Hard X-ray Properties of Relativistically Beamed Jets from Radio- and Gamma-Ray-Bright Blazars

Dissertation zur Erlangung des naturwissenschaftlichen
Doktorgrades der Julius-Maximilians-Universität Würzburg

vorgelegt von

Marcus Langejahn

aus Wernigerode

Würzburg 2021

Eingereicht am: 29.10.2021
bei der Fakultät für Physik und Astronomie

1. Gutachter: Prof. Dr. Matthias Kadler
2. Gutachter: Prof. Dr. Jörn Wilms
der Dissertation

Vorsitzende: Prof. Dr. Adriana Pálffy-Buß

1. Prüfer: Prof. Dr. Matthias Kadler
2. Prüfer: Prof. Dr. Jörn Wilms
3. Prüfer: Prof. Dr. Bert Hecht
im Promotionkolloquium

Tag des Promotionskolloquiums: 20.05.2022
Doktorurkunde ausgehändigt am: . . . .

Abstract

From all known galaxy types, active galaxies are easily the most remarkable in areas such as variability or pure energy output. Their central region, the active galactic nuclei, can often be brighter than their host galaxy. The most distinguishing factor, however, is their prominent emission that can reach throughout the entire electromagnetic spectrum, from radio waves up to highly energetic gamma-rays and sometimes even TeV energies. AGN are testing grounds for physics in extreme environments, including the interaction of magnetic fields with particles and their acceleration on large scales, the re-processing of the emitted radiation via multiple components of the central engine of the AGN, and the production of cosmic neutrinos. The most extreme type of AGN from the observational standpoint are blazars, a type that features highly beamed emission from a jet directly pointed at the observer, very high luminosity, rapid variability, and a pronounced X-ray and gamma-ray component. The distinction of AGN from other source types becomes easier at very low and very high energies, where the (thermal) emission of non-active galaxies is much lower than at optical wavelengths. Great numbers of AGN have been found in the past, with millions in the optical and X-ray range. However, source detections in surveys are always subject to selection biases, such as source variability, the flux limitation of the survey, misidentification, or the wavelength-dependent brightness, especially between different AGN / blazar types. In the hard X-ray band ($\gtrsim 10\,\mathrm{keV}$), by contrast, only a few hundred AGN have been cataloged, with a small fraction being blazars, which in contrast to this constitute a dominant part of the extragalactic sky at gamma-rays.

In this thesis, I perform dedicated analyses of the hard X-ray characteristics of pre-defined samples of beamed AGN using the 105-month all-sky survey maps from the Burst Alert Telescope (BAT) on board of the satellite observatory *Swift*, encompassing archival spectral data from 2004 to 2013. I employ the radio-selected AGN samples of the MOJAVE and TANAMI programs, which observe the radio-brightest sources on the Northern and Southern hemispheres, respectively. Also, I use the sizable and most recent gamma-ray-selected *Fermi*/LAT 4LAC catalog, that covers AGN detected at GeV energies over the entire sky. Comparing the results of these radio- and gamma-ray-selected samples as well as the listed sources of recent hard X-ray source catalogs (*Swift*/BAT, *INTEGRAL*) allows for the assessment of selection biases, including the influence of different AGN / blazar sub-types. Besides compiling a set of spectral characteristics, one central question that I want to address is why the detection statistic of beamed AGN in this frequency band is so comparatively low. Is this fact due to sensitivity issues of the observing instruments, or the intrinsic faint nature or evolution of this source class at hard X-rays? If there is a hidden blazar population at low flux limits, could it potentially contribute significantly to the cosmic X-ray background? In comparing the hard X-ray parameters of the relevant AGN sub-types (FSRQs, BL Lacs, and radio galaxies), I aim to make restrictions regarding the true source class of yet unclassified sample entries, which are especially numerous in the 4LAC catalog.

From the archival BAT survey maps, the spectra in the $20\,\mathrm{keV} - 100\,\mathrm{keV}$ band as well as the total S/N values in the extended $14\,\mathrm{keV} - 150\,\mathrm{keV}$ range are read out at the coordinates of the pre-defined sample sources. All spectra with sufficient counts are fitted with a simple power law, while the flux of fainter sources is estimated based on template spectra. I implement and utilize the dedicated PGSTAT fit statistic for background-dominated spectra with low count rates. In order to determine the distribution of the sample sources in space and to derive biases through sample selection and the evolution of the emission, I calculate the respective $\log N$-$\log S$ distributions. Furthermore, I derive luminosity functions to determine whether the evolutionary path of the emission is different for the X-ray band and the original wavelength at which the samples were defined. Because of the substantial uncertainties of the calculated spectral characteristics, such as the flux, the comparison of the parameter distributions makes use of Monte Carlo methods.

In the first part of this work I present the detailed analysis of the hard X-ray characteristics of the radio-selected MOJAVE and TANAMI samples and show that a great majority of the sources, albeit not listed in the recent hard X-ray catalogs, are significantly detected, just below the conservative catalog signal thresholds of about $5\,\sigma$. Around 90% of all 135 MOJAVE-1 sources are not compatible with random background noise, and still 80% of the TANAMI sample, which counts 126 sources. All blazar sub-types and the radio galaxies show characteristic ranges of X-ray flux, luminosity, and photon index, where in the case of many of the individual sources these properties are correlated with the corresponding SED's shape / peak frequency. Also, the BAT photon indices of gamma-ray-faint MOJAVE sources suggest that the high-energy SED bump peaks at lower frequencies than for gamma-ray-bright sources, explaining the non-detections by *Fermi*/LAT. The relatively flat $\log N$-$\log S$ distributions of the blazars in the radio-selected samples expresses a scarcity of blazars that are in the middle and lower X-ray flux range of the samples. This fact can be interpreted as being due to the differing evolutionary paths between radio and X-ray emission. Variability of the X-ray band can be excluded as a leading factor regarding the flat slope of the distribution. Furthermore, the X-ray output of these radio-selected blazars only constitutes a small fraction to the CXB, about 0.2% to 0.3%. The less uniformly composed TANAMI sample, which includes many gamma-ray-bright and TeV sources, shows similar characteristics as the MOJAVE-1 and MOJAVE-1.5 samples, but is somewhat less X-ray-bright on average. The larger MOJAVE-1.5 sample (181 sources) and the radio-loud TANAMI sub-sample together form a robust radio-selected set of highly beamed AGN, which could serve as a solid basis for future sample studies of this object type in the hard X-rays over the entire sky.

The second part of this work centers around the hard X-ray analysis of the 4LAC sample, counting 3207 sources. In comparison to the radio samples, the 4LAC sources are on average significantly less bright in the BAT band, with the vast majority notably below a signal strength of $5\,\sigma$, and with only $35\,\% - 41\,\%$ of the sample being not compatible with background noise. Although the fitted 459 X-ray-bright sources show similar luminosity ranges than the radio samples, the spectral shapes / photon indices differ notably, especially for the BL Lacs that are distributed around $\Gamma = 2.5$, indicating high-peaked SED types. In general, the sample features a variety of spectral shapes in the X-rays, corresponding to a range of SED peak frequencies. The high fraction of 4LAC sources with the spectral gap region between the big SED emission bumps coinciding with the BAT band explains why a sizable amount of the sample is X-ray-faint. In any case, the characterization of the sources of all analyzed samples makes it possible to ascertain the likely true AGN type of a number of yet unclassified sources, especially in the 4LAC sample. Here, using the parameter space of X-ray and gamma-ray photon indices, 35 blazar candidate sources can be assigned either the FSRQ or BL Lac type with high certainty. This methodology will allow the classification of many more candidate sources in the future. I present a list of 46 blazar candidates from the 4LAC catalog that are the most likely to benefit from additional X-ray observations in this regard, together with more FSRQs and BL Lacs that would help further narrow down the corresponding photon index distributions.

The hard X-ray band, as observed by the coded mask instrument BAT, although technically challenging for weaker sources, has proven to be a viable tool for studying and classifying the high-energy part of blazar SEDs. In this thesis I show that the reason why many blazars are weak in this energy band can be traced back to a number of factors: the selection bias of the initial sample, differential evolution of the X-rays and the wavelengths in which the sample is defined, and the limited sensitivity of the observing instruments. The study of the hard X-ray range provides an important asset for the characterization of the high-energy bump of SEDs, which will help to define interesting sets of targets for dedicated observations at GeV and TeV energies, with instruments like the CTA.

Zusammenfassung

Von allen bekannten Galaxienarten sind Aktive Galaxien mit Abstand die bemerkenswertesten in Bereichen wie der Variabilität oder der abgestrahlten Energie. Deren Zentralregionen, die aktiven Galaxienkerne (engl. active galactic nuclei, AGN) können dabei oft heller sein als ihre Heimatgalaxie. Das wichtigste Unterscheidungsmerkmal gegenüber nichtaktiven Galaxien ist aber ihre auffällige Emission über das gesamte elektromagnetische Spektrum, von Radiowellen bis in den Hochenergiebereich der Gammastrahlen, die in manchen Fällen sogar zu TeV-Energien reicht. AGN sind Testgebiete für die Physik extremer Bedingungen, wie etwa die Interaktion von Magnetfeldern mit Teilchen und deren Beschleunigung auf großen Skalen, die Wechselwirkung emittierter Strahlung mit mehreren Komponenten im Zentrum der AGN und die Produktion kosmischer Neutrinos. Der extremste Typ der AGN aus Beobachtungssicht sind die Blazare, welche sich durch stark gebeamte Emission der Jets auszeichnen, welche direkt auf den Beobachter gerichtet sind, sowie sehr hohe Leuchtkraft, schnelle Variabilität und eine ausgeprägte spektrale Komponente im Röntgen- und Gammastrahlenbereich. Die Unterscheidung der AGN von anderen Quelltypen wird bei sehr hohen und sehr niedrigen Energien deutlicher, wo die (nicht-thermische) Emission von normalen Galaxien sehr viel geringer im Vergleich zu optischen Wellenlängen ist. In der Vergangenheit wurden eine sehr große Anzahl von AGN gefunden, mit Millionen Objekten im optischen und Röntgen-Bereich. Die Detektion in AGN und Himmelsdurchmusterungen ist jedoch von Auswahleffekten betroffen, wie etwa Quellvariabilität, die Helligkeitlimitierung der Durchmusterung, mögliche Fehlidentifikationen, oder die wellenlängenabhängige Helligkeit der Quellen, besonders zwischen AGN- und Blazar-Unterklassen. Im harten Röntgenband ($\gtrsim 10\,\mathrm{keV}$) wurden im Gegensatz dazu nur einige hundert AGN katalogisiert, mit nur einem kleinen Anteil an Blazaren, wobei diese Quellklasse dann wiederum im Gammastrahlenbereich einen Großteil der extragalaktischen Quellen darstellt.

Unter Verwendung von Archivdaten der 105-month Survey-Maps (2004 bis 2013) des Burst Alert Telescope (BAT) an Bord des Satellitenobservatoriums *Swift* führe ich in dieser Arbeit eine detaillierte Analyse der Charakteristiken im harten Röntgenband von vordefinierten Listen (Samples) gebeamter AGN durch. Dabei verwende ich die radio-selektierten AGN der MOJAVE und TANAMI Programme, welche jeweils die nördliche und südliche Hemisphäre abdecken. Ebenfalls nutze ich die noch größere Quellliste des neusten gammastrahlen-selektierten *Fermi*/LAT AGN Katalogs, dem 4LAC, welcher Quellen über den ganzen Himmel erfasst, die im GeV-Bereich detektiert wurden. Der Vergleich der Ergebnisse der radio- und gammastrahlen-selektierten Samples sowie und die Einbeziehung der neusten Quellkataloge aus dem harten Röntgenband (*Swift*/BAT, *INTEGRAL*) erlaubt es, Auswahleffekte einzugrenzen, wie auch den Einfluss verschiedener AGN- und Blazar-Quellklassen. Neben der Zusammenstellung der spektralen Charakteristik der genannten Samples will ich in einer weiteren zentralen Fragestellung betrachten, warum die Statistik der entdeckten gebeamten AGN im harten Röntgenbereich so vergleichsweise gering ist. Ist die limitierte Empfindlichkeit der Beobachtungsinstrumente ein wichtiger Faktor, oder die intrinsisch geringe Emission der Quellen im Bereich harter Röntgenstrahlen? Wenn es eine verborgene Blazarpopulation gibt, welche eher bei geringen Röntgenflüssen strahlt, kann diese in signifikantem Maße zur kosmischen Röntgenhintergrundstrahlung beitragen? Durch den Vergleich der spektralen Parameter der relevanten AGN-Unterklassen (FSRQs, BL Lacs, Radiogalaxien) will ich weiterhin die wahre Quellklasse von noch unklassifizierten AGN eingrenzen, welche

besonders zahlreich im 4LAC-Katalog sind.

Aus den Archivdaten der BAT Survey-Maps werden die Spektralinformationen im Bereich von 20 keV – 100 keV an den Koordinaten der Quellen ausgelesen und das Signal-zu-Rausch-Verhältnis S/N im erweiterten Band von 14 keV – 150 keV bestimmt. Alle Spektren mit genügend hoher Anzahl an Photonen werden per einfachem Potenzgesetz gefittet. Der Fluss aller anderen Quellen wird anhand der spektralen Form der hellen Quellen abgeschätzt. Für diesen Prozess implementiere ich die für geringe Zählraten und hintergrunddominierte Spektren vorgesehene Fit-Statistik PGSTAT. Um die Verteilung der Quellen im Raum zu bestimmen und Auswahleffekte durch die Definition der Quell-Samples abzuleiten, errechne ich die entsprechenden $\log N$-$\log S$-Verteilungen. Ebenfalls bestimme ich die Leuchtkraftfunktionen um einzugrenzen ob die Entwicklung der Röntgenemission sich vom Wellenlängenbereich unterscheidet in welcher die Quell-Samples zusammengestellt worden sind. Aufgrund der deutlichen Unsicherheiten der sich ergebenden spektralen Parameter, wie etwa dem Fluss, werden beim Vergleich der Parameterverteilungen Monte-Carlo-Methoden mit einbezogen.

Im ersten Teil dieser Arbeit präsentiere ich die detaillierte Analyse der Charakteristik der harten Röntgenemission der radio-selektierten MOJAVE- und TANAMI-Samples und zeige, dass der überwiegende Großteil der Quellen als detektiert beschrieben werden kann. Die meisten Quellen zeichnen sich durch S/N-Werte knapp unter $5\,\sigma$ aus, sodass diese nicht in den neusten Katalogen harter Röntenquellen gelistet worden sind. Etwa 90% der 135 MOJAVE-1-Quellen sind nicht mit zufälligem Hintergrundrauschen vereinbar, sowie immer noch 80% der 126 TANAMI-Quellen. Alle Blazar-Unterklassen und Radiogalaxien zeigen charakteristische Bereiche des Röntgenflusses, der Leuchtkraft und des Photon-Indexes. Bei vielen Quellen sind diese Eigenschaften mit der Form der SED / der Frequenz des spektralen Maximums korreliert. Die BAT Photon-Indices von gammastrahlen-schwachen MOJAVE-Quellen deuten auf ein Maximum der Hochenergiekomponente der entsprechenden SEDs bei relativ geringen Frequenzen hin, was die fehlenden Detektionen von *Fermi*/LAT in diesem Sample erklärt. Die vergleichsweise flache $\log N$-$\log S$-Verteilung der radio-selektierten Samples deutet auf einen Mangel an schwachen bis mäßig hellen (Röntgen-)Quellen hin. Dieser Umstand kann als eine unterschiedliche Entwicklung der Röntgen- und Radioemission interpretiert werden. Hingegen kann Variabilität als ein signifikanter Einfluss auf die Steigung der $\log N$-$\log S$-Verteilung im Röntgenbereich ausgeschlossen werden. Die Abstrahlung der radio-selektierten Blazare stellt nur einen kleinen Anteil des Röntgenhintergrundes dar, etwa 0.2% bis 0.3%. Das TANAMI-Sample, welches weniger strengen Auswahlkriterien unterliegt, und welches viele gammastrahlen-helle und TeV-Quellen beinhaltet, zeigt ähnliche Eigenschaften wie die MOJAVE-1- und MOJAVE-1.5-Samples, ist aber generell etwas weniger Röntgen-hell. Das erweiterte MOJAVE-1.5-Sample mit 181 Quellen und das radio-laute TANAMI-Unter-Sample bilden zusammen ein robustes radio-selektiertes Sample von stark gebeamten AGN, welches als Basis für zukünftige Studien dieses Quelltyps im harten Röntgenbereich dienen kann.

Der zweite Teil dieser Arbeit befasst sich mit der Röntgenanalyse des 4LAC-Samples, welches 3207 Quellen enthält. Verglichen mit den Radio-Samples sind die 4LAC-Quellen deutlich weniger hell im BAT-Band, wobei der weitaus größte Teil des Samples einen S/N-Wert deutlich unterhalb von $5\,\sigma$ aufweist. Nur etwa 35% – 41% des Samples ist nicht mit Hintergrundrauschen vereinbar. Die 459 Röntgen-hellen Quellen im Sample zeigen zwar eine ähnliche Charakteristik der Leuchtkräfte wie die Radio-Samples, unterscheiden sich aber deutlich in den Formen der Spektren / Photon-Indices, besonders bei BL Lacs, deren Indices um $\Gamma = 2.5$ verteilt sind, was auf SEDs mit hochfrequenten Maxima deutet. Generell zeichnet sich das Sample durch eine breite Verteilung der Photon-Indices und entsprechenden SED-Maxima aus. Dabei befindet sich bei einem hohen Anteil des 4LAC-Samples der Lückenbereich der SED zwischen den beiden großen spektralen Maxima nahe der Position des BAT-Bandes, was die geringe Detektionsstatistik dieser Quellen im harten Röntgenbereich erklärt. Die Analyse der Röntgeneigenschaften der helleren Quellen erlauben es jedoch die wahrscheinliche Quellklasse vieler noch unklassifizierter heller Röntgenquellen im Sample festzulegen. Der Parameterraum der Photon-Indices aus den BAT- und LAT-Datensätzen erlaubt somit die Einteilung von 35 Blazar-Kandidatenquellen in FSRQs und BL Lacs mit hoher Sicherheit. Diese Methodik wird in Zukunft die Klassifizierung von noch mehr Kandidatenquellen ermöglichen. Ich liste 46 Blazar-Kandidatenquellen, welche am meisten von gezielten Röntgenbeobachtungen in diesem Zusammenhang profitieren würden, zusammen mit einer Anzahl von FSRQs und BL Lacs aus dem Sample, die für der Eingrenzung der jeweiligen Photon-Index-Verteilungen wichtig sind.

Obwohl technisch anspruchsvoll für schwächere Quellen, hat sich der Bereich harter Röntgenstrahlung, welcher vom Coded-Mask-Detektor BAT abgetastet wird, als praktisches Instrument für die Charakterisierung und Klassifizierung der Hochenergiekomponente von Blazar-SEDs erwiesen. In dieser Arbeit zeige ich, dass der Grund warum viele Blazare im harten Röntgenband so schwach sind, einer Reihe von Faktoren entstammt: dem Auswahleffekt des initialen Quellsamples, der sich unterscheidenden Entwicklung im Röntgenbereich und der Wellenlänge der ursprünglichen Sample-Definition, sowie der limitierten Empfindlichkeit der Beobachtungsinstrumente. Die Studie dieses Energiebereichs liefert ein wichtigen Beitrag für die Charakterisierung der Hochenergiekomponente der SEDs, und wird dabei helfen, interessante neue Ziele für die dedizierte Beobachtung im GeV- und TeV-Bereich zu definieren, mit neuen Instrumenten wie dem CTA.

Contents

1. The turbulent and color-rich sky

The most extreme environments that we know of are found in astrophysics. The intense gravitational fields of black holes, very high-energy particles, whose interactions can be detected millions of light years away, intense magnetic fields of neutron stars or truly exotic states of matter cannot be probed in the traditional laboratory. This provides unique opportunities regarding high-energy research, albeit with the restriction that the objects of interest cannot be manipulated, but only observed.

For the longest time only observations in the optical regime ($\lambda \approx 400\,\mathrm{nm} - 700\,\mathrm{nm}$) were possible. This domain corresponds to the maximum of ordinary black-body emission of hot gases of a few thousand K, the temperature of the light-emitting outer layers of stars. With the second half of the 20th century a multitude of new astronomical instruments like radio antennas and balloon experiments with X-ray detectors revealed that the sky is populated by a vast array of different astronomical objects, which emit light in characteristic parts of the extremely broad electromagnetic spectrum. Figure 1.0.1 shows a composite of different all-sky images from the radio, optical, X-ray, and gamma-ray bands in Galactic coordinates. Apart from the narrow horizontal band of the Milky Way, light emission from single objects as well as diffuse regions that are distinct for a specific energy range can be recognized. Besides dedicated observations in only one regime of the spectrum, many fields of research benefit from multiwavelength studies, providing new insights and a more complete understanding of the subject matter. This is especially significant for objects and phenomena that are characterized by a very broad spectrum, such as active galactic nuclei (AGN).

Ground observatories are able to detect optical, adjacent parts of ultra-violet (UV), near infra-red (NIR), radio, millimeter, and sub-millimeter light, as Earth's atmosphere is largely transparent in these bands. While the thermal light emission in the optical and NIR and near UV parts of the spectrum is mainly due to stars, either directly or by scattering on gas and dust, other energy bands are associated with increasingly extreme and exotic sources. In the IR colder objects like brown dwarfs or red giants are prevalent, as are sources with a high cosmological redshift. At longer wavelengths, namely mm and sub-mm, molecular lines from rotational transitions can be observed, as well as the cosmic microwave background (CMB) radiation and the higher-energy end of processes in the radio regime. One of the main subjects of radio astronomy, with its broad band of wavelengths from millimeters to several meters, is the study of regions of relativistic electrons in magnetic fields, indicating synchrotron radiation from very hot relativistic plasmas of giant radio galaxies and AGN, as well as supernova remnants (SNR) and radio pulsars. On the opposite side of the electromagnetic spectrum, the UV and X-ray bands are characterized by high-temperature objects, for example white dwarfs, SNRs, accreting X-ray binaries, or the hot gas in galaxy clusters. Also, non-thermal processes are starting to dominate at higher energies. Synchrotron radiation and Compton up-scattered emission via, for example, relativistic electrons in the inner regions of AGN are especially characteristic for this part of the spectrum. Above a couple of hundred keV, in the wide gamma-ray band, Compton up-scattering and the decay of neutral

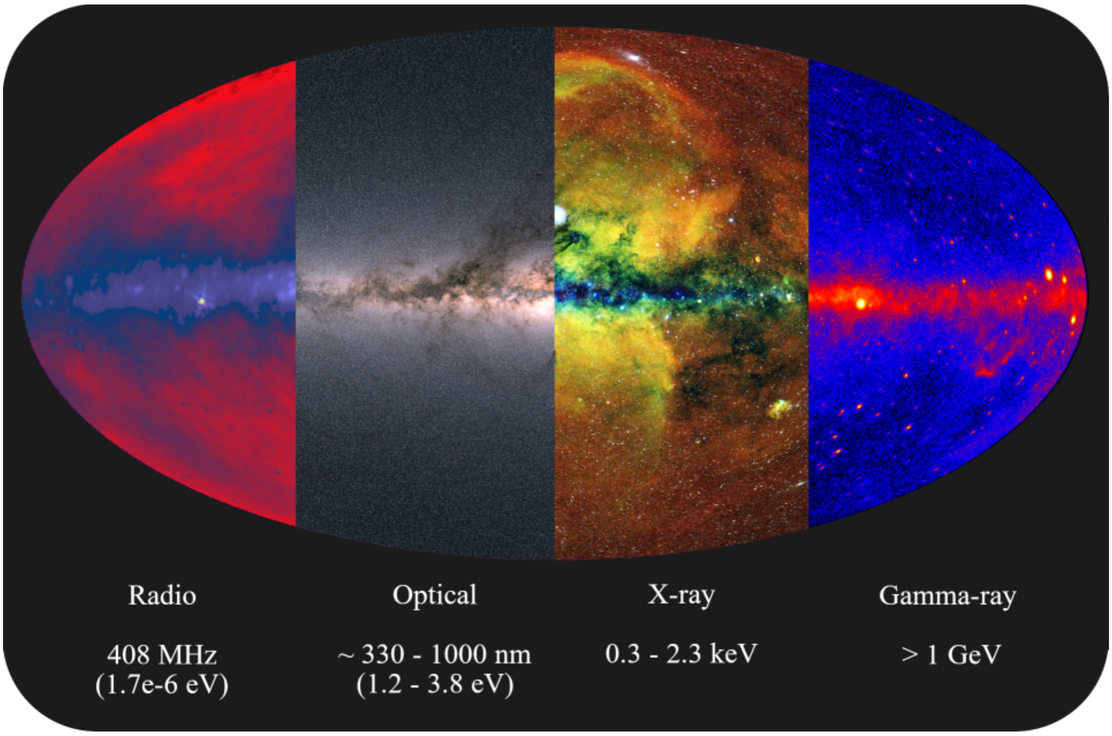

Figure 1.0.1.: Hammer-Aitoff projection of the sky in Galactic coordinates in different wavelengths. From left to right, with image credits: Radio (Max Planck Institute for Radio Astronomy, generated by Glyn Haslam), optical (ESA/Gaia/DPAC), X-ray (Jeremy Sanders, Hermann Brunner and the eSASS team (MPE); Eugene Churazov, Marat Gilfanov (on behalf of IKI)), and gamma-ray (NASA/DOE/Fermi LAT Collaboration). The labels of the energy range correspond to the shown sky image, but do not indicate strict definitions of the different bands.

pions are the prevalent emission mechanisms. At high Galactic latitudes, beamed AGN jets and gamma-ray bursts (GRB) are the most common phenomena to be detected. Besides the observation of the extremely broad electromagnetic spectrum, other windows for astrophysical observation have emerged in the past, specifically the measurement of energetic neutrino signals (e.g., Mannheim, 1995; Bradascio, 2019) and gravitational waves (e.g., Accadia et al., 2012; Abbott et al., 2016).

Beamed AGN are still an enigmatic class of objects, whose multiwavelength properties are subject to large observation campaigns. Especially their characteristics in the high-energy domain, starting at X-rays, is still not well understood. This work focuses on the properties of beamed AGN in the hard X-ray band of 20 keV to 100 keV, a part of the spectrum that is notoriously difficult to study because of technical challenges and relatively low emission of beamed AGN in this band. In this first chapter, in Sect. 1.1, astrophysical emission processes are introduced that are relevant specifically in high-energy observations of active galactic nuclei, before discussing the different types and the unification model of AGN in Sect. 1.2, as well as the field of all-sky surveys in the context of AGN in Sect. 1.3. A short outline of this thesis is given in Sect. 1.4. This introductory chapter including various definitions and most of the illustrative calculations are based on the text books of Longair (2011), Seward & Charles (2010), Carroll & Ostlie (2007), and Krolik (1999).

1.1 High-energy emission and absorption processes

The many different environmental conditions in astrophysical phenomena, for example, the chemical composition, pressure, density, temperature, and magnetic field strength, harbor many different processes / interactions of matter and light, which emerge in specific parts of the electromagnetic spectrum. This allows conclusions to be drawn about the nature of the emission processes and the classification of the object in an astronomical context. In this overview, the basic interactions are described, which are specifically relevant to the high-energy / X-ray domain. However, processes that are prevalent in other frequency regimes like synchrotron radiation in the ratio band, are also discussed, because of their significant influence on the X-ray and gamma-ray domain through related radiation mechanisms, like, in this case, inverse Compton scattering.

Photoelectric absorption

A beam of light, here specifically X-rays, loses intensity when it passes though a medium of the thickness x. Its intensity behaves like $\sim e^{-\sigma x}$, with the absorption coefficient σ, which is equivalent to the cross-section of the interaction. The thickness or length x of the material or gas in astronomy is named n_{H}, given as the number of (hydrogen) atoms in a column per cm^2. The interactions of X-rays in the soft band ($0.1\,\mathrm{keV}$ – $10\,\mathrm{keV}$, $h\nu \ll m_{\mathrm{e}}c^2$) with the interstellar medium is dominated by the photoelectric effect, where an atom absorbs a photon and loses an electron, that has the energy of the initial photon subtracted by the electron's binding energy. The light transmission increases for higher energies, but shows sharp edges that correspond to the binding energy of the K and L shells of the specific element.

At even higher energies, Compton scattering becomes more important: at 10 keV, only about 4% of the energy of a Compton-scattered photon can be transferred to an electron, whereas a 100 keV photon can transfer up to 28% of its energy. Above 1.02 MeV, twice the rest mass of an electron, all of the photon energy can be used by electron-positron pair production. Not only play these absorption and scattering processes an important role in astrophysical environments, but also in the physical detectors in telescopes. Thus, depending on the energy range of the detector, different absorption mechanisms need to be taken into account for the detector to register a signal and work effectively (see Sect. 2.2.3).

The photoelectric cross-section is determined by deriving the absorption coefficients and cosmic abundances for all relevant elements i and performing a weighted summation:

$$\sigma_{\mathrm{ph}}(\nu) = \frac{1}{n_{\mathrm{H}}} \sum_{\mathrm{i}} n_{\mathrm{i}} \sigma_{\mathrm{i}}(\nu). \tag{1.1.1}$$

For low energies ($h\nu \ll m_{\mathrm{e}}c^2$) and for the electron ejecting from the K shell each individual cross-section is:

$$\sigma_{\mathrm{K}} \sim Z^5 \nu^{-7/2}, \tag{1.1.2}$$

which is also proportional to the cross-section for Thomson scattering σ_{T}[1]. The interaction via the photoelectric effect has a very strong dependency of the atomic number, making an absorption by heavier elements much more effective. In any case, the removal of a 1s electron represents the dominant source opacity in this process.

---

[1] The cross-section for Thomson scattering with an electron is $\sigma_{\mathrm{T}} = e^4/(6\pi\epsilon_0^2 m_{\mathrm{e}}^2 c^4)$.

Spectra of interstellar sources often show a turnover at lower X-ray energies, because the optical depth

$$\tau_\mathrm{e}(\nu) = \int \sigma_\mathrm{e} N_\mathrm{H} dx \tag{1.1.3}$$

is very low in relative terms. Here, the parameter N_H identifies the number of atoms per volume, not the column density. For example, a gas density for interstellar hydrogen of $10^6\,\mathrm{m}^{-3}$ restricts the optical depth of X-rays at 1 keV to only 1 kpc. Consequently, photons of higher energies are only significantly scattered for large densities. The hard X-ray range is therefore well-suited for studies of comparatively dense regions, like the central engines of AGN or X-ray surveys even in the Galactic plane (e.g., Krivonos et al., 2012; Hong et al., 2016; Oh et al., 2018).

Black-body radiation

Objects or gases that are in thermal equilibrium, which do not reflect and just absorb and re-emit electromagnetic radiation, are called black-bodies. Their emitted continuous spectrum depends only on the temperature, while the spectrum's maximum is described by Wien's Law:

$$\lambda_\mathrm{max} T = 0.002898\,\mathrm{m\,K}. \tag{1.1.4}$$

With an effective temperature of the Sun's surface of $\approx 5800\,\mathrm{K}$ its spectrum peaks at the visible wavelength of $\approx 500\,\mathrm{nm}$, whereas the spectrum of a white dwarf ($T \approx 10^5\,\mathrm{K}$) peaks at 29 nm, in the extreme UV. The idea of quantization of energy led to the expression of Planck's Law, describing the emissive power per area, solid angle, and wavelength interval:

$$B_\lambda(T) = \frac{2hc^2/\lambda^5}{\exp\left[\frac{hc}{\lambda k T}\right] - 1} \quad \left[\mathrm{W\,m^{-2}\,nm^{-1}\,sr^{-1}}\right] \tag{1.1.5}$$

with the Boltzmann constant k and the Planck constant h. An astrophysical object or region that emits light in this regard is therefore characterized by a specific temperature, and ratio of the emitted power at different wavelengths, the spectrum, or the perceived color in the case of stars. Many complex astrophysical objects, however, are not necessarily in thermodynamic equilibrium, and only locally, like in the case of large-scale gas and dust clouds or highly dynamic accretion discs. Extreme environments such as supernova remnants (SNR) or the accretion discs of X-ray binaries even produce a notable part of their black-body radiation in the gamma-ray band.

Line emission and absorption

Studied and formalized in the 19th century by Kirchhoff, Bohr, Balmer, and Planck, line emission and absorption could be attributed to the quantized energy levels of electrons bound to the atomic nucleus. Transitions between the energy levels release or capture energy in form of a photon in case of an emitted line or an absorption line, respectively. Since the transition energies are unique to each element, a detailed spectral analysis allows conclusion to be drawn about the source's chemical composition and even structure, such as a colder absorbing gas layer in front of a hot emitting gas.

Spectral lines undergo different processes that create a finite width in the spectrum. The quantum-mechanical uncertainty principle broadens every line because of blurred energy levels, while the non-zero thermal energy of a system creates statistically distributed Doppler shifts, exacerbating the effect. In astrophysical systems with contributions of large velocity components in reference to the observer, like in accretion discs, the rotational velocity and the black hole mass can be determined using, for example, the FeKα emission line (e.g., Fabian et al., 2000; Reynolds & Fabian, 2008).

Bremsstrahlung

Also referred to as free-free emission, bremsstrahlung describes the scattering of a free election with an ion though the acceleration in the ion's Coulomb field, leading to the emission of a photon. An electron population that is in thermal equilibrium creates a characteristic spectrum when scattering, which only depends on the temperature and is appropriately named thermal bremsstrahlung. The emitted power per unit volume, or emissivity, is:

$$e_{\mathrm{ff}} \sim Z^2 n_{\mathrm{e}} n_{\mathrm{i}} \, (kT)^{-1/2} \exp\left[\frac{h\nu}{kT}\right] g_{\mathrm{ff}}(T,\nu), \tag{1.1.6}$$

with the ion charge Z, the number density of electrons n_{e} and ions n_{i}. The Gaunt factor g_{ff} is of the order of 1 and only changes slowly with energy.

The emissivity falls off exponentially towards higher energies. The hotter the gas, however, the farther does the function of emissivity extend along the energy axis. A hot gas, which consists of heavy elements, is not completely ionized even at temperatures of millions of K. Thus, election-ion scattering transfers energy to the ions, that are exited, producing emission lines when returning to their previous states, and thus mixing the continuous free-free spectrum with emission lines of specific transitions. The presence of particular spectral lines and the shape of the continuum allow calculating the observed source's temperature. Also, the chemical composition can be derived from the strength of the measured lines.

For the non-relativistic case, the electron-ion/proton interaction dominates over electron-electron and ion-ion collisions because of the significant electric dipole. Other moments like the electric quadrupole, however, gain importance for relativistic velocities of the electrons, that is, when kT is comparable to $m_{\mathrm{e}}c^2$. Thus, contributions from these processes have to be added to the expression for the emission. At radio wavelengths bremsstrahlung traces ionized winds and HII regions, while X-ray observations of galaxy clusters reveal a hot intracluster medium with $T \approx 10^7\,\mathrm{K} - 10^8\,\mathrm{K}$ (e.g., Lea et al., 1973; Cavaliere & Lapi, 2013), where bremsstrahlung acts as a significant cooling mechanism.

Compton / inverse Compton effect

Compton scattering describes the interaction of a free charged particle and a photon whereby energy is transferred from the photon to the particle. In the following, the most relevant case of an electron is addressed. Should the energy of the photon be much less than the electron rest mass, that is, $h\nu \ll m_{\mathrm{e}}c^2$, the interaction can be approximated by Thomson scattering (cross section σ_{T}), where no energy is transferred. For relativistic cases (Lorentz factor[2] $\gamma \gg 1$) the relevant cross section for Compton scattering is expressed by the Klein-Nishima cross section, which falls like $(h\nu)^{-1}$ for higher energies. Scattering of photons with atomic nuclei (mass m_{N}) can often be neglected compared to the electron case because the process is in the order of $(m_{\mathrm{e}}/m_{\mathrm{N}})^2$ less effective.

---

[2] The Lorentz factor is defined as $\gamma = (1 - v^2/c^2)^{-1/2}$.

Inverse Compton (IC) scattering is the process where highly energetic electrons of often relativistic velocities interact with lower-energy photons, which are up-scattered to higher frequencies. For $\gamma h\nu \ll m_\mathrm{e}c^2$ the loss rate of energy is given by:

$$\frac{\mathrm{d}E}{\mathrm{d}t} = \frac{4}{3}\sigma_\mathrm{T} c u_\mathrm{rad}\gamma^2 \left(\frac{v}{c}\right)^2, \tag{1.1.7}$$

with the electron's velocity v and the radiation energy density u_rad. The produced photon spectrum is proportional to the energy for lower frequencies. The spectral emissivity is $I(\nu) \sim \nu$. It features a sharp turnover and then rapidly declines, with a maximum photon energy of $h\nu_\mathrm{max} = 4\gamma^2 h\nu_0$ for a radiation field of monochromatic frequency ν_0.

Astrophysical environments involving relativistic electrons with very high Lorentz factors up-scatter photons of nearby sources or even the CMB significantly. Bulk Lorentz factors of ultra-relativistic jets in blazars (see Sect. 1.2) have been measured to be in the typical range of 10 to 30 and up to approximately 50 (see, e.g., Lister et al., 2009b), while Lorentz factors up to 1000 have been found in studies of gamma-ray bursts (GRBs, e.g., Piran, 2005; Liang et al., 2010). In the extreme case of $\gamma = 1000$, seed photons of the CMB ($\nu_0 \approx 2 \cdot 10^{11}\,\mathrm{Hz}$) can be re-processed into an output IC spectrum which reaches X-rays ($\nu \approx 3\,\mathrm{keV}$), whereas an optical seed-photon population ($\nu_0 \approx 500\,\mathrm{nm}$) can also be scattered into the same band for typical blazar Lorentz factors. IC scattering is a significant process that cools relativistic electron populations. In the context of active galactic nuclei IC scattering becomes especially important in powerful jets with high u_rad and consequently high energy loss rates (see Sect. 1.2.2).

Synchrotron radiation

Covering the radio domain up to X-rays, synchrotron radiation is one of the most prevalent emission mechanisms that can be observed in astronomy. The acceleration of charged particles, usually high-energy electrons, by a magnetic field perpendicular to their velocity vectors, creates a continuous non-thermal spectrum. The relativistic electrons move in a spiral around the magnetic field lines with the pitch angle α. In reality, the distribution of pitch angles is randomized and assumed to be isotropic due to streaming instabilities and the magnetic field, which has an irregular distribution. For an averaged pitch angle the resulting energy loss rate can be determined to:

$$\frac{\mathrm{d}E}{\mathrm{d}t} = \frac{4}{3}\sigma_\mathrm{T} c u_\mathrm{mag}\gamma^2 \left(\frac{v}{c}\right)^2, \tag{1.1.8}$$

with the magnetic field density u_mag.

The emission of a relativistic electron is beamed in the direction of its motion, corresponding to a greatly elongated beam pattern in the observer's frame. The frequency with which the emission cone hits the observer during the gyration of the electron determines the frequency ν of the emitted synchrotron radiation. The frequency at which most of the radiation is emitted is approximately:

$$\nu_\mathrm{c} \approx \gamma^2 \nu_\mathrm{g}, \tag{1.1.9}$$

with the non-relativistic gyrofrequency:

$$\nu_\mathrm{g} = \frac{eB}{2\pi m_\mathrm{e}}, \tag{1.1.10}$$

and the magnetic field strength B. The synchrotron spectrum is sharply peaked around ν_c. In order to generate a radio signal at 10 GHz from a magnetic field of $B = 10^{-4}\,\mathrm{G}$, highly relativistic electrons ($\gamma \approx 10^5$) are required. Since electrons are characterized by a power-law energy distribution, the resulting synchrotron emissivity using Eq. 1.1.8 is:

$$e_\mathrm{sy} \sim B^{(p+1)/2} \nu^{-(p-1)/2}, \tag{1.1.11}$$

with the spectral index of the electron energy spectrum p. The superposition of all electron power-law spectra again leads to a power law for the emissivity.

The synchrotron radiation of a source is self-absorbed at lower frequencies where the optical depth is $\tau \gtrsim 1$. In this case the radiation of the relativistic electron is re-absorbed, significantly altering the synchrotron spectrum, and producing a steeply rising power law with a flux of $S_\nu \sim \nu^{2.5}$ for $\nu \to 0$ and a turnover before following the standard power-law index at higher frequencies (Eq. 1.1.11). Highly energetic sources of synchrotron radiation in astrophysics include supernova remnants, such as Cassiopeia A or the Crab pulsar, which emits over most of the observable spectrum, and extragalactic radio sources like AGN and massive jet structures and radio lobes, for example Cygnus A. The process of synchrotron emission can also be accompanied by IC scattering of the emitted photons with the same relativistic electron population. This is known as synchrotron self-Compton (SSC) scattering, and it is able to create extraordinarily energetic radiation, reaching the GeV band. This mechanism is likely the source of a significant part of the X-ray and gamma-ray output of AGN (see Sect. 1.2.5).

Electron-positron annihilation

A high-energy photon or interacting photons can produce an electron-positron pair. This pair can then annihilate again, producing gamma-rays. For the pair production to happen, the photon energy must reach the equivalent of twice the rest mass of an electron. Head-on collisions of, for example, a photon in the optical range ($\approx 2\,\mathrm{eV}$) would need a second photon in the GeV regime ($\approx 10^{11}\,\mathrm{eV}$) for a pair production. The cross-section for this process is:

$$\sigma_{\gamma\gamma} = \pi r_\mathrm{e}^2 \left(1 - \frac{m_\mathrm{e}^2 c^4}{E_{12}^2}\right)^{1/2}, \tag{1.1.12}$$

with the classical electron radius r_e and:

$$E_{12} = (E_1 E_2)^{1/2} \approx m_\mathrm{e} c^2, \tag{1.1.13}$$

for the photon energies E_1 and E_2. The production of electron-positron pairs functions as sources of opacity for high-energy gamma-rays. This way, photons at GeV energies and above can be absorbed by pair production processes with the extragalactic background light (EBL).

One further common mechanism that creates positrons is the collision of cosmic ray protons with other nuclei, resulting in positively charged pions π^+, which decay into positrons. Also, the decay of radioactive isotopes from stellar nucleosynthesis and supernova explosions (e.g., $^{26}\mathrm{Al}$) releases them. In case the positron has a low velocity, the interaction can also result in a bound electron-positron state, a positronium atom. A singlet $^1\mathrm{S}_0$ state decays into two photons at the characteristic 511 keV line. Should the initial particles have a significant velocity dispersion then the line will also broaden. In the majority of cases, a $^3\mathrm{S}_3$ triplet state is present, that decays into three photons, which have a continuous energy spectrum up to 511 keV.

The annihilation process of $e^+ + e^- \rightarrow 2\gamma$ results in an emission line at 511 keV regarding both photons when both initial particles are at rest. If not, the photon energies will be characterized by a certain dispersion. In the ultra-relativistic limit the cross-section for the annihilation is:

$$\sigma_{\mathrm{an,rel}} = \frac{\pi r_{\mathrm{e}}^2}{\gamma}(\log 2\gamma - 1). \tag{1.1.14}$$

Other sources of gamma-rays from these processes and especially the 511 keV line are AGN and their jets (e.g., Giblin & Shertzer, 2012; Kamraj et al., 2018), the wide region around the Galactic center, and potentially low-mass X-ray binaries (see, e.g., Prantzos et al., 2011, and references therein).

Particle acceleration mechanisms

The presence of high-energy photons and cosmic rays of up to $\approx 10^{20}$ eV point towards powerful non-thermal acceleration mechanisms, both in Galactic and extragalactic environments. A charged particle of the mass m, charge e, and with the velocity $\boldsymbol{v}$ is accelerated by electric and magnetic fields, according to:

$$\frac{\mathrm{d}}{\mathrm{d}t}(\gamma m \boldsymbol{v}) = e(\boldsymbol{E} + \boldsymbol{v} \times \boldsymbol{B}). \tag{1.1.15}$$

The resulting Lorentz force is exerted on the particle by the magnetic field if its path and the magnetic field are not parallel. In contrast, the electric field component in Eq. 1.1.15 is less relevant in most astrophysical settings: gases often exist in their ionized state, which impedes static electric fields because of the high conductivity of the gas/plasma. However, high-intensity electromagnetic waves or a time-wise variable magnetic field, inducing an electric field, constitute a non-stationary case, and consequently exert a force on the particle. The re-connection of magnetic field lines in, for example, the solar magnetosphere, also produces electric fields. Here, the particle collides with other particles in the ionized gas. The resulting equation of motion is given as:

$$\frac{\mathrm{d}\boldsymbol{v}}{\mathrm{d}t} = -e\boldsymbol{E} - \nu_{\mathrm{c}} m \boldsymbol{v}, \tag{1.1.16}$$

with the collision frequency between particles ν_{c}.

Shock waves that travel through a medium, like in supernova remnants or AGN, can also interact with charged particles via a process called Fermi acceleration. These shock waves of interstellar gas reflect the particles through the interaction with carried magnetic fields. The particles gain energy, so that:

$$\left\langle \frac{\Delta E}{E} \right\rangle \sim \left(\frac{v_{\mathrm{s}}}{c}\right)^2, \tag{1.1.17}$$

with the characteristic velocity of the shock wave v_{s}. This process in an environment of random motion of the gas cloud is named second-order Fermi acceleration, because of the order of dependence between energy gain and the velocity of the gas cloud as well as the internal magnetic field. Since the shock front is moving, collisions with particles are more likely head-on than trailing. The number of particles with an energy in the interval $E \dots E + \mathrm{d}E$ is:

$$\mathrm{d}EN(E) \sim \mathrm{d}EE^{-x}, \tag{1.1.18}$$

including the exponent:

$$x \equiv 1 + \left(\frac{4}{3}\frac{v_\mathrm{s}^2}{cL}\tau_\mathrm{esc}\right)^{-1}, \tag{1.1.19}$$

with the escape time from the cloud τ_esc and the mean free path L. The charged particles get stochastically scattered and gain energy. However, some collisions also result in the loss of energy of the particle.

If the particles have a high velocity compared to the shock front, the difference between a particle hitting the front head-on or from the trailing end is negligible. After the collisions the energy gain is thus symmetrical, and expressed by:

$$\left\langle \frac{\Delta E}{E} \right\rangle = \frac{4}{3}\frac{v_\mathrm{s}}{c}, \tag{1.1.20}$$

which is appropriately named first-order Fermi acceleration or diffuse shock acceleration. The corresponding exponent x in the power law describing the number of particles (Eq. 1.1.18) becomes approximately $x = 2$ in this case.

1.2 Active Galactic Nuclei

Radio surveys in the 1950s revealed a great number of astronomical sources within our galaxy as well as extragalactic ones, which were associated with galaxies at relatively high redshifts, like Cygnus A at $z = 0.057$. In the case of Cygnus A, very strong radio emission was detected from large lobes, oriented symmetrically around the center (Jennison & Das Gupta, 1953), see also Fig. 1.2.1, left. The emission from supernova remnants like the Crab nebula and jet-like structures in these new radio-luminous galaxies like Cygnus A and M 87 were found to be non-thermal in nature and due to synchrotron radiation possibly from relativistic electrons. The source of energy release, which is up to millions of times larger in the radio band compared to the Milky Way, had to be very efficient and different in these radio galaxies.

The next step in the discovery of what was later named active galaxies, was the association of radio-loud galaxies with a star-like optical appearance in the 1960s. Measuring the redshift from the hydrogen Balmer series, these quasi-stellar radio sources (Quasars) were found to be very distant, with the famous observation of the source 3C 273 ($z = 0.158$, Schmidt, 1963). Besides the radio output, the optical luminosity was magnitudes higher than our own galaxy, about a factor of 100 more in the case of 3C 273 (see Fig. 1.2.1, right). Sandage (1965) revealed the first radio-quiet quasars, a new sub-class of active galaxies. In the following years, more sub-classifications were created, depending on observables like the radio-to-optical flux, variability, radio morphology, emission line width, and others.

The accretion of matter in a strong gravitational field of a supermassive black hole (SMBH) and the subsequent release of potential energy has become a widely accepted model, giving birth to the idea of the relatively compact active galactic nucleus (AGN). Several observed

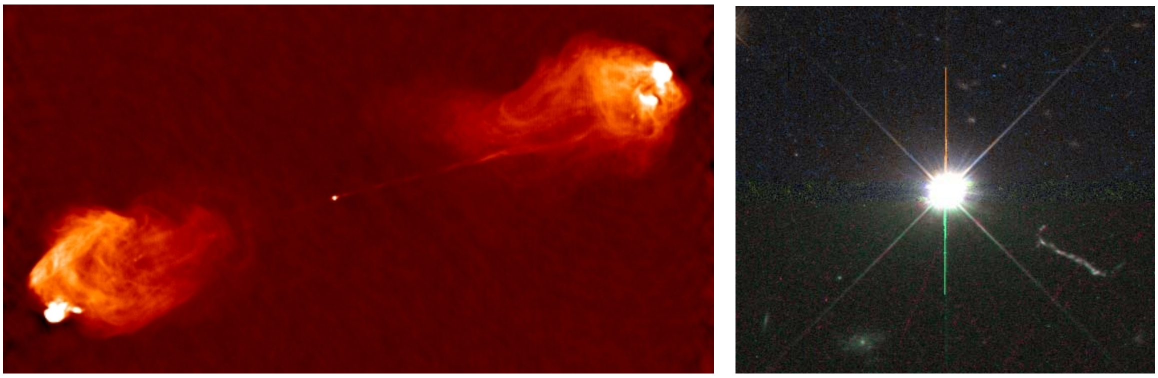

Figure 1.2.1.: Left: Radio galaxy Cygnus A with jets and extended lobes, imaged with the VLA at 6 cm, image credit: Chris Carilli, right: optical image of the quasar 3C 273, image credit: J. Bahcall, STScI.

properties contributed to a complex model of the central engine (see Sect. 1.2.1). With respect to their host galaxies, AGN often appear as bright point sources, exhibiting very small angular size, and a luminosity that often reaches and surpasses that of their host galaxy. However, the luminosity of AGN is also wavelength-dependent and underlies strong evolution on cosmological time scales. Known AGN are characterized by a broad range of luminosities, roughly $L \approx 10^{42}\,\mathrm{erg\,s^{-1}} - 10^{48}\,\mathrm{erg\,s^{-1}}$. In the following, the general properties of AGN from an observational standpoint are addressed. Section 1.2.1 gives an overview of the different AGN classifications, while Sect. 1.2.2 discusses the building blocks of the central engine and adjacent components which are responsible for the broadband energy output of AGN. Sections 1.2.3, 1.2.4, and 1.2.5 cover AGN jets, which are a particularly important feature of source classes that produce highly beamed emission like blazars. Lastly, the broadband spectrum of AGN and the search of AGN in the context of surveys are discussed in Sect. 1.3.

1.2.1. AGN: general properties and classifications

One of the most striking characteristics of AGN is the spectral range on which they can be observed. Regular galaxies host billions of stars, which emit, roughly approximated, black-body spectra, showing the main energy output around the optical regime, not wider than a decade in wavelength. AGN on the other hand exhibit broadband spectra that are also notably bright in the radio and X-ray to GeV energies. This makes distinguishing AGN from normal galaxies easy in radio or X-ray surveys. The exceptionally broad spectral energy distribution (SED) lends itself to several different emission mechanisms (see also Sect. 1.1). AGN spectra also prominently feature emission lines like the often observed Balmer series, Lyα, or the FeKα line in the X-ray band. In some cases, the emission lines are particularly broadened, equivalent to several thousand $\mathrm{km\,s^{-1}}$, while others are comparatively narrow, only exhibiting a few hundred $\mathrm{km\,s^{-1}}$. This circumstance is closely related to Doppler broadening and the dynamic and geometry of the AGN's central engine (Sect. 1.2.2). Objects of both classes feature permitted and semi-forbidden lines, whereas objects with narrow lines can also show forbidden emission lines in their spectra.

Besides their high flux output, AGN are also known for their variability in this regard, depending on the wavelength, time scale, and the individual source. In general, the variability amplitude across the electromagnetic spectrum correlates with the time scale and the rest-frame frequency of the observed emission, but anti-correlates with the luminosity (see, e.g., Sartori et al., 2019, and references therein). Time scales from hours to decades have been recorded in the past, with especially blazars showing significant short-term variability (e.g., Abdo et al., 2010d; MacLeod et al., 2012; Sandrinelli et al., 2014). Since the emitting region and the variable region need to be causally related, the characteristic variability time scale corresponds to the size of said region, giving thus a rough estimation on its dimension. In contrast to other source types like Cepheid variables or pulsars, AGN do not show concrete periodicity. On time scales of days to weeks AGN X-ray light curves were found to vary from a few to approximately 40%, while observational data comprising a decade or more suggests variability in their light curves of up to 50% (see, e.g., Maughan & Reiprich, 2019, and references therein). Short-term flux and spectral variations are measured on time scales of a few thousand down to a few hundred seconds (Ponti et al., 2004; Vaughan & Fabian, 2004). In the hard X-ray band ($\gtrsim$ 10 keV) radio-loud and radio-quiet AGN have also shown significant variability, comparable to the soft X-ray band[3], as recorded by the *Swift*/BAT all-sky monitor (e.g., Soldi et al., 2014), see also Sect. 2.3.1. The strongly variable sky at GeV energies has been studied in numerous works in the past using the comprehensive coverage of the *Fermi*/LAT monitor (see Sect. 2.4). Light curve timing analyses as well as time-critical multiwavelength campaigns regarding the observations of neutrinos are just some fields of recent AGN research (e.g., Adrián-Martínez et al., 2012; Abdollahi et al., 2017; Sahakyan et al., 2018). There are also a number of high-peaked beamed AGN (blazars), which show frequent and intense variability in the TeV regime, which is observed by Imaging Air Cherenkov Telescopes like MAGIC and FACT. Prominent examples of the few highly variable blazars that are the target of continuous monitoring are Mrk 421 (e.g., Gokus et al., 2022) and Mrk 501 (e.g., MAGIC Collaboration et al., 2020). Another distinctive feature of the obscured light in many wavelength bands is the notable degree of linear polarization, more so than from standard stellar environments, which has been observed to be time-dependent (e.g., Gaskell et al., 2012), and is indicative of scattering mechanisms and synchrotron radiation.

Since the discovery of the first radio galaxies, the number of different AGN types, or classifications, has grown, leading to an array of types and related sub-types. The following list gives a short overview over the most relevant ones. Additionally, Table 1.2.1 summarizes some of the most important properties. After introducing the different AGN types, Sect. 1.2.2 illustrates how a unified model aims to reconcile them.

Quasars and QSOs

As stated above, this prominent AGN class was discovered in connection with their significant radio output and point-like optical appearance, as well as high redshifts. Like most AGN, quasars possess an extremely broad SED, starting in the radio regime, before producing a turnover roughly in the far IR, possibly by synchrotron self absorption. The optical spectrum has an excess of blue light, giving rise to the spectral component called the big blue

---

[3] Historically, the soft and hard X-ray bands were associated with the 0.2 keV – 2 keV and 2 keV – 10 keV, respectively. In the context of this work, the entire X-ray band below 10 keV is labeled soft, whereas 10 keV – 200 keV, associated with the *Swift*/BAT sensitivity range, is called hard.

Table 1.2.1.: General observational properties of the most prevalent AGN classifications.

	Radio morphology	Radio loudness	Luminosity	Emission lines$^{(a)}$	Variability	Jet	Example
Quasar	FR II	loud	high	b, n	high	yes	3C 273
QSO	-	quiet	high	b, n	high	-	QSO B1246+377
FSRQ	compact	loud	high	b, n	high	yes	3C 279
BL Lac	compact	loud	high	-	high	yes	Mrk 421
Seyfert 1	-	quiet	low	b, n	high	-	NGC 4151
Seyfert 2	-	quiet	low	n	high	-	Mrk 3
LINER	-	quiet	low	n	low	-	NGC 4379
BLRG	FR I / II	loud	low / high	b, n	low	yes	3C 111
NLRG	FR I / II	loud	low / high	n	low	yes	Centaurus A

Notes. The listed properties of the classifications are not completely exclusive, since further sub-classifications exist. The table includes the most predominant properties of the listed classifications. $^{(a)}$ emission line width is generically marked with 'b' for broad and 'n' for narrow. After Krolik (1999) and Longair (2011).

bump. The radio-quiet variant of quasars with steep radio spectra, sometimes referred to as QSOs or RQQs, are actually about ten times as numerous when compiling optically-selected quasar samples. A certain type of QSOs was shown to exhibit especially strong polarization measures of almost 20% (Berriman et al., 1990; Zakamska et al., 2005). In the greater picture of the AGN phenomenon this sub-class is associated with Type 2 AGN or here Type 2 QSOs (see Sect. 1.2.2).

Radio Galaxies

Distinctive of their radio jet and lobe structure, and spanning in some cases tens of kpc, radio galaxies were the first specimen of AGN that were studied via observations using radio interferometry. A radio galaxy may also emit strongly from a halo, extending approximately as far as the host galaxy, or the emission may be restricted to a bright core in its center. The radio lobes, or plumes, are connected to the central region by jets, with cases of one-sided and two-sided jets. Radio galaxies can be sub-divided into broad-line radio galaxies (BLRGs) and narrow-line radio galaxies (NLRGs). The former sub-type constitutes sources with bright centers and faint surroundings, featuring broad and narrow emission lines, while the latter type is connected to giant elliptical galaxies, showing only narrow lines. Two further sub-types are compact steep-spectrum sources (CSS) and the gigahertz-peaked sources (GPS), which are characterized by a very small emission region in the radio galaxy and a spectrum that steeply rises at lower radio frequencies, having a sharp peak, and then declining steeply again at higher frequencies.

The classification of luminosity and morphology introduced by Fanaroff & Riley (1974) sorts all radio-loud AGN into two main categories. The FR I type describes AGN which are brighter in the center with diminishing brightness farther away, also showing two jets, and with a specific luminosity of $< 10^{25}\,\mathrm{W\,Hz^{-1}}$ at 1.4 GHz. More luminous sources also tend to have a different morphology, named the FR II type, which exhibit edge-brightened lobes and often only one visible and very straight jet. Cygnus A (Fig. 1.2.1) is a classic example of an FR II type, as are quasars.

Blazars

The most extreme sort of all AGN in many fields is given by blazars, which can be subdivided into further types. Blazars are characterized by their high amount of variability, down to hours. They have a very small angular size while being radio-loud and core-dominated, and feature a high degree of radio and optical polarization, which has been observed to be as high as $\approx 40\,\%$ (Jorstad et al., 2007). In the X-ray range, blazars show power-law spectra and a wide range of spectral indices, which also depend on their current activity state (e.g., Pandey et al., 2018; Yoo & An, 2020). A significant element of the blazar model is the jet from the central engine that is pointed directly or at a small angle to the observer (Sect. 1.2.2), creating relativistically beamed emission. All-sky surveys found, that blazars easily dominate the extragalactic sky at gamma-ray energies and the even more energetic TeV regime (Abdollahi et al., 2020; Wakely & Horan, 2008).

Some blazars were later associated with luminous and distant quasars with a flat radio spectrum ($I_\nu \sim \nu^0$) and consequently named flat spectrum radio quasars (FSRQ). The second category of blazars comprises the BL Lacs, named after BL Lacertae, the first prototypical case. BL Lacs are usually less luminous, but highly variable sources with typically low redshifts of about $z \lesssim 0.2$. Their power-law continua are often devoid of any emission or absorption lines, making an assessment of their redshift difficult, if not impossible. Both FSRQs and BL Lacs feature a double-humped broadband SED, which, depending on the source, is characterized by a certain position along the frequency axis, referred to as the peak frequency. While FSRQs are often lower-peaked sources, a wide array of different peak frequencies were found for BL Lacs (e.g., Ajello et al., 2020). Blazars also include the type of optically violent variables (OVV), that are similar to the BL Lac type, but with strong and broad emission lines.

Seyferts

In contrast to large quasars, Seyfert galaxies are optically bright, but generally radio-quiet spiral galaxies with point-like luminous nuclei. Their spectra feature high-excitation emission lines, together with broad Balmer and forbidden lines. Seyferts also show a dichotomy regarding their emission line characteristics: So-called Seyfert-1 galaxies exhibit permitted lines with a FWHM of up to a $10{,}000\,\mathrm{km\,s^{-1}}$ equivalent in velocity regarding Doppler broadening. Also, Sy1s have forbidden lines with only $\approx 1000\,\mathrm{km\,s^{-1}}$. The category of Seyfert 2 galaxies have exclusively narrow permitted lines corresponding to $1000\,\mathrm{km\,s^{-1}}$. Most Seyferts show relatively low polarization levels of a few per cent (Miller & Goodrich, 1990; Smith et al., 2002).

Since the production of the lines must be correlated to moving emission regions, it can be concluded that the different broadening also happens in different parts of the AGN's central engine, moving at different distinctive velocities (see Sect. 1.2.2). Intermediate classifications were introduced later (Sy 1.2, 1.5, 1.8, 1.9), describing varying degrees of permitted Sy1-like lines that are superimposed with a narrow line. A peculiar and relatively recent discovery is the sub-type of narrow-line Seyfert-1s (NLSy1), which show small emission line widths but high variability, the latter being typical of Sy1s. Some of which can even be described as radio-loud while having a relativistic jet and producing gamma-ray emission (e.g., Komossa et al., 2006; Paliya & Stalin, 2016), mixing blazar-like and non-blazar-like properties, such as a low-mass black hole.

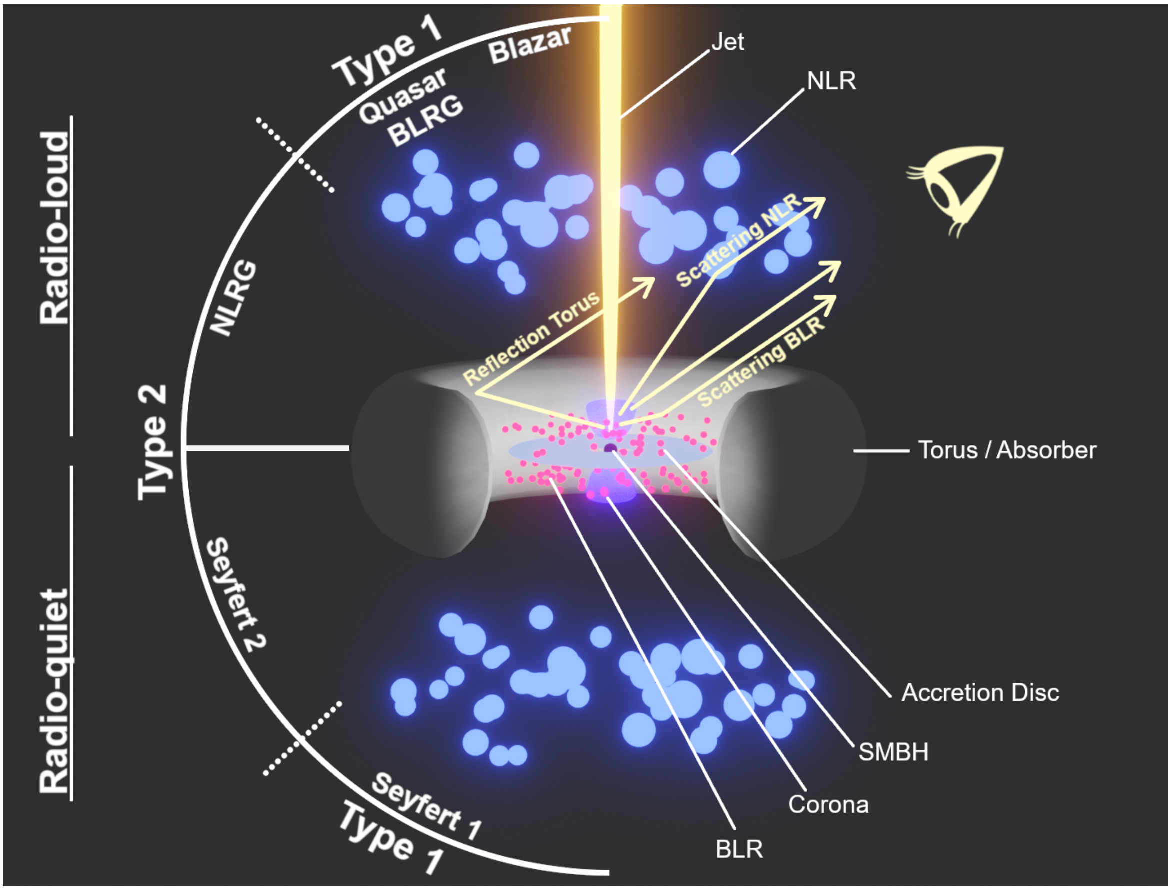

Figure 1.2.2.: AGN unification model, representing radio-loud AGN including the jet in the top half, and radio-quiet AGN without a (prominent) jet in the bottom half, as well as different AGN types which are dependent on the inclination angle between the observer and the rotational axis. The model is not to scale. The hot electron corona in the central engine is modeled as a conical shape only for illustration. The yellow lines indicate different re-processed radiation from the corona, which is seen by the observer.

LINERs

Akin to Seyferts, low ionization nuclear emission regions, or LINERs, are low-luminosity but fairly common AGN types. They feature even narrower and weaker emission lines from strongly ionized atoms, but reasonably strong lines from neutral or weakly ionized atoms. Luminous infra-red galaxies are often LINERs.

1.2.2. Anatomy of an AGN and unification

In the past, unified models (e.g., Antonucci, 1993; Urry & Padovani, 1995) have aimed to reconcile the multitude of observational data into a consistent picture of the central engine of AGN and their surroundings (see also, e.g., Netzer, 2015; Padovani et al., 2017, for a more recent review). The fact that enormous energy generation takes place in the smallest regions while showing a wide variety of behaviors hinted at a complex interaction of different mechanisms in a novel astrophysical context. Today, the widely accepted general idea of the compact central region of AGN puts a spinning supermassive black hole in the center, surrounded by an accretion disc, which releases potential energy far more efficiently than, for example, nuclear fusion processes[4]. Many experiments have delivered supportive evidence for the existence of black holes in the mass range of 10^6 to 10^{10} solar masses (e.g., Kollmeier et al., 2008; Zaw et al., 2020, and references therein), with most prominently the recent images of the black hole shadow from the center of elliptical galaxy M 87 (Event Horizon Telescope Collaboration et al., 2019). The surface of a non-rotating black hole (Schwarzschild black hole) is described by the Schwarzschild radius / gravitational radius:

$$r_\mathrm{S} = \frac{2GM}{c^2}, \tag{1.2.1}$$

which, for example, would be 2 AU for a black hole mass of $M = 10^7\,M_\odot$. The closest stable orbit around the black hole is given by $r = 3 \cdot r_\mathrm{S}$. For a spinning black hole (Kerr black hole), that is maximally rotating, the gravitational radius is $\frac{1}{2}\,r_\mathrm{S}$, equal to the closest stable orbit. The spin is often described by the spin parameter a, which can assume the values $-1 \leq a \leq 1$. A useful, if very rough, constraint of the black hole mass is provided by the maximum allowed luminosity that scales linearly with the mass, that is, the Eddington luminosity L_E, given for spherical symmetric emission:

$$L_\mathrm{E} = 1.3 \cdot 10^{31} (M/M_\odot). \tag{1.2.2}$$

In many cases, the luminosity of AGN is observed to be mainly 0.01 to a few ten per cent of L_E (e.g., Lusso et al., 2012; Suh et al., 2015). The matter in the accretion disk around the black hole has viscous forces acting upon it, which leads to the emission of thermal optical and UV radiation, and the decreasing of the angular momentum. Although too small to be imaged directly, the size of the accretion disc can been estimated via light curve data, since the size of the accretion disc correlates with the longest time scale of a significant amount of variability. For example, Hawkins (2007), using a large quasar sample, estimated the size of AGN accretion discs to be approximately 10^{-2} pc. The high temperatures as well as the high luminosity lead to the formation of an extremely hot (relativistic) electron gas near the disc, called the corona, whose precise geometry is not yet well understood (Fig. 1.2.2 shows the corona as a conical shape for illustration purposes). Thermal UV radiation from the disc is inverse Compton-scattered by the hot electrons into the X-ray regime and beyond, creating a power-law spectrum. The accretion disc often exhibits strong fluorescent lines from ionized iron, most commonly the FeKα transition, initiated by the removal of K-shell electrons by X-rays. The line was found to be asymmetrically broadened, due to the strong gravitational field in the black hole's vicinity (e.g., Cadež & Calvani, 2005; Brenneman & Reynolds, 2009). Observations concerning the time lag between a variation of the optical / UV continuum and the broad emission lines (e.g., Ulrich et al., 1984) led to the conclusion that a re-processing of the thermal emission must take place in even more distant regions / clouds (the BLR, see below).

A central part of the AGN unification model(s) is the consideration of a (non-isotropic) geometry that explains why certain classes exhibit broadened lines and others do not, like the distinction of Seyfert 1 / Seyfert 2 or BLRG / NLRG (see Sect. 1.2.1). Light from the center is scattered by a photo-ionized medium, which populates a) the region relatively

---

[4] Up to 42% of the rest mass is able to escape when the mass enters the black hole, in contrast to only 0.7% from nuclear fusion of H to He.

close to the accretion disc, creating broad lines through a high velocity dispersion (broad line region, BLR), and b) a significantly more distant and larger region of lower density away from the center, consequently only creating narrow lines when scattering (narrow line region, NLR). An obscuring medium of gas and dust, in its simplest form thought to be of toroidal shape, restricts the view to the BLR, making the Type 1 / Type 2 dichotomy of AGN types a matter of orientation to the observer. The term Type 1 AGN thereby refers to an orientation of a low inclination angle (the angle of the rotational axis and the line of sight). Type 2 AGN consequently denote orientations that are more edge-on, that is, of higher inclination angles. The size of the torus needs to be larger than the BLR, but smaller than the extend of the NLR, whose dimensions are estimated to be roughly 100 pc to several 100 pc (Wilson & Tsvetanov, 1994; Barbosa et al., 2009; Ruschel-Dutra et al., 2021), see also Fig. 1.2.2. The radiation from the central area produces thereafter the NLR in a conical shape via photo-ionization in an axisymmetric structure. Although being reasonably effective as a basic AGN unification model, the thick and uniform pc-scale torus geometry underwent conceptual changes towards a more clumpy structure following studies in the past years using IR and X-ray observations (e.g., Ramos Almeida et al., 2009; Markowitz et al., 2014; Esparza-Arredondo et al., 2021).

A dusty / molecular torus can absorb photons via a number of mechanisms, depending on the photon energy and the composition of the absorber (Krolik, 1999): Dust particles are able to scatter as well as absorb mid-IR to UV photons, re-emitting the energy in the IR. Hydrogen gas that is not fully ionized constitutes a certain opacity for photons that are energetic enough to ionize it, that is, UV radiation of at least 13.6 eV (Lyman limit), being more effective than dust. Photons of higher energy interact with the absorber via photo-ionization, producing further opacity of the material, while X-rays above $\approx 10\,\mathrm{keV}$ are hindered by Compton scattering. A column density of $\approx 10^{24}\,\mathrm{cm}^{-2}$ is called Compton-thick, effectively obscuring even harder X-rays. The observed power-law continuum and line spectrum of Type 2 AGN in the X-ray band is therefore significantly absorbed, with additional reflection components from the BLR and the torus itself (see also Fig. 1.2.2). The opacity falls, however, for higher energies where the scattering process is expressed by the Klein-Nishima cross-section. One of the most prominent features of radio-loud AGN, especially blazars, is the relativistic jet, which is discussed in the following sections.

1.2.3. Relativistic jets

AGN that are classified as radio-loud usually feature a prominent beam of particles, called a jet, parallel to the central engine's rotational axis on both sides, that can extend for kpc. Depending on the case, jets can be resolved into large individual components, or knots. Outside of the radio regime, jets are sometimes also visible in the optical and X-ray bands. The jets are created in the vicinity of the inner accretion disc and the black hole, carrying magnetic fields and charged particles that are accelerated into the two opposite outflows. Often, the jet components have seemingly superluminal speeds (e.g., Pearson et al., 1981; Jorstad et al., 2001; Kellermann et al., 2004), which is a projection effect (see Sect. 1.2.4). Radio images have shown a closest component to the black hole as a stationary emission region, also named the core (e.g., Lister et al., 2018). The position of the observed radio core shifts further upstream of the jet with decreasing wavelength (Blandford & Königl, 1979).

The mechanism that is responsible for the launching of the jet from the central engine has not yet been identified conclusively. The rotational energy of the black hole or the accretion disc, or a combination of both could drive the launching: Blandford & Znajek (1977) introduced a mechanism, which describes the extraction of energy and angular momentum from a Kerr black hole by a solely electromagnetic process. External currents in the surrounding disc support magnetic field lines which create an electric potential difference, leading to electron-positron pair production in the induced magnetosphere. In the case that the resulting field lines are paraboloidal in shape, the anti-parallel jets are predicted to be beamed. Blandford & Payne (1982) described a process in which the angular momentum is removed from the disc. Therein, magnetic field lines are carried off the disc, whereas the matter outflow is driven centrifugally into the jets above and below. Close to the disc, gas pressure drives the launching of matter, while at larger distances the outflow can stay collimated by the magnetic field components. Both models are used in recent studies and simulations of possible jet launching scenarios. For example, Xie et al. (2012), proposed a two-component jet with both processes in the framework of a spine-sheath model. In a study by Feng & Wu (2017), the spin of the SMBH of the giant radio galaxy M 87 was estimated using a hybrid jet formation model including contributions of both mechanisms. Most recently, Dihingia et al. (2021) performed axisymmetric GRMHD simulations of the central engine including the resulting ejection of jets using both processes for a relativistic jet and disc winds.

The precise mechanisms that are responsible for the collimation of the jet, leading to opening angles of less than 1° up to kpc-scales, are still debated. For a recent review see Blandford et al. (2019). Starting in the acceleration and collimation zone (ACZ), the jet is magnetically dominated and becomes particle-dominated further downstream. At the base, the jet is characterized by a wide opening angle and is accelerated in the ACZ through magnetic forces, which are also likely to be crucial for the confinement of the jet over long distances. Helical magnetic fields can exert "hoop stress" through their toroidal component while the poloidal component might also produce pressure (e.g., Spruit et al., 1997; Mirabel & Rodríguez, 1999). Furthermore, disc winds and the ambient medium may also contribute in an important way in confining the jet close to the accretion disc and then farther away (e.g., Komissarov et al., 2007; Bromberg et al., 2011; Globus & Levinson, 2016).

As of yet, it is still unclear what the composition of AGN jets actually is. The discussed launching mechanisms imply an electrically neutral jet, but the question whether the jet is purely leptonic (electrons, positrons) or also includes hadronic particles (see, e.g., Mannheim, 1993; Böttcher et al., 2013) remains open. However, the latter scenario has been encouraged by recent results in the detection of neutrino events that are most likely extragalactic in origin. After the first significant detections of PeV neutrinos (IceCube Collaboration, 2013), a high-energy neutrino event could be associated with the blazar TXS 0506+056 in a gamma-ray flaring state (IceCube Collaboration et al., 2018). Neutrinos from blazars are theorized to be produced in the beamed jets together with gamma-rays by cascade reactions of accelerated protons, which can produce pions that decay into electron and muon neutrinos (e.g., Mannheim, 1995; Tavecchio & Ghisellini, 2015; De Angelis & Mallamaci, 2018).

The most luminous radio sources (FR II galaxies) show extended radio structures: hot spots are often visible at the outer edges of the lobes, where accelerated particles from shocks within the jet meet the intergalactic medium (IGM). The lobes themselves are created by the expansion of the gas in magnetic field structures. FR I galaxies, which have significantly lower luminosity, have radio lobes that do not contain any hot spots and form a low-density bubble.

1.2.4. Beaming and superluminal motion

As already stated above, AGN jets are outflows of particles, accelerated to relativistic speeds, and, in the case of blazars, under very small inclination angles of the jet axis to the observer. The source / emitting region, here a jet component, moves at a speed v towards the observer under the inclination angle θ. It follows (e.g., Longair, 2011), that the frequency shift of the observed radiation can be expressed as:

$$\nu' = D\,\nu_0, \tag{1.2.3}$$

with the Doppler factor D:

$$D = \frac{1}{\gamma\left(1 - \frac{v\,\cos\theta}{c}\right)}. \tag{1.2.4}$$

Under the assumption that the source's luminosity can be described by a power law:

$$L(\nu_0) \sim \nu_0^{-\alpha}, \tag{1.2.5}$$

the measured flux density becomes:

$$S(\nu) = \frac{L(\nu_0)}{4\pi d^2} D^{3+\alpha}, \tag{1.2.6}$$

with the distance d to the source. The emission in the observer's frame is highly beamed in the direction of the source's movement, significantly increasing its measured flux. The otherwise isotropic emission of the source is focused by this relativistic effect, as the solid angle over which the source is emitting decreases with a factor of D^{-2}. The same way, the flux of the counter-jet of the AGN, pointing away from the observer, loses the flux output in the same direction, leading to a de-boosting effect and a great difference of the observed luminosities of both jets. Thus, the apparent picture of only one-sided jets for even moderate Doppler factors and only slight jet inclinations becomes plausible. For example, Saikia et al. (2016) have studied a sizable blazar sample, deriving the distribution of Doppler factors, whereas many sources showed factors in the range of around 10 to 20, and up to approximately 40. Furthermore, the variability or the duration of a flare from a highly beamed source in the jet component's frame due to changing physical conditions gets enhanced by the beaming and compressed with a factor of D, producing rapid variations.

VLBI observations of relativistic AGN jets have shown that the jet components often move with apparent transversal superluminal speeds v_{app} with reference to the radio core. Lister et al. (2013), for example, presented the pc-scale kinematics of 200 radio-selected AGN jets. Most jets with robust measurements showed median apparent speeds in the range of 0 to 20 c. However, it has been widely accepted that this contradiction to relativity in regard to the speed of light is an effect of the emitting jet component being only marginally slower than its own emitted light and the low inclination angle θ. Through simple geometrical considerations (e.g., Longair, 2011) it can be derived that the projected apparent velocity is:

$$v_{\mathrm{app}} = \frac{v\,\sin\theta}{1 - v\,\cos\theta/c}. \tag{1.2.7}$$

Thus, a speed of the jet component of $v = 0.995\,\mathrm{c}$ can result in a projected jet speed of up to $v_{\mathrm{app}} = 10\,\mathrm{c}$, depending on the angle. A little less extreme case of $v = 0.986\,\mathrm{c}$ would still result in up to $v_{\mathrm{app}} = 5\,\mathrm{c}$. The observed superluminal speeds therefore imply highly relativistic jets, which have to be driven by efficient and powerful central engines (see Sect. 1.1).

1.2.5. Multiwavelength emission from jets

The emission from jets over large parts of the electromagnetic spectrum, from the radio to the optical and beyond is caused by synchrotron radiation of the charged particles in the transported magnetic fields. Their orientation can be traced by the strong polarization up into the optical regime (e.g., Pavlidou et al., 2014). Synchrotron radiation in an astrophysical context has been theorized early by, for example, Shklovsky (1953) and Burbidge (1956). Due to the self-absorption in the synchrotron-emitting region in the jet, one single region is not able to explain the higher-energy spectral component in AGN broadband spectra, that is, in the optical regime and above. Modeling the synchrotron-dominated part of AGN spectra thus requires more than one emission region: a large one of low density where the radio emission is created, and a more dense and compact part of the jet, giving rise to the high-energy part of the spectrum. The geometry of such a two-zone model is still unclear, but could be realized through an inner and outer jet (see Cerruti, 2020, and references therein). In a recent study, Bruni et al. (2021) analyzed VLBI observations of the jet of the quasar 3C 273, indeed indicating that a stratification of the emission region, meaning a spine-sheath structure, would be required to explain the observational data.

The second major component in an AGN's broadband spectrum is a similar bump as the synchrotron component, but at X-ray to gamma-ray energies. This bump is generally associated with inverse Compton (IC) emission (see Sect. 1.1) from various potential photon fields in the vicinity of the jet. Since this spectral component is not yet attributed with certainty to IC processes or a specific population of up-scattering particles, it is also referred to as the high-energy (HE) bump. In any case, many works have suggested various scenarios of high-energy jet emission through IC scattering. The corresponding seed photon fields can for once be provided by the same photons that are the product of the synchrotron processes in the jet. This is also called the Synchrotron Self-Compton mechanism (SSC, Maraschi et al., 1992; Bloom & Marscher, 1996). Other sources from outside the jet are summarized as external-Compton models (EC), providing seed photons from the accretion disc (Dermer et al., 1992; Sikora et al., 1994), the torus (Błażejowski et al., 2000; Sikora et al., 2008), or even the cosmic microwave background radiation (Böttcher et al., 2008; Zacharias & Wagner, 2016). Also, studies have suggested that the BLR functions as a source of the seed photons, putting restrictions in the size and shape of the BLR (Sikora et al., 1994; Blandford & Levinson, 1995; Hartman et al., 2001). Finke (2016) performed detailed calculations of IC scattering for different regions, drawing the conclusion, that gamma-rays from flares are unlikely to originate outside of the BLR, or may be created in a sheath surrounding the initial emission region in the jet.

1.3 AGN: broadband emission and surveys

No other astrophysical source type is as prevalent throughout the entire electromagnetic spectrum as active galactic nuclei. A multitude of emission and re-emission mechanisms are responsible for the extremely wide spectral energy distribution (SED) of AGN. Since the entire spectrum of the most powerful radio- as well as gamma-ray-bright source types cover a frequency range of roughly 20 decades, searching for AGN and their sub-types can be highly biased regarding the observed frequency window. However, the wide spectrum can also be utilized for differentiating AGN from normal galaxies or stars when surveying

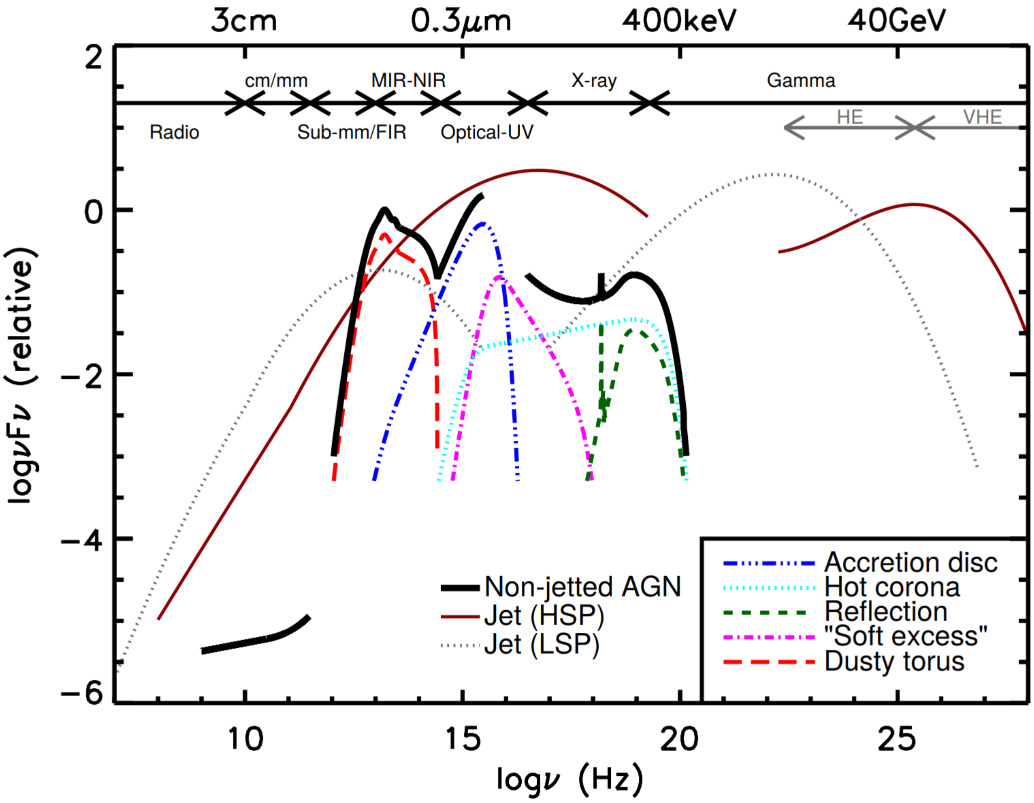

Figure 1.3.1.: Schematic SED of non-jetted and jetted AGN in the νF_ν format, including the individual emission and re-processing mechanisms as well as the two dominant emission processes for jetted AGN, the synchrotron and high-energy bumps. The gray dotted curve indicates a low-peaked source in this regard, while the brown curve illustrates a high-peaked one. Image credit: Padovani et al. (2017).

the sky. Figure 1.3.1 shows a schematic SED of AGN with and without a jet, illustrating the grave difference between both types, especially in the gamma-ray regime. The typical representation in the $F_\nu \nu$ against ν format shows the energy emitted per frequency interval, instead the more usual spectrum where the energy flux F_ν is graphed. The overall flux spectrum of an AGN can be approximated by a power law, $F_\nu \sim \nu^{-\alpha}$, with the spectral index α. The discussed broadband properties and selection effects in this section follow the review by (Padovani et al., 2017).

1.3.1. The synchrotron regime: radio and optical

AGN that are selected in the broad radio regime feature a power-law spectrum in this part of the SED, which is caused by the synchrotron emission of the jet (Sect. 1.2.3). Besides AGN, star-forming galaxies (SFG) also emit via the synchrotron process, albeit at lower luminosities. The blazar sub-types of FSRQs and BL Lacs both feature flat radio spectra ($\alpha < 0.5$) and dominate radio surveys at high brightness levels, making radio observations an effective tool for finding (beamed) AGN (e.g., Kuehr et al., 1981). While radio-loud AGN radiate a substantial fraction of their energy output via non-thermal processes, the output of radio-quiet types is characterized by thermal emission in a more significant way (e.g., Padovani, 2016). The first surveys in the radio band discovered hundreds of point-sources throughout the sky, resulting in catalogs like the 3C (3rd Cambridge, Edge et al., 1959), whose sources were classified later by the means of optical spectroscopy. Subsequent surveys for later iterations of the catalog and in the range of 38 MHz up to 15 GHz covered large portions of the sky while providing sensitivities in the range of mJy. The precise identification of source types in radio surveys at very low flux densities, however, is difficult, because of the low optical brightness. At these flux densities, well below 1 mJy, it has been shown that the observed populations of radio sources are a mix of radio-quiet AGN and SFGs (e.g., Padovani et al., 2014). Some of the more recent and notable surveys that revealed a large number of point sources, mostly targeting high Galactic latitudes, include the GMRT survey (150 MHz, $\approx 6 \cdot 10^5$ sources, Intema et al., 2017), the NVSS survey (1.4 GHz, $\approx 2 \cdot 10^6$ sources, Condon et al., 1998), and the LOFAR multiwavelength snapshot survey (MSSS, 74 MHz / 151 MHz, $\approx 2.5 \cdot 10^4$ sources, Heald et al., 2015; Jackson et al., 2022).

Among the largest AGN surveys are those conducted in the optical band over years. These include large-area surveys that cover a great part of the sky, such as the Sloan Digital Sky Survey (SDSS, York et al., 2000), or very localized but deep observations over longer time spans, like Hubble Deep Field (HDF, Williams et al., 1996). The SDSS catalog of the most recent 16th data release lists approximately $1.2 \cdot 10^9$ objects, including nearly 5 million spectra, with almost 3 million from galaxies and 1 million from quasars. The optical band of the spectrum often features a component with strong lines, called the big blue bump, which is thought to originate from thermal emission of the accretion disc (e.g., Malkan & Sargent, 1982), peaking in the extreme UV, which is the main source of ionizing radiation in the central engine. The host galaxy also contributes to the spectrum in the range between the big blue bump and the IR emission of the AGN. AGN and their types are identified and distinguished from other sources using, for example, the presence of broad lines or measured color indices. The optical emission lines also permit the calculation of the source's redshift. Generally, optical surveys suffer from a bias towards higher-luminosity and unobscured AGN[5]. At low brightness levels it becomes difficult to distinguish AGN from stars or normal galaxies at specific redshift intervals, especially without dedicated spectroscopy (e.g., Ross et al., 2013). Compared to other wavelengths like radio or X-rays, optical surveys exhibit a relatively low fraction of AGN, which is however mitigated by the massive sky coverage and huge numbers of total cataloged sources.

1.3.2. The high-energy regime: X-rays and gamma-rays

The X-ray part of an AGN's SED is created by many different emission processes that cause a multitude of spectral shapes. Their spectra are generally characterized by a power law with an index of $\alpha = 0.7 - 1$, originating from the up-scattering hot electrons in the corona. The power law features a high-energy cut-off at several hundred keV. A soft excess / thermal component at the lower part of the X-ray spectrum is due to direct emission from the accretion disc. Also, the disc reflects X-rays from the corona, creating a spectral component starting at a few keV, including fluorescent lines, like the FeKα line at 6.4 keV. These emission lines also undergo a broadening both to the motion of the scattering AGN components and the gravitational redshift close the black hole (e.g., Brenneman & Reynolds, 2009). The

---

[5] The classification obscured and unobscured AGN also depends of the observed wavelength, but is roughly equivalent to the Type 2 / Type 1 classification, respectively.

composition of an AGN's X-ray spectrum can vary greatly from source to source, depending on factors like the inclination angle or the geometry of the emitting components (e.g., Murphy & Yaqoob, 2009; Chen et al., 2012). The hard X-ray range ($\approx 10\,\mathrm{keV}-200\,\mathrm{keV}$) continues the primary power law of the soft band. The overall SEDs of blazars, however, are superimposed with the synchrotron and HE (high-energy) emission bumps, which can additionally influence the spectral shape of the hard X-ray power law. A detailed study of the spectral properties of different blazar samples is the main subject of this work, see Chpts. 4, 5, and 6. The absorption of X-rays is a major selection effect that depends on the X-ray energy, with lower energies suffering from stronger absorption (e.g., Wilms et al., 2000). However, the detection of more obscured / Compton-thick AGN becomes more likely for higher redshifts, since the harder X-rays are shifted towards lower energies regarding the observer. Hard X-rays are only significantly obscured by high column densities ($N_\mathrm{H} \gtrsim 3 \cdot 10^{23}\,\mathrm{cm}^{-2}$). Moreover, higher column densities, even for sources at significant redshifts, can become difficult to observe due to the Compton scattering of the X-rays to lower energies, which get absorbed more easily.

In any case, a great majority of all AGN types can be tracked by their non-thermal X-ray emission. This led to the discovery of a large number of AGN at a wide range of cosmological distances. Numerous deep surveys in the soft X-ray bands have been performed in the past decades. For a detailed review, see Brandt & Hasinger (2005). Notable entries in the list of past surveys are, for example, the highly localized but extremely deep *XMM-Newton* observations of the Lockman Hole (Mateos et al., 2005), or the *Chandra* Deep Field South Survey (Luo et al., 2017), which revealed around 1000 sources with a density of approximately $5 \cdot 10^4$ sources per square degree, half of them being AGN. The study also showed that a major part of the cosmic X-ray background (CXB) can indeed be resolved into individual sources, with the actual fraction depending on the observed energy band. The first and for the longest time only all-sky survey of all X-ray sources in the soft band was performed by *ROSAT* (Voges et al., 1999, 2000), resulting in the more recent Second *ROSAT* all-sky survey (2RXS) source catalog (Boller et al., 2016), including approximately $7 \cdot 10^4$ high-confidence sources. The largest and most thorough X-ray survey has been started with the eROSITA mission (Predehl et al., 2010; Merloni et al., 2012) with its four-year long all-sky survey (eRASS). The mission is projected to sample at least a few million AGN, as well as 10^5 galaxy clusters and $7 \cdot 10^5$ active stars (Predehl et al., 2021). All-sky data from the hard X-ray regime is comparatively scarce. This is due to a number of factors like a comparatively low detector sensitivity and spatial resolution. In the case of jetted AGN, hard X-rays often fall between both large SED emission bumps, exacerbating the situation. Long-term missions like the *INTEGRAL*/IBIS surveys (Krivonos et al., 2015; Malizia et al., 2016) or the *Swift*/BAT 105-month survey (Oh et al., 2018) cover the entire sky up to a few hundred keV, but at notably lower sensitivities. Figure 1.3.2 shows the result of the *Swift*/BAT survey, consisting of 1632 sources, about half of them Seyfert galaxies and additionally 158 beamed AGN.

The gamma-ray regime can be divided into the HE and the VHE (very-high-energy) parts, with the latter being around 100 GeV to several TeV, where the most energetic photons of extragalactic origin are recorded from blazars and GRBs. Although the general power-law shape of AGN broadband spectra only provides low amounts of photons in the HE and VHE domains, thousands of AGN have been cataloged here. This is mainly due to the intense relativistic beaming of the jets of blazars, which dominate the gamma-ray sky, together with a low number of close-by radio galaxies (Casandjian & Grenier, 2008; Abdollahi et al.,

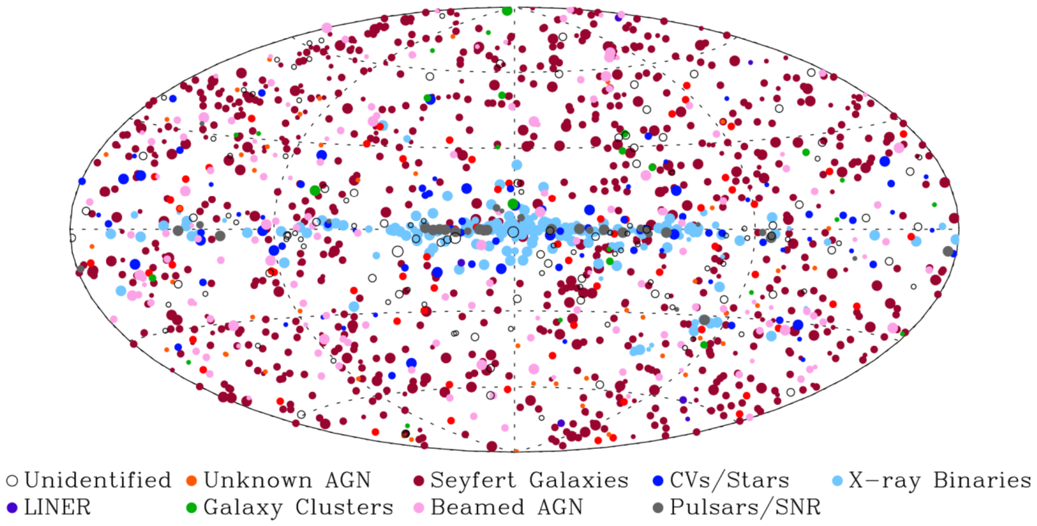

Figure 1.3.2.: Hammer-Aitoff map of the 105-month *Swift*/BAT all-sky survey in Galactic coordinates. The size of the symbols indicates quantity of the flux of the sources in the 14 keV – 195 keV band. Image credit: Oh et al. (2018).

2020). The SEDs of gamma-ray-bright sources show the peak or the declining part of the large HE bump, which is likely due to IC emission in the jet (see Sect. 1.1). While the GeV band has been observed by telescopes on satellite observatories, such as EGRET, *AGILE*, or *Fermi*, TeV energies have become accessible by the use of Imaging Atmospheric Cherenkov Telescopes (IACT) on the ground, like MAGIC or FACT. The largest and most complete catalog of gamma-ray sources in the range of 50 MeV to 1 TeV is the *Fermi*/LAT Fourth Source Catalog (4FGL, Abdollahi et al., 2020), listing 5064 sources, 3207 of them AGN, of which the overwhelming majority are blazars. Like with the *Swift*/BAT all-sky survey, the *Fermi*/LAT all-sky survey was performed blind, meaning without prior data on gamma-ray source positions. In the VHE band, especially above 1 TeV, comparatively few sources have been detected. Because of pair production via the (gamma-ray) extragalactic background light, photons in this part of the spectrum are significantly attenuated. Like in the X-ray band, long-term gamma-ray observation campaigns including the near gap-less measurement of light curves have been made possible by the use of satellite observatories. The Third Catalog of Hard *Fermi*/LAT Sources (3FHL, Ajello et al., 2017), contains 1231 extragalactic sources, detected in the 10 GeV to 2 TeV band, with 1163 of them being blazars or blazar candidates. Of the currently only 89 extragalactic TeV sources that were detected from the ground[6] 82 are AGN, including 77 blazars.

Besides the instrumental selection effects, like the bias towards hard spectra in the LAT detector, a detection in the broad gamma-ray band depends strongly on the position of the SED along the frequency axis, described by the synchrotron peak frequency of the SED. This effect is especially visible at hard X-rays and gamma-rays, where the photon flux from AGN is considerable less compared to, for example, the optical / IR band.

The emission of different AGN populations throughout the electromagnetic spectrum has been shown to follow an evolution on cosmological time scales in numerous studies in the past

---

[6] From the TeVCat webpage, accessed Sep. 2021: `http://tevcat2.uchicago.edu/`

(e.g., Croton et al., 2006; Aird et al., 2015; Caplar et al., 2015). For a comprehensive review on this issue see, for example, Merloni & Heinz (2013) or Brandt & Alexander (2015). The knowledge of the field of AGN evolution on these time scales has changed significantly over the recent decades, driven by new observational tools and more sensitive instruments. With the advent of instruments like *Chandra* and *XMM-Newton* a notable excess of faint sources was found. Furthermore, it is apparent that the evolution of the AGN and the stellar population of the host galaxy are not independent from each other, implying feedback mechanisms of the matter-consuming SMBH. Environmental factors such as the gas temperature and density, which are linked to the host galaxy's state, can therefore induce a time-dependence of the AGN's emission. Even factors like the obscuration and extinction in the inner parts of the AGN might play a role in the evolution with time. For the description of the state and the evolutionary path of an AGN population, the $\log N$-$\log S$ distributions and luminosity functions have become standard tools. In Sect. 3.4 and 3.6 these procedures are introduced in more detail.

1.3.3. The blazar sequence

The double-humped structure of the SED of jetted AGN (Fig. 1.3.1) has been measured for a multitude of sources, which can be categorized according to the position of the SED along the frequency axis. A common metric is the frequency of the synchrotron bump's peak, $\nu_{\rm synch}^{\rm peak}$. This distinction led to the types low-, intermediate-, and high-synchrotron-peaked blazars, or LSPs, ISPs, and HSPs, respectively. Peak frequencies $\nu_{\rm synch}^{\rm peak} < 10^{14}\,\rm Hz$ are labeled LSPs, whereas $\nu_{\rm synch}^{\rm peak} > 10^{15}\,\rm Hz$ denote HSPs, with ISPs in-between. FSRQs are mainly LSPs, whereas BL Lacs tend to cover a wide range of peak frequencies, but are especially characteristic for ISPs and HSPs (Giommi et al., 2012; Ajello et al., 2020). A systematic relation of the SED shape, peak frequency and bolometric luminosity of blazars was found by Fossati et al. (1998) and Donato et al. (2001), and dubbed the blazar sequence. Thereafter, the blazar SEDs with lower bolometric luminosity are high-peaked and vice versa. Additionally, the ratio of HE to synchrotron peak heights in the $\nu L_\nu - \nu$ format (Compton Dominance, CD) is higher for lower-peaked sources. According to the shifting of the SED, the spectral indices in a given band change, with, for example, harder indices in the X-rays for lower luminosity / high-peaked blazars. This phenomenon was theorized by Ghisellini et al. (1998) to be caused by the cooling of the electron populations that emit the observed spectrum, where the different amount of the cooling depends on the individual source. In this context, the lower peak frequencies of FSRQs stem from a stronger cooling compared to BL Lacs.

Ghisellini et al. (2017) argued that the blazar sequence could originate from a sequence of accretion rates, dividing blazars into radiatively efficient and inefficient cases. One major argument in past studies has been whether the observed relations are actually caused by survey selection effects, despite unprecedentedly sensitive instruments and deep surveys (e.g., Perlman et al., 2001; Ghisellini & Tavecchio, 2008; Giommi et al., 2012). In a more recent work, Ghisellini (2016), employing the *Fermi*/LAT 3LAC survey catalog, generally confirm the properties of the blazar sequence, but also show that the SEDs of low bolometric luminosity are a mix of FSRQs with low black hole masses and BL Lacs with high black hole masses. For a more in-depth review of the historic developments of the blazar sequence see, for example, Ghisellini et al. (2017). In their study, the authors introduce a variant named the Fermi blazar sequence, a systematic anti-correlation of $\nu_{\text{synch}}^{\text{peak}}$ and the gamma-ray luminosity derived from the sizable 3LAC sample of gamma-ray-bright blazars. The analysis of fitted SEDs showed that the SED shape of FSRQs largely stays the same while having a relatively small range of $\nu_{\text{synch}}^{\text{peak}}$, producing harder X-ray spectra for higher luminosities. BL Lacs exhibit a much broader parameter space in this regard, showing increased luminosity for lower peak frequencies. Since large luminosities are almost exclusively given by FSRQs and lower ones by BL Lacs, the sequence harbors a wide dynamic range, reminiscent of the original blazar sequence, although with less extreme slopes in the gamma-rays.

The blazar sequence and its validity are still a matter of hot debate, trying to unite the different cases of rather extreme blazar sub-types and the general idea of a unified AGN model (see, e.g., Meyer et al., 2011; Boula et al., 2022; Keenan et al., 2021)

1.4 Context and outline

Active galactic nuclei have been studied at all accessible wavelengths, with large surveys cataloging millions of individual sources all over the sky. By far, the energy regime in which AGN have been observed the least are the hard X-rays / soft gamma-rays, above roughly 10 keV. Here, the numbers of detected AGN, especially blazars remains comparatively low, with only a few hundred listed in recent catalogs. In this thesis a detailed analysis of the spectral and statistical properties of pre-defined blazar samples in the hard X-ray band is performed to address the following main points:

- What are the spectral properties of a statistically complete blazar sample that is not selected at hard X-rays?
- What are the main reasons for the low detection statistic of blazars in this energy band and what role does blazar evolution play?
- Do known bright blazars exhibit significant hard X-ray emission at lower flux thresholds than those in the recent survey catalogs?
- In what way do these blazars contribute to the hard X-ray background?
- Are the spectral characteristics as well as the overall signal strength dependent on the wavelength at which the object samples are compiled?
- Can the derived spectral parameters be utilized to classify beamed AGN of yet unknown type?

In order to approach these issues, the *Swift*/BAT hard X-ray 105-month all-sky survey data set is processed and analyzed in the 20 keV to 100 keV band. Chapter 2 introduces the relevant observing instruments and source monitoring programs, while Chpt. 3 focuses on the data retrieval, reduction and analysis steps. The hard X-ray data products of the statistically complete radio-selected MOJAVE-1 AGN sample are presented and discussed in Chpt. 4, which is also expanded to the larger MOJAVE-1.5 sample, providing a comprehensive radio-bright AGN sample on the Northern and parts of the Southern hemisphere. The TANAMI sample of the corresponding AGN radio monitoring program on the Southern hemisphere completes the sky coverage. Its X-ray sample analysis is presented in Chpt. 5. Lastly, the sizable *Fermi*/LAT 4LAC AGN gamma-ray catalog is analyzed and compared with the data sets obtained from the radio samples in Chpt. 6. A summary and conclusions are given in Chpt. 7, followed by the appendices A (table of 4LAC X-ray results), B (BAT spectra), and C (supplementary studies). The latter includes a short summary of other studies that I was involved in during the work on this thesis, which employed the processing and interpretation of *Swift*/BAT data.

2. Observing instruments and detectors

Since beamed AGN can be registered over most of the accessible electromagnetic spectrum, a great many types of instruments and telescopes are required to cover this extremely wide range, from radio waves up to TeV energies in the gamma-ray domain. In this chapter, the instrument types which are most relevant to this work are introduced, but with a focus on the hard X-ray regime and the *Swift*/BAT coded-mask aperture telescope.

Observations of beamed AGN jets at very high resolutions are facilitated by arrays of radio telescopes, which also define the AGN survey samples that are the basis of this work. In Sect. 2.1, the fundamental principles and measurement techniques of single radio antennas and interferometric arrays as well as the monitoring campaigns MOJAVE and TANAMI are introduced, which provide not only radio flux monitoring of selected sources, but the foundation for such data products as jet speed, variability indices, or Doppler factors. Detectors that operate in the X-ray regime and even higher at GeV and TeV energies operate fundamentally different than the observatories at the opposite side of the spectrum. Whereas radio antennas process the observed signals via their wave-like characteristic, X-ray and gamma-ray instruments detect individual photons. X-ray detection and imaging are discussed in more detail in Sect. 2.2, with an emphasis on the data reduction from the Burst Alert Telescope (BAT) and the *Neil Gehrels Swift Observatory* (Sect. 2.3), on which it is mounted. The Large Area Telescope (LAT) of the *Fermi Gamma-ray Observatory* is also briefly covered (Sect. 2.4).

2.1 Radio instruments and AGN monitoring

The radio regime, which is accessible with current instruments, is an exceptionally wide band, from a few meters of wavelength (tens of MHz) down to 1 millimeter (300 GHz). Consequently, the field offers many applications in the context of astronomical research, such as the observation of thermal processes like free-free emission and line emission, for example, the 21 cm line from neutral hydrogen, as well as non-thermal ones, like the synchrotron radiation of charged particles in magnetic fields. Many astronomical objects have been probed by the use of radio telescopes, such as supernova remnants, pulsars, active galactic nuclei, or the cosmic microwave background (CMB). The following section outlines the basic principles of radio observation using a single radio telescope as well as the 2-element interferometer, which can be generalized to even bigger arrays. After, the MOJAVE and TANAMI AGN monitoring programs are introduced.

2.1.1. Fundamental workings of a radio telescope and interferometry

Radio antennas come in many shapes an sizes, which is due to the observed frequency bands, and their modes of operation. In its simplest version a radio telescope is a dipole antenna, whose gain characteristic depends on its orientation. Large parabolic telescope dishes are used to track targets along their path across the sky while providing a large collecting area. Finally, the simultaneous use of interferometric telescope arrays across the globe achieves the best angular resolutions of all current telescope types in astronomy. This section largely follows the introductory chapters in Burke & Graham-Smith (2010).

The spectral distribution S_ν of the observed flux S is the energy per time and area that is received[1]. Because of the angular extend of sources the specific brightness $B_\nu(\theta, \phi)$ for spherical coordinates can be defined, which is the flux per unit solid angle per frequency interval. Thus, the total flux is:

$$S = \int \int B_\nu(\theta, \phi)\ d\Omega\ d\nu. \tag{2.1.1}$$

The sensitivity of single aperture telescopes is proportional to the collecting area, whereas the angular resolution depends on the size of the telescope. However, due to mechanical limitations, the largest current (steerable) reflector dishes are around 100 m in diameter, such as the Effelsberg Radio Telescope or NRAO's Green Bank Telescope. The aperture of radio telescopes is realized by a reflector, horns/waveguides and the receiver dipoles. The telescope power gain G is the equivalent of the instrument response or point spread function (PSF) and exhibits a primary beam and weaker so-called side-lobes that define the field of view. This pattern follows the Airy function, producing zero gain outside the main beam at:

$$\sin\theta = 1.22\,\lambda/D, \tag{2.1.2}$$

for circular apertures of the size D at the wavelength λ. This relation determines approximately the angular resolution of the instrument (Rayleigh criterion). For example, this gives an angular resolution of 0.8' for a 100 m telescope observing at 15 GHz / 2 cm. Large arrays of radio telescopes are able to achieve significantly higher angular resolutions. In the following, the 2-element interferometer for observing astronomical objects at large distances is described, whose working is transferable to larger multi-element arrays.

A Michelson or 2-element interferometer consists of two radio antennas, which observe the same object (Fig. 2.1.1, left) in the direction $\boldsymbol{s}$. The vector $\boldsymbol{b}$ is called the baseline between both instruments. The geometrical lag of the received signal can be expressed by the corresponding time lag τ. Receiving signals from at least two detectors causes interference, the so-called fringe-pattern, and is characterized by an amplitude and phase. The goal is to obtain the fringe amplitude, which is achieved by cross-correlating the amplitude of both signals while taking into account the time delay τ. It is advantageous to define a reference direction $\boldsymbol{s}_0$, also called the phase tracking center, whereas a source has a distance of $\boldsymbol{\sigma}$ to the phase tracking center, that is, $\boldsymbol{s} = \boldsymbol{s_0} + \boldsymbol{\sigma}$. The total time delay is composed of the geometric delay and a component for the individual off-center source, and thus, $\tau = \tau_\mathrm{g} + \tau_\mathrm{i}$. The total correlator output is the cross spectrum power density and can be written as follows:

$$S(\boldsymbol{s}_0) = \int_{4\pi} A(\sigma)\, B_\nu(\sigma) \exp\left[i 2\pi (\boldsymbol{b}_\lambda \cdot (\boldsymbol{s}_0 + \boldsymbol{\sigma}) - \nu\tau_\mathrm{i})\right]\, \mathrm{d}\Omega, \tag{2.1.3}$$

with the relative antenna area A (1 for $\boldsymbol{s}_0$), the specific brightness $B_\nu(\sigma)$ of the source element at $\boldsymbol{s}$, and the baseline vector $\boldsymbol{b}_\lambda$ in units of wavelength λ. This quantity is also known as the complex visibility V, which is the Fourier transform of antenna area and specific brightness. In multi-element arrays with N antennas, there are $N(N-1)/2$ individual baselines $\boldsymbol{b}_{\lambda,ij}$.

---

[1] This quantity is also called the flux density, and is usually given in Jansky; $1\,\mathrm{Jy} = 10^{-26}\,\mathrm{W\,m^{-2}\,Hz^{-1}}$.

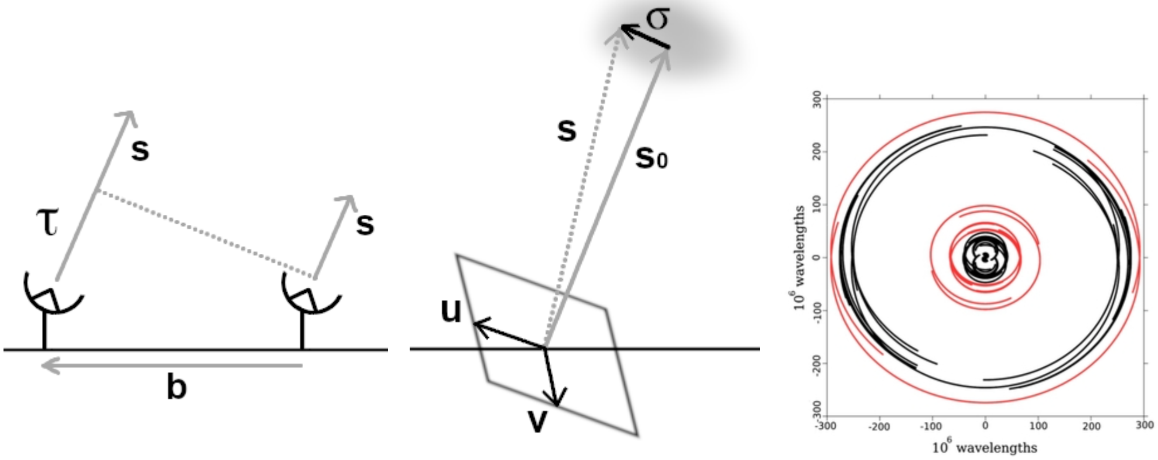

Figure 2.1.1.: Left: Concept of 2-element interferometer, comprising two antennas with the baseline $\boldsymbol{b}$, observing the same source in the direction $\boldsymbol{s}$. The geometric lag is expressed by the time lag τ. Middle: Schematic of the array observing a source in the reference direction $\boldsymbol{s}_0$ and distance $\boldsymbol{\sigma}$. The u, v-plane is oriented perpendicular to the reference direction. Right: illustrative u, v-plane coverage of a 12-hour long observation of the source 1934–638 with the WARK30M telescope (New Zealand) and two Australian radio telescopes Hobart 26-m and Ceduna 30-m (Petrov et al., 2015).

The correlator response exists in the so-called u, v-plane, which is parallel to the baseline vector $\boldsymbol{b}_{\lambda,ij}$ and the offset vector $\boldsymbol{\sigma}$ and perpendicular to the source direction (Fig. 2.1.1, middle). The actual source brightness distribution is obtained by the inverse Fourier transform of the interferometer output (brightness distribution in the u, v-plane). One measurement equals one complex Fourier component. Therefore, many observations cover a higher portion of the u, v-plane, and extended observations with telescope arrays (aperture synthesis array) produces baselines that change their length and orientation because of the Earth's rotation, resulting in an even higher coverage, see Fig. 2.1.1. Besides local arrays like the VLA (resolution of 0.1”, 15 GHz), VLBI (Very Long Baseline Interferometry) offers the best achievable angular resolutions of milliarcseconds and below by collecting data from observing stations thousands of kilometers apart. After the calibration of the recorded visibilities, an analysis chain, the CLEAN algorithm (Högbom, 1974), produces a final “clean” map with the unit of intensity of Jy/beam. This process involves the iterative (partial) subtraction of sources from the initial “dirty” map in order to remove all components due to the sidelobes. All identified source components are added to the map and convolved with a Gaussian approximation of the beam, producing the final image.

2.1.2. The MOJAVE and TANAMI programs

An essential part of the study of the powerful AGN jets on pc scales has been facilitated by VLBI techniques, providing resolutions in the GHz regime down to milliarcseconds. In order to restrict parameters of jet models, individual measurements are carried out by the VLBA (Very Long Baseline Array) of the NRAO (National Radio Astronomy Observatory) in the Northern hemisphere. Since its inception in the 1990s, numerous interferometric arrays in the MHz and GHz bands like the expanded VLA (Karl G. Jansky Very Large Array Perley

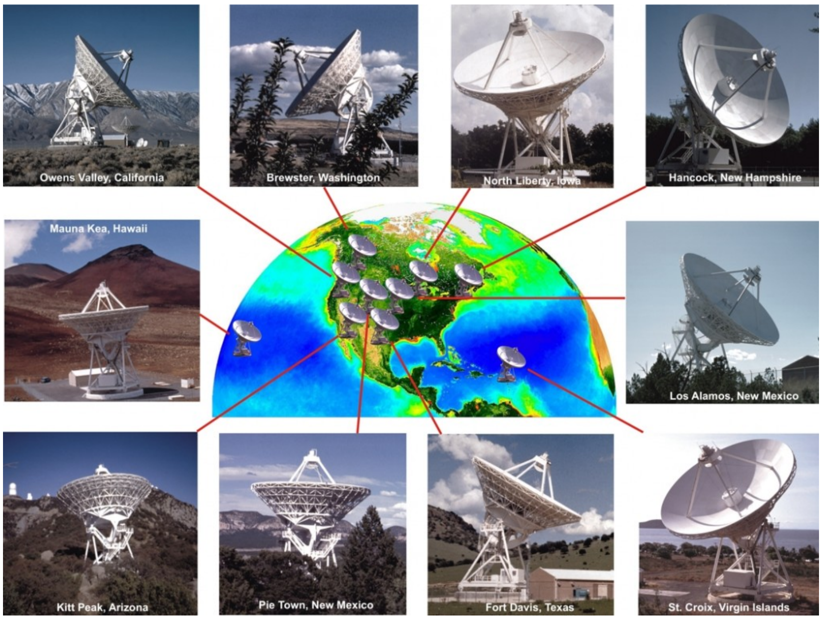

Figure 2.1.2.: Arrangement of the radio telescopes of the Very Long Baseline Array. Image rights: NRAO/AUI and Earth image courtesy of the SeaWiFS Project NASA/GSFC and ORBIMAGE.

et al., 2011) ALMA (Atacama Large Millimeter/submillimeter Array, Wootten & Thompson, 2009), and LOFAR (Low Frequency Array, van Haarlem et al., 2013) began operation.

The first major AGN survey using the VLBA was the 2 cm survey (Kellermann et al., 1998), which was carried out from 1997 to 2002, observing more than 150 AGN with the goal of studying the jet kinematics of a larger source sample. This survey, however, did only focus on the total intensity in the given waveband, and did suffer from statistical incompleteness regarding beamed jet emission (Lister & Homan, 2005). As its successor, the MOJAVE program (Monitoring Of Jets in Active galactic nuclei with VLBA Experiments, Lister et al., 2018), was build upon the previous survey with the intent to study the evolution of magnetic fields and the polarization in a large radio-loud sample at 15 GHz. The source sample is considered statistically complete. Further goals of the program are the investigation of jet kinematics and the subsequent relations between characteristics like jet power, variability, or the gamma-ray brightness.

Observations of the long-term campaigns are performed every couple of months up to every year, depending on the speed of moving components in the jets. The consistent observation of larger samples enables the study of a wide range of sources of different optical classifications, that is, FSRQs, BL Lacs, or radio galaxies and other non-blazar AGN regarding their radio luminosity and kinematic jet parameters. Most jet features have been found to be superluminal with changes in speed within the jet (Homan et al., 2015), while on pc scales Lorentz factors of up to 50 are indicated (Lister et al., 2016). During its operation, the MOJAVE program monitored several hundred AGN over 2/3 of the sky, which have been compiled into different samples and of which a large part is not observed regularly at the present time. In this work, primarily two object samples of the MOJAVE program are investigated. The first one, the MOJAVE-1 sample, was initially composed of the 133 radio-loudest AGN in the Northern hemisphere, down to a declination of $\delta = -20°$, and above the Galactic plane ($|b| \geq 2\overset{\circ}{.}5$) (Lister & Homan, 2005). At any epoch, starting 1994.0 and until 2004.0, a sample source's flux density was required to be at least 1.5 Jy and at least 2 Jy below the celestial equator. The sample was later extended by two additional sources, that were found during the processing of archival data and that met the selection criteria (Lister

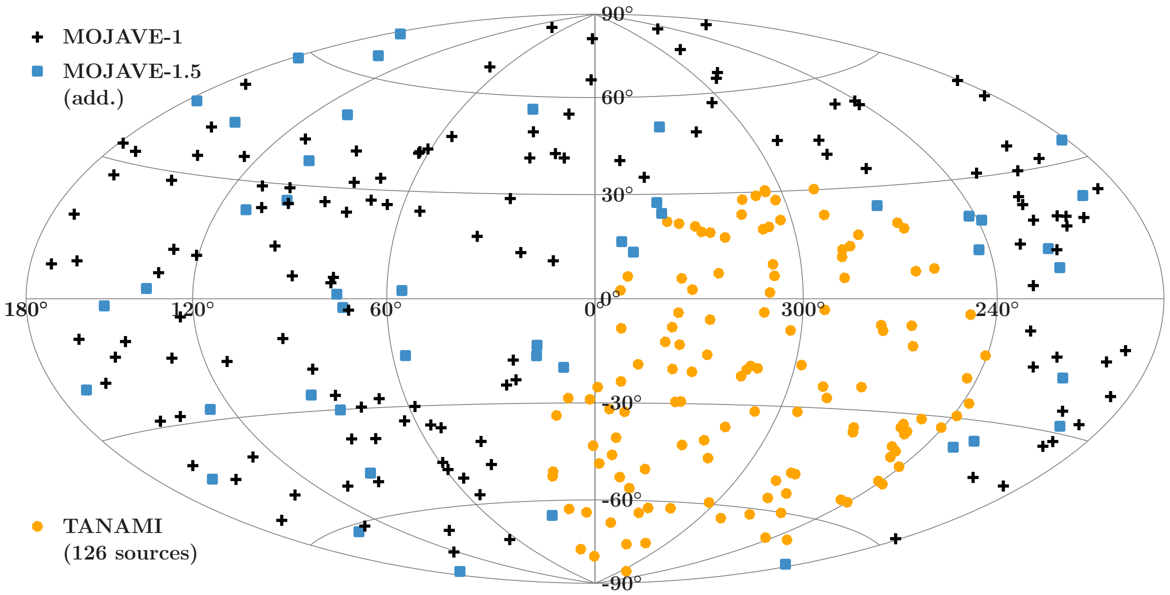

Figure 2.1.3.: Hammer-Aitoff projection of the sky in Galactic coordinates. Plotted are the MOJAVE-1 AGN sample, the extended MOJAVE-1.5 sample (only additional sources relative to MOJAVE-1 sample are shown), and the TANAMI sample (version of 2020 with 126 sources).

et al., 2009a). The second object sample is the larger MOJAVE-1.5 sample, including the Galactic plane and all radio-loud sources down to $\delta = -30°$ with a uniform flux density requirement of 1.5 Jy, yielding 181 sources (Lister et al., 2013). For a more detailed description of the samples including their composition, see Sect. 4 and Sect. 4.3. Figure 2.1.3 shows the MOJAVE samples plotted in a Hammer-Aitoff projection. Later samples targeted further AGN populations, like the hard spectrum gamma-ray-loud AGN sample (129 sources) or the complete Fermi flux-limited sample (1FM, 116 sources, Lister et al., 2011).

Introduced as a complementary program to MOJAVE, TANAMI (Tracking Active Galactic Nuclei with Austral Milliarcsecond Interferometry, Ojha et al., 2010) monitors a sample of more than 100 AGN jets below the declination of $\delta = -30°$. It incorporates data from the Australian Long Baseline Array (LBA) and several other telescopes in Australia, South Africa, New Zealand, Argentina, and Antarctica at the frequencies of 8.4 and 22.3 GHz. A radio flux monitoring program at frequencies of 4.8 GHz to 40 GHz is additionally carried out by ATCA (Australian Telescope Compact Array). Based on the first observation epoch in 2007, the initially compiled source sample consisted of most of the radio-loud jets in the Southern sky that were also gamma-ray detections or candidates. Besides the monitoring of AGN jets at radio wavelengths as well as determining their spectral indices and their change with time, the program aims to coordinate and gather comprehensive multiwavelength data, from NIR/optical to UV/X-ray and gamma-ray measurements, especially for sources that are bright in the GeV band. A number of instruments like the REM telescope, the TNG telescope, or the Nordic Optical Telescope observe in the NIR/optical regime, while the UV/X-ray bands are covered by satellite observatories, such as *Swift*, *XMM-Newton*, *Suzaku*, and *INTEGRAL*. A continuous all-sky monitoring of the gamma-ray sky is performed by *Fermi*/LAT in the 100 MeV to 300 GeV band.

Later additions of further sources to the most recent sample are described in detail in

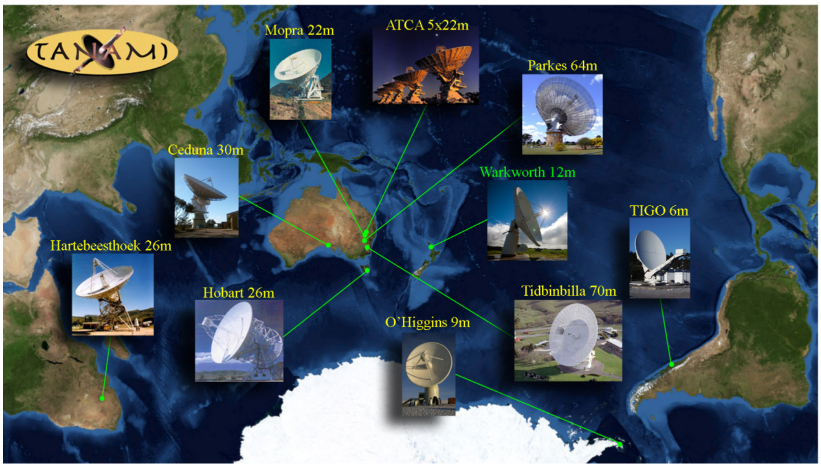

Figure 2.1.4.: Telescopes of the TANAMI array in the Southern hemisphere. Image rights: M. Kadler & J. Wilms.

Sect. 5. In this work the TANAMI sample version of 2020 is used, counting 126 sources, with a majority of them being blazars. The sample is also graphed in Fig. 2.1.3. Early results from the program include, for example, the finding that gamma-ray brightness correlates with the jet's morphology (Ojha et al., 2010) and the detailed high-resolution imaging and kinematic analysis of the nearby radio galaxy Centaurus A (Müller et al., 2014). One of the primary goals of the program is to provide quasi-simultaneous multiwavelength data of beamed and mis-aligned AGN, which is essential for fitting physical models (e.g., leptonic vs. hadronic emission) to the broadband SEDs, taking into account the significant short- to long-term variability of these sources. One specific application of the TANAMI data coverage is, for example, the study of the correlation of high-energy neutrino events with the emission characteristics throughout the electromagnetic spectrum (e.g., Krauß et al., 2014).

2.2 X-ray telescopes and imaging

Earth's atmosphere is opaque to X-rays and thus the collection of X-ray photons is restricted to observatories in space and balloon experiments in the upper atmosphere. Imaging astronomical objects in the X-ray band, spanning approximately 0.1 keV–100 keV, is related to many concepts from optical astronomy. The usage of charge-coupled devices (CCDs) as direct imaging instruments in the focal plane, as well as for the measurement of spectral information, has similarities with the optical band. Significantly different technical solutions are however required for the part of focusing the X-ray light onto the detector assembly (see Sect. 2.2.1 and 2.2.2). There are furthermore a number of different X-ray detector types (Sect. 2.2.3) in space observatories for specialized applications, like high spatial resolution or spectroscopy. The most common X-ray imaging concepts that are in use today are introduced in the following. This section is based on Arnaud et al. (2011).

2.2.1. Focusing X-ray optics

In order to measure physical information from the emitted X-rays by imaging or spectroscopy the incident X-rays that pass through the aperture of the instrument need to be focused on the detector plane. Due to the large energy of X-ray photons, they have the property to be generally absorbed or fully transmitted by metallic mirrors for large angles

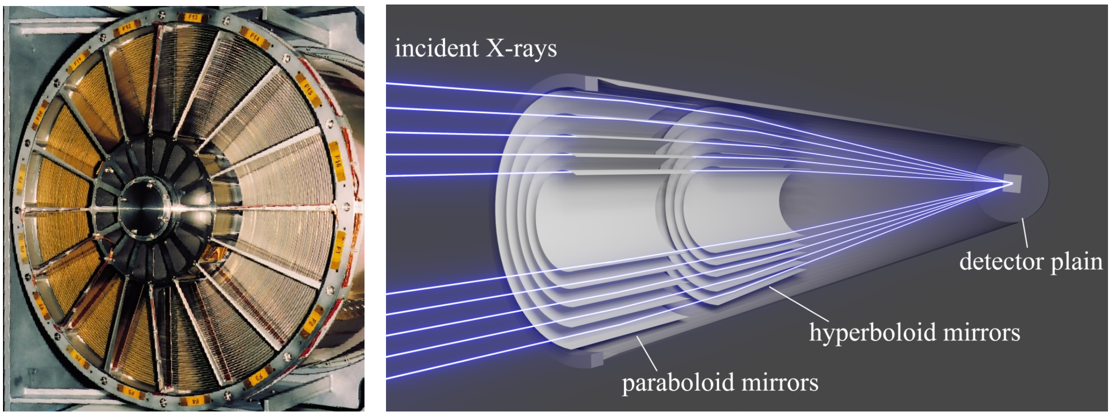

Figure 2.2.1.: Left: Focusing optics mirror module of *XMM-Newton*, image credit: ESA, right: Wolter-1 telescope architecture with co-axial paraboloid and hyperboloid mirror elements and the light path.

between the incident light path and the mirror surface. The focusing of X-rays at lower energies / the soft X-ray band ($\lesssim 10\,\mathrm{keV}$) is instead facilitated by the total external reflection of the incident X-ray light. Therefore, focusing optics need to use reflective surfaces at shallow angles (grazing incidence). The reflection of a photon from vacuum on the mirror material is governed by the complex refractive index,

$$n = 1 - \delta + i\beta, \tag{2.2.1}$$

with imaginary unit i and the optical constants δ and β, typically for X-rays in the range of 10^{-5} and 10^{-6}, respectively (Atwood & Sakdinawat, 2017). Thus, the real part of the refractive index, which describes the reflected part of in incident wave, becomes slightly smaller than 1, allowing total external reflection from vacuum on the metallic mirror material. Using Snell's law and assuming total reflection, a critical incident grazing angle θ_c can be found, that is proportional to the square root of the atomic number Z and inverse proportional to the photon energy E:

$$\theta_c \sim \sqrt{Z}/E, \tag{2.2.2}$$

where the critical angle θ_c is defined as the maximum angle of the incident X-rays to the mirror surface for which total external reflection occurs. For typical soft X-ray energies elements with high atomic numbers, which are also easy to apply on the substrate material of the mirror's surface, like gold, iridium, or platinum are used, resulting in grazing angles in the range of about 0.5°–1°. To ensure a large collecting area and adequate FOV, the reflective surface is constructed in a paraboloid shape. Multiple layers are nested in each other (see Fig. 2.2.1). Depending on the specific so-called Wolter-type mirror structure, the X-rays are then reflected onto the focal point on the detector plane by another set of nested mirrors that are hyperboloid or ellipsoid in shape. Many X-ray observatories also include a grating array in the light path, which diffracts the X-rays onto a separate detector that measures the spectrum of the incident light.

In order to also effectively reflect X-rays at higher energies than around 10 keV using the same Wolter structure, multi-layer mirrors have been used in the past. Normally, extremely low grazing angles for highly energetic X-rays are impractical. However, using high-Z and low-Z materials that are applied to the substrate alternatingly several times many coherently reflecting beams can be created. This construction method has for example been used in the optics of the *NuSTAR* satellite observatory (Harrison et al., 2013). A different approach for the tracing and imaging of hard X-ray photons is the introduced in the following section.

2.2.2. Coded mask aperture systems

While focusing incident X-rays stops to be technically feasible at higher energies, a different approach has been implemented in many astronomical instruments since the 1960s. Due to its compact construction and large field of view the coded mask aperture system has been used in early rocket and balloon experiments that imaged the sky from several keV to MeV[2]. Modern instruments on satellite observatories utilize one of several optics configurations to provide wide-field coverage of the hard X-ray and low-energy gamma-ray sky. Currently operating X-ray telescopes that make use of coded mask aperture systems are, for example, *Swift*/BAT, *INTEGRAL*/IBIS, SPI, JEM-X, and *AstroSat*/CZTI. The following description is based on in't Zand (1992) and in't Zand (1996).

The basic idea of a coded mask system is the detection of an X-ray source through a pinhole aperture. The effect, thereby, is additive for multiple sources in the field of view. In order to receive the directional information of the X-ray light and retain a high signal to noise ratio a mask with a unique pattern of opaque and transparent elements instead of a single hole is used. Usually, the area that is occupied by both the opaque and transparent elements is close to 50%. The created additive pattern of several light sources, which is encoded by the mask, is transformed back to the original signal, that is, the distribution of X-ray photons in the instrument's FOV. Figure 2.2.2, left, illustrates this additive technique of the coded aperture system, also known as spatial multiplexing. The strength of every image that is cast on the detector reflects a source's X-ray count rate. Unlike focusing optics, the signal of a point source is always influenced by all other sources that are imaged on the detector. Once a certain exposure time is reached the accumulated pattern of multiple sources can be decoded and the strength of every possible cast pattern and corresponding direction of illumination determined.

The performance of the imaging system depends on the configuration of the coded mask itself: every possible direction of a light source needs to have a unique encoding. This means than the mask needs to be of a non-repeating and unique pattern, equivalent to a autocorrelation function of the pattern that is a delta function. The generation of these patterns is based on cyclic difference sets, which have been described by Gunson & Polychronopulos (1976) and Fenimore & Cannon (1978). Figure 2.2.2, right, shows the difference between fully and partially coded imaging. The autocorrelation characteristic only remains a delta function in the case of fully coded exposure. Imaging using a partially coded field of view, meaning only a fraction of the coded mask that is projected onto the detector, introduces sidelobes into the autocorrelation function and consequently more noise into the image signal.

In practice, simple optics configurations using collimators on top of the detector plane can be applied, as well as a configuration featuring shielding around the detector space from X-rays and high-energy particles that do not originate in the field of view of the instrument. A basic condition for the optimal function of the coded mask telescope is that the detector pixel size needs to resolve at least the individual projected coded mask elements. In practice

---

[2] `https://universe.gsfc.nasa.gov/archive/cai/coded_inss.html`

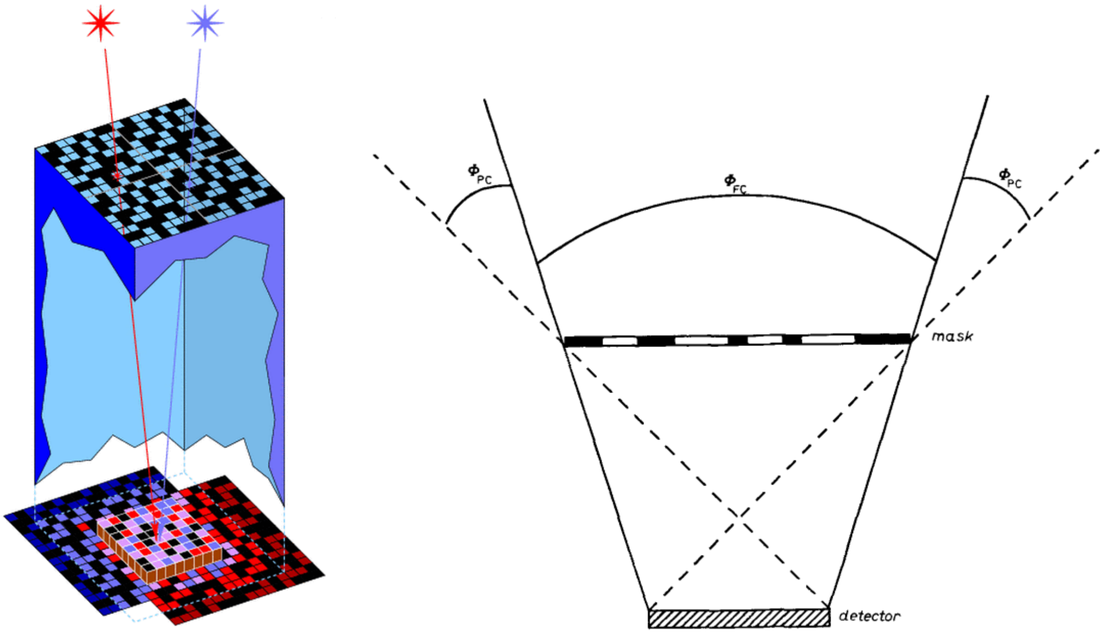

Figure 2.2.2.: Left: Illumination of a coded mask aperture system by two separate sources, image credit: ISDC/M. Türler, right: fully and partially coded fields of view in the coded mask aperture instrument, indicated by the angles Φ_{FC} and Φ_{PC}, respectively, image credit: Caroli et al. (1984)

Figure 2.2.3.: Left: Coded mask aperture of the *Swift* BAT imager, image credit: NASA/Goddard, right: hexagonal coded mask of the *INTEGRAL* SPI spectrometer, image credit: INTA, Spain.

the geometry of the mask and the fraction of number of mask tiles to detector elements is often governed by limitations in spacecraft design. A more detailed discussion of coded mask optics configurations can be found in Hammersley et al. (1992). Different mask patterns have distinguishing properties like angular resolution, sensitivity, background suppression, and the observable energy band. Often-used patterns are so-called uniformly redundant arrays (URA) forming a checkerboard or hexagonal structure (Fig. 2.2.3). A number of instruments, like *Swift's* Burst Alert Telescope, use a optimized random pattern (see Sect. 2.3.2).

The registered distribution of light, the so-called shadowgram D on the detector, can be described by the convolution of the aperture mask A and the true sky image / signal S plus a signal-independent background noise component B. Following the description of Caroli et al. (1987), the registered signal on the detector can be expressed as:

$$D = A \otimes S + B, \tag{2.2.3}$$

which can also be written in discrete form as a correlation:

$$D_{jk} = \sum_l \sum_i A_{j+l,k+i} S_{li} + B_{li}. \tag{2.2.4}$$

The entries of the aperture mask A are either 1 for transparent or 0 for opaque mask elements. In order to reconstruct the true signal S a decoding function G can be applied:

$$S' = G \otimes D, \tag{2.2.5}$$

so that the estimate S' of the signal S is

$$S' = G \otimes A \otimes S + G \otimes B. \tag{2.2.6}$$

This expression of S' can also be written in the discrete case as a cross correlation of the matrix G with D:

$$S'_{jk} = \sum_l \sum_i G_{j+l,k+i} D_{li}. \tag{2.2.7}$$

To preserve the true image features within the system's resolution the cross correlation $G \star A$ must be as close as possible to a delta function, which gives:

$$S' = S + G \star B, \tag{2.2.8}$$

where the second term is constant and independently measurable. The true sky image S can then easily be determined using Eq. 2.2.5 and Eq. 2.2.8. There are a number of choices for the specific construction of the decoding matrix G depending on the fraction of transparent to opaque matrix elements and the overall transparency of the mask (see Caroli et al., 1987). Because this approach involves a weighting of the opaque elements, it is often referred to as balanced correlation.

Furthermore, there are a range of other reconstruction methods for the coded mask image: a straight-forward approach is the deconvolution by Fourier transformation of Eq. 2.2.6, reducing the convolution to a multiplication. However, this method is generally not preferred because of significant noise amplification due to small values in the Fourier transform of A. Even for high-S/N signals the image can undergo major degradation. If the number of detected photons with respect to the number of mask elements is low or if only a fraction of the observed sky is to be observed, the process of a backprojection can also be performed. In this special case the procedure can be computationally less expensive than the often used cross correlation method. Here, the path of each photon is reconstructed individually, assigning it to the source signal, should the path coincide with an open mask element, and to the background if it does not. Several iterative processes, such as the Maximum Entropy Method (MEM), are also available for the image reconstruction. MEM has found numerous applications in image reconstruction of badly degraded signals and was later applied to coded mask systems (Willingale, 1979). The process requires the maximization of an entropy function, which includes a minimum of information, or, in other words, only the required data that is needed to fit the observed image. Also, the reconstruction creates a minimum of image artifacts. On the other hand, iterative methods are generally more computationally intensive than a cross correlation.

2.2.3. X-ray detectors

Decades of imaging applications in the X-ray band led to a number of different detector concepts: The most simple detector for X-ray photons is the proportional counter, consisting of a medium, for example a gas, that is ionized by the X-ray photon. The created electrons/ions are drawn to an anode/cathode under high voltage, where the registered signal height is proportional to the energy of the photon. Scintillation counters include a gas or more often a high-Z material, like NaI or CsI, that absorb the X-ray that ionizes atoms, which then recombine and emit a flash of optical light. This signal can then be amplified by the use of photomultiplier tubes. An application of this technique for the detection of gamma-rays is employed in the *Fermi*/LAT instrument (Sect. 2.4). Very similar in working to photomultipliers are microchannel plates, which are composed of a large number of parallel micrometer-sized channels. In-falling photons liberate single electrons, which produce a cascade of electrons in a microchannel, that are accelerated by a high voltage to be registered by a position-sensitive readout assembly. *Chandra*'s HRC sensor, for example, utilizes a microchannel plate. One of the newer developments for X-ray detectors are the transition edge sensors (TES, see, e.g., Bastia, 2019). This detector type consists of an array of highly temperature-sensitive microcalorimeters, made of a superconducting material. The individual pixels are held at the transition temperature between the superconducting and the normal state. The temperature increase through the absorption of X-rays changes the resistance significantly, facilitating a very high spectral resolution. The mission concept for the future X-ray observatory Athena (Barret et al., 2018) includes the cryogenic microcalorimeter array X-IFU for the soft X-ray band.

One of the most used detector systems in astronomy from the IR to the X-rays, however, is the charge-coupled device (CCD), which is placed on the focal plane of the instrument to measure the collected light. In this section the most relevant detector types for the used X-ray data in this work are introduced, that is, CCD sensors and CZT detectors for higher energies. The following description is based on Howell (2006) and McLean (2008). For the soft X-ray part of the spectrum (0.2 keV – 10 keV) and lower energy domains, CCDs, or charge-coupled devices, have been the go-to solution for decades in astronomy. This includes both imaging and spectrographic measurements alike. The spatial resolution that is required is facilitated by an array of pixels of semiconductor material, like doped silicon. Incident light generates a signal through charge separation in a pixel. The absorption of a photon

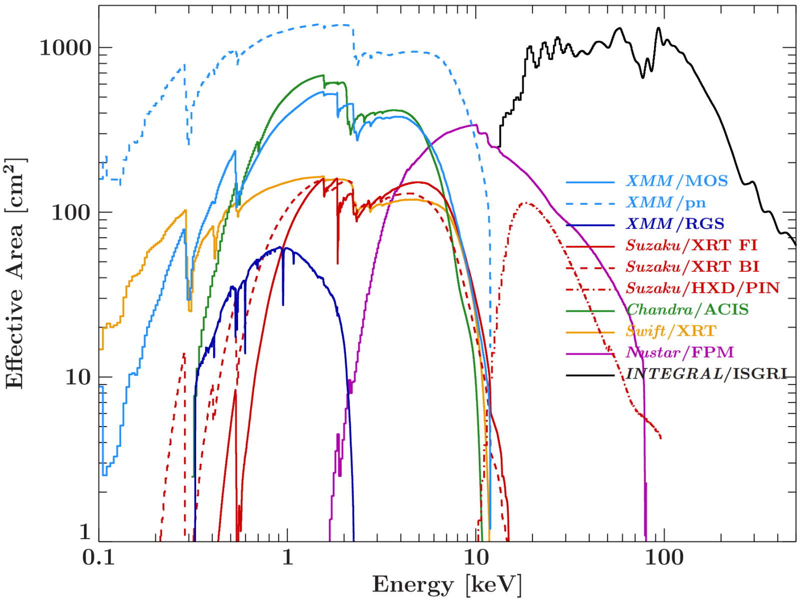

Figure 2.2.4.: Effective area of currently operating X-ray telescopes, image credit: Beuchert (2017)

creates an electron-hole pair, where the electron has an energy of:

$$E = h\nu - b, \tag{2.2.9}$$

with the photon frequency ν and the electron binding energy b. The electron then collides with other orbital electrons of silicon atoms in the detector pixel, creating other electron-hole pairs, which each require on average 3.65 eV to be separated. The resulting charge cloud can be distributed over several pixels depending on the point of impact in the pixel (see, e.g., Tsunemi et al., 1999). The electrons are raised into the conduction band of the semiconductor and can be transferred. A fraction of the energy of the photon is also transferred into the crystal lattice structure of the detector material, leading to a certain variance in electron-hole pairs that can be created per incident photon. This limits the photon energy resolution of the detector and is expressed by the Fano factor F, which is approximately 0.1 for silicon. The FWHM of the energy uncertainty δE is proportional to the square root of F and the photon energy E:

$$\delta E = 2.355 \left(\frac{F\,E}{3.65}\right)^2 . \tag{2.2.10}$$

In order to measure the created charge separation the electrons are stored in a potential well of each pixel. Then, the charge of one pixel is transferred via an applied voltage to the neighboring pixel and so on to the readout electronics, where the output amplifier and analog/digital converters produce a digital signal. Either the number of counts or analog-to-digital units (ADU) are then stored in the instrument's memory. After the entire CCD is read out sequentially the detected distribution of incident photons, that is, the image, can be reconstructed.

The ability of a CCD to register and output a photon signal compared to the number of incident photons is expressed by the quantum efficiency QE of the detector. Modern X-ray CCDs have a high QE, although this characteristic depends on the precise photon energy. The EPIC PN sensor of the *XMM-Newton* X-ray observatory, for example, reaches more than 95% over most of the soft X-ray band. Amongst other factors, the QE depends greatly on the thickness of the detector layer. The photon absorption length is a function of the incident wavelength because more energy-rich photons create larger numbers of electron-hole pairs within the medium. Both the QE and the X-ray mirror effective area, which focuses the X-ray light, determine the effective area of the detector. Also, X-ray telescopes often feature filters that reduce contamination by IR, optical, and UV light. Figure 2.2.4 shows the effective area of CCDs of several currently operating X-ray observatories as a function of photon energy. While a number of instruments like *XMM-Newton* or *Swift*/XRT work primarily in the soft X-ray band, up to approximately 10 keV, different sets of optics and sensors are specifically constructed to exceed this limit, such as in *NuSTAR*, *INTEGRAL*, or *Swift*/BAT (see Sect. 2.3.2).

All electronic detection of astronomical data, be it in imaging, photometry, or spectrometry, is subject to different noise terms in addition to the pure signal. The noise generated with the usage of CCDs can be divided into the background sky contribution N_B, the thermal noise component of the sensor, or dark current N_D, and the readout noise of the CCD N_R. All noise terms are given as a photon count number. The fraction of real detected source photons to the noise is given by the signal-to-noise ratio,

$$S/N = \frac{N_S}{\sqrt{N_S + n_{\mathrm{pix}}(N_B + N_D + N_R^2)}}, \tag{2.2.11}$$

with the number of source photons N_S and the number of pixels n_{pix} for which the S/N is calculated. The dark current and readout noise are measured separately. The background sky contribution is determined by the extraction of the photon data from the image. Usually an area of the sky near the source position is chosen.

To gain spectroscopic information using CCDs in the X-ray band mainly two different methods are applied. A dedicated spectrometer uses a reflection grading in the optical path to diffract the X-ray light onto a single or a row of CCDs, directly imaging the spectral energy distribution (see Fig. 2.2.5, left). Also, the CCDs can be used directly to derive spectral information from the registered image data. Contrary to CCDs that operate at optical wavelengths, X-ray CCDs count individual photons and not the pure light intensity over a longer readout cycle. Since every photon is registered individually and the number of created electron-hole pairs is dependent on the incident photon energy, the signal also carries the wavelength information. This means that especially for bright sources, short readout cycles in the order of microseconds are necessary to avoid two or more photons hitting the same pixel in one cycle, which would lower the real intensity by assuming only one photon hit the pixel. This effect commonly referred to as pile-up.

The measurement of X-rays on the focal plane with imaging sensors becomes not feasible using standard silicon CCDs above approximately 15 keV, where hard X-rays penetrate the detector. In order to facilitate the direct measurement of hard X-rays Cadmium Zinc Telluride (CZT) detectors with pixel sizes of several millimeters are often used. The material is a wide band gap semiconductor, which can be operated at room temperatures. CZT detectors have an effective energy measurement region of about 10 keV to a few MeV. While CZT devices in current coded mask systems provide an energy resolution of a few keV at around 100 keV, newer instruments, such as *NuSTAR*, reach less than 1 keV. Each pixel has thin metal electrodes, which have a bias voltage applied to them and cause a difference in the electric potential in the pixel. An incident hard X-ray photon ionizes the CZT medium, creating electron-hole pairs that move to their respective electrodes. The registered charge

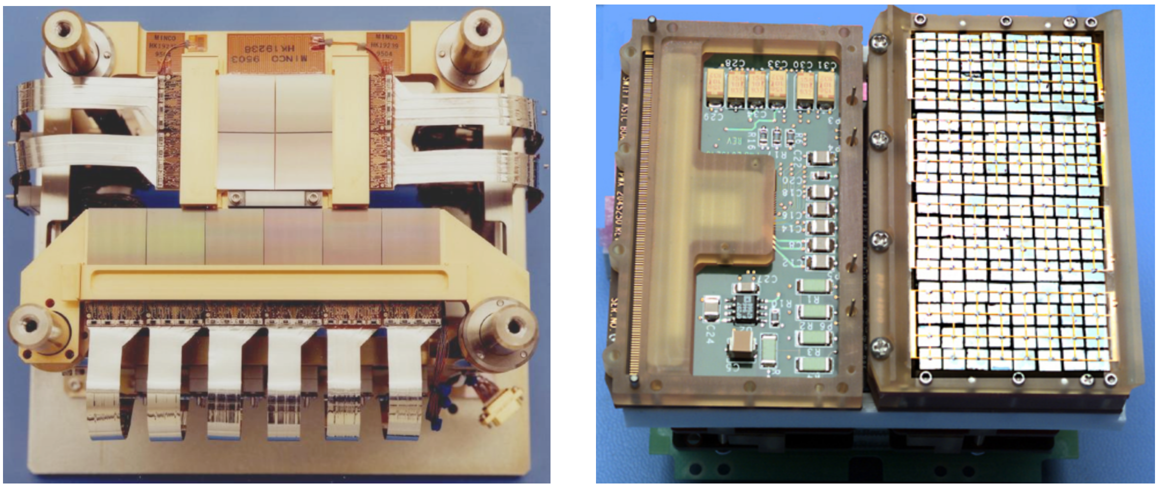

Figure 2.2.5.: Left: *Chandra* Advanced CCD Imaging Spectrometer (ACIS), image credit: NASA/CXC/SAO, right: one of the *Swift*/BAT detector CZT module, image credit: NASA/Goddard Space Flight Center.

is amplified proportionally to the photon energy. The resulting voltage pulse is then transferred to the readout electronics. The *Swift*/BAT detector (Fig. 2.2.5, right) uses an array of CZT detector modules.

The detector hardware registers counts per time, area, and energy interval from the sources in the field of view as well as counts from the background. Each photon that is registered produces signal with a corresponding (discrete) pulse height, which equals the photon energy. Thus, the total number of expected counts n in the energy channel i can be expressed as:

$$n(i) = t_{\text{eff}} \int_E R(E,i) \cdot F(E)\; dE + B(i), \tag{2.2.12}$$

with the source photon flux density $F(E)$ (source flux in units of $\mathrm{ph\,s^{-1}\,cm^{-2}\,keV^{-1}}$) and the background counts $B(i)$, which are registered during the effective exposure time t_{eff} (see, e.g., Davis, 2001). The instrument response $R(E,i)$ is usually the product of the redistribution matrix file (RMF) and the ancillary response file (ARF),

$$R(E,i) = \mathrm{RMF}(E,i) \cdot \mathrm{ARF}(E), \tag{2.2.13}$$

but can also be used as a single response file (.rsp). The unit-less RMF describes the probability of a photon with energy E to be detected in channel i and encodes the spectral detector resolution. A perfect detector would have only a narrow diagonal component in the matrix, assigning one input energy value to one output value, when an arbitrary high spectral resolution is given. In reality, a number of output energy channels are likely to produce a signal for one specific input photon energy. The ARF encodes the effective area in cm^2 of the instrument as a function of photon energy. It is the product of the telescope's collecting area, filter efficiency, and the QE of the detector. Also, the ARF incorporates errors like malfunctioning pixels. Generally, the effective area of the instrument is higher for angles close to perpendicular to the detector plane compared to higher angles, that is, areas near the edge of the field of view, an effect also known as vignetting. Figure 2.2.6, left, shows the normalized response of the *Swift*/BAT detector. The full spectral resolution shows 80

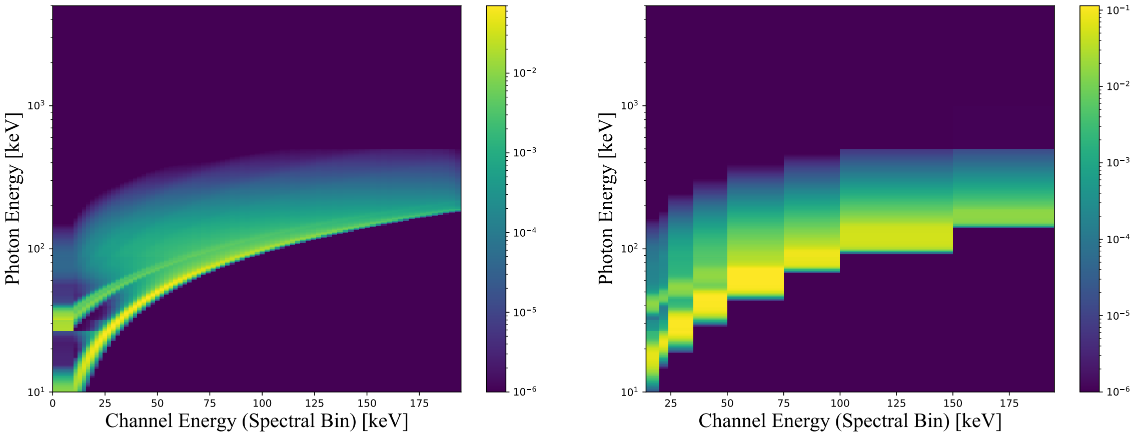

Figure 2.2.6.: Left: *Swift*/BAT instrument response for the full range of 80 spectral bins, right: reduced response for eight bins of the BAT all-sky survey maps. All response entries below 10^{-6} are omitted.

bins, whereas the reduced response (Fig. 2.2.6, right) is used for the fitting process, because the extraction of BAT spectra is performed for the eight spectral bands of the all-sky BAT survey maps.

The background of the photon count measurement of an X-ray source may originate from a number of different sources of its own. There can be resolved emission that is diffuse, like hot gas, or unresolved emission with no discernible point of origin. Also, a particle-induced signal contributes to the overall background. Usually, when observing individual point sources, such as AGN, the background is extracted separately near the point source. When performing a spectral fit, the background is added to the term describing the source flux in Eq. 2.2.12. This way, the fit can incorporate the background without subtracting it directly from the source signal, avoiding a loss of information.

2.3 The Neil Gehrels Swift Observatory

Next to the dedicated X-ray imaging and spectroscopy missions that were launched in the late 1990s and early 2000s like *XMM-Newton* (Jansen et al., 2001), *Chandra* (Weisskopf et al., 2002), *INTEGRAL* (Winkler et al., 2003), or *Suzaku* (Mitsuda et al., 2007), *Swift* (Gehrels et al., 2004) was conceptualized as a multiwavelength observatory, covering the optical up to the hard X-ray regime. Part of NASA's medium explorer (MIDEX) program, *Swift* was started in November of 2004 and brought into a low-Earth orbit. One of the observatory's main objectives, using its three instruments, is the detection and quick and automatic observation of Gamma-ray Bursts (GRBs) and their afterglows. Besides this automatic observation mode, the spacecraft performs a long-term hard X-ray survey of the entire sky. Since the the start of *Swift*'s mission, its ability to take simultaneous multiwavelength data and the coordinated measurements with other observatories have contributed greatly to the field blazar research, like the discovery of the most distant blazars, or the classification of blazars of unknown source type. For a comprehensive review on the impact of *Swift* on blazar research see, for example, Ghisellini (2015).

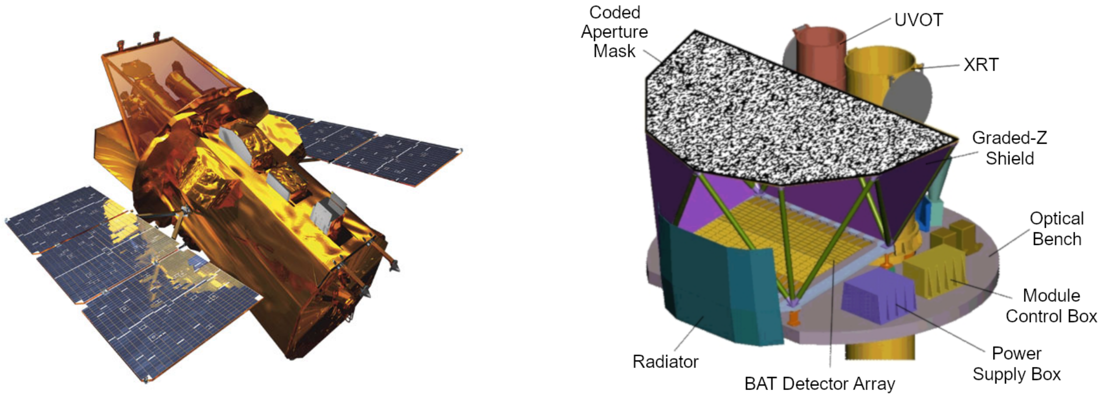

Figure 2.3.1.: Left: *Neil Gehrels Swift Observatory*, image credit: NASA E/PO, right: schematic display of *Swift* optical bench and mounted instruments, after Myers (2006).

More detailed information about *Swift* and its instruments is given in the following sections. This work focuses mainly on survey data gathered with the Burst Alert Telescope (BAT), whose function is described in more detail in Sect. 2.3.2. This overview of the *Swift* satellite and its instruments follows the *Swift* Technical Handbook[3] and the *Swift* BAT Software Guide (Markwardt et al., 2007).

2.3.1. Swift

The study of GRBs has long been hindered by the low detection statistic of satellite observatories and by slow response times for follow-up observations. With the *Neil Gehrels Swift Observatory* a dedicated set of instruments was brought forward that is able to detect GRBs within 1'–3', send a position estimate to the ground stations within 15 seconds, and point itself to the position in less than 75 seconds. All three instruments then begin observation of the GRB and its afterglow: the optical and UV telescope UVOT (Roming et al., 2005), the (soft) X-ray telescope XRT (Burrows et al., 2005), and the hard X-ray coded mask imager BAT (Barthelmy et al., 2005). Spectral energy distributions and lightcurves are measured with all instruments and are belayed to the ground. During the GRB the positional information is transferred via the Gamma-Ray Burst Coordinates Network (GCN)[4] in order to alert observers that operate radio, optical, X-ray, gamma-ray, and TeV instruments. At the time of writing, *Swift* detected 1656 GRBs (Jul. 2021), a number which is comparable to GRBs detected by *Fermi* (von Kienlin et al., 2020).

During its 95-minute orbit *Swift* continuously observes the sky using the Burst Alert Telescope, looking for GRBs and collecting count-rate data in 5-minute bins, producing a deep hard X-ray survey from 14 keV–195 keV (see also Sect. 2.3.2). The analysis of the BAT surveys maps for source coordinates from other AGN samples is the main focus of this work.

Additionally, during standard survey mode, BAT collects near real-time count rate data in the range of 15 keV–50 keV, accessible on-line through the *Swift* BAT transient monitor[5] (Krimm et al., 2013). The purpose of the monitor is the detection of previously unknown

---

[3] *Swift* Technical Handbook, v.14.0,
`https://swift.gsfc.nasa.gov/proposals/tech_appd/swiftta_v14.pdf`

[4] `https://gcn.gsfc.nasa.gov/`

[5] `https://swift.gsfc.nasa.gov/results/transients/`

transient X-ray sources, recording abrupt changes in X-ray flux of known sources, as well as the generation of light curves for 1050 Galactic and extragalactic objects (Jul. 2021).

Although dedicated to the study of GRBs and the mission to gather all-sky X-ray data, *Swift* has been used for a multitude of applications since its start in 2004. The long-term observation of the Milky Way's center and its supermassive black hole in the X-ray band (e.g., Degenaar et al., 2015), the cataloging of a large number of X-ray-bright sources (e.g., Liu et al., 2015; Oh et al., 2018), or the detailed multi-color mapping of the nearest galaxies in the UV are some of the projects that are being conducted[6].

Dedicated joint observations in conjunction with other X-ray observatories, such as *XMM-Newton* or *NuSTAR*, and NRAO facilities can also be proposed to obtain better spectral coverage of a source. *Swift's* mission design also allows astronomers to submit Target of Opportunity (ToO) requests in order to observe transient or flaring sources. Monitoring campaigns with other instruments, both satellites and ground facilities, can be set up to include *Swift* observations in the event of, for example, the flaring of a source in the TeV band.

2.3.2. Burst Alert Telescope (BAT)

Swift's Burst Alert Telescope is a coded mask instrument with a large FOV for the dedicated detection of GRBs and the long-term study of the entire sky in the band of 14 keV–195 keV. Figure 2.3.1, right, shows the basic schematic of the instrument. The D-shaped coded mask has an area of 2.7 m^2, measuring 2.4 m × 1.2 m. Approximately 54,000 lead tiles (5 mm × 5 mm × 1 mm) compose the unique random pattern of the mask, leaving 50% of the total area opaque and 50% transparent (Fig. 2.2.3, left). The mask is positioned 1 m above the CZT detector array, which consists of 32,768 pixels (4 mm × 4 mm × 2 mm) that compose the 256 modules with 128 pixels per module (Fig. 2.2.5, right). The entire structure allows for a large FOV of $100° \times 60°$ / 1.4 sr (half coded illumination), equal to 1/9 of the entire sky at any given time.

The division of the detector array into 16 smaller blocks, then modules, and finally individual pixels also functions as a layer of redundancy. In case any of the elements should stop working the whole instrument will still be able to locate GRBs and measure X-ray spectra, although with somewhat decreased accuracy and sensitivity. Additionally, the coded-mask principle does not depend on individual elements the way focusing X-ray detectors do in order to maintain its core functionality.

The positional accuracy of a source detection is around 1'–3'. Due to its setup, the BAT is limited to a relatively large Gaussian-shaped PSF of 22' within its effective energy range. For the purpose of locating GRBs and performing subsequent observations with the other on-board instruments XRT and UVOT, however, this precision is sufficient. The detecting area on the detector plane is 5240 cm^2. Each detector module is a self-triggered device, which will recognize an event in one of the 128 individual input channels (one for each pixel per module). The analog-to-digital converter transforms the pulse-height signal into a digitized output, blocking all other remaining channels at the same time. The registration and readout of a single event happens within 0.1 ms. The block controller and data handler produces a data stream of all events within a certain time and transmits it to the imaging processor. This central component scans the data stream for a sudden rate increase (bursts), calculates

---

[6] `https://www.nasa.gov/mission_pages/swift/bursts/magellanic-uv.html`

the sky image, accumulates data for the all-sky survey, and determines if a burst is worth a slewing maneuver and subsequent observation by the other telescopes. In the standard survey mode the detector plane count rate maps are calculated for 80 energy channels after a nominal exposure time of five minutes.

The survey reaches a sensitivity of $2 \cdot 10^{-10}\,\mathrm{erg\,s^{-1}cm^{-2}}\,(t/20\,\mathrm{ks})^{-0.5}$ with the exposure time t in the 15 keV – 150 keV band for a $5\,\sigma$ signal, equivalent to about 1 mCrab for two years. The data end products of the standard survey comprise light curves of all transient sources, for 1-day and 1-orbit time bins, as well as the long-term all-sky survey maps in eight energy channels in FITS format (see Sect. 3.2.1). Newly registered or highly variable sources are considered transients. Should the position of a new source not match the position of any source in an on-board catalog it is classified as a GRB (Markwardt et al., 2007).

2.3.3. XRT and UVOT

The focusing X-ray telescope on the *Swift* observatory (XRT, Burrows et al., 2005) is a standard Wolter-1-type setup, which is used for the automatic and dedicated observation of X-ray sources in the energy range of 0.2 keV–10 keV. In its role as an instrument for GRB studies the XRT is capable of measuring the spectra, flux information, and light curves of GRB afterglows, as fast as 60 to 80 seconds after the initial burst detection. The FOV of the XRT is $23.6' \times 23.6'$ with a PSF of 18 arcsec HPD (half-power diameter) at 1.5 keV. The silicon-based CCD in the focal plane (600 × 602 pixels) has a spectral resolution of 50 eV (FWHM) at 0.1 keV to 190 eV at 1.5 keV. Several readout modes are available during the XRT's operation. The imaging mode provides the measurement of an integrated image, forfeiting spectroscopic information. The photo-counting mode on the other hand offers spatial and full spectral information from the measurement. Brighter sources, whose count rates exceed 0.5 counts / s, however, can cause pile-up. A timing measurement with a resolution of 2.2 ms is achievable in the windowed timing mode with limited positional and spectroscopic information.

Co-aligned with the XRT is *Swift*'s Ultraviolet and Optical Telescope (UVOT, Roming et al., 2005), providing spectral coverage in the range of 160 nm–600 nm. The telescope is a modified Ritchey-Chrétien construction with an aperture of 30 cm and an FOV of 17' × 17'. Within the telescope unit there are two detectors that operate in photon counting mode. Light that is gathered by the telescope passes through a filter that can be chosen by rotating the filter wheel with several band pass filters and grisms for optical and UV light, which allow low-resolution spectroscopy. The angular resolution of the entire instrument is characterized by a PSF of 2.5 arcsec (FWHM). Contrary to *Swift*'s two X-ray instruments, the detector of UVOT does not register the incident light directly. Instead, a photo-cathode, a set of micro-channel plates, and a phosphor screen amplify the light by factor of approximately 10^6. Besides the automatic study of GRB afterglows the UVOT is also utilized to observe pre-planned sources.

2.4 Fermi Gamma-ray Space Telescope

In 2008 the *Fermi Gamma-ray Space Telescope* was launched into a low-Earth orbit, carrying two detector arrays, the Large Area Telescope (LAT, Atwood et al., 2009) and the

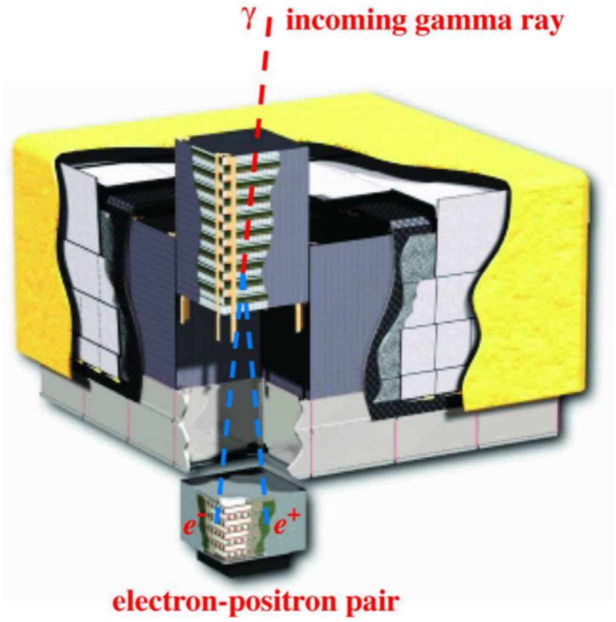

Figure 2.4.1.: Schematic of *Fermi*/LAT. The illustration shows a pair conversion process in the tracking module into a electron-positron pair, which reaches the calorimeter. Image credit: Atwood et al. (2009).

Gamma-ray Burst Monitor (GBM Meegan et al., 2009). The LAT has since been instrumental to studies of the variable sky in the band of 20 MeV to 300 GeV, offering light curves and continuous survey data of the entire sky. Because of its large FOV of 2.4 sr, the LAT samples the sky very evenly, once every three hours, or two orbits. Among the key science objectives, which *Fermi*/LAT is designed to address, is the understanding of particle acceleration mechanisms that produce the observed gamma-ray emission of Galactic and extragalactic sources, resolving the gamma-ray sky and determining the nature of unidentified gamma-ray sources, and the study of GRBs. Especially as a part of multiwavelength studies of transient events, for example, flare activities of AGN, the LAT has proven to be essential for not only contributing valuable spectral coverage but trigger coordinated observations with other telescopes (see, e.g., Karamanavis et al., 2016; Pushkarev et al., 2019, and references therein).

The LAT registers incident gamma-rays not directly. Instead, a e^+e^--pair is detected, which is produced when gamma-rays interact with layers of high-Z material within the detector. The tracking units measure the electron's and positron's trajectory via several layers of silicon strip detectors, allowing the reconstruction of the gamma-ray source coordinates. After their path through the tracking units, the particles hit the calorimeter modules. Using an arrangement of scintillating CsI crystals in an x,y (hodoscopic) array the energy deposition can be read out by photo diodes. The positional accuracy of single photon events increases with energy, achieving 0.6° at 1 GeV and $\leq 0.15^\circ$ at 10 GeV and above. The conversion process and resulting e^+e^--pair also have a unique signature when compared to other cosmic rays that continuously hit the detector. Figure 2.4.1 shows a schematic diagram of the individual components of the LAT.

Online accessible data products of *Fermi*/LAT[7] comprise already processed photon files in time resolutions down to 1 second. High-level data products include source catalogs like the most recent 4FGL (see Sect. 6), photometry light curves for cataloged and flaring sources, the LAT GRB catalog, extended sources, and background models. After the past

---

[7] `https://fermi.gsfc.nasa.gov/ssc/data/access/lat/`

years in operation, a significant improvement of the event-level analysis framework could be achieved. Specifically the full instrument response functions of the Pass 8 event selection (Atwood et al., 2013) furthered the scientific capabilities of LAT on various levels, that is, the Monte Carlo simulations of the detector, an optimization of the event reconstruction, and the background rejection process. The sensitivity for ten years of accumulated data of point sources with assumed flat spectra ($\Gamma = 2$) at a background level of the North Galactic pole is approximately $10^{-12}\,\mathrm{erg\,s^{-1}cm^{-2}}$ at $100\,\mathrm{MeV}$ and again at $300\,\mathrm{GeV}$ with the highest sensitivity at a few GeV with around $2 \cdot 10^{-13}\,\mathrm{erg\,s^{-1}cm^{-2}}$.

Fermi's second instrument, the GBM, is designed to detect and measure GRBs in the X-ray to gamma-ray range ($8\,\mathrm{keV} - 40\,\mathrm{MeV}$) with several arrays of scintillation detectors arranged around the spacecraft. Besides extending the effective range of the LAT in this regard, the GBM can trigger a reorientation of *Fermi* in order to observe a GRB with LAT. Online accessible data products[8] include daily trigger and burst data as well as GRB candidate catalogs and listed gamma-ray flashes from Earth itself.

---

[8] `https://fermi.gsfc.nasa.gov/ssc/data/access/gbm/`

3. Data reduction and analysis

Following the description of the relevant instruments in the previous chapter, this part introduces the data extraction chain as well as a number of crucial analysis methods used in this work. Although the standard *Swift*/BAT data extraction methods from the literature are applied, the analysis of the extracted data is performed using a custom procedure, which is necessitated by the low to medium signal strength of the majority of analyzed sources, whose spectral data are not well described using standard fitting methods.

This chapter begins with the source identification between the BAT data set and other source catalogs, such as radio and gamma-ray-selected source samples. The data extraction from the survey maps and spectral fitting are described in the following. After that, a number of application-specific methods are introduced: the comparison of signal-to-noise radios (S/N) of different object samples, the the calculation of source count distributions, the contribution of the emitted flux of an object sample to the cosmic X-ray background (CXB), and the luminosity functions (LF) for radio and X-ray emission.

3.1 Source identification and association

The association of a detected signal with a counterpart at the same or different wavelength is a crucial step when comparing the multiwavelength properties of an object sample. Whereas the measured coordinates of certain energy bands and observation techniques allow great precision down to the milliarcsecond scale other regimes have uncertainty ranges of several magnitudes larger. Radio-interferometric observations of point sources, for example, distant blazars, generally provide the best positional measurements. The high-energy regime, starting at hard X-rays, is often characterized by an instrument PSF of several arcminutes. When associating one source with a counterpart these error ranges need to be addressed accordingly. In this study, the positional information of the radio-selected and interferometically observed samples like MOJAVE and TANAMI (see Sect. 2.1.2) is assumed to be absolute. The X-ray and gamma-ray catalogs that have been used in this study (see Sect. 1.3) also provide the positional uncertainties and already identified counterparts.

For the hard X-ray band the *Swift*/BAT 105-month blind survey source catalog (Oh et al., 2018), the *INTEGRAL*/IBIS AGN survey catalog (Malizia et al., 2012), and the *INTEGRAL*/IBIS 11-year survey catalog (Krivonos et al., 2015) have been used. Although the BAT catalog gives absolute coordinates of the detected source signal, a positional uncertainty is still present. The 90% error radius can be calculated using an empirical relation (Oh et al., 2018) that depends on the S/N:

$$r_{\mathrm{error}}^{\mathrm{BAT}}(\mathrm{arcmin}) = \left(\left(\frac{30.5}{\mathrm{S/N}}\right)^2 + 0.1^2\right)^{\frac{1}{2}} . \tag{3.1.1}$$

Thus, a source with an S/N value of $5\,\sigma$ would have an error radius of 6.1’. Moderately high

S/N values of sources measured by the *INTEGRAL*/IBIS result in a very comparable positional resolution of 5'–10'. The GeV sources samples of the *Fermi*/LAT 3LAC (Ackermann et al., 2015) and 4FGL catalog (Abdollahi et al., 2020), are provided with error ranges that typically are less than approximately 6' for blazar types sources, and a factor of 10 less for the brightest objects.

Since cross-checking two catalogs via the listed counterpart name is far from practical and positional uncertainties can be substantial, a two-part process is used to correlate sources across catalogs. First, for any source 1 of a catalog the distance to each of the sources 2 in the second catalog is determined using the great-circle distance θ:

$$\cos\theta = \sin\delta_1 \sin\delta_2 + \cos\delta_1 \cos\delta_2 \cos(\alpha_1 - \alpha_2) \tag{3.1.2}$$

with the right ascension α and declination δ of the positions 1 and 2. If the separation is significantly smaller than the combined error radii of both sources the counterpart is usually the same. If the separation is significantly larger both catalog entries are regarded as non-identical sources. The second step is performed should both distances be in the same order of magnitude. Then, the counterparts are checked manually in NED[1] or SIMBAD[2].

3.2 BAT data pipeline

In the following sections the BAT data pipeline is described, from data extraction to the computation of flux and spectral slope, to other end products like the all-sky sensitivity function. The hard X-ray spectra, including uncertainties and the crab-weighted S/N for each source, are extracted from the *Swift*/BAT 105-month all-sky survey maps. Both the count rate and exposure maps have been provided by the *Swift*/BAT team at NASA GSFC. For the model fitting and analysis of all BAT spectra the Interactive Spectral Interpretation System (ISIS, Houck & Denicola (2000), version 1.6.2-43) was used. Additional scripts and functions for analysis were provided by ISISscripts, which are written and maintained by ECAP / the Dr. Karl Remeis Observatory and MIT.

Here, the data processing chain describes the extraction of flux data and the subsequent procedure for sources of various brightness classes. Although the method of extraction is always the same, very bright sources are processed differently than faint ones (S/N $\lesssim 4\,\sigma$) in terms of spectral fitting. The individual source signal significance is always given by the relation of count rate to the background of the source position.

Besides the quantity of significance for each source, a new way of estimating the percentage of sources in a sample, which differs from random fluctuation, is introduced in Sect. 3.2.3. Further, with the count rate and background maps as well as exposure it is possible to calculate the sensitivity of the survey in terms of minimal achievable flux per area sky. This step is required by later analyses, where the number of sources per area sky are determined, the calculation of the CXB contribution, and luminosity functions.

---

[1] NASA/IPAC Extragalactic Database NED, (Jet Propulsion Laboratory, California Institute of Technology / NASA)

[2] SIMBAD database (CDS, Strasbourg, France)

3.2.1. Data extraction

The hard X-ray data set in this work is based on is the 105-month *Swift*/BAT all-sky survey. The survey maps are background-subtracted count rate maps, whose photon count information have been accumulated nearly continuously between 2004-12-11 and 2013-08-31. The survey is condensed into two different count rate maps: one set is Crab-spectrum-weighted in the energy band of 14 keV–150 keV, one with full spectral information in 8 energy bands (in keV) of 14–20, 20–24, 24–35, 35–50, 50–75, 75–100, 100–150, and 150–195. Former data set is uniformly used to extract the signal to noise ratio (S/N) of any given source or position compared to the surrounding background.

Data extraction is performed using the sliding cell algorithm `batcelldetect`[3] from the `FTOOLS` software package. The algorithm can be used to detect all sources in an image above a certain S/N threshold and extract S/N and spectrum. Alternatively, it can be used to extract S/N and spectrum at any given position. The systematic background from the coded mask imager is already subtracted from all count rate maps. Individual contributions of all sources in an image need to be taken into account while extracting spectral information of any position, however. In order to determine the background prior to extraction a list of known hard X-ray sources is specified in the beginning. Here, this list comprises the 105-month survey catalog as well as the source sample of interest.

The entire BAT all-sky survey is described by a set of six survey maps (facets 0–5) that form a cube around the observer (see Fig. 3.2.1), with the Galactic center in the middle of facet 1, where the Galactic plane is parallel to the X-axis. For the data extraction the convention of Baumgartner et al. (2013) is adopted: a source extraction radius of 40.5' (15 pixels) and a surrounding ring of 4.5 degrees (100 pixels), whose rms value determines the error of the source flux. Also, one has to take into account spectral contamination of nearby sources. The convention by Baumgartner et al. (2013) is followed in this regard: the `batcelldetect` return value of contamination ratio must not be larger than 0.02, otherwise the flux of a source is considered an upper limit. In order to determine the number of counts per spectral bin a second set of six survey maps that describe the distribution of exposure is required. Compared to many other all-sky surveys, the BAT exposure is very uniform over the sky with the largest difference of a factor of 2.5. The maps of background-subtracted count rate, source background, and exposure for one facet are plotted in Fig. 3.2.2.

All past *Swift*/BAT survey source catalogs (Tueller et al., 2008; Baumgartner et al., 2013; Oh et al., 2018) were blind surveys, in which all signals above a set S/N value of 4.8 sigma were cataloged and counterparts were searched based on position and spectral and variability properties. In this work, data extraction is performed by using independent AGN samples and consequently set coordinates, whose S/N values and spectral bin count rates are extracted at these positions. Because the individual sky maps overlap a few degrees, due to the given projection and redundancy, in certain cases a source may appear on two or even three maps. For the extraction the source with the smallest distance to its respective map center is chosen.

The extraction of the S/N values and spectra is carried out for the central pixel of the source coordinates. For bright sources this pointing is usually within a few pixels of the

---

[3] An overview and help page for batcelldetect can be found on the High Energy Astrophysics Science Archive Research Center (HEASARC) of NASA at:
https://swift.gsfc.nasa.gov/analysis/threads/batsrcdetect.html
https://heasarc.gsfc.nasa.gov/lheasoft/ftools/caldb/help/batcelldetect.html

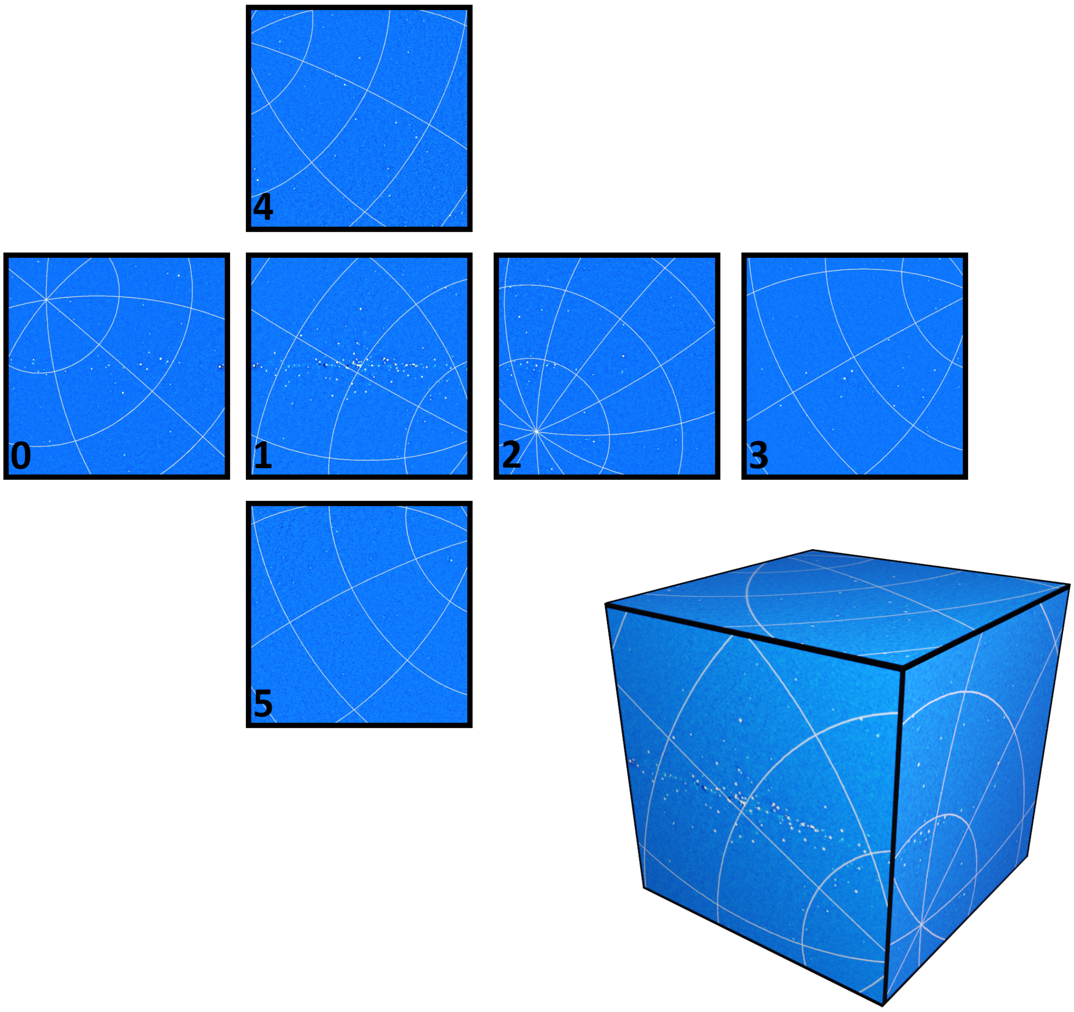

Figure 3.2.1.: BAT 105-month background-subtracted survey maps. All six facets compose the entire sky when folded into a cube, overlapping on the edges. The center of facet 1 is co-aligned with the Galactic center (bottom left side on the cube rendering). The equatorial coordinate grid is plotted in white.

(previously) registered BAT catalog source position. From the results of the extraction using `batcelldetect`, the spectral information is written into standard `pha` files in `fits` format. Per spectral bin the central pixel count rates and uncertainties derived from background region are saved. The exposure from the position in the BAT exposure maps is read out separately using the software package `wcstools` and the routine `sky2xy` (Mink, 2014).

3.2.2. Choosing a fitting statistic

This overview of fitting methods and statistics follows Arnaud et al. (2011) and the X-Ray Spectral Fitting Package XSPEC Users' Guide, version 12.10.1 (Arnaud et al., 2018). The process of finding a theoretical model that describes a measured data set includes the calculation of the best-fit model parameters and a goodness-of-fit test, which states how well the data is described by the model. The data set can be a time series, a 2D image, or in

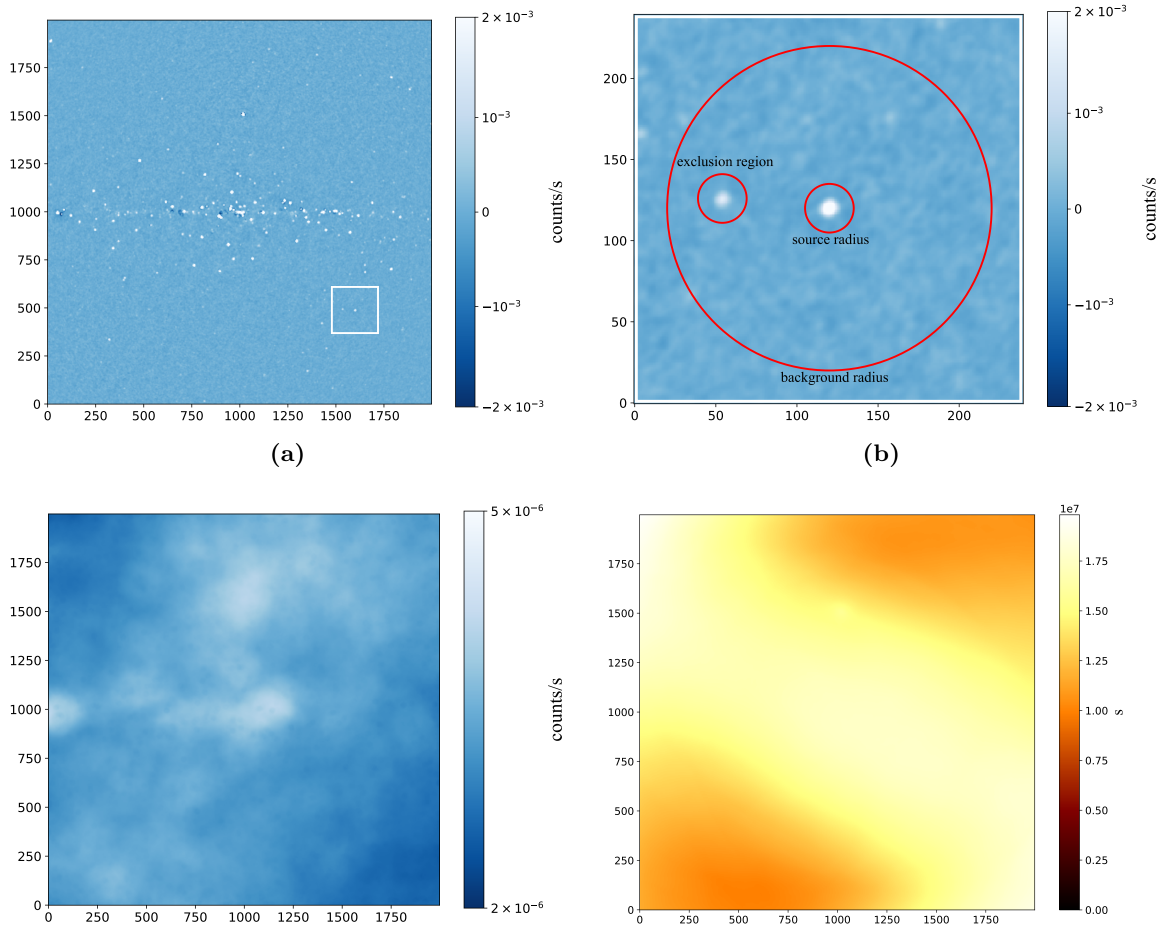

(a) **(b)**

(c) **(d)**

Figure 3.2.2.: BAT survey maps for facet 1: (a) background-subtracted and crab-weighted count rate map, (b) detail of count rate map (white square) with source extraction (15 pixels) and background radius (100 pixels), (c) modeled source background map, (d) exposure distribution in seconds.

this case an X-ray spectrum. The general approach is to find the model parameters that maximize the probability (or likelihood) $\mathcal{L}$ of measuring the given data under the assumption of the model. In doing so, the fitting algorithm iteratively maximizes $\mathcal{L}$, which is defined as:

$$\mathcal{L}(\{S_i\}) = \prod_{i=1}^{N} \mathcal{P}(S_i|m_i(\theta)), \tag{3.2.1}$$

with the probability $\mathcal{P}(S_i|m_i(\theta))$ that the data point i has the value S_i and the expected value m_i, given the set of model parameters θ. The expected count rate m_i of photons in the spectral bin i is the energy integral over the spectral model $F(\theta, E)$ and the detector response,

$$m_i = \int \mathrm{RMF}(i, E)\ \mathrm{ARF}(E)\ F(\theta, E)\ dE. \tag{3.2.2}$$

The response matrix file (RMF) is the spectral response of the X-ray detector, a proportional photon counter. The ancillary response file (ARF) describes the effective area and quantum efficiency in cm^2 depending on the photon energy. See also Sect. 2.2.3 for more details on the X-ray detector responses.

The two main probability distributions $\mathcal{P}$ for fitting (and spectral modeling in astronomy) are for Poisson- and Gaussian-distributed data. In the Poisson case the probability of receiving n photons within the exposure time t is given by:

$$\mathcal{P}_{\mathrm{P}}(n, t\mu) = \frac{e^{-t\mu}(t\mu)^n}{n!}, \tag{3.2.3}$$

where $t\mu$ is the mean of the events, and $\mu(= m_i)$ equal to the count rate. Using Eq. 3.2.1 and 3.2.3 the likelihood for n events in the exposure time t becomes:

$$\mathcal{L}_{\mathrm{P}}(\{S_i\}) = \prod_{i=1}^{N} (tm_i)^{S_i} e^{-tm_i}/S_i! \tag{3.2.4}$$

with the observed number of counts S_i. In practice the desired fit statistic is often expressed as twice the negative logarithm of the likelihood. Following Cash (1979) the fit statistic for Poisson-distributed data, also simply named C, can thus be written as:

$$C = -2ln\mathcal{L}_{\mathrm{P}} = \sum_{i=1}^{N} tm_i - S_i ln(tm_i) + ln(S_i!). \tag{3.2.5}$$

Since the last term is independent of the fitting model it can be neglected in the fitting algorithm, resulting in:

$$C = \sum_{i=1}^{N} tm_i - S_i ln(tm_i). \tag{3.2.6}$$

In the limit of large numbers the Poisson distribution becomes Gaussian. Because of this, the C statistic approaches a fitting statistic commonly used for good quality data sets (more than about 30 counts per bin). This is often referred to as S^2 or χ^2, since the fit statistic follows approximately the χ^2 probability distribution. Starting with the expression for Gaussian probability, the fit statistic can be derived:

$$\mathcal{P}_{\mathrm{G}}(n, t\mu, \sigma) = \frac{1}{\sigma\sqrt{2\pi}} exp\left(\frac{-(n - t\mu)^2}{2\sigma^2}\right), \tag{3.2.7}$$

with the variance σ. Applying Eq. 3.2.1 and 3.2.7 and again dropping a term independent of the model gives:

$$S^2 = \sum_{i=1}^{N} \frac{(S_i - m_i)^2}{\sigma_i^2}. \tag{3.2.8}$$

The commonly used quantity of the reduced S^2 is the S^2 value divided by the number of degrees of freedom in the fit (number of fitted data points / bins subtracted by the number of free parameters), which approaches unity for an optimal fit. All measured counts of X-ray photons comprise pure source and noise contribution. Depending on the probability distribution of the measured data and noise a specific fit statistic must be used. If the only source of noise in the signal is due to the number of counted photons the C statistic is favored. Should a different dominant noise term be present S^2 is applied. For example, in many cases the background has to be modeled in addition to the source signal.

Should a source spectrum retain a high number of counts per spectral bin the S^2 fit statistic can be used. However, in the case of the hard X-ray spectra, which have been extracted from the BAT maps in this work, the collected counts in many bins are very low, and sometimes even of negative value due to over-subtraction of the background in the maps. Although the C statistic describes low count spectra it assumes no background at all. In order to properly fit the background-subtracted count rate maps the recommended likelihood statistic PGSTAT from the XSPEC statistics appendix (Arnaud et al., 2018) is implemented. It assumes Poisson-distributed source counts as well as Gaussian background counts, which are here set to 0. The statistic can be derived as:

$$PG = 2\sum_{i=0}^{N} t_s(m_i + f_i) - S_i ln(t_s m_i + t_s f_i) + \frac{1}{2\sigma_i^2} t_b^2 f_i^2 - S_i(1 - lnS_i), \tag{3.2.9}$$

where

$$f_i = \frac{-t_s\sigma_i^2 - t_b^2 m_i + d_i}{2t_b^2} \tag{3.2.10}$$

and

$$d_i = \sqrt{(t_s\sigma_i^2 + t_b^2 m_i)^2 - 4t_b^2(t_s\sigma_i^2 m_i - S_i\sigma_i^2)}, \tag{3.2.11}$$

with the exposure time for both source t_s and background t_b. The calculation of the model confidence errors of the PG statistic is shown in Sect. 3.2.4.

In a specific application in Sect. 3.2.3 the C statistic is used, in this case not to fit a spectrum with subtracted background, but in order to fit a simple parameter distribution / histogram.

3.2.3. Source detection

To determine if a source can be called detected, or significant, the S/N is a simple measure that also takes into account the local background and exposure variation over the entire sky. Especially source samples that are not X-ray-selected, and maybe originate from flux-limited surveys in the radio domain, can have substantially lower signal strength than the conservative BAT detection threshold value of about 5 σ. In order to make statements about the general trend of signal strength of a source sample or state if a sample is significantly different from the random background fluctuations, the sample S/N distribution needs to be compared to the random S/N distribution in the sky. Figure 3.2.3 (left) shows the distribution of S/N values that have been measured at 1000 random positions in the sky, at least 4.5 degrees away from any BAT catalog source. The result is a symmetric bell-shaped characteristic centered around 0 σ with minimum and maximum values of -3.3 σ and 3.5 σ respectively. A least-squares fit with a Gaussian curve describes the distribution very well. Negative S/N values stem from the fact that the average background is already subtracted from the count rate maps, which vary mildly. For comparison, the right side of Fig. 3.2.3 shows the S/N distribution of the MOJAVE-1 AGN sample, which is radio-loud but generally not bright at X-ray for all sources. Both distributions are clearly different in overall profile and location on the S/N axis.

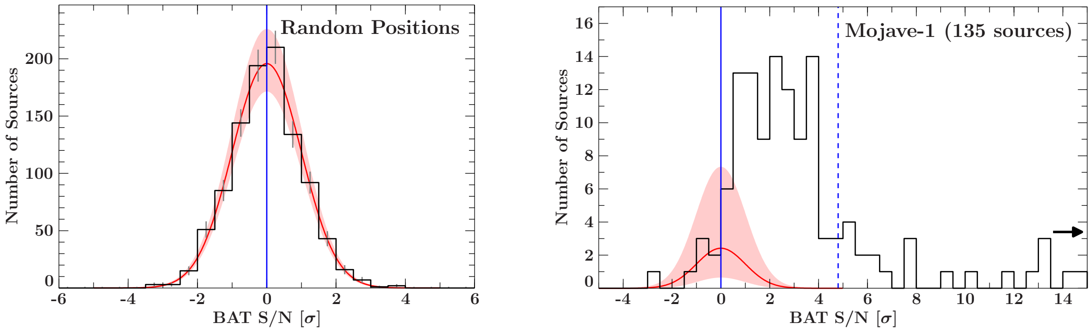

Figure 3.2.3.: Left: BAT S/N distribution of 1000 random positions in the sky, and at least 15 pixels from each catalog source, right: S/N distribution of the MOJAVE-1 AGN sample (see Sect. 4.1.2). The dashed line indicates the usual BAT catalog survey threshold of 4.8 σ. The red line represents the Gaussian fit to the negative S/N bins. The corresponding 3 σ uncertainty range of the norm is plotted as the red shaded area. For better readability, the X-axis is truncated at 15 σ.

This way it can be estimated what percentage of the source sample is not compatible with random background fluctuations. The approach is as follows: the negative part of the S/N distribution of the source sample is assumed to be due to random fluctuations. The histogram below 0 σ is fitted using a Gaussian curve with a set center of 0 σ and a width of 1 σ (see Fig. 3.2.3, right). Because the number of used data points for real source samples can be low (less than 10) Cash-statistics instead of χ^2-statistics are applied for the fit (see also Sect. 3.2.2). A histogram binning is chosen that results in the best fit statistics. Usually a bin size of around 0.5 σ gives the best results in this regard. Then, each bin in the original source S/N distribution is subtracted by the value of the fit curve at that bin. The remaining histogram is summed up, omitting all values smaller than 0 and all bins below 0 σ. This procedure is done for the Gaussian fit curve itself and a curve that correspond to the 3 σ error maximum and minimum of the norm, respectively. For any histogram in this work, purely statistical error bars based on the Poisson distribution are applied, with the value of the error equal to the square root of the number in the respective histogram bin. With the sum S of the subtracted histogram bin values under the aforementioned restrictions the error ΔS is equal to the individual error bars added in quadrature. The number of sources in the respective source sample, which is not compatible with random fluctuations and the corresponding error, are thus:

$$S = \sum_{i=1}^{N} S_i, \tag{3.2.12}$$

and

$$\Delta S = \sqrt{\sum_{i=1}^{N} \Delta S_i}, \tag{3.2.13}$$

for N positive bins larger than 0 σ significance. The resulting value of S as well as minimum and maximum values are rounded to the next lower integer in the later analysis.

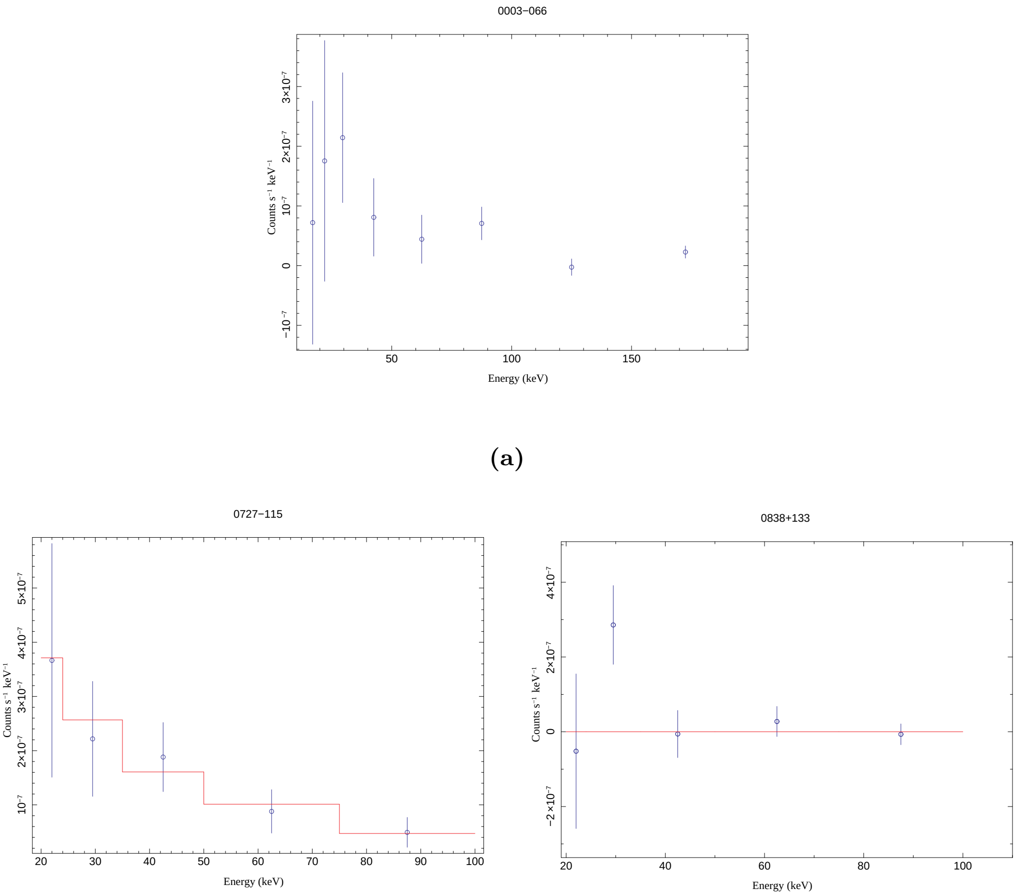

(a)

(b) **(c)**

Figure 3.2.4.: Examples of BAT spectra: (a) full 8-channel BAT spectrum of blazar 0003-066 ($2.34\,\sigma$), the count rate data point in the seventh channel (100–150 keV) has a negative value, (b) reduced 5-channel BAT spectrum of blazar 0727–115 ($3.83\,\sigma$), well fitted using a simple power-law model, (c) reduced 5-channel BAT spectrum of blazar 0803+113 ($0.61\,\sigma$), no fit is viable due to the negative count rate bins.

3.2.4. Spectral fitting

Spectra that are measured in the entire X-ray band, starting at around 0.5 keV, intrinsically suffer from a scarcity of photons compared to optical or UV. Especially extragalactic sources often require long exposure times of several hours in the soft X-ray band in order to register a sufficient number of photons to apply a fitting statistic that requires a minimum number of data points. For the hard X-ray band above around 10 keV the combination of even less photons per frequency interval and the penalty of less sensitive instruments intensifies this trend. However, the all-sky exposure of the *Swift*/BAT survey in the order of 10^7 seconds allows for a substantial accumulation of photon data. In this work the full 8-channel spectra of 14 keV–195 keV spectra are extracted for every source in the corresponding source samples. The fitting procedure is performed for only 5 channels, starting at the original second channel at 20 keV, ending at 100 keV. This reduction is considered necessary because of very low count rates (in some cases negative) in the omitted energy channels (14 keV–20 keV, 100 keV–150 keV, and 150 keV–195 keV). Figure 3.2.4 (a) shows a full 8-channel BAT survey spectrum of the MOJAVE-1 source, 0003–066, a blazar, which demonstrates the aforementioned issues of BAT spectra with relatively low S/N.

The BAT spectra extracted from the 105-month survey maps are fitted using the XSPEC power-law model `pegpwlw`:

$$f(E) = KE^{-\Gamma}, \tag{3.2.14}$$

with normalization K, the energy E, and the spectral slope / photon index Γ. The model's input parameters also include the lower and upper energy range. This allows the fitting process to return the physical flux value F in cgs units in place of the the normalization K, which is equal the photon flux in the energy band.

Earlier works analyzing BAT spectra (Tueller et al., 2008; Baumgartner et al., 2013; Oh et al., 2018) utilized the standard χ^2 fitting method. The here used PGSTAT fit statistic leads to model parameter values that are compatible with the results obtained using the χ^2 statistic for significant sources (approximately larger than $3\,\sigma$) within the 90% uncertainty ranges (see also Fig. 3.2.7).

When computing the model parameters of the power law and their uncertainty ranges different methods need to be applied depending on the quality of the specific spectrum. For simplicity, all cases in which all spectral bins have count rates larger than zero are labeled category A, and all cases with at least one spectral bin containing negative count rates are labeled category B. This distinction is necessitated by the use of the PGSTAT fit statistic: the second logarithmic term in Eq. 3.2.2 does not allow negative numbers. Thus, for category A spectra the PGSTAT statistic can be used as intended, whereas a direct fit is not possible for category B. In the following, the analysis chain for both sorts of spectra and the error derivation of fit parameters are shown.

The calculation of the flux F and photon index Γ of category A spectra is straightforward. See also Fig. 3.2.5 for an overview of the process. A simple `pegpwlw` model fit is performed and both parameters F and Γ are saved for the next step, which is the error calculation via a Monte Carlo approach. Using `XSPEC`, a new `pegpwlw` model is defined with arbitrary high exposure time. The command `fakeit` produces a simulated spectrum src_{sim} assuming the flux F and photon index Γ from the original fit in the previous step.

In order to determine the uncertainty range of the initial fit parameters, this ideal spectrum without errors is randomized. First, the statistical errors of the spectrum per channel i are calculated, using:

$$err_{\mathrm{sim}}(i) = \sqrt{\frac{2 \cdot bkg(i) + src_{\mathrm{sim}}(i)}{\alpha_{\mathrm{BAT}} \cdot n_{\mathrm{pixels}} \cdot t}}, \tag{3.2.15}$$

which follows the calculation that is implemented in the `ftools` program `batphasimerr`. The typical BAT background spectrum bkg has been taken from the NASA HEASARC Calibration Database[4]. The imaging efficiency of the BAT instrument α_{BAT} has a value of 0.28; the effective number of pixels n_{pixels} with a source in the direction of pointing is 32768. The exposure time is labeled t. This error term (per channel i) is multiplied with a Gaussian-distributed random number r_{Gauss} of mean 0 and width 1, and added to the simulated spectrum,

$$src_{\mathrm{sim,err}}(i) = src_{\mathrm{sim}}(i) + r_{\mathrm{Gauss}} \cdot err_{\mathrm{sim}}(i). \tag{3.2.16}$$

---

[4] https://heasarc.gsfc.nasa.gov/docs/heasarc/caldb/caldb_intro.html

This procedure is repeated a large number of times and the resulting distribution of F and Γ are fitted using a Gaussian curve (see Fig. 3.2.6). A number of 2000 iterations for each error calculation has been proven to be a viable compromise between accuracy and computation time. Finally, the results for flux / photon index and the uncertainty range are determined by the respective center of the Gaussian fit curve and the width corresponding to 90% of the fit curve's area.

As an example, in Fig. 3.2.7 the fitting results of the aforementioned reduced BAT spectra (five channels, 20 keV–100 keV) for S^2, Cash, and PGSTAT statistics are shown. Here, the X-ray-brightest sources in the MOJAVE-1 AGN sample (see Sect. 2.1.2 and Sect. 4.1) are fitted with all three fit statistics using the same power-law model `pegpwlw`. Especially for the brightest sources, the deviation in flux and photon index values between all used statistics are well within the 90% uncertainty range. One exception is the bright radio galaxy 3C 84 in the range of $\Gamma = 3 - 3.5$, whose spectral form is not well fit by the described power law in any case ($S^2 = 29.02, C = 34.94, PG = 14.82$ with three degrees of freedom).

If the error range of the derived flux value is relatively large the flux is considered an upper-limit value. In the case that the value of the $3\,\sigma$ error is larger than the flux itself the flux becomes by definition an upper limit with the value equal to the $3\,\sigma$ error. Furthermore, as stated in Sect. 3.2.1, every source that is found to be contaminated by another close source is also treated as an upper limit. In this case, the upper-limit value is equal to the derived flux with no error.

For the calculation of the source flux F from category B spectra a direct power-law fit is not viable. Hence, the count rates in the spectra are added up and the equivalent norm (equal to source flux in the model `pegpwlw`) is determined by assuming a certain spectral shape (photon index). Should the source spectrum originate from a larger sample, the weighted mean photon index of all category A spectra in that sample is applied. In the case of different sub-classes in that sample, like radio galaxies and BL Lacs, the according sub-class photon index is used. This constitutes the template photon index Γ_{temp} and the error of the mean $d\Gamma_{\text{temp}}$.

Next, the factor that translates a given total count rate of the spectrum to the flux F is determined. A spectrum with frozen photon index Γ_{temp} is created using `fakeit` and the `pegpwlw` model. Both flux F_B and exposure time t_B are set to arbitrarily high values, and the total number of counts src_{sim} is read out. The relation of count rate to norm is then calculated:

$$b(\Gamma_{\text{temp}}) = \frac{src_{\text{sim}}(\Gamma_{\text{temp}})/t_{\text{B}}}{F_{\text{B}}}, \tag{3.2.17}$$

as well as its error based on the error of the template photon index,

$$db(\Gamma_{\text{temp}}) = |b(\Gamma_{\text{temp}}) - b(\Gamma_{\text{temp}} - d\Gamma_{\text{temp}})|. \tag{3.2.18}$$

All count rates in the real spectrum are then summed up and the corresponding error is computed:

$$src_{\text{sum}} = \sum_i src(i), \tag{3.2.19}$$

and

$$err_{\text{sum}} = \sqrt{\sum_i src(i)^2}. \tag{3.2.20}$$

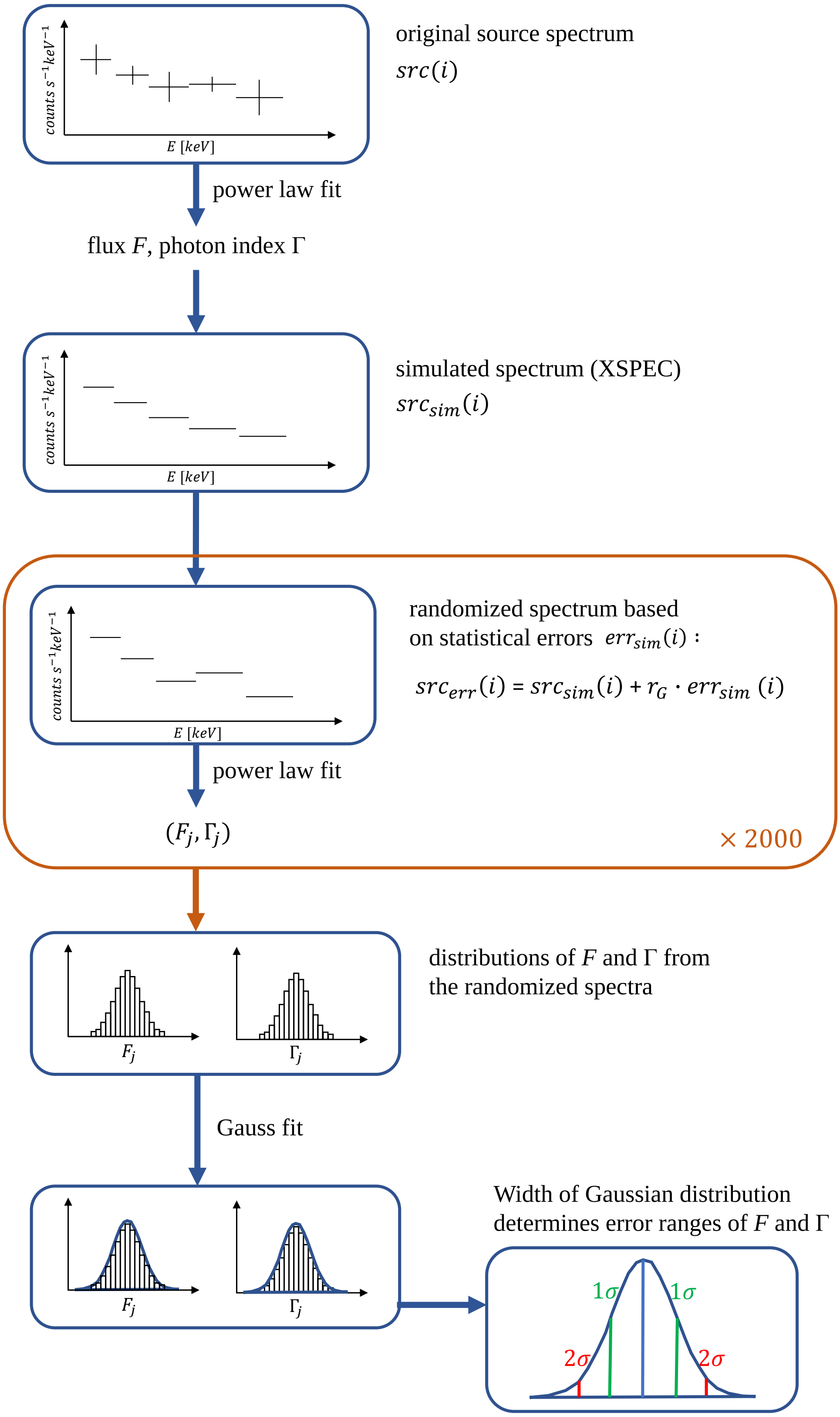

Figure 3.2.5.: Schematic process of the derivation of the flux and photon index uncertainty ranges for BAT spectra, category A.

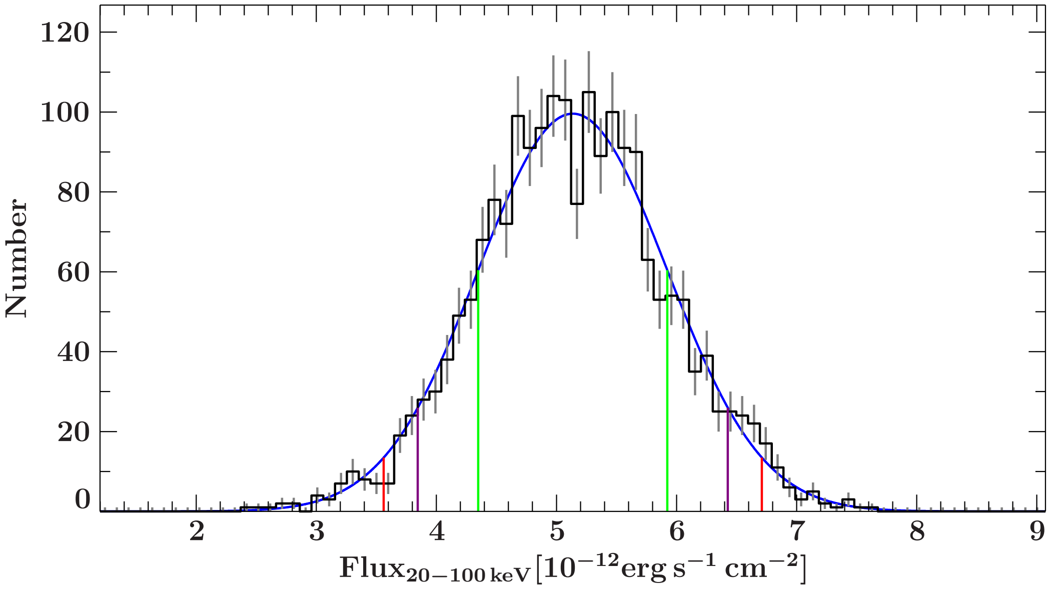

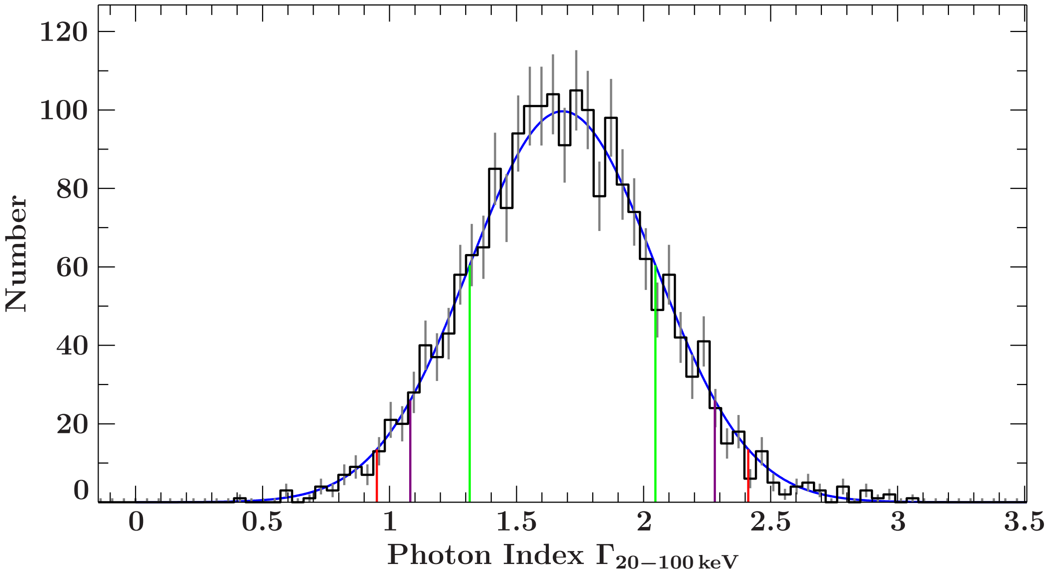

Figure 3.2.6.: Distribution of BAT flux (top), and photon index (bottom) of the Monte Carlo error calculation for blazar 1803+784. The blue line indicates the fitted Gaussian curve, the colored lines the uncertainty ranges for both quantities: green for $1\,\sigma$, purple for 90% errors, and red for $3\,\sigma$.

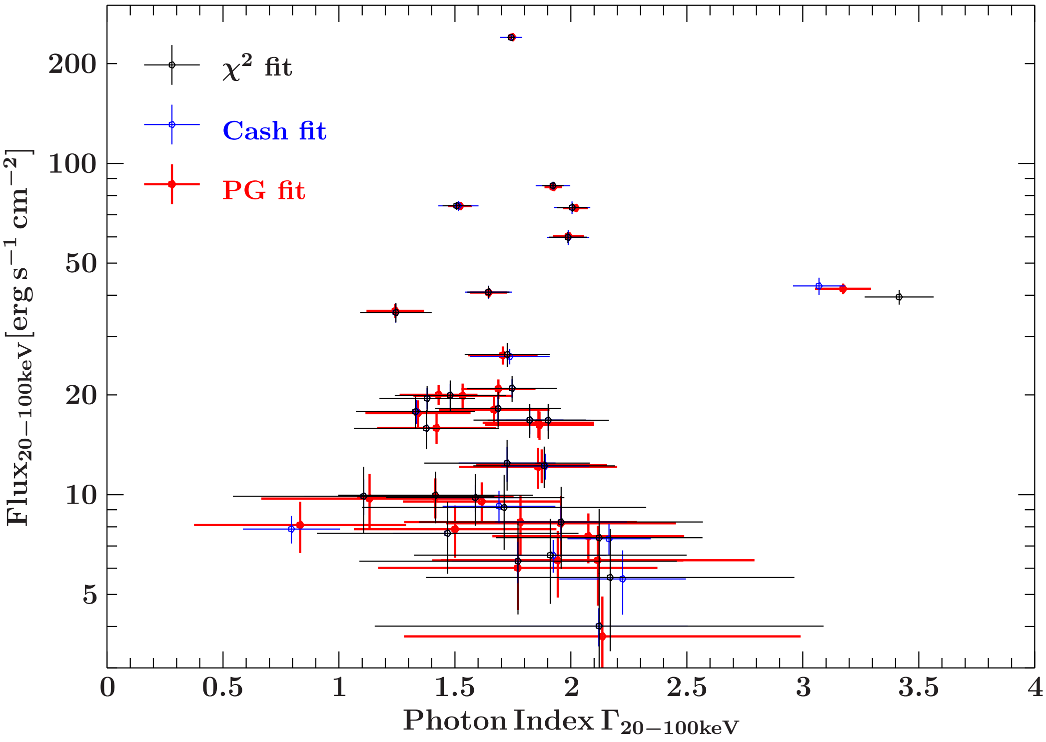

Figure 3.2.7.: Hard X-ray flux plotted against photon index for S^2 (χ^2), Cash, and PGSTAT fit statistics. Graphed are the measurements for all sources in the MOJAVE-1 sample with an S/N value larger than $5\,\sigma$.

The final expression for the flux F of the category B spectrum as well as its error range following Gaussian error propagation becomes thus:

$$F = \frac{src_{\mathrm{sum}}}{b}, \tag{3.2.21}$$

and

$$dF = \sqrt{\left(\frac{err_{\mathrm{sum}}}{b}\right)^2 + \left(\frac{K \cdot db}{b^2}\right)^2}. \tag{3.2.22}$$

The same criterion of whether the flux is a $3\,\sigma$ upper limit is applied from the method for category A spectra. Lastly, the luminosity values for all corresponding fluxes are calculated using the K-correction:

$$L = \frac{1}{(1+z)^{2-\Gamma}} 4\pi d_{\mathrm{L}}^2 F, \tag{3.2.23}$$

with the redshift z and the luminosity distance d_{L}, which has been computed assuming the cosmological parameters $H_0 = 70.0\,\mathrm{km\,s^{-1}\,Mpc^{-1}}$, $\Omega_{\mathrm{M}} = 0.30$ and $\Omega_\lambda = 0.70$. Its error can be derived to:

$$dL = \sqrt{l_1^2 + l_2^2}, \tag{3.2.24}$$

where

$$l_1 = 4\pi d_{\mathrm{L}}^2 dF (1+z)^{\Gamma-2}, \tag{3.2.25}$$

and

$$l_2 = 4\pi d_{\mathrm{L}}^2 F (1+z)^{-\Gamma-2} log(1+z) d\Gamma. \tag{3.2.26}$$

3.3 Survey sensitivity and area

After the new data reduction methods, outlined in the sections before, the following parts describe specific data analysis procedures for the given source samples. For all of the analyses the sky survey area Ω_s as a function of flux is required. This section describes how Ω_s is derived from the 105-month count rate survey maps.

One of the applications that necessitate such function is the so-called source count distribution, or $\log N$-$\log S$ (Sect. 3.4). Here, the number of sources in a sample is graphed against the source flux F. However, since the majority of surveys for various kinds of astronomical objects do not cover the entirety of the sky, the number of sources in this instance is always given per square degree. Thus, a characteristic curve for the specific survey is needed, which expresses the empirical sky survey area as a function of the minimal flux F_min that corresponds to a detection. For large surveys that incorporate a number of different instruments and detectors this function, or sensitivity profile, can have a rather complex shape (see, e.g., Ebrero et al. (2009)).

The format of sky projection of the individual sets of six BAT survey maps is known as Lambert's zenithal equal area (ZEA), which is a projection from a sphere to a plane where the area is accurately represented, but not the angle. It is described by the radius R_θ in degrees as a function of native latitude θ:

$$R_\theta = \frac{360^\circ}{\pi} \sin\left(\frac{90^\circ - \theta}{2}\right). \tag{3.3.1}$$

Because the entire sky is not projected down to a single plain but six squares separately, the skewing of the maps is kept to a minimum. For a review of spherical map projections including the ZEA variant see also Snyder (1993) and Calabretta & Greisen (2002).

In order to effectively sum up the area of the pixels with a certain flux the overlap of all maps needs to be addressed. As already mentioned in Sect. 3.2.1, due to redundancy and the chosen projection, certain areas of the sky are mapped twice on the edges of two and three times on the corners of three maps (Fig. 3.3.1, left). The basic approach is to find a mask with the same dimensions as a survey map (1998 × 1998 pixels) that marks all pixels as 1 that belong to each individual map and 0 for pixels that belong to the neighbouring map. Thus, projecting all original maps onto a sphere with the mask applied to each map eliminates any overlap, leaving a spherical map with pixel values unambiguously assigned to every coordinate (within the map resolution).

In doing so one can utilize the fact that each map is oriented along the Galactic coordinate system. The maps are standard `fits` files with dimensionless axes and only x and y coordinates. Using the program `xy2sky` from the software package `wcstools` (Mink, 2014) it is possible to assign every pixel Galactic coordinate pairs. As an example, one can choose facet 1, which and centered on the coordinates $(0^\circ, 0^\circ)$. Since every of the six maps (facets) must span $90^\circ \times 90^\circ$ all pixels in the new mask with Galactic longitudes $l > 45^\circ$ and $l < 315^\circ$ must be set to 0. The same criterion can be set for the latitude with $|b| > 45^\circ$. All remaining mask pixels are set to 1. The result is shown in Fig. 3.3.1, right. Finally, the mask is multiplied with the survey maps in order to obtain the maps with no overlap. Before the multiplication each map has a total number of 3992004 pixels. After, 3157149 unique pixels are remaining. The area for each pixel is equal and it is set to the corresponding fraction of the $41252.96\,\mathrm{deg}^2$, or $12.67\,\mathrm{sr}$, which is the solid angle of a full sphere.

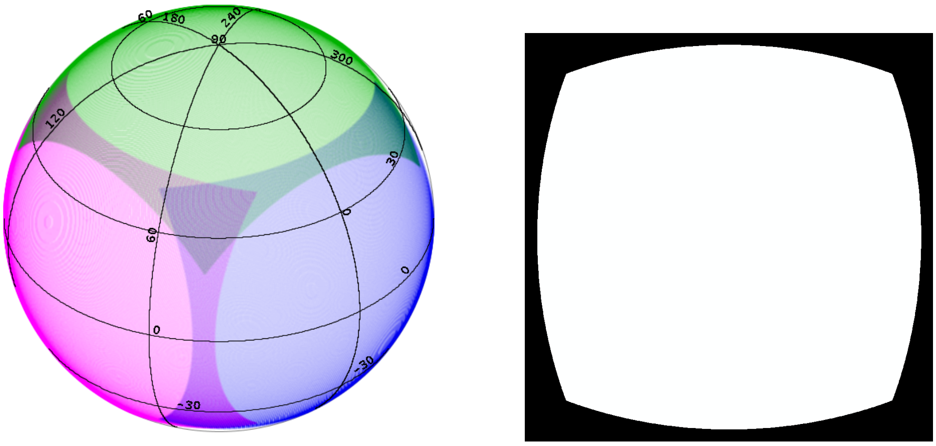

Figure 3.3.1.: Left: facets 0, 1, and 4 projected onto a sphere with a Galactic coordinate system, right: facet mask that shows all pixels that unambiguously belong to a single facet in white, and the rest in black.

The survey maps that are used in calculating the sensitivity characteristic are not the original count rate maps themselves but the background fluctuation maps that are created during the extraction routine (Sect. 3.2.1, Fig. 3.2.2). The approach is to multiply the Gaussian-distributed background pixel values with a certain factor that corresponds to the significance of a detection, for example, 5 for a sensitivity curve of a survey where all sources with $5\,\sigma$ signals are declared detections. A full sky survey's curve starts at high fluxes at the complete sky area and decreases towards fainter fluxes.

For determining the survey sensitivity curve a certain flux value is chosen and the area of all pixels with fluxes that are lower or equal are summed up, resulting in the corresponding sky area. This area is accessible for this flux level at the given significance. The pixel values in the background maps, however, are photon count rates and not energy fluxes. To convert the count rates in to fluxes in cgs units a template spectrum of the background has to be assumed. To obtain a reasonable mean photon index Γ of the background all bright X-ray sources ($> 4.8\,\sigma$), Galactic and extragalactic, are fitted in the band of 20 keV–100 keV. The limit of $4.8\,\sigma$ is equal to the cut-offs of the past official source catalogs (Tueller et al., 2008; Baumgartner et al., 2013; Oh et al., 2018). All source types are included in the calculation because the original surveys were blind surveys, that is, not source-specific. In other words, the registered sources and their spectra mirror the capability of the instrument and sensitivity of the survey. The mean index of $\Gamma = 2.356 \pm 0.024$ is determined from 1437 bright sources of the 105-month catalog. Figure 3.3.2 displays the curves of sky coverage as a function of minimal observable flux for the detection significances 1, 3, and $5\,\sigma$.

While using a sensitivity characteristic corresponding to a high certainty like $5\,\sigma$ is suggested for blind surveys, targeted studies (known source positions) allow for lower significances. In this work, independent AGN samples, which are radio- or gamma-ray-selected, are analyzed in terms of hard X-ray emission properties. From counterparts in other wavelengths the exact coordinates of the given objects are already known. Unless stated otherwise for the analyses, that are described in the following, the $1\,\sigma$ sensitivity characteristic is used.

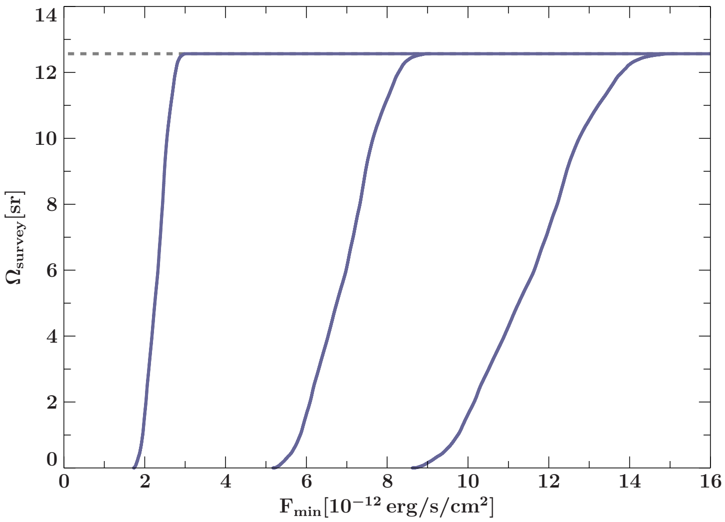

Figure 3.3.2.: *Swift*/BAT 105 month survey sky coverage as the function of minimal flux. The curves correspond to a 1, 3, and 5 σ detection (left to right) in the 20 keV–100 keV band. The dashed line indicates the full sky.

3.4 Number count distribution: logN-logS

Astronomical surveys that look for specific source types are characterized by the distribution of several key parameters of the observed sources, such as flux and flux density, distance, luminosity, spectral shape, variability of flux and spectral shape, the correlation of these parameters with those in other wavelength regimes, and many more. These population studies of, for example, a certain AGN class, and especially for sizable samples, are facilitated by graphing the number count distribution. This is also called the $\log N$-$\log S$ because the logarithm of the number of sources is graphed against the logarithm of the flux, often labelled S instead of F. In the following the physical quantity of flux is consistently named F. The $\log N$-$\log S$ diagram conveys a number of statistical properties of the emission of flux by any given sample, as well as possible selection effects, incompleteness, or flux intensity fluctuations. It can also be used to find differences between the spatial distributions of source types. Many studies in the past have utilized this tool for Galactic objects like X-ray binaries (e.g., Grimm et al., 2002), and extragalactic sources from single galaxies, AGN (e.g., Mateos et al., 2008; Warwick et al., 2012), to whole galaxy clusters (e.g., Kitayama et al., 1998). The path of each curve in the $\log N$-$\log S$ diagram can have cosmological implications, namely the evolution of a source population over large time scales. In addition, this toolset is often used to test and compare the capabilities of observing instruments (e.g., Akylas & Georgantopoulos, 2019).

In this work, a number of AGN samples are analyzed via their $\log N$-$\log S$ distributions. From a fit of the curve the distribution can be extrapolated to lower fluxes. Thus, it can be determined how complete a sample is in terms of flux coverage. Furthermore, the number of missing sources at low fluxes can be calculated. In performing a fit of the distribution it is also possible to test if only a small portion of bright sources dominate the slope, meaning, how consistent the distribution is. In addition, different systematic factors like selection biases and the implications of random flux fluctuations and flares can be studied. One specific field that benefits from the measurements of the $\log N$-$\log S$ distributions is the study of the contribution of a source population to the cosmic X-ray background (CXB), which is described in Sect. 3.5.

A limiting factor regarding the usage of $\log N$-$\log S$ distributions of X-ray flux, or any other flux measurement for that matter, is that the analysis does not directly take into account the variation of intrinsic luminosity between sample sources of equal flux, potentially skewing the result. By calculating the luminosity function of a source sample the luminosity and redshift distributions are directly factored in (see Sect. 3.6).

3.4.1. Shape of the logN-logS

There are several methods to express the $\log N$-$\log S$ diagram. Data points that correspond to the flux of each source in the sample can be shown as a cumulative differential or integral graph. Here, the integral diagram plot method is used. The cumulative source number per area sky with fluxes F_i larger that F_j of source j is given by:

$$N(\geq F_j) = \frac{\Omega_{\text{survey}}}{\Omega_{\text{sky}}} \sum_{i}^{n} \frac{1}{\Omega_i}, \tag{3.4.1}$$

with the number of sources n brighter and including F_j (after, e.g., Mateos et al., 2008). Ω_{sky} describes the total sky area and Ω_{survey} the covered area by the specific survey, for example, part of the Northern hemisphere or in certain cases the whole sky. The error bars of each data point in the diagram are calculated using Poisson statistics:

$$N_{\text{err}}(> F_j) = \frac{N(> F_j)}{\sqrt{N}}. \tag{3.4.2}$$

The general shape of a cumulative $\log N$-$\log S$ distribution is a falling trend with increasing flux. It can often be approximated by a single or broken power law. The single power law case with normalization A and exponent / slope α is described by:

$$N_{\text{err}}(> F) = AF^{-\alpha}. \tag{3.4.3}$$

Assuming that the emission from objects does not change with time, that is redshift, and that the objects are distributed uniformly in space the negative index becomes $\alpha = 3/2$. The value of the index can be derived from the ratio of volume to surface of a spherical region in space, corresponding to Euclidean, or flat, geometry. Figure 3.4.1 shows a simulated case of the $\log N$-$\log S$ distribution of an ideal non-evolving sample in Euclidean geometry, and the same sample under the influence of fluctuating flux. The ideal case, plotted as red circles, is a sample of 250 sources, which simply follow the slope of $-3/2$ (gray dashed lines), starting at an arbitrary flux value of 10. Plotted as blue squares is the same sample with a random factor applied to the majority of flux values. In addition, an increasing number of sources is randomly filtered out the fainter the sources are. This simulates the detection bias created by some flaring sources that temporarily climb over the detection threshold of the survey. A more detailed discussion of the impact of variability amplitudes and flaring can be found in Sect. 3.4.2. Both distributions serve as an illustration how the ideal $\log N$-$\log S$ graph and a realistic and potentially biased one (for larger distances) may look like. Many larger surveys in multiple wavelength regimes show very similar distributions compared to the simulation (e.g., La Franca et al., 2005; Krivonos et al., 2015; Massaro et al., 2014).

Besides the variation in intrinsic luminosity for sources within a sample, a variety of factors influence the shape of the $\log N$-$\log S$ distribution. Many of these factors can be analyzed separately and, if possible, excluded in order to determine the statistical properties with a

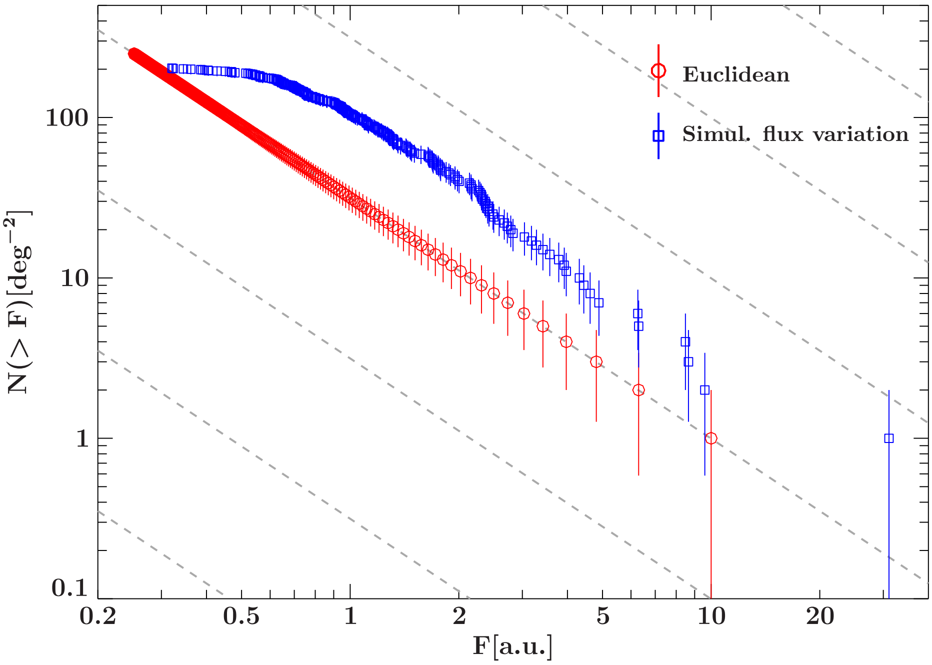

Figure 3.4.1.: Simulated ideal log N-log S distribution of uniform luminosity in Euclidean Universe (red circles), and induced variable flux overall and missing sources at low fluxes (blue squares). The gray dashed lines indicate a slope of $-3/2$.

minimum of biases. These factors can be characterized as either physical or systematic. In the following, both categories are discussed in terms of the sources counts of galaxies.

A slope of the log N-log S distribution that differs from the Euclidean case can be regarded as a relative over-abundance of bright, or faint sources. The sort of influence that is of physical nature generally describes the true volumetric density of sources that emit in a specific observed band. Since most modern beamed-AGN surveys span large redshift ranges of $z > 1$ the homogeneous and isotropic structure of the Universe excludes the impact of naturally large density variations on small scales. The observation of sources on large scales introduces the possibility of source evolution, however. In this case, a shape of the log N-log S distribution that has not the ideal slope of $-3/2$ indicates a different luminosity output of sources throughout their existence. This can also be interpreted as a variation in density when sources start or stop to emit radiation, or even merge to decrease their numbers. A larger flux-limited survey with a number of different source classes in it can have significantly different looking log N-log S statistics. For example, the distribution of redshift for the two largest sub-classes in the *Fermi*/LAT 3LAC catalog (Ackermann et al., 2015), FSRQs and BL Lacs, are noticeably varied, with BL Lacs being much closer. Thus, the covered time scales for observable evolution are also different.

The systematic effects that are present in a data set can be severe and give the impression of intrinsic evolution and other natural effects. Because of this it is important to narrow the extend of said influences. Every survey has two main limiting factors: sensitivity and finite observation time. The sensitivity of an instrument in a given band is usually well known and can be expressed by the sky coverage (see Sect. 3.3). Since many astrophysical sources can show high variability on the time scales from minutes to years, the limited observation time can skew the mean flux that can be expected from such a source. When compiling a source sample, a certain flux threshold is regarded as the lower limit for which the survey within the observed sky area can be called statistically complete. High variability, especially close to the detection threshold, can include or exclude sources from the sample. Because the number of fainter sources is typically larger than brighter sources the false inclusion of lower flux sources is more probable (Eddington Bias). Should the source selection criterion be such that a source flux has to reach a certain value within an observation period but the cataloged flux is the mean value from multiple observations, the effective cataloged flux is lower than the completeness of the sample would allow. This effect adds a small number of sources to the lower flux end which rapidly level off (blue curve in Fig. 3.4.1).

A third category of biases that influence the shape of a $\log N$-$\log S$ distribution stems from the sample definition using one instrument, for example, a radio survey, and the analysis in a different wavelength band, such as X-rays. This bias is often difficult to isolate since the transition of one wavelength band to another one can yield different results, even for the same source type. Beamed AGN, for instance, that have been defined in a flux-limited sample at a few GHz do not all have the same factor of radio to X-ray flux. The broadband spectral energy distribution (SED) of a beamed AGN / blazar has a different shape in both bands (see, for example, Fig. 4.2.3). If the SED is shifted marginally to higher or lower energies the contribution of synchrotron emission or Compton up-scattering can change significantly for the X-ray band. Because of this it is useful to compare the results of both $\log N$-$\log S$ distributions with source samples that are defined in their native energy band.

3.4.2. Variable sample sources

Numerous observations in all wavelength regimes have shown that active galaxies, and especially blazars, are highly variable sources (see Sect. 1.2.1). The significant increase of flux on short time scales and the long-term development of the flux are simultaneously studied with a wide array of instruments. Such as radio observation campaigns (e.g., MOJAVE and TANAMI, see Sect. 2.1.2) to the monitoring in the X-ray and gamma-ray regime using *Swift*/BAT (Sect. 2.3) and *Fermi*/LAT (Sect. 2.4), and the very-high-energy band via Imaging Air Cherenkov Telescopes like MAGIC (Aleksić et al., 2012) and FACT (Biland et al., 2014). In this section, the influence of flux variability on the shape of an ideal $\log N$-$\log S$ function of Euclidean-distributed sources is tested using a number of simplified assumptions. Specifically, the typical flaring amplitude and the percentage of the flaring sources are considered.

As already mentioned in Sect. 3.4.1, the effects of random flux increase are simulated in two separate steps. Each simulated diagram starts with the ideal Euclidean case with the brightest source set at $N = 1\,\mathrm{deg}^{-2}$ and a flux of $F = 10$ in arbitrary units. All data points follow the cumulative integral form of the $\log N$-$\log S$ distribution (Eq. 3.4.1) and therefore a power-law index of $-3/2$. In Fig. 3.4.2a this case is graphed for 400 sources. For 200 randomly chosen sources in the distribution each flux is multiplied with the factor:

$$f_{\mathrm{var}} = r_{0\ldots1} * a_{\mathrm{var}} + 1, \tag{3.4.4}$$

with a uniformly distributed random number $r_{0\ldots1}$ and the amplitude factor a_{var}. This gives, for example, a multiplication factor to the original flux of 1...3 for $a_{\mathrm{var}} = 2$. The factor starts at unity because an increase just above normal flux for the observation period is

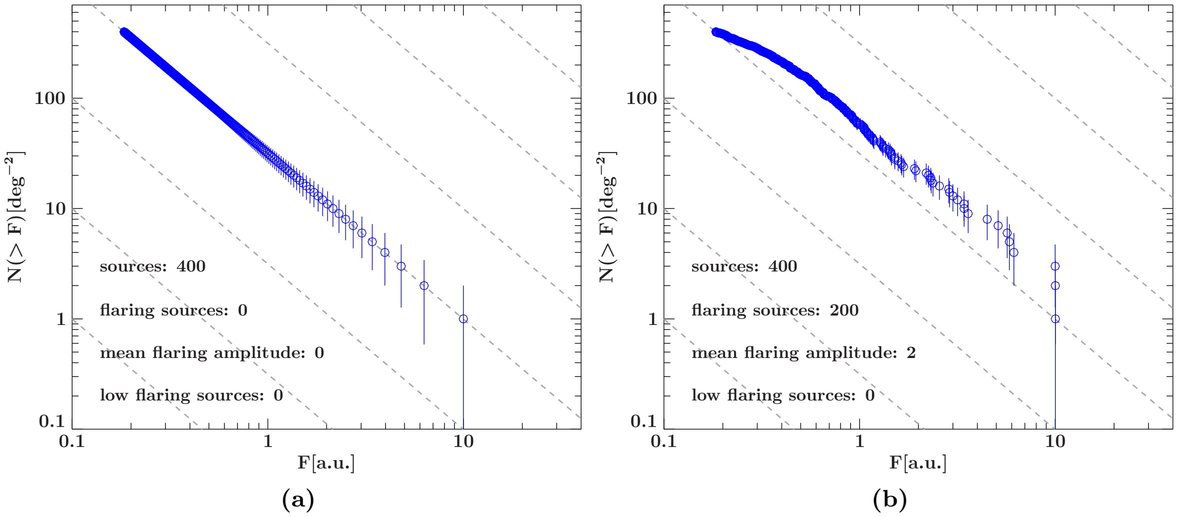

Figure 3.4.2.: log N-log S distributions of (a) ideal Euclidean flux distribution and (b) with randomly increased flux for 200 out of all 400 sources.

assumed in this approach. Figure 3.4.2b shows the result of the simulated flux variation. In essence, a random half of all sources is shifted by a factor of 1...3 to the right. The diagram is then sorted and graphed anew. Compared to the normal Euclidean case, the log N-log S distribution is also characterized by a slope of or at least very close to $-3/2$, with a flattening at the lower flux end, where most sources are concentrated. The randomly chosen shifting by flux increase already changes the shape of the distribution noticeably.

This trend can be amplified further by raising the number of sources that are affected by flux increase and by raising a_{var}. Both effects are illustrated in Fig. 3.4.3, where the amplitude increase is expressed by two different values of a_{var}, here, for example, 2 and 6. Each of which are applied to half of the sources in question. This second variant produces not only a stronger flaring effect but can also be understood as two independent causes for the flux increase, or a mixture of two source types with characteristic amplitudes. Additionally, the effect of random flux increase of sources normally below the detection threshold at the low flux end is simulated by randomly removing around 100 sources at the low end. This is done by removing the more sources the closer the flux is to the lowest one in the diagram using a linear function. Finally, the fluxes are sorted and the log N-log S diagram is graphed with Poisson errors. The end result is a realistic depiction of a typical log N-log S graph of a flux-limited source survey with slight variation within the curve and a flattening lower end that thins out rapidly. Although the repeating random creation of each diagram yields small variations in shape, the overall trend in each case stays the same.

3.5 Contribution to the CXB

In the past, a number of studies aimed to characterize the cosmic X-ray background (CXB) and its shape from around 0.5 keV to several hundred keV, including its maximum in energy density at approximately 30 keV. Figure 3.5.1 displays the CXB, sampled by various missions in the past. Also, many previous works aimed to deconstruct the individual contribution

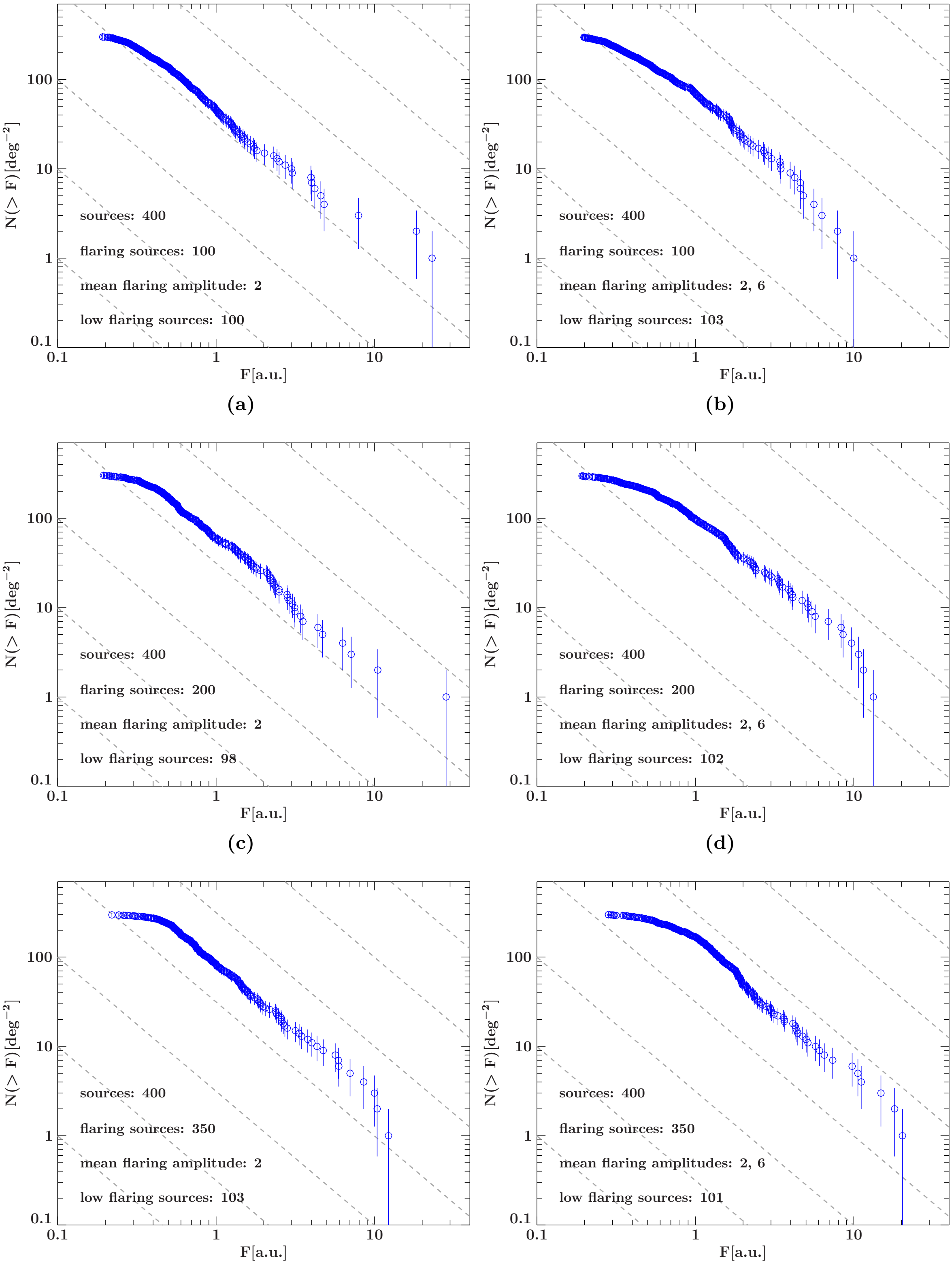

(a) (b)

(c) (d)

(e) (f)

Figure 3.4.3.: $\log N$-$\log S$ distributions with randomly increased flux. Left: for the mean increase factor of 2, right: for the mean increase factor of 2 and 6 for both halves of the flaring sources. Top to bottom: growing percentage of flaring sources. All cases have around 100 sources randomly removed at the lower flux end.

of sources. It is still debated how large a Compton-thick source population is, which might by strongly under-represented in soft X-ray surveys. In the past, several surveys were able to associate individually detectable objects with the CXB. Moretti et al. (2003) studied combined deep X-ray surveys in the soft range of 0.5 keV–10 keV with *Chandra*, *XMM-Newton*, and *ROSAT*, with the result that a great majority of the CXB can indeed be resolved into specific sources. Ajello et al. (2008b) found that in the hard X-ray band of 14 keV–170 keV band 1%–2% of the CXB can be resolved into AGN. However, the authors used only a relatively small sample with the majority being close Seyferts. In a study by Ajello et al. (2009) the contribution to the hard CXB for Seyfert and blazar samples was conducted using evolutionary luminosity function models (see also Sect. 3.6). The work produced strongly varying contribution percentages from a few percent to over 100% for certain models. The approach was also based on measured data from a small number of sources (38 blazars). Recently, Giommi & Padovani (2015) found that the blazar contribution to the CXB in the 1 keV–50 keV range can be confined to 4%–5%, and to approximately 10% at 100 keV, with as much as the complete background for energies exceeding 10 GeV. This, however, was done for a simulated data set of a $\log N$-$\log S$ distribution that was extrapolated from soft X-ray data. The complication of deriving the blazar contribution stays the same: a reliable data basis requires directly measured hard X-ray spectra from a larger blazar sample. In this work, the calculation of the CXB blazar contribution is based on a number of blazar samples, which stem from larger surveys, conducted in the radio, X-ray, and gamma-ray regime.

To determine which percentage of the CXB is resolved in a given source sample, the CXB flux in the interval of 20 keV–100 keV and 14 keV–195 keV is calculated. The first interval is the reduced band for which the majority of the spectral analysis in this work has been conduced. The full band is also determined for comparison with the official BAT catalog beamed AGN sub-sample. The CXB spectrum itself, which has been fitted with a smoothly joined broken power law by Ajello et al. (2008a), is integrated numerically and converted to cgs units. The spectrum is given in units of $\mathrm{keV}^2\,\mathrm{photons\,cm}^{-2}\,\mathrm{s}^{-1}\,\mathrm{sr}^{-1}\,\mathrm{keV}^{-1}$. During the integration over energy, keV is converted to erg, sr to deg^2, and at each integration step the expression is divided by the center energy of each step. The resulting CXB fluxes per solid angle are:

$$I_{\mathrm{CXB}}^{20-100\,\mathrm{keV}} = 3.14 \cdot 10^{-11} \mathrm{erg\,s}^{-1}\mathrm{cm}^{-2}\mathrm{deg}^{-2}, \qquad (3.5.1)$$

and

$$I_{\mathrm{CXB}}^{14-195\,\mathrm{keV}} = 4.61 \cdot 10^{-11} \mathrm{erg\,s}^{-1}\mathrm{cm}^{-2}\mathrm{deg}^{-2}. \qquad (3.5.2)$$

Having derived the spectral fluxes of a sample and therefore the $\log N$-$\log S$ distribution allows the calculation of the flux per sky area that can be attributed to the sample. Following, for example, Giommi et al. (2006), the flux can be calculated as the integral over the differential $\log N$-$\log S$ fit function multiplied with the flux:

$$I_{\mathrm{sample}} = \int_{F_{\mathrm{min}}}^{F_{\mathrm{max}}} \frac{\mathrm{d}N}{\mathrm{d}F} F dF, \qquad (3.5.3)$$

with the lower limit F_{min} and top limit F_{max} of source fluxes in the sample. The top limit can also be set to a higher value. This, however, does not influence the result of Eq. 3.5.3 significantly because of the declining trend of the function. The integral can also be evaluated with a lower F_{min} than the flux of the faintest source, but only under the assumption of a consistent slope of the $\log N$-$\log S$ distribution below the measured flux.

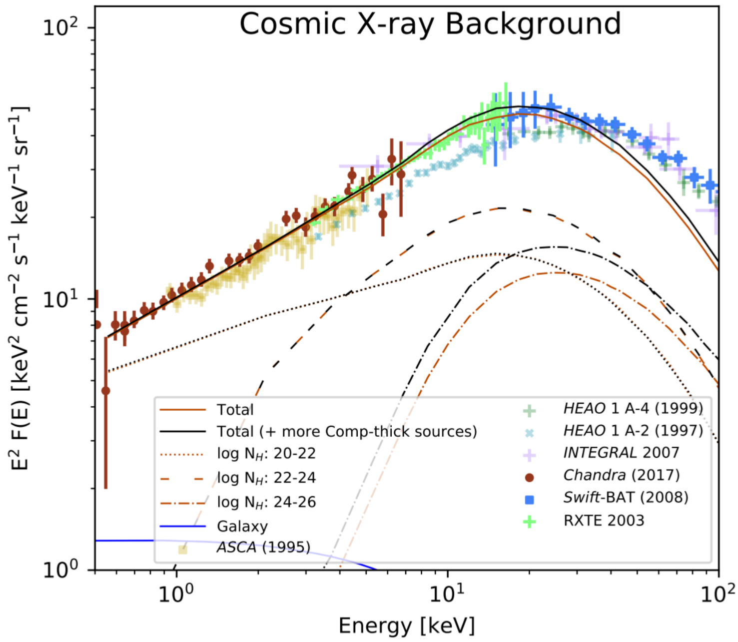

Figure 3.5.1.: The cosmic X-ray background as measured by various missions. Graphed is the energy density per solid angle against energy from the soft to the hard X-ray range. Image credit: Ananna et al. (2020) and references therein.

3.6 Luminosity Function (LF)

The so-called luminosity function is often used as a versatile tool for population and statistical analysis as well as a complementary method to the $\log N$-$\log S$ analysis for a known object sample. How can the distinct distribution of the flux F and luminosity L values be explained in the given data set? Why are there too many or too few bright or faint sources in the source sample compared to uniform distribution in Euclidean space? How many sources are there at a certain time within the evolutionary path of the population, and how does the luminosity change with time? A number of issues like selection bias or intrinsic evolution with time are inaccessible by graphing and fitting the $\log N$-$\log S$ distribution alone. The differential luminosity function (LF) $d\Phi/dlogL$ of a data set expresses the number of sources per unit redshift z, or co-moving volume, and luminosity L. The LF can be calculated in two ways: as a binned version and analytic model fit. The following approach for the calculation of the binned and analytic versions follows the methods described in Ajello et al. (2009), Ebrero et al. (2009), and Miyaji et al. (2015).

3.6.1. Definition

The binned LF is expressed by the number of sources N in a logarithmic luminosity bin $L_{\text{bin,min}} - L_{\text{bin,max}}$, divided by the integral over the co-moving volume dV/dz. The integral limits for luminosity $L_{\min} - L_{\max}$ and $z_{\min} - z_{\max}$ correspond to the measured minimum and maximum values in the source sample. The binned LF thus becomes:

$$\frac{d\Phi}{dlogL} = \frac{N}{\int_{L_{\min}}^{L_{\max}} \int_{z_{\min}}^{z_{\max}} \frac{dV}{dz}\; dz\; dlogL}, \tag{3.6.1}$$

and

$$\frac{d\Phi}{dlogL} = \frac{N}{\int_{logL_{\min}}^{logL_{\max}} \int_{z_{\min}}^{z_{\max}} \frac{dV}{dz} \frac{1}{L\; log(10)}\; dz\; dlogL}, \tag{3.6.2}$$

with the co-moving volume:

$$\frac{dV}{dz} = d_H \left(\frac{d_L}{1+z}\right)^2 \frac{\Omega(L,z)}{\sqrt{\Omega_{\mathrm{M}}(1+z)^3 + \Omega_\Lambda}}, \tag{3.6.3}$$

and the luminosity distance d_{L}, and the accessible sky area $\Omega(L,z)$ of a source with L and z. The cosmological parameters in the above equation are set to $\Omega_{\mathrm{M}} = 0.3$ and $\Omega_\Lambda = 0.7$. The Hubble distance is defined by:

$$d_H = \frac{c}{H_0}, \tag{3.6.4}$$

in Mpc with the Hubble constant H_0 set to $70\,\mathrm{kms}^{-1}\mathrm{Mpc}^{-1}$. The derivation of the cosmological quantities needed in this approach is performed using the `cosmolopy` package, which implements the equations outlined in Hogg (1999).

The data set is binned by luminosity and for each bin Eq. 3.6.2 is evaluated. In doing so, the integral is solved numerically on a 50×50 log$L$-z grid: the integrand is calculated for every element and is multiplied by the step size in log$L$ and z. The resulting sum of all elements equals the expression in the denominator in Eq. 3.6.2. Usually, the integration over the logarithmic luminosity is chosen, because of the multiple orders of magnitude for the most source samples. Solving a numerical integral for linear luminosity scaling tends to deliver inaccurate results due to numerical effects caused by insufficient resolution. The grid on which the double integral is computed is shown in Fig. 3.6.1. The relation of flux in the log$L$-z plain is illustrated in Fig. 3.6.1a for a generic blazar spectral photon index of $\Gamma = 1.7$. Using the function of the accessible sky area depending on minimal flux (Fig. 3.3.2, $1\,\sigma$ sensitivity), the sky area corresponding to the BAT survey in 20 keV–100 keV is plotted in Fig. 3.6.1b. Because of the slow rise of the sky area curve, the transition between 0 and the complete sky area is distributed over several grid elements. The co-moving volume (Eq. 3.6.3), which is also calculated depending on L and z coordinate, is shown in Fig. 3.6.1c.

Figure 3.6.2 shows the binned LF for an X-ray data set for the MOJAVE-1 blazar sample (see Sect. 4.2.5). Luminosity functions show a typical falling trend, often fitted via a single or broken power law. The errors of each data point are purely statistical (Poisson distributed).

A function that fits the data can not only be applied to characterize the shape of the distribution with a number of parameters such as slope, normalization, or turnover luminosity in the case of a broken power law. The advantage of finding a fitting functional relation between source density and luminosity and redshift is that a evolutionary term can be included. This term describes if intrinsic evolution is present and how it can be characterized, for example, by a critical redshift, or strength of evolution with redshift. An analytic model of the LF is fitted to the data using a maximum likelihood approach. The following sections describe the fitting algorithm and the used analytical models.

3.6.2. Maximum Likelihood estimation

Finding the optimal set of model parameters that describe a given data set is often facilitated by using a likelihood function $\mathcal{L}$. This function is the product of the probability density f_i of each measured data point $[x_1, x_2, ..., x_n]$ (see, e.g., Blobel & Lohrmann, 2012):

$$\mathcal{L}(a) = \prod_{i=1}^{n} f(x_i|a), \tag{3.6.5}$$

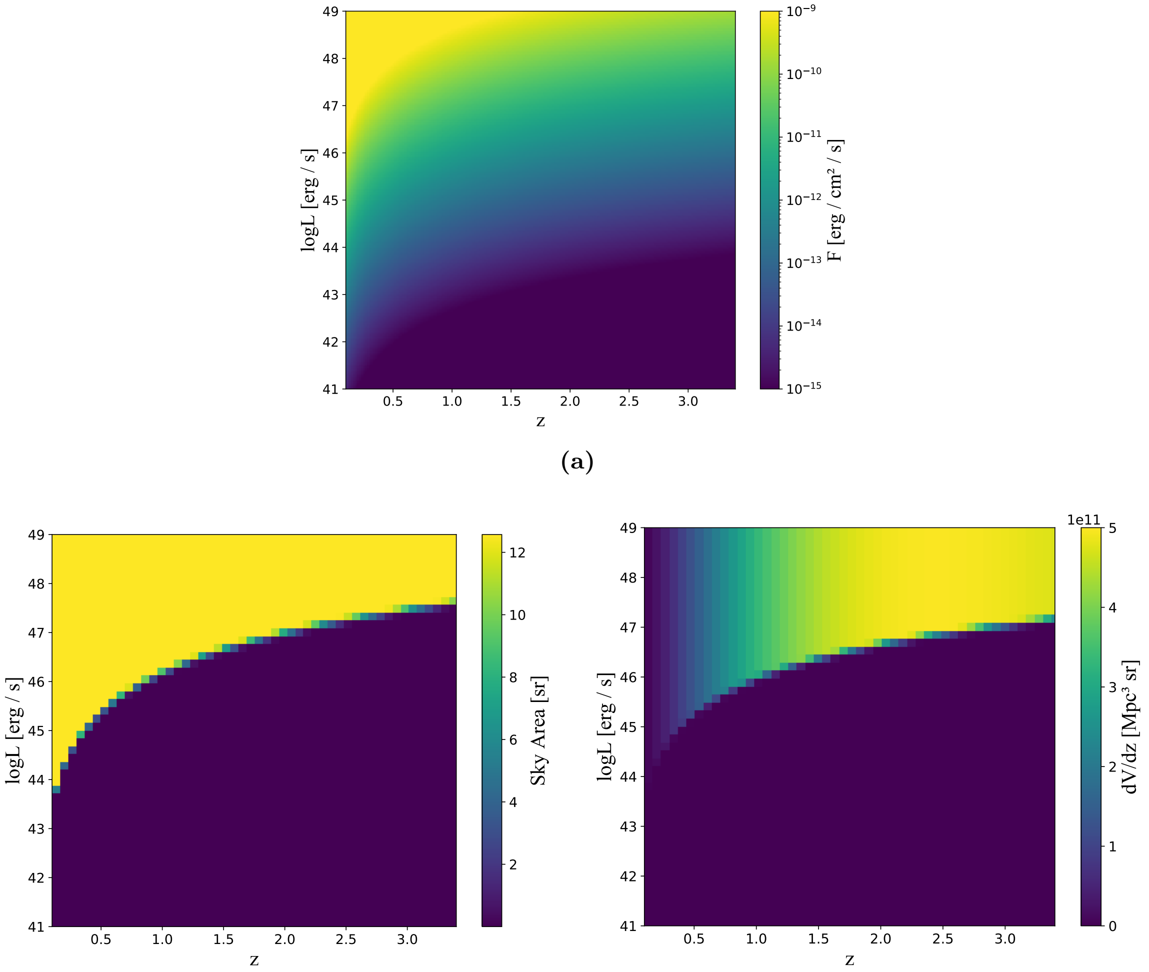

(a)

(b)

(c)

Figure 3.6.1.: Luminosity L of a generic blazar power law spectrum ($\Gamma = 1.7$) plotted against redshift z on a 50×50 grid: (a) distribution of flux in the $\log L - z$ plain, (b) corresponding sky area derived by using the BAT $1\,\sigma$ survey coverage (Fig. 3.3.2), (c) co-moving volume computed from Eq. 3.6.3.

for n measurements and a set of parameters a. It gives the likelihood of measuring x_i if the model parameters are assumed to be true. The objective in this approach is to maximize $\mathcal{L}$ which corresponds to the best estimate model parameters $\hat{a}$. All probability densities need to be normalized to 1 for all parameters a:

$$\int f(x|a)dx = 1 \;\forall\; a. \tag{3.6.6}$$

In practice, the negative logarithmic likelihood function $\mathcal{F}$ is often used, which has to be minimized:

$$\mathcal{F}(a) = -\log \mathcal{L}(a) = -\sum_{i=1}^{n} f(x_i|a). \tag{3.6.7}$$

Many implemented optimization algorithms already perform a minimization instead of a

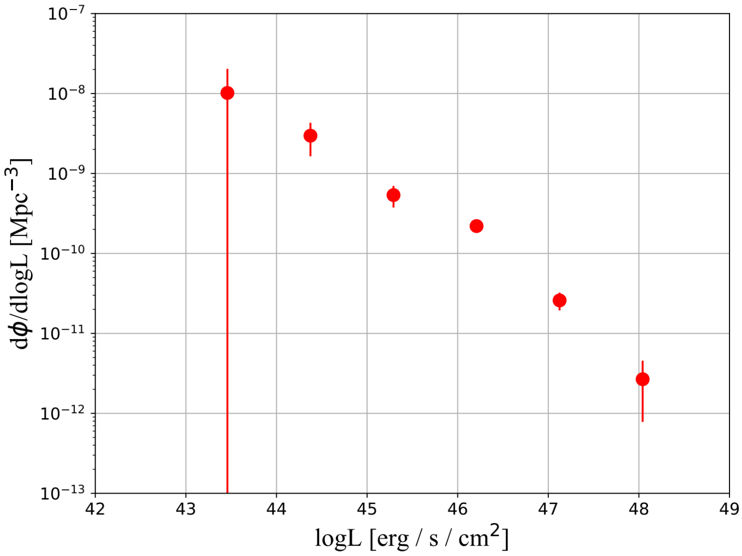

Figure 3.6.2.: Binned X-ray luminosity function of data set from the MOJAVE blazar sample (70 sources), see Sect. 4.2.5.

maximization, like the used MINUIT software package (James, 1994). The transformation into the logarithmic expression makes the algorithm numerically more stable, because the probability densities are usually small numbers would be multiplied after Eq. 3.6.5. Finite precision in any software implementation can therefore easily lead to numerical errors, skewing the results. Summing the logarithmic values instead leads to much more consistent results. For all model parameters a_i, represented by the vector $\bar{a}$, the partial derivative of $\mathcal{F}$ must become 0,

$$\frac{\partial \mathcal{F}}{\partial a_i} = 0. \tag{3.6.8}$$

Using a minimization algorithm like MINUIT also creates the covariance matrix C of the vector $\bar{a}$ at the minimum $\hat{a}$. Its entries are the second derivatives of $\mathcal{F}$,

$$C = G^{-1}, \tag{3.6.9}$$

with

$$G_{ij} = \frac{\partial^2 \mathcal{F}}{\partial a_i \partial a_j}. \tag{3.6.10}$$

The errors of the model parameters are the square roots of the diagonal matrix elements. To determine which assumed model describes the data best the Akaike information criterion (Akaike, 1973) is applied. The process provides a balanced approach between choosing a preferably simple model and the goodness of fit of the model. The AIC value is defined by the maximum likelihood value $\mathcal{F}$ and number of free parameters k:

$$\mathrm{AIC} = 2k - 2log\mathcal{F}, \tag{3.6.11}$$

and is minimal for the best fit LF model. The difference of the AIC values,

$$\Delta_j = \mathrm{AIC}_j - \mathrm{AIC}_{\mathrm{min}} \tag{3.6.12}$$

of model j to the model with the minimal AIC value, states whether the model is equally or less probable to be true (Burnham & Anderson, 2004). A relative probability p_j can be assigned that determines how likely model j describes the data compared to the best fit model:

$$p_j = e^{-\Delta_j/2}. \tag{3.6.13}$$

Although the AIC is used frequently for choosing a model that best describes a given data set, alternative approaches exist in this regard. The Bayesian Information Criterion (Schwarz, 1978), for example, uses a similar likelihood-based method. However, it possesses a number of disadvantages to the AIC for the specific application in this study. One factor is that the AIC provides better results in case that the list of models does not include the exact true model. In turn, the AIC method chooses a model that asymptotically minimizes the difference of data and prediction (Vrieze, 2012).

3.6.3. Luminosity Function models

The analytic form of luminosity functions (LF) is often used to constrain the characteristics of certain AGN populations and to create population synthesis models that can be compared with the observed data. Luminosity functions of the radio flux density of AGN have been used, for example, to characterize and study morphology, accretion modes, and jet power (e.g., Kaiser & Best, 2007; Cara & Lister, 2008). Large surveys in the soft and, to an extend, hard X-ray bands aim to determine the different AGN class evolution scenarios, or pinpoint the composition of the CXB (e.g., Sazonov et al., 2007; Mateos et al., 2008; Ebrero et al., 2009).

In this work the LF models are used to analyze the difference between the observed emission characteristics of the same source sample in the radio and hard X-ray bands. Also, varying AGN sub-classes are compared based on their best fit model parameters. Often, the binned luminosity function shows a behavior that can be described by an analytical form in the shape of a single or broken power-law model. The present day LF ($z = 0$) can be expressed as:

$$\frac{d\Phi}{dlogL} = A\left(\frac{L}{L_*}\right)^{-\gamma_1}, \tag{3.6.14}$$

and

$$\frac{d\Phi}{dlogL} = A\left[\left(\frac{L}{L_*}\right)^{\gamma_1} + \left(\frac{L}{L_*}\right)^{\gamma_2}\right]^{-1}, \tag{3.6.15}$$

for the single and smoothly joined broken power-law, respectively. The free parameters are the normalization A, the power-law indices γ_1 and γ_2, and the break luminosity L_* (fixed for single power-law models). The evolutionary behaviour of the LF can be expressed by the redshift-dependent function:

$$e = (1+z)^{(k+gz)}, \tag{3.6.16}$$

with the parameters k and g. Here, two separate basic models of the LF are used: the pure density evolution (PDE) assumes a changing number of sources with steady luminosity output per volume with time. In contrast, pure luminosity evolution (PLE) solely assumes changing luminosity with a constant source number. The LF becomes thus:

$$\left.\frac{d\Phi}{dlogL}(L,z)\right|_{\mathrm{PDE}} = \frac{d\Phi}{dlogL}(L, z=0)\cdot e \tag{3.6.17}$$

and

$$\left.\frac{d\Phi}{dlogL}(L,z)\right|_{\mathrm{PLE}} = \frac{d\Phi}{dlogL}(L/e, z=0). \tag{3.6.18}$$

It is beneficial to further subdivide the introduced models regarding their complexity of the evolutionary term e. In the PLE and PDE models the exponent g is set to 0. In the case that g is allowed to vary the models will be labelled PLEg and PDEg, respectively. This allows to test whether less free parameters are sufficient compared to more complex models in terms of describing the measured data.

Figure 3.6.3 illustrates single and broken power-law models in the PLE and PDE variant for the typical blazar X-ray luminosity range. The single power-law models area created assuming $A = 10^{-8}\,\mathrm{Mpc}^{-3}$, $\gamma_1 = 0.7$, $k = 1$ and $L_* = 10^{44}\,\mathrm{erg\,s^{-1}}$. Whereas for $z = 0$ the LF is the same for both PLE and PDE, the distance between the LF for increasing values of z is larger. This stems from the fact that the slope in this case is flatter than 1, which produces a larger change in the source number per volume (y-axis / PDE) than a change in luminosity (x-axis, PLE). This is shown even more clearly in the broken power-law models, which feature a flat ($\gamma_1 = 0.7$) and a steep ($\gamma_2 = 1.5$) slope. The break luminosity is set to $L_* = 10^{45}\,\mathrm{erg\,s^{-1}}$. For the assumed model parameters sources become generally more luminous or denser with higher redshift.

More complex models can reveal an evolutionary path that is not linear and might exhibit a maximum or minimum. The PLEg and PDEg models are plotted in Fig. 3.6.4 using the same parameters like before for both the single and broken power law, but with the parameters $k = 2.5$ and $g = -0.5$. The combination of these parameters in the evolutionary term of the LF produce a behaviour that lets the LF rise in luminosity or density and then, after a certain critical redshift, decrease again.

Previous studies of larger AGN samples incorporated models that express not only the evolution of luminosity or density, but include both as parallel or interconnected processes (e.g., Ueda et al., 2003; Miyaji et al., 2015; Ranalli et al., 2016). Common versions are the luminosity and density evolution (LADE), the luminosity-dependent density evolution (LDDE), or the independent luminosity density evolution (ILDE). The individual models incorporate either the evolutionary factor e, which is multiplied with the LF and the luminosity, or two different factors and allow different behaviors of the LF with z at high and low luminosities. The used data sets in this work are characterized by a significant number of upper-limit luminosity values, especially in the X-ray band, leading to lower sample sizes, and thus, a reduced number of data points. Therefore, the fitting of the LF in the different wavelength regimes focuses on the PLE / PDE and PLEg / PDEg models.

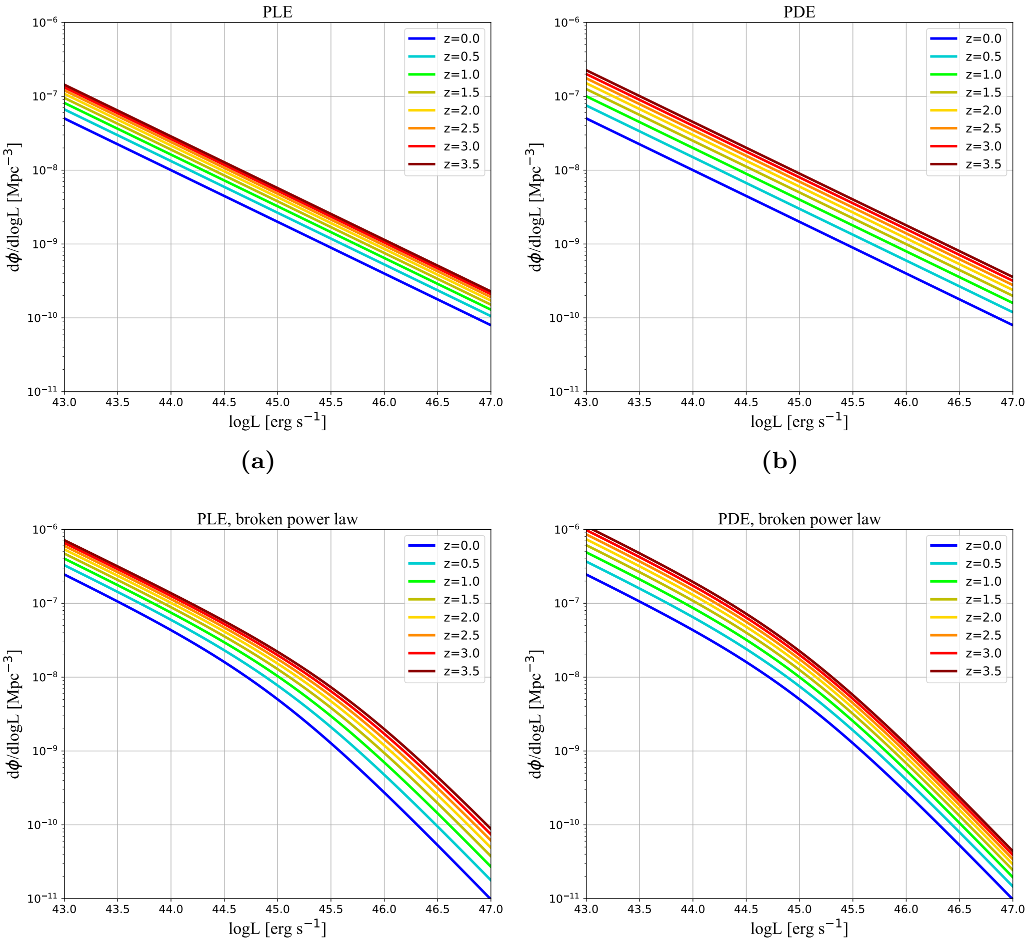

(a) **(b)**

(c) **(d)**

Figure 3.6.3.: Example luminosity function models PLE and PDE: for the single power-law models in (a) and (b) the model parameters $A = 10^{-8}\,\mathrm{Mpc}^{-3}$, $\gamma_1 = 0.7$, $k = 1$ and $L_* = 10^{44}\,\mathrm{erg\,s^{-1}}$ were used. For the broken power-laws in (c) and (d) the parameters $\gamma_2 = 1.5$ and $L_* = 10^{45}\,\mathrm{erg\,s^{-1}}$ are assumed.

3.7 Tests for parameter distributions and correlation

This section describes the basic statistical tests for the comparison of parameter distributions in this study. In order to test if the distribution of a certain measured variable x_{A} follows a given theoretical distribution or is drawn from the same parent distribution of another measured variable x_{B} a number of tests can be applied. Besides the method introduced in Sect. 3.7.2 the results in this work have been obtained using the implementation of the statistical tests in the ISISscripts[5]. The formalism in this section follows Bosch (1998).

---

[5] Provided by ECAP/Remeis observatory and MIT (`https://www.sternwarte.uni-erlangen.de/isis/`)

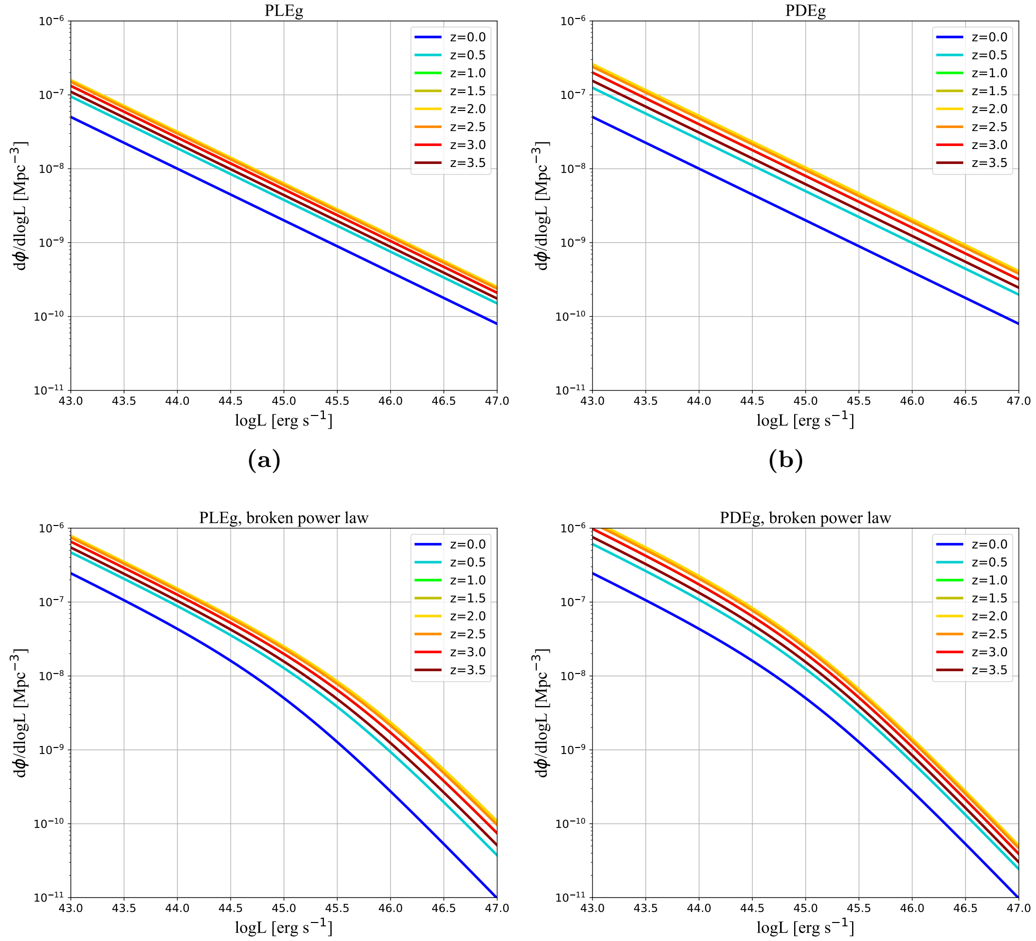

(a) **(b)**

(c) **(d)**

Figure 3.6.4.: Example luminosity function of the models PLEg and PDEg: the same parameters from Fig. 3.6.3 are used, except for $k = 2.5$ and $g = -0.5$.

3.7.1. Kolmogorov-Smirnov test

Besides the already discussed maximum likelihood approach using the χ^2 fit statistic (Sect. 3.2.2), an often used method is the Kolmogorov-Smirnov test (KS test) to compare the data sets to a distribution function or other data sets. This section focuses on a two-sided KS test.

In a 1-sample KS test the random variable X is assumed to have a distribution function $F(x)$, which is unknown. Let $G(x)$ be a known continuous distribution function. The hypothesis

$$\begin{aligned} H_0 &: F(x) = G(x), \text{ for all } x \\ H_1 &: F(x) \neq G(x), \text{ for at least one } x \end{aligned} \tag{3.7.1}$$

is tested. From a sample $(x_1, x_2, ..., x_n)$ of size n an empirical distribution function $F_n(x)$ is determined, which is defined as:

$$F_n(x) = \frac{\text{number sample values} < x}{n}. \tag{3.7.2}$$

The test statistic value D, which is the maximum distance between $F_n(x)$ and $G(x)$, is then calculated,

$$D = \sup_{x\in\mathbb{R}} |F_n(x) - G(x)|. \tag{3.7.3}$$

For the test a significance level α is assumed, for instance $\alpha = 0.05$[6]. The $(1-\alpha)$ quantile of the test is determined,

$$D_{1-\alpha} \approx \sqrt{-\frac{1}{2n}\log\frac{\alpha}{2}}, \tag{3.7.4}$$

whose approximation is valid for $n \geq 40$. If

$$D \geq D_{1-\alpha} \tag{3.7.5}$$

then the null hypothesis of $F(x) = G(x)$ for all x can be rejected, and the hypothesis of $F(x) \neq G(x)$ for at least one x accepted. In this case, the distribution $F(x)$ of the random variable X is likely (at a level α) not the same as the distribution $G(x)$.

The 2-sample KS test works analogously to the 1-sample test. Here the empirical distribution functions $F_\mathrm{A}(x)$ and $F_\mathrm{B}(x)$ of the two independent variables X_A and X_B are compared. It is tested whether both distributions are drawn from the same parent distribution. The hypothesis

$$\begin{aligned} H_0 &: F_\mathrm{A}(x) = F_\mathrm{B}(x), \text{ for all } x \\ H_1 &: F_\mathrm{A}(x) \neq F_\mathrm{B}(x), \text{ for at least one } x \end{aligned} \tag{3.7.6}$$

is tested for. The test statistic value D_AB for this 2-sample test is thus determined:

$$D_\mathrm{AB} = \sup_{x\in\mathbb{R}} |F_\mathrm{A}(x) - F_\mathrm{B}(x)|. \tag{3.7.7}$$

For the $(1-\alpha)$ quantile follows (for $n_\mathrm{A} + n_\mathrm{B} \geq 40$ and $1-\alpha \geq 0.8$):

$$D_{1-\alpha} \approx \sqrt{-\frac{1}{2}\log\frac{\alpha}{2}} \cdot \sqrt{\frac{n_\mathrm{A}+n_\mathrm{B}}{n_\mathrm{A}\cdot n_\mathrm{B}}} \tag{3.7.8}$$

with the sample sizes n_A and n_B, respectively. Thus, the null hypothesis, of both data sets X_A and X_B to be drawn from the same distribution, can be rejected at a level α if

$$D_\mathrm{AB} \geq D_{1-\alpha}. \tag{3.7.9}$$

Like is the case for most statistical tests, the result can also be expressed with the p-value, which denotes a probability. It corresponds to the smallest significance level at which the null hypothesis can still be rejected. Many modern implementations of various tests return the test statistic and additionally the p-value.

---

[6] If not stated otherwise, this convention is set for all KS tests in this work.

3.7.2. Incorporating measurement errors

When comparing two distributions of the same parameter, for example, flux or photon index, the 2-sample KS test or the Z-test may be used. The resulting test statistic or probability value provides information of whether the null hypothesis of the two samples being drawn from a common distribution can be rejected or not. These tests, however, neglect the uncertainty of the measured values. In the following, a modified method, based on the 2-sample KS-test, is introduced, which takes into account the measurement uncertainty ranges when comparing two distributions of values, such as, model fit parameters. Especially in the analysis of data of low signal quality the extend of the parameter uncertainty can be substantial (see Sect. 4.2.2).

Let $X_{\rm A}$ and $X_{\rm B}$ be two samples of data of the same parameter x, for example, X-ray photon index, ($x_{\rm A,i}$, $x_{\rm B,i}$) and of the sample sizes $n_{\rm A}$ and $n_{\rm B}$, respectively. The uncertainties of the sample values are accordingly named $dx_{\rm A,i}$ and $dx_{\rm B,i}$. The distribution of the sample values can be graphed in form of a simple histogram, see Fig. 3.7.1 (a) and (b). If the error of each sample value is, for example, Gaussian in nature, the uncertainty range of said values can be understood as a Gaussian function:

$$A(x) = \frac{K}{dx_i\sqrt{2\pi}}\exp\left(\frac{-(x-x_i)^2}{2dx_i^2}\right), \tag{3.7.10}$$

with the expected value equal to the sample value x_i, the width of dx_i, and normalization K. In Fig. 3.7.1 (c), all individual sample values are assigned random error ranges for illustration. If a sample value is precisely known / has a small error (e.g., flux value of a bright source with high S/N) the Gaussian curve is expressed as a sharp peak. Otherwise, the function distributes over a larger space. Panel (d) in Fig. 3.7.1 shows the cumulative distributions of each sample from panel (c) as well as the sum of both samples (black line).

In order to make an assessment of how distinct both sample distributions $X_{\rm A}$ and $X_{\rm B}$ are, the sum of both samples is used. From this combined distribution a random test sample $X_{\rm A,test}$ of the size $n_{\rm A}$ as well as a random test sample $X_{\rm B,test}$ of the size $n_{\rm B}$ are drawn. The process is carried out on a discrete grid of 1000 bins on which the combined distribution is defined. The distribution's value at any given step of x is equal to the probability of a value to be drawn. For the two test samples a 2-sample KS test is performed. This step is repeated a large number of times, in this case 10^5 iterations. The KS test statistic D of all runs gives a distribution that is compared to the initial KS test statistic $D_{\rm AB}$ of the real sample distributions $X_{\rm A}$ and $X_{\rm B}$. The fraction of test statistic values D larger than $D_{\rm AB}$ indicates how likely the random distinct samples $X_{\rm A}$ and $X_{\rm B}$ are. Figure 3.7.2 illustrates the process for uncertainty ranges of random independent samples. The left panels (a), (c), and (e) show uncertainty distributions of different distances to one another, including the summed uncertainty range (black line). The right panels (b), (d), and (f) show the corresponding distribution of KS test statistic values D and the corresponding $D_{\rm AB}$ of the initial two samples. As the two initial distributions are moved away from each other, they become more distinct, which is reflected in the increasing KS test statistic $D_{\rm AB}$. In this example the test sample sizes are $n_{\rm A} = 20$ and $n_{\rm B} = 30$. The KS test statistic $D_{\rm AB}$ for all three cases, from top to bottom, is 0.21, 0.55, and 0.95. After 10^5 random draws the percentage of cases with $D > D_{\rm AB}$, is 57.94%, 0.08%, and 0.00%, respectively. This fraction directly indicates how likely it is that both samples are drawn from the same parent distribution, while taking into account the measurement uncertainties.

The shape of the distributions of D values is always (mostly) the same because the random draws are performed for the sum of both samples (black line). Although for a very small number of draws the distributions of D values will differ notably, a large number of draws leads to a much more even sampling of the tested quantity, leading to, on average, the same distribution of D values. On the other hand, said distribution is influenced by the test sample sizes n_A and n_B.

3.7.3. Kendall's τ rank correlation coefficient

In order to measure the dependence of one data set to another of equal length, such as, two spectral parameters like flux and photon index, the rank correlation coefficient is often used. The rank correlation of two ordinal data sets (categorical data that is ordered) expresses the relation, or dependency, of the rankings of both data sets. Often-used non-parametric statistics that implement a rank correlation measure are, for example, Spearman's ρ or Kendall's τ.

The Kendall's τ rank correlation coefficient (Kendall, 1938) is defined as follows. The two random variables x and y have n pairs of values (x_i, y_i). The pairs (x_i, y_i) and (x_j, y_j) are called concordant if either $x_i < x_j$ and $y_i < y_j$ or $x_i > x_j$ and $y_i > y_j$, which means that the order of sorting, or ranking, is the same. Analogously, if the ranking is not equal, that is, either $x_i < x_j$ and $y_i > y_j$ or $x_i < x_j$ and $y_i > y_j$, the pair is called discordant. The difference between the number of concordant pairs n_c and discordant pairs n_d, divided by the number of possible orders of the rank, is defined as the rank correlation coefficient:

$$\tau = \frac{n_\mathrm{c} - n_\mathrm{d}}{n(n-1)/2}. \tag{3.7.11}$$

The coefficient can assume values within [–1,1], whereas a value near 1 indicates a high probability of correlated / dependent data sets. No significant correlation is suggested by a coefficient near 0, and negative correlation around a value of –1. In this work, the Kendall's τ rank correlation coefficient is applied to a number of data sets because of a number of advantages compared to other correlation tests. The dependence of both data sets is not necessarily assumed to be linear, like for Pearson's r. Additionally, it is robust against outliers in the data. The implementations of the test in many software environments return the p-value, which expresses the rejection level of the null hypothesis of zero correlation. Furthermore, the test, which is implemented in ISIS / ISISscripts, also provides support for data sets that include censored data, that is often given for flux and luminosity values for faint X-ray sources (upper limits).

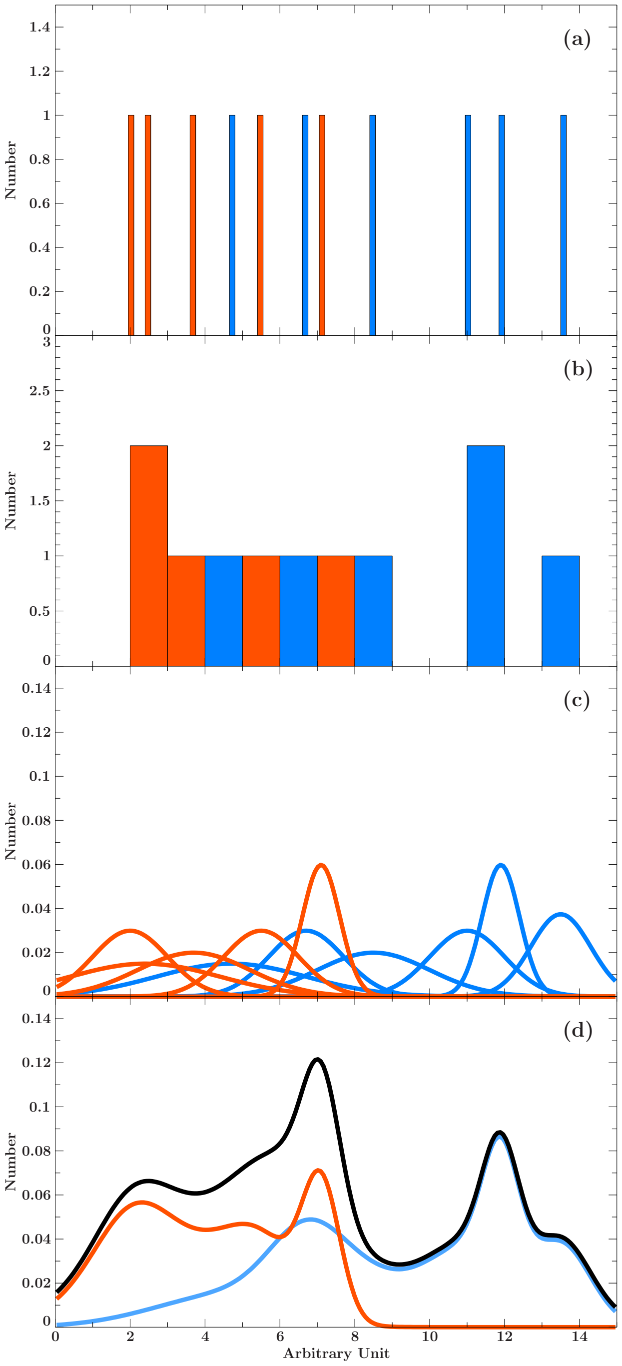

Figure 3.7.1.: Distribution of measurement values of two independent samples (orange and blue, respectively). (a) The (random) measurement values themselves, (b) larger binning of panel a, (c) display of the (random) Gaussian-shaped uncertainty ranges of the measurement values, (d) sum of the individual curves in panel c for both samples as well as for both samples combined (black line).

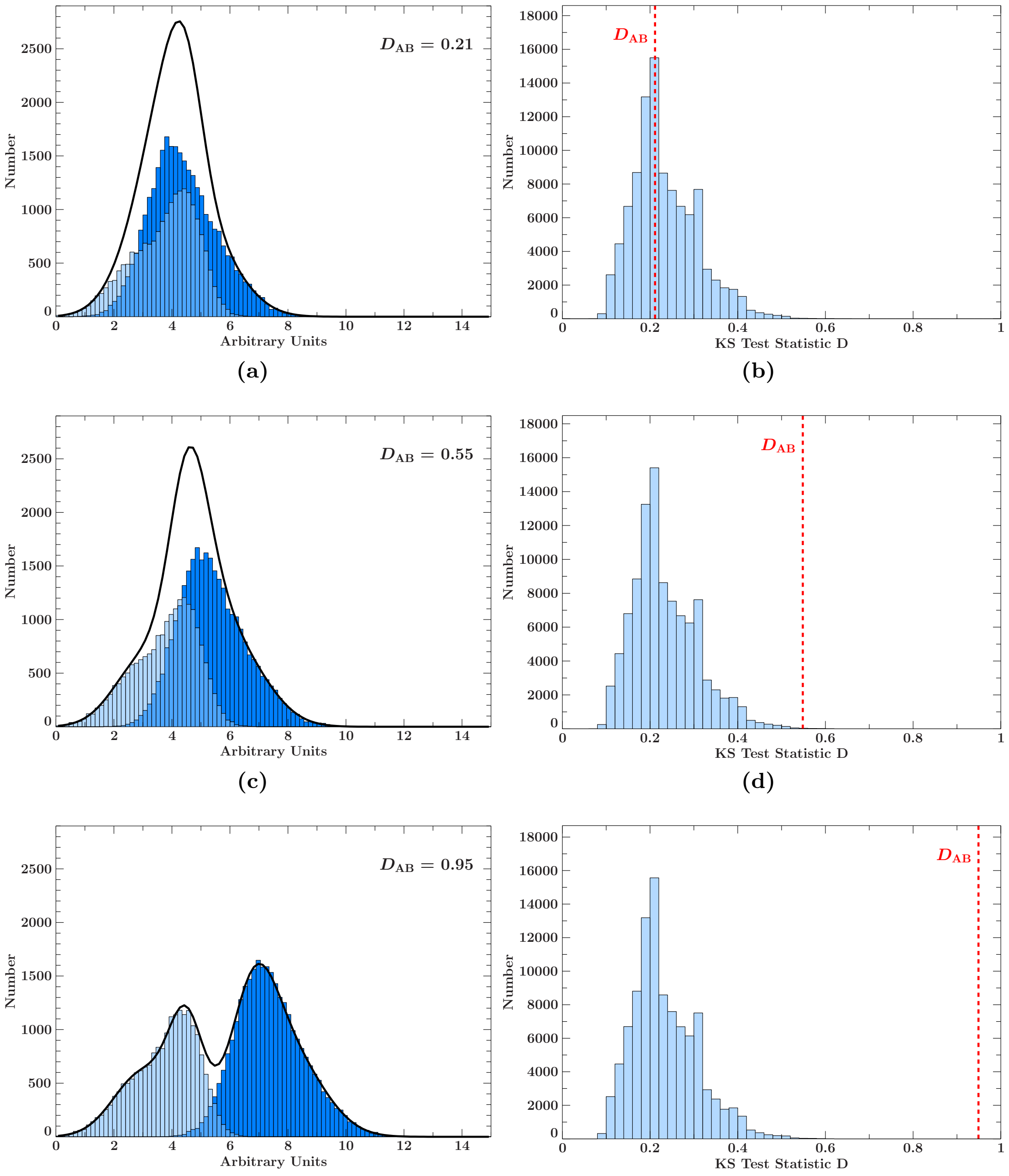

(a) (b)

(c) (d)

(e) (f)

Figure 3.7.2.: Illustration of the extended KS test using added uncertainty regions (see text). Left (a, c, e): distribution of two random added uncertainty ranges of random sample values (analogous to Fig. 3.7.1, d). Bright and dark blue indicate the two distributions with various distances to each other, the medium blue tone marks the intersection. The black line indicates the added distribution functions of both samples. The KS test statistic value D_{AB} refers to a standard 2-sample KS test of both distributions. Right (b, d, f): distributions of 10^5 KS tests for the value distribution on the left. In each case 20 random values of sample A and 30 random values of sample B are used for the tests. The dashed line shows the D_{AB} value of the corresponding sample.

4. The Northern blazar sky at hard X-rays: the MOJAVE sample

Due to their extreme broadband emission, AGN, and specifically blazars, have been studied using a large variety of telescopes and detectors over the past decades (e.g., Villata et al., 2008; Ojha et al., 2010; Jorstad & Marscher, 2016). While radio and gamma-ray surveys have brought forward catalogs containing vast amounts of blazars, catalogs of the spectral band of hard X-rays, starting at around 10 keV, show a different picture (see Sect. 1.3). The comparatively low amount of blazars, that is registered in the hard X-ray band, is at least partially due to the minimum between the characteristic spectral bump from synchrotron emission at radio to X-ray frequencies and the high-energy emission bump that reaches from MeV to TeV energies. Consequently, the definition of a hard-X-ray-selected blazar sample is not only limited to a low sample size, but also subject to a selection effect. Either the spectral minimum, the falling side of the synchrotron bump, or the rising side of the high-energy bump provide a selection bias regarding signal strength. Blazars with a slightly different position of their SED along the frequency axis due to, for example, different amounts of cooling of the emitting electrons (Sect. 1.3.3) / different blazar sub-types or the redshift are selected differently in hard X-ray surveys. Additionally, technical difficulties of detecting and tracing hard X-ray photons lead to signals that are highly dominated by a prominent background component and noise.

In order to study the hard X-ray characteristics of blazars, while taking into account these factors, a statistically complete radio-selected sample[1] is chosen: the MOJAVE-1 beamed AGN sample (Lister & Homan, 2005). The MOJAVE program (Lister et al., 2009a, see also Sect. 2.1.2) provides regular monitoring of the radio-brightest AGN jets in the Northern hemisphere. The definition of the MOJAVE-1 sample specifically includes all flat-spectrum sources with a declination of $\delta \geq -20^\circ$, and a minimum distance from the Galactic plane of $|b| \geq 2\overset{\circ}{.}5$. At any epoch, starting 1994.0 and until 2004.0, a sample source's flux density was required to be at least 1.5 Jy and at least 2 Jy for sources below the celestial equator. The MOJAVE-1 sample itself is mostly composed of low-peaked sources, that is, beamed AGN with the peak frequency of the synchroton bump below 10^{14} Hz. It can be divided further by the optical spectral classification after Véron-Cetty & Véron (2003) into 104 Flat Spectrum Radio Quasars (Q), 21 BL Lacs (B), eight Radio Galaxies (G), and two unidentified types (U).

Previously published studies of hard X-ray properties of blazars and all-sky surveys were limited by a conservatively high significance cutoff at around 5 σ, leading to small sample sizes (see, e.g., Baumgartner et al., 2013; Krivonos et al., 2015). In this chapter, the overall hard X-ray characteristics of a statistically complete beamed AGN / blazar sample are

---

[1] In this context, the term statistical completeness means that the characteristics of the chosen source sample is representative to the source population that is detected at the given survey limit. The MOJAVE program is considered statistical complete because of the long survey time, minimizing the risk of missing sources due to flux variability.

presented, including the type-specific distribution of S/N, flux, luminosity, and photon index (Sect. 4.1.2, 4.1.3, and 4.1.4). Furthermore, the MOJAVE-1 sample serves as a case study of the enigmatic group of gamma-ray-faint blazars in the intermediate region of X-rays (Sect. 4.2.2). While the majority of the sample is detected in the GeV band a number of blazars is not. Here, the hard X-ray emission characteristics give insight into the spectral shape in-between both SED emission bumps, and, thereby, make statements and predictions for past and present gamma-ray detections. Additional contributing factors that might lead to the low hard X-ray detection rate of blazars are discussed in the second part of this chapter. In Sect. 4.2.3 the proportion of high- and low-flux sources is studied using $\log N$-$\log S$ distributions of the X-ray and radio flux of the same object sample. A study of a possible effect of source variability and source evolution in terms of luminosity with time are presented in Sect. 4.2.4 and 4.2.5, respectively.

Lastly, the assessment of the emission properties of a well-defined blazar sample in the hard X-ray band offers the opportunity to study the composition of the cosmic X-ray background (CXB) in this energy range. Many earlier studies have found that the soft X-ray band can indeed be resolved into individual sources, for the vast majority AGN (e.g. Hickox & Markevitch, 2006). The modeling of soft and hard X-ray luminosity functions by, for example Ueda et al. (2003) and Ajello et al. (2009), lead to the conclusion that blazars must be a major contributor to the hard X-ray and MeV background. However, the studies concerning the CXB contribution of AGN and, specifically blazars, were conducted on the basis of X-ray-selected source samples. Here, the contribution of a radio-selected beamed AGN sample with a broad range of X-ray brightness is analyzed in the hard X-ray band of 20 keV–100 keV. The results of the analysis are presented in Sect. 4.2.6.

As a step of verification in terms of sample completeness, the X-ray properties of the extended MOJAVE-1.5 sample (Lister et al., 2013) are presented in Sect. 4.3. This larger version of the earlier MOJAVE-1 sample features more consistent selection criteria regarding position and flux density. The sample consists of all flat-spectrum radio sources with $\delta \geq -30^\circ$, including the Galactic plain, and a 15 GHz flux density larger than 1.5 Jy. This chapter is based on Langejahn et al. (2020), sections 4 and 5.

4.1 Hard X-ray characteristics

In this section, the basic spectral characteristics, derived from the hard X-ray data set of the well-defined radio-selected MOJAVE-1 beamed AGN sample, are presented. The results, which are described in this part, are the basis for further analyses in Sect. 4.2, including possible selection effects, flux evolution, and the composition of the hard X-ray background. The derived values of the X-ray flux, luminosity, S/N, and photon index are displayed in Table 4.1.1, at the end of this section, together with general properties like redshift and the source detection in other high-energy survey catalogs.

Furthermore, the MOJAVE-1 sample serves as a control group regarding the TANAMI AGN sample (Chpt. 5), which has not been composed with the same strict selection criteria. Comparing the hard X-ray properties can, among others, address the question of sample completeness. Also, the radio-selected blazars can be compared to the large set of gamma-ray-selected *Fermi*/LAT catalog samples (Chpt. 6), shedding light on the X-ray properties of different blazar sub-classes, which have been selected in two very distant energy bands.

4.1.1. Previous high-energy detections

In order to determine the nature of the broadband spectral properties of the MOJAVE-1 beamed AGN sample, a number of source catalogs of high-energy surveys are compared. To check if a source is also identified in another catalog, the analysis steps described in Sect. 3.1 are carried out.

The most recent *Swift*/BAT survey catalog (Oh et al., 2018) includes 1632 sources, both Galactic and extragalactic. The catalog, which is based on the same 105-month survey maps as this study, however, features a sharp significance cutoff at $4.8\,\sigma$, with a few exceptions due to significant detections in previous catalogs (Tueller et al., 2008; Baumgartner et al., 2013). The catalog features 158 "beamed AGN", which includes blazars and/or FSRQs, and also 129 hard X-ray sources without a certain classification, as well as an additional 114 AGN of yet unidentified type. A positional correlation analysis of the MOJAVE-1 sample and the BAT survey catalog results in a number of 36 common sources, comprising 28 FSRQs, three BL Lacs, and five radio galaxies. All sources are classified as beamed AGN except 0415+379 (3C 111) and 1957+405 (Cygnus A), which are listed as Seyfert galaxies in the BAT catalog.

The largest separation between two associated sources in the catalogs is $0.'03$ (2201+315). On average, the separation of unassociated MOJAVE-1 sources with the nearest BAT catalog AGN is $3.^\circ 11$, several orders larger. It can be estimated how high the probability of a chance association between both source samples is. Starting from the accessible sky area of the MOJAVE-1 survey ($26556.15\,\mathrm{deg}^2$), one can calculate the density of the common sources. Then, the result is multiplied with the area of 36 error circles, assuming the largest error range of source 2201+315. This gives the average number of the 36 MOJAVE-1 sources in this (conservatively maximum) area of the BAT catalog sources:

$$n = \frac{36}{26556.15\,\mathrm{deg}^2} \cdot 36 \cdot A^{90\%}_{2201+315} = 3.8 \cdot 10^{-8}. \tag{4.1.1}$$

For a Poisson probability function with zero hits and an expected value of n the probability of a chance association is approximately $4 \cdot 10^{-8}$ and, thus, negligible.

Besides *Swift*, the X-ray and gamma-ray observatory *INTEGRAL* performed deep surveys of the entire sky, albeit not as uniformly distributed as *Swift*. Here, the coordinates of the MOJAVE-1 sources are compared with the source catalogs of two studies: the *INTEGRAL*/IBIS 11-year survey (Krivonos et al., 2015) and the *INTEGRAL*/IBIS AGN catalog (Malizia et al., 2012) as well as its updated catalog (Malizia et al., 2016). The former consists of a list of 35 AGN, that have been detected in the 100 keV to 150 keV band above $4\,\sigma$. Only six sources are present in the survey catalogs as well as in the MOJAVE-1 sample: four FSRQs and two radio galaxies. With the exception of the FSRQ 1219+044 at $13\,\sigma$, all sources are brighter than $37\,\sigma$ (BAT S/N). The larger *INTEGRAL*/IBIS AGN catalog includes 272 AGN that have been observed in the 2 keV–10 keV and 20 keV–100 keV bands. A fraction of 57% of the catalog is given by Type 1 AGN, which comprises blazars, Seyferts 1 to 1.5, and a number of sources with multiple classifications (e.g., 3C 273, Sy1 / QSO). Both the *INTEGRAL* AGN catalog and the MOJAVE-1 sample have 18 sources in common: thirteen blazars and five radio galaxies (MOJAVE classification, Seyfert or QSO in the *INTEGRAL* AGN catalog).

To date, the deepest and most uniform gamma-ray all-sky survey has been performed by the *Fermi*/LAT instrument, accumulating years of spectral survey data in the 50 MeV–1 TeV band. The most recent 8-year / 4FGL catalog (Abdollahi et al., 2020) includes 5098 sources with a significance in the observed band of $4\,\sigma$ or higher. With 2940 blazars or blazar candidates, the 4FGL catalog consists to a large extent of highly beamed AGN. A total number of 112 sources with a wide range of BAT S/N values are common between the 4FGL catalog and the MOJAVE-1 sample, which comprises 86 FSRQs, 21 BL Lacs, as well as three radio galaxies and two sources of unidentified type. While 83% of the MOJAVE-1 sample has a counterpart in the 4FGL catalog, the BAT 105-month survey catalog ("beamed AGN" sub-sample) only has 65%. This endorses the well-known correlation of radio flux density to gamma-ray flux (see, e.g., Ackermann et al., 2011; Mufakharov et al., 2015). Since blazars that emit in the LAT-observed gamma-ray band are known to be highly variable (see, e.g., Abdo et al., 2010d; Rajput et al., 2020) a comparison with the detection statistic of the older 3LAC Fermi/LAT catalog (Ackermann et al., 2015) is also presented. The older catalog is based on integrated all-sky gamma-ray data, whose time frame is much more compatible with the BAT 105-month observation length (2008–2012 and 2004–2013, respectively).

In Sect. 4.1.4 the relation of the gamma-ray detection statistic and the spectral shape in the BAT band is discussed.

4.1.2. Signal-to-noise ratio

As suggested by the low number of common registered sources in the MOJAVE-1 sample and the BAT 105-month survey catalog, a large number of the MOJAVE-1 sources must be characterized by low S/N values. While the aforementioned BAT catalog has a sharp cutoff at $4.8\,\sigma$ the significance values for the MOJAVE-1 sample are extracted at the given coordinates. The extraction is performed using the Crab-weighted 105-month survey maps in the energy range of 14 keV–150 keV. The resulting distribution of S/N values is presented in Fig. 4.1.1, also showing the different optical AGN classes by color, omitting the brightest source 1226+023 (3C 273) for better readability. Hatched areas indicate all sources for which only upper-limit flux values could be derived. The most significant sources in the BAT band, three FSRQs and four radio galaxies, clearly separate from the rest of the sample below $20\,\sigma$. There are 27 sources below $20\,\sigma$, but above the BAT catalog limit of $4.8\,\sigma$. The by far most significant BL Lac type source in that range is 2200+420 at $16.8\,\sigma$, BL Lac itself. For the most part, radio galaxies appear relatively bright, which is due to the low redshifts of this AGN class in the sample. While the average redshift $\langle z \rangle$ of radio galaxies in the sample is 0.06, FSRQs ($\langle z \rangle = 1.16$) and BL Lacs ($\langle z \rangle = 0.39$) are, on average, significantly more distant.

The vast majority (101 sources) of the MOJAVE-1 sample is characterized by S/N values below $4.8\,\sigma$, even including negative values, which are reasonable because of the fact that the count rate maps area already subtracted by an average background component. In some cases, the position of a source, that is very X-ray-faint to begin with, coincides with an over-subtracted region of random fluctuation in the count rate map, hence the negative signal. In any case, the S/N distribution shows a clear offset from $0\,\sigma$ towards positive significances.

Following the method outlined in Sect. 3.2.3, the fraction of sources, which are not compatible with random background noise, can be determined by subtracting the S/N distribution by a Gaussian fit curve to the negative side of the distribution. Both the distributions of the MOJAVE-1 S/N before and after the subtraction are presented in Fig. 4.1.2. The histogram errors are purely statistical. From 135 initial samples source $121.94^{+4.39}_{-11.16}$ remain, equal to 82.06%–93.58%. This fraction of the MOJAVE-1 sample is thus characterized as hard X-ray emitters, regarding the achievable flux limit after 105 months of integrated observation with

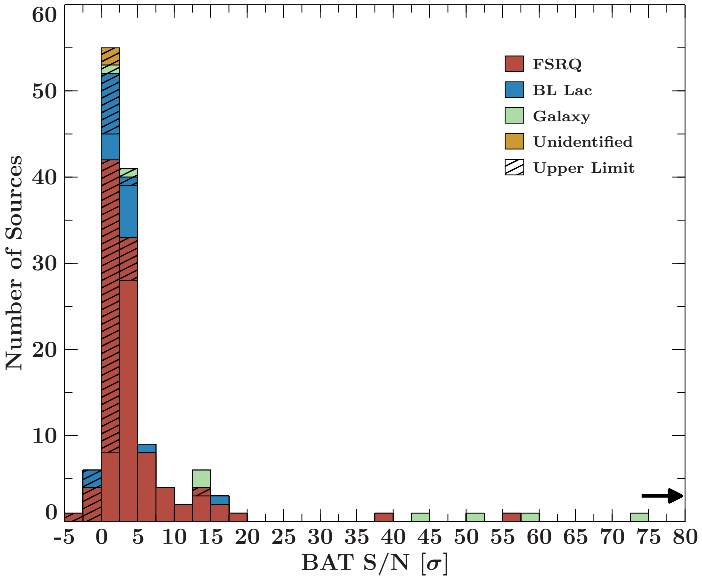

Figure 4.1.1.: Distribution of BAT S/N values of the MOJAVE-1 sample for the different source classes. For better readability, the brightest source 3C 273 at 192 σ has been omitted, indicated by the black arrow.

Swift/BAT in the given energy band.

However, this estimate is only applicable to the entire source sample. A statement about single low-significance sources has to be made in using an alternate approach: one single S/N value, which is expressed in the corresponding histogram bin, is compared to the expected background contribution, that is the Gaussian fit curve. The fraction of the bin value (number of sources) and the Gaussian curve at that bin (significance) equals the probability of a source in that bin not being random fluctuation. As an example, thirteen sources are included in the bin of 0.5 σ–1 σ, while the fit curve has a value of approximately five. Thus, the probability of any source in that bin to be not due to random fluctuation is $1 - 5/13$, or 0.62. Naturally, the probability increases for sources in bins at a higher S/N value.

4.1.3. Hard X-ray flux and luminosity

The hard X-ray flux of the MOJAVE-1 sample sources, which is calculated following the procedure outlined in Sec. 3.2.4, is presented in Fig. 4.1.3. Like the distribution of the S/Ns, most values are concentrated at the lower end. From all 135 sources the majority of 127 lies below $30 \cdot 10^{-12}$ erg s^{-1} cm^{-2}. The brightest source types are constituted by FSRQs and radio galaxies. On average, the BL Lacs and sources of unidentified type are relatively faint in the hard X-ray band. The flux values of 59 sources are upper limits, which includes the sources 0917+624, 1502+106, and 1928–179, whose spectra allow the fitting of a power law, but which are also affected by spectral contamination of nearby sources. Due to the calculation of the upper-limit values, which correspond to the uncertainty ranges of the determined flux (see Sect. 3.2.4) the correlation of flux to S/N is only approximately linear above a certain signal quality. This relation is illustrated in Fig. 4.1.4, which shows a flattening of the distribution of data points in the flux vs. S/N space at around $2\,\sigma$ / $(3-4) \cdot 10^{-12}$erg s^{-1} cm^{-2}, because of the upper limits (arrow symbols). Above approximately 2 σ, the relation is characterized by a slope of approximately unity, as expected. Interestingly, the linear relation of both quantities continues well below the 4.8 σ BAT catalog cutoff. Although numerous upper limits start to appear, spectral data of a large amount of hard X-ray sources can be derived, as demonstrated by the MOJAVE-1 sample.

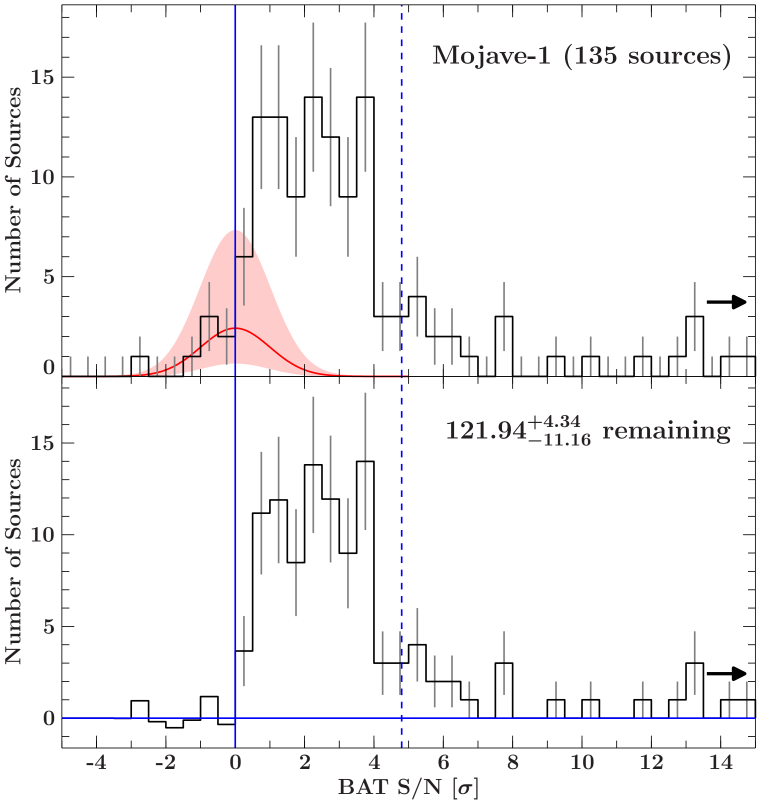

Figure 4.1.2.: Top panel: S/N distribution of the MOJAVE-1 source sample, truncated at $15\,\sigma$. The fit of a Gaussian curve to the negative side of the distribution with center of $0\,\sigma$ and width of $1\,\sigma$ is indicated by the red line. The $3\,\sigma$ uncertainty range of the fit is shown by the red shaded area. Bottom panel: histogram after the subtraction of the original S/N distribution from the fit curve. The resulting number of remaining sources is given in the plot, summing all histogram bins larger than $0\,\sigma$. The dashed line indicates the BAT catalog threshold of $4.8\,\sigma$.

The hard X-ray luminosity is determined following Eq. 3.2.23, and Eq. 3.2.24 for the error calculation. Because of missing redshift information, two BL Lac-type sources and two sources of unidentified type are left out. The resulting luminosity distribution is presented in Fig. 4.1.5. The broad distribution, spanning approximately eight orders of magnitude, centers around $(10^{46} - 10^{47})\,\mathrm{erg\,s^{-1}}$ in log space. The most luminous class are the FSRQs, stretching up to $10^{48}\mathrm{erg\,s^{-1}}$ (0836+710), while the corresponding luminosities of the upper limits following approximately the same distribution up to $5 \cdot 10^{47}\mathrm{erg\,s^{-1}}$. The next luminous class is that of BL Lacs in the range of $(10^{43} - 10^{46})\,\mathrm{erg\,s^{-1}}$. In comparing the luminosities of FSRQs and BL Lacs with a KS test, the null hypothesis that both distributions are drawn from the same parent distribution can be rejected at a level of $\alpha = 3.2 \cdot 10^{-6}$. By far, the least luminous class of source samples is the radio galaxies, reaching just $(10^{41} - 10^{45})\,\mathrm{erg\,s^{-1}}$, which, again, is likely explained by the fact that the redshift of all radio galaxies is significantly lower compared to the other classes.

4.1.4. Hard X-ray photon index

Because a large fraction of the MOJAVE-1 sample resides at low S/N values, spectral fitting results in some cases in considerable uncertainty ranges for the spectral slope / the photon index Γ. This is mirrored by the broad distribution of the photon index for the 77 sources, for which a spectral fit is viable. In Fig. 4.1.6 the photon index distribution is shown, including indices for lower significance sources (hatched area), which are characterized by a somewhat broader distribution. This is a direct consequence of the higher uncertainty ranges, which are as large as about 1–2 for the faintest fitted sources. The rest of the sample is processed using template spectra (see Sect. 3.2.4). The photon indices of FSRQs form

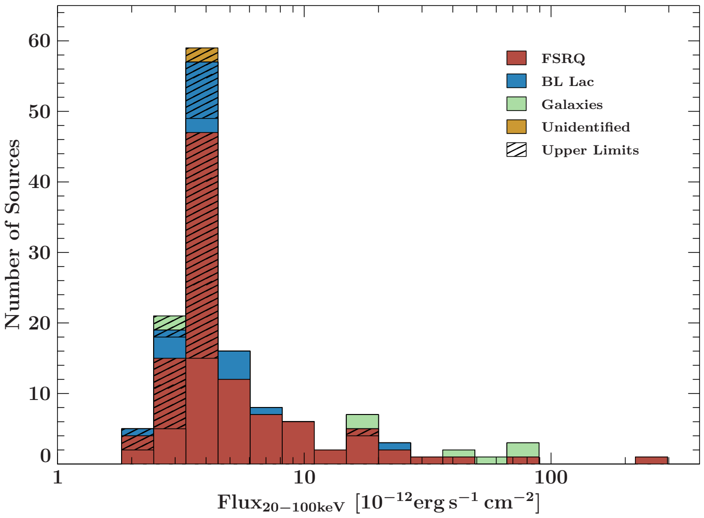

Figure 4.1.3.: Distribution of flux values of the MOJAVE-1 sample in the 20 keV–100 keV band.

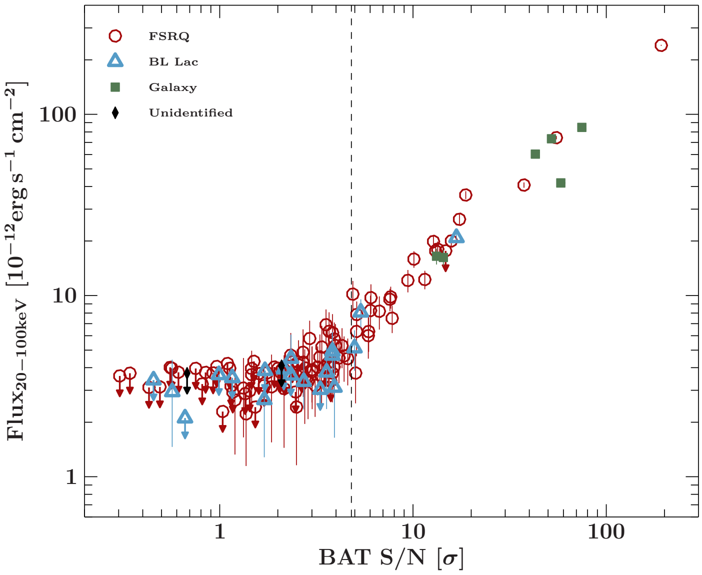

Figure 4.1.4.: Plot of the flux against S/N values of the MOJAVE-1 sample in the 20 keV–100 keV band. The BAT catalog's threshold of 4.8 σ is indicated by the dashed line. For readability the data point of source 1504–166 at 0.01 σ has been omitted.

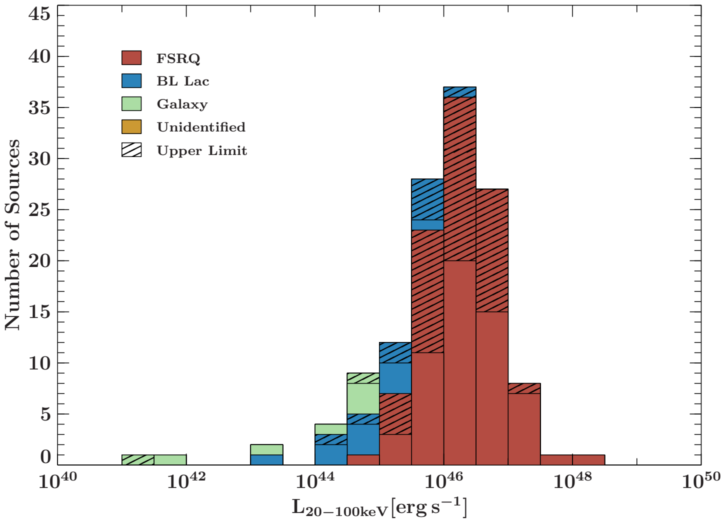

Figure 4.1.5.: Distribution of luminosity values of the MOJAVE-1 sample in the 20 keV–100 keV band.

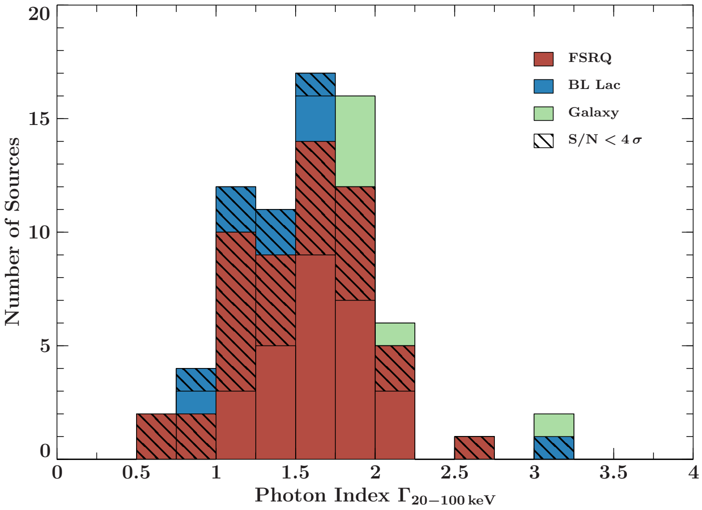

Figure 4.1.6.: Distribution of photon index Γ of all fitted MOJAVE-1 source spectra in the 20 keV–100 keV band. The Hatched Boxes show the fainter half of the subsample (S/N below $4\,\sigma$).

a bell-shaped distribution around $\Gamma = 1.6$, and extending from approximately 0.5 to 2.7. The BL Lac distribution is comparatively flat, with values from 0.8 to 3. The smaller range can also be attributed to the relatively small number of BL Lacs in the sample. Radio galaxies concentrate around $\Gamma = 2$, with the exception of 0316+414 (3C 84) at 3.2. The source spectrum is not well described by a simple power-law fit ($PG = 14.8$) in this analysis and also the BAT survey catalog ($\chi^2 = 3.8$, Oh et al., 2018). In a study by Churazov et al. (2003), it has been found that the source's broadband spectrum is indeed dominated by thermal emission instead of synchrotron or inverse Compton processes. However, a more typical blazar spectrum in the BAT band could usually be fit well with a simple power law.

In the νF_ν representation of a broadband blazar SED a photon index $\Gamma < 2$ indicates a rising slope, like the left flank of the HE emission peak from X-rays to gamma-rays. Photon indices with $\Gamma > 2$ consequently show the falling part of an emission component, typically the synchrotron peak. A flat part of the spectrum is expressed by $\Gamma = 2$, which usually means the maximum of the HE emission peak or in some cases the emission minimum between the synchroron an HE emission peaks. The analysis of the photon indices of the MOJAVE-1 sample shows that the majority of SED's rising flank of the HE peak is located in the observed hard X-ray band. Nine sources, which have an index $\Gamma > 2$ are likely located at the falling synchrotron flank. However, these sources, except the radio galaxy 0316+414, also have 90% error ranges, which would place them well below $\Gamma = 2$ in the typical blazar index of approximately 1.7. The hard photon indices measured in this sample fit into the classification of low-peaked blazars, and to an extend, intermediate-peaked blazars if the synchrotron flank of the SED is considered. Besides 0316+413, the BL Lac 0754+100 has also a very soft photon index of $\Gamma = 3.04 \pm 1.56$. The BAT band is located at the rising part of the HE bump in the fitted SED of the source (Chang, 2010), implying a photon index smaller than 2, which seems likely due to the large uncertainty range of the BAT measurement.

On the other end of the distribution the BL Lac type object 0716+714 is located at $\Gamma = 0.83 \pm 0.46$, placing the spectral measurement at the steepest section of the rising HE bump. The source, however, is characterized by large variability at many wavelengths (e.g., Wagner et al., 1996), including the X-ray regime. Deriving a photon index above approximately 10 keV has proven challenging due to this aspect and the fact that the source is only fairly bright (BAT survey S/N = $5.4\,\sigma$). Past studies like, for example, Pian et al.

(2005) or Beckmann et al. (2009), were able to present meaningful flux values in this energy regime, but under the restriction of a fixed photon index. Wierzcholska & Siejkowski (2016) have shown, using observations of the source during a flaring state with *Swift* and *NuSTAR*, that the SED exhibits a clear minimum at $E = (8.01 \pm 0.56)\,\mathrm{keV}$. A modeled photon index of 2.40 ± 0.01 at lower energies, and 1.61 ± 0.05 at higher energies places the BAT energy band of 20 keV – 100 keV at the beginning of the rising flank of the HE bump. The source is also listed in the *Fermi*/LAT catalogs, which is consistent with the assumption that the HE bump is positioned at a relatively high frequency, making the source bright enough for a detection in the keV and GeV bands. The source's synchrotron peak frequency of $\log\nu = 14.4$ is presented in Lister et al. (2015), which already classifies the BL Lac as intermediate, or even high-peaked.

Table 4.1.1.: Results of the spectral hard X-ray analysis of the MOJAVE-1 sample in the 20 keV–100 keV band.

Name[a]	Common Name	RA[b]	Dec[b]	S/N[c]	Γ[d]	$F_{20-100\,\mathrm{keV}}$[e]	$L_{20-100\,\mathrm{keV}}$[f]	Type[g]	z[h]	Detections[i]
0003–066	NRAO 005	1.558	-6.393	2.34	1.04 ± 1.02	4.49 ± 1.6	$(1.36 \pm 0.53) \cdot 10^{45}$	B	0.3467	F_4
0007+106	III Zw 2	2.629	10.975	13.24	1.86 ± 0.24	16.48 ± 1.65	$(3.24 \pm 0.33) \cdot 10^{44}$	G	0.0893	B
0016+731	S5 0016+73	4.941	73.458	3.65	1.5 ± 0.78	4.26 ± 1.27	$(5.53 \pm 1.66) \cdot 10^{46}$	Q	1.781	F_4
0048–097	PKS 0048–09	12.672	-9.485	0.99		$< 3.66^*$	$< 5.07 \cdot 10^{45}$	B	0.635	F_3 F_4
0059+581	TXS 0059+581	15.691	58.403	2.87	0.92 ± 1.14	3.37 ± 1.29	$(3.49 \pm 1.55) \cdot 10^{45}$	Q	0.644	F_3 F_4
0106+013	4C +01.02	17.162	1.583	2.17		$< 3.67^*$	$< 6.88 \cdot 10^{46}$	Q	2.099	F_3 F_4
0109+224	S2 0109+22	18.024	22.744	1.16		$< 3.52^*$	$< 7.04 \cdot 10^{44}$	B	0.267442**	F_3 F_4
0119+115	PKS 0119+11	20.423	11.831	0.34		$< 3.73^*$	$< 3.96 \cdot 10^{45}$	Q	0.571	
0133+476	DA 55	24.244	47.858	3.0	1.87 ± 0.91	3.9 ± 1.33	$(1.29 \pm 0.45) \cdot 10^{46}$	Q	0.859	F_3 F_4
0202+149	4C +15.05	31.21	15.236	0.92		$< 3.74^*$	$< 1.84 \cdot 10^{45}$	Q	0.405	F_3 F_4
0202+319	B2 0202+31	31.271	32.208	–0.6		$< 3.55^*$	$< 3.08 \cdot 10^{46}$	Q	1.466	F_3 F_4
0212+735	S5 0212+73	34.378	73.826	15.79	1.43 ± 0.17	20.03 ± 1.4	$(4.37 \pm 0.31) \cdot 10^{47}$	Q	2.367	B I_A F_3 F_4
0215+015	OD 026	34.454	1.747	1.53		< 2.42	$< 2.95 \cdot 10^{46}$	Q	1.715	F_3 F_4
0224+671	4C +67.05	37.209	67.351	3.9	2.68 ± 0.9	4.04 ± 1.26	$(5.76 \pm 1.81) \cdot 10^{45}$	Q	0.523	F_4
0234+285	4C +28.07	39.468	28.802	4.14		4.53 ± 1.24	$(2.56 \pm 0.7) \cdot 10^{46}$	Q	1.206	F_3 F_4
0235+164	AO 0235+164	39.662	16.616	2.56	1.73 ± 1.02	4.14 ± 1.53	$(1.56 \pm 0.58) \cdot 10^{46}$	Q	0.94	F_3 F_4
0238–084	NGC 1052	40.27	-8.256	14.36	1.86 ± 0.23	16.23 ± 1.6	$(9.1 \pm 0.9) \cdot 10^{41}$	G	0.005037	B I_A
0300+470	4C +47.08	45.897	47.271	3.57	1.53 ± 1.03	3.77 ± 1.41		B		F_3 F_4
0316+413	3C 84	49.951	41.512	58.16	3.17 ± 0.12	41.83 ± 1.53	$(2.98 \pm 0.11) \cdot 10^{43}$	G	0.0176	B I_A F_3 F_4
0333+321	NRAO 140	54.125	32.308	17.4	1.71 ± 0.15	26.35 ± 1.66	$(1.92 \pm 0.12) \cdot 10^{47}$	Q	1.259	B I_A F_3 F_4
0336–019	CTA 26	54.879	-1.777	2.71	1.81 ± 0.95	4.25 ± 1.49	$(1.33 \pm 0.48) \cdot 10^{46}$	Q	0.852	F_3 F_4
0403–132	PKS 0403-13	61.392	-13.137	5.87	1.77 ± 0.6	6.01 ± 1.52	$(7.17 \pm 1.86) \cdot 10^{45}$	Q	0.571	B F_3 F_4
0415+379	3C 111	64.589	38.027	52.05	2.02 ± 0.05	73.31 ± 1.65	$(4.18 \pm 0.09) \cdot 10^{44}$	G	0.0491	B I_A I_{11} F_3 F_4
0420–014	PKS 0420–01	65.816	-1.343	1.33	1.53 ± 1.47	3.09 ± 1.43	$(9.56 \pm 4.62) \cdot 10^{45}$	Q	0.9161	F_3 F_4
0422+004	PKS 0422+00	66.195	0.602	0.57	1.14 ± 1.6	2.94 ± 1.48	$(5.34 \pm 2.94) \cdot 10^{44}$	B	0.268	F_3 F_4
0430+052	3C 120	68.296	5.354	42.95	1.99 ± 0.07	60.34 ± 1.7	$(1.52 \pm 0.04) \cdot 10^{44}$	G	0.033	B I_A
0446+112	PKS 0446+11	72.282	11.358	1.5		$< 4.33^*$	$< 8.57 \cdot 10^{46}$	Q	2.153	F_3 F_4
0458–020	S3 0458–02	75.303	-1.987	1.46		$< 3.96^*$	$< 8.88 \cdot 10^{46}$	Q	2.286	F_3 F_4
0528+134	PKS 0528+134	82.735	13.532	4.88	1.06 ± 0.46	10.18 ± 1.85	$(1.12 \pm 0.21) \cdot 10^{47}$	Q	2.07	B I_A F_3 F_4
0529+075	OG 050	83.162	7.545	2.38		$< 4.31^*$	$< 2.65 \cdot 10^{46}$	Q	1.254	F_3 F_4
0529+483	TXS 0529+483	83.316	48.381	1.13		$< 3.97^*$	$< 2.06 \cdot 10^{46}$	Q	1.16	F_3 F_4
0552+398	DA 193	88.878	39.814	6.03	1.78 ± 0.5	8.27 ± 1.73	$(2.76 \pm 0.58) \cdot 10^{47}$	Q	2.363	B F_4
0605–085	OC–010	91.999	-8.581	2.11		$< 3.94^*$	$< 1.08 \cdot 10^{46}$	Q	0.87	F_3 F_4
0607–157	PKS 0607–15	92.421	-15.711	0.85		$< 3.76^*$	$< 1.12 \cdot 10^{45}$	Q	0.3226	
0642+449	OH 471	101.633	44.855	3.3	1.57 ± 0.89	4.58 ± 1.52	$(2.51 \pm 0.84) \cdot 10^{47}$	Q	3.396	
0648–165	PKS 0648–16	102.602	-16.628	0.68		$< 3.72^*$		U		F_3 F_4
0716+714	TXS 0716+714	110.473	71.343	5.37	0.83 ± 0.46	8.1 ± 1.43	$(2.98 \pm 0.54) \cdot 10^{44}$	B	0.127**	B F_3 F_4
0727–115	PKS 0727–11	112.58	-11.687	3.83	1.5 ± 0.64	6.24 ± 1.66	$(6.37 \pm 1.71) \cdot 10^{46}$	Q	1.591	F_3 F_4
0730+504	TXS 0730+504	113.469	50.369	–1.01		$< 3.47^*$	$< 6.19 \cdot 10^{45}$	Q	0.72	F_3 F_4
0735+178	OI 158	114.531	17.705	0.66		< 2.11	$< 1.34 \cdot 10^{45}$	B	0.45**	F_3 F_4
0736+017	OI 061	114.825	1.618	3.68	1.52 ± 0.66	6.35 ± 1.74	$(5.94 \pm 1.67) \cdot 10^{44}$	Q	0.1894	F_3 F_4
0738+313	OI 363	115.295	31.2	2.0		$< 3.96^*$	$< 5.26 \cdot 10^{45}$	Q	0.631	

Table 4.1.1.: continued.

Name^a	Common Name	RA^b	Dec^b	S/N^c	Γ^d	$F_{20-100\,\mathrm{keV}}{}^e$	$L_{20-100\,\mathrm{keV}}{}^f$	Type^g	z^h	Detections^i
0742+103	PKS B0742+103	116.388	10.187	3.97	2.0 ± 0.8	5.29 ± 1.66	$(2.96 \pm 0.93) \cdot 10^{47}$	Q	2.624	
0748+126	OI 280	117.717	12.518	2.7	1.08 ± 0.97	4.86 ± 1.65	$(1.06 \pm 0.39) \cdot 10^{46}$	Q	0.889	F_3 F_4
0754+100	PKS 0754+100	119.278	9.943	3.93	3.04 ± 1.56	3.11 ± 1.47	$(8.71 \pm 4.18) \cdot 10^{44}$	B	0.266	F_3 F_4
0804+499	OJ 508	122.165	49.843	1.2	1.04 ± 1.56	2.65 ± 1.32	$(1.44 \pm 0.79) \cdot 10^{46}$	Q	1.436	F_3 F_4
0805–077	PKS 0805–07	122.065	-7.853	2.76	1.2 ± 1.36	3.5 ± 1.54	$(3.57 \pm 1.63) \cdot 10^{46}$	Q	1.837	F_3 F_4
0808+019	OJ 014	122.861	1.781	–0.6		$< 3.92^*$	$< 2.08 \cdot 10^{46}$	B	1.148	F_3 F_4
0814+425	OJ 425	124.567	42.379	0.45		$< 3.42^*$		B		F_3 F_4
0823+033	PKS 0823+033	126.46	3.157	2.15		$< 3.93^*$	$< 3.24 \cdot 10^{45}$	B	0.505	F_3 F_4
0827+243	OJ 248	127.717	24.183	3.38	1.07 ± 0.79	5.2 ± 1.61	$(1.26 \pm 0.42) \cdot 10^{46}$	Q	0.94	F_3 F_4
0829+046	OJ 049	127.954	4.494	1.72		$< 3.85^*$	$< 3.03 \cdot 10^{44}$	B	0.174	F_3 F_4
0836+710	4C +71.07	130.352	70.895	37.52	1.65 ± 0.08	40.73 ± 1.38	$(1.0 \pm 0.03) \cdot 10^{48}$	Q	2.218	B I_A I_{11} F_3 F_4
0838+133	3C 207	130.198	13.207	0.61		$< 3.77^*$	$< 5.92 \cdot 10^{45}$	Q	0.68	F_3 F_4
0851+202	OJ 287	133.704	20.109	3.82	1.31 ± 0.89	4.68 ± 1.53	$(1.17 \pm 0.41) \cdot 10^{45}$	B	0.306	F_3 F_4
0906+015	4C +01.24	137.292	1.36	2.19		$< 3.72^*$	$< 1.46 \cdot 10^{46}$	Q	1.024	F_3 F_4
0917+624	OK 630	140.401	62.264	2.47		$< 2.94\dagger$	$2.48 \cdot 10^{46}$	Q	1.447	F_3 F_4
0923+392	4C +39.25	141.763	39.039	3.12		3.19 ± 1.05	$(5.3 \pm 1.75) \cdot 10^{45}$	Q	0.697	
0945+408	4C +40.24	147.231	40.662	4.59	1.87 ± 0.75	4.49 ± 1.3	$(3.66 \pm 1.06) \cdot 10^{46}$	Q	1.25	F_3 F_4
0955+476	OK 492	149.582	47.419	1.43		$< 2.98^*$	$< 4.43 \cdot 10^{46}$	Q	1.884	F_3 F_4
1036+054	PKS 1036+054	159.695	5.208	0.3		$< 3.6^*$	$< 2.51 \cdot 10^{45}$	Q	0.473	
1038+064	4C +06.41	160.322	6.171	3.01	2.05 ± 1.06	3.81 ± 1.45	$(3.71 \pm 1.41) \cdot 10^{46}$	Q	1.265	
1045–188	PKS 1045–18	162.028	-19.16	0.55		$< 4.02^*$	$< 4.67 \cdot 10^{45}$	Q	0.595	
1055+018	4C +01.28	164.623	1.566	3.69		4.05 ± 1.23	$(1.17 \pm 0.36) \cdot 10^{46}$	Q	0.893	F_3 F_4
1124–186	PKS 1124–186	171.768	-18.955	0.97		$< 4.06^*$	$< 1.68 \cdot 10^{46}$	Q	1.048	F_3 F_4
1127–145	PKS 1127–14	172.529	-14.824	13.42	1.67 ± 0.24	18.05 ± 1.81	$(1.11 \pm 0.11) \cdot 10^{47}$	Q	1.184	B F_3 F_4
1150+812	S5 1150+81	178.302	80.975	1.17		$< 2.93^*$	$< 1.79 \cdot 10^{46}$	Q	1.25	F_4
1156+295	4C +29.45	179.883	29.246	4.4	1.55 ± 0.7	4.65 ± 1.3	$(8.6 \pm 2.49) \cdot 10^{45}$	Q	0.725	B F_3 F_4
1213–172	PKS 1213–17	183.945	-17.529	2.09		$< 4.09^*$		U		F_4
1219+044	4C +04.42	185.594	4.221	13.09	1.34 ± 0.23	17.63 ± 1.64	$(5.41 \pm 0.52) \cdot 10^{46}$	Q‡	0.966	B I_A I_{11} F_3 F_4
1222+216	4C +21.35	186.227	21.38	11.51	1.87 ± 0.28	12.26 ± 1.44	$(7.98 \pm 0.96) \cdot 10^{45}$	Q	0.433	B I_A F_3 F_4
1226+023	3C 273	187.278	2.052	192.37	1.75 ± 0.02	240.34 ± 1.67	$(1.59 \pm 0.01) \cdot 10^{46}$	Q	0.1583	B I_A I_{11} F_3 F_4
1228+126	M 87	187.706	12.391	2.82		$< 3.17^*$	$< 1.33 \cdot 10^{41}$	G	0.00436	F_3 F_4
1253–055	3C 279	194.047	-5.789	12.76	1.53 ± 0.21	19.88 ± 1.76	$(1.85 \pm 0.17) \cdot 10^{46}$	Q	0.536	B I_A F_3 F_4
1308+326	OP 313	197.619	32.345	1.36		$< 2.87^*$	$< 1.06 \cdot 10^{46}$	Q	0.997	F_3 F_4
1324+224	B2 1324+22	201.754	22.181	0.43		$< 3.11^*$	$< 2.43 \cdot 10^{46}$	Q	1.398	F_3 F_4
1334–127	PKS 1335–127	204.416	-12.957	5.1	2.12 ± 0.68	6.34 ± 1.72	$(7.67 \pm 2.11) \cdot 10^{45}$	Q	0.539	B F_3 F_4
1413+135	PKS B1413+135	213.995	13.34	1.7	1.0 ± 1.64	2.66 ± 1.38	$(3.94 \pm 2.24) \cdot 10^{44}$	B	0.247	F_3 F_4
1417+385	B3 1417+385	214.944	38.363	1.37	1.76 ± 1.55	2.22 ± 1.08	$(4.02 \pm 1.95) \cdot 10^{46}$	Q	1.831	F_3 F_4
1458+718	3C 309.1	224.782	71.672	3.83	2.01 ± 0.81	3.73 ± 1.16	$(1.53 \pm 0.48) \cdot 10^{46}$	Q	0.904	B F_4
1502+106	OR 103	226.104	10.494	14.76		$< 17.65\dagger$	$< 2.49 \cdot 10^{47}$	Q	1.838	F_3 F_4
1504–166	PKS 1504–167	226.77	-16.875	0.01		$< 4.38^*$	$< 1.21 \cdot 10^{46}$	Q	0.876	
1510–089	PKS 1510–08	228.211	-9.1	18.74	1.24 ± 0.12	35.88 ± 1.81	$(1.25 \pm 0.07) \cdot 10^{46}$	Q	0.36	B I_A F_3 F_4
1538+149	4C +14.60	235.206	14.796	2.34		$< 3.64^*$	$< 4.54 \cdot 10^{45}$	B	0.606	F_3 F_4
1546+027	PKS 1546+027	237.373	2.617	2.69		4.29 ± 1.37	$(2.22 \pm 0.71) \cdot 10^{45}$	Q	0.414	F_3 F_4

Table 4.1.1.: continued.

Name^a	Common Name	RA^b	Dec^b	S/N^c	Γ^d	$F_{20-100\,\mathrm{keV}}{}^e$	$L_{20-100\,\mathrm{keV}}{}^f$	Type^g	z^h	Detections^i
1548+056	4C +05.64	237.647	5.453	1.92		$< 4.03^*$	$< 3.25 \cdot 10^{46}$	Q	1.417	F_3 F_4
1606+106	4C +10.45	242.193	10.485	2.33	0.81 ± 0.94	4.69 ± 1.53	$(1.58 \pm 0.61) \cdot 10^{46}$	Q	1.232	F_3 F_4
1611+343	DA 406	243.421	34.213	1.7		$< 3.18^*$	$< 2.5 \cdot 10^{46}$	Q	1.4	F_3 F_4
1633+382	4C +38.41	248.815	38.135	3.92	1.59 ± 0.57	5.76 ± 1.34	$(8.57 \pm 2.0) \cdot 10^{46}$	Q	1.814	F_3 F_4
1637+574	OS 562	249.556	57.34	3.21	1.49 ± 0.8	4.03 ± 1.22	$(7.81 \pm 2.45) \cdot 10^{45}$	Q	0.751	F_3 F_4
1638+398	NRAO 512	250.123	39.779	1.15		$< 3.16^*$	$< 3.65 \cdot 10^{46}$	Q	1.672	F_3 F_4
1641+399	3C 345	250.745	39.81	7.67	1.42 ± 0.34	9.83 ± 1.36	$(1.09 \pm 0.16) \cdot 10^{46}$	Q	0.593	B F_3 F_4
1655+077	PKS 1655+077	254.538	7.691	2.65		$< 3.8^*$	$< 4.87 \cdot 10^{45}$	Q	0.621	
1726+455	S4 1726+45	261.865	45.511	1.46	0.51 ± 1.08	3.66 ± 1.3	$(3.77 \pm 1.85) \cdot 10^{45}$	Q	0.717	F_3 F_4
1730–130	NRAO 530	263.261	-13.08	3.55	1.24 ± 0.53	6.9 ± 1.48	$(1.72 \pm 0.39) \cdot 10^{46}$	Q	0.902	I_A F_3 F_4
1739+522	4C +51.37	265.154	52.195	4.3	1.34 ± 0.61	5.29 ± 1.31	$(3.46 \pm 0.88) \cdot 10^{46}$	Q	1.379	B F_3 F_4
1741–038	PKS 1741–03	265.995	-3.835	2.92	1.15 ± 0.63	5.79 ± 1.47	$(1.87 \pm 0.5) \cdot 10^{46}$	Q	1.054	I_A F_3 F_4
1749+096	OT 081	267.887	9.65	3.83	1.27 ± 0.72	4.93 ± 1.38	$(1.36 \pm 0.4) \cdot 10^{45}$	B	0.322	F_3 F_4
1751+288	B2 1751+28	268.427	28.801	3.76		$< 3.38^*$	$< 1.61 \cdot 10^{46}$	Q	1.118	F_4
1758+388	B3 1758+388B	270.103	38.809	–0.71		$< 3.24^*$	$< 6.02 \cdot 10^{46}$	Q	2.092	
1800+440	S4 1800+44	270.385	44.073	0.49		$< 3.13^*$	$< 4.65 \cdot 10^{45}$	Q	0.663	F_3 F_4
1803+784	S5 1803+784	270.19	78.468	4.98	1.68 ± 0.6	5.14 ± 1.29	$(8.79 \pm 2.26) \cdot 10^{45}$	B	0.6797	B F_3 F_4
1807+698	3C 371	271.711	69.824	2.72		3.35 ± 1.0	$(2.02 \pm 0.61) \cdot 10^{43}$	B	0.051	F_3 F_4
1823+568	4C +56.27	276.029	56.85	3.31		$< 3.03^*$	$< 4.65 \cdot 10^{45}$	B	0.664	F_3 F_4
1828+487	3C 380	277.382	48.746	7.6	1.62 ± 0.34	9.54 ± 1.35	$(1.64 \pm 0.24) \cdot 10^{46}$	Q	0.692	B F_3 F_4
1849+670	S4 1849+67	282.317	67.095	5.05	2.14 ± 0.85	3.73 ± 1.19	$(7.44 \pm 2.41) \cdot 10^{45}$	Q	0.657	B F_3 F_4
1928+738	4C +73.18	291.952	73.967	7.8	2.08 ± 0.41	7.49 ± 1.29	$(2.24 \pm 0.39) \cdot 10^{45}$	Q	0.302	B
1936–155	PKS 1936–15	294.861	-15.429	–2.86		$< 4.03^*$	$< 4.56 \cdot 10^{46}$	Q	1.657	F_4
1957+405	Cygnus A	299.868	40.734	74.71	1.92 ± 0.04	84.77 ± 1.32	$(6.34 \pm 0.1) \cdot 10^{44}$	G	0.0561	B I_A I_{11}
1958–179	PKS 1958–179	300.238	-17.816	3.48		$< 4.02\dagger$	$< 5.74 \cdot 10^{45}$	Q	0.652	F_3 F_4
2005+403	TXS 2005+403	301.937	40.497	5.12	1.5 ± 0.44	7.86 ± 1.41	$(9.71 \pm 1.76) \cdot 10^{46}$	Q	1.736	B
2008–159	PKS 2008–159	302.815	-15.778	6.7	1.96 ± 0.5	8.19 ± 1.7	$(6.23 \pm 1.3) \cdot 10^{46}$	Q	1.18	B F_4
2021+317	4C +31.56	305.829	31.884	–0.48		$< 3.51^*$	$< 1.3 \cdot 10^{45}$	B	0.356	F_3 F_4
2021+614	TXS 2021+614	305.528	61.616	0.97		$< 2.99^*$	$< 4.45 \cdot 10^{44}$	G	0.227	
2037+511	3C 418	309.654	51.32	3.37	1.5 ± 0.93	3.62 ± 1.25	$(4.18 \pm 1.46) \cdot 10^{46}$	Q	1.686	F_3 F_4
2121+053	OX 036	320.935	5.589	0.56		$< 3.97^*$	$< 6.3 \cdot 10^{46}$	Q	1.941	F_3 F_4
2128–123	PKS 2128–12	322.897	-12.118	2.53		$< 4.3^*$	$< 3.4 \cdot 10^{45}$	Q	0.501	
2131–021	4C –02.81	323.543	-1.888	2.15	0.72 ± 1.76	3.06 ± 1.62	$(1.03 \pm 0.71) \cdot 10^{46}$	Q	1.284	F_3 F_4
2134+004	PKS 2134+004	324.161	0.698	1.04		< 2.29	$< 3.63 \cdot 10^{46}$	Q	1.94	F_4
2136+141	OX 161	324.755	14.393	2.05		$< 3.79^*$	$< 9.63 \cdot 10^{46}$	Q	2.427	
2145+067	4C +06.69	327.023	6.961	9.41	1.86 ± 0.34	12.13 ± 1.71	$(5.73 \pm 0.82) \cdot 10^{46}$	Q	0.999	B F_4
2155–152	PKS 2155–152	329.526	-15.019	1.1		$< 4.22^*$	$< 6.45 \cdot 10^{45}$	Q	0.672	F_3 F_4
2200+420	BL Lac	330.68	42.278	16.79	1.69 ± 0.16	20.87 ± 1.41	$(2.34 \pm 0.16) \cdot 10^{44}$	B	0.0686	B I_A F_3 F_4
2201+171	PKS 2201+171	330.862	17.43	1.59		$< 3.71^*$	$< 1.63 \cdot 10^{46}$	Q	1.076	F_3 F_4
2201+315	4C +31.63	330.812	31.761	5.89	1.94 ± 0.54	6.33 ± 1.44	$(1.73 \pm 0.4) \cdot 10^{45}$	Q	0.2947	B F_3
2209+236	PKS 2209+236	333.025	23.928	2.5	1.91 ± 1.71	2.43 ± 1.27	$(1.58 \pm 0.84) \cdot 10^{46}$	Q	1.125	F_3 F_4
2216–038	PKS 2216–03	334.717	-3.594	2.77		$< 3.98^*$	$< 1.17 \cdot 10^{46}$	Q	0.901	F_4
2223–052	3C 446	336.447	-4.95	1.86	1.11 ± 1.59	3.14 ± 1.59	$(1.74 \pm 0.95) \cdot 10^{46}$	Q	1.404	F_3 F_4

Table 4.1.1.: continued.

Name^a	Common Name	RA^b	Dec^b	S/N^c	Γ^d	$F_{20-100\,\mathrm{keV}}{}^e$	$L_{20-100\,\mathrm{keV}}{}^f$	Type^g	z^h	Detections^i
2227–088	PHL 5225	337.417	-8.548	6.06	1.13 ± 0.47	9.73 ± 1.81	$(6.75 \pm 1.3) \cdot 10^{46}$	Q	1.56	B F_3 F_4
2230+114	CTA 102	338.152	11.731	10.11	1.42 ± 0.26	15.89 ± 1.67	$(6.01 \pm 0.65) \cdot 10^{46}$	Q	1.037	B F_3 F_4
2243–123	PKS 2243–123	341.576	-12.114	0.75		< 3.96*	$< 5.28 \cdot 10^{45}$	Q	0.632	
2251+158	3C 454.3	343.491	16.148	55.16	1.52 ± 0.05	74.34 ± 1.56	$(1.98 \pm 0.04) \cdot 10^{47}$	Q	0.859	B I_A I_{11} F_3 F_4
2331+073	TXS 2331+073	353.553	7.608	1.76		< 3.75*	$< 1.81 \cdot 10^{45}$	Q	0.401	F_3 F_4
2345–167	PKS 2345–16	357.011	-16.52	–0.14		< 3.65*	$< 3.94 \cdot 10^{45}$	Q	0.576	F_3 F_4
2351+456	4C +45.51	358.59	45.885	0.81		< 3.25*	$< 5.41 \cdot 10^{46}$	Q	1.986	F_3 F_4

Notes. $^{(a)}$ Name in IAU B1950 format, $^{(b)}$ Equatorial coordinates (J2000) in degrees, $^{(c)}$ *Swift*/BAT S/N, $^{(d)}$ Photon Index for 20 keV – 100 keV, $^{(e)}$ X-ray flux in $10^{-12}\mathrm{erg\,s^{-1}\,cm^{-2}}$ (* indicates fluxes calculated by assuming a photon index based on sub-sample of bright sources; † for upper limits caused by contamination of a nearby source) $^{(f)}$ X-ray luminosity in $\mathrm{erg\,s^{-1}}$, $^{(g)}$ Optical classification (Véron-Cetty & Véron, 2003): Q: Flat Spectrum Radio Quasar, B: BL Lac, G: Radio Galaxy, U: Unidentified, $^{(h)}$ Redshift, taken from the MOJAVE webpage (http://www.physics.purdue.edu/astro/MOJAVE/), ** indicates a redshift value from (Lister et al., 2015), $^{(i)}$ Published hard X-ray / gamma-ray detection in: B: *Swift*/BAT 105-month survey catalog (Oh et al., 2018), I_A: *INTEGRAL*/IBIS AGN catalog (Malizia et al., 2012) and the updated catalog (Malizia et al., 2016), I_{11}: *INTEGRAL* 11-year Hard X-ray Survey (Krivonos et al., 2015), F_3: *Fermi*/LAT 3LAC catalog (Ackermann et al., 2015), and F_4: 4FGL catalog (Abdollahi et al., 2020). ‡: the source has been re-classified as a NLSY1 galaxy by Yao et al. (2015). The original classification of Q is kept here because of the FSRQ-typical values for luminosity and photon index.)

4.2 Implications for blazar evolution, selection effects, and variability

After the hard X-ray analysis in the previous section, the distribution of measured parameters and their implications regarding sample statistics and physical characteristics are discussed in this part in more detail. The cross section of the MOJAVE-1 sample sources with multiple high-energy survey catalogs is investigated. Why are certain groups of sources detected in one energy band, but not in another? For the analysis of this issue, the general trend of the detection behavior as well as individual outliers are studied in Sect. 4.2.1. Following the results of the measured X-ray parameters in the BAT band, the correlation of photon index to the detection statistic in the *Fermi*/LAT band is discussed in Sect. 4.2.2.

A central question, which needs to be addressed using a number of analysis methods, is the disparity of low-flux to high-flux sources in the sample. Is the fact that generally sources are concentrated at low fluxes a result of selection effects? By determining the $\log N$-$\log S$ distribution of the sample the disparity is revealed to be more complex (Sect. 4.2.3). Two possible contributors to the unusual flux distribution, that is, source variability and intrinsic luminosity evolution, are studied in Sect. 4.2.4 and Sect. 4.2.5, respectively. With the characteristics derived from the $\log N$-$\log S$ distribution the MOJAVE-1 sample's contribution to the CXB is determined in Sect. 4.2.6.

4.2.1. Common sources with other high-energy catalogs

The cross section of the MOJAVE-1 sample with the BAT 105-month catalog is governed by the catalog S/N cutoff at $4.8\,\sigma$, with some minor deviations due to slightly offset extraction coordinates. In this section, the detection statistics of the *INTEGRAL*/IBIS and *Fermi*/LAT catalogs are analyzed in terms of correlation to BAT flux and radio flux density in order to examine potential outliers and selection effects. The radio flux density data is taken from Lister et al. (2015). A Kendall's τ test reveals that the hard X-ray flux and radio flux density of the complete MOJAVE-1 sample are indeed correlated. Taking into account only sources that are not upper limits results in a p-value of 0.0063 for the rejection of the null hypothesis of zero correlation, whereas a test that includes all sources results in an even more significant p-value of $4.6 \cdot 10^{-6}$.

The *INTEGRAL* AGN catalog (Malizia et al., 2012) and the 11-year catalog (Krivonos et al., 2015) comprise the brightest X-ray sources that have been registered in the corresponding survey time span in the energy bands of 20 keV–100 keV, and 100 keV–150 keV, respectively. Figure 4.2.1 shows the BAT flux against radio flux density of the MOJAVE-1 sample with all sources in the *INTEGRAL* catalogs marked accordingly. The *INTEGRAL* AGN catalog in the plot is supplemented by the updated AGN catalog Malizia et al. (2016), adding four new detections of MOJAVE-1 sources: 1222+216, 1510–089, 1730–130, and 1741–038.

There is no apparent correlation between radio emission and the detection by *INTEGRAL*, as indicated by the Kendall's τ p-value of 0.45. From Fig. 4.2.1 a tentative correlation of radio flux density and the *INTEGRAL* detections might be indicated for the 11-year catalog entries, but is uncertain due to the low number of data points. As expected, the tendency of a detection by *INTEGRAL* follows the flux distribution of the BAT data. A band at around $(6-12)\cdot 10^{-12}\,\mathrm{erg\,s^{-1}\,cm^{-2}}$ is occupied by both sources that are detected and not detected

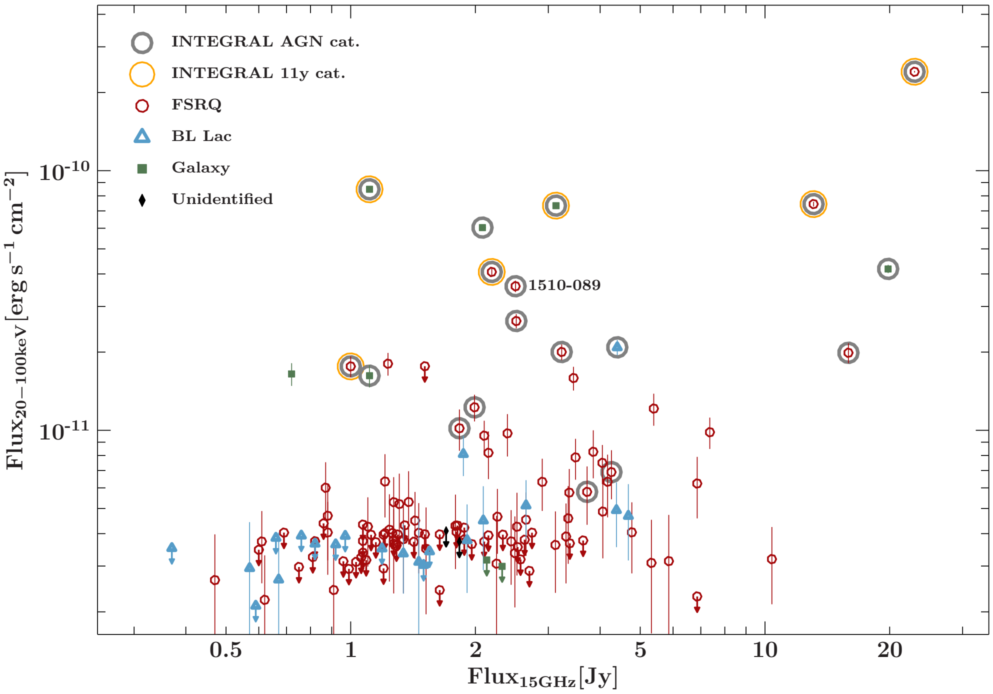

Figure 4.2.1.: Hard X-ray flux plotted against radio flux density. All sources with a corresponding entry in the *INTEGRAL* 11-year catalog or the AGN catalog are marked.

by *INTEGRAL*, indicating the catalog sensitivity cutoff.

Until the publication of the updated AGN catalog (Malizia et al., 2016; Bird et al., 2016), the source 1510–089, an FSRQ, has been a notable outlier, although a comparatively bright X-ray source. Malizia et al. (2016) report a hard X-ray flux of $38.5\cdot10^{-12}\,\mathrm{erg\,s^{-1}\,cm^{-2}}$, on the basis of the *INTEGRAL* survey from 2002 to 2010. The BAT survey data set (2004 to 2013) gives a very comparable flux value of $(35.9\pm1.8)\cdot10^{-12}\,\mathrm{erg\,s^{-1}\,cm^{-2}}$ in the same energy band. The question remains whether the non-detection of the source was due to variability or other effects. The surveys that have been performed by *INTEGRAL* show an irregular exposure over the entire sky, with regions in the Galactic plane observed significantly more often. In the exposure map of AO11[2] the source has a cumulative exposure time of $2\cdot10^6$ s, which is an order of magnitude less than many regions of the Galactic plane. However, different sources, which are in the older catalog (Malizia et al., 2012), like BL Lac, show very comparable exposure times, in this case $3\cdot10^6$ s. Furthermore, both sources are highly significant in the BAT band after 105 months of observation: 1510–089 with $18.7\,\sigma$ and BL Lac with $16.8\,\sigma$. Thus, a selection effect on the basis of low exposure time is estimated to be unlikely. In the catalog paper Malizia et al. (2012) state that in order for a source to be included in the sample it is required to have X-ray spectral information, that is, flux values in the 2 keV−10 keV and 20 keV−100 keV bands. In 2010, at the time of the catalog release, one *Chandra* pointed observation and multiple *Swift*/XRT observations were available[3]. An estimation[4] of the number of spectral counts in the 2 keV−10 keV band on the basis of the BAT flux reveals

---

[2] `https://www.cosmos.esa.int/web/integral/exposure`

[3] NASA HEASARC mission archive, `https://heasarc.gsfc.nasa.gov/docs/archive.html`

[4] NASA HEASARC WebPIMMS, `https://heasarc.gsfc.nasa.gov/cgi-bin/Tools/w3pimms/w3pimms.pl`

approximately 0.4 counts/s in the 10 ks exposure time of said observation, giving 4000 counts for the soft X-ray spectrum, which is more than sufficient for a meaningful flux calculation. An additional requirement for an inclusion in the catalog were available spectral data in the optical band as well as a precise optical identification and classification of a source, supported by numerous previous works (see Malizia et al., 2012, and references therein). The authors do not state why certain X-ray-bright sources are excluded and/or which factor lead to the exclusion. Ultimately, the results regarding the question why 1510–089 was not included in the first catalog are inconclusive, but point to significant flux variability instead of selection effects.

The case of the source 1730–130 could be indicative of this scenario. While significantly lower in flux than the majority of MOJAVE-1 sources in the *INTEGRAL* AGN catalogs, its listed flux of $13 \cdot 10^{-12}\,\mathrm{erg\,s^{-1}\,cm^{-2}}$ (Malizia et al., 2016) is approximately twice the flux obtained from the BAT survey data ($(6.9 \pm 1.5) \cdot 10^{-12}\,\mathrm{erg\,s^{-1}\,cm^{-2}}$), while being in the same energy band of 20 keV–100 keV. Although the observation time frames of both surveys overlap (2002–2010, 2004–2013) the registered flux changed notably, likely due to a variable flux output, which decreased with time. The X-ray-faintest *INTEGRAL* source in Fig. 4.2.1 is represented by the source 1741–038, at $(5.8 \pm 1.5) \cdot 10^{-12}\,\mathrm{erg\,s^{-1}\,cm^{-2}}$ (BAT), or $7 \cdot 10^{-12}\,\mathrm{erg\,s^{-1}\,cm^{-2}}$ (*INTEGRAL* AGN catalog), at the detection limit of the survey. This, on the other hand, indicates a very consistent flux output in the given observation time frames.

While *Swift*/BAT and *INTEGRAL*/IBIS measure in most cases the rising part of the high-energy bump in the typical blazar SED, *Fermi*/LAT observations gather data in the GeV band, that is, the falling flank of the same spectral component. Figure 4.2.2 shows the same plot of hard X-ray flux against radio flux density as in Fig. 4.2.1, with all sources marked that were not listed in the 3LAC or 4FGL catalogs. For better readability the non-detections instead of detections are marked, since the vast majority of the MOJAVE-1 sample is indeed detected by *Fermi*/LAT.

The distribution of the hard X-ray flux for *Fermi*/LAT-detected and undetected sources is not significantly different from each other, as shown by a 2-sample KS test for the X-ray flux (excluding upper limits) and the resulting p-value of 0.37. Almost all BL Lac type sources are *Fermi*/LAT-detected contrary to both FSRQs and radio galaxies. This result can be attributed to the SED characteristic of the AGN types. Depending on the SED shape and position of the emission bumps on the frequency axis, a LAT detection is more likely for certain scenarios. Since the source detection of the instrument favors hard spectra, corresponding to a high-peaked source (HSP), BL Lacs are detected disproportionately often compared to their low-peaked relatives, the FSRQs and radio galaxies (mostly LSP). Radio surveys on the other hand register mainly low-peaked sources. This dependence is illustrated in the latest *Fermi*/LAT source catalog (4FGL), listing 1102 BL Lacs and 681 FSRQs, while, in contrast, the MOJAVE-1 sample, compiled through measurements at 15 GHz, consists of a number of only 21 BL Lacs and 104 FSRQs. Also, radio galaxies are predominantly low-peaked sources, as indicated by the flat photon index in the hard X-ray band (Sect. 4.1.4), resulting in a low detection rate for this AGN type by *Fermi*. In the 4FGL catalog, only 41 radio galaxies have been associated over the entire sky. Figure 4.2.3 shows the SEDs of three MOJAVE-1 sources as an example: the FSRQ 0923+392 (4C 29.25), the radio galaxy 0430+052 (3C 120), and 2200+420 (BL Lac itself). The first two sources do not have any *Fermi*/LAT catalog counterpart, while the third one does. The spectra illustrate the

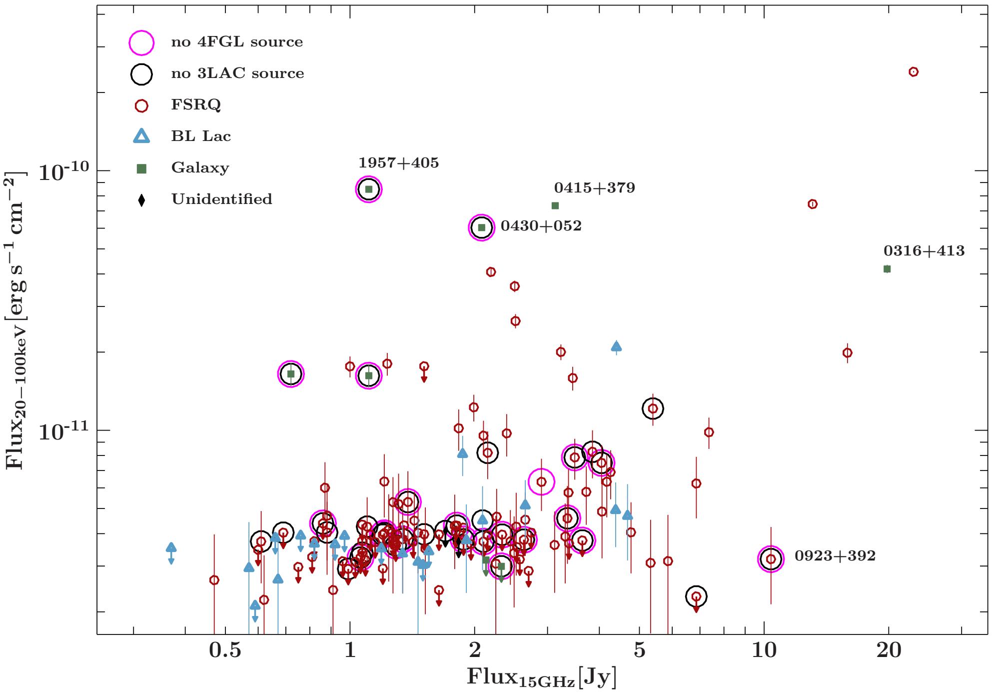

Figure 4.2.2.: Hard X-ray flux plotted against radio flux density. All sources which do not have a corresponding entry in the 3LAC or 4FGL catalogs are marked. Note the different convention compared to Fig. 4.2.1 for better readability.

distinctive shape and SED positions (peak frequencies) of the individual AGN types.

The four X-ray-brightest MOJAVE-1 sources, which are not registered by *Fermi*/LAT in the most recent survey catalog (4FGL), are all radio galaxies, with 1957+405 (Cygnus A) and 0430+052 (3C 120) being the X-ray-brightest. Two more radio galaxies in the same range but at higher radio-flux densities are *Fermi*/LAT-detected: 0415+379 (3C 111) and 0316+413 (3C 84). In the case of the X-ray brightest radio galaxies, gamma-ray flux output, or at least a detection-strength signal, is dependent on the variability of the source. This, for example, is illustrated by the source 0430+052, which was included in the *Fermi*/LAT source catalogs 1FGL (1 year, Abdo et al., 2010b), 3FGL (4 years), and 4FGL (8 years), but not in the 2FGL catalog (2 years, Nolan et al., 2012).

The radio-loudest source in the sample that has no *Fermi*/LAT association is the FSRQ 0923+392. A the same time, the source is X-ray-faint at $(3.19 \pm 1.05) \cdot 10^{-11}\,\mathrm{erg\,s^{-1}\,cm^{-2}}$. The SED of the source in Fig. 4.2.3 reveals a very low-peaked spectrum with no data available above the X-ray regime. The shape of the spectral distribution does not rule out a high-energy bump, which falls off significantly just before the GeV band. Even if the broadband spectrum does extend into the LAT band, the spectrum would almost certainly be characterized by very low count rates and an extremely steep slope, making a LAT detection highly unlikely. On VLBI images of 5 GHz (Kollgaard et al., 1990) and 15 GHz (Lister et al., 2018) the source's jet morphology changes radically with scale[5], suggesting a relatively small inclination angle of line-of-sight to jet axis. While relativistically moving plasma would boost the observed flux especially in this case in the direction of travel, the magnitude greatly de-

---

[5] For an overview see `https://www.physics.purdue.edu/astro/MOJAVE/index.html`

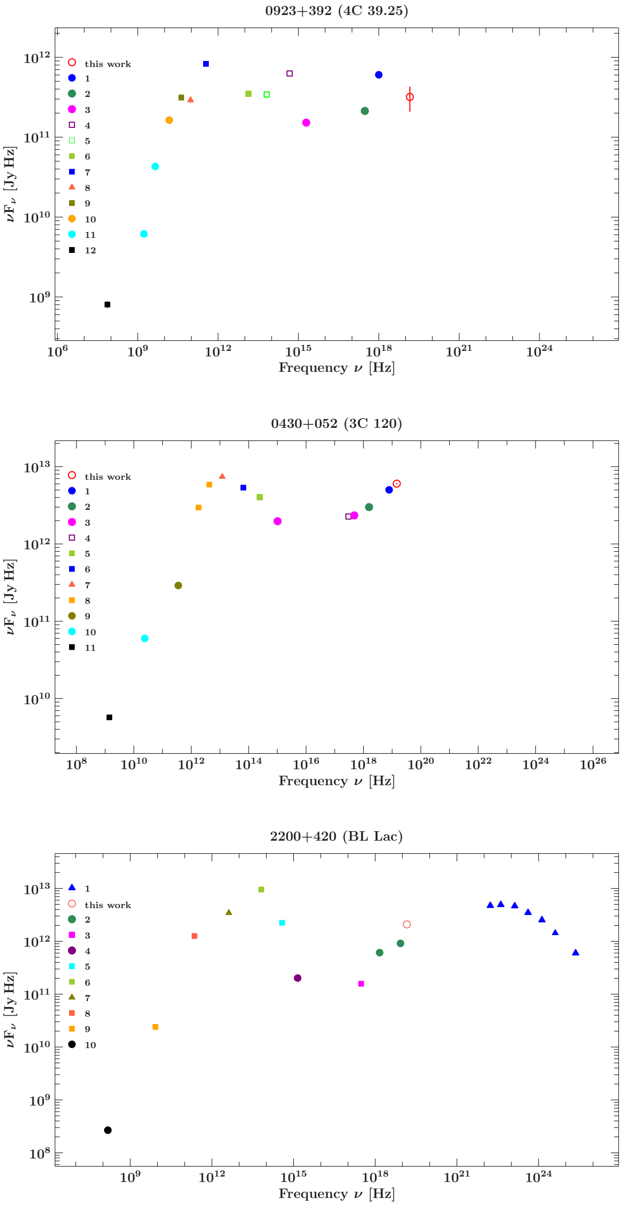

Figure 4.2.3.: Non-simultaneous broadband SEDs of the FSRQ 0923+392 (4C 39.25, top), the radio galaxy 0430+052 (3C 120, middle), and 2200+420 (BL Lac, bottom). The first two sources are not detected in the most recent *Fermi*/LAT source catalog (4FGL), while the third one is.
Data references for 0923+392: [1]Wang et al. (2016), [2]Massaro et al. (2009), [3]Seibert et al. (2012), [4]Healey et al. (2008), [5]Cutri et al. (2013), [6]Wu et al. (2012), [7]Jenness et al. (2010a), [8]Gold et al. (2011), [9]Lee et al. (2017), [10]Lister et al. (2011), [11]Orienti et al. (2007), [12]Cohen et al. (2007).
Data references for 0430+052: [1]Winter et al. (2012), [2]Kataoka et al. (2007), [3]Ogle et al. (2005), [4]Maselli et al. (2010a), [5]Skrutskie et al. (2006a), [6]Cutri et al. (2013),[7]Sargsyan et al. (2011), [8]Meléndez et al. (2014), [9]Jenness et al. (2010b), [10]Lanyi et al. (2010a), [11]Allison et al. (2014).
Data references for BL Lac: [1]Abdollahi et al. (2020), [2]Ricci et al. (2017), [3]Massaro et al. (2009), [4]Raiteri et al. (2009), [5]Larionov et al. (2010), [6]Cutri et al. (2013), [7]Hanish et al. (2015), [8]Agudo et al. (2014), [9]Kovalev (2009), [10]Arshakian et al. (2010).

pends on the jet's speed. Past works found that gamma-ray-bright radio jets tend to have significantly higher apparent jet speeds compared to gamma-faint sources (e.g., Kellermann et al., 2004; Lister et al., 2015). Also, in a recent study, Lister et al. (2019) suggested that a high apparent jet speed is a minimum requirement for gamma-ray and TeV detections of LSP and ISP sources. The low median apparent speed of 1.567c (Lister et al., 2019) of 0923+392 is therefore a likely cause for the non-detection by *Fermi*/LAT.

4.2.2. Fermi vs. MeV blazars

As already described in Sect. 4.2.1, the LAT gamma-ray detector on-board *Fermi* favors high-peaked sources. Even with the new improved Pass 8 event selection process of the continuous LAT survey, bringing more sensitivity to the MeV range, *Fermi*/LAT detections are still biased towards harder spectra. More distant sources, blazars in particular, provide an additional challenge, since the SED and the declining part of the HE bump are shifted towards lower energies, away from the LAT band. This scenario is the case with a certain blazar sub-type, adequately named MeV blazars, for their HE peak frequency in the or very much near the MeV regime. This radio-loud blazar type, predominantly found at high redshifts, is characterized by hard X-ray but soft gamma-ray spectra and exhibits relatively high jet speeds and often a massive SMBH in their nuclei, billions of solar masses heavy. Following the concept of the blazar sequence (Ghisellini et al., 1998), MeV blazars are particularly strong in the hard X-ray regime. This is because of two factors: the shift of the SED to lower energies due to redshift, and the high-z FSRQs, which on their own tend to be more luminous (e.g., Ajello et al., 2012b). While only a few blazars are detected by *Fermi*/LAT above $z = 3$ in the recent catalogs, luminous blazars that are strong in the hard X-ray band have their activity maximum at around $z = 4$ (e.g., Ajello et al., 2009).

The MOJAVE-1 sample is mostly composed of low-peaked radio-loud sources. Similarly, the fraction of gamma-ray-bright sources is very high: 112 of a total of 135 sources have a counterpart in the 4FGL catalog. If the photon index in the hard X-ray band indicates, as previously suggested, a tendency of a gamma-ray detection, then the distribution of BAT photon indices should mirror this behavior. Furthermore, yet gamma-ray-undetected sources near the parameter space of detected sources would be prime candidates for detections in the near future. Figure 4.2.4 shows the BAT photon indices of the MOJAVE-1 sample in the spectral band of 20 keV–100 keV plotted against the HE peak frequency where available, taken from Chang (2010), for the rest frame and the observed frame. For the most part the distribution of the data points does not change significantly between both graphs and the overall trend stays the same. That is, most *Fermi*/LAT-detected sources have notably higher peak frequencies than non-detected sources. While former concentrate around $\log \nu_{\mathrm{HE}}^{\mathrm{peak}}$ of 22.5 to 23.5 the non-detections span a much larger range of approximately 19 to 24 (rest frame). Sources that have been newly listed in the 4FGL catalog are specifically marked. Two previously non-detected sources (1458+718, 2145+067) are also located in the cluster of detected sources around $\log \nu_{\mathrm{HE}}^{\mathrm{peak}} = 23$ in the new catalog. Lister et al. (2015) found the same trend using the extended MOJAVE-1.5 sample, but by analyzing the synchrotron bump peak frequency. The authors also explained the behavior by the SED position and therefore reduced flux in the LAT sensitivity range, but also by low relativistic boosting due to comparatively low jet speed and a low radio variability level. In their study Lister et al. (2015) suggested a probable *Fermi*/LAT detection in the near future for three blazars on the basis of high jet speed and radio modulation index. All three blazars in the sample (III Zw 2, PKS 0119+11, and 4C +69.21) were still not listed in the 4FGL catalog, which comprises twice the integration time and improved event selection compared to the previous 3FGL/3LAC catalogs.

Here, an alternative approach is introduced for the prediction of which source could likely be detected in a future source catalog of the LAT survey. Instead of properties which are only specific to the radio regime, the HE peak position is deemed a more robust indicator. Also, the photon index, derived from the BAT survey, implies the shape of the HE emission bump, although with less accuracy (see below for a more detailed discussion). Between the bulk of all gamma-ray-bright sources at around $\log \nu_{\mathrm{HE}}^{\mathrm{peak}} = 23$ and the rest at lower frequencies, two non-gamma-ray-detections stand out: the FSRQs 2005+403 and 0742+103. The former has a hard BAT photon index of $\Gamma = 1.50 \pm 0.44$ and moderately high jet speed of 9.9c, while the latter has a less hard X-ray spectrum, but higher HE peak frequency of

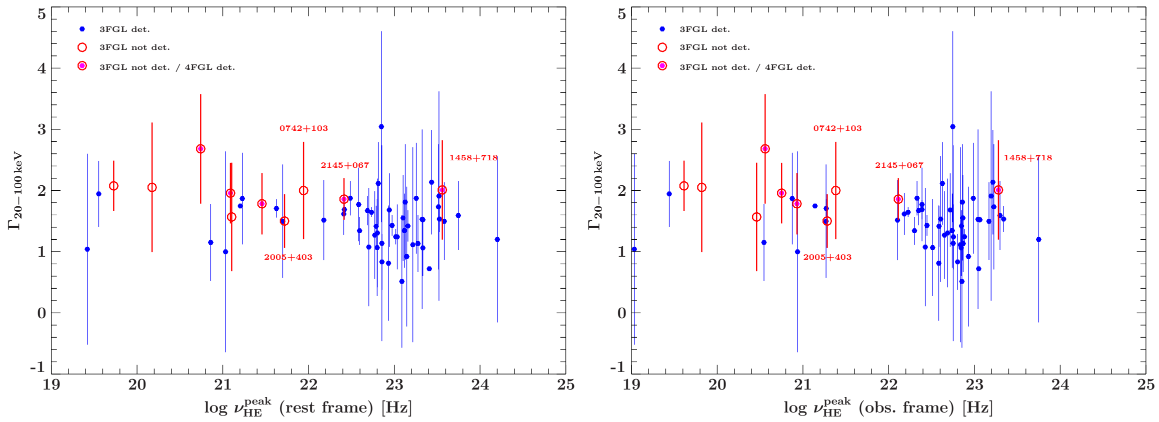

Figure 4.2.4.: BAT photon index against SED HE peak frequency (data from Chang, 2010). Left: rest frame peak frequency, right: observed frame frequency.

approximately log $\nu_{\mathrm{HE}}^{\mathrm{peak}} = 22$. While the critical radio properties listed by Lister et al. (2015) are far from ideal for this source (jet speed $v = 2.8c$, variability index $m = 0.016$) compared to the mean values of the study ($v_{\mathrm{mean}} = 10.1c$, variability index $m_{\mathrm{mean}} = 0.2$) a future *Fermi*/LAT detection would be of particular interest and could indicate which approach is the more reliable in this regard.

In the following, a more detailed analysis of the BAT photon index distribution of gamma-ray-bright and gamma-ray-faint blazars is described. Since the X-ray photon index mirrors the slope of the HE emission bump (or the declining synchrotron bump in a few isolated cases) it is determined if the distributions of this parameter of both sub-samples are indeed significantly different from each other. However, as already shown in Fig. 4.2.4, the derived photon indices from spectral fitting feature substantial uncertainty ranges. In order to estimate how large the impact of said uncertainty ranges is and to make a meaningful statistical statement, the expanded 2-sample KS-test is applied (Sect. 3.7.2). For this analysis the definition of the sub-samples of LAT-detected and non-detected MOJAVE-1 blazars follows the 4-year catalog (3FGL/3LAC), since the integration time is very close to the 105-month BAT survey. Figure 4.2.5 shows the distributions of BAT photon index for the 3LAC-detected sources (sub-sample A) and 3LAC-non-detected sources (sub-sample B). The bottom panel displays the added Gaussian distributions of every photon index measurement. This is equal to the probability distribution of measuring a certain photon index in one of the sub-samples, or the combined sample (black line). A standard 2-sample KS-test on both sub-samples results in the rejection of the null hypothesis that both parameter distributions are drawn from the same parent distribution at a level of $\alpha = 0.008$ and with a test statistic of $D_{\mathrm{sample}} = 0.497$. The expanded 2-sample KS test, which incorporates the measurement errors, reveals that only 0.9% of randomly chosen sub-samples reach a test statistic D for the null hypothesis equal or larger than the initial test of sub-samples A and B without uncertainties. Hence, both LAT-detected and non-detected MOJAVE-1 blazars show significantly different spectral slopes in the hard X-ray regime. As expected, the LAT-detected blazars have harder X-ray photon indices compared to LAT-non-detections. If one includes the group of radio galaxies into the sum-samples, an even more distinct result is derived: the null hypothesis of a common parent distribution of A and B can be rejected at a level of $\alpha = 0.002$ and $D_{\mathrm{sample}} = 0.55$. The corresponding fraction of the test statistic D equal or

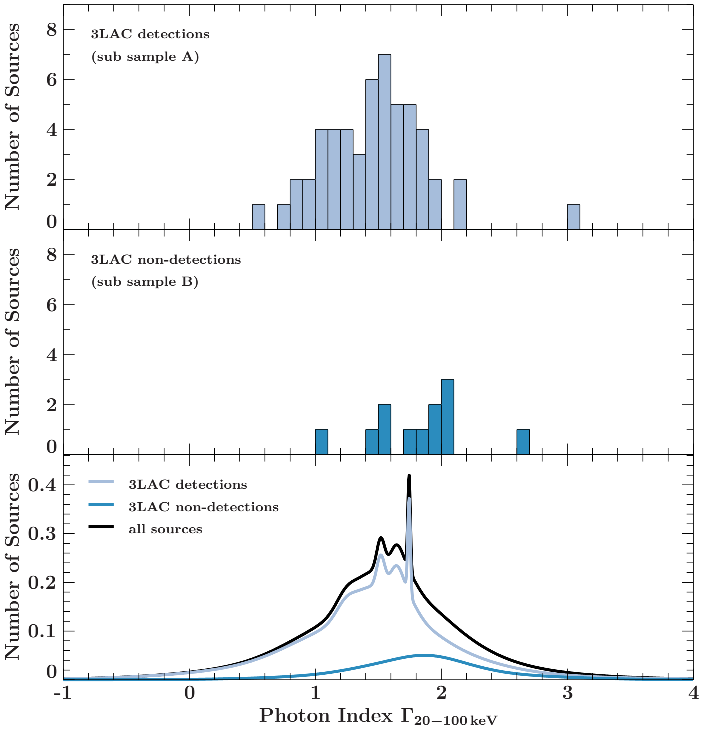

Figure 4.2.5.: Distribution of MOJAVE-1 hard X-ray photon indices in the 20 keV–100 keV band. Top: MOJAVE-1 blazars that are listed in the 3LAC catalog, middle: sources that are not listed in the 3LAC, bottom: added Gaussian probability curves of all photon indices. The X-ray-bright source 3C 273 creates a sharp peak at $\Gamma = 1.75$ because of its small uncertainty range.

larger than D_{sample} is only 0.05%. The increased significance is mainly due to the clustering of photon index values around $\Gamma = 2$ in sub-sample B.

Abdo et al. (2010a) found the same general relation for gamma-ray-bright blazars in terms of gamma-ray photon index and synchrotron and HE peak frequency. Also, the authors showed a strong correlation between gamma-ray and X-ray photon indices, as expected from a shifted SED of typical double-peaked structure.

4.2.3. Number count distributions: logN-logS

The cumulative distribution, or $\log N$-$\log S$, of the MOJAVE-1 AGN sample allows to deduce a number of characteristics specific to this population of radio-loud low-peaked blazars in the hard X-ray regime, such as the distribution of the sources in space compared to their respective flux output. The calculation of the distribution follows the steps outlined in Sect. 3.4. Both the $\log N$-$\log S$ graph for the hard X-ray flux and radio flux density are presented in Fig. 4.2.6. The fitting results are summarized in Table 4.2.1. Following Eq. 3.4.3, the index / slope of the fitted power law is defined as a negative parameter. The left panel of the graph shows the distribution for hard X-ray flux data (70 MOJAVE-1 blazars, excluding upper limits), which follows the shape of a power law with a norm of $A_{\text{Moj,BAT}} = (8.25{\pm}0.57) \cdot 10^{-3}\,\text{deg}^{-2}$ and a slope of $\alpha_{\text{Moj,BAT}} = 1.13 \pm 0.04$ for all fluxes $F \gtrsim 2.2 \cdot 10^{-12}\text{erg}\,\text{s}^{-1}\,\text{cm}^{-2}$. Within the uncertainty interval the distribution's slope is not compatible with the Euclidean case, that is, 3/2. Like in most flux-limited cumulative $\log N$-$\log S$ distributions, the graph saturates at the low-flux end, in this case around $3 \cdot 10^{-12}\text{erg}\,\text{s}^{-1}\,\text{cm}^{-2}$. Within the power-law fit error interval the data point of the faintest source (1417+385) is not compatible with the fit. The source density per sky area is read off at the flux of the faintest source and gives $(3.33 \pm 0.22) \cdot 10^{-3}\text{deg}^{-2}$, which equals 88 ± 6 sources in the sky area that is covered by the MOJAVE-1 survey. The flattening of the distribution and the consequent discrepancy

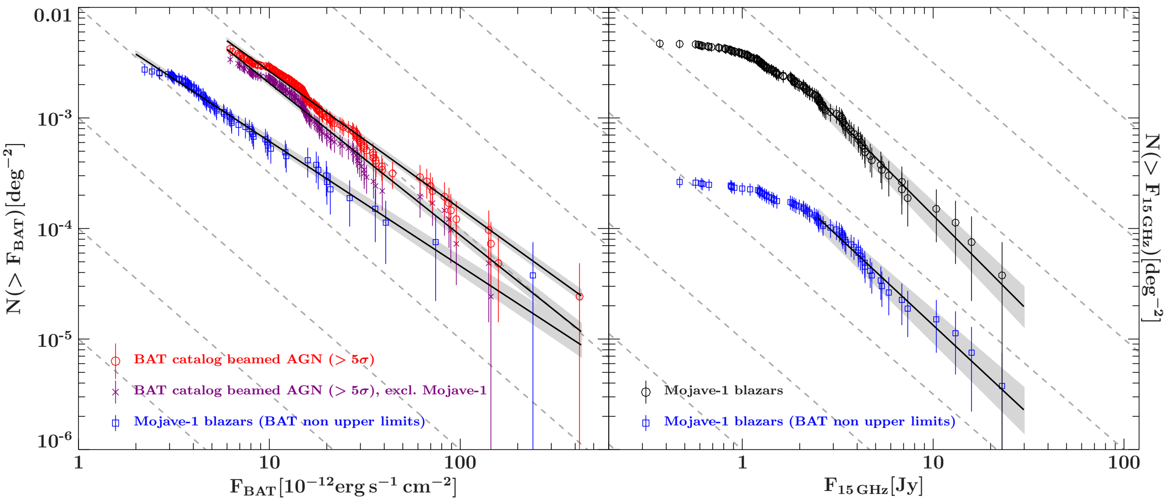

Figure 4.2.6.: Left: $\log N$-$\log S$ distribution of all MOJAVE-1 blazars in the 20 keV–100 keV band (excluding upper limits) and the all sources from the BAT 105-month catalog listed as beamed AGN, derived from fluxes in the range of 14 keV–195 keV. Also, the same sub-sample is graphed without all MOJAVE-1 sources. Right: distribution derived from 15 GHz flux density measurements (Lister et al., 2015). The complete MOJAVE-1 sample and the same X-ray sub-sample from the left plot are graphed. The norm of latter distribution has been multiplied with 0.1 for better readability. Power-law fits to all distributions are shown as black lines with the gray area indicating the error interval. For the power-law fits of the radio data only fluxes higher than 2.5 Jy are taken into account. A general slope of $-3/2$ is indicated by the dashed lines.

between the projected number of sources to the 70 sources in the plot likely stems from the upper limits, which have been excluded from the distribution.

The approach of subtracting a background S/N contribution from a source sample's S/N distribution (Sect. 3.2.3, 4.1.2) is endorsed by the fact that even the low-flux end of the $\log N$-$\log S$ distribution is generally very consistent, showing no notable signs of a selection bias or strong saturation.

The unusually flat slope of the hard X-ray $\log N$-$\log S$ of the MOJAVE-1 sample can be subject to a number of different causes. In the following, it determined which factors are likely responsible. In order to exclude a strong selection effect that is introduced by only selecting radio-bright sources, the distribution of the beamed AGN sub-sample of the BAT catalog (Oh et al., 2018) is also graphed in Fig. 4.2.6, albeit for the full catalog flux band of 14 keV–195 keV. Since the catalog is compiled on the basis of a blind survey and it is purely dependent on the source significance in the hard X-ray band and not the flux characteristics of a different wavelength, it functions as a reference point. The sample is composed of 158 AGN, from which all sources with a significance lower than $5\,\sigma$ are excluded as well as the brightest source, Centaurus A, because of its more common classification as a radio galaxy (e.g., Steinle, 2006), leaving 143 beamed AGN. Interestingly, the resulting $\log N$-$\log S$ distribution is also characterized by a notably flat slope of $\alpha_{\mathrm{cat,BAT}} = 1.24 \pm 0.02$. Even the entire sub-sample of 955 AGN in the BAT catalog results in a very similar value of $\alpha_{\mathrm{BAT\ AGN}} = 1.27 \pm 0.01$. The AGN from the BAT catalog also exhibit a non-Euclidean distribution in space in terms of flux output, which could be explained by intrinsic and redshift-dependent evolution of the X-ray luminosity or variability. In any case, the slope of

Table 4.2.1.: $\log N$-$\log S$ distribution power-law fit results. The fitted distribution of the MOJAVE-1 sample (20 keV–100 keV) only includes blazars and sources that do not have an upper-limit flux value. The fit results regarding the BAT catalog sources are obtained for the full 14 keV–195 keV flux. The last group of two rows corresponds to the power-law fits of the radio flux density data (15 GHz).

Sample	Fitted Sources	normalization A $[10^{-3}\,\mathrm{deg}^{-2}]$	slope α	Original Sample
MOJAVE-1, BAT	70	8.25 ± 0.57	1.13 ± 0.04	Lister et al. (2009a)
BAT cat. (beamed AGN)	143	46.20 ± 2.50	1.24 ± 0.02	Oh et al. (2018)
BAT cat. (beamed AGN)^{a}	115	$48.96^{+3.57}_{-3.09}$	1.38 ± 0.03	Oh et al. (2018)
BAT cat. (AGN)	955	$338.99^{+2.72}_{-2.70}$	1.27 ± 0.01	Oh et al. (2018)
MOJAVE-1, 15 GHz^{b}	40	$7.17^{+1.19}_{-0.99}$	$1.74^{+0.13}_{-0.12}$	Lister et al. (2009a)
MOJAVE-1, 15 GHz^{c}	32	$5.46^{+1.1}_{-0.89}$	$1.61^{+0.15}_{-0.14}$	Lister et al. (2009a)

Notes. $^{(a)}$ Excluding all MOJAVE-1 sources. $^{(b)}$ Power-law fit restricted to all 125 MOJAVE-1 blazars with radio flux densities larger than 2.5 Jy. $^{(c)}$ Power-law fit restricted to the 70 non-upper-limit (BAT flux) MOJAVE-1 blazars with radio flux densities larger than 2.5 Jy.

the MOJAVE-1 $\log N$-$\log S$ distribution is not compatible with the most recent BAT catalog AGN sample or the beamed-AGN sub-sample within $2\,\sigma$ of the respective error intervals. The similarly flat slopes of all samples in the hard X-ray band, however, suggests a common responsible property. The strong tendency of the MOJAVE-1 (blazar) sample to produce a very flat slope in the hard X-ray $\log N$-$\log S$ distribution is also expressed by the fact that the beamed AGN sample of the BAT catalog without any MOJAVE-1 sources shows a steeper slope of $\alpha_{\mathrm{cat,BAT,noMoj}} = 1.38 \pm 0.03$, closer to a static distribution in a Euclidean universe. Typically, AGN samples that result from the hard X-ray surveys are not mainly composed of blazars but Seyfert galaxies. For example, the studies conducted by Beckmann et al. (2006), Ajello et al. (2012a), or Akylas & Georgantopoulos (2019) exhibit distribution slopes that are indeed compatible with $-3/2$. The here found deviation from this behavior in the studied blazar samples describes the difference in intrinsic emission and potentially the luminosity evolution in the hard X-rays.

The $\log N$-$\log S$ distribution for hard X-ray as well as the BAT catalog's beamed AGN sample both show remarkably flat slopes. It has to be pointed out, however, that the 243 unclassified sources in the BAT catalog could include a significant number of blazars, which would change the corresponding beamed AGN $\log N$-$\log S$ distribution and almost certainly its slope. The same argument cannot be made for the MOJAVE-1 sample, which mostly consists of blazars with only two sources of unidentified type (0648–165 and 1213–172).

The MOJAVE-1 sample shows an entirely different behavior in the radio regime. The right panel of Fig. 4.2.6 presents the $\log N$-$\log S$ distribution at 15 GHz for all 122 MOJAVE-1 blazars as well as all 70 blazars that are not upper limits in the BAT band, that is, the same sample as in the left panel, also colored blue. The radio flux density data are taken from Lister et al. (2015). The measurement values (median) derived by the authors cover the time span of 2008–2012. Compared to the X-ray $\log N$-$\log S$ distribution the radio data reveal a much steeper slope and significant flattening at the lower-flux end. The flux density data set has been compiled as part of a larger flux-limited MOJAVE-1.5 sample (Lister et al., 2015). Since the vast majority of additional sources to the MOJAVE-1 sources in the larger sample is located below the flux density of 2.5 Jy, the power-law fit to the distribution is restricted to

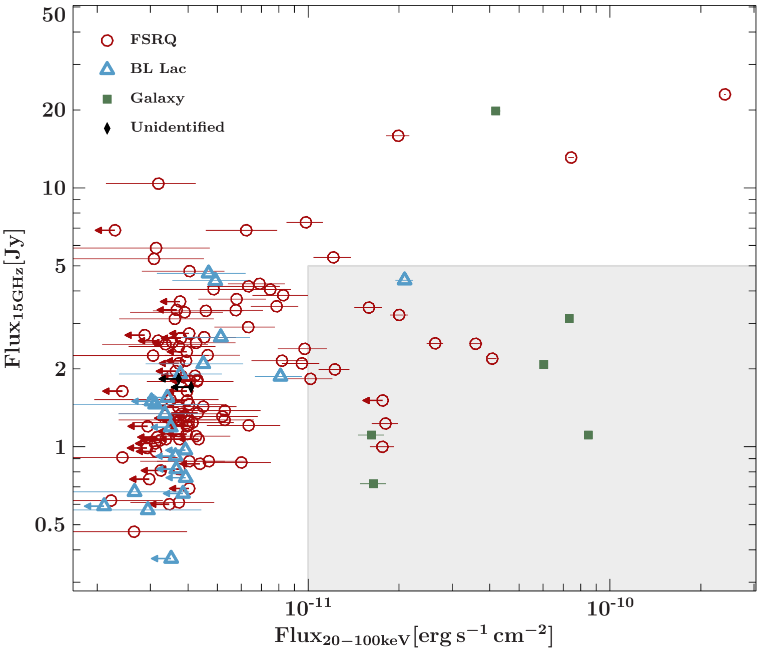

Figure 4.2.7.: MOJAVE-1 15 GHz flux density vs. hard X-ray flux. The gray area indicates a number of X-ray-bright but radio-faint sources (see text).

all values above that limit. This way, the flux values can be applied to the MOJAVE-1 sample without a possible bias at the low-flux end. The power-law slopes of the full MOJAVE-1 blazar sample and the reduced X-ray-bright sub-sample are $\alpha^{122}_{\mathrm{Moj,15GHz}} = 1.74^{+0.13}_{-0.12}$, and $\alpha^{70}_{\mathrm{Moj,15GHz}} = 1.61^{+0.15}_{-0.14}$, respectively. Both slopes are not compatible with the results in the BAT band, and the complete MOJAVE-1 blazar sample is even steeper than the canonical value 3/2 for an Euclidean distribution within the uncertainty interval. The flattening of both radio distributions is very likely due to the fact that median values are graphed, but the source selection criterion states that only one of multiple flux measurements must reach a certain value. Consequently, the median flux is often lower at the low end of the distribution, below the survey flux cutoff. In order to test for residual selection biases while reducing the larger MOJAVE-1.5 sample to the MOJAVE-1 source sample, in Sect. 4.3 the $\log N$-$\log S$ distributions of the MOJAVE-1.5 sample in the radio and BAT band are analyzed and compared.

For the hard X-ray MOJAVE-1 $\log N$-$\log S$ distribution to be more compatible with the pure Euclidean case the relative number of X-ray-bright to faint sources needs to be balanced differently. Either bright sources are too numerous or faint ones are missing. The sources, which are not graphed due to them being upper limits, are not responsible for the general flat slope of the distribution, because their values only extend to approximately $4 \cdot 10^{-12}\mathrm{erg\,s^{-1}cm^{-2}}$. A potential group of sources, that has greater influence on the distribution's slope, is given by a number of X-ray-bright, but radio-quiet sources, shown in the plot of X-ray against radio flux in Fig. 4.2.7. The gray area (with arbitrary limits) marks the corresponding sub-set, including nine FSRQs and one BL Lac (BL Lac itself). Also, five radio galaxies are included, which, however, are not incorporated in the $\log N$-$\log S$ distribution in any case. Removing this sub-set from the list of MOJAVE-1 blazars results in a new $\log N$-$\log S$ distribution with a slope of 1.54 ± 0.06, in accordance with the radio $\log N$-$\log S$ and Euclidean distribution. Using the modeling of luminosity functions this dependency of source population and the shape of the $\log N$-$\log S$ is analyzed further in Sect. 4.2.5.

Generally, no significant correlation is present between the hard X-ray flux and radio flux density, as indicated by Spearman's rank correlation coefficient of $\rho = 0.31$. However, the distribution of flux in both energy bands is notably different. BAT fluxes are concentrated at low values, partially due to the high number of upper limits. The radio flux densities are spread much more uniform over about two decades of frequency. In the following Sect. 4.2.4 the difference of radio and hard X-ray $\log N$-$\log S$ slope is studied regarding the possible influence of variability in the BAT band.

4.2.4. Influence of blazar variability

In Sect. 3.4.2, a method for estimating the influence of source variability on the $\log N$-$\log S$ shape was introduced. The method incorporates the typical flaring amplitude and the percentage of flaring sources. Here, it is tested whether typical blazar flaring behavior can explain the significantly flatter slope of the MOJAVE-1 sample at hard X-rays compared to the radio band, which is compatible with the Euclidean slope of $-3/2$.

Because the hard X-ray data set of the used BAT survey was accumulated during 105 months of observation, and since blazars are well known for their irregular flux output, the measured source fluxes are possibly not representative of the flux's mean values or even quiet states. In the case that a number of sources exhibit a flaring state during observation, the flux values are shifted to higher values in the $\log N$-$\log S$ distribution, flattening its slope. This scenario is consistent with the observation from Sect. 4.2.3, which shows an disproportionately high fraction of bright sources in the BAT data set (or too few at the low-flux end).

Using the first 66 months of *Swift*/BAT observations in the full 14 keV–195 keV band, Soldi et al. (2014) found significant variation in AGN light curve data. The intrinsic variability of each source has been determined using the variability amplitude estimator S_v. This quantity is derived from the light curve flux values and their uncertainties using the maximum-likelihood estimate of the variability parameter σ_{Q} (Soldi et al., 2014, Eq. 1). Approximately 80% of the AGN in the study were found to exhibit variability on scales from months to years. The variability amplitude estimator for the blazar sub-sample was calculated to $\langle S_v \rangle = 33\% \pm 2\%$, which was the highest variability in the study. A small sub-set of two gamma-ray-bright blazars were characterized by an even higher variability ($\langle S_v \rangle = 90\%$).

Here, it is also assumed, that 80% of all sources are variable. The maximum of the possible flux increase for such a source is equal to S_v. The maximum value of this random factor would thus be 1.33 for $S_v = 33\%$. Table 4.2.2 shows the derived values of S_v on the basis of the 70-month and 105-month BAT light curves[6] for the 70 X-ray bright MOJAVE-1 blazars. Because of the tentative difference between gamma-ray-bright and faint blazars in Soldi et al. (2014), the light curves are sorted by 3FGL associations. *Fermi*/LAT-detected sources reveal an hard X-ray variability amplitude estimator S_v of approximately 33% to 65%, even larger than the previous study. The *Fermi*/LAT-non-detected sources show a similar, but somewhat larger range, that is approximately 30% to 80%. However, this result is only based on the light curves of three sources. The data sets of the 105-month light curves also tends to produce larger values of S_v. In order not to underestimate the variability of the BAT flux a conservative value of $S_v = 100\%$ is chosen. Thus, the fraction of variable sources of a simulated test sample is assumed to increase their flux value randomly, but not more than

---

[6] https://swift.gsfc.nasa.gov/results/bs105mon/, https://swift.gsfc.nasa.gov/results/bs70mon/

Data Set	non-3FGL $\langle S_v \rangle$	3FGL $\langle S_v \rangle$
70-month	45 ± 12 (3)	39 ± 6 (12)
105-month	69 ± 9 (3)	56 ± 9 (17)

Table 4.2.2.: Mean variability amplitude estimator $\langle S_v \rangle$ of the 70 X-ray-bright MOJAVE-1 blazars. The calculation is based on the BAT light curve data (number of used light curves per set in parentheses), accessible through the BAT survey website.

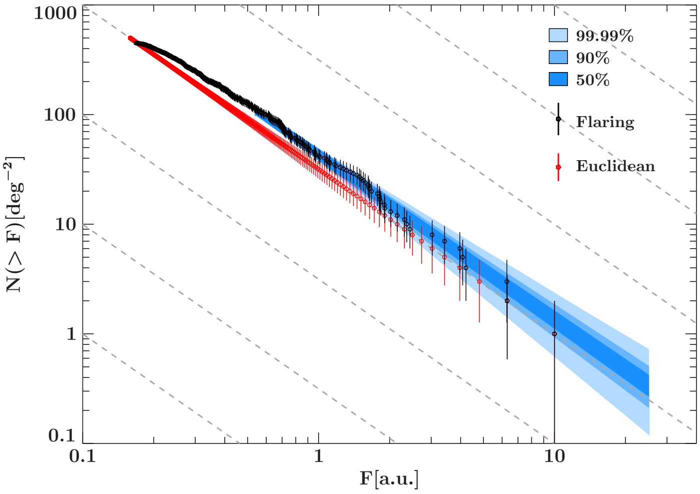

Figure 4.2.8.: log N-log S diagram of ideal source sample with uniform luminosity and distribution in Euclidean space (red). An instance of the log N-log S graph of randomly flaring sources is plotted in black. The blue shaded areas indicate the range of fitted power laws from simulated flaring samples (see text). The outer shaded area comprises 99.99% of all fitted power laws. The dashed lines represent a slope of $-3/2$.

twice the original / start value.

A set of 500 sources is simulated, which all share the same luminosity and are distributed uniformly according to Euclidean geometry. The resulting ideal log N-log S graph is plotted in Fig. 4.2.8, with the brightest source set to 10 arbitrary flux units. Two separate effects are simulated that change the shape of the distribution. First, the flattening at the low-flux end, which is observed in the MOJAVE-1 radio data set (see Sect. 4.2.3). A number of 100 sources of a simulated sample at the low-flux end is randomly removed in order to account for the effect of randomly flaring sources below the detection threshold (Sect. 3.4.2). And, secondly, the random flaring with a factor in the range of $[1-2]$ is simulated for 400 out of all 500 sources. Here, only one single maximum flaring amplitude (one population) is considered for simplicity. Each randomized flaring distribution is fit by a power law above 0.5 of the arbitrary flux unit to avoid fitting the part of the distribution that levels off. The process is repeated $5 \cdot 10^4$ times. Figure 4.2.8 shows one instance of a simulated flaring log N-log S distribution together with the regions that the fitted power laws describe. Different colored regions indicate the 50%, 90%, and 99.99% of all slopes closest to the overall median slope. The vast majority of 99.99% of all runs has slopes larger than 1.28, which are thus not compatible with the hard X-ray MOJAVE-1 blazars (1.13 ± 0.04), equal to a $4\,\sigma$ uncertainty range. It can be stated that the X-ray flaring of the blazars in the MOJAVE-1 sample is very unlikely to be a major contributing factor to the unusually flat slope of the hard X-ray log N-log S distribution.

4.2.5. Evolution of hard X-ray emission: blazar XLF

In this section the results of the luminosity function fits to the hard X-ray and radio data of the MOJAVE-1 blazar sample are presented. Since the general variability in the BAT

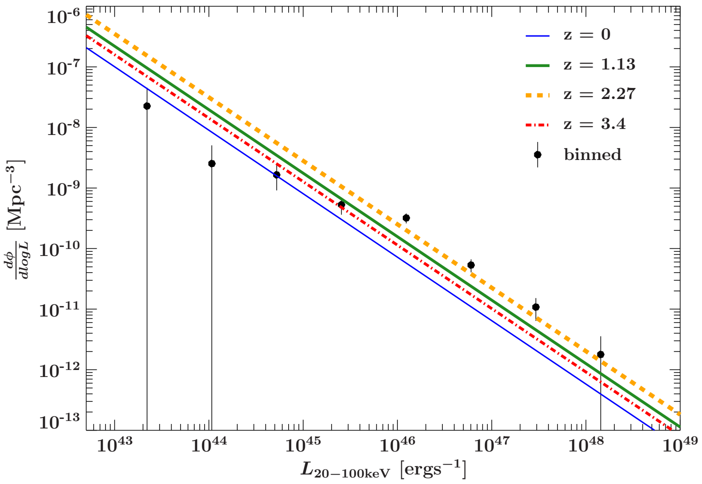

Figure 4.2.9.: The binned XLF and best-fit analytic model PLEg for the MOJAVE-1 blazar sub-sample (70 sources, upper limits excluded).

band can be excluded to be primarily responsible for the comparatively flat slope of the hard X-ray log N-log S distribution (Sect. 4.2.4), a different evolution of intrinsic emission at radio and X-ray energies is tested for. The hard X-ray luminosity function (XLF) is calculated for all blazars in the MOJAVE-1 sample minus one source with no redshift information (0300+470), leaving 69 sources. The 15 GHz radio luminosity function (RLF) is determined for the complete set of 123 blazars with redshift information in the MOJAVE-1 sample. Additionally, the AIC values (Eq. 3.6.11) are calculated for all model fits. The corresponding probability p_j of each model j is calculated, which expresses if said model fits the data, that is, maximizes the likelihood compared to the best fit. This section follows the methods outlined in Sect. 3.6.

The LF models PDE, PLE, PDEg, and PLEg (Sect. 3.6.3) are fitted using a single power law form. Furthermore, a model of PLE with no evolution ($k = g = 0$) is tested. Double power-law models are also fitted and generally provide viable results ($p_i \approx 0.05 - 0.70$). Despite of introducing additional free parameters to the fit model, however, there is no significant improvement in the fit for the analyzed source samples. Consequently, it can be reasoned that double power-law models are less suitable in describing the analytic LFs. All parameters of the fitted LF models are listed in Table 4.2.3. Although previous works, deriving the XLFs of AGN, also applied luminosity-dependent density evolution models (e.g., Ueda et al., 2003; Miyaji et al., 2015; Ranalli et al., 2016), simpler models with less free parameters are chosen in this analysis because of the small sample sizes. The X-ray data set is described best with the single power-law PDEg and PLEg models, and considerably less optimal with the double power-law versions ($p_{\mathrm{PLE}} = 0.247$, $p_{\mathrm{PLEg}} = 0.320$). No evolution at all can be excluded with a corresponding relative probability of $p_{\mathrm{no\ evol}} = 0.0269$ for describing the data adequately. Figure 4.2.9 shows the binned XLF (Sect. 3.6.1) of the MOJAVE-1 blazar sample as well as the PLEg model for different redshifts and exhibit the typical falling trend with luminosity. Additionally, a standard V/V_{max} test (Schmidt, 1968) is performed in order to validate the result obtained from the XLF fit. The test value including its mean absolute error $\langle V/V_{\mathrm{max}}\rangle = 0.451 \pm 0.184$ also indicates a trend of negative evolution, which is in qualitative agreement with the previous result.

For the radio data set but the same sub-sample of 69 sources the simple PDE and PLE models are preferred. Also, the extended PDEg and PLEg models with $p_{\mathrm{PLEg}} = p_{\mathrm{PDEg}} = 0.737$ are reasonably probable. Again, no evolution is least probable with $p_{\mathrm{no\,evol}} = 0.12$.

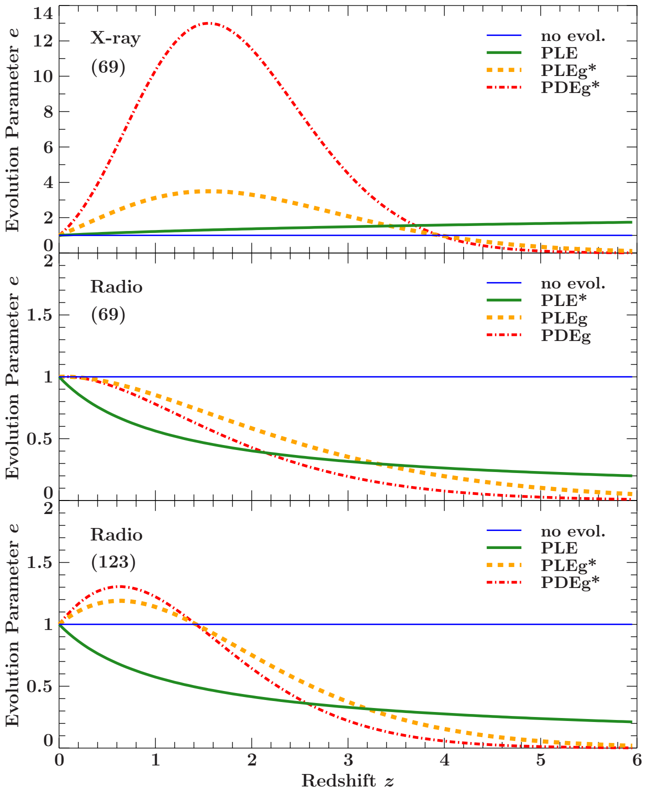

Figure 4.2.10.: Evolution parameter e against redshift for the MOJAVE-1 sample (see Table 4.2.3). A selection of fitted models is plotted, with the best fit models marked with an *.

The RLF fit to the complete set of 123 MOJAVE-1 blazars with redshift information results in a preferred PDEg / PLEg model, and, again, a highly unlikely no-evolution scenario ($p_{\text{no evol}} = 0.003$). In any case, luminosity or density evolution is always preferred for all samples against a static model. Although all samples show similar trend in this regard, the individual model parameters reveal different evolutionary behavior. Figure 4.2.10 presents the evolutionary parameter e as a function of redshift for different LF models and all three analyzed samples. The best-fit models are marked accordingly. The X-ray sample as well as the full radio sample (123 sources) show a trend of positive evolution up to a certain redshift value, that is $z \approx 1.5$ for the X-ray data set and $z \approx 0.6$ for the radio data. Beyond this redshift mark the evolution shows a negative trend, which is equal to sources that are less luminous or less dense. The luminosity output for the sampled population of sources per co-moving volume increased for both data sets up to a point in time and then decreased again. The same sample of 69 X-ray-bright sources in the radio regime shows a different characteristic. All RLF models show only a continuously falling trend of e with redshift. It can be stated, however, that the evolutionary properties between hard X-ray and radio energies are clearly different, while a scenario where no evolution of intrinsic luminosity is present can be excluded.

Comparable blazar studies in the soft and hard X-ray band (e.g., Hasinger et al., 2005; Sazonov et al., 2007; Ajello et al., 2009) derived very similar parameters of the XLF evolutionary term. In contrast to the MOJAVE-1 blazar sample, however, previous works reveal relatively steep (single) power-law slopes of the XLF, approximately $\gamma = 2 - 3$. The best fit MOJAVE-1 XLF models are characterized by slopes of $\gamma \approx 1$. For the corresponding RLF fits the slope is even flatter with $\gamma \approx 0.5 - 0.65$. The derived blazar XLFs from Ajello et al. (2009) in the energy band of 15 keV – 55 keV are also characterized by source densities comparable to the MOJAVE-1 data-set at the low-luminosity end ($L \approx 10^{44}\,\mathrm{erg\,s^{-1}}$). In contrast, the density diverges strongly for the high-luminosity part of the XLFs, with approximately 10^3 times more for the MOJAVE-1 data at around $L \approx 10^{48}\,\mathrm{erg\,s^{-1}}$. Relatively, the difference of both functions can also be interpreted as a scarcity of low-luminosity sources in the MOJAVE-1 sample, or at least in the analyzed sub-set of 69 X-ray-bright sources. For the analysis 52 sources have been omitted due to insufficient signal strength, that is, only upper-limit values could be determined for these cases. Interestingly, the RLF of the MOJAVE-1 blazars (full number of 122 sources) exhibits a similar property. In this instance the influence of a X-ray-related selection bias cannot be present. It can be concluded that the results indicate different blazar populations as well as evolutionary behavior regarding the radio-selected MOJAVE-1 blazars and the X-ray-bright samples of previous studies. Also, the redshift distribution of both samples is already indicative of a different population selection. Whereas the MOJAVE-1 sample sources have a wide range of redshift, with the majority around $z = 0.5 - 1.5$, the 38 blazars from Ajello et al. (2009) feature a distribution that looks comparatively bi-modal: 18 sources have a redshift of $z < 0.5$, and ten sources are at $z > 2$. Accordingly, higher redshift values influence a probable detection in the hard X-ray band by shifting the HE emission bump to lower energies. Furthermore, the BL Lac type sources in the sample are almost exclusively high-peaked.

The introduction of a selection effect when reducing the full source sample (123) to 69 sources in the radio band may not be fully excluded, but it is not a compelling explanation for the difference in X-ray and radio $\log N$-$\log S$ distributions. The different XLF and RLF fitting results and the fact that disproportionally many X-ray-bright sources exist in the X-ray distribution of consistent slope support this conclusion. An evolutionary path for the X-ray emission, which describes a notable increase in luminosity per volume until $z \approx 1.5$ compared to the falling trend in the radio band, corresponds to a relatively low fraction of X-ray-faint sources. It is therefore suggested that this characteristic is at least to some extend responsible for the observed disparity of low to high X-ray flux sources in the respective $\log N$-$\log S$ distribution.

The results in this part are generally supported by a recent study by Ighina et al. (2019), who have found significantly different trends of the emitted luminosity in the soft X-ray (0.2 keV – 10 keV) and radio bands at low and high ($z > 4$) redshifts, respectively. The fraction of X-ray to radio emission was found to be 2–3 times as large in the high-redshift compared to the low-redshift sample. In this work, in the MOJAVE-1 data set an earlier emission maximum in the hard X-ray range is detected regarding to the radio emission, which simply declines with redshift, starting at $z = 0$. Ighina et al. (2019) argue that the interaction of extended jet regions via IC upscattering with the CMB, which is highly redshift-dependent, reflects the evolution of the observed emission of X-ray to radio. A number of previous studies that center around X-ray and radio-selected AGN samples (e.g., Ajello et al., 2009; Caccianiga et al., 2019) show results that do not confirm this trend. The studies can be reconciled by arguing that the extended / compact emission ratio is not constant between sources (Ighina et al., 2019).

4.2.6. Cosmic hard X-ray background - the contribution of blazars

The specific origin of the cosmic background radiation, especially in the X-ray regime (CXB), is still subject of debate. The soft X-ray band, below approximately 10 keV, has been resolved for the most part into individual sources. Hickox & Markevitch (2006) attribute

Table 4.2.3.: Fitting results of the luminosity functions for the hard X-ray and radio data of the MOJAVE-1 blazar sub-sample. The value p_j expresses the relative probability that the corresponding model also fits the data compared to the best fit. The numbers in parentheses in the first column denote the sample sizes. Sect. 3.6.3 introduces the fitting models and parameters.

LF Model	A $[10^{-10}\,\mathrm{Mpc}^{-3}]$	L_* $[\mathrm{erg\,s^{-1}}]$	γ_1	γ_2	k	g	p_j
BAT (69)							
PLEg	89.9	10^{44}	1.05 ± 0.12		2.20 ± 0.65	-0.56 ± 0.19	1.000
PDEg	35.7	10^{44}	1.05 ± 0.12		4.51 ± 1.54	-1.14 ± 0.41	1.000
PLEg (dpw)	2.11	$(0.52 \pm 1.56) \cdot 10^{46}$	1.35 ± 0.31	0.68 ± 0.32	1.57 ± 0.86	-0.35 ± 0.25	0.320
PLE (dpw)	1.97	$(1.62 \pm 2.05) \cdot 10^{46}$	0.54 ± 0.19	1.52 ± 0.29	0.38 ± 0.30		0.247
PLE	74.4	10^{44}	0.89 ± 0.09		0.29 ± 0.31		0.015
PDE	74.4	10^{44}	0.89 ± 0.09		0.54 ± 0.61		0.015
no evol.	74.1	10^{44}	0.82 ± 0.05		0		0.027
Radio (69)							
PLE	5.06	10^{34}	0.50 ± 0.08		-0.83 ± 0.39		1.000
PDE	5.07	10^{34}	0.50 ± 0.08		-1.25 ± 0.54		1.000
PLEg	2.61	10^{34}	0.53 ± 0.09		0.03 ± 0.86	-0.26 ± 0.25	0.737
PDEg	3.33	10^{34}	0.53 ± 0.09		0.05 ± 1.32	-0.41 ± 0.38	0.737
no evol.	2.92	10^{34}	0.65 ± 0.05		0		0.120
Radio (123)							
PLEg	2.00	10^{34}	0.53 ± 0.07		0.64 ± 0.65	-0.45 ± 0.19	1.000
PDEg	2.01	10^{34}	0.53 ± 0.07		0.98 ± 1.01	-0.69 ± 0.30	1.000
PLE	4.17	10^{34}	0.48 ± 0.06		-0.80 ± 0.29		0.105
PDE	4.17	10^{34}	0.48 ± 0.06		-1.19 ± 0.39		0.105
no evol.	2.38	10^{34}	0.63 ± 0.04		0		0.003

around 80% of the background flux in the 1 keV – 8 keV band to AGN, while luminosity function modeling by Ueda et al. (2003) based on AGN surveys by *HEAO-1*, *ASCA*, and *Chandra* showed that blazars are required to be a major constituent for the background above a few hundred keV. In a more recent study, Giommi & Padovani (2015) estimated the CXB blazar contribution through Monte Carlo simulations. The authors found that 4% – 5% at 1 keV – 50 keV can be attributed to blazars, whereas in the 100 MeV – 10 GeV band the fraction is 40% – 70%, and as much as 100% above. Using *NuSTAR*, the dedicated X-ray telescope for soft and hard X-ray bands, Harrison et al. (2016) found that up to 39% of the CXB in the 8 keV – 24 keV band is due to individual AGN. Past *NuSTAR* observations provided deep surveys over small sections of the sky (e.g., Masini et al., 2018). Furthermore, the *NuSTAR* legacy survey program[7] targeted over a hundred known sources, most of them AGN. However, the effective energy range of *NuSTAR* in the majority of cases stops at ≈ 24 keV (e.g., Brandt & Alexander, 2015). In an earlier study of a small sub-sample from the *Swift*/BAT survey, Ajello et al. (2009) found that 10% – 20% CXB in the 15 keV – 55 keV band can be explained by blazar emission. Generally, the composition of the CXB in terms of source type has been studied using X-ray or gamma-ray-bright samples (see, e.g., Mateos et al., 2008; Ajello et al., 2009; Bottacini et al., 2012). Due to different sample definition and analytic approaches, the results of CXB contribution per source type vary significantly.

In this work a well-defined and statistically complete blazar sample is used to determine the CXB contribution in the energy band of 20 keV – 100 keV of beamed AGN, which, for the most part are low-peaked radio-loud sources that do not suffer from any X-ray selection

---

[7] For an overview see `https://www.nustar.caltech.edu/page/legacy_surveys`

bias. The power-law fit to the $\log N$-$\log S$ hard X-ray flux distribution of the MOJAVE-1 blazars (Fig. 4.2.6) gives the normalization A and power-law index (slope) α, which are reported in Table 4.2.1. Following Eq. 3.5.3 the integrated flux of the blazar sample above $2.2 \cdot 10^{-12}\mathrm{erg\,s^{-1}\,cm^{-2}}$ is calculated to:

$$\begin{aligned} F_{\mathrm{contrib}}^{\mathrm{deg}^2,\,\mathrm{MOJAVE}} &= \int_{2.2\cdot 10^{-12}}^{\infty} \alpha \cdot A \cdot F^{-\alpha} dF \\ &= (6.47^{+2.83}_{-1.51}) \cdot 10^{-14}\mathrm{erg\,s^{-1}\,cm^{-2}\,deg^{-2}}. \end{aligned} \tag{4.2.1}$$

Compared to the total CXB intensity in the 20 keV – 100 keV band (Eq. 3.5.1) this result represents 0.21% within an error interval of 0.16% – 0.31%. In contrast to the $\log N$-$\log S$ slope, which has a major impact on the CXB flux contribution, a lowering of the integration limit of $2.2 \cdot 10^{-12}\mathrm{erg\,s^{-1}\,cm^{-2}}$ (flux of the faintest source) only increases the contribution marginally. For example, for the same $\log N$-$\log S$ slope of $\alpha = 1.13$ (negative slope) of the MOJAVE-1 blazars and an estimated contribution of 20% to the background (for 15 keV – 55 keV, Ajello et al., 2009), the lower integration limit has to be $F = 1.15{\cdot}10^{-27}\mathrm{erg\,s^{-1}\,cm^{-2}}$, already around 13 orders of magnitude lower than the reached flux limit for *NuSTAR* in the study by Harrison et al. (2016). This limit would correspond to a density of 10^{14} sources per deg^2. For comparison, the total number of galaxies over the entire sky up to a redshift of $z = 8$ has been determined to be approximately $2 \cdot 10^{12}$ (Conselice et al., 2016). A much more realistic scenario is met with a theoretical $\log N$-$\log S$ slope of 3/2, which produces a necessary lower integration limit of $F = 5 \cdot 10^{-15}\mathrm{erg\,s^{-1}\,cm^{-2}}$ (421 sources per deg^2) when the distribution is normalized on the brightest sample source. Similarly, Ajello et al. (2009) found relatively steep slopes throughout the analyzed blazar samples, approximately $\alpha = 1.7 - 2.1$. Although the authors derived a substantially different CXB contribution fraction for blazars than in this work, the results originate in the analysis of very differently defined source samples, that is, hard X-ray against radio flux selection.

Figure 4.2.6 also shows the $\log N$-$\log S$ distribution of the BAT survey catalog beamed AGN sub-sample, which also has a notably flat slope ($\alpha = 1.24$). The same calculation as above for the catalog's listed 14 keV – 195 keV flux values results in a CXB contribution of 0.31% (0.29% – 0.35%) for the $\log N$-$\log S$ distribution above $6.3{\cdot}10^{-12}\mathrm{erg\,s^{-1}\,cm^{-2}}$ (faintest source). Applying the same consideration of an associated target contribution of 20%, the necessary lower integration limit becomes $F = 2.5 \cdot 10^{-19}\mathrm{erg\,s^{-1}\,cm^{-2}}$, corresponding to a density of $7.3 \cdot 10^6$ per deg^2. Although the MOJAVE-1 blazars and the BAT beamed AGN sub-sample contribute very comparable quantities to the CXB, the necessary number of sources to reach the previously estimated percentage of 20% differs greatly when extrapolated to fainter sources. Thus, it can be concluded that the radio-loud MOJAVE-1 blazars and the X-ray-bright sources of the BAT beamed AGN sub-sample behave like two different and distinct source populations in this regard, with the former only having a negligible contribution.

4.3 Expanding to the MOJAVE-1.5 sample

The primary focus of this chapter is the model study of the MOJAVE-1 AGN sample at hard X-rays. This sample of radio-loud low-peaked jetted sources has been chosen because of its well-defined and statistically complete nature. As a further step of verification of the results in Sect. 4.1 and Sect. 4.2 the hard X-ray characteristics of the extended MOJAVE-1.5 sample are presented in this section. The MOJAVE-1 sample definition was based on a somewhat inconsistent radio flux requirement, that is, a total 15 GHz flux density larger than 1.5 Jy for all sources above $\delta = 0°$ and a flux density larger than 2 Jy for $0° > \delta > -20°$. Also, the Galactic plane ($|b| \leq 2.^\circ 5$) was excluded. In order to test whether the analysis of the MOJAVE-1 sample is subject to any significant selection biases in this regard the extended MOJAVE-1.5 sample (Lister et al., 2013) is analyzed for comparison. The later extension to the larger MOJAVE-1.5 sample featured all flat-spectrum radio sources with 15 GHz flux density larger than 1.5 Jy for $\delta > -30°$, also including the Galactic plane. To the original 135 sources in the MOJAVE-1 sample, 46 source were added, making a total of 181 sample sources, of which 142 are classified as FSRQs and 29 as BL Lacs. The remaining eight as radio galaxies and two unclassified sources are the same as in the MOJAVE-1 sample. In the following Sect. 4.3.1 an overview of the MOJAVE-1.5's hard X-ray characteristics is presented. The derived X-ray data products of both samples are compared in Sect. 4.3.2.

4.3.1. Hard X-ray characteristics

In this section the X-ray properties of the MOJAVE-1.5 sample are presented. In the following, in the interest of brevity, the terms MOJAVE-1 and MOJAVE-1.5 are designated M1 and M1.5, respectively. Additionally, the sub-sample of sources, which are exclusive to the M1.5 sample, is written as M1.5e.

In general, the derived properties of all sources are very similar to the results from the M1 sample. Figures 4.3.1 and 4.3.2 show the distributions of hard X-ray S/N, flux, luminosity, and photon index, analogously to Sect. 4.1. Additionally, the lower panels show the distribution of the derived parameters only for the M1.5 sample sources, excluding all M1 sources.

The following description of the results refers to only the additional 46 sources, which are added in the M1.5 sample compared to the earlier M1 sample. The S/N distribution for the Crab-weighted 14 keV – 150 keV band shows that the majority of 35 sources has an S/N value below the BAT catalog thresholds of $4.8\,\sigma$, down to $-0.8\,\sigma$ (1642+690). The six sources with the highest S/N values are all FSRQs, with the by far brightest source 0241+622 at $48\,\sigma$. Consequently, the flux distribution (20 keV – 100 keV) follows a very similar shape. However, the accumulation of upper-limit values at low fluxes create a high number of sources in the bin around $3 \cdot 10^{-12}\mathrm{erg\,s^{-1}\,cm^{-2}}$. Overall, the spectral fit and the calculation of the flux for 22 out of 46 sources results in upper limits. Compared to the M1 sample, where the majority of sources has flux values $< 30 \cdot 10^{-12}\mathrm{erg\,s^{-1}\,cm^{-2}}$, almost the entire M1.5 sub-sample of 45/46 sources lies below $15 \cdot 10^{-12}\mathrm{erg\,s^{-1}\,cm^{-2}}$.

Although the source 0241+622 is very bright in the BAT band, no association in the most recent *Fermi*/LAT catalog (4FGL) is found. An increased X-ray signal through source confusion can be excluded. Although the radio source 7C 0241+6159 is only approximately 15' distant from 0241+622, just within the BAT instrument's PSF, the spectral analysis

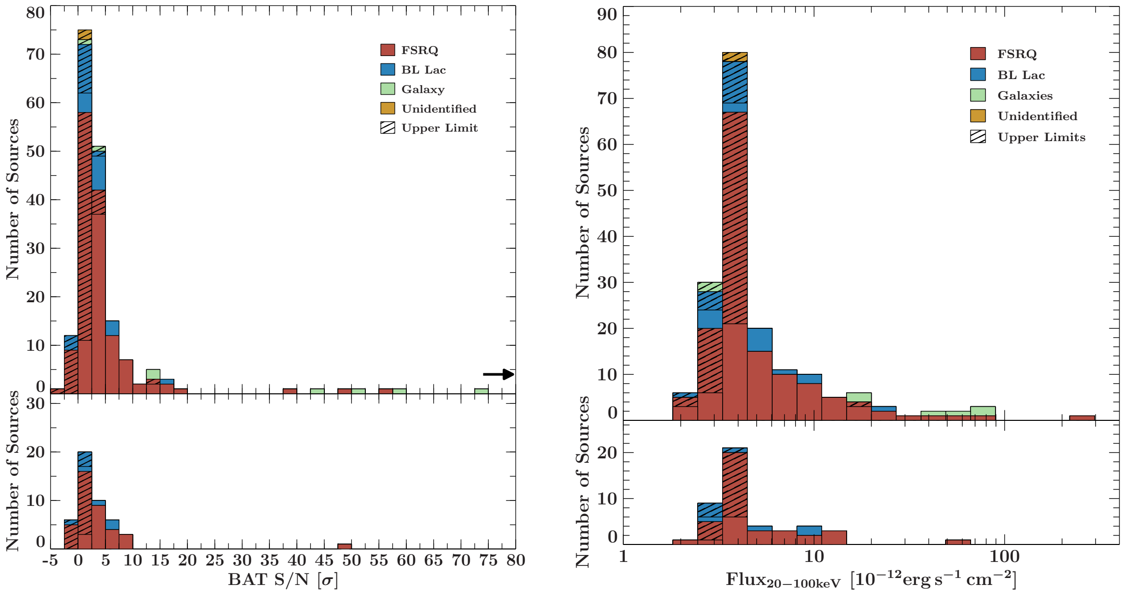

Figure 4.3.1.: Left: distribution of BAT S/N for the M1.5 sample, right: distribution of BAT flux. The bottom panels of each graph show only the M1.5 sources, excluding the M1 sources (M1.5e).

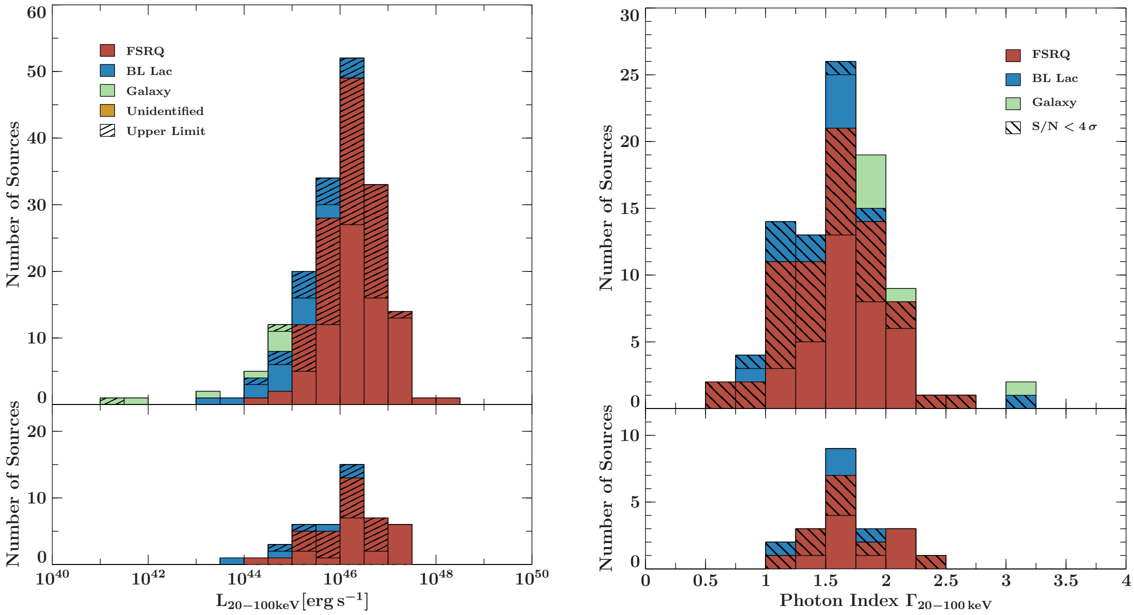

Figure 4.3.2.: Left: distribution of BAT luminosity for the M1.5 sample, right: distribution of BAT photon index Γ. The bottom panels of each graph show only the M1.5 sources, excluding the M1 sources (M1.5e).

shows no sign of spectral contamination by nearby sources. In Fig. 4.3.3 the SED of 0241+622 is shown. No data above the BAT range at around 10^{19} Hz is present in the SED. The broadband spectrum is not particularly low-peaked (synchrotron peak) when compared with more extreme sources in the sample (e.g., 0923+391). However, the graph and the measured BAT photon index of 2.05 ± 0.06 strongly suggest that BAT range measures the peak of the HE bump, which likely falls off rapidly above the hard X-ray regime, leading to a insignificant amount of flux in the GeV band.

The broad distribution of hard X-ray luminosity for the sub-sample extends over several orders of magnitude, from approximately $5 \cdot 10^{43} \mathrm{erg\,s^{-1}}$ to $2 \cdot 10^{47} \mathrm{erg\,s^{-1}}$. Only one source without known redshift, the BL Lac 1923+210, is not graphed. The most luminous source is the FSRQ 0834–201 at a relatively high redshift of $z = 2.87$. Of all sources in the sub-sample only 21 have a spectrum that can be fitted due to signal quality, that is, all positive count rate values in the spectral bins from 20 keV – 100 keV. The resulting distribution of photon indices is less broad than the complete M1.5 sample. However, both the lowest and highest photon indices of the broader M1.5 sample originate from low-significance sources, which on their own have large uncertainty ranges. Similarly, the distribution of the sub-sample, which extends from 1.03 ± 0.64 (1923+210) to 2.37 ± 0.8 (1128+385), is characterized by low-significance sources at the edges, both just over S/N $= 3\,\sigma$. All results of the spectral analysis of the additional M1.5 sources are also presented in Table 4.3.1.

Fig. 4.3.4 shows the S/N distribution and the subtraction of the fitted S/N background component for all 181 sources. After the subtraction, $157.59^{+5.64}_{-12.50}$ remain, which equals 80.16% – 90.18%. This fraction is very consistent with the results from the M1 sample, and only marginally lower than the fraction of 82.06% – 93.58%.

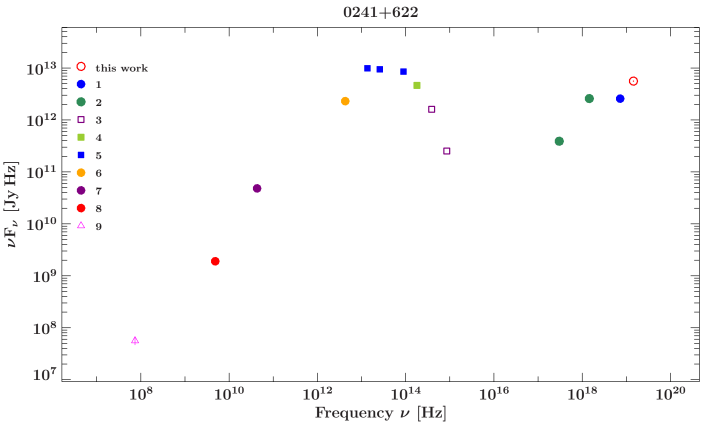

Figure 4.3.3.: SED of the M1.5 source 0241+622. The SED has been compiled using non-simultaneous data from: [1]Bird et al. (2007), [2]Winter et al. (2009), [3]Koss et al. (2011), [4]Skrutskie et al. (2006b), [5]Cutri et al. (2013),[6]Meléndez et al. (2014), [7]Lanyi et al. (2010b), [8]Becker et al. (1991), [9]Cohen et al. (2007).

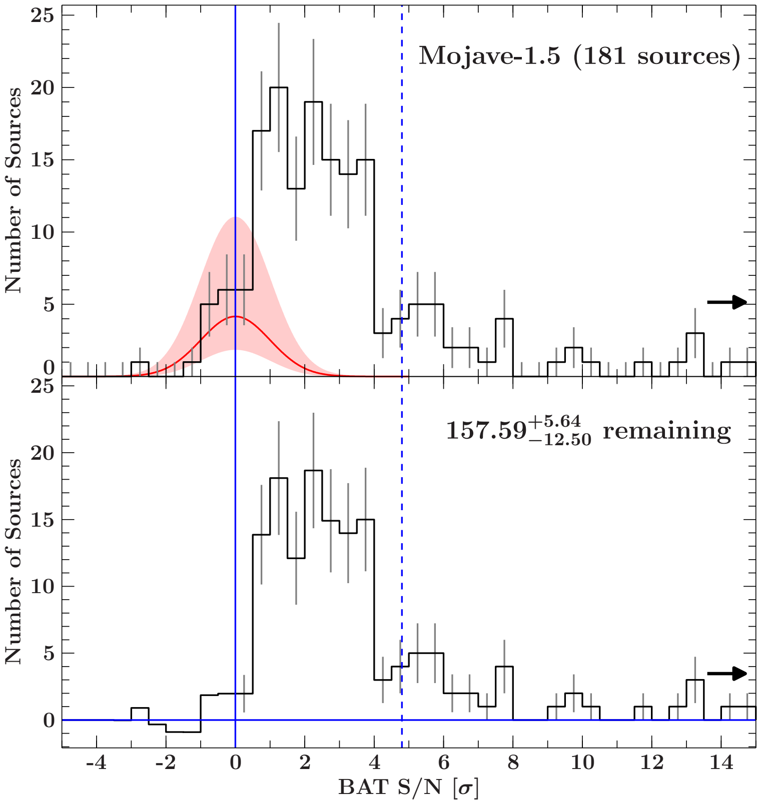

Figure 4.3.4.: Top panel: S/N distribution of the M1.5 source sample, truncated at 15 σ. The fit of a Gaussian curve to the negative side of the distribution with center of 0 σ and width of 1 σ is indicated by the red line. The 3 σ uncertainty range of the fit is shown by the red shaded area. Bottom panel: histogram after the subtraction of the original S/N distribution from the fit curve. The resulting number of remaining sources is given in the plot, summing all histogram bins larger than 0 σ. The dashed line indicates the BAT catalog threshold of 4.8 σ.

Table 4.3.1.: Results of the spectral hard X-ray analysis of the MOJAVE-1.5 sample in the 20 keV–100 keV band (only additional sources to the MOJAVE-1 sample listed).

Name[a]	Common Name	RA[b]	Dec[b]	S/N[c]	Γ[d]	$F_{20-100\,\mathrm{keV}}$[e]	$L_{20-100\,\mathrm{keV}}$[f]	Type[g]	z[h]
0109+351	B2 0109+35	18.054	35.372	1.52		$< 3.39^*$	$< 2.11 \cdot 10^{45}$	Q	0.45
0122–003	UM 321	21.37	-0.099	2.72		3.95 ± 1.23	$(1.73 \pm 0.54) \cdot 10^{46}$	Q	1.076
0130–171	OC -150	23.181	-16.913	2.74		3.81 ± 1.17	$(1.49 \pm 0.45) \cdot 10^{46}$	Q	1.02
0202–172	PKS 0202-17	31.24	-17.022	3.74		5.28 ± 1.12	$(6.63 \pm 1.41) \cdot 10^{46}$	Q	1.739
0229+131	4C +13.14	37.941	13.382	1.1		$< 3.8^*$	$< 6.84 \cdot 10^{46}$	Q	2.059
0241+622	TXS 0241+622	41.24	62.468	48.52	2.05 ± 0.06	55.9 ± 1.41	$(2.66 \pm 0.0) \cdot 10^{44}$	Q	0.045
0355+508	NRAO 150	59.874	50.964	7.44	1.72 ± 0.33	11.67 ± 1.59	$(1.33 \pm 0.18) \cdot 10^{47}$	Q	1.52
0400+258	CTD 026	60.773	26.0	0.58		$< 4.19^*$	$< 7.94 \cdot 10^{46}$	Q	2.109
0440–003	NRAO 190	70.661	-0.295	1.76	1.51 ± 1.01	4.21 ± 1.56	$(1.07 \pm 0.41) \cdot 10^{46}$	Q	0.845
0451–282	OF -285	73.311	-28.127	2.42		$< 3.22^*$	$< 9.14 \cdot 10^{46}$	Q	2.559
0454–234	PKS 0454-234	74.263	-23.414	2.77	1.55 ± 1.13	3.42 ± 1.36	$(1.31 \pm 0.53) \cdot 10^{46}$	Q	1.003
0539–057	PKS 0539-057	85.409	-5.697	-0.07		$< 3.96^*$	$< 9.94 \cdot 10^{45}$	Q	0.838
0723–008	PKS 0723-008	111.461	-0.916	5.89	1.51 ± 0.47	9.17 ± 1.77	$(3.66 \pm 0.72) \cdot 10^{44}$	B	0.127
0743–006	OI -072	116.475	-0.738	1.01		$< 3.98^*$	$< 1.47 \cdot 10^{46}$	Q	0.996
0745+241	S3 0745+24	117.15	24.007	0.88		$< 3.97^*$	$< 2.0 \cdot 10^{45}$	Q	0.409
0821+394	4C +39.23	126.231	39.278	-0.05		$< 3.47^*$	$< 1.99 \cdot 10^{46}$	Q	1.216
0834–201	PKS 0834-20	129.163	-20.283	5.06	1.56 ± 0.6	6.54 ± 1.62	$(2.3 \pm 0.57) \cdot 10^{47}$	Q	2.752
0847–120	PMN J0850-1213	132.54	-12.227	1.61		$< 3.72^*$	$< 3.87 \cdot 10^{45}$	Q	0.566
0859–140	PKS B0859-140	135.57	-14.259	1.11		$< 3.79^*$	$< 2.69 \cdot 10^{46}$	Q	1.339
0917+449	S4 0917+44	140.244	44.698	3.15	1.98 ± 0.96	3.66 ± 1.29	$(1.28 \pm 0.45) \cdot 10^{47}$	Q	2.188
0954+658	S4 0954+65	149.697	65.565	2.15		$< 2.76^*$	$< 1.19 \cdot 10^{45}$	B	0.368
1030+415	S4 1030+41	158.265	41.268	0.9		$< 2.97^*$	$< 1.42 \cdot 10^{46}$	Q	1.118
1034–293	PKS 1034-293	159.317	-29.567	2.05		$< 3.85^*$	$< 1.06 \cdot 10^{45}$	Q	0.312
1128+385	B2 1128+38	172.722	38.255	3.43	2.37 ± 0.8	4.07 ± 1.21	$(1.22 \pm 0.36) \cdot 10^{47}$	Q	1.741
1150+497	4C +49.22	178.352	49.519	7.75	1.9 ± 0.41	7.28 ± 1.26	$(2.62 \pm 0.46) \cdot 10^{45}$	Q	0.334
1406–076	PKS B1406-076	212.235	-7.874	-0.19		$< 4.06^*$	$< 3.67 \cdot 10^{46}$	Q	1.494
1435+638	VIPS 0792	219.191	63.611	-0.53		$< 2.74^*$	$< 4.97 \cdot 10^{46}$	Q	2.068
1514+197	PKS 1514+197	229.237	19.537	0.5		$< 3.18^*$	$< 1.44 \cdot 10^{46}$	B	1.07
1514–241	AP Librae	229.424	-24.372	5.51	1.75 ± 0.44	9.36 ± 1.7	$(5.24 \pm 0.95) \cdot 10^{43}$	B	0.049
1519–273	PKS 1519-273	230.657	-27.503	-0.17		$< 3.74^*$	$< 2.61 \cdot 10^{46}$	B	1.297
1622–253	PKS 1622-253	246.445	-25.461	2.35		$< 3.83^*$	$< 8.32 \cdot 10^{45}$	Q	0.786
1622–297	PKS 1622-29	246.525	-29.858	5.75	1.61 ± 0.44	8.38 ± 1.5	$(2.09 \pm 0.38) \cdot 10^{46}$	Q	0.815
1642+690	4C +69.21	250.533	68.944	-0.84		$< 2.96^*$	$< 5.8 \cdot 10^{45}$	Q	0.751
1842+681	S4 1842+68	280.64	68.157	1.05	1.44 ± 1.65	2.16 ± 1.11	$(1.45 \pm 0.81) \cdot 10^{45}$	Q	0.472
1908–201	PKS B1908-201	287.79	-20.115	1.19	1.12 ± 1.43	3.0 ± 1.39	$(1.07 \pm 0.54) \cdot 10^{46}$	Q	1.119
1920–211	OV -235	290.884	-21.076	1.64		$< 3.97^*$	$< 1.96 \cdot 10^{46}$	Q	1.136
1921–293	PKS B1921-293	291.213	-29.242	6.89	2.12 ± 0.4	9.3 ± 1.54	$(4.05 \pm 0.69) \cdot 10^{45}$	Q	0.3526
1923+210	PKS B1923+210	291.498	21.107	3.26	1.03 ± 0.64	5.7 ± 1.47		B	
2007+777	S5 2007+77	301.379	77.879	2.0		$< 2.78^*$	$< 9.6 \cdot 10^{44}$	B	0.342
2013+370	TXS 2013+370	303.87	37.183	9.89	2.17 ± 0.31	11.31 ± 1.41	$(4.5 \pm 0.56) \cdot 10^{46}$	Q	0.859
2023+335	B2 2023+33	306.295	33.717	4.87	1.55 ± 0.51	6.94 ± 1.44	$(8.94 \pm 1.92) \cdot 10^{44}$	Q	0.219

Table 4.3.1.: continued.

Name[a]	Common Name	RA[b]	Dec[b]	S/N[c]	Γ[d]	$F_{20-100\,\mathrm{keV}}$[e]	$L_{20-100\,\mathrm{keV}}$[f]	Type[g]	z[h]
2029+121	PKS 2029+121	307.979	12.328	1.25		$< 3.56^*$	$< 2.04 \cdot 10^{46}$	Q	1.213
2223+210	DA 580	336.409	21.302	3.06	1.65 ± 0.62	5.97 ± 1.55	$(1.12 \pm 0.29) \cdot 10^{47}$	Q	1.959
2234+282	CTD 135	339.094	28.483	1.07	1.83 ± 1.56	2.58 ± 1.26	$(6.83 \pm 3.42) \cdot 10^{45}$	B	0.79
2255–282	PKS 2255-282	344.525	-27.973	3.1	1.32 ± 0.71	5.83 ± 1.69	$(1.62 \pm 0.49) \cdot 10^{46}$	Q	0.927
2325+093	OZ 042	351.89	9.669	9.5	1.38 ± 0.29	14.36 ± 1.68	$(1.77 \pm 0.21) \cdot 10^{47}$	Q	1.841

Notes. (a) Name in IAU B1950 format, (b) Equatorial coordinates (J2000) in degrees, (c) *Swift*/BAT S/N, (d) Photon Index for 20 keV – 100 keV, (e) X-ray flux in $10^{-12}\mathrm{erg\,s^{-1}\,cm^{-2}}$ (* indicates fluxes calculated by assuming a photon index based on sub-sample of bright sources, (f) X-ray luminosity in $\mathrm{erg\,s^{-1}}$, (g) Optical classification (Véron-Cetty & Véron, 2003): Q: Flat Spectrum Radio Quasar, B: BL Lac, G: Radio Galaxy, U: Unidentified, (h) Redshift, taken from the MOJAVE webpage (http://www.physics.purdue.edu/astro/MOJAVE/)

Table 4.3.2.: Mean values and standard errors for the derived parameters of the BAT spectral analysis (20 keV – 100 keV) for the MOJAVE-1 and MOJAVE-1.5 samples.

Samples	M1	M1.5	M1.5e (M1.5 excl. M1)
S/N	7.25±1.69	6.36±1.29	3.72±1.07
F^a	$(14.91 \pm 3.57) \cdot 10^{-12}$	$(13.37 \pm 2.77) \cdot 10^{-12}$	$(8.49 \pm 2.16) \cdot 10^{-12}$
$\log L^b$	45.96 ± 0.12	45.97 ± 0.10	46.05 ± 0.21
Γ^c	1.58 ± 0.06	1.61 ± 0.05	1.67 ± 0.07

Notes. For the tests of flux and luminosity the upper-limit sources are excluded. (a) in 10^{-12}erg s^{-1} cm^{-2}, (b) in log erg s^{-1} (c) only fitted source spectra are included.

4.3.2. Comparison to the MOJAVE-1 sample

The spectral analysis of the BAT data of the M1.5 sample shows that the distribution of spectral parameters, such as flux and photon index, is very similar to the earlier M1 sample. In order to compare the S/N, flux, luminosity, and photon index distributions shown in Fig. 4.3.1 and 4.3.2 with the M1 sample, the mean values for the corresponding distributions of the M1, M1.5, and M1.5e samples are calculated, see Table 4.3.2. Furthermore, 2-sample KS tests are performed, whose results are presented in Table 4.3.3. No significant difference is found between any two distributions of the same quantity. While the resulting p-values are close to 1 when testing the M1 against the M1.5 sample, the test of the M1 against the M1.5e sample reveals lower values of $\approx 0.2 - 0.6$, but still no significant difference.

The S/N and flux distributions for both M1 and M1.5 samples are very much compatible with each other within the derived standard errors. The M1.5 sample is somewhat fainter on average than the M1 sample, as evidenced by the even lower mean S/N and flux values of the M1.5e sources. This is due to the relative lack of high-significance sources that have been added to form the M1.5 sample, that is, for the most part nearby radio galaxies and a small number of bright FSRQs in the original M1 sample. The mean values of the logarithmic luminosity are compatible between all samples. The distribution for the M1.5e sources is a little less broad compared to M1 and M1.5, which is probably due to the smaller sample size. Also, the mean photon indices are compatible with each other within the respective standard errors. Compared to M1, the M1.5e sources tend to have somewhat softer indices on average, with 1.67 ± 0.07.

In Sect. 4.2.3 the M1 blazar sub-sample's flux characteristic is analyzed using the $\log N$-$\log S$ distribution of both the hard X-ray fluxes (70 sources fitted) and the native radio flux densities (40 sources fitted). Both hard X-ray and radio $\log N$-$\log S$ distributions exhibit a significantly different shape and fitted power-law slope, with the X-ray slope being very flat at 1.13 ± 0.04, while the radio slope is comparatively steep at 1.74 ± 0.13 (for sources brighter than 2.5 Jy). The radio flux densities of M1 $\log N$-$\log S$ distribution is based on the VLBI measurements from Lister et al. (2013), who define the M1.5 AGN sample on the basis of uniform sky area coverage and a minimum flux density of 1.5 Jy during the observation time span.

A fit to the full M1.5 radio flux density $\log N$-$\log S$ distribution (170 sources fitted) reveals a power law slope of $1.72^{+0.11}_{-0.10}$ with a normalization of $(7.20^{+0.98}_{-0.84}) \cdot 10^{-3}\,\mathrm{deg}^{-2}$. Compared to the fitting results of the M1 sample (Table 4.2.1), this result is well compatible within the

Samples	M1 / M1.5	M1 / M1.5e
S/N	0.999	0.465
F	0.999	0.519
L	1.000	0.637
Γ	0.901	0.246

Table 4.3.3.: Two-sample KS test results (p-values) between M1, M1.5 / M1.5e X-ray parameter distributions for the S/N, flux F, luminosity L, and photon index Γ.

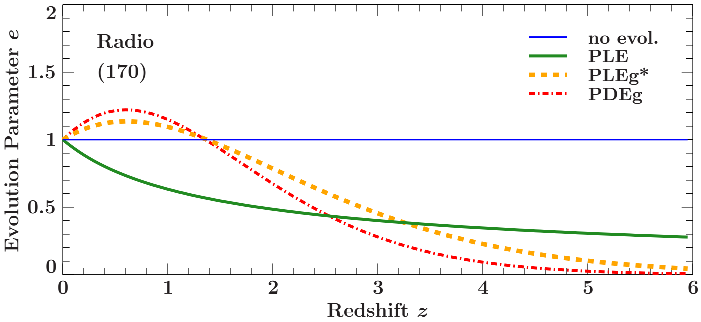

Figure 4.3.5.: Evolution parameter e against redshift for the MOJAVE-1.5 sample (see Table 4.3.4). A selection of fitted models is plotted, with the best fit models marked with an *.

$1\,\sigma$ error range. Also, the power-law fit of the $\log N$-$\log S$ distribution of the derived BAT fluxes (92 sources fitted) shows a normalization of $(9.22 \pm 0.45) \cdot 10^{-3}\,\mathrm{deg}^{-2}$ and a slope of 1.13 ± 0.04, which is equal to the fit performed for the M1 sample. Extending the analysis to the M1.5 sample revealed that the smaller M1 sample, albeit less consistent in terms of (radio flux) source selection, performs identically within the uncertainty ranges. Therefore, the initial approach of using the M1 sample for a case study of the hard X-ray characteristic of a statistically complete and well defined blazar sample is deemed justified.

In Sect. 4.2.5 the properties of flux evolution between the hard X-ray and radio bands are compared. Again, a fundamental difference between both emission regimes is shown. Switching from the M1 to the larger M1.5 sample shows that the basic evolution characteristic does not change significantly. All fitted RLF models are compatible with the parameters that are derived for the M1 sample (123 sources). Like before, the case of no evolution at all can be rejected. Interestingly, the model of pure density evolution PLDg is less likely than pure luminosity evolution PLEg. The model parameters of the fitted RLFs are presented in Table 4.3.4. A number of models including the most likely PLEg model are plotted in Fig. 4.3.5. The favored models show a maximum for the evolutionary parameter e of $z \approx 0.6$, which matches the results from the M1 sample in the radio band. Both the M1 and extended M1.5 samples show the same behavior in the 15 GHz radio band, which validates the initial use of the smaller M1 sample for the purpose of comparing the luminosity function between X-ray and radio band.

In conclusion, there is no evidence that the addition of the 46 sources of the larger M1.5 sample to the M1 blazar sample produces significantly different properties in terms of hard X-ray parameter distributions, that is, S/N, flux, luminosity, and photon index. Furthermore, the behavior of the M1 versus M1.5 sample in the hard X-ray and radio bands regarding flux and luminosity distribution with respect to redshift / evolution of emission is found to be well compatible with each other. The initial question, whether the somewhat inconsistent selection criteria of the M1 sample compromise the statistically complete nature of the sample for this analysis, can be denied.

Table 4.3.4.: Fitting results of the radio luminosity functions for the radio data of the M1.5 blazar sub-sample. The value p_j expresses the relative probability that the corresponding model also fits the data compared to the best fit. Sect. 3.6.3 introduces the fitting models and parameters.

LF Model	A $[10^{-10}\,\mathrm{Mpc}^{-3}]$	L_* $[\mathrm{erg\,s}^{-1}]$	γ_1	γ_2	k	g	p_j
Radio (170)							
PLEg	2.17	10^{34}	0.57 ± 0.06		0.48 ± 0.53	-0.35 ± 0.15	1.000
PDEg	2.21	10^{34}	0.57 ± 0.06		0.76 ± 0.83	-0.56 ± 0.24	0.368
PLE	3.97	10^{34}	0.53 ± 0.05		-0.66 ± 0.24		0.118
PDE	3.97	10^{34}	0.53 ± 0.05		-1.01 ± 0.34		0.118
no evol.	2.45	10^{34}	0.65 ± 0.03		0		0.004

4.4 Summary

In this chapter the hard X-ray properties of the well-defined and statistically complete MOJAVE-1 AGN sample are presented. The sample of 135 sources, as well its extended version, the MOJAVE-1.5 sample with 181 sources are composed of radio-loud and for the most part low-peaked blazars. The hard X-ray characteristics are derived for the 20 keV−100 keV band on the basis of the 105-month *Swift*/BAT all-sky survey maps. The main results of this study are listed in the following.

- Although the radio-selected MOJAVE-1 and MOJAVE-1.5 samples are characterized by mostly low S/N values in the hard X-ray band, a modeling of the S/N background component shows that the great majority of both samples is not compatible with random fluctuations, that is, 121 / 135 and 157 / 181 sources, respectively.

- The AGN sub-types of FSRQs, BL Lacs and radio galaxies occupy distinct ranges in the parameter spaces of the derived hard X-ray flux, luminosity, and photon index. Besides the AGN type and redshift, these spectral parameters can be associated with the specific SED and its position regarding the BAT range.

- The sub-sets of *Fermi*/LAT-detected and non-detected MOJAVE-1 blazars have significantly different distributions of the hard X-ray photon index. A major contributor against previous radio-based estimators for a future detection in the GeV regime is demonstrated to be the spectral position of the HE bump.

- The X-ray-brightest MOJAVE-1 sources are also registered in recent *INTEGRAL* all-sky surveys. The same relation is not present for the *Fermi*/LAT source catalogs. A detection in the GeV band is in this case dominated rather by the individual blazar's synchrotron peak frequency and / or source type.

- Compared to the radio data, the hard X-ray $\log N$-$\log S$ distribution shows a significantly flatter and clearly non-Euclidean slope ($\alpha = 1.13 \pm 0.04$). It can be concluded that the relative rarity of low-flux hard X-ray sources in the sample is likely due to different evolutionary paths in both energy bands, with a maximum X-ray evolution at $z \approx 1.5$.

- The contribution to the CXB in the BAT band from blazars of the MOJAVE-1 selection type is determined to be 0.2% – 0.3%. This fraction is approximately only 0.01 to 0.1 of the contribution derived in previous X-ray-selected blazar studies in the past, which strongly implies a different blazar population in this regard.

In conclusion, the MOJAVE-1 and the extended MOJAVE-1.5 samples of mainly low-peaked compact and beamed AGN give a unique perspective on the field of ongoing blazar research in the high-energy regime. Areas such as broadband SED modeling or the blazar sequence will benefit from the derived characteristics that the hard X-ray analysis from the BAT survey provides. Future projects, like the new deep X-ray survey using eROSITA will add greatly to issues regarding population synthesis and CXB composition. Because the modeling of an AGN's SED and especially its HE bump massively depends on the observational coverage in the complete X-ray regime, future studies will be crucial in finding target sources for observation campaigns with telescopes in the GeV and TeV domain, like, for example, the Cherenkov Telescope Array (CTA).

5. A comparative hard X-ray analysis of the TANAMI AGN sample

The previous Chpt. 4 details the analysis of the hard X-ray characteristics of the statistically complete and robust MOJAVE-1 and the extended MOJAVE-1.5 sample. The samples of jetted, beamed radio-loud AGN are mainly composed of low-, and to an extend, intermediate-peaked blazars. The coverage of the sky, however, is mostly limited to the Northern hemisphere with $\delta \geq -20°$ for the MOJAVE-1, and $\delta \geq -30°$ for the MOJAVE-1.5 sample, covering 64% and 75% of the sky, respectively. The TANAMI program (tracking active galactic nuclei with austral milliarcsecond interferometry, Ojha et al., 2010) aimed to close this gap of sky coverage for multiwavelength jet monitoring and VLBI imaging at 8.4 GHz and 22 GHz while including radio- and gamma-ray-bright sources as well as many special cases and neutrino candidates, counting 43 individual sources (see also Sect. 2.1.2). The radio sub-sample was based on the catalog of Stickel et al. (1994), including all sources (22) with $\delta < -30°$, a 5 GHz flux density of $S > 2$ Jy, and a flat spectrum ($\alpha > -0.5$, $S \sim \nu^{\alpha}$) in the band of $\nu = 2.7\,\mathrm{GHz} - 5\,\mathrm{GHz}$. In terms of completeness, this sub-sample is thought to be very comparable with the MOJAVE samples. The gamma-ray-bright sub-sample was first defined as all known blazars detected by EGRET in the same area of the sky. Furthermore, a number of intra-day-variable sources in the GeV band have been added, such as 0405–385, or 1144–373.

Müller et al. (2018) presented the VLBI images of an additional 39 sources, including eight sources from the study of multi-epoch blazar SEDs (Krauß et al., 2016), 28 sources from the study by Böck et al. (2016) of radio- and gamma-ray-bright extragalactic jets, and three more sources from the works of Nesci et al. (2011a,b) and Dutka et al. (2013). The TANAMI sample in the state as studied by Müller et al. (2018) comprised 88 sources, adding gamma-ray-bright sources with a radio counterpart, and a flux density of $S \geq 100$ mJy. The 22 gamma-ray-brightest sources in in terms of *Fermi*/LAT flux (Ackermann et al., 2015) were designated as the gamma-ray-bright sub-sample.

Since, a number of sources have been dropped from the increasing list of monitored TANAMI sources. This was due to an insufficient radio brightness, low variability, or the fact that the source could not be resolved in the VLBI observations. New sources have been added if they exhibited at least 100 mJy of radio flux density and were newly discovered or flaring sources in the GeV or TeV band below $\delta = -30°$. Also, neutrino candidate sources with the same radio flux criterion were included. As of 2020, the most recent list of monitored TANAMI sources in the sample is 126, consisting of 59 FSRQs, 28 BL Lacs, 18 radio galaxies, and 21 sources of unidentified type. The classification of all sources follows the 4FGL catalog (Abdollahi et al., 2020), and Véron-Cetty & Véron (2010) if no 4FGL classification was available. The list is maintained by the TANAMI collaboration. In this study, the most recent version of the sample with 126 sources is analyzed.

In the following, the original radio sub-sample (Ojha et al., 2010; Müller et al., 2018) and the newer *Fermi*/LAT-detected gamma-ray-bright (3LAC) sub-sample (Müller et al., 2018) are also compared to the main sample. They are designated M18R and M18G, respectively. In a recent study, Angioni et al. (2019) presented the analysis of the evolution of parsec-scale radio emission of TANAMI radio galaxies and the corresponding relation to their gamma-ray properties. Here, it is assessed to what extend the hard X-ray characteristics of this sub-sample, designated A19, differ from the typical blazar populations from the other sub-samples.

Performing the X-ray analysis of the BAT survey data for the Southern hemisphere not only provides a more complete picture of the hard X-ray characteristics of the radio-loudest low-peaked blazars, but also for a number of VHE-detected and high-peaked sources (mostly BL Lacs). The general hard X-ray properties derived from the *Swift*/BAT 105-month all-sky survey are presented in Sect. 5.1. Since the TANAMI sample is the subject of recent and ongoing studies (e.g., Krauß et al., 2018b; Angioni et al., 2019; Lucchini et al., 2019), and it is extended perpetually, the issue of sample completeness needs to be addressed. Not only in the radio band, but especially in the high-energy regime. In Sect. 5.2, the hard X-ray emission profile of the sample is compared to the reference samples MOJAVE-1 and MOJAVE-1.5 in terms of completeness. Also, it is analyzed whether the TANAMI sample is suited as a robust basis for blazar studies in the hard X-ray band, although it is not as statistically complete as the MOJAVE samples by definition.

5.1 General properties

In this section the results of the hard X-ray analysis of the TANAMI source sample are presented. The following Sect. 5.1.1 includes the characteristics derived from the *Swift*/BAT 105-month survey maps, analogously to the MOJAVE-1 sample in Sect. 4.1. Previous detections of the TANAMI sources in other high-energy source catalogs are discussed in Sect. 5.1.2. The results of the hard X-ray analysis of the TANAMI sources are also listed in Table 5.1.1.

5.1.1. Hard X-ray characteristics

From all 126 sources in the TANAMI sample, flux values and 90% uncertainty ranges for 42 sources can be calculated, and only upper-limit values for the remaining 84 sources. Approximately 39% of both FSRQs and radio galaxies are non-upper-limit sources within their respective sub-samples. BL Lacs feature a fraction of 29%, and unidentified types are around 19%.

The hard X-ray S/N distribution of the entire sample is presented in Fig. 5.1.1, omitting the brightest sources, the radio galaxies 1322–428 (Centaurus A) at S/N $= 607\,\sigma$ and 1409–651 (Circinus) at S/N $= 146\,\sigma$. The vast majority of the sample (116 sources) has S/N values less than $10\,\sigma$, 108 sources are below the BAT catalog threshold of $4.8\,\sigma$. Below the significance of S/N $\approx 3\,\sigma$ the fraction of sources with upper-limit flux values increases rapidly. Throughout the extend of the S/N characteristic the different sub-types are distributed rather evenly, with all types present at the high- as well as the low-significance regions. In order to discuss the specific distribution of the different sub-types in terms of brightness, the flux, which incorporates properly derived upper-limit values, is deemed more suited than the signal-to-noise ratio (see below).

Figure 5.1.2 again shows the S/N characteristic of the TANAMI sample. Following the methodology from Sect. 3.2.3 and analogous to the MOJAVE samples (Sect. 4.1.2, 4.3.1),

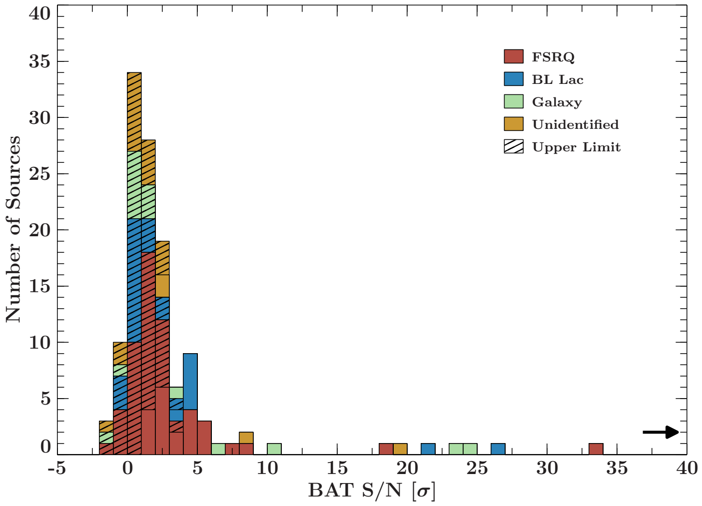

Figure 5.1.1.: Distribution of S/N values of the TANAMI sample in the Crab-weighted 14 keV–150 keV band. The black arrow indicates a truncated axis for better readability. The radio galaxies 1409–651 at 146 σ and 1322–428 (Centaurus A) at 607 σ are not shown.

a Gaussian component is fitted to the negative S/N histogram. The bottom panel of the figure shows the distribution of the background-subtracted S/N characteristic, indicating the fraction of the sample that is not compatible with random fluctuation in the survey maps, which amounts to 79.54% (68.25% – 85.75%), equal to approximately 100 (86 – 108) sources.

The distributions of the hard X-ray flux (20 keV–100 keV) for the entire TANAMI sample and the corresponding sub-samples from Müller et al. (2018) and Angioni et al. (2019) are displayed in Fig. 5.1.3, left panel. Similar to the S/N characteristic, most fluxes are located at the lower end of the distribution, in the range of approximately $(2-5)\cdot10^{-12}\mathrm{erg\,s^{-1}\,cm^{-2}}$. This accumulation of sources in the lower flux bins mainly stems from the upper-limit values, which are typically distributed in this range for BAT spectra that have one or more channels with a negative count rate. The flux values excluding upper limits peak around $5\cdot10^{-12}\,\mathrm{erg\,s^{-1}\,cm^{-2}}$. A 2-sample KS test regarding the different sub-types in the TANAMI sample revealed that only FSRQs and radio galaxies most certainly do not share the same parent distribution when the upper limits are ignored ($p = 9\cdot10^{-4}$). Compared to radio galaxies the majority of the FSRQs are distributed at the lower flux end. Excluding the brightest two sources, which are both radio galaxies, in order to test the influence of these extreme cases, produces a similarly significant result ($p = 6\cdot10^{-3}$). The A19 sub-sample, which consists for the most part of radio galaxies, also shows a significantly different flux distribution (ignoring upper limits) when compared to the complete TANAMI sample ($p = 0.012$), the M18R sub-sample ($p = 0.024$), and the M18G sub-sample ($p = 0.003$). Also, the results remain highly significant if the two brightest sources are removed.

A similar distinctiveness between the AGN types and sub-samples can be observed for the hard X-ray photon index. Figure. 5.1.3, right panel, shows the corresponding distributions for all sources whose spectra were fit (36 for the main TANAMI sample). FSRQ photon indices range from 0.69 ± 0.86 (0920–397) to 2.17 ± 1.74 (0252–549). Former source has an extremely hard spectrum while being moderately faint (S/N = 3.16). The hard photon index likely indicates the steepest part of the rising HE bump, which coincides with the BAT energy band at around 10^{19} Hz. BL Lacs show a more narrow distribution, from 1.02 ± 0.71 (0537–441) to 2.08 ± 0.15 (0548–322). The sub-set of unidentified sources is similarly narrow. The distribution of the radio galaxies shows a majority of sources around a photon index of 2, while the outlier 1814–637 at 1.11 ± 0.48 represents an unusually hard spectrum for a radio galaxy. Although the SED of radio galaxies feature a not very pronounced HE bump, if any,

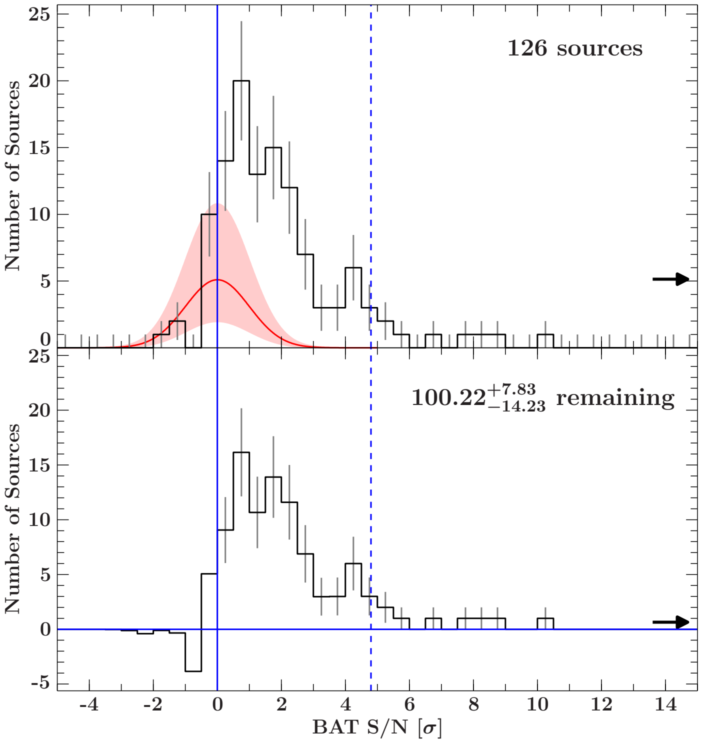

Figure 5.1.2.: Top panel: S/N distribution of the TANAMI source sample, truncated at 15 σ. The fit of a Gaussian curve to the negative side of the distribution with center of 0 σ and width of 1 σ is indicated by the red line. The 3 σ uncertainty range of the fit is shown by the red shaded area. Bottom panel: histogram after the subtraction of the original S/N distribution from the fit curve. The resulting number of remaining sources is given in the plot, summing all histogram bins larger than 0 σ. The dashed line indicates the BAT catalog threshold of 4.8 σ.

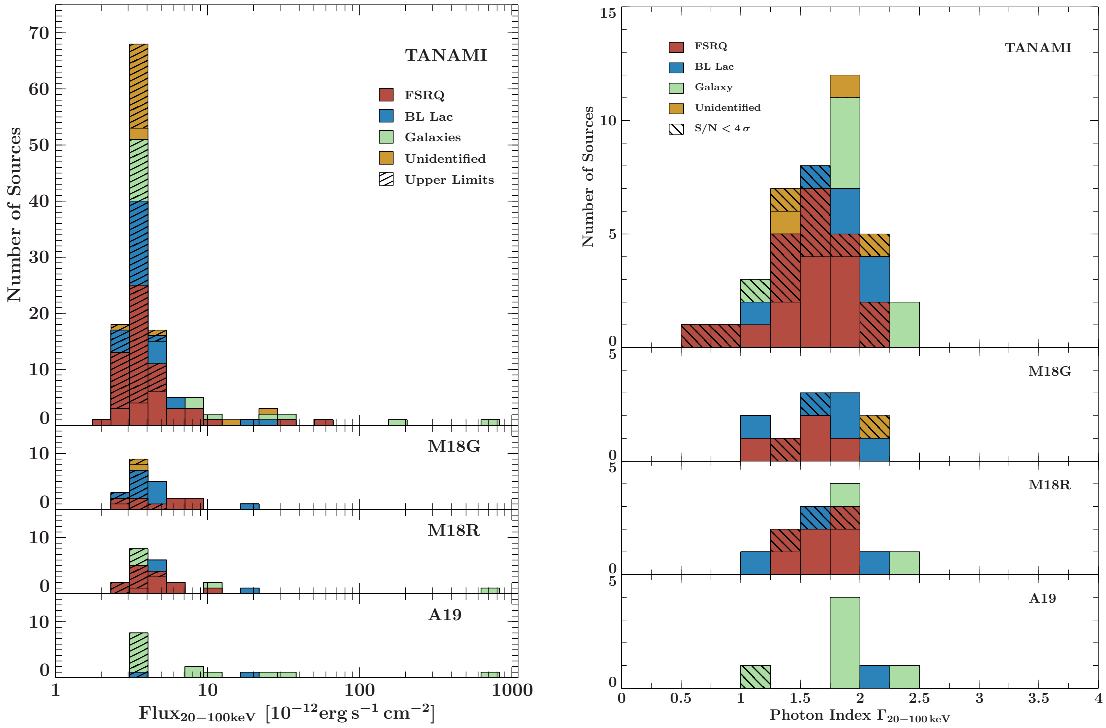

Figure 5.1.3.: Left: distribution of the hard X-ray flux (20 keV–100 keV) for the TANAMI sample and the sub-samples from Müller et al. (2018) and Angioni et al. (2019) (see text), right: distribution of the hard X-ray photon index. The hatched area indicates low S/N sources (S/N < 4 σ).

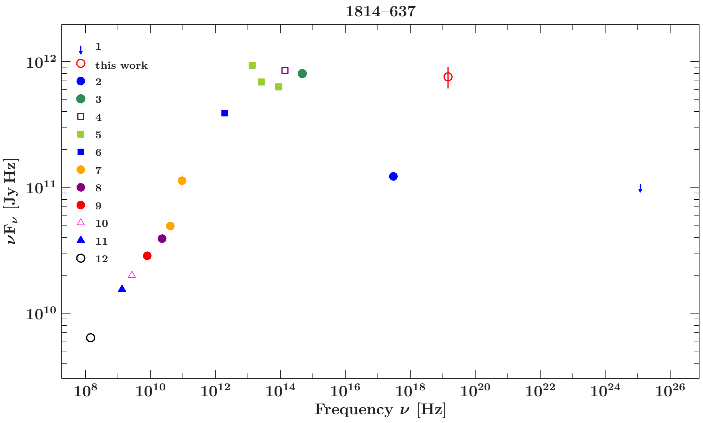

Figure 5.1.4.: SED of the TANAMI radio galaxy 1814–637. The SED has been compiled using non-simultaneous data from: [1]Angioni et al. (2020), [2]Maselli et al. (2010b), [3]Ramos Almeida et al. (2011), [4]Inskip et al. (2010), [5]Cutri et al. (2013), [6]Dicken et al. (2008), [7]Wright et al. (2009), [8]Gold et al. (2011), [9]Murphy et al. (2010), [10]Wright & Otrupcek (1990), [11]Morganti et al. (2011a), [12]Jacobs et al. (2011).

this result points towards the measurement of the rising part of the HE bump in the hard X-ray band, while the vast majority of this source type coincides with the flat peak region of the HE emission component. Figure 5.1.4 shows the SED of the source using archival data, which supports this assumption. While the synchrotron bump reaches the soft X-ray regime, the HE component rises around $(10^{18} - 10^{19})$ Hz.

The photon index distributions of the main TANAMI sample and the different sub-samples do not show any substantial difference. Although a possible difference of radio-loud (tentatively low-peaked) and gamma-ray-bright (high-peaked) sources could be visible in the spectral slope of the SEDs, no such trend is evident from the BAT data. Both the M18G and M18R sub-samples share seven sources. Even when excluding these sources in both sub-samples a KS test does not indicate different distributions ($p = 0.780$). Also, it could be argued that the gamma-ray-bright sources, which are generally more compact and have higher Doppler factors compared to gamma-ray-faint ones, also exhibit a measurable difference in flux, not only in the gamma-ray band, but also at hard X-rays. However, no such tendency is present between both sub-sets: a KS test for flux non-upper-limits of the M18G sub-sample and the rest of the main TANAMI sample reveals a p-value of 0.59. In terms of flux and spectral shape the gamma-bright sources in the TANAMI sample do not show any sign of distinctive behavior in the BAT data. Even the standard deviation is nearly identical, that is, 0.41 for the TANAMI sample without the M18G sources and 0.40 for the M18G sub-sample. This result, however, can also be distorted by the large uncertainty ranges of flux and photon index as well as the fact that only a small part of the entire TANAMI sample could be analyzed because of the low signal quality of many sources.

Figure 5.1.5 shows the distribution of the hard X-ray luminosity in the 20 keV to 100 keV band of the main TANAMI sample. All sub-types occupy distinct ranges in luminosity. The brightest type by far is the group of FSRQs with up to $1.26 \cdot 10^{48}\,\mathrm{erg\,s^{-1}}$ (2149–306), followed by BL Lacs with the most luminous source at $4.19 \cdot 10^{46}\,\mathrm{erg\,s^{-1}}$ (0332–403). The radio galaxies are located over a wide range on the lower end of the distribution, with the most luminous one at $6.44 \cdot 10^{44}\,\mathrm{erg\,s^{-1}}$ (1549–790). The upper-limit values of all types generally follow the distributions of the non-upper-limits, whereas the low-luminosity tail ends of all distributions are almost exclusively occupied by upper-limit sources, which, for the most part, are characterized by very slow signal strength (S/N $\approx 0\,\sigma - 2\,\sigma$) and below average redshifts ($z \approx 0.5$ for FSRQs and $z \approx 0.1$ for BL Lacs). A KS test between the source types, excluding upper limits, reveals that FSRQs, BL Lacs, and radio galaxies all have significantly distinctive distributions compared to each other (FSRQ - BL Lac: $p = 0.01$, FSRQ - radio

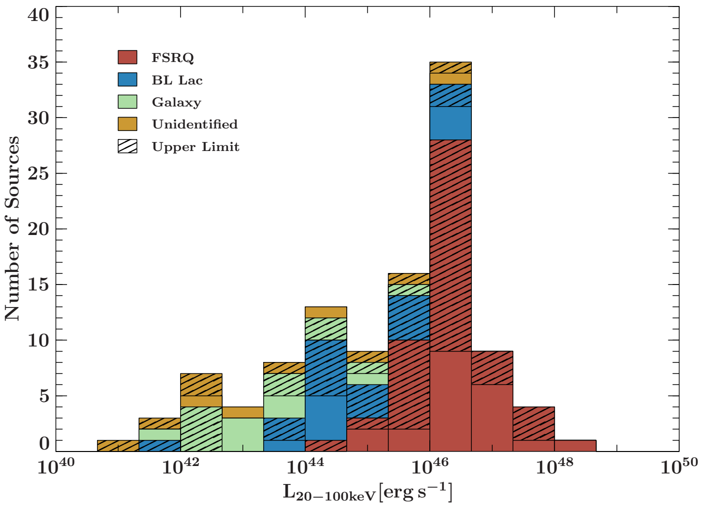

Figure 5.1.5.: Distribution of luminosity values of the TANAMI sample in the 20 keV–100 keV band.

galaxy: $p = 1.7 \cdot 10^{-6}$, BL Lac - radio galaxy: $p = 4.7 \cdot 10^{-3}$). The low number of four sources with unidentified type seem to be differently distributed than FSRQs ($p = 0.022$). However, because of the low source number the result lacks significance. Also, excluding the source with the lowest luminosity (2206–474) from the test leads to a even less significant result ($p = 0.13$). In any case, since the unidentified sources cover a large range of luminosities, it is possible to formulate at least qualitative statements about the probability which source type they belong to. Unidentified sources below approximately $10^{43}\,\mathrm{erg\,s^{-1}}$, of which many are upper limits, are most likely not FSRQs. Taking the hard X-ray luminosity as a proxy, it is thus suggested, that these sources (0131–522, 0958–314, 1521–300, 2206–474, 2254–367) are either BL Lac type objects or radio galaxies. All five sources have redshift values between 0.005 and 0.02, which is much more compatible with the radio galaxies ($z_{\mathrm{G}}^{\mathrm{median}} = 0.035$) than the BL Lacs ($z_{\mathrm{B}}^{\mathrm{median}} = 0.223$). The only source in this small sub-set for which a photon index could be derived is the source 2206–474 with $\Gamma = 1.9 \pm 0.18$. The (weighted) mean photon index of radio galaxies and BL Lacs in the sample is $\Gamma_{\mathrm{G}} = 1.86 \pm 0.17$ and $\Gamma_{\mathrm{B}} = 1.57 \pm 0.14$, respectively. This result therefore also suggests a classification of 2206–474 as a radio galaxy, which generally falls in line with previous studies. Earlier works classified the source as a Sy1 galaxy (Phillips, 1979), while later studies put forward a classification as a LINER (e.g., Starling et al., 2005). The most luminous source of unidentified type in the sample is 1505–496 with $(2.42 \pm 0.30) \cdot 10^{46}\,\mathrm{erg\,s^{-1}}$, which likely belongs to the FSRQ class. This is also suggested by its high flux of $(13.18 \pm 1.54) \cdot 10^{-12}\,\mathrm{erg\,s^{-1}\,cm^{-2}}$ and redshift of 0.776 (see also Fig. 5.1.6). A possible classification of the other unidentified type sources using BAT luminosity values becomes more difficult because of the shared luminosity range with all other source types.

A 2-sample KS test between FSRQs and radio galaxies reveals that a common parent distribution of photon indices can be rejected ($p = 0.018$). In a previous study of a large number of beamed AGN and their broadband SED shapes, Meyer et al. (2011) found that the difference of (synchrotron) peak frequencies and peak luminosities for these sources can be associated with a difference of alignment of the jet axis to the line of sight. Thereafter, radio galaxies are only found at low peak luminosities and low peak frequencies, whereas FSRQs produce generally larger luminosites at the peak frequency and BL Lacs a wide range of peak frequencies at moderate luminosities. While the misaligned radio galaxies are characterized by high inclination angles and low amounts of relativistic beaming, the

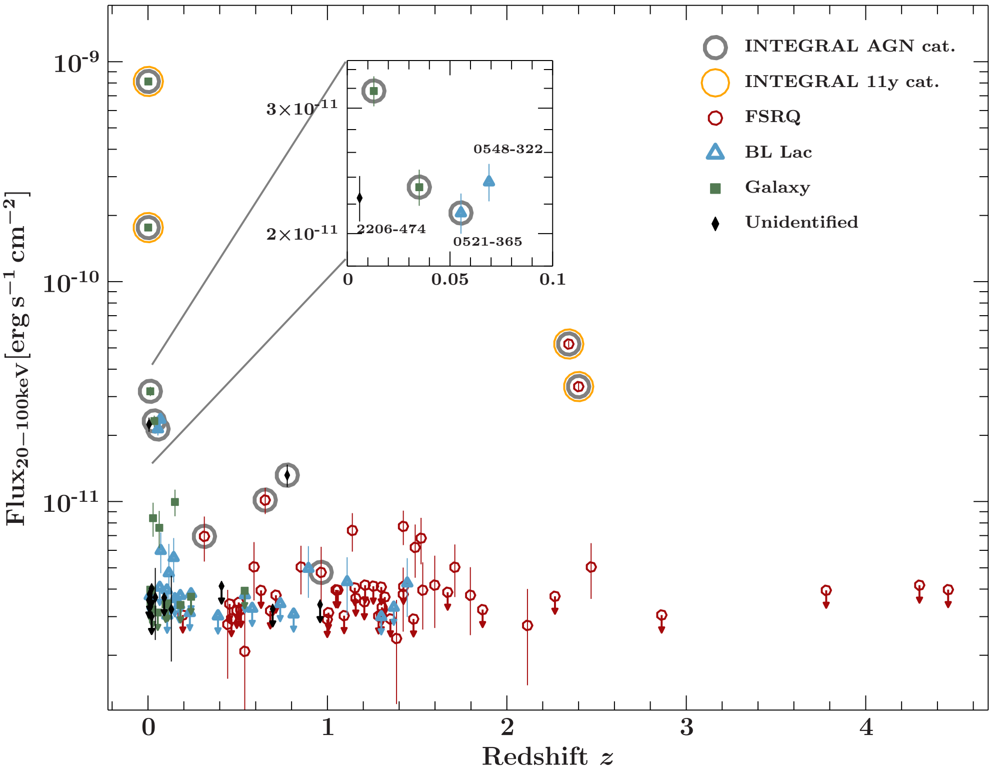

Figure 5.1.6.: Hard X-ray flux plotted against redshift. All sources with a corresponding entry in the *INTEGRAL* 9-year AGN catalog and *INTEGRAL* 11-year survey catalog are marked.

highly beamed blazars have low inclination angles. The distribution of photon indices that are presented in this chapter confirms the results for the MOJAVE sources (Sect. 4). Also, the overall picture supports the general concept that has been suggested by Meyer et al. (2011): lower luminosity radio galaxies have lower SED peak frequencies and, therefore, the BAT band coincides with the flat HE peak region of the SED ($\Gamma \approx 2$). In case of the higher peaked blazar SEDs, the rising part of the HE component is measured ($\Gamma \approx 1-2$). It is reasonable to assume that part of the total hard X-ray flux that is observed originates from the relativistically boosted jet as well as the corona of hot electrons near the accretion disk. Thus, the hard X-ray emission of radio galaxies must originate from the corona, but must also have a non-negligible contribution from the jet itself.

5.1.2. Common sources with other high-energy catalogs

Since the TANAMI sample has been compiled to include radio- and gamma-ray-bright AGN as well as a number of interesting special cases like neutrino candidates or sources with high variability, the cross section with other high-energy catalogs can be expected to follow the properties of the MOJAVE samples. In the following, the TANAMI sample's overlap with the high energy survey catalogs of *Swift*/BAT, *INTEGRAL*/IBIS and *Fermi*/LAT is presented. A short introduction to the catalogs is already given in Sect. 4.1.1.

Of the 126 sources in the main TANAMI sample only 17 are listed in the 105-month BAT catalog, with most of them having an extracted S/N value higher than the catalog threshold of $4.8\,\sigma$. The catalog source with the lowest S/N value in the data set extracted in this work is the BL Lac 0537–441 with $4.26\,\sigma$. The BAT catalog lists the sources at $5.15\,\sigma$, which is likely due to slightly offset extraction centers, since the extraction position in this work is taken from the source samples, in this case the TANAMI radio source coordinates. Figures 5.1.6 and 5.1.7 show the graph of the hard X-ray flux of the TANAMI sample versus redshift z, with the counterparts in the *INTEGRAL* and *Fermi*/LAT catalogs marked, respectively. In the analysis of the counterpart statistic of the MOJAVE-1 sample (Sect. 4.2.1) the X-ray flux and radio flux density are used. Because no reliable long-term radio flux densities at one single frequency for all TANAMI sources are yet available, the graph of X-ray flux against redshift is used instead in order to gauge the influence of source distance, and therefore the shift of the SED shape to lower energies, on the source detection.

The sources, which are brightest in the BAT band, are generally more likely to also be listed in the *INTEGRAL* survey catalogs, as shown in Fig. 5.1.6. There is a number of notable outliers, however, whose occurrence can be understood by addressing the rather inhomogeneous distribution of the accumulated exposure until the end of AO10[1], marking the time of the catalog's release. The source with the lowest BAT flux, which is still listed in the *INTEGRAL* AGN catalog, is the FSRQ 1933–400 (S/N $= 2.9\,\sigma$, $F_{20-100\,\mathrm{keV}} = 4.76 \cdot 10^{-12}\,\mathrm{erg\,s^{-1}\,cm^{-2}}$). Although a few FSRQs and BL Lacs around the same flux are not registered in any *INTEGRAL*/IBIS survey, this source is. This could either be the case because of long-term variability, or the fact that the source is located in a part of the sky which is characterized by a relatively high accumulated exposure time ($\approx 3.3\,\mathrm{Ms}$, AO10) in the survey, near the Galactic center. A more peculiar case is given by a group of sources at very low redshift ($z = 0 - 0.07$) that are also moderately bright in the BAT band ($(2-3.5) \cdot 10^{-11}\,\mathrm{erg\,s^{-1}\,cm^{-2}}$). While the two radio galaxies and the BL Lac 0521–365 in that group are listed in the *INTEGRAL* AGN catalog, the BL Lac 0548–322 and the source of unidentified type 2206–474 are not (see zoomed panel in Fig. 5.1.6). The photon index of 0548–322 in the BAT band is relatively soft (2.08 ± 0.15) while the *INTEGRAL* survey's exposure time is low ($\approx 1\,\mathrm{Ms}$, AO10) compared to many other areas of the sky in the survey. However, 0521–365 is very much similar in BAT photon index (2.06 ± 0.16) and flux, as well as in the *INTEGRAL* exposure time. Although these parameters would highly suggest that both sources have been listed in the *INTEGRAL* survey paper (Malizia et al., 2012), the catalog was limited only to AGN with secure optical identification and a precise measurement of the spectrum as well as already known soft X-ray characteristics. Additionally, it can be argued that the true spectral slope in the *INTEGRAL* observation phases was fairly soft, making a detection less likely. The BL Lac 0548–322 has been classified previously as an extreme blazar, meaning an extremely high synchrotron emission peak, as evidenced by hard photon indices in the soft X-ray band (Costamante et al., 2001; Biteau et al., 2020) and the fact that it is a hard TeV source (see, e.g., Costamante, 2020). This is supported by the broadband SED of the source (e.g., Tavecchio et al., 2011; Perri et al., 2007), showing the soft and hard X-ray bands covering the flat peak region of the SED's synchrotron bump.

The relatively bright source 2206–474 (unidentified type) is only listed in the BAT survey catalog. As established in Sect. 5.1.1, a possible and likely classification from the hard X-ray spectral slope is that of a radio galaxy. This matches the circumstance of no available gamma-ray data for this source, meaning no *Fermi*/LAT catalog counterparts. Other radio galaxies in the TANAMI sample, that are fainter than $F \approx 10^{-11}\,\mathrm{erg\,s^{-1}\,cm^{-2}}$ in the BAT band also

---

[1] `https://www.cosmos.esa.int/web/integral/exposure`

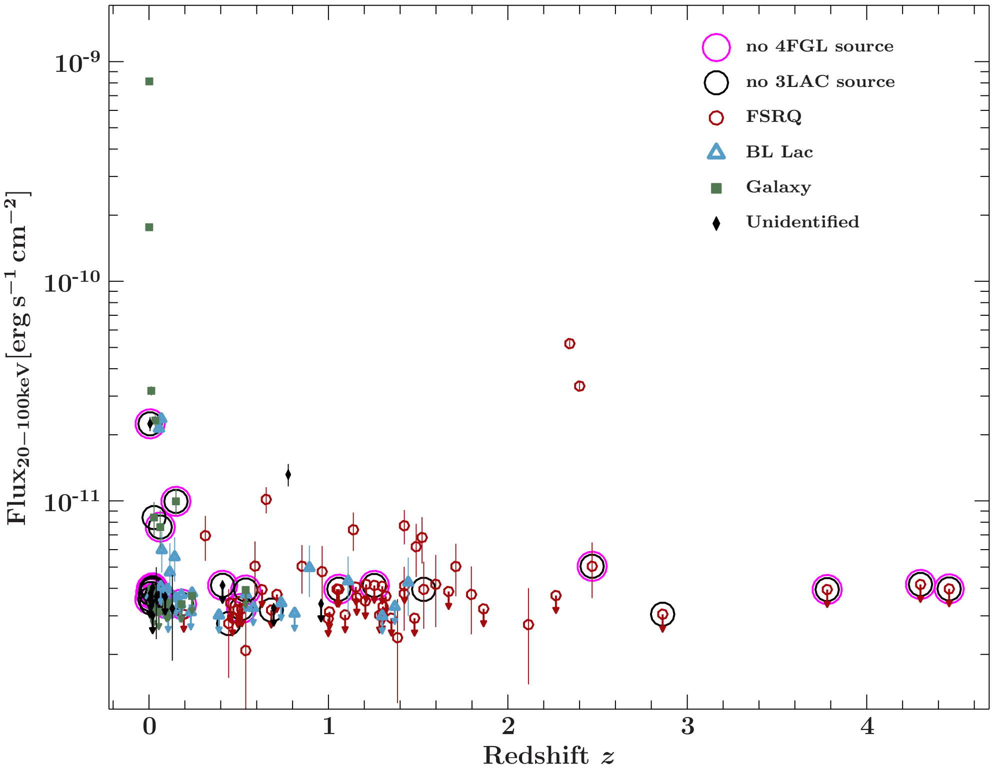

Figure 5.1.7.: Hard X-ray flux plotted against redshift. All sources which do not have a corresponding entry in the 3LAC or 4FGL catalogs are marked. Note the different convention compared to Fig. 5.1.6 for better readability.

do not have a gamma-ray counterpart (see Fig. 5.1.7). In any case, the non-detection by *INTEGRAL*, again, is likely due to a particularly low exposure time of 0.25 Ms.

The detection characteristic of the TANAMI sample is notably different in the gamma-ray band compared to the hard X-rays. Of all 126 sources in the sample 101 are listed in the 4FGL catalog, and 93 in the previous 3FGL catalog. One source is only listed in the 2FGL catalog but not in later editions: 1114–483 (2FGL J1117.2–4844). Higher peaked sources tend to be detected by *Fermi*/LAT and even TeV instruments. In the original 43-source TANAMI sample (Ojha et al., 2010) twelve TeV sources are present, all of which are high-frequency-peaked BL Lacs such as 2005–489 or 2155–304 ($\nu_{\mathrm{synch}}^{\mathrm{peak}} \approx 10^{16}$ Hz), with the exception of the radio galaxies 0625–354 and 1322–428 (Centaurus A).

Generally, the X-ray-brightest sources in the sample are also gamma-ray-bright with the exception of a number of radio galaxies. Because of the typically large inclination angles of jet axis and line of sight, the Doppler-boosted jet emission in radio galaxies is low compared to blazars, that dominate the gamma-ray sky. In addition, all sources with redshifts larger than $z \approx 2.4$ are not listed in the 3FGL catalog, and also the 4FGL catalog with the exception of the FSRQ 0438–436. The specific issue of the redshift distribution of FSRQs in the *Fermi* source catalogs has been addressed in a number of previous studies. The most recent *Fermi*/LAT AGN catalog (4LAC, Ajello et al., 2020) reveals a broad redshift distribution for FSRQs around $z = 1$, which corroborates an earlier study by Ajello et al. (2012b) that showed a modeled number density of FSRQs with its maximum in the range of $z = 0.5 - 2$ and a significant decline for higher values. A different cause of the scarcity of high-redshift blazars above $E \approx 10\,\mathrm{GeV}$ has been put forward to be the redshift-dependent attenuation of gamma-rays through the extragalactic background light (EBL) in the IR to UV range (e.g., Abdo et al., 2010c) Also, most FSRQs are low-peaked-type blazars, already shifting the broadband SED away from the gamma-ray range towards lower energies; an effect that is exacerbated by a high redshift. Objects at low to moderately high redshifts at the lower X-ray flux end also tend to be gamma-ray-faint (20 FSRQs, radio galaxies and unidentified sources with redshift information), while all BL Lacs with redshift information are gamma-ray-bright.

A peculiar case is given by the radio galaxy 1814–637, which is not listed in any of the previously mentioned high-energy source catalogs, and is also characterized by a very hard photon index of 1.11 ± 0.48 in the BAT band (see Sect. 5.1.1). However, the source is too faint for the BAT survey catalog ($\mathrm{S/N} = 3.91\,\sigma$) and likely for the *INTEGRAL* surveys as well. The non-detection in the GeV regime can be attributed to a low Doppler factor / large inclination angle, typical for radio galaxies, and, hence, a low boosting of the high-energy emission of the jet. In a study based on optical data, Morganti et al. (2011b) have found that the source is indeed viewed nearly edge-on to the line of sight. Also, the authors argue that the source is unusually bright in the radio compared to other wavelengths, which has been attributed to the interaction of the jet with a dense ISM, as well as potentially an atypically powerful jet and high black hole mass for its source class.

Table 5.1.1.: Results of the spectral hard X-ray analysis of the TANAMI sample in the 20 keV–100 keV band.

Name^a	Common Name	RA^b	Dec^b	S/N^c	Γ^d	$F_{20-100\,\mathrm{keV}}{}^e$	$L_{20-100\,\mathrm{keV}}{}^f$	Type^g	z^h	Detections^i
0007–325	IC 1531	2.398	-32.277	1.78		$< 3.23^*$	$< 4.55 \cdot 10^{42}$	G	0.025^{1}	F_3 F_4
0010–401	PKS 0010-401	3.25	-39.907	-0.05		$< 3.29^*$		B		
0027–426	PKS 0027-426	7.573	-42.413	2.19		$< 3.2^*$	$< 2.46 \cdot 10^{45}$	Q	0.495^{2}	F_3 F_4
0047–579	[HB89] 0047-579	12.498	-57.641	3.93	1.89 ± 0.91	3.75 ± 1.28	$(7.41 \pm 2.54) \cdot 10^{46}$	Q	1.8^{3}	F_3 F_4
0055–328	PKS 0055-328	14.509	-32.572	-0.27		$< 3.3^*$	$< 2.6 \cdot 10^{46}$	B	1.37^{4}	F_3 F_4
0131–522	PKS 0131-522	23.274	-52.001	0.32		$< 3.0^*$	$< 2.69 \cdot 10^{42}$	U	0.02^{2}	F_3 F_4
0208–512	[HB89] 0208-512	32.693	-51.017	1.5		$< 2.91^*$	$< 1.08 \cdot 10^{46}$	Q	0.999^{5}	F_3 F_4
0226–559	PKS 0226-559	37.09	-55.768	-0.3		$< 2.89^*$		Q		
0227–369	PKS 0227-369	37.369	-36.732	1.76	0.94 ± 1.46	2.73 ± 1.27	$(2.71 \pm 1.37) \cdot 10^{46}$	Q	2.115^{6}	F_3 F_4
0235–618	PKS 0235-618	39.222	-61.604	1.12		$< 2.93^*$	$< 1.96 \cdot 10^{45}$	Q	0.465^{7}	F_3 F_4
0236–314	1RXS J023832.6-311658	39.635	-31.283	1.99		$< 3.12^*$	$< 4.57 \cdot 10^{44}$	B	0.233^{8}	F_3 F_4
0244–470	PKS 0244-470	41.5	-46.855	1.31	1.32 ± 1.57	2.38 ± 1.18	$(1.54 \pm 0.8) \cdot 10^{46}$	Q	1.385^{9}	F_3 F_4
0252–549	PKS 0252-549	43.372	-54.698	1.21	2.17 ± 1.74	2.08 ± 1.09	$(2.58 \pm 1.38) \cdot 10^{45}$	Q	0.539^{2}	F_3 F_4
0302–623	PKS 0302-623	45.961	-62.19	2.29		$< 2.93^*$	$< 2.12 \cdot 10^{46}$	Q	1.351^{7}	F_3 F_4
0308–611	PKS 0308-611	47.484	-60.978	1.01		$< 2.92^*$	$< 2.59 \cdot 10^{46}$	Q	1.48^{7}	F_3 F_4
0332–376	PMN J0334-3725	53.564	-37.429	2.8		$< 3.01^*$	$< 1.39 \cdot 10^{45}$	B	0.39^{8}	F_3 F_4
0332–403	[HB89] 0332-403	53.557	-40.14	3.77	1.69 ± 0.78	4.26 ± 1.27	$(4.19 \pm 1.26) \cdot 10^{46}$	B	1.445^{11}	F_3 F_4
0402–362	PKS 0402-362	60.974	-36.084	7.73	1.75 ± 0.43	7.72 ± 1.37	$(7.76 \pm 1.39) \cdot 10^{46}$	Q	1.422838^{12}	B F_3 F_4
0405–385	[HB89] 0405-385	61.746	-38.441	1.63		$< 3.02^*$	$< 1.96 \cdot 10^{46}$	Q	1.28^{3}	F_3 F_4
0426–380	PKS 0426-380	67.168	-37.939	4.5	1.98 ± 0.76	4.31 ± 1.27	$(2.88 \pm 0.85) \cdot 10^{46}$	B	1.11^{13}	B F_3 F_4
0438–436	[HB89] 0438-436	70.072	-43.553	2.58		$< 3.05^*$	$< 1.09 \cdot 10^{47}$	Q	2.863^{14}	F_4
0447–439	PKS 0447-439	72.353	-43.836	0.99		$< 3.04^*$	$< 8.53 \cdot 10^{43}$	B	0.107^{15}	F_3 F_4
0454–463	[HB89] 0454-463	73.962	-46.266	4.46	1.99 ± 0.63	5.04 ± 1.26	$(1.77 \pm 0.45) \cdot 10^{46}$	Q	0.8528^{16}	F_3 F_4
0454–810	PKS 0454-81	72.523	-81.017	1.85	2.04 ± 1.34	2.77 ± 1.2	$(2.03 \pm 0.91) \cdot 10^{45}$	Q	0.444^{2}	F_4
0506–612	[HB89] 0506-612	76.683	-61.161	2.1		$< 3.03^*$	$< 1.38 \cdot 10^{46}$	Q	1.093^{11}	F_3 F_4
0514–459	PKS 0514-459	78.939	-45.945	1.8		$< 3.05^*$	$< 3.0 \cdot 10^{44}$	Q	0.194^{2}	F_3 F_4
0516–621	PKS 0516-621	79.187	-62.118	0.89		$< 2.99^*$	$< 2.1 \cdot 10^{46}$	B	1.3^{9}	F_3 F_4
0518–458	PICTOR A	79.957	-45.779	23.98	1.97 ± 0.14	23.24 ± 1.36	$(6.6 \pm 0.39) \cdot 10^{43}$	G	0.035058^{17}	B I_A F_3 F_4
0521–365	ESO 362- G 021	80.742	-36.459	21.39	2.06 ± 0.16	21.38 ± 1.39	$(1.56 \pm 0.1) \cdot 10^{44}$	B	0.056546^{12}	B I_A F_3 F_4
0524–485	PKS 0524-485	81.569	-48.51	-1.05		$< 3.06^*$	$< 2.04 \cdot 10^{46}$	Q	1.3^{9}	F_3 F_4
0530–485	PMN J0531-4827	82.994	-48.46	0.24		$< 3.08^*$	$< 7.19 \cdot 10^{45}$	B	0.8116^{18}	F_3 F_4
0534–340	PKS 0534-340	84.118	-34.02	3.02		$< 3.18^*$	$< 5.03 \cdot 10^{45}$	Q	0.682^{2}	F_4
0537–441	[HB89] 0537-441	84.71	-44.086	4.26	1.02 ± 0.71	4.96 ± 1.31	$(1.05 \pm 0.31) \cdot 10^{46}$	B	0.892^{19}	B F_3 F_4
0548–322	PKS 0548-322	87.669	-32.271	26.13	2.08 ± 0.15	23.63 ± 1.43	$(2.75 \pm 0.17) \cdot 10^{44}$	B	0.069^{20}	B F_3 F_4
0625–354	PKS 0625-35	96.778	-35.488	1.07		$< 3.13^*$	$< 2.21 \cdot 10^{43}$	G	0.056212^{21}	F_3 F_4
0637–752	PKS 0637-752	98.944	-75.271	8.78	1.91 ± 0.33	10.16 ± 1.39	$(1.78 \pm 0.25) \cdot 10^{46}$	Q	0.653^{22}	B I_A F_3 F_4
0646–306	PKS 0646-306	102.059	-30.739	1.15		$< 3.42^*$	$< 2.18 \cdot 10^{45}$	Q	0.455^{23}	F_3 F_4
0700–661	PKS 0700-661	105.13	-66.179	0.84		$< 3.02^*$	$< 1.4 \cdot 10^{45}$	B	0.39^{10}	F_3 F_4
0736–770	PKS 0736-770	113.681	-77.187	2.57	1.32 ± 0.89	3.97 ± 1.3		Q		
0745–330	PKS 0745-330	116.832	-33.18	0.95		$< 3.34^*$		B		
0749–514	PMN J0751-5134	117.749	-51.579	0.49		$< 3.19^*$		U		
0823–500	PKS 0823-500	126.362	-50.177	0.51		$< 3.27^*$		G		

Table 5.1.1.: continued.

Name[a]	Common Name	RA[b]	Dec[b]	S/N[c]	Γ[d]	$F_{20-100\,\mathrm{keV}}$[e]	$L_{20-100\,\mathrm{keV}}$[f]	Type[g]	z[h]	Detections[i]
0851–577	PMN J0852-5755	133.161	-57.925	-0.42		$< 3.24^*$		U		
0902–350	NVSS J090442-351423	136.176	-35.24	1.33		$< 3.53^*$		U		
0903–573	PKS 0903-57	136.222	-57.585	2.49		$< 3.25^*$	$< 5.36 \cdot 10^{45}$	U	0.695[24]	F_3 F_4
0920–397	[HB89] 0920-397	140.69	-39.993	3.16	0.69 ± 0.86	5.05 ± 1.49	$(3.96 \pm 1.43) \cdot 10^{45}$	Q	0.591[11]	F_3 F_4
0958–314	PKS 0958-314	150.17	-31.664	0.03		$< 3.79^*$	$< 6.8 \cdot 10^{41}$	U	0.009[25]	
1008–310	1RXS J101015.9-311909	152.567	-31.319	4.82		$5.56 \pm 1.27^*$	$(2.85 \pm 0.65) \cdot 10^{44}$	B	0.143[20]	F_3 F_4
1055–403	PMN J1057-4039	164.366	-40.661	2.11		$< 3.72^*$		U		
1057–797	PKS 1057-79	164.68	-80.065	0.11		$< 3.26^*$	$< 3.7 \cdot 10^{45}$	B	0.581[26]	F_3 F_4
1101–536	PKS 1101-536	165.968	-53.95	0.88		$< 3.61^*$	$< 2.05 \cdot 10^{44}$	B	0.15[10]	F_3 F_4
1104–445	[HB89] 1104-445	166.786	-44.819	2.29	1.43 ± 0.98	4.17 ± 1.51	$(4.02 \pm 1.47) \cdot 10^{46}$	Q	1.598[27]	F_3 F_4
1114–483	PMN J1117-4838	169.308	-48.637	-1.11		$< 3.74^*$		U		F_2
1116–462	PKS 1116-46	169.612	-46.571	1.61		$< 3.75^*$	$< 6.56 \cdot 10^{45}$	Q	0.713[2]	F_3 F_4
1121–640	PMN J1123-6417	170.828	-64.297	1.06		$< 3.49^*$		U		
1144–379	[HB89] 1144-379	176.756	-38.203	1.8		$< 3.97^*$	$< 1.64 \cdot 10^{46}$	Q	1.048[28]	F_3 F_4
1152–308	PMN J1155-3107	178.763	-31.133	-0.14		$< 4.17^*$	$< 3.37 \cdot 10^{47}$	Q	4.3[2]	
1248–350	PKS 1248-350	192.913	-35.311	0.56		$< 4.13^*$	$< 2.09 \cdot 10^{45}$	U	0.41[25]	
1251–407	PKS 1251-407	193.498	-40.992	0.39		$< 3.98^*$	$< 3.46 \cdot 10^{47}$	Q	4.46[29]	
1251–713	PKS 1251-71	193.75	-71.638	-0.03		$< 3.45^*$		U		
1257–326	PKS 1257-326	195.177	-32.887	0.91		$< 4.12^*$	$< 2.55 \cdot 10^{46}$	Q	1.256[30]	
1258–321	ESO 443- G 024	195.253	-32.441	0.25		$< 3.94^*$	$< 2.57 \cdot 10^{42}$	G	0.017042[31]	
1312–423	1ES 1312-423	198.764	-42.614	3.24		$< 3.96^*$	$< 1.07 \cdot 10^{44}$	B	0.105[20]	F_3 F_4
1313–333	[HB89] 1313-333	199.033	-33.65	1.69		$< 4.17^*$	$< 2.37 \cdot 10^{46}$	Q	1.21[32]	F_3 F_4
1322–428	Cen A	201.365	-43.019	606.52	1.87 ± 0.0	813.12 ± 1.68	$(5.96 \pm 0.01) \cdot 10^{42}$	G	0.001825[33]	B I_{A} I_{11} F_3 F_4
1323–526	PMN J1326-5256	201.703	-52.939	-0.22		$< 3.81^*$	$< 6.01 \cdot 10^{44}$	B	0.24[10]	F_3 F_4
1325–558	PMN J1329-5608	202.255	-56.134	2.24	2.24 ± 1.29	3.24 ± 1.36	$(1.48 \pm 0.64) \cdot 10^{44}$	U	0.13[10]	F_3 F_4
1333–337	IC 4296	204.163	-33.966	1.31		$< 3.98^*$	$< 1.38 \cdot 10^{42}$	G	0.012465[31]	
1343–601	Centaurus B	206.704	-60.408	24.59	1.95 ± 0.12	31.72 ± 1.54	$(1.18 \pm 0.06) \cdot 10^{43}$	G	0.012916[34]	I_{A} F_3 F_4
1344–376	PMN J1347-3750	206.918	-37.844	0.85		$< 4.09^*$	$< 2.72 \cdot 10^{46}$	Q	1.3[35]	F_3 F_4
1409–651	Circinus Galaxy	213.291	-65.339	145.96	2.37 ± 0.02	176.00 ± 1.51	$(6.10 \pm 0.05) \cdot 10^{41}$	G	0.001254[36]	B I_{A} I_{11} F_3 F_4
1424–418	[HB89] 1424-418	216.985	-42.105	4.21	1.62 ± 0.57	6.81 ± 1.63	$(7.1 \pm 1.7) \cdot 10^{46}$	Q	1.522[37]	F_3 F_4
1440–389	PKS 1440-389	220.988	-39.144	2.33		$< 4.07^*$	$< 4.1 \cdot 10^{43}$	B	0.065454[38]	F_3 F_4
1451–375	[HB89] 1451-375	223.614	-37.793	4.06	1.76 ± 0.55	6.95 ± 1.61	$(2.08 \pm 0.5) \cdot 10^{45}$	Q	0.314054[12]	I_{A} F_3 F_4
1454–354	PKS 1454-354	224.361	-35.653	1.79		$< 4.11^*$	$< 3.34 \cdot 10^{46}$	Q	1.424[6]	F_3 F_4
1505–496	PMN J1508-4953	227.162	-49.884	8.21	1.26 ± 0.29	13.18 ± 1.54	$(2.42 \pm 0.3) \cdot 10^{46}$	U	0.776[35]	B I_{A} F_3 F_4
1510–324	PKS 1510-324	228.412	-32.583	0.82		$< 4.05^*$	$< 2.07 \cdot 10^{46}$	Q	1.153[35]	F_3 F_4
1521–300	PKS 1521-300	231.139	-30.206	1.37		$< 4.02^*$	$< 3.61 \cdot 10^{42}$	U	0.02[25]	
1549–790	PKS 1549-79	239.245	-79.234	10.33	2.43 ± 0.35	9.95 ± 1.38	$(6.44 \pm 0.91) \cdot 10^{44}$	G	0.1501[38]	B
1600–445	PMN J1604-4441	241.129	-44.692	1.6		$< 3.72^*$	$< 8.26 \cdot 10^{41}$	B	0.01[10]	F_3 F_4
1600–489	PMN J1603-4904	240.962	-49.068	0.65		$< 3.73^*$	$< 3.13 \cdot 10^{44}$	B	0.18[39]	F_3 F_4
1610–771	[HB89] 1610-771	244.455	-77.288	4.06	1.33 ± 0.67	5.03 ± 1.35	$(5.05 \pm 1.38) \cdot 10^{46}$	Q	1.71[40]	F_3 F_4
1613–586	PMN J1617-5848	244.325	-58.803	2.84		$3.79 \pm 1.22^*$	$(3.07 \pm 0.99) \cdot 10^{46}$	Q	1.422[1]	F_3 F_4
1637–771	PKS 1637-77	251.067	-77.263	2.09	1.37 ± 0.99	3.67 ± 1.32	$(1.4 \pm 0.51) \cdot 10^{43}$	U	0.041[25]	
1646–506	PMN J1650-5044	252.571	-50.748	1.98		$< 3.65^*$	$< 7.1 \cdot 10^{43}$	U	0.09[10]	F_3 F_4

Table 5.1.1.: continued.

Name^a	Common Name	RA^b	Dec^b	S/N^c	Γ^d	$F_{20-100\,\mathrm{keV}}{}^e$	$L_{20-100\,\mathrm{keV}}{}^f$	Type^g	z^h	Detections^i
1653–329	Swift J1656.3-3302	254.07	-33.036	18.42	1.44 ± 0.1	33.33 ± 1.45	$(7.57 \pm 0.33) \cdot 10^{47}$	Q	2.4^{41}	B I_A I_{11} F_3 F_4
1713–518	PMN J1717-5155	259.397	-51.922	1.41		$< 3.64^*$	$< 1.88 \cdot 10^{46}$	Q	1.158^{1}	F_3 F_4
1714–336	PMN J1717-3342	259.4	-33.703	0.52		$< 3.83^*$		B		
1716–771	PKS 1716-771	260.96	-77.231	0.56		$< 3.39^*$		U		
1718–649	NGC 6328	260.921	-65.01	0.14		$< 3.42^*$	$< 1.59 \cdot 10^{42}$	G	0.014428^{42}	F_4
1733–565	PKS 1733-56	264.399	-56.568	0.06		$< 3.41^*$	$< 8.16 \cdot 10^{43}$	G	0.098^{43}	
1743–525	PMN J1747-5236	266.774	-52.609	2.04		$< 3.57^*$		U		
1759–396	PMN J1802-3940	270.678	-39.669	0.88		$< 3.68^*$	$< 2.54 \cdot 10^{46}$	Q	1.32^{44}	F_3 F_4
1814–637	PKS 1814-63	274.896	-63.763	3.91	1.11 ± 0.48	7.6 ± 1.47	$(6.82 \pm 1.33) \cdot 10^{43}$	G	0.0627^{45}	
1824–582	PKS 1824-582	277.302	-58.232	2.84	1.61 ± 0.89	3.96 ± 1.34	$(4.11 \pm 1.40) \cdot 10^{46}$	Q	1.531^{7}	F_4
1839–486	PKS 1839-48	280.811	-48.606	-1.6		$< 3.45^*$	$< 1.08 \cdot 10^{44}$	G	0.111^{2}	F_4
1915–458	PKS 1915-458	289.82	-45.727	2.49	1.66 ± 0.73	5.04 ± 1.43	$(1.59 \pm 0.45) \cdot 10^{47}$	Q	2.47^{6}	
1933–400	PKS 1933-400	294.318	-39.967	2.9	1.67 ± 0.8	4.76 ± 1.47	$(1.82 \pm 0.57) \cdot 10^{46}$	Q	0.965^{46}	I_A F_3 F_4
1934–638	PKS 1934-63	294.854	-63.713	0.82		$< 3.39^*$	$< 3.06 \cdot 10^{44}$	G	0.18129^{47}	
1936–623	PKS 1936-623	295.341	-62.189	5.28	1.57 ± 0.48	7.61 ± 1.51		Q		
1954–388	[HB89] 1954-388	299.499	-38.752	0.26		$< 3.95^*$	$< 5.22 \cdot 10^{45}$	Q	0.63^{48}	F_3 F_4
2000–330	PKS 2000-330	300.85	-32.863	-0.15		$< 3.95^*$	$< 2.48 \cdot 10^{47}$	Q	3.78^{49}	
2004–447	PKS 2004-447	301.98	-44.579	0.47		$< 3.69^*$	$< 6.21 \cdot 10^{44}$	G	0.24^{46}	F_3 F_4
2005–489	[HB89] 2005-489	302.356	-48.832	4.53		$5.98 \pm 1.26^*$	$(7.14 \pm 1.5) \cdot 10^{43}$	B	0.071^{50}	B F_3 F_4
2027–308	PKS 2027-308	307.741	-30.657	-0.09		$< 3.93^*$	$< 4.26 \cdot 10^{45}$	G	0.539^{7}	
2052–474	[HB89] 2052-474	314.068	-47.247	5.52	1.69 ± 0.65	6.19 ± 1.68	$(6.53 \pm 1.78) \cdot 10^{46}$	Q	1.489^{51}	B F_3 F_4
2106–413	[HB89] 2106-413	317.388	-41.173	0.55		$< 3.96^*$	$< 1.67 \cdot 10^{46}$	Q	1.058^{37}	
2123–463	PKS 2123-463	321.628	-46.097	2.21		$< 3.87^*$	$< 4.45 \cdot 10^{46}$	Q	1.67^{52}	F_3 F_4
2136–428	PMN J2139-4235	324.851	-42.589	1.53		$< 3.76^*$	$< 3.61 \cdot 10^{45}$	B	0.54^{9}	F_3 F_4
2137–644	PMN J2141-6411	325.443	-64.187	0.64		$< 3.4^*$	$< 1.15 \cdot 10^{46}$	U	0.959^{18}	F_3 F_4
2142–758	PKS 2142-75	326.803	-75.604	5.34	1.01 ± 0.5	7.39 ± 1.47	$(2.51 \pm 0.54) \cdot 10^{46}$	Q	1.139^{53}	B F_3 F_4
2149–306	PKS 2149-306	327.981	-30.465	33.13	1.53 ± 0.08	52.04 ± 1.82	$(1.26 \pm 0.04) \cdot 10^{48}$	Q	2.345^{11}	B I_A I_{11} F_3 F_4
2152–699	ESO 075- G 041	329.275	-69.69	6.96	1.81 ± 0.42	8.4 ± 1.49	$(1.53 \pm 0.27) \cdot 10^{43}$	G	0.028273^{54}	B F_4
2154–838	PKS 2155-83	330.582	-83.637	0.47		$< 3.23^*$	$< 4.7 \cdot 10^{46}$	Q	1.865^{35}	F_3 F_4
2155–304	[HB89] 2155-304	329.717	-30.226	4.08	1.91 ± 0.96	4.73 ± 1.68	$(1.63 \pm 0.59) \cdot 10^{44}$	B	0.116^{55}	F_3 F_4
2204–540	[HB89] 2204-540	331.932	-53.776	1.41		$< 3.5^*$	$< 1.98 \cdot 10^{46}$	Q	1.206^{11}	F_3 F_4
2206–474	NGC 7213	332.318	-47.167	19.32	1.9 ± 0.18	22.44 ± 1.65	$(1.79 \pm 0.13) \cdot 10^{42}$	U	0.006^{25}	B
2232–488	PKS 2232-488	338.805	-48.6	2.7		$< 3.48^*$	$< 2.81 \cdot 10^{45}$	Q	0.506^{2}	F_3 F_4
2245–328	PKS 2245-328	342.161	-32.598	0.5		$< 3.71^*$	$< 8.18 \cdot 10^{46}$	Q	2.268^{27}	F_3 F_4
2254–367	IC 1459	344.294	-36.462	0.85		$< 3.56^*$	$< 1.96 \cdot 10^{41}$	U	0.005^{25}	
2300–683	PKS 2300-683	345.931	-68.127	0.93		$< 3.24^*$	$< 2.74 \cdot 10^{45}$	Q	0.516^{2}	
2322–409	1ES 2322-409	351.186	-40.68	0.7		$< 3.39^*$	$< 2.63 \cdot 10^{44}$	B	0.17359^{1}	F_3 F_4
2326–477	[HB89] 2326-477	352.324	-47.505	1.11		$< 3.31^*$	$< 2.22 \cdot 10^{46}$	Q	1.304169^{12}	F_3 F_4
2326–502	PKS 2326-502	352.337	-49.928	-0.16		$< 3.23^*$	$< 2.75 \cdot 10^{45}$	Q	0.518^{51}	F_3 F_4
2351–309	PKS 2351-309	358.448	-30.63	0.27		$< 3.43^*$	$< 6.46 \cdot 10^{45}$	B	0.737^{10}	F_3 F_4
2355–534	[HB89] 2355-534	359.472	-53.187	1.8		$< 3.13^*$	$< 1.18 \cdot 10^{46}$	Q	1.006^{51}	F_3 F_4

Notes. (a) Name in IAU B1950 format, (b) Equatorial coordinates (J2000) in degrees, (c) *Swift*/BAT S/N, (d) Photon Index for 20 keV – 100 keV, (e) X-ray flux in 10^{-12}erg s^{-1} cm^{-2} (* indicates fluxes calculated by assuming a photon index based on sub-sample of bright sources), (f) X-ray luminosity in erg s^{-1}, (g) Optical classification after (Abdollahi et al., 2020) or (Véron-Cetty & Véron, 2010) if no 4FGL entry is available: Q: Flat Spectrum Radio Quasar, B: BL Lac, G: Radio Galaxy, U: Unidentified, (h) Redshift, (i) Published hard X-ray / gamma-ray detection in: B: *Swift*/BAT 105-month survey catalog (Oh et al., 2018), I_A: *INTEGRAL*/IBIS AGN catalog (Malizia et al., 2012) and the updated catalog (Malizia et al., 2016), I_{11}: *INTEGRAL* 11-year Hard X-ray Survey (Krivonos et al., 2015), F_3: *Fermi*/LAT 3LAC catalog (Ackermann et al., 2015), and F_4: 4FGL catalog (Abdollahi et al., 2020). The source 1114–483 is only listed in the 2FGL catalog (Nolan et al., 2012), indicated by F_2)

References. [1]Ackermann et al. (2015), [2]Mahony et al. (2011), [3]Truebenbach & Darling (2017), [4]Rau et al. (2012), [5]Wisotzki et al. (2000), [6]Jackson et al. (2002), [7]Healey et al. (2008), [8]Arsioli et al. (2015), [9]Shaw et al. (2012), [10]Shaw et al. (2013), [11]Hewitt & Burbidge (1989), [12]Jones et al. (2009), [13]Heidt et al. (2004), [14]Stickel et al. (1994), [15]Craig & Fruscione (1997), [16]Sulentic et al. (2004), [17]Lauberts & Valentijn (1989), [18]Titov et al. (2017), [19]Mao (2011), [20]Kapanadze (2013), [21]Lauer et al. (2014), [22]Hunstead et al. (1978), [23]Johnston et al. (1995), [24]Thompson et al. (1990), [25]Véron-Cetty & Véron (2010), [26]Sbarufatti et al. (2009), [27]Peterson et al. (1979), [28]Stickel et al. (1989), [29]Shaver et al. (1996), [30]Perlman et al. (1998), [31]Smith et al. (2000), [32]Jauncey et al. (1982), [33]Graham (1978), [34]West & Tarenghi (1989), [35]Ackermann et al. (2011), [36]Corwin & Emerson (1982), [37]White et al. (1988), [38]Jones et al. (2004), [39]Müller et al. (2015), [40]Hunstead & Murdoch (1980), [41]Masetti et al. (2008), [42]Callingham et al. (2017), [43]Tadhunter et al. (1993), [44]Massaro et al. (2009), [45]Danziger & Goss (1979), [46]Drinkwater et al. (1997), [47]Holt et al. (2008), [48]Browne et al. (1975), [49]Peterson et al. (1982), [50]Falomo et al. (1987), [51]Jauncey et al. (1984), [52]Otrupcek & Wright (1991), [53]Jauncey et al. (1978), [54]da Costa et al. (1991), [55]Falomo et al. (1993)

5.2 Sample completeness

Since the source sample of the TANAMI observing program was not established using the same long-term selection criterion of radio flux density as it was done for the MOJAVE program, the issue of sample completeness needs to be addressed. Many sources were added to the sample because of a measured VLBI flux density of $S \geq 100\,\mathrm{mJy}$ within one single observation and other factors like gamma-ray brightness, variability, high X-ray flux, or a potential neutrino emission counterpart. In the framework of this study, it is of particular interest if the TANAMI main sample can serve as a statistically sound extension to the MOJAVE samples of the Northern hemisphere in terms of high-energy / hard X-ray studies of beamed extragalactic jets. Can the TANAMI sample or its sub-samples be treated as statistically complete in this regard? Is there a substantial difference in hard X-ray properties compared to the well defined MOJAVE-1 and MOJAVE-1.5 sample?

In the following, these issues are discussed. AGN studies are known to suffer from selection biases depending on the observation wavelength, time frame, and source activity among others. Therefore, the mixed TANAMI source sample, which is compiled of different beamed AGN populations, needs to be treated accordingly when compiling the broadband spectral characteristics and deriving physical properties. This aspect is taken into account for the presentation and discussion of the hard X-ray characteristics of the TANAMI sample sources in this chapter.

5.2.1. Comparison with the MOJAVE samples

Analog to the MOJAVE-1 and MOJAVE-1.5 samples, the background-subtracted S/N distribution of the TANAMI sample shows a clear positive offset to $0\,\sigma$ (Fig. 5.1.2). However, the offset is less prominent. While the MOJAVE samples show a fraction of sources that are not compatible with random noise of close to 90%, the TANAMI sources reveal a lower amount with large spread, that is, 68.2% – 85.7%. This is also expressed by the fact that 86.5% of the TANAMI sources are below the BAT catalog threshold of $4.8\,\sigma$, whereas MOJAVE-1 is characterized by a fraction of 74.8%.

The subtraction of the random noise component is not viable for the relatively small TANAMI sub-samples. In the case of M18G and A19 only one source has a negative S/N value, and the M18R sub-sample has no such source. The number of available data points is too low for a meaningful description of random noise component. Instead, the measure of the S/N median and percentage of bright sources (non-upper-limits) is used. Table 5.2.1 lists the corresponding values for the MOJAVE and TANAMI samples. The median values of the MOJAVE samples are around $2.7\,\sigma$, well below the BAT catalog threshold, whereas the TANAMI main sample is relatively low at $1.6\,\sigma$. The sub-samples reveal a different picture, however: the MOJAVE-like M18R sub-sample has a S/N median of 2.58, while the gamma-ray-selected M18G sub-sample is characterized by a median of only 1.98. Although no significant correlation between radio flux density and hard X-ray flux could be found for the MOJAVE-1 sample (Sect. 4.2.3, Fig. 4.2.7), the S/N median difference of M18R and M18G in the TANAMI sample points towards a tentative favoritism of radio-bright against gamma-ray-bright sources in terms of hard X-ray emission. In any case, the percentage of non-upper-limit sources in both sub-samples is very similar, 54.5% and 52.4%, respectively. Interestingly, these values are consistent with the value for MOJAVE-1 with 56%, instead

Table 5.2.1.: Comparison of the MOJAVE samples with the TANAMI sample and gamma-ray- and radio-selected sub-samples in terms of BAT signal strength and *Fermi*/LAT detections.

	MOJAVE-1	MOJAVE-1.5	TANAMI	M18G	M18R	A19	TANAMI[d] (log N-log S)	MOJAVE-1[d] (log N-log S)
sample size	135	181	126	22	22	15	34	70
S/N subtr.[a]	$90.3^{+3.3}_{-8.3}\%$	$87.1^{+3.1}_{-6.9}\%$	$79.5^{+6.2}_{-11.3}\%$	–	–	–	–	–
S/N median	2.71	2.65	1.60	1.98	2.58	1.60	4.06	3.83
non-UL[b]	56.3%	55.2%	33.3%	52.4%	54.5%	46.7%	100%	100%
LAT det.[c]	83.7%	84.5%	81.7%	100.0%	86.4%	53.3%	94.1%	91.4%

Notes. [a] Percentage of the source sample that is not compatible with random background noise, [b] percentage of sources in each sample whose spectral fit did result in a flux value that is not an upper limit, [c] percentage of sources that have counterparts in at least one of the 2FGL, 3FGL, or 4FGL *Fermi*/LAT catalogs, [d] only includes non-upper-limit sources of the blazar log N-log S distribution (Fig. 5.2.1).

of the TANAMI main sample of only 33%. Thus, radio- and gamma-ray-bright sources also tend to be brighter in the hard X-ray band.

In Sect. 4.2.1 / Fig. 4.2.1 the hard X-ray flux is graphed against the 15 GHz radio flux density for the MOJAVE-1 sample. Although no significant correlation between both quantities is found, a clear lack of X-ray-bright sources below $\approx 1\,\mathrm{Jy}$ of the median flux density can be seen. The main TANAMI source sample comprises roughly the same number of sources than the MOJAVE-1 sample, but on a sky area that is only 39% as large. Consequently, the sample comprises a large number of sources that are tentatively lower in radio flux density, which is the case because of TANAMI's lower radio flux density threshold regarding the sample definition. The tendency of radio sources of low flux density also being weak in the BAT band is also suggested by the TANAMI data set. The relatively large number of sources shows a notably lower BAT S/N mean value, $1.6\,\sigma$ compared to $2.7\,\sigma$ for MOJAVE-1. The radio galaxy / BL Lac sub-sample of A19 shows the same median S/N values as the main TANAMI sample. This, however, is mere coincidence. Calculating the mean S/N value reveals the large difference of both distributions with $9.0\,\sigma$ (TANAMI) and $46.8\,\sigma$ (A19). Compared to the MOJAVE samples the AGN sub-types of the TANAMI sample are distributed much more evenly over the entire covered S/N range. Notably, the radio galaxies follow all other types, peaking around $1\,\sigma - 2\,\sigma$, contrary to the MOJAVE distributions that are characterized by mostly high-S/N radio galaxies.

The *Fermi*/LAT detection rate of the sample sources is above 80% throughout all samples, with the exception of A19 (53%), which stems from the low gamma-ray profile of radio-galaxies (see discussion in Sect. 5.1.2). Otherwise, the main TANAMI sample is lowest, with 82%. Interestingly, the M18R sub-sample shows a very similar proportion of LAT detections compared to the MOJAVE samples.

Overall, the distribution of fitted photon indices between TANAMI and MOJAVE samples is very similar. The mean photon index of the radio galaxies is always notably softer than the index of FSRQs and BL Lacs. Furthermore, no significant difference between the corresponding sub-types in the samples have been found using 2-sample KS tests. The photon index distribution of the TANAMI sample, however, also includes four sources of unidentified type. This group of sample sources is also represented in the distribution of X-ray luminosity, where their specific position in the overall distribution may suggest a tentative source classification (Sect. 5.1, Fig. 5.1.5).

If the TANAMI main sample and the MOJAVE samples do not show significantly different parameter distributions of the hard X-ray emission it could be concluded that the TANAMI sample or at least the M18R sub-sample is the extension of the observing program on the Northern hemisphere for hard X-ray beamed AGN sample studies, but only to the precision that the Swift/BAT survey data provides in this energy range. In order to gauge the validity of such statement, other blazar samples with different selection criteria need to be analyzed. Should a, for example, gamma-ray-selected blazar sample reveal the same ambiguity in relation to the MOJAVE blazars, the above results for the TANAMI blazars need to be re-evaluated. To address this issue, the hard X-ray analysis of the *Fermi*/LAT 4LAC source sample and the comparison with the radio-selected AGN samples is presented in Sect. 6.1.1.

Due to the high fraction of upper limits in the BAT data set of the TANAMI sample, an analysis of the contribution to the CXB and of the hard X-ray luminosity functions for the comparison with the MOJAVE results is problematic. However, the calculation and analysis of the $\log N$-$\log S$ distribution is still viable for the X-ray-brightest sources. Figure 5.2.1 shows the $\log N$-$\log S$ distribution of all TANAMI blazars (excluding radio galaxies and the source of unknown type 2206–474), whose fluxes are not upper limits. The unidentified sources in the sample are also included, because of the high probability of them being a type of blazar themselves. Also, the graph features the MOJAVE-1 blazar $\log N$-$\log S$ distribution from Sect. 4.2.3 for comparison. There are three different segments of the TANAMI distribution that show a different shape. First, the lowest-flux sources (four sources, $(2–3)\cdot 10^{-12}\mathrm{erg\,s^{-1}\,cm^{-2}}$) show a very flat slope. Both the MOJAVE-1 and TANAMI distribution saturate at around $3\cdot 10^{-12}\mathrm{erg\,s^{-1}\,cm^{-2}}$, which in both cases indicates a relative rarity of faint sources, and is likely due to a large number of missing sources that have been excluded because of their flux values being upper limits. The black lines and shaded areas represent the power-law fits to the $\log N$-$\log S$ distributions and the $1\,\sigma$ uncertainty regions. The fit of the TANAMI data set reveals a very flat slope of $\alpha_{\mathrm{Tan,BAT}} = 1.11\pm 0.08$ and a norm of $A_{\mathrm{Tan,BAT}} = 9.55^{+1.26}_{-1.12}\cdot 10^{-3}\,\mathrm{deg}^{-2}$, and is thus compatible with the fit to the MOJAVE-1 blazars ($\alpha_{\mathrm{Moj,BAT}} = 1.13\pm 0.04$). However, it needs to be emphasized that only a small fraction of the entire TANAMI sample (34/126 sources) is presented by the distribution due to low signal quality of many sources. A potentially different shape at the low-flux end might be able alter the overall slope. Remarkably, the cumulative source number per unit sky for the weakest graphed source of both MOJAVE-1 ($(2.73\pm 0.33)\cdot 10^{-3}\,\mathrm{deg}^{-2}$) and TANAMI ($(3.20\pm 0.57)\cdot 10^{-3}\,\mathrm{deg}^{-2}$) distribution are well compatible within their uncertainty ranges.

Using the MOJAVE-1 $\log N$-$\log S$ distribution the number of expected MOJAVE-like and X-ray-bright blazars on the TANAMI part of the sky can be predicted. For the same density of the 70 X-ray-bright blazars on the MOJAVE-1 area, 27 sources are expected for one forth of the entire sky (TANAMI area). Instead, it is 34 with three unidentified source types included, of which a small number could be non-blazars. Furthermore, the slight excess can also be interpreted as a number of blazars that simply do not fit the MOJAVE selection criteria. In any case, the number of sources per sky area are compatible for both the MOJAVE-1 and TANAMI samples on the basis of the hard X-ray $\log N$-$\log S$ distributions. The selection process of sources for both observation programs therefore seems consistent in this regard.

The four sources on the higher flux end ($> 1.1\cdot 10^{-11}\mathrm{erg\,s^{-1}\,cm^{-2}}$) of the TANAMI distribution can be regarded as a complete, although very small, sub-sample. Interestingly, the three brightest sources are not featured in the M18R and M18G samples. Only the fourth-brightest source in the distribution (BL Lac 0521–365) is present in both lists. The five brightest sources in the MOJAVE-1 $\log N$-$\log S$ distributions are exclusively FSRQs with an average redshift of approximately 1, with only one outlier (0836+710, $z = 2.22$). In the

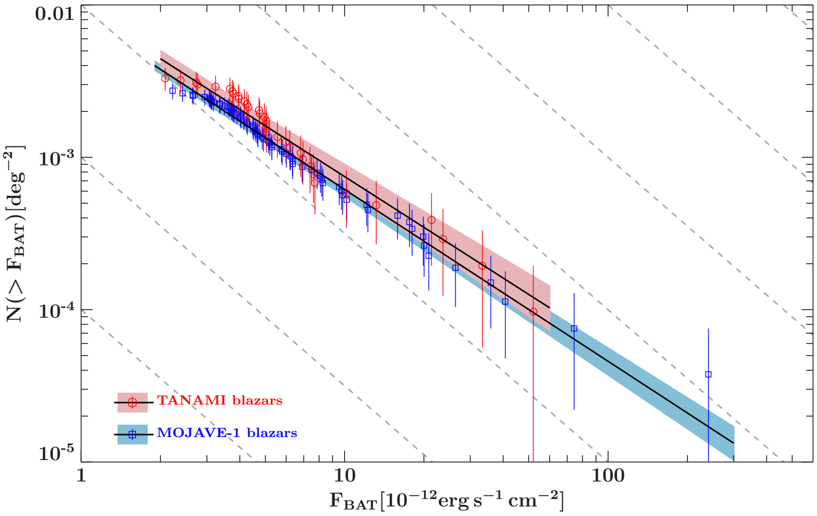

Figure 5.2.1.: TANAMI blazar log N-log S distribution in the 20 keV–100 keV band (excluding upper limits) in red. The same MOJAVE-1 blazar log N-log S distribution as in Fig. 4.2.6 is shown for comparison. Power-law fits are shown as black lines with the shaded area indicating the error interval. A general slope of −3/2 is indicated by the dashed lines.

TANAMI distribution the high-flux end is populated by a highly irregular set of sources. The two brightest sources are the high-redshift FSRQs 2149–306 ($z = 2.35$) and 1653–329 ($z = 2.4$), where the latter was added to the TANAMI sample because of the high *Swift*/BAT signal. These are followed by the BL Lac 0548–322, which is an extreme blazar at the low redshift of $z = 0.069$, and 0521–365 ($z = 0.055$).

The MOJAVE and TANAMI samples share a very comparable fraction of gamma-ray-bright sources in the respective sub-set of X-ray-bright blazars (log N-log S distributions). MOJAVE-1 and MOJAVE-1.5 have 91.4% (64/70) and 91.3% (84/90) LAT-detected X-ray-bright blazars, respectively. The X-ray-bright TANAMI blazars are charaterized by 94.1% (32/34). The two missing gamma-ray faint sources are 1637–771 and 1915–458. The former is a source of unidentified type and $z = 0.041$, while latter is an FSRQ at $z = 2.47$. Both sources have a very low BAT S/N value of ≈ 2, and are at the low-flux end of the log N-log S distribution. Also, both sources fit into the characteristic of LAT detections depicted in Fig. 5.1.7: 1637–771 has been classified as a LINER / weak-line radio galaxy (WLRG) by Lewis et al. (2003), which is relatively weak in the BAT band, following the behavior of gamma-ray (non-)detections of radio galaxies in this regard. 1915–458 is a high-z FSRQ, which is a source type that is notoriously hard to detect in the GeV band. In Sect. 4.2.2, a number of blazars are proposed to be likely future *Fermi*/LAT detections based on the peak frequency of the HE emission bump. For the above cases no such high-energy SED archival data is available. Therefore, a similar prediction is not viable. However, due to the nature of said sources a near-future gamma-ray detection seems unlikely.

The MOJAVE samples, for which strict radio flux density criteria have been applied, consist for the great majority out of low-peaked blazars. The derived log N-log S distributions are characterized by a very flat, but still consistent slope. Blazar variability in the hard X-ray band is found to be not the dominating factor regarding the flat slope in case of the MOJAVE sample (Sect. 4.2.4). Instead, intrinsically evolving luminosity is likely a major contributor (Sect. 4.2.5). Since the TANAMI source sample is partially gamma-ray-selected as well as chosen because of high variability, or potential neutrino counterparts, it depicts not necessarily the X-ray characteristics of a MOJAVE-like sample of the radio-brightest beamed AGN in the Southern sky. As such, it is not a priori expected to follow the same peculiar log N-log S distribution of the MOJAVE samples. Yet, the results for both distributions are very much compatible with each other.

The initial question remains, whether the TANAMI sample can be seen as an extension of the MOJAVE samples in terms of sample studies, especially in the hard X-ray band. For the radio sub-sample M18R similarly strict selection criteria of the MOJAVE program were applied. Consequently, the distributions of signal strength are very similar between this sub-sample and the MOJAVE samples (Sect. 5.2.1, Table 5.2.1). The hard X-ray S/N distribution and the fraction of LAT detections for the M18G and A19 sub-samples are notably different, likely due to the source type, and / or SED peak frequency and intensity. Because of this, both sub-samples cannot be regarded as statistically complete in the radio band and are not suited for the extension of the MOJAVE samples. Generally, the distribution of the BAT photon indices of the main TANAMI and the MOJAVE sample should be slightly different, originating from a wider range of HE peak frequencies in the TANAMI sources, changing the spectral slope in the measured BAT band. However, the comparison of the spectral shape / photon indices is inconclusive because of low the number of fitted sources and large uncertainty ranges due to low data quality.

Although the extension of the MOJAVE samples by the M18R sub-sample provides a larger and relatively consistent group of beamed AGN, the set is incomplete. Assuming the same density of sources per sky area, (181 sources of the MOJAVE-1.5 sample, $\delta \geq -30°$) the remaining part of the Southern sky should be populated by approximately 60 sources of the general MOJAVE selection criteria, instead of the 22 of the M18R sub-sample. The low number of radio-loud AGN is likely due to several factors, primarily the different observation practices. The original definition of the radio-loud (M18R) sample (Stickel et al., 1994; Kuehr et al., 1981) was derived using only single observations, whereas the MOJAVE program incorporated multiple observation epochs, in which the source flux had to reach the target flux density only once, also including generally weaker but more variable objects. Another potential cause of the difference between the expected source number and the M18R sample size is the different sample selection criterion ($S > 2\,\mathrm{Jy}$ at 5 GHz vs. $S > 1.5\,\mathrm{Jy}$ at 15GHz). A flux density of 2 Jy at 5 GHz equals 1.5 Jy at 15 GHz for a spectral index $\alpha \approx -0.26$, which is within the specification of the M18R sample definition ($\alpha > -0.5$). However, a certain range of different spectral indices would effectively lead to a somewhat unequal selection limit for the flux density. For illustration, a flux density of 1.5 Jy at 15 GHz and a spectral index of $\alpha = -0.5$ would translate to a flux density of 2.6 Jy at 5 GHz and 1.3 Jy for $\alpha = 0.1$. Since the sources are indeed expected to have flat radio spectra ($\alpha \approx 0$), the original flux density limit of 2 Jy is thus likely too high for a consistent comparison with the MOJAVE samples.

It can be stated that the M18R sub-sample is missing sources regarding the MOJAVE selection criteria. In other words, a combined MOJAVE and M18R AGN beamed AGN sample is not statistically complete in the radio regime. The M18R sub-sample, on the other hand, seems to be representative of the MOJAVE-like sources in the Southern sky in the hard X-ray band. Additionally, the density of X-ray-bright sources of the main TANAMI sample is consistent with the results obtained with the MOJAVE-1 sample. The main TANAMI sample is characterized by 34 blazars which are X-ray-bright (non-upper-limits), that are also graphed in the $\log N$-$\log S$ distribution. Compared to this, the MOJAVE-1.5 sample has 92 blazars that are X-ray-bright, which corresponds to 31 predicted blazars in the remaining part of the sky, that is, the area covered by TANAMI. The slight difference might possibly be due to the later inclusion of interesting cases such as neutrino candidates or TeV emitter or pure statistical fluctuation. The sources with the lowest X-ray flux at the BAT detection limit in the $\log N$-$\log S$ distributions for the MOJAVE samples and TANAMI are also compatible with each other within their uncertainties (MOJAVE-1: $(2.73 \pm 0.32)\,\mathrm{deg}^{-2}$, MOJAVE-1.5: $(2.97 \pm 0.31)\,\mathrm{deg}^{-2}$, TANAMI: $(3.20 \pm 0.56)\,\mathrm{deg}^{-2}$). Altogether, the hard X-ray emission statistic from blazars of both the Northern (MOJAVE) and Southern (TANAMI) observation programs is very consistent, contrary to the radio emission, which is characterized by a lack of radio-loud sources and abundance of sources with low radio flux density. Therefore, the MOJAVE-1.5 + M18R group is deemed a suitable and robust source sample for studies in the hard X-ray band of radio-loud beamed AGN. This conclusion, however, is based on the available BAT survey data set, which offers limited sensitivity, especially for weaker sources, which are excluded from the analysis. A comparison with a beamed AGN sample with truly different selection criteria, for example, high-peaked sources such as gamma-ray-bright blazars, would help to discuss the importance of sample composition in this regard. In the following chapter, Sect. 6.1.2 the recent *Fermi*/LAT catalog sample is analyzed accordingly. The corresponding conclusions are given therein.

5.3 Summary

In this chapter the hard X-ray (20 keV – 100 keV) emission characteristics of the entire TANAMI sample are analyzed on the basis of the *Swift*/BAT 105-month all-sky survey maps. The following points comprise the main results of the analysis and discussion of the X-ray characteristics and the comparison to the MOJAVE samples:

- The derived spectral properties of the TANAMI sample sources are generally very similar to the characteristics of the MOJAVE-1 / MOJAVE-1.5 samples (Chpt. 4). However, on average, the BAT signal quality and consequently the flux are lower for the TANAMI sample. This is mirrored by the lower fraction of sources that are not compatible with random background noise, that is, 80% (100 out of 126 sources) compared to 90% in the MOJAVE-1 sample.

- The radio galaxies in the TANAMI and MOJAVE samples exhibit on average a notably softer photon index compared to the blazar sub-classes. It can be concluded that the observed hard X-ray emission must originate from the jet and the accretion disk / hot corona, but in the case of radio galaxies with a lower contribution from the jet to the total signal.

- The radio-loud (M18R) and gamma-ray-bright (M18G) sub-samples are more comparable to the MOJAVE-1 sample in terms of BAT signal strength than to the main TANAMI sample, as indicated by the median S/N values and the fraction of sample sources that are bright enough for spectral fitting.

- Different source classes are characterized by distinct hard X-ray luminosities, similar to the MOJAVE samples. Several sources of unidentified type can be assigned a likely classification based on the location in luminosity space, such as 1505–496 (likely FSRQ), or 0131–522 and 2206–474 (likely radio galaxies or BL Lacs).

- Overall, the brightest TANAMI sources in the BAT survey are also detected by *INTEGRAL*. The moderately bright unidentified source 2206–474 and BL Lac 0548–322 are exceptions. Gamma-ray-bright sources (*Fermi* detections) are not strongly correlated with BAT signal strength. Generally, all BL Lacs (with z information) in the TANAMI sample, most FSRQs, and the X-ray-brightest radio galaxies are listed in the most recent *Fermi*/LAT catalogs.

- Compared with the MOJAVE-1 and MOJAVE-1.5 samples, the hard X-ray $\log N$-$\log S$ distribution of the TANAMI blazars is similarly flat ($\alpha_{\mathrm{Tan,BAT}} = 1.11 \pm 0.08$). This suggests that the same source population and sample composition is present in the (blazar) samples of both monitoring programs. This is strengthened by the fact that the number of sources per sky area at the BAT flux limit is compatible between TANAMI and MOJAVE within the given uncertainties.

Since its inception the TANAMI program served as a strong and versatile basis for multi-wavelength studies of beamed AGN and even neutrino candidates, with an excellent coverage over most of the electromagnetic spectrum, from radio (GHz) to gamma-ray and TeV energies (e.g., Kadler et al., 2015; Krauß et al., 2016). Compared to the statistically complete MOJAVE-1 sample and its extended version, MOJAVE-1.5, the current main TANAMI source sample (126 sources, 2020), however, has clear limitations for the purpose of sample studies regarding completeness and its mixed source type composition. Although studies using the entire TANAMI sample for any given wavelength range need to take into account this aspect, the combined MOJAVE-1.5 and M18R group is a statistically solid basis for hard X-ray analyses ($E \gtrsim 10\,\mathrm{keV}$) of the radio-loud blazar population of the full sky. Future works regarding multi-wavelength observations involving instruments in a similar energy range, like *INTEGRAL*, *Astrosat*, or *NuSTAR*, could benefit from this larger pre-defined source sample.

6. Gamma-ray-bright blazars in the Swift/BAT survey: the 4LAC sample

The gamma-ray observation window has proven to be effective and necessary at tracking and understanding high-energy astrophysical phenomena (see, e.g., Massaro et al., 2015, for a review). In the fairly wide GeV and TeV bands the (extragalactic) sky is easily dominated by highly beamed AGN jets compared to other wavelength regimes. Started in 2008, the *Fermi Gamma-ray Space Telescope* and its main instrument, the Large Area Telescope (LAT), (Atwood et al., 2009, see Sect. 2.4) have become imperative for coordinated multi-wavelength campaigns for the study of AGN (e.g., TANAMI, Ojha et al., 2010). Also, its contribution to the availability of long-term gamma-ray data made the instrument essential for broadband AGN SEDs, covering several orders of magnitude at the high-energy end of the spectrum (e.g., Krauß et al., 2016; Ghisellini et al., 2017; Paliya et al., 2019).

Besides the nearly real-time monitoring of gamma-ray activity in the entire observable sky, the results of the *Fermi*/LAT data products include source catalogs which incorporate years of integrated GeV band data. The most recent source catalog release by the time of writing is the *Fermi*/LAT Fourth Source Catalog, or 4FGL (Abdollahi et al., 2020). The catalog is derived from the first eight years of integrated observation in the energy range of 50 MeV to 1 TeV, and comprises 5064 individual sources and their spectral characteristics. A large fraction of the catalog is composed of AGN, that is 3207 sources, which are presented in the Fourth Catalog of AGN detected by *Fermi*/LAT (4LAC, Ajello et al., 2020).

This chapter focuses on the 4LAC source sample and primarily its hard X-ray properties, extracted from the *Swift*/BAT 105-month survey maps. Its composition is outlined in Table 6.0.1, distinguishing between the main sample, and the high- and low-latitude sample ($|b| > 10°$, $|b| < 10°$). An overwhelming fraction of approximately 98% of the 4LAC catalog can be classified as blazar-type AGN, with the remainder being radio galaxies and other AGN, such as CSS or Seyferts. Compared to the radio-selected blazar samples of the MOJAVE and TANAMI programs (Chpt. 4 and Chpt. 5), the majority of the 4LAC sample is composed of BL Lacs (35.3%) and unidentified blazar candidate sources (BCUs, 40.9%). The sub-type of FSRQs represent the smallest group (21.6%). The low-latitude sub-set of the 4LAC sample is characterized by a relatively high amount of BCUs (69.2%) and low source count overall. This is due to a higher flux detection limit, the issue of Galactic extinction, and the contamination by Galactic sources in counterpart catalogs (Ajello et al., 2020). Additionally, the catalog lists the SED type for 2369 blazars, that is, the classification of an SED regarding the peak frequency $\nu_{\mathrm{synch}}^{\mathrm{peak}}$ of the synchrotron component: low-synchrotron-peaked blazars (LSP, $\nu_{\mathrm{synch}}^{\mathrm{peak}} < 10^{14}\,\mathrm{Hz}$), intermediate (ISP, $10^{14}\,\mathrm{Hz} < \nu_{\mathrm{synch}}^{\mathrm{peak}} < 10^{15}\,\mathrm{Hz}$), and high-synchrotron-peaked blazars (HSP, $\nu_{\mathrm{synch}}^{\mathrm{peak}} > 10^{15}\,\mathrm{Hz}$).

This most recent *Fermi*/LAT AGN sample permits the hard X-ray analysis on the basis of the *Swift*/BAT survey data set of a large number of blazars and blazar candidate sources with minimal selection bias because of the long-term nature of the survey, mitigating the

	complete 4LAC sample		high latitude ($\|b\| > 10\,^{\circ}$)		low latitude ($\|b\| < 10\,^{\circ}$)	
FSRQ	694	21.6%	658	23.0%	36	10.5%
BL Lac	1131	35.3%	1067	37.3%	64	18.6%
BCU$^{(a)}$	1312	40.9%	1074	37.5%	238	69.2%
radio gal.	42	1.3%	38	1.3%	4	1.2%
other$^{(b)}$	28	0.9%	26	0.9%	2	0.6%
total	3207		2863		344	

Notes. $^{(a)}$ Blazar candidates of uncertain type, $^{(b)}$ remaining AGN classes including CSS, NLSY1, Seyfert, SSRQ and other AGN.

Table 6.0.1.: Composition of the 4LAC source catalog including high- and low-latitude sub-samples

influence of variability. The 4LAC catalog can be regarded as a very consistent source sample that allows the comparison of the hard X-ray characteristics of blazars, which have been selected on the opposite side of the electromagnetic spectrum compared to the previously analyzed radio-based samples. This chapter is structured after the following key aspects: In Sect. 6.1 the general hard X-ray properties of the 4LAC sample are presented. Similarities and differences to the radio-loud MOJAVE and TANAMI AGN samples are described therein. One especially important aspect is the property of X-ray brightness for both sample types. In connection to the previous chapters, it is analyzed whether the low number of cataloged X-ray-bright blazars is especially characteristic to the source selection at radio wavelengths. The distribution of X-ray-bright *Fermi* catalog sources is studied using the $\log N$-$\log S$ in Sect. 6.1.2 both for the X-ray and gamma-ray bands. Additionally, the influence of the SED type / peak position is discussed in Sect. 6.1.3. Furthermore, it is determined whether the 4LAC source sample can be regarded as a solid basis for hard X-ray blazar studies. The combination of the *Fermi*/LAT and *Swift*/BAT survey data offers a unique description of the high-energy SED characteristic of a large number of blazars and blazar candidate sources. Section 6.2 covers the BCU sub-type and the specific distribution of these sources within the X-ray and gamma-ray parameter space compared to the FSRQs and BL Lacs of the sample in order to make statements about possible source classifications.

6.1 General properties

In this section the hard X-ray spectral characteristics of the 4LAC sample based on the *Swift*/BAT 105-month survey maps are presented. Following the previous chapters, Sect. 6.1.1 describes the distributions of the spectral properties like X-ray flux, luminosity, and photon index in the 20 keV – 100 keV band, as well as the S/N distribution compared to random background noise. It is analyzed whether gamma-ray-bright beamed AGN are significantly brighter or fainter at hard X-rays compared to radio-selected sources of this type. Furthermore, the issue of a lack of X-ray-faint radio-bright blazars (Sect. 4.2.3, Sect. 5.2.1) can be viewed from the perspective of a large well-defined gamma-ray sample. The hard X-ray $\log N$-$\log S$ distributions are discussed in Sect. 6.1.2. Since the 4LAC data set includes the values of the SED synchrotron peak frequencies, the impact of the SED position on the hard X-ray flux can be addressed (Sect. 6.1.3). The results of the spectral fits of the 4LAC BAT spectra are listed in the appendix in Table A.0.1[1].

---

[1] Due to the size of the sample only sources that are bright enough to allow spectral fitting are listed in the table, together with non-fitted sources, which produce non-upper-limit flux values. The remaining upper-limit values of flux and luminosity are saved in a fits-format table in the attached zip file.

6.1.1. Hard X-ray characteristics

The 4LAC source sample consists of a variety of gamma-ray-bright AGN types. Most of the sample, however, is relatively faint in the observed hard X-ray band of 20 keV – 100 keV. Only 504 out of a total of 3207 sources are bright enough to facilitate a spectral fit. The fitting process for 86 sources in this sub-set leads to upper-limit flux values, leaving 417 AGN for which fluxes and photon indices can be derived. The BAT spectra of eleven sources of this group are contaminated by close-by sources. Hence, the extracted photon indices are omitted, and flux and luminosity values are marked as upper limits. 42 source spectra, which cannot be fitted using the approach detailed in Sect. 3.2.4 due to one or more spectral bins with negative counts, produce fluxes that are non-upper-limits.

The average signal strength of the sources tends to be somewhat correlated with the AGN type, which is mirrored by the S/N distribution, shown in Fig. 6.1.1. The distributions of all types are offset from $0\,\sigma$, although not as pronounced as the radio-selected MOJAVE and TANAMI samples (see also Table 5.2.1). The group of FSRQs is the brightest set with a median S/N value of $1.10\,\sigma$, while the BL Lacs ($0.49\,\sigma$) and BCUs ($0.38\,\sigma$) show only a small offset. In total, the vast majority of 96.7% of the 4LAC catalog has S/N values lower than the BAT catalog threshold of $4.8\,\sigma$. The S/N distributions of all types are characterized by a high-significance tail. Several bright sources are omitted from the plot, like the FSRQ J1229.0+0202 (3C 273, $192.14\,\sigma$), the radio galaxy J1325.5–4300 (Centaurus A, $606.89\,\sigma$), or the BL Lac J1104.4+3812 (Mrk 421, $120.30\,\sigma$).

Subtracting the fitted random noise component (see Sect. 3.2.3) from the S/N distribution of the whole sample and each of the blazar sub-sets reveals the fraction of each set that is not compatible with the expected random noise. The resulting S/N distributions are presented in Fig. 6.1.2. Of the complete 4LAC sample 34.74% – 40.72% remain after the subtraction, which is considerably less than for the MOJAVE ($\approx 90\%$) and TANAMI sample ($\approx 80\%$). The relatively high signal strength of the small number of FSRQs is reflected in the higher fraction of 54.94% – 65.21%, whereas BL Lacs are characterized by only 28.70% – 39.18%. The weakest sub-type of the whole sample are the blazar candidate sources, showing a fraction of only 22.75% – 32.87%.

Figure 6.1.3 shows the distribution of the X-ray fluxes, offering a very similar picture. The top panel includes all upper-limit values, which dominate the region of $\approx (2.5 - 5.0) \cdot 10^{-12}\,\mathrm{erg\,s^{-1}\,cm^{-2}}$. In the bottom panel all sources whose fluxes are not upper limits are plotted. The distribution is still concentrated at low values, around $(2-4)\cdot 10^{-12}\,\mathrm{erg\,s^{-1}\,cm^{-2}}$, and 90% of all values are below $10^{-11}\,\mathrm{erg\,s^{-1}\,cm^{-2}}$. A 2-sample KS test between FSRQs and BL Lacs reveals no significant difference between both distributions ($p = 0.088$). A difference between FSRQs and BCUs is more pronounced ($p = 6 \cdot 10^{-5}$), suggesting that only a fraction of the BCU sub-sample would likely be identified as FSRQs. Comparing the fluxes of the 4LAC blazars to the MOJAVE-1.5 blazars shows that the distributions of FSRQs themselves are significantly different from each other ($p = 0.003$), while the same cannot be stated for BL Lacs ($p = 0.186$). Again, the 4LAC blazars are, on average, fainter in the BAT band than the previously analyzed radio-selected samples. Additionally, the tests omit the upper-limit flux values, which are far more numerous in the 4LAC data set. Hence, the true difference between all the X-ray fluxes of gamma-ray- and radio-selected samples would be even larger. Table 6.1.1 lists the 20 X-ray-brightest sources in the 4LAC sample (BAT S/N value), as well as their source types. The list consists of eight FSRQs, four BL Lacs, and eight radio galaxies and other non-blazar AGN, which otherwise constitute a

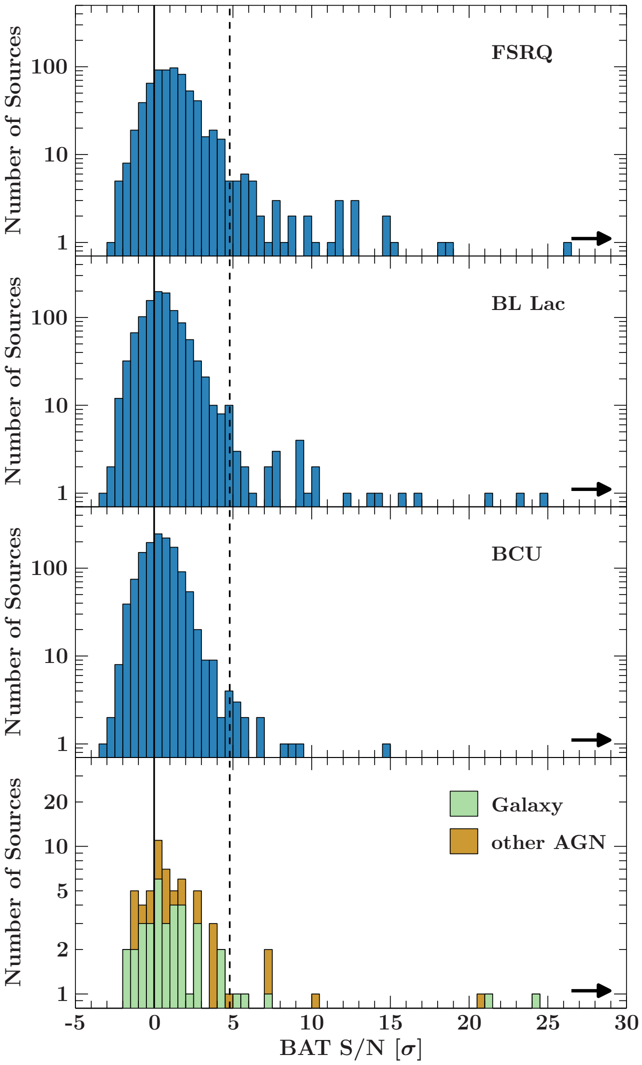

Figure 6.1.1.: BAT S/N distribution of the different sub-types of the 4LAC source sample. The dashed line marks the 4.8 σ threshold of the BAT survey catalog. The black arrows indicate sources brighter that 30 σ that are omitted for better readability.

small minority of the entire sample. Similar to the MOJAVE and TANAMI samples, low-redshift radio galaxies are prominently featured among the X-ray-brightest sample sources. The radio galaxy Centaurus B is featured in the list with an S/N of 21.11 σ. However, the source is spectrally contaminated by the close-by and X-ray-bright Seyfert-1 4U 1344–60. The *Swift*/BAT survey is not capable of resolving both sources because of the low angular separation of approximately 14'. At lower X-ray energies both sources can be imaged separately (e.g., Katsuta et al., 2013, Fig. 5). Since the extracted BAT spectrum of Centaurus B is dominated by 4U 1344–60, only an upper limit can be derived for the flux, that is, $27.61 \cdot 10^{-12}\,\mathrm{erg\,s^{-1}\,cm^{-2}}$.

The hard X-ray analysis of the MOJAVE and TANAMI samples (Chpt. 4 and Chpt. 5) revealed that a substantial part of these radio-loud beamed AGN are detected in the X-ray range, for MOJAVE-1 more so than for TANAMI, as shown by the corresponding S/N and flux distributions. However, only a minor part of both samples has a conservatively high BAT S/N value of 5 σ, that is 32/135 (23.7%) and 16/126 (12.7%), respectively. Compared to this, the 4LAC sample only features 97/3207 sources above this limit, equal to 3.0% of all sources. Although, it has to be taken into account, that MOJAVE and TANAMI monitor

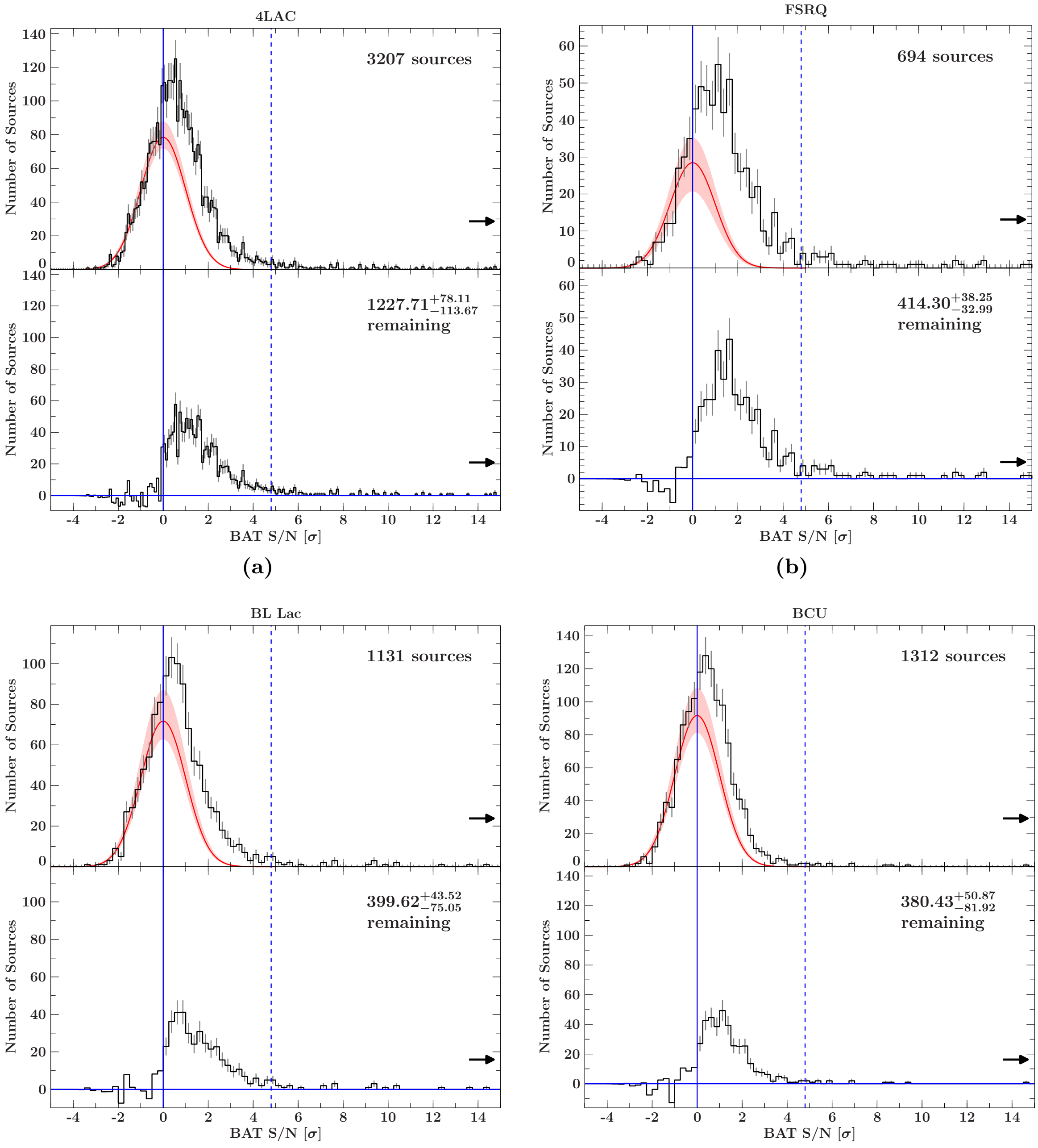

(a) (b) (c) (d)

Figure 6.1.2.: Distribution of the BAT S/N values for the entire 4LAC sources sample, and the different blazar sub-types. The graph is truncated at 15 σ. The top panels of each graph depict the respective S/N distribution with a Gaussian curve fitted to the negative side, centered at 0 σ and with a width of 1 σ (red line, shaded area for 3 σ uncertainty range). All lower panels show the S/N distributions after the subtraction of the fitted Gaussian. The dashed lines indicate the BAT catalog threshold of 4.8 σ.

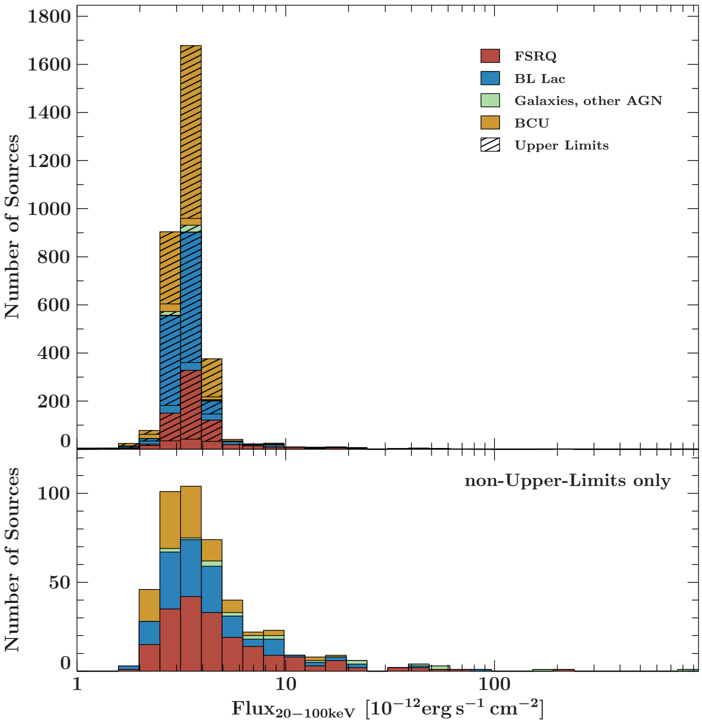

Figure 6.1.3.: Distribution of the hard X-ray flux (20 keV – 100 keV) of the 4LAC sample. Top: complete sample including the large number of upper-limit values. Bottom: non-upper-limit values only.

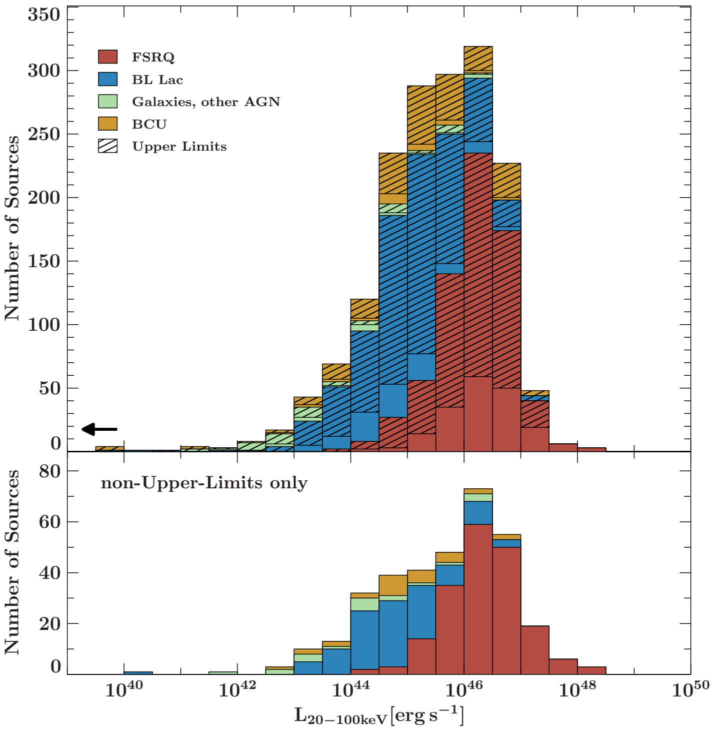

Figure 6.1.4.: Distribution of hard X-ray luminosity (20 keV – 100 keV) of the 4LAC sample. Top: all sources with redshift information (1695), bottom: all sources with redshift information that are not upper-limits in the BAT band (345). The plot range is truncated at 10^{39} erg s^{-1} for better readability, omitting two sources, the BCU 4FGL J0654.0–4152 at $1.97 \cdot 10^{36}$ erg s^{-1}, and the BL Lac 4FGL J0719.7–4012 at $9.33 \cdot 10^{36}$ erg s^{-1}.

Table 6.1.1.: The 20 X-ray-brightest sources in the 4LAC sample.

4FGL Name[a]	Common Name	S/N[b]	$F_{20-100\,\mathrm{keV}}$[c]	Type[d]	SED Type[e]
J1325.5–4300	Cen A	606.89	813.08 ± 1.7	G	LSP
J1229.0+0202	3C 273	192.14	240.34 ± 1.67	Q	LSP
J1413.1–6519	Circinus galaxy	145.91	176.17 ± 1.52	Sey	
J1104.4+3812	Mkn 421	120.3	80.24 ± 1.28	B	HSP
J2253.9+1609	3C 454.3	55.05	74.41 ± 1.6	Q	LSP
J0418.2+3807	3C 111	41.58	58.15 ± 1.67	G	LSP
J0433.0+0522	3C 120	41.55	57.85 ± 1.71	G	LSP
J2151.8–3027	PKS 2149–306	32.8	52.03 ± 1.83	Q	LSP
J1653.8+3945	Mkn 501	48.98	44.38 ± 1.33	B	HSP
J1833.6–2103	PKS 1830–211	26.05	44.22 ± 1.47	Q	LSP
J0319.8+4130	NGC 1275	58.5	41.85 ± 1.53	G	LSP
J0841.3+7053	4C +71.07	37.53	40.73 ± 1.38	Q	LSP
J1512.8–0906	PKS 1510–089	18.75	35.9 ± 1.8	Q	LSP
J1656.3–3301	2MASS J16561677–3302127	18.43	33.35 ± 1.45	Q	LSP
J1346.3–6026	Cen B	21.11	$< 27.61\dagger$	G	LSP
J0336.4+3224	NRAO 140	15.42	23.76 ± 1.66	Q	LSP
J0519.6–4544	Pictor A	24.11	23.23 ± 1.36	G	LSP
J0550.5–3216	PKS 0548–322	24.59	21.89 ± 1.42	B	HSP
J0522.9–3628	PKS 0521–36	20.92	20.91 ± 1.39	AGN	LSP
J2202.7+4216	BL Lac	16.9	20.64 ± 1.4	B	LSP

Notes. (a) Name listed in 4FGL catalog, (b) *Swift*/BAT S/N (14 keV – 150 keV), (c) hard X-ray flux in $10^{-12}\mathrm{erg\,s^{-1}\,cm^{-2}}$, (d) Classification from 4FGL catalog (Abdollahi et al., 2020) Q: Flat Spectrum Radio Quasar, B: BL Lac, BCU: Blazar candidate of uncertain type, G: radio galaxy, Sey: Seyfert, NLSY1: Narrow-Line Seyfert-1, CSS: Compact Steep Spectrum radio source, AGN: non-blazar active galaxy, (e) SED classification from the 4LAC catalog (Ajello et al., 2020), † upper-limit value because of spectral contamination of nearby source.

a relatively small sample of the radio-brightest sources in the sky, whereas the *Fermi*/LAT catalog provides a deeper survey of a much larger sample, accessing many more sources that have not been detected previously in the GeV band due to low flux. In any case, the gamma-ray-bright 4LAC sample includes many sources that are also X-ray bright, but make out a tiny percentage of the total sample, making it a viable resource for hard X-ray studies while probably suffering a gamma-ray selection bias. Radio-bright samples on the other hand have proven as a more reliable if not ideal basis for the study of blazar's hard X-ray characteristics. The LAT survey is less optimal for detecting low-peaked blazars, which have their HE peak in or near the MeV band. FSRQs that are very luminous and are located at high redshifts (MeV blazars, see discussion in Sect. 4.2.2) are usually bright at X-rays. The MOJAVE survey on the other hand also includes gamma-ray-faint sources which tend to have low-peaked SEDs.

The hard X-ray luminosity distribution for the 4LAC sample is presented in Fig. 6.1.4. Since the large number of upper-limit flux values and due to the fact that only for about half of the 4LAC sample a redshift is reported (Ajello et al., 2020), the number of viable luminosity values is also relatively small. The figure displays all 345 resulting non-upper-limit values (bottom panel) and all 1695 luminosities including upper limits (top panel), omitting two sources at unusually low luminosites, the BCU J0654.0–4152 and the BL Lac J0719.7–4012 (see below). The distribution and location of the individual source types is very similar to the MOJAVE and TANAMI samples, with the FSRQs being most luminous, followed by the BL Lacs, and then, radio galaxies and other AGN. Like for the TANAMI sample, BCUs are distributed over most of the occupied range, reaching up to $4.29 \cdot 10^{46}\,\mathrm{erg\,s^{-1}}$ (J1418.4+3543). Comparing the luminosities (non-upper-limits) of the different sub-types of the MOJAVE-1.5 and 4LAC samples using a 2-sample KS test does not indicate a significant difference of the distributions. It cannot be stated that FSRQs ($p = 0.87$) and BL Lacs ($p = 0.90$) are drawn from different parent distributions when comparing the radio- and gamma-ray-selected blazar samples.

The most luminous FSRQs are all high-redshift sources, with the most luminous source J2151.8-302 (PKS 2149–306, $z = 2.35$, $L = (1.26 \pm 0.04) \cdot 10^{48}$), then J1833.6–2103 (PKS 1830–211, $z = 2.51$), and J0841.3+7053 (4C +71.07, $z = 2.22$). The BL Lac with the highest luminosity is J0208.5-0046 (PKS 0205–010, $z = 2.03$, $L = (9.9 \pm 3.0) \cdot 10^{46}$), being also a source with a high redshift, especially among the group of BL Lac sources. Non-blazar AGN, including radio galaxies, are distributed over a wide range of luminosities, reaching $1.70 \cdot 10^{46}\,\mathrm{erg\,s^{-1}}$ with J1829.5+4845, a compact Steep-Spectrum radio source (CSS). In fact, the three most luminous non-blazar AGN in the sample are all sources of the CSS type, while radio galaxies only reach up to $3.91 \cdot 10^{44}\,\mathrm{erg\,s^{-1}}$ (J0312.9+4119), approximately two orders of magnitude below. The very luminous nature of CSS sources in quasars in the (soft) X-ray band has been described in previous works (e.g., O'Dea, 1998, for a review). Two of the three most luminous sources in the data set, J0521.2+1637 and J1459.0+7140, are listed in the 4LAC catalog as CSS sources that are hosted in quasars. The third source, J1829.5+4845, was listed as an SSRQ/CSS source in the 3LAC calalog (Ackermann et al., 2015). The source features a flat spectrum core as well as superluminal motion of the jet on pc scales, which indicates an orientation close to the line of sight, a non-typical case for SSRQs (Ackermann et al., 2015, and references therein). Also, all CSS sources in the 4LAC sample show gamma-ray luminosities that are at least two orders of magnitude larger than those from radio galaxies, and therefore well compatible with the typical luminosites of blazars. Blazar candidate sources (BCUs) are distributed rather like the BL Lacs, whereas the most luminous among those, J1418.4+3543 and J2318.2+1915 are located in a luminosity range that is dominated by FSRQs, making this classification more likely than a BL Lac.

Two sources that show extraordinarily low emission and for which only upper-limit luminosity values could be determined are the BCU J0654.0–4152 at $1.97 \cdot 10^{36}\,\mathrm{erg\,s^{-1}}$ ($z = 1.7 \cdot 10^{-5}$), and the BL Lac J0719.7–4012 at $9.33 \cdot 10^{36}\,\mathrm{erg\,s^{-1}}$ ($z = 3.7 \cdot 10^{-5}$). The redshift of the former source in the 4LAC catalog (Lott et al., 2020) was taken from the 6dFGS DR3 catalog (Jones et al., 2009). Sadler et al. (2014) presented a newly measured redshift value of $z = 0.0908$ and argue that the older value was falsely derived from foreground Galactic absorption lines. Also, the authors classify the source as a FR I radio galaxy. The updated redshift leads to a hard X-ray luminosity for J0654.0–4152 of $6.28 \cdot 10^{43}\,\mathrm{erg\,s^{-1}}$ (upper limit), which is much more compatible with the luminosity distribution of radio galaxies / other AGN. The extremely low redshift value of BL Lac J0719.7–4012 from the 4LAC list is the only measurement available in the literature. Possibly, a similar measurement error like in the case of the former source falsified the given redshift value. The relatively low Galactic latitude ($b = -12°$) points towards a case of source confusion. Furthermore, the BL Lac J0828.3+4152 is characterized by a very low luminosity in both the gamma-ray and X-ray bands, that is $4.92 \cdot 10^{39}\,\mathrm{erg\,s^{-1}}$ and $1.00 \cdot 10^{40}\,\mathrm{erg\,s^{-1}}$, respectively. The most likely explanation is a wrong redshift, which is given as $z = 1.32 \cdot 10^{-3}$ in the 4LAC list (Lott et al., 2020). The referenced counterpart catalog 2WHSP (Chang et al., 2017) only gives estimated lower limits of the object's redshift. In another study, Kapanadze (2013) referenced the object's

Sub-sample	S/N	$\langle\Gamma\rangle$	$\langle\Gamma\rangle^{a}_{\text{weighted}}$	sources
FSRQ	all	1.58 ± 0.03	1.69 ± 0.01	189
	$< 50\,\sigma$	1.58 ± 0.03	1.54 ± 0.03	187
	$< 10\,\sigma$	1.58 ± 0.03	1.60 ± 0.06	171
	$< 5\,\sigma$	1.56 ± 0.04	1.54 ± 0.08	144
BL Lac	all	1.83 ± 0.05	2.49 ± 0.03	144
	$< 50\,\sigma$	1.82 ± 0.05	2.21 ± 0.04	143
	$< 10\,\sigma$	1.77 ± 0.05	1.87 ± 0.08	132
	$< 5\,\sigma$	1.73 ± 0.05	1.71 ± 0.11	120
BCU	all	1.61 ± 0.05	1.75 ± 0.08	132
	$< 50\,\sigma$	1.61 ± 0.05	1.75 ± 0.08	132
	$< 10\,\sigma$	1.61 ± 0.05	1.68 ± 0.09	131
	$< 5\,\sigma$	1.58 ± 0.05	1.58 ± 0.12	121

Notes. [a] The weighting is performed using the photon index uncertainty. Brighter sources with smaller uncertainties are weighted more.

Table 6.1.2.: Mean values of the BAT photon indices of the 4LAC blazars (only fitted source spectra).

redshift as $z = 0.226$, which is much more typical for a BL Lac type source. This would bring the gamma-ray and X-ray luminosity values to $1.96 \cdot 10^{44}\,\mathrm{erg\,s^{-1}}$ and $3.50 \cdot 10^{44}\,\mathrm{erg\,s^{-1}}$, being much more compatible with the rest of the BL Lac distribution.

The distribution of the X-ray photon indices of all fitted source spectra is shown in Fig. 6.1.5. The brightest radio galaxies and non-blazar AGN are located around $\Gamma = 2$. This result is in accordance with the radio-selected samples in the previous Chpt. 4 and Chpt. 5, which fits the concept of the blazar envelope, presented by Meyer et al. (2011); see the discussion in Sect. 5.1. The blazar classes occupy a wide range of indices, with mean values around 1.6 – 1.9. Weaker sources ($\mathrm{S/N} < 4\,\sigma$) are marked by the hatched areas. Sources with lower signal strength and lower counts per spectrum consequently show higher uncertainties in the fitted parameters of flux and photon index[2]. Hence, the very hard and very faint ends of the photon index distribution are dominated by fainter sources, whose true values likely are more in line with the rest. Compared to the MOJAVE and TANAMI samples the distribution of the larger 4LAC sources is generally broader because of this factor. Furthermore, the distribution of BL Lacs notably extends to higher indices around $\Gamma = 3$ compared with the radio-selected samples. These sources with softer spectra are, for the most part, high-peaked BL Lacs, whose declining SED synchrotron component coincides with the hard X-ray band, producing the soft index (see also the discussion in Sect. 6.1.3). A 2-sample KS test of the FSRQ photon index distributions of the MOJAVE-1.5 and 4LAC samples shows that both do not have the same parent distribution ($p = 2.33 \cdot 10^{-7}$), as is the case for the BL Lacs ($p = 0.005$). Excluding the fainter sources ($\mathrm{S/N} < 4$) from the tests still shows the same trend, with $p = 1.25 \cdot 10^{-3}$ and $p = 0.009$, respectively. Although the tests show that both blazar types have on average different spectral shapes depending on the energy regime in which they were selected, this result only applies to the X-ray-bright (fitted) sources, described here, and not necessarily the entire blazar samples. This is especially significant in the case of the 4LAC sample, where 84% of all sources are not bright enough for a spectral fit, and therefore ignored.

The mean values of the photon index of all blazar sub-types in the sample are reported

---

[2] The figure includes all sources that are fitted but have flux resulting upper limits. All sources with $\Gamma < 0.25$ fall into this category.

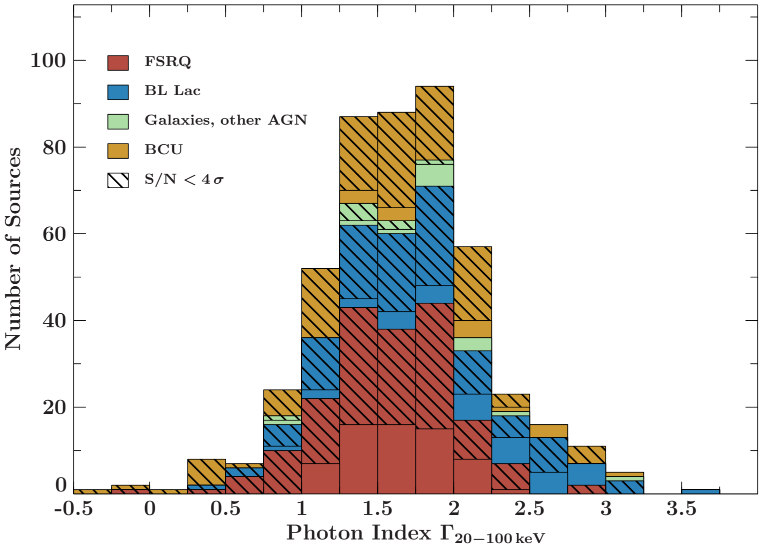

Figure 6.1.5.: Distribution of the hard X-ray photon indices (20 keV − 100 keV) of the fitted sources in the 4LAC sample. The hatched areas mark fainter sources (S/N $< 4\,\sigma$). Sixteen sources at unusually high and low photon indices outside of the plot range are omitted (see text).

in Table 6.1.2, as well as the weighted means, which are derived using the uncertainties of the photon index values. The means are relatively consistent for different ranges of source brightness (S/N). Interestingly, the weighted mean values show a different behavior, that is, a notable decline of the value for ranges that only include successively fainter sources. This trend is particularly strong for the BL Lacs, where $\langle\Gamma\rangle_{\mathrm{weighted}} = 2.49 \pm 0.03$ for all applicable BL Lacs, and $\langle\Gamma\rangle_{\mathrm{weighted}} = 1.71 \pm 0.11$ for all BL Lacs below $5\,\sigma$. A similar dependency can be observed in the MOJAVE and TANAMI data sets: a combined set of all available photon indices from spectral fitting of the MOJAVE-1.5 sample and the TANAMI M18R sub-sample (107 sources total) also shows on average a decline of the photon index for fainter sources. The weighted index for the FSRQs is 1.73 ± 0.01 and 1.49 ± 0.12 for all sources below $5\,\sigma$. BL Lacs are characterized by 1.74 ± 0.09 and 1.38 ± 0.25, respectively. A more detailed analysis of this aspect is presented in Sect. 6.1.3, where the role of SED peak position and the dependency of emitted flux to spectral shape is discussed.

Besides the bell-shaped distribution of photon indices there are sixteen fitted sources in the 4LAC sample at unusually high and low values, which have been omitted in Fig. 6.1.5 (all fitted parameters are reported in Table A.0.1). The fitting process for these faint sources $(0.1, \sigma - 2\,\sigma)$ resulted in a) very hard indices in the range of -2.6 to -2.0, and b) very soft indices at the maximum allowed parameter range of $\Gamma = 5$. All spectral bins for these sources are characterized by very low counts, which are almost all compatible with 0 within their error ranges. In case a) the last bin or two bins show somewhat increased counts compared to the rest, leading to a rising spectrum and unusually hard (negative) photon indices. The corresponding 90% error ranges of 1.0 – 1.5 suggest that a more canonical photon index is possible. Case b) shows a similar scenario, although with overall low spectral counts except for the first spectral bin, often exhibiting a factor of ≈ 10 difference, leading to a exceptionally high index after fitting. Altogether, a great majority of the total 3207 4LAC sources has corresponding BAT spectra that are characterized by at least one spectral bin with negative counts. It seems likely that of the remaining sources with only positive counts in their spectral bins a small number of sources randomly shows one or two bins with somewhat higher counts, dominating the fit, and creating the observed anomalous indices. As a consequence, the corresponding sixteen photon indices are excluded from all statistical tests.

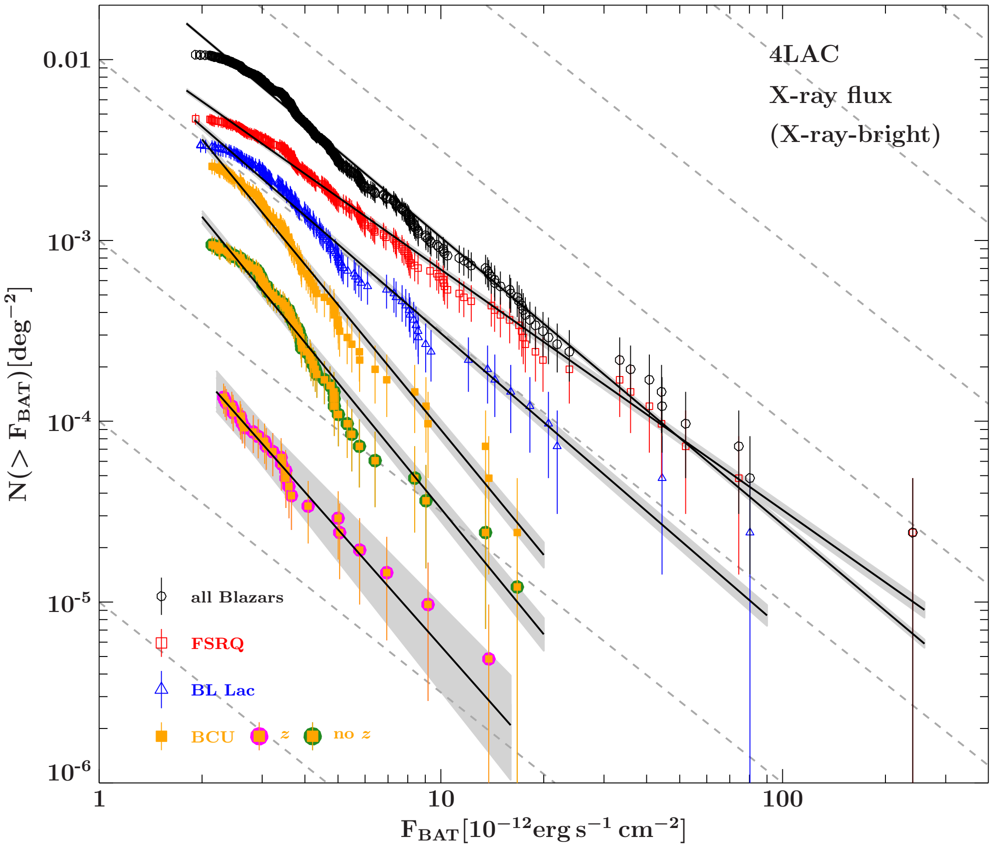

Figure 6.1.6.: log N-log S distribution of 4LAC blazars in the BAT band of 20 keV – 100 keV. Only X-ray-bright sources (non-upper-limits) are graphed. The black lines and gray areas mark the power-law fits and corresponding uncertainty range. For better readability the distribution of BCUs with z information has been been shifted down using a factor of 0.2, and the BCU distribution without z information using a factor of 0.5. The dashed lines indicate a Euclidean slope of $-3/2$.

6.1.2. Number count distibutions: logN-logs

In the source count / log N-log S distribution regions of abundant or missing sources are represented as changes in slope and shape. Comparing the distributions derived from the BAT flux with other different observation windows, for example the available gamma-ray data set, provides an insight to which flux range is dominant at which part of the broadband spectrum, be it by observational selection biases, survey limits, or SED type. The results of the analysis of the distributions and their power-law fits are presented in the following.

Because of the relatively low BAT signal strength of the majority of the 4LAC sample, only a small fraction can be used to determine hard X-ray log N-log S distribution. Figure 6.1.6 shows the distribution for the non-upper-limit blazars in the sample, as well as the individual distributions of FSRQs, BL Lacs, and BCUs. The corresponding power-law fits as well as their uncertainty range are indicated by the black lines and gray areas. The fitting power-law parameters (see Eq. 3.4.3) of the normalization A and the slope α are shown in Table 6.1.3. Similar to the results from the radio-loud MOJAVE samples (Sect. 4.2.3), the shapes of the distributions follow the fitted power law down consistently to the lower flux

Table 6.1.3.: $\log N$-$\log S$ distribution power-law fit results. The fitted distribution of the 4LAC sample (20 keV–100 keV) only includes blazars and sources that do not have an upper-limit flux value.

Sample	Energy band	Flux range $[10^{-12}\mathrm{erg\,s^{-1}\,cm^{-2}}]$	Fitted sources	Normalization A $[10^{-2}\,\mathrm{deg}^{-2}]$	Slope α
4LAC, X-ray-bright$^{(a)}$					
all blazars	BAT	complete range	439	4.03 ± 0.05	1.59 ± 0.01
FSRQ	BAT	complete range	194	1.47 ± 0.03	1.33 ± 0.02
BL Lac	BAT	complete range	139	1.32 ± 0.05	1.63 ± 0.03
BCU	BAT	complete range	106	1.78 ± 0.10	2.30 ± 0.05
BCU (with z)	BAT	complete range	28	$0.39^{+0.09}_{-0.11}$	$2.14^{+0.23}_{-0.25}$
BCU (without z)	BAT	complete range	78	$1.34^{+0.10}_{-0.11}$	2.31 ± 0.07
all blazars	LAT	$3 - 10$	166	1.68 ± 0.04	0.58 ± 0.02
FSRQ	LAT	$3 - 10$	71	0.75 ± 0.04	0.44 ± 0.03
BL Lac	LAT	$3 - 10$	48	0.50 ± 0.04	0.56 ± 0.05
BCU	LAT	$3 - 10$	47	0.59 ± 0.07	1.19 ± 0.08
all blazars	LAT	> 10	183	3.72 ± 0.13	0.89 ± 0.01
FSRQ	LAT	> 10	112	2.39 ± 0.14	0.90 ± 0.02
BL Lac	LAT	> 10	57	0.95 ± 0.09	0.79 ± 0.03
BCU	LAT	> 10	14	$1.40^{+0.75}_{-1.40}$	$1.62^{+0.29}_{-0.34}$
4LAC, all					
all blazars	LAT	$3 - 10$	1353	14.01 ± 0.05	0.97 ± 0.00
FSRQ	LAT	$3 - 10$	307	2.89 ± 0.04	0.64 ± 0.01
BL Lac	LAT	$3 - 10$	497	4.95 ± 0.04	0.88 ± 0.01
BCU	LAT	$3 - 10$	549	9.13 ± 0.11	1.59 ± 0.01
all blazars	LAT	> 10	594	25.80 ± 0.39	1.24 ± 0.01
FSRQ	LAT	> 10	270	8.65 ± 0.25	1.11 ± 0.01
BL Lac	LAT	> 10	250	11.44 ± 0.40	1.25 ± 0.01
BCU	LAT	> 10	74	29.05 ± 5.72	2.19 ± 0.08

Notes. $^{(a)}$ Non-upper-limits for the fluxes in the BAT band.

end of $(2 - 3) \cdot 10^{-12}\mathrm{erg\,s^{-1}\,cm^{-2}}$, where they level off.

The slope of the distributions of all blazar types are significantly different from each other, however, and none of them are consistent with $-3/2$, indicating that they are not equally distributed for a Euclidean geometry. The FSRQs exhibit a particularly flat slope of $\alpha = 1.33 \pm 0.02$, whereas the BL Lacs are characterized by a notably steep slope of $\alpha = 1.63 \pm 0.03$. Also, the distribution of BL Lacs shows a scarcity of sources in the intermediate flux band of approximately $(5 - 7) \cdot 10^{-12}\mathrm{erg\,s^{-1}\,cm^{-2}}$, which could as well be a simple statistical fluctuation that is emphasized by the already low number of sources in this flux band. Generally, the slopes indicate that BL Lacs have a relatively low amount of high-flux sources compared to FSRQs and/or a low amount of low-flux sources in case of the FSRQs.

Extrapolating the power-law fits of the FSRQ and BL Lac distributions shows that the source density of both classes becomes equal at approximately $F = 7 \cdot 10^{-13}\mathrm{erg\,s^{-1}\,cm^{-2}}$. The steepest slope in the sample is given by the BCUs, which, although not an AGN class in a strict sense, have a disproportionally high fraction of low-flux sources. At a flux of around $F = 1.2 \cdot 10^{-12}\mathrm{erg\,s^{-1}\,cm^{-2}}$ the (extrapolated) distribution would match the source density of the FSRQs. However, the large number of BCUs at very low fluxes is also often a result of a more difficult classification of a source using spectral features due to poor data quality because of a low photon count / low flux to begin with. Graphing the distributions of BCUs that have a known redshift and those without redshift information separately shows similar slopes but notable differences in shape. While the BCUs with redshift information form a distribution that is rather consistent towards lower fluxes, the distribution for the sources without any redshift association exhibits a relatively uneven shape, including a prominent hump at lower fluxes similar to the BL Lacs. The steep slope of the distribution, especially around $(3-4) \cdot 10^{-12}\mathrm{erg\,s^{-1}\,cm^{-2}}$, and the fact that no redshift is available, as is often the case for BL Lacs due to the lack of spectral features, implies a high probability that a significant fraction of this BCU sub-sample is composed of BL Lacs. The brighter part of the full BCU's $\log N$-$\log S$ distribution shows a flatter slope, more compatible with FSRQs. Overall, this gradual division seems plausible when comparing the S/N characteristics of both blazar classes, showing that the FSRQs of the 4LAC sample are notably brighter than BL Lacs in the observed hard X-ray band.

The slope found for the $\log N$-$\log S$ distribution of the MOJAVE-1 blazars is similarly flat ($\alpha = 1.13 \pm 0.04$, Sect. 4.2.3) as the slope of the 4LAC's FSRQ distribution, although not compatible within the uncertainties. Since both (sub-)samples are mainly composed of low-peaked blazars, it is suggested, that the source's synchrotron peak frequency is an important contributor to the shape of the $\log N$-$\log S$ distribution of a given sample. This aspect is discussed further in Sect. 6.1.3.

Figure 6.1.7 presents the $\log N$-$\log S$ distributions of the 4LAC sample that are derived from the flux data of the 0.1 GeV − 100 GeV LAT band (Abdollahi et al., 2020), both for the full sample (top) and only for sources that are X-ray-bright (bottom). Compared to the previous results in the BAT band (Sect. 4.2.3 and Sect. 5.2.1) the graph for the full sample shows a number of notable differences. The distributions are not well fit using a single power-law[3], because they exhibit a continuous flattening, most notably below $\approx 10^{-11}\mathrm{erg\,s^{-1}\,cm^{-2}}$ and then again on the low flux end, saturating below $\approx (2-3) \cdot 10^{-12}\mathrm{erg\,s^{-1}\,cm^{-2}}$. In order to describe the distributions, two separate power laws are fitted: one in the range of $(3-10) \cdot 10^{-12}\mathrm{erg\,s^{-1}\,cm^{-2}}$, and a second power law for all fluxes larger than $10^{-11}\mathrm{erg\,s^{-1}\,cm^{-2}}$[4]. The aforementioned low-flux region where distributions saturate are omitted. The resulting fitting parameters are also presented in Table 6.1.3. With the exception of the BCUs all distributions have extremely flat slopes with $\alpha < 1$ for the low-flux interval, especially FSRQs with $\alpha = 0.64 \pm 0.01$. The high-flux part of the distributions is generally steeper, but still lower than $\alpha \approx 1.3$, except BCUs. At the high-flux end, the order of all graphed distributions equals the results of the BAT data. The predicted crossing of the distributions of the sub-types at low fluxes in the BAT data set can indeed be observed in the gamma-ray data set. The fact that the gamma-ray $\log N$-$\log S$ distributions are poorly fit with a single power-law suggests that the pictured gamma-ray-bright blazar populations are not uniformly distributed in space, at least less so than for the observed hard X-ray band.

---

[3] A power-law fit of the entire blazar $\log N$-$\log S$ distribution results in a reduced χ^2 value of 36.11. Fitting all fluxes above $3 \cdot 10^{-12}\mathrm{erg\,s^{-1}\,cm^{-2}}$ gives a reduced χ^2 value of 1.81.

[4] The reduced χ^2 values for power-law fits of the distribution of all blazars are 0.30 and 0.33 for the low-flux and high-flux interval, respectively.

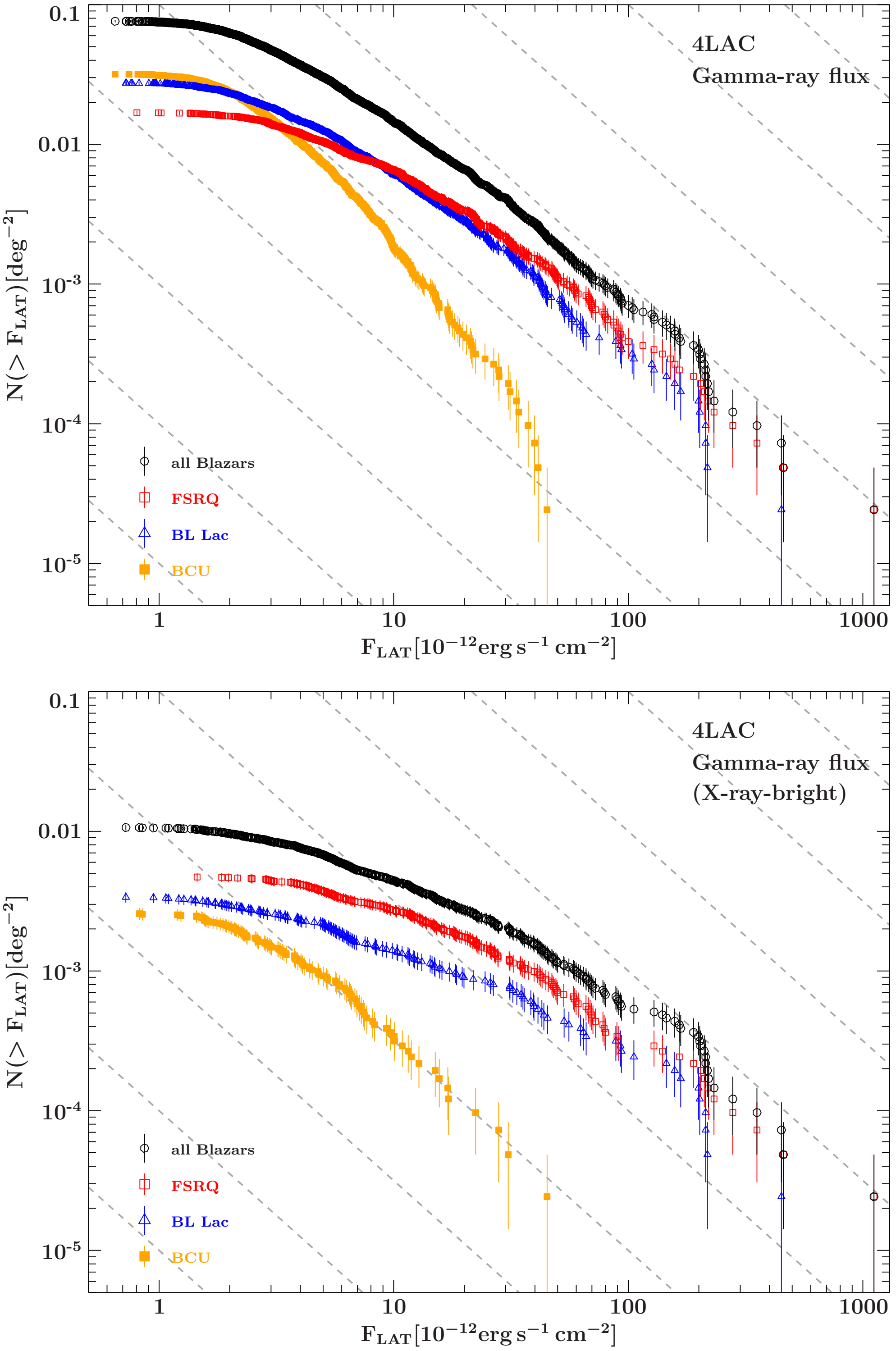

Figure 6.1.7.: log N-log S distribution of 4LAC blazars in the LAT band of 0.1 GeV – 100 GeV. Top: all blazars from the 4LAC sample, bottom: only X-ray-bright sources (BAT non-upper-limits). Power-law fits (see text) have been omitted in the plots for better readability. The dashed lines indicate a Euclidean slope of $-3/2$.

These results are for the most part in accordance with a recent study by Marcotulli et al. (2020), who analyzed the first eight years of *Fermi*/LAT survey data in the 100 MeV – 1 TeV band, paying special attention to survey and data analysis biases. The authors derived the gamma-ray $\log N$-$\log S$ distribution for point sources above the Galactic plane ($|b| > 20°$), which are heavily dominated by blazars. By using detailed Monte Carlo simulations of the entire gamma-ray sky on the basis of the measurement data, the authors also derived a flux-dependent parameter describing the survey detection efficiency $\omega(S_i)$, corresponding to the flux bin S_i in the $\log N$-$\log S$ distribution. Figure 6, bottom right in Marcotulli et al. (2020) presents the (binned) $\log N$-$\log S$ that is the result of the point-source data extraction and the implementation of the detection efficiency parameter. The $\log N$-$\log S$ of the 4LAC blazars derived here closely follows this distribution, except for the larger variation at the high-flux end as well as the strong saturation on the low-flux end. The latter can be attributed to the detection efficiency, which quickly drops below $\approx 2 \cdot 10^{-12}\mathrm{erg\,s^{-1}\,cm^{-2}}$ (Marcotulli et al., 2020, Fig. 5). The derived slope of the (differential) $\log N$-$\log S$ distribution of $\gamma = 1.96 \pm 0.04$ from Marcotulli et al. (2020) is furthermore compatible with the slope of the low-flux portion of the blazar distribution analyzed here ($\alpha = 0.97$)[5]. Although the value of the slope for $F > 10^{-11}\mathrm{erg\,s^{-1}\,cm^{-2}}$ is higher ($\alpha = 1.24 \pm 0.01$), other factors, like the inclusion of low-altitude sources or the different convention of binning the $\log N$-$\log S$ distribution might be contributors to this discrepancy. In terms of an evolving population of sources, the authors calculate and compare the gamma-ray luminosity functions and state that the model of pure density evolution (PDE) is able to describe the data set best when put against PLE and LDDE models.

Reducing the number of 4LAC sources to the X-ray-bright ones and graphing the $\log N$-$\log S$ of the gamma-ray fluxes again (Fig. 6.1.7, bottom) shows a similar behavior to the X-ray distribution, but with significantly flatter slopes ($\alpha < 1$). Again, the BCUs exhibit a relatively steep slope, which is compatible with an Euclidean distribution for $F_{\mathrm{LAT}} > 10^{-11}\mathrm{erg\,s^{-1}\,cm^{-2}}$, although with large uncertainties ($\alpha = 1.62^{+0.29}_{-0.34}$). The individual distributions do not cross and instead level off at low fluxes. The fact that these distributions are even flatter than in the case of the full gamma-ray data set implies that generally more sources at the lower-flux end are removed. This is also the case for the $\log N$-$\log S$ distribution of the X-ray fluxes, however, only notably for FSRQs. Furthermore, the flattening when only selecting X-ray-bright sources in the gamma-ray $\log N$-$\log S$ is more pronounced for BL Lacs compared to the FSRQs. The fluxes in both energy bands of the 4LAC sample can be characterized as strongly correlated, as shown by a Kendall's τ test[6]. Since BL Lacs / BCUs are on average X-ray-fainter in the BAT data set, the flattening becomes more significant for BL Lacs / BCUs.

To conclude, the $\log N$-$\log S$ distributions of the hard X-ray and gamma-ray bands that have been analyzed in this section show a variety of shapes due to multiple factors like SED peak frequency, different data selection biases, and flux evolution. In the BAT frequency range, using only X-ray-bright blazar sources, FSRQs exhibit a slope that is very much comparable with the MOJAVE-1 $\log N$-$\log S$ distribution in the BAT band, likely because of the similar composition of the samples, that is, low-peaked blazars. BL Lacs show a steeper

---

[5] The derivative of the here applied fit function $N(>F) = A \cdot F^{-\alpha}$ is used in Marcotulli et al. (2020), i.e., $\frac{\mathrm{d}N}{\mathrm{d}S} = K \cdot S^{-\gamma}$, leading to $-\alpha - 1 = -\gamma$

[6] A Kendall's τ correlation test between X-ray and gamma-ray fluxes of all X-ray bright 4LAC blazars returns p-value of 0, and 10^{-10} just for FSRQs, as well as 10^{-3} for BL Lacs.

slope, since this sub-set includes more sources and also intermediate- and high-peaked ones. This context is discussed further in the following Sect. 6.1.3. The log N-log S slopes for the gamma-ray fluxes of the full sample are relatively flat and, again, more so for FSRQs, while the overall very steep slope of BCUs is likely due to the faint nature of many of these sources and the associated difficulty to determine the source type because of the data quality. The observed flattening for all blazar types at lower fluxes can be explained by the declining detection efficiency in the LAT band. A combination of the above factors is present in the case of graphing the gamma-ray log N-log S distribution for only the X-ray-bright sources.

6.1.3. SED type and peak position

In this section the relation of the hard X-ray flux and corresponding BAT photon index (Sect. 6.1.1) is analyzed using the characteristic of source luminosity and SED type. It is tested whether the observed spectral characteristics of the individual blazar types can be attributed to the SED's shape and peak frequency. Figure 6.1.8a shows the behavior of the X-ray-bright blazar types and their spectral slope for different flux bins. While the FSRQs indicate no significant change of the photon index Γ with flux, the BL Lacs exhibit a softer Γ for higher flux bins. The LAT band (Fig. 6.1.8b) shows no such distinctive behavior. Very high- and low-flux FSRQs tend to have somewhat harder indices than the rest. Interestingly, the BCUs show in the gamma-ray band that their spectral slope is on average much more compatible with BL Lacs at low fluxes, and with FSRQs at the high-flux end. The photon indices of the BCUs in the BAT band on the other side follow more closely the FSRQs, with the exception of the second-highest bin. However, the two highest bins only include three sources each and have substantial uncertainties. The tendency of X-ray-bright BL Lacs to have softer spectra could also be the effect of a scarcity of BL Lacs with hard photon indices in the sample. On average, BL Lacs are less X-ray-bright than FSRQs, as demonstrated in the comparison of the corresponding S/N distributions (Fig. 6.1.2).

The log N-log S distribution of the individual blazar types in the sample reveals a significant difference of the slopes of BL Lacs and FSRQs (Sect. 6.1.2, Fig. 6.1.6). The relatively steep slope of the BL Lacs can be interpreted as an abundance of low-flux sources and / or missing high-flux sources. If X-ray-bright BL Lacs are indeed missing in the BAT data set, can this be the result of a systematic luminosity / redshift bias? Figure 6.1.9 shows the luminosity graphed against the flux for the various blazar types for both the BAT data set and the available gamma-ray data from the 4LAC sample. The distribution of FSRQs is notably similar between both energy bands, describing a curved shape from low to high luminosity and flux values. As in the hard X-ray band, the sources accumulate more strongly at the low-flux end. However, the same distributions for the BL Lacs are remarkably different between both bands. While the overall distribution is similar and shifted towards smaller luminosities compared to FSRQs in the case of the gamma-ray data, the shape of the graphed sources in the X-ray band is concentrated at low fluxes and / or luminosities with a sharp border to higher values. It is suggested, that, compared to the FSRQs and BL Lacs in the GeV band, the X-ray-bright BL Lacs suffer from a systematic effect, which excludes sources that are both bright and luminous at the same time. In order to ensure comparability between both the X-ray and gamma-ray data sets in this regard the gamma-ray luminosity is also graphed against the X-ray flux (Fig. 6.1.10, left). The same overall shape is the result, also exhibiting the empty region as before. To test whether this region is created through a redshift-related bias in the analysis, the luminosity is again graphed against the flux for various hypothetical

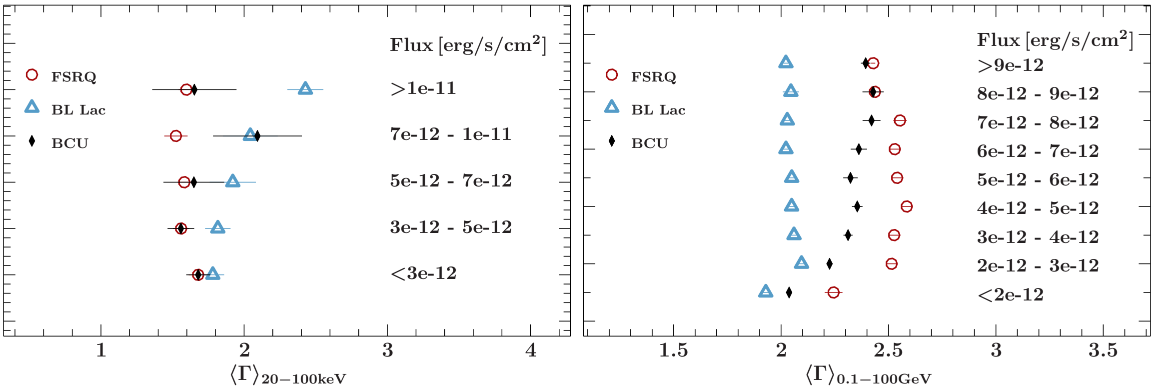

(a) Flux binning **(b)** Flux binning

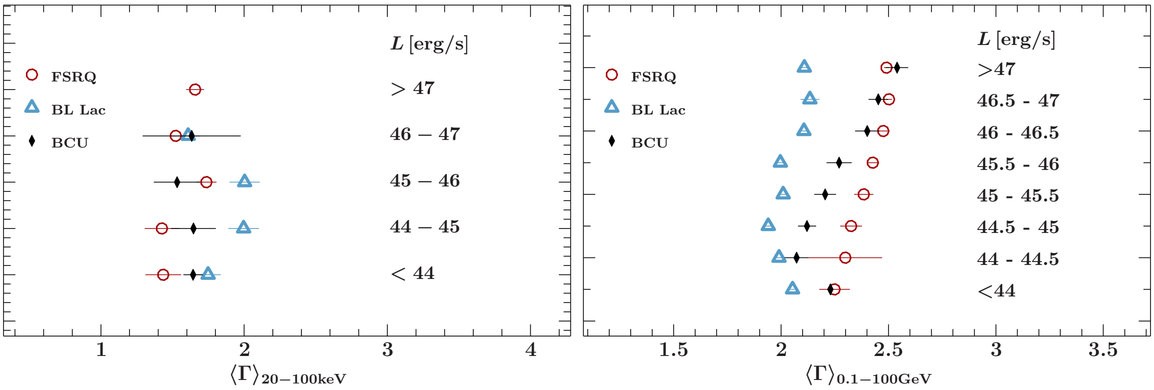

(c) Luminosity binning **(d)** Luminosity binning

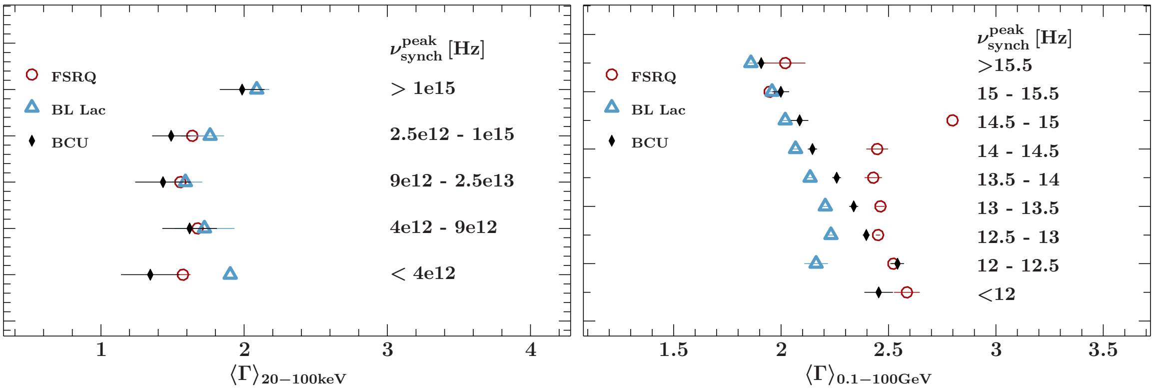

(e) Peak frequency binning **(f)** Peak frequency binning

Figure 6.1.8.: Mean photon index in the hard X-ray band (20 keV – 100 keV, left) and gamma-ray band (0.1 GeV – 100 GeV, right) for bins of flux (top), luminosity (middle), and synchrotron peak frequency (bottom). The photon index range of the figures on the right-hand side are zoomed in slightly to emphasize the trend of the plotted data.

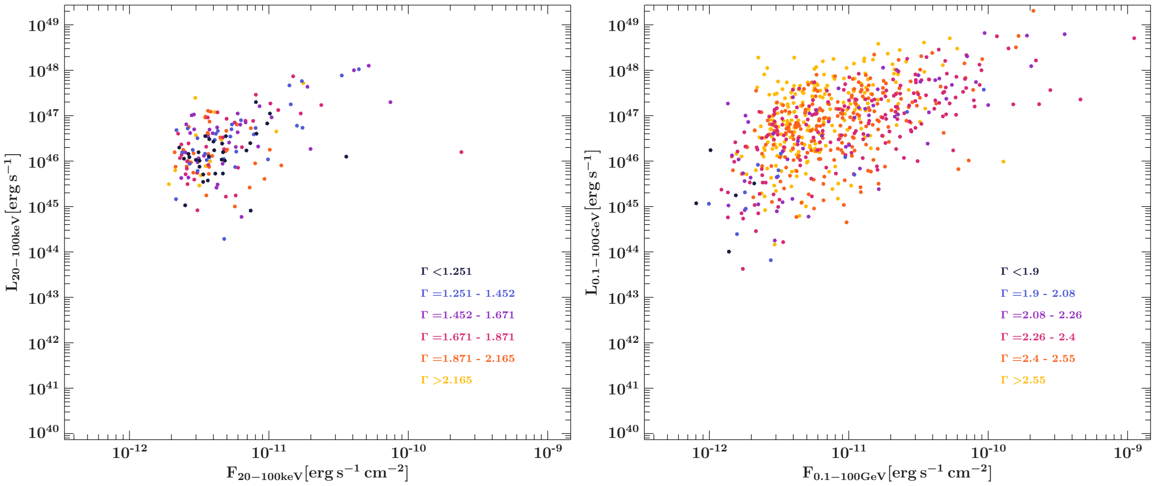

(a) FSRQ **(b)** FSRQ

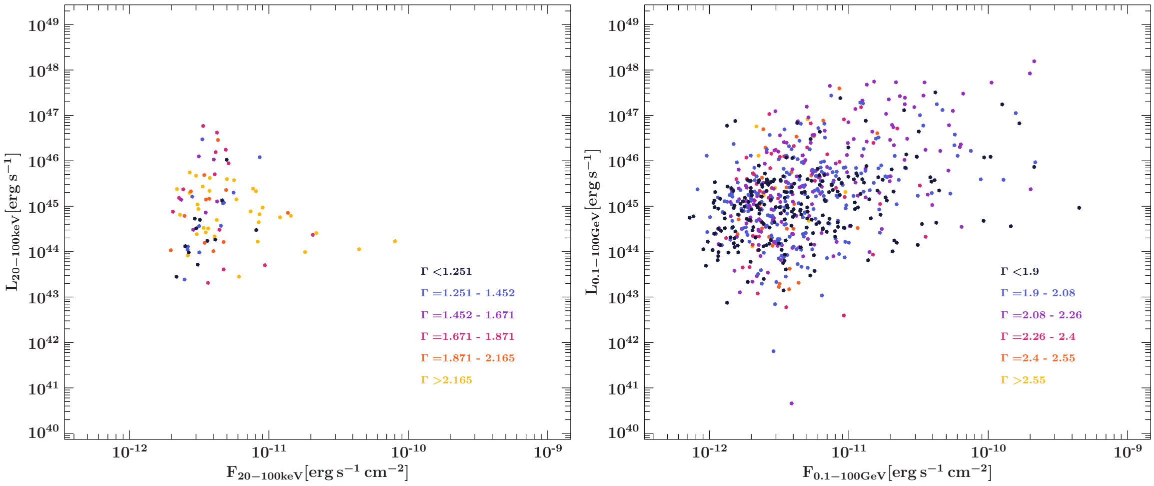

(c) BL Lac **(d)** BL Lac

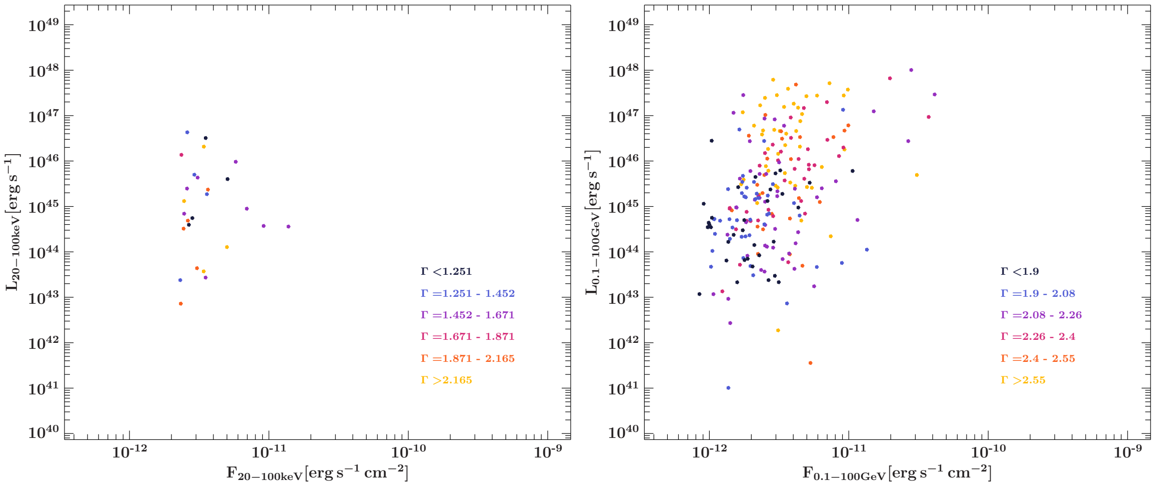

(e) BCU **(f)** BCU

Figure 6.1.9.: Luminosity against flux in the BAT band (left) and LAT band (right) for the blazar types in the 4LAC sample of FSRQs (top), BL Lacs (middle), and BCUs (bottom). The color scales for the photon indices are chosen to divide the complete sets of blazars in either band into bins with equal numbers of sources within.

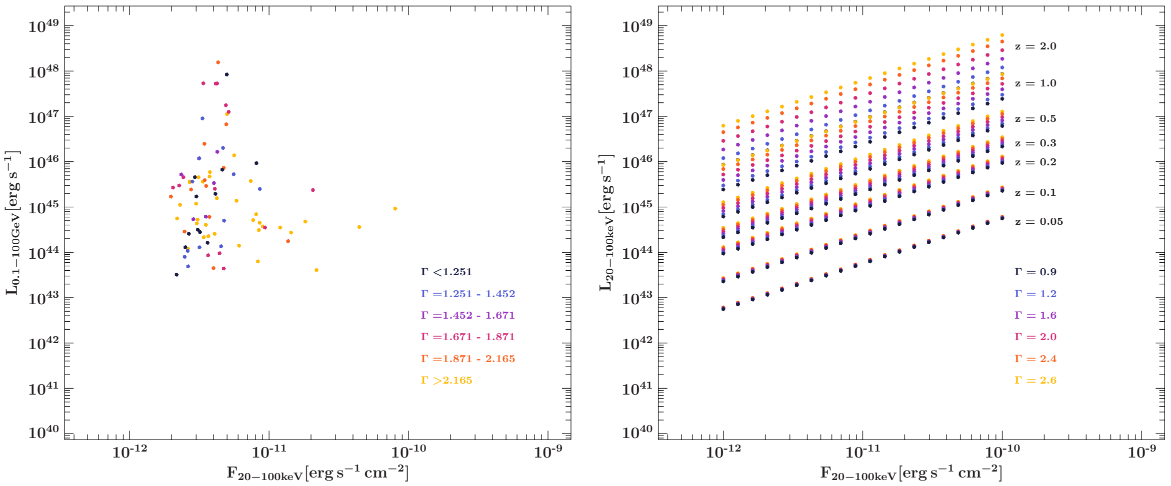

Figure 6.1.10.: Left: luminosity in the LAT band plotted against hard X-ray flux in the BAT band for the X-ray-bright BL Lacs in the 4LAC sample (see text), right: Distribution of luminosity for hypothetical sources at specific values of flux, photon index Γ, and redshift z in the BAT band.

values of source redshift and photon index (Fig. 6.1.10, right). Especially the region for $z \lesssim 1$ would be expected to be covered by BL Lacs, which concentrate at lower values of z, indicated by the mean redshift of all BL Lacs in the 4LAC sample (with redshift information) $\langle z\rangle^{\mathrm{4LAC}}_{\mathrm{BLLac}} = 0.44$. This, although, is clearly not the case. Also, different photon indices do not have a significant impact on the distribution of the hypothetical sources.

Generally, the BAT data of the BL Lacs in the 4LAC sample show that X-ray-bright sources have SEDs that are typically high-peaked, and that faint sources tend to have low-peaked SEDs. In an earlier work by Ghisellini et al. (2017), it has been demonstrated that (gamma-ray-bright) BL Lacs are characterized by a strong anti-correlation of the luminosity and SED synchrotron peak frequency $\nu^{\mathrm{peak}}_{\mathrm{synch}}$. More luminous sources thereby are notably lower peaked compared to cases of lower luminosity. Figure 6.1.11 shows the fitted broadband SEDs from Ghisellini et al. (2017) based on data extracted from the earlier 3LAC source catalog and further archival spectral data. The class of highly luminous low-peaked BL Lacs in this scenario produces on average hard photon indices in the BAT frequency band, observing the rising part of the HE emission bump. The behavior of the SEDs, named the *Fermi* Blazar Sequence by Ghisellini et al. (2017), is in accordance with the here derived data sets for the 4LAC blazars in both energy bands: In the BAT band high-luminosity sources have hard photon indices Γ / a rising spectrum in the $\nu L - \nu$ format, while sources of lower luminosity have a softer Γ, measuring the declining part of the synchrotron bump in case of BL Lacs. The lowest bin ($L < 10^{44}\,\mathrm{erg\,s^{-1}}$) even shows hard indices again, likely indicating the spectral region at even lower frequencies than $\nu^{\mathrm{peak}}_{\mathrm{synch}}$. The characteristic pictured for BL Lacs follows the discussed blazar sequence scheme for luminosities but not for fluxes (Fig. 6.1.8a, 6.1.8c). This supports that sources of a wide variety of redshifts are indeed missing in Fig. 6.1.9c compared to the gamma-ray picture in Fig. 6.1.9d.

The distribution of luminosity-binned gamma-ray photon indices in Fig. 6.1.8d also fits the scenario shown by the fitted SEDs. BL Lacs have somewhat soft photon indices at high luminosity, while the indices get harder for lower luminosity. The lowest bins also exhibit

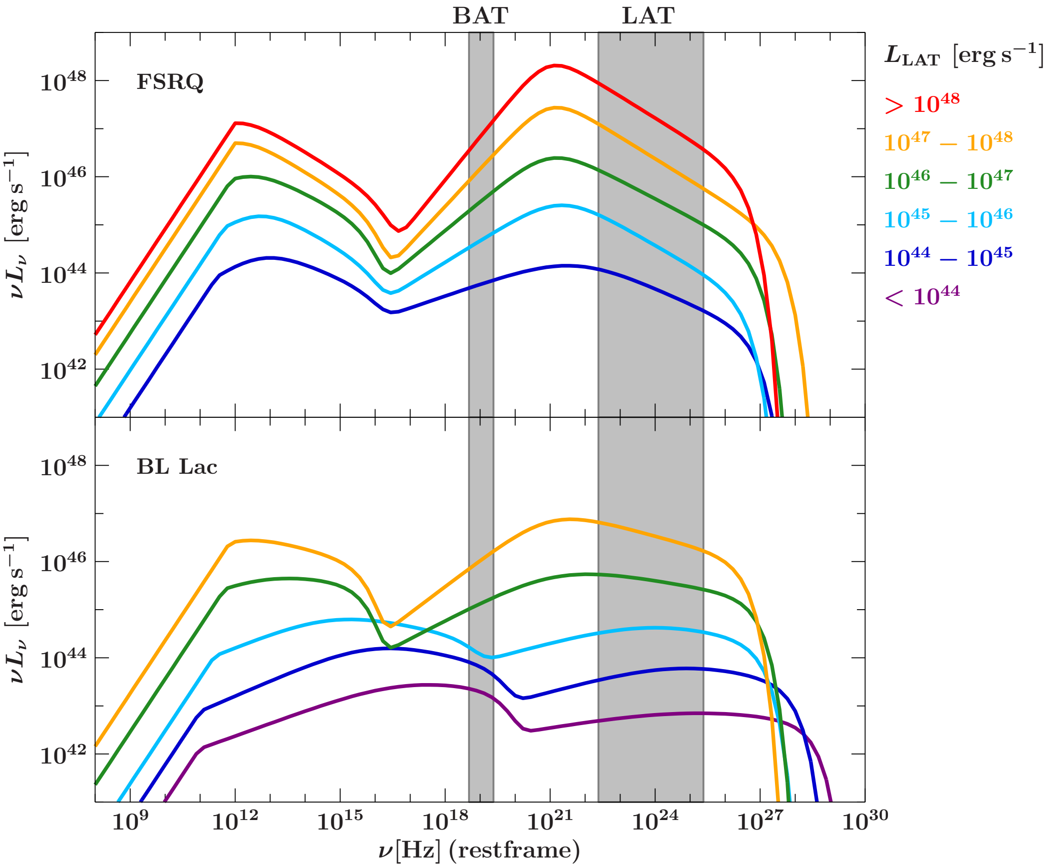

Figure 6.1.11.: Fitted broadband SEDs of gamma-ray-bright blazars after the fitting parameters from Ghisellini et al. (2017). The individual fits are grouped following the gamma-ray (*Fermi*/LAT, 3LAC) luminosity bins, with the labels in erg s^{-1}. The detection ranges of the *Swift*/BAT survey in $(20-100)$ keV and *Fermi*/LAT in $(0.1-100)$ GeV are marked accordingly.

higher values. Much more consistent is the characteristic of the FSRQs in the LAT band, which show a clear correlation of luminosity and photon index value, which increases (gets steeper in the SED). A distinct trend of the FSRQs or BCUs in the BAT band in terms of luminosity bins cannot be recognized.

Especially for the group of BL Lacs, the characteristic of photon index to $\nu_{\mathrm{synch}}^{\mathrm{peak}}$ (Fig. 6.1.8e, Fig. 6.1.8f) is relatively discernible as well as consistent with the *Fermi* Blazar Sequence in both energy bands. In the BAT band the sources with the lowest peak frequencies have almost a flat slope ($\Gamma \approx 2$), indicating the near-peak region of the HE bump. BL Lacs with higher peak frequencies coincide with the rising part of the same SED component, resulting in a harder index ($\Gamma < 2$). The sources with the highest peak frequencies again feature softer indices, marking the near-peak region of the synchrotron bump. BL Lacs show an inverted behavior in the LAT band, which is solely governed by the HE component, producing hard indices for high-peaked sources and vice versa. The lowest peak frequency bin indicates a turn of the trend. However, the relatively low number of twelve sources in the this bin could skew the result. Analog to their relatively static SED, FSRQs show only a small change in the photon index with varying peak frequency, being somewhat steeper for lower-peaked sources and flatter for higher-peaked sources. The outliers at very high peak frequencies are likely due to the low number of sources in those bins, with only four sources in the highest bin, and only one source in the next two bins each. The group of BCUs fall in-between both main source classes, and are more FSRQ-like in the case of SEDs with the lowest peak frequencies.

In order to estimate the influence of the SED type and its broadband spectral features towards the X-ray detection statistic, the distribution of $\nu_{\rm synch}^{\rm peak}$ is discussed in the following. Figure 6.1.12 presents the peak frequency distribution for all blazar sub-types of the 4LAC sample. Additionally, the distributions of all corresponding X-ray-bright sources are displayed. Both BL Lacs and BCUs occupy a wide range of synchrotron peak values while FSRQs are typically located at low values around $10^{12}\,{\rm Hz} - 10^{14}\,{\rm Hz}$, with few exceptions[7]. Although more FSRQs are X-ray-bright compared to BCUs, in both cases the total and X-ray-bright distributions are not significantly different from each other, as indicated by 2-sample KS-tests ($p_{\rm FSRQ} = 0.22$, $p_{\rm BCU} = 0.23$). The picture for BL Lacs is notably different. The total and X-ray-bright distributions do most likely not originate from the same parent distribution ($p_{\rm BLLac} = 1.9 \cdot 10^{-3}$). It can be stated that the group of *Swift*/BAT-detected BL Lacs is not randomly drawn from the gamma-ray-bright 4LAC sample. Where the peak frequencies of the total number of BL Lacs describe a bell-shaped distribution, the X-ray-bright sub-sample is relatively flat. The biggest difference between both distributions can be located at intermediate frequencies of approximately $10^{14}\,{\rm Hz} - 10^{16}\,{\rm Hz}$ and at the very low end.

Figure 6.1.13 shows the X-ray-bright BL Lac sub-set and the corresponding percentage of missing sources relative to the complete set of BL Lacs in the sample. Approximately 95% of sources are missing in the intermediate region, falling off to ≈ 80% towards the low-peaked end and as low as 50% – 60% for high-peaked sources. This asymmetry again expresses the relative scarcity of low-peaked BL Lacs, which, following the model SEDs, would also be characterized by high luminosity and a hard spectrum. BL Lacs, which have rather extreme (high) peak frequencies, are detected more easily in the *Swift*/BAT survey. A likely explanation for the clear scarcity of intermediate-peaked X-ray-bright BL Lacs is the spectral gap region between both broad emission bumps in the SEDs. The corresponding frequency band of $\nu_{\rm synch}^{\rm peak} \approx 10^{14}\,{\rm Hz} - 10^{16}\,{\rm Hz}$ matches the fitted SEDs in Fig. 6.1.11, namely the cyan-colored curve ($L_\gamma = (10^{45} - 10^{46})\,{\rm erg\,s^{-1}}$), and consequently SEDs with slightly lower peak frequencies. Hence, a more suitable way of classifying a wide range of BL Lacs in the context of X-ray surveys would not be the peak, but the spectral gap frequency, leading to low-, mid-, and high-gap sources. Since a substantial part of the catalog's BL Lacs could be classified as mid-gap sources, hard X-ray surveys seem not especially well suited for comparative population studies in this regard.

Although the presented data are consistent with the model SEDs that have been derived in the study of Ghisellini et al. (2017), the issue of missing X-ray-luminous BL Lacs persists. The distribution of synchrotron peak frequencies (Fig. 6.1.12, Fig. 6.1.13) indicates that low- and intermediate-peaked BL Lacs are strongly underrepresented compared to high-peaked sources. In order to test the source sample for flux-related selection biases in the X-ray band, it is useful to graph the previous model SEDs in a νF_ν display against frequency ν instead

---

[7] The FSRQ 4FGL J1557.9–1404 (PKS 1555–140) has an exceptionally high synchrotron peak frequency of $1.5 \cdot 10^{18}\,{\rm Hz}$. However, the source also has an unusually low redshift of $z = 0.097$, which is more in line with a radio galaxy or BL Lac. The source has been cited as a radio galaxy or member of a galaxy group in a number of studies (e.g. Véron-Cetty & Véron, 2006; Healey et al., 2008; Tempel et al., 2016)

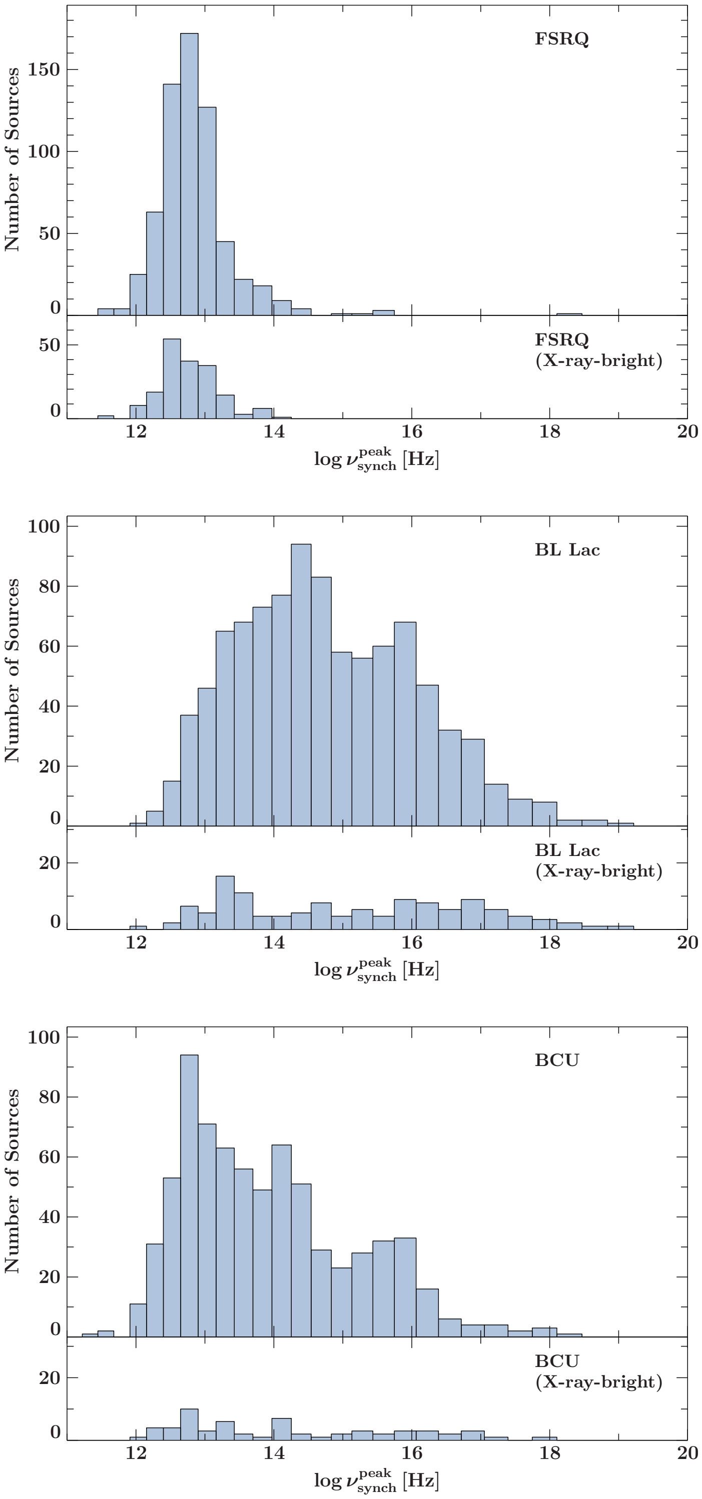

Figure 6.1.12.: Distributions of the synchrotron peak frequency of the 4LAC blazars for all sources with available frequency measurements (Ajello et al., 2020). The lower panels show the X-ray-bright sources (non-upper-limits) within the same sub-set.

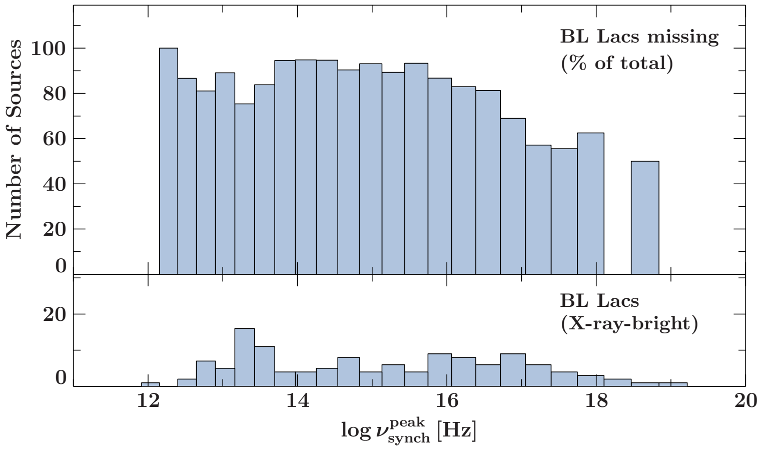

Figure 6.1.13.: Distribution of the synchrotron peak frequencies of the X-ray-bright 4LAC BL Lacs for all sources with available frequency measurements. Top: percentage of missing sources compared to the total number of BL Lacs in Fig. 6.1.12. Bottom: absolute numbers. Frequencies are taken from Ajello et al. (2020).

of νL_ν. Figure 6.1.14 (top) shows the same SEDs as in Fig. 6.1.11, with the flux values derived from the median redshift values in each corresponding luminosity bin. The middle panel presents a zoomed-in version of the BAT band (νF_ν). The bottom panel shows the same data as in the middle panel, but with only the flux per frequency interval as a function of frequency (F_ν). The plots reveal an asymmetry of flux / power output for the different L_{LAT} bins regarding high- versus low-peaked sources. In order to incorporate the different numbers of sources in each bin an additional curve is introduced. In the middle and bottom panels the dashed lines indicate the flux equivalent that is derived from the tenth-lowest redshift in each L_{LAT} bin. Since the source numbers per bin can differ greatly, these lines indicate the upper region (brightest) of all curves in this bin[8]. At the approximate detection limit for sources in the *Swift*/BAT survey of $(3-4)\cdot 10^{-12}\,\mathrm{erg\,s^{-1}\,cm^{-2}}$, most of the sources in the L_{LAT} bins larger than $10^{45}\,\mathrm{erg\,s^{-1}}$ are not registered detections (upper-limits). While the detection limit is just below the dashed lines and above the median curves of the lower two L_{LAT} bins (high-peaked), the dashed lines of all higher L_{LAT} bins (intermediate and low-peaked) are below the limit or just barely intersecting it. The covered flux of the dashed lines in the BAT band in the three higher L_{LAT} bins is roughly 50% of that of the two lower L_{LAT} bins, which cover around $(4-8)\cdot 10^{-12}\,\mathrm{erg\,s^{-1}\,cm^{-2}}$.

An abundance of BL Lacs with high L_{BAT} values is initially expected from the SEDs of gamma-ray-bright sources (Fig. 6.1.11), which is not observed. The SED's spectral gap region as well as the relatively low flux output in the BAT band for low-peaked sources (Fig. 6.1.14) is able to explain at least qualitatively the observed scarcity of this source class in the *Swift*/BAT data set. Compared to the radio-loud and predominantly low-peaked MOJAVE and TANAMI samples the gamma-ray-selected 4LAC sample is overall fainter in the hard X-ray range. Although the 4LAC catalog also incorporates a sizable fraction of low-peaked blazars, only a relatively small number of sources, especially BL Lacs and BCUs, show a strong BAT signal. Low-peaked FSRQs do not exhibit a strong $\nu_{\mathrm{synch}}^{\mathrm{peak}} - L_{\mathrm{LAT}}$ correlation. Therefore, they are not affected as much as BL Lacs.

The 4LAC catalog's content of BL Lacs suffers, as would be expected, from a gamma-ray bias, which favors sources of high gamma-ray luminosity and flux and rather low X-ray flux

---

[8] Since the BAT photon index Γ for the lowest two L_{LAT} bins is expected to be softer than a flat spectrum it has been set to $\Gamma = 2.2$ for the calculation of the flux curves. Similarly, the photon index for the two highest L_{LAT} bins, which are expected to be hard, are set to $\Gamma = 1.8$. The curves for the middle L_{LAT} bin have been derived for $\Gamma = 2.0$.

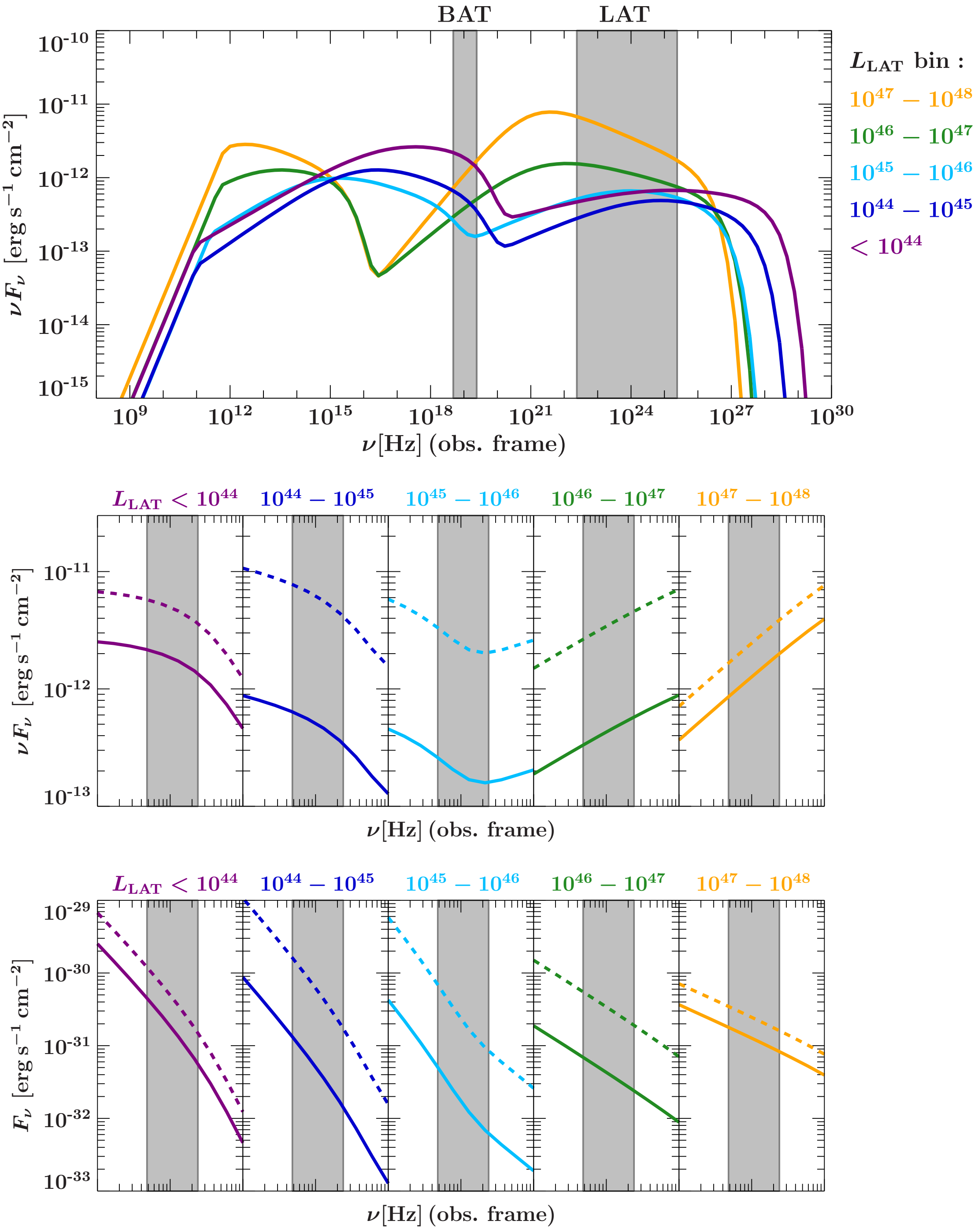

Figure 6.1.14.: Top: Fitted broadband SEDs of gamma-ray-bright blazars after the fitting parameters from Ghisellini et al. (2017), translated to the νF_ν display, following Fig. 6.1.11. The colored curves of the flux correspond to the luminosity bins in erg s^{-1} and median redshift of the sources in the corresponding luminosity bin. Middle: Zoomed-in plots of the SEDs in the top graph around the BAT frequency band in gray (20 keV – 100 keV / $4.8 \cdot 10^{18}$ Hz – $2.4 \cdot 10^{19}$ Hz). The dashed lines indicate the tenth-lowest redshift in the corresponding luminosity bin (see text). Bottom: Same graph as in the middle, but in F_ν display.

values. Subsequently, the 4LAC AGN sample is only partially suitable for blazar studies in the hard X-ray regime. The source count statistics are not representative regarding an X-ray-focused or blind survey due to the issues discussed above, and need to be treated accordingly. The sample can therefore not be considered a statistically complete one in the BAT survey band of 20 keV – 100 keV.

6.2 X-ray - gamma-ray parameter space

Both the X-ray and gamma-ray energy bands offer important insight into the workings of active galactic nuclei and the high-energy processes that are believed to be harbored within. Further, the parameter spaces of flux, luminosity, photon index, and other quantities that are spanned by both observation bands uniquely describe the given AGN populations in the high-energy regime. In this section the given AGN classes of FSRQs, BL Lacs, BCUs, and non-blazar AGN are analyzed in terms of their behavior in said parameter spaces. In the following Sect. 6.2.1 the general distribution trend of all classes is discussed with an emphasis on outlier sources which may point towards extreme cases or misclassifications. Section 6.2.2 focuses on the sizable group of yet unclassified blazar candidate sources (BCUs) and whether they can be attributed to either FSRQs or BL Lacs by analyzing their location in the X-ray-gamma-ray photon index parameter space.

6.2.1. Overall trend and outliers

The distribution of the X-ray-bright 4LAC sources in the X-ray- and gamma-ray flux plane is shown in Fig. 6.2.1. The sources accumulate at low X-ray fluxes whereas the distribution over gamma-ray fluxes is notable more even. Kendall's τ tests show that the X-ray and gamma-ray fluxes of all X-ray-bright sources are correlated. This is also true for all individual blazar classes ($p_{\mathrm{blazar}} = 0$, $p_{\mathrm{FSRQ}} = 10^{-10}$, $p_{\mathrm{BLLac}} = 10^{-3}$, $p_{\mathrm{BCU}} = 10^{-3}$). The Kendall's τ correlation test is robust against outliers. However, these special cases are of particular interest, and are discussed in the following. In general, it is expected that sources of the same AGN class have different X-ray to gamma-ray flux ratios, which naturally also applies to luminosity: hard X-ray and gamma-ray emission should be dominated by the beamed jet, therefore, the ratio between the flux in both bands for all blazar classes should be independent of the inclination angle and Doppler boosting. Other factors that are more likely to be responsible for a wide scatter are different photon indices between sources / SED peak frequencies, and the issue of variability in both bands, exacerbated by the slightly different survey time ranges.

Radio galaxies and other non-blazar AGN show a more X-ray-bright distribution compared to the blazars, also indicating a lack of sources that are X-ray-faint and / or gamma-ray-bright at the same time. The origin of X-ray and especially gamma-ray emission in these source types is still a debated issue. While the high-energy bands of blazars are heavily dominated by beamed emission from the jets, radio galaxies, or misaligned AGN, are also characterized by other contributing components. Of the plotted X-ray-bright sources in the 4LAC sample J0319.8+4130 (NGC 1275, only classified as an AGN in the 4LAC catalog) has the highest gamma-ray flux. As previously stated, the extracted information in the BAT band reveals high brightness but also spectral contamination by a nearby source. On the other hand, J0319.8+4130 is located in the large Perseus galaxy cluster. These clusters feature

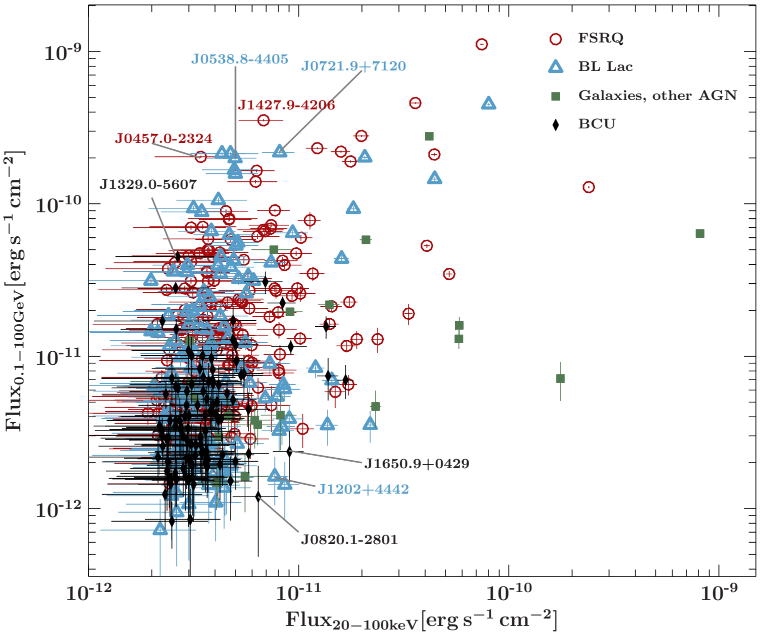

Figure 6.2.1.: Hard X-ray flux against gamma-ray flux for all X-ray-bright sources in the 4LAC sample. A number of outlier sources are marked and discussed in the text.

significant X-ray emission from the hot intracluster medium (ICM), which is dominated by bremsstrahlung and are characterized by a temperature of several 10^7 K and a spectral peak in keV to MeV, notably lower than the LAT band (see, e.g., Böhringer & Werner, 2010).

A larger number of radio galaxies and other similar sources in the 4LAC sample are not located in large galaxy clusters, however. Prominent examples are J1325.5–4300 (Centaurus A), J0418.2+3807 (3C 111), or J0519.6–4544 (Pictor A). Multiple studies present detailed discussions of the multiwavelength nature of these objects and the possible origin of the high-energy SED components. The hard X-ray (*INTEGRAL*) spectrum of Centaurus A, for example, has been presented and discussed by Beckmann et al. (2011). A spectral cut-off at around 400 keV was found, as well as no significant sign of X-ray emission from the radio lobes themselves. While the emissions in the *Fermi*/LAT band are generally thought to be due to non-thermal jet processes, a non-thermal origin of the emissions the keV to GeV range can also not be ruled out by the authors. Brown & Adams (2012) presented the discovery of GeV emission from the BLRG Pictor A. While the radio lobes of certain broad line radio galaxies have been resolved into hotspots up into the X-ray regime, *Fermi*/LAT data suggest an origin of the gamma-ray emission within the jet itself. Gamma-rays are likely not produced via SSC processes within these hotspots like other wavelengths. Using a small sample of radio galaxies from the TANAMI sample, Angioni et al. (2019) have shown that the VLBI core flux of these sources correlates with the gamma-ray flux like in blazars. However, data presented in the study also implies that the gamma-ray emission from radio galaxies is not subject to the orientation of the jet regarding the observer's line of sight. To conclude, gamma-ray emission from radio galaxies is very likely solely due to emission processes in the jet, while X-rays are also produced in the radio lobe hotspots and ICM in galaxy clusters. In the case of blazars the (non-thermal) jet emission towards the observer is highly boosted and heavily dominates compared to other emission mechanisms, which gain importance for (mis-aligned) non-blazar sources, such as radio galaxies. The observed faintness of gamma-rays compared to the BAT data for radio galaxies in the 4LAC sample supports this picture.

Both the gamma-ray and X-ray-brightest FSRQs and BL Lacs tend to have fairy restricted photon indices ($\Gamma_{\mathrm{LAT}}^{\mathrm{FSRQ}} \approx 2.4 - 2.8$ and $\Gamma_{\mathrm{LAT}}^{\mathrm{BLLac}} \approx 1.7 - 1.9$). The spectral shape in the X-ray band shows a somewhat inverted trend ($\Gamma_{\mathrm{BAT}}^{\mathrm{FSRQ}} \approx 1.2 - 1.7$ and $\Gamma_{\mathrm{BAT}}^{\mathrm{BLLac}} \approx 2.4 - 2.7$). This characteristic mirrors the distribution of synchrotron peak frequencies in the sample, that is, predominantly low values for FSRQs (BAT: rising HE bump, LAT: declining HE bump) and intermediate and high values for BL Lacs (BAT: declining synchrotron bump, LAT: rising HE bump). The outliers, which are marked in Fig. 6.2.1, are also listed in Table 6.2.1, including their spectral properties in both energy bands and the synchrotron peak frequencies.

Many of the FSRQs and BL Lacs that are gamma-ray-bright and X-ray-faint share the spectral characteristics of a hard X-ray photon index ($\Gamma_{\mathrm{BAT}} < 2$) and an index in the gamma-ray band that is relatively flat, or somewhat soft ($\Gamma_{\mathrm{LAT}} \approx 2$).

Compared to the mean index of this sub-sample ($\langle\Gamma\rangle_{\mathrm{LAT}}^{\mathrm{FSRQ}} = 2.56 \pm 0.01$) the FSRQs J0457.0–2324 ($\Gamma_{\mathrm{LAT}} = 2.20 \pm 0.01$) and J1427.9–4206 ($\Gamma_{\mathrm{LAT}} = 2.19 \pm 0.01$) stand out. Also, most of these sources have relatively low synchrotron peak frequencies, comparable with the average value for the (low-peaked) FSRQs in this sub-sample ($\langle\nu\rangle_{\mathrm{synch}}^{\mathrm{FSRQ}} = (9.40 \pm 1.02) \cdot 10^{12}\,\mathrm{Hz}$). These cases correspond to the scenario of a generally low-peaked SED, which has the rising part of the HE bump coincide with the hard X-ray band, hence a rather low signal strength and hard index, and the top part of the HE bump, near and past the peak, that is described by the gamma-ray band. The BCU J1329.0–5607 is very much characterized like a typical low-peaked FSRQ, with $\nu_{\mathrm{synch}}^{\mathrm{peak}} = 7.66 \cdot 10^{12}\,\mathrm{Hz}$ and $\Gamma_{\mathrm{LAT}} = 2.43 \pm 0.02$. The large X-ray photon index of 2.78 ± 1.64 is atypical, but also features large uncertainties.

Most of the gamma-ray-faint but X-ray-bright blazars in the sample are BL Lacs and BCUs. The BL Lac J1202.4+4442 could be classified as an intermediate-peaked blazar. The soft X-ray photon index of $\Gamma_{\mathrm{BAT}} = 2.45 \pm 0.40$ suggests that the peak region or the declining part of the synchrotron bump is measured while the gamma-ray band should observe near the peak region of the HE bump. The corresponding relatively high index of $\Gamma_{\mathrm{LAT}} = 2.46 \pm 0.18$ indicates a measurement on the declining part of the component. A somewhat inverted case is presented by the BCU J0820.1–2801, which features unusually hard photon indices in both bands ($\Gamma_{\mathrm{BAT}} = 1.49 \pm 0.59$, $\Gamma_{\mathrm{LAT}} = 1.41 \pm 0.20$), suggesting that the measurement pinpoints the rising flanks of the synchrotron and HE bumps in the SED, respectively. No synchrotron peak frequency is available for this source. However, the data strongly imply an extremely high-peaked SED and therefore likely classification as a BL Lac, similar to the case of the BCU J2251.7–3208, with $\nu_{\mathrm{synch}}^{\mathrm{peak}} = 2.09 \cdot 10^{18}\,\mathrm{Hz}$. In a related scenario, the BCU J1650.9+0429 likely also depicts an intermediate to high-peaked BL Lac, with $\Gamma_{\mathrm{BAT}} = 2.19 \pm 0.4$, and $\Gamma_{\mathrm{LAT}} = 1.95 \pm 0.16$.

In many cases the position of the outliers in the gamma-ray-X-ray flux plane can be rationalized using the synchrotron peak frequency and subsequently the SED position in respect to the observation bands. The results are consistent with Sect. 6.1.3 (Fig. 6.1.14): high-peaked BL Lacs (and BCUs that are likely BL Lacs), where the synchrotron peak frequency is near the observed X-ray band ($\approx 10^{19}\,\mathrm{Hz}$), feature a higher flux value (νF_ν) compared to the LAT band. The case is reversed for low- and intermediate-peaked BL Lacs, for which the HE peak region is near the LAT band, but the SED gap and rising HE bump coincide with the hard X-ray regime.

Figure 6.2.2 shows the luminosity of the hard X-ray and gamma-ray bands graphed against

Table 6.2.1.: Outliers and their spectral properties that are either particularly X-ray-faint and gamma-ray-bright or vice-versa, see Fig. 6.2.1.

Source	Type	Γ_{BAT}	Γ_{LAT}	$\nu_{\mathrm{synch}}^{\mathrm{peak}}$ [Hz]
Gamma-ray-bright / X-ray-faint				
J0457.0–2324	FSRQ	1.55 ± 1.13	2.20 ± 0.01	$7.31 \cdot 10^{12}$
J1427.9–4206	FSRQ	1.63 ± 0.57	2.19 ± 0.01	$1.40 \cdot 10^{13}$
J0538.8–4405	BL Lac	1.03 ± 0.7	2.11 ± 0.01	$6.24 \cdot 10^{12}$
J0721.9+7120	BL Lac	0.84 ± 0.46	2.06 ± 0.01	$1.48 \cdot 10^{14}$
J1329.0–5607	BCU	2.78 ± 1.64	2.43 ± 0.02	$7.66 \cdot 10^{12}$
X-ray-bright / Gamma-ray-faint				
J1202.4+4442	BL Lac	2.45 ± 0.4	2.46 ± 0.18	$1.38 \cdot 10^{14}$
J0820.1–2801	BCU	1.49 ± 0.59	1.41 ± 0.20	
J1650.9+0429	BCU	2.19 ± 0.4	1.95 ± 0.16	
J2251.7–3208$^{(a)}$	BCU	2.24 ± 0.49	1.72 ± 0.16	$2.09 \cdot 10^{18}$

Notes. All photon indices Γ_{LAT} for the gamma-ray band and synchrotron peak frequencies have been taken from Ajello et al. (2020). The labels X-ray-faint and gamma-ray-faint describe the fraction of sources with relatively low flux, which are still not upper-limits. $^{(a)}$The spectral fitting of the source only resulted in an upper limit for the flux, but still viable photon index values. As such, it is still classified as X-ray-faint in this context.

each other[9]. The power-law fits to the sources classes of FSRQs, BL Lacs, and BCUs are displayed as well as labels for several outliers that are discussed in the following. The great majority of all data points is distributed along a slope with the index of one, as is to be expected from a plot that covers sources with a wide range of redshifts. However, the high-luminosity sources, independent of source class but mostly FSRQs, tend to be more luminous in the gamma-ray band. Since the luminosity strongly correlates with the redshift, it can be stated that the ratio of X-ray to gamma-ray emission of blazar sources was notably different for earlier periods / larger redshifts. This conclusion points towards a different evolution of X-ray and gamma-ray luminosity, similar to the results that are reported in Sect. 4.2.5 for the X-ray and radio bands. A correlation between the gamma-ray and X-ray luminosities is present for the entire sub-sample and all individual source classes individually. Using a partial correlation test (Akritas & Siebert, 1996), in order to exclude the influence of the redshift, shows that the null hypothesis of zero correlation can be rejected at a level of 0.05 or better in all cases. All classes occupy distinctive regions in the plot with large areas of overlap between sources of different classes. Power-law fits are applied to all source classes in the form of $L_\gamma = A \cdot (L_X)^\alpha$, which confirm the steep slope: BL Lacs are steepest[10] ($A = 2.22 \cdot 10^{-16}$, $\alpha = 1.36$), while FSRQs are flatter ($A = 1.59 \cdot 10^{-11}$, $\alpha = 1.25$), similar to the BCUs ($A = 1.28 \cdot 10^{-12}$, $\alpha = 1.27$).

Compared to the power-law fits, several sources are also unusually bright in the gamma-ray band, especially BL Lacs. Some sources at around $L_{\mathrm{BAT}} = 10^{45}\,\mathrm{erg\,s^{-1}}$ are J0721.9+7120,

---

[9] The gamma-ray luminosities are derived using flux values in the 0.1 – 100 GeV band and the same conventions for the cosmological parameters as for the X-ray band (Sect. 3.2.4). All displayed uncertainties are converted from $1\,\sigma$ to 90%-errors.

[10] The source J0828.3+4152 has been excluded from the fit since its cited redshift value is likely wrong and extremely low, see discussion in Sect. 6.1.1.

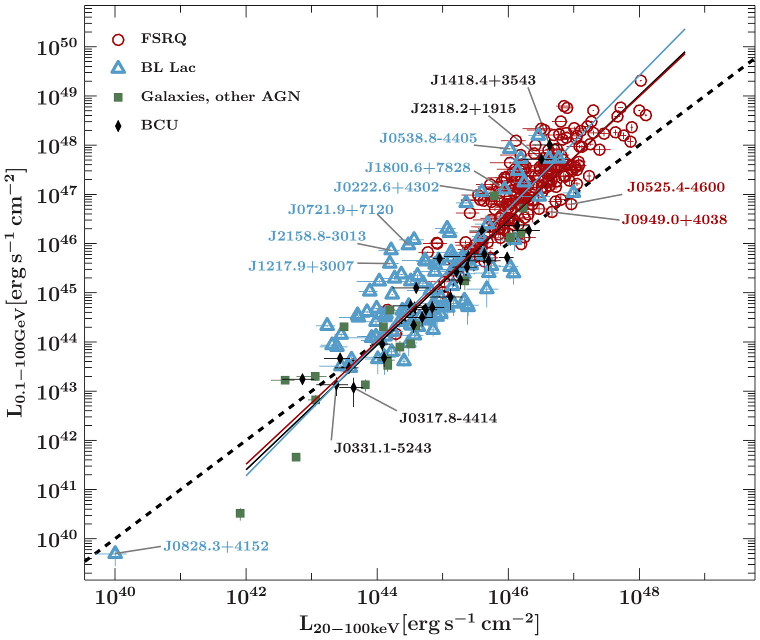

Figure 6.2.2.: Hard X-ray against gamma-ray luminosity for all X-ray-bright sources in the 4LAC sample. A number of outlier sources are marked and discussed in the text. The dashed line indicates the angle bisector. The red, blue, and black solid lines mark the power-law fits of the data for FSRQs, BL Lacs, and BCUs, respectively. The source J0828.3+4152 is omitted in the fit.

J1217.9+3007, and J2158.8–3013, all of which have redshifts between 0.1 and 0.3. This is a factor 3–4 smaller than comparable BL Lacs at this X-ray luminosity, and more compatible with BL Lacs at lower X-ray luminosity values, indicating a relatively increased gamma-ray emission for these sources in the survey time span. J0721.9+7120, however, is also found to be significantly gamma-ray-bright and X-ray-faint in terms of flux, likely due to the SED's position (see discussion above).

A number of BL Lacs, that are also disproportionally luminous in the gamma-ray band and reach the area that is mainly occupied by FSRQs are J0538.8–4405, J1800.6+7828, and J0222.6+4302. Their redshift values are comparable with those of FSRQs in the sample, but follow a photon index distribution that is typical for BL Lacs ($\Gamma_{\mathrm{LAT}} = 1.9 - 2.3$). Again, J0538.8–4405 is characterized by a unusually high gamma-ray flux compared to the X-ray emission (discussion above). In any case, the three sources also feature relatively high Doppler factors of $\delta = 4.5 - 6.0$, where the median value for BL Lacs is $\delta_{\mathrm{med}} = 2.8$ (based on the available data from Lin et al. (2017)), which suggests that the high luminosity on both bands is due to increased relativistic beaming.

The FSRQs J0949.0+4038 and J0525.4–4600 are characterized by a low gamma-ray and relatively high X-ray luminosity. Both sources feature somewhat higher redshift values compared to FSRQs of similar gamma-ray luminosity, that is 1.25 and 1.48 against the more typical range of 0.8 – 1.0. An inverted trend can be seen for the BL Lacs J0721.9+7120, J1217.9+3007, and J2158.8–3013, which may indicate an increased gamma-ray and / or decreased X-ray output during the respective survey times.

The majority of the BCUs are close to the bisector line and only show an increased slope of the fitted power law because of the two high-luminosity sources J2318.2+1915 and J1418.4+3543 at unusually high redshift values of 2.16 and 2.09, respectively. Former source has a very low synchrotron peak frequency of $\nu_{\mathrm{synch}}^{\mathrm{peak}} = 5.75 \cdot 10^{12}$ Hz and a very soft gamma-ray photon index of $\Gamma_{\mathrm{LAT}} = 2.61 \pm 0.09$, strongly suggesting a likely classification as an FSRQ, as stated previously. J1418.4+3543, however, shows characteristics that are much more compatible with a BL Lac classification, with $\nu_{\mathrm{synch}}^{\mathrm{peak}} = 2.82 \cdot 10^{15}$ Hz and $\Gamma_{\mathrm{LAT}} = 2.11 \pm 0.02$.

BCUs at the low-luminosity end can also very likely be classified as BL Lacs. The two sources J0331.1–5243 and J0317.8–4414 are somewhat less luminous in the gamma-rays / more luminous in the X-rays. However, they also feature relatively large uncertainties in both dimensions.

The distribution of (fitted) sources in the plane of X-ray and gamma-ray photon indices is plotted in Fig. 6.2.3. FSRQs and BL Lacs clearly occupy unique domains in the plot, while the distinction is far more pronounced for the gamma-ray photon index, where sources with $\Gamma_{\text{LAT}} \gtrsim 2.3$ are mostly FSRQs and sources with $\Gamma_{\text{LAT}} \lesssim 2.2$ mostly BL Lacs. A distinction in the X-ray band is visible for the BL Lacs, which are somewhat shifted to higher photon indices compared to FSRQs, notably for $\Gamma_{\text{BAT}} \gtrsim 2.5$. From the entire distribution sources are lacking that either have both very hard or very soft X-ray and gamma-ray photon indices. This characteristic can be explained by the behavior of the SED, described by the Fermi blazar sequence (Ghisellini et al., 2017), which is discussed in Sect. 6.1.3, see also Fig. 6.1.11 and 6.1.14. Following this model, BL Lacs with hard X-ray photon indices (low-peaked) also have soft gamma-ray indices ($\Gamma_{\text{LAT}} \gtrsim 2$), a trend that is visible in Fig. 6.2.3. The model SEDs demonstrate that FSRQs only tend to have hard X-ray photon indices within the given sample. However, since the model SEDs were compiled using a large number of sources, averaging their broadband spectrum, some FSRQs with $\Gamma_{\text{BAT}} \gtrsim 2$ are likely to exist. Also, the uncertainty ranges of many FSRQs in that region of the photon index plot are substantial, that is, around $d\Gamma_{\text{BAT}} \approx 0.5 - 1$. The blazar candidate sources (BCUs) are distributed over the entire area where FSRQs and BL Lacs are located. The radio galaxies and other non-blazar sources are distributed similarly, albeit more towards the center, being restricted to $\Gamma_{\text{LAT}} \approx 1.8 - 2.9$. Sources that are located on the edges of the distribution generally tent to have relatively large uncertainties with $d\Gamma_{\text{BAT}} \gtrsim 1$ and $d\Gamma_{\text{LAT}} \approx 0.13 - 0.2$ for FSRQs that have soft gamma-ray spectra[11]. Thus, many of these apparent outliers are compatible with the denser more central region of the distribution.

In the following, several individual sources that can be considered outliers are discussed. They are also marked in Fig. 6.2.3. The FSRQ J0043.8+3425 features an extraordinarily flat gamma-ray spectrum ($\Gamma_{\text{LAT}} = 1.94 \pm 0.02$) and is comparatively high-peaked ($\nu_{\text{synch}}^{\text{peak}} = 5.89 \cdot 10^{13}$ Hz) for the source class. This suggests that the source may be a misclassified BL Lac. However, the corresponding luminosity in both emission bands is more typical for FSRQs, as is the redshift of $z = 0.966$. Furthermore, the given photon index has been derived using a log-parabola fit instead of a power-law fit, as is the case of most other blazars in the catalog. In the earlier 3FGL catalog (Acero et al., 2015), the source was reported to have a (power-law) photon index of $\Gamma_{\text{LAT}} = 2.04 \pm 0.05$, which is still somewhat low for the source class but less than the 4FGL value. In the FSRQ area of the distribution, there are a number of BL Lacs, especially the three sources with notably soft gamma-ray spectra at $\Gamma_{\text{BAT}} \approx 1$ and $\Gamma_{\text{LAT}} \approx 2.6$: J0037.9+2612 is characterized by significant uncertainties ($\Gamma_{\text{BAT}} = 1.17 \pm 1.72$, $\Gamma_{\text{LAT}} = 2.59 \pm 0.17$) due to a low flux and luminosity in both bands. Similar cases are J0812.3+1143 ($\Gamma_{\text{BAT}} = 0.95 \pm 1.33$, $\Gamma_{\text{LAT}} = 2.61 \pm 0.15$) and J2056.7–3209 ($\Gamma_{\text{BAT}} = 1.07 \pm 0.96$, $\Gamma_{\text{LAT}} = 2.61 \pm 0.15$). Latter source, however, is fairly low-peaked with $\nu_{\text{synch}}^{\text{peak}} = 4.79 \cdot 10^{12}$ Hz. This set of BL Lacs is likely all LSPs which are faint in the X-ray band, suggesting that the BAT band is just observing the rising part of the SED's HE bump, but

---

[11] Unless explicitly specified, the uncertainties of the gamma-ray data set are $1\,\sigma$ values, taken directly from the released 4FGL tables (Abdollahi et al., 2020). All uncertainties in the X-ray data set are by default 90% values.

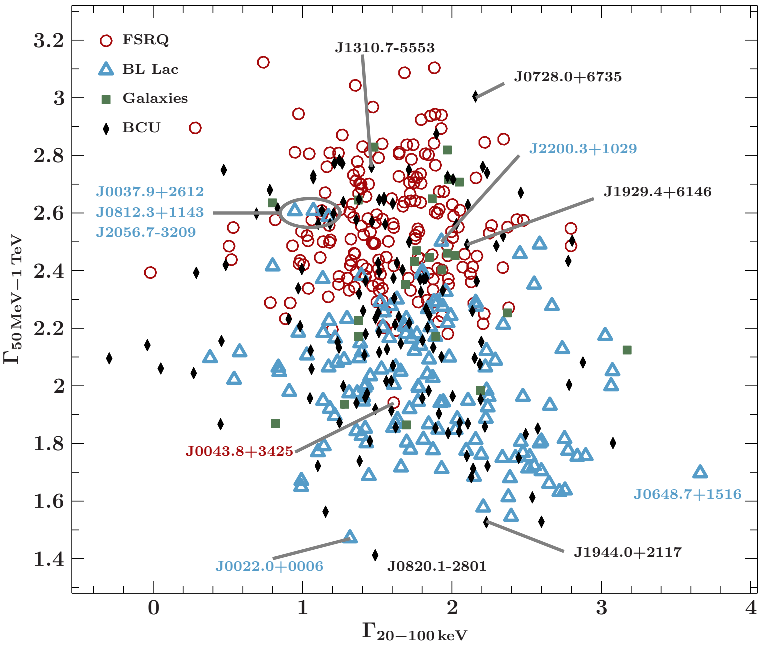

Figure 6.2.3.: Hard X-ray against gamma-ray photon indices for all sources that have fitted X-ray spectra in the 4LAC sample. A number of outlier sources are marked and discussed in the text. Error bars are omitted for better readability. All sources with $\Gamma_{\mathrm{BAT}} < -2$ are omitted in the plot due to very poor signal quality.

near the spectral gap region, while the LAT band measures a sharply declining HE bump. The values of the corresponding photon indices have significant uncertainties associated with them. However, they still pose notable outliers from the rest of the BL Lac distribution in the plot. The source J2200.3+1029 also stands out as a BL Lac with a soft gamma-ray spectrum that has a more typical BAT photon index ($\Gamma_{\mathrm{BAT}} = 1.93 \pm 0.25$, $\Gamma_{\mathrm{LAT}} = 2.50 \pm 0.12$). However, the source's X-ray spectrum suffers from the contamination of a nearby source and is therefore not representative. Overall, the peak frequency of $\nu_{\mathrm{synch}}^{\mathrm{peak}} = 1.1 \cdot 10^{13}$ Hz indicates a similar case as above. The source with the highest X-ray photon indices in the sample is the rather X-ray-faint BL Lac J0648.7+1516 with $\Gamma_{\mathrm{BAT}} = 3.66 \pm 1.18$ and a low index in the LAT band with $\Gamma_{\mathrm{LAT}} = 1.70 \pm 0.04$. The high peak frequency of $\nu_{\mathrm{synch}}^{\mathrm{peak}} = 6.31 \cdot 10^{16}$ Hz describes a high-peaked source, where the BAT band coincides with the declining part of the synchrotron bump near the spectral gap. Consequently, the LAT band observes the rising HE bump. In the case of the BL Lac J0022.0+0006, both spectral bands measure a particularly low photon index ($\Gamma_{\mathrm{BAT}} = 1.32 \pm 0.90$, $\Gamma_{\mathrm{LAT}} = 1.47 \pm 0.17$) and a very high-peaked SED with $\nu_{\mathrm{synch}}^{\mathrm{peak}} = 1.35 \cdot 10^{17}$ Hz. Although the X-ray photon index suggests a measurement of the rising flank of one of the SED emission peaks, the spectral band around 10^{19} Hz has to be on the declining part or near the peak of the synchrotron bump, which is well compatible within the corresponding uncertainties. Thus, the gamma-ray data describe the rising flank of the HE bump.

The description of the BCUs in the photon index parameter space is especially interesting regarding the possible classification of sources as FSRQs or BL Lacs. In this section, a number of notable outlier sources are discussed. For this purpose, Fig. 6.2.4 also shows the gamma-ray photon index plotted against the (available) values of synchrotron peak frequencies. A more elaborate Monte-Carlo-based approach is presented in the following Sect. 6.2.2. Generally, it seems likely, that the great majority of BCUs with $\Gamma_{\mathrm{LAT}} > 2.3$ are FSRQs, while sources with $\Gamma_{\mathrm{LAT}} < 2.2$ are likely BL Lacs. The high-peaked source J1310.7–5553 ($\nu_{\mathrm{synch}}^{\mathrm{peak}} = 2.49 \cdot 10^{15}$ Hz) has a gamma-ray spectral slope which is typical for FRSQs ($\Gamma_{\mathrm{LAT}} = 2.76 \pm 0.14$) but a peak frequency which would be exceptionally high, approximately 100 to 1000 times higher than

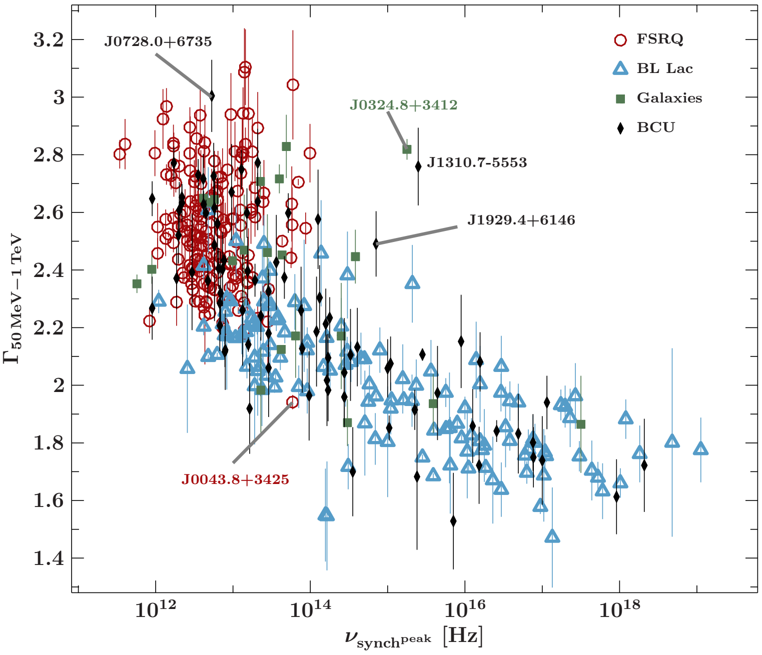

Figure 6.2.4.: Gamma-ray photon index for all sources that have fitted X-ray spectra in the 4LAC sample plotted against (available) synchrotron peak frequencies. A number of outlier sources are marked and discussed in the text.

expected for this photon index. In Fig. 6.2.4, the source is relatively close to J0324.8+3412, a NLSy1 galaxy. This inconsistency might be explained by either a misclassification as a blazar candidate instead of a non-blazar AGN or a wrong measurement of the peak frequency. For determining the peak frequency Ajello et al. (2020) reference archival data available from the SED builder tool from the ASI Science Data Center (ASDC)[12]. However, a search for the source and its common name PMN J1310–5552 did not match any entry in the data base. A wrong source classification or peak frequency calculation could therefore be the result of a simple source confusion. Furthermore, other works like Panessa et al. (2015), Bird et al. (2016), or Paliya et al. (2019), all of them referencing the source as a Sy1, only list broadband spectral flux data in the radio and X-ray regime with large gaps remaining in-between. Even if a spectral fit over the entire range was performed, a restriction the peak frequency would likely be attached to large uncertainties, which are not given in the literature.

A very similar case is given by the source J1929.4+6146 in the intermediate region between FSRQs and BL Lacs ($\Gamma_{\mathrm{LAT}} = 2.49 \pm 0.11$). Its peak frequency is also relatively high ($\nu_{\mathrm{synch}}^{\mathrm{peak}} = 7.08 \cdot 10^{14}\,\mathrm{Hz}$), about 10 to 100 times as high as expected from its photon index. Again, only scarce SED data is available in the literature, with no data between the infrared and *Fermi*/LAT band at the time of publication of the 4LAC catalog. No corresponding entry could be found in the online SED builder tool. Although the value of the peak frequency remains uncertain, a previous study of a catalog of *WISE* sources (D'Abrusco et al., 2014) references J1929.4+6146 as a BL Lac, which fits better than a classification as an FSRQ when taking into account the moderately large error of the gamma-ray photon index and its position in Fig. 6.2.4.

On the other hand, the source J1944.0+2117, which is notably X-ray-bright ($14.52\,\sigma$), is very likely a BL Lac with its exceptionally low photon index $\Gamma_{\mathrm{LAT}} = 1.53 \pm 0.09$. Although without any available synchrotron peak frequency value, the X-ray photon index of $\Gamma_{\mathrm{BAT}} = 2.23 \pm 0.22$ suggests that the SED's declining synchrotron component coincides with the

---

[12] `https://tools.ssdc.asi.it/SED/`

BAT band, whereas *Fermi*/LAT observes the rising part of the HE component, making the SED almost certainly intermediate- to high-peaked. The fairly X-ray- and gamma-ray-faint source J0820.1–2801 ($\Gamma_{\mathrm{BAT}} = 1.49 \pm 0.59$, $\Gamma_{\mathrm{LAT}} = 1.41 \pm 0.20$) is probably also intermediate- to high-peaked; see the discussion earlier in this section.

Lastly, the BCU J0728.0+6735 is characterized by a extremely high gamma-ray photon index of $\Gamma_{\mathrm{LAT}} = 3.00 \pm 0.13$, which is very soft, even for FSRQs. Due to very poor signal quality, the X-ray photon index features significant uncertainties with $\Gamma_{\mathrm{BAT}} = 2.16 \pm 2.05$. The gamma-ray data and peak frequency of $\nu_{\mathrm{synch}}^{\mathrm{peak}} = 5.31 \cdot 10^{12}\,\mathrm{Hz}$, however, highly suggest a low-peaked FSRQ. Figure 6.2.3 also includes a number of BCUs at $\Gamma_{\mathrm{LAT}} \approx 2.1$, but at very hard X-ray slopes around $\Gamma_{\mathrm{BAT}} = 0$. All sources feature large uncertainties, which are due to poor signal quality ($1.3\,\sigma - 1.8\,\sigma$). Although more compatible with the distribution of BL Lacs a founded estimation of a likely classification remains difficult.

6.2.2. Classifying BCUs in the Γ-Γ plane

In the previous Sect. 6.2.1 a number of sources, including ten BCUs, are discussed regarding their individual hard X-ray and gamma-ray characteristics like flux, luminosity, spectral slope with respect to the overall trend of the X-ray-bright 4LAC sub-sample. In doing so, the BCUs are attributed different to likely blazar classes, that is, FSRQs or BL Lacs. This section focuses on the classification of all of the 132 blazar candidate sources (BCU) of the sub-sample, using two different approaches, which also serve as a step of verification for the previous results.

The following analyses are based on the distribution of the FSRQs and BL Lacs in the plane of gamma-ray photon index to X-ray photon index (see Fig. 6.2.3). All sources in the graph are characterized by partly significant uncertainty regions, predominantly in the X-ray data set. It is assumed that the two-dimensional Gaussian error profile of each source in the plane describes the probability density function (pdf) of each measurement, that is:

$$f_{\Gamma} = \frac{1}{d\Gamma_{\mathrm{x}}\, d\Gamma_{\mathrm{y}}\, 2\,\pi} \exp\left[-\left(\frac{(\Gamma_{\mathrm{x}} - \mathrm{E}(\Gamma_{\mathrm{x}}))^2}{2\, d\Gamma_{\mathrm{x}}^2} + \frac{(\Gamma_{\mathrm{y}} - \mathrm{E}(\Gamma_{\mathrm{y}}))^2}{2\, d\Gamma_{\mathrm{y}}^2}\right)\right], \tag{6.2.1}$$

with the expected values $\mathrm{E}(\Gamma)$ and the uncertainties of the photon index $d\Gamma$ for the X-ray/BAT and gamma-ray/LAT data sets x and y, respectively. The probability of finding a random variable in the parameter space is equal to the integral over the probability density function:

$$\Pr(\Gamma_{\mathrm{x}}, \Gamma_{\mathrm{y}}) = \int_{\Gamma_{\mathrm{x}}} \int_{\Gamma_{\mathrm{y}}} f_{\Gamma}\; d\Gamma_{\mathrm{y}}\, d\Gamma_{\mathrm{x}}, \tag{6.2.2}$$

which is equal to 1 for the entire parameter space. The cumulative profile of all sources in each separate blazar class describe the probability density of finding a (X-ray-bright) source of the corresponding class at a specific point in the parameter space. The cumulative functions are shown in Fig. 6.2.5a and Fig. 6.2.5b. For illustration, the distribution of BCU sources together with the added FSRQ and BL Lac probability densities is shown in Fig. 6.2.5c[13].

---

[13] Because the functions feature sources that have a low (1σ) error in the gamma-ray axis, but a comparatively large error in the X-ray axis, the overall 2D-function can exhibit strong streaks, which are dominated by a few individual sources. In order to mitigate this bias, the used overall function is composed of the individual sources with an error range of $3 \times 1\sigma$, providing a more gradual and less fractured function.

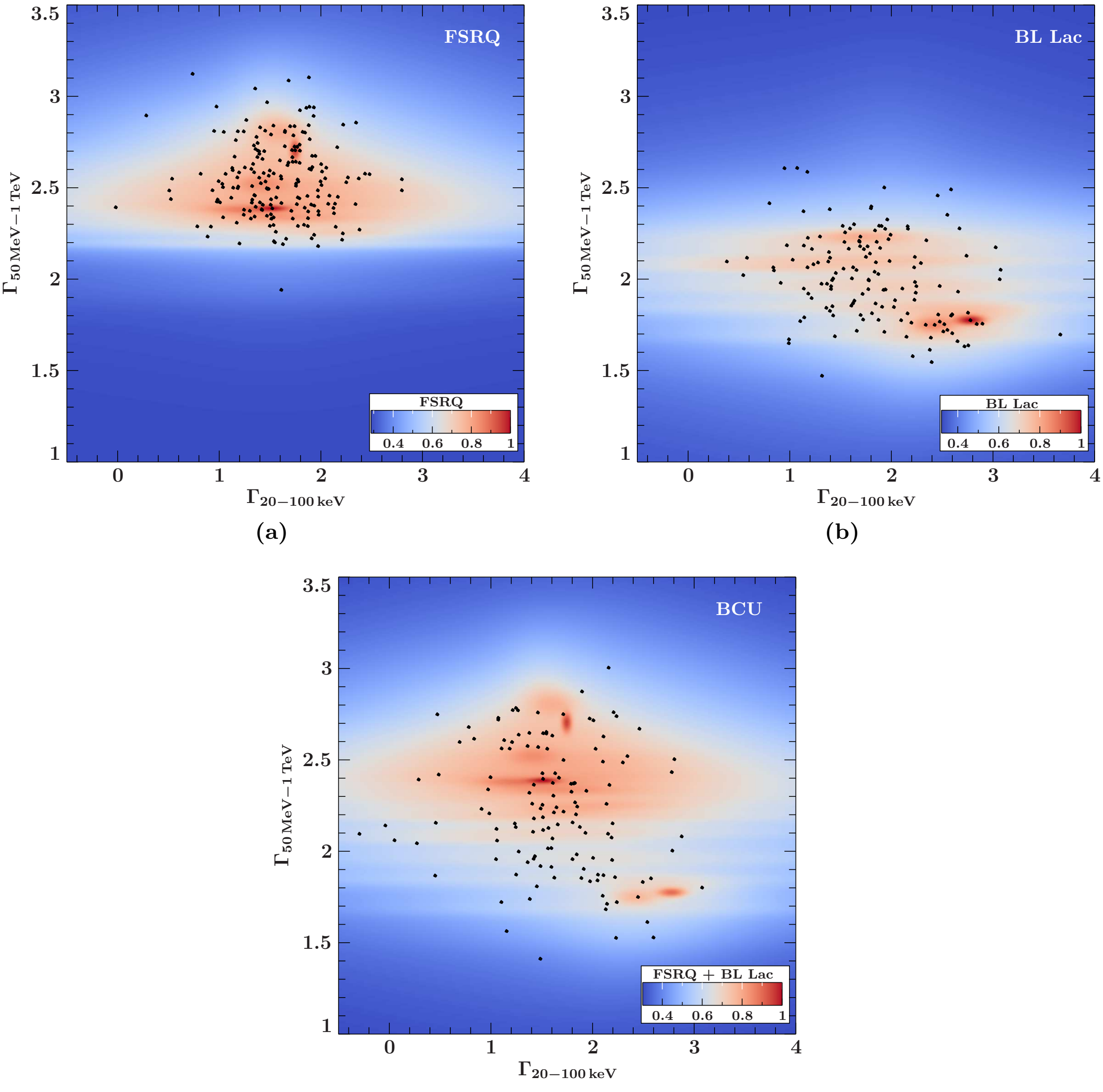

(a)

(b)

(c)

Figure 6.2.5.: Gamma-ray against X-ray photon indices of all X-ray-bright blazars in the 4LAC sample (black dots). The uncertainty regions are modeled as 2D Gaussians on the basis of $3 \times 1\sigma$ uncertainty values of the corresponding measurements. All individual regions are added up. The color scale is logarithmic and normalized to the 2D function's maximum value. (a) shows the distribution for FSRQs, (b) for BL Lacs, and (c) for BCUs (only sources) including the combined 2D Gaussians of both FSRQs and BL Lacs.

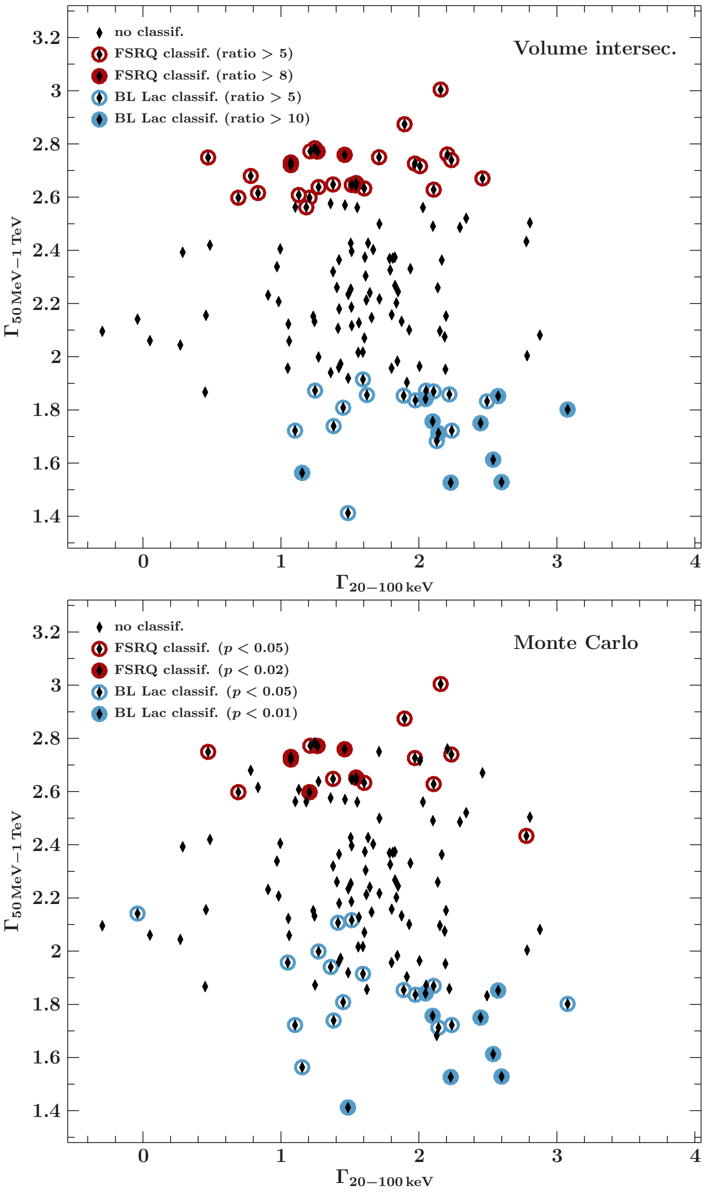

Figure 6.2.6.: Gamma-ray versus X-ray photon index, showing all X-ray-bright BCUs in the 4LAC sample. Top: classification of the BCUs as either FSRQs or BL Lacs depending on the ratio of the volume intersection of the BCU's 2D Gaussian function and the respective cumulative function of the FSRQ and BL Lac sub-samples. Bottom: classification of the BCUs of the Monte Carlo approach of counting simulated sources based on the FSRQ and BL Lac function in the $3\,\sigma$ BCU source ellipses. Different grades of significance (p-values) are marked accordingly. See the text for details.

In the following, two methods are introduced which provide a quantitative assertion of the possible classification of the BCUs in this sample.

In the first approach, each BCU is treated like before, that is, it is represented by a two-dimensional Gaussian probability density function with a width corresponding to the associated photon index uncertainties. The intersection of volume between this function and the cumulative function of the FSRQs and BL Lacs is calculated numerically. This represents a measure of how well the individual source is compatible with the probability density of either the FSRQs or BL Lacs. The ratio of both results expresses in a quantitative way how compatible the source with one classification is on the basis of X-ray and gamma-ray photon index compared to the alternative classification. Table 6.2.2 at the end of this section lists the sources of the BCU sub-sample and their likely classification depending on the corresponding ratio of intersections (only the larger ratio and not its inverse is given since it determines the classification). A value notably larger than unity suggests a distinctive result. In the table, all ratios larger than five are highlighted. In total, 28 sources are classified as FSRQs with ratios larger than five, and one source with a volume ratio larger than ten (J1508.5–4951). Also, sources with a ratio larger than approximately eight have an X-ray photon index lower than $\Gamma_{\text{BAT}} = 1.6$, on the left half of the distribution in Fig. 6.2.3. A comparable number of 25 sources could be classified as BL Lacs, having a ratio larger than five. Also, ten sources have a ratio larger than ten, nine of which with a X-ray photon index larger than $\Gamma_{\text{BAT}} = 2$. In Fig. 6.2.6 the photon index plane is plotted again with only the BCUs and the classification following this method. Generally, the BCUs that can be more confidently associated with either a classification as FSRQ or BL Lac tend to be well separated along the axis of the gamma-ray photon index. As stated above, the sources with the highest confidence of a correct classification also show a dependency of the X-ray photon index, which may partially be caused by the slight offset of both blazar populations along the X-ray axis (Fig. 6.2.3). In any case, the most likely classifications for BCUs as FSRQs are characterized by soft gamma-ray and hard X-ray photon indices ($\Gamma_{\text{LAT}} \approx 2.7, \Gamma_{\text{BAT}} \approx 1.0 - 1.6$), while a likely classification as a BL Lac is strongest in the opposite of the parameter space, that is, a hard gamma-ray and soft X-ray photon index ($\Gamma_{\text{LAT}} \approx 1.5 - 1.8, \Gamma_{\text{BAT}} \approx 2.0 - 3.1$).

The second method for testing which of the BCUs could be classified as one of the two blazar types incorporates a Monte Carlo approach, providing a p-value as a result. The null hypothesis of a BCU being an FSRQ type can then be rejected at a low enough p-value, for example 0.05, and therefore be classified as a BL Lac, and vice versa. Starting again with the probability density function of the cumulative FSRQ and BL Lac functions ($3 \times 1\sigma$ uncertainty), a large number of sources are simulated that follow the respective functions, approximately 130.000 FSRQs and 100.000 BL Lacs, which mirrors the ratio of both blazar types in the sample. The number of simulated sources that fall into the $3\,\sigma$ uncertainty area of a certain BCU divided by the total number of simulated sources of this type gives the p-value at which the classification of this type can be rejected. For example, if in Fig. 6.2.5a a BCU's uncertainty region is located at approximately $\Gamma_{\text{LAT}} = 1.5$ only a low number of simulated sources would be located in that area. Consequently, the null hypothesis of an FSRQ classification can be rejected at the corresponding level of the p-value, and thereby sources must be classified as a BL Lac object. This approach assumes that BCUs can only be FSRQs or BL Lacs. Figure 6.2.6 shows the result of the classification following the Monte Carlo method. Similar to the previous approach, the classification into FSRQs and BL Lacs is largely governed by the gamma-ray photon index, whereas the X-ray photon index shows the same behavior of the most significant classifications associated with soft X-ray photon indices for BL Lacs and hard indices for FSRQs. In total, 19 BCUs can be classified as FSRQs at a p-value of 0.05. Six sources even correspond to a p-value of 0.02 or lower. A number of 26 sources can be classified as BL Lacs at a p-value of 0.05, with eight highly significant classifications with p-values below 0.01.

It has to be stated, that the p-value limits as well as the ratios regarding the presented numbers of sources with high confidence of a correct classification are to an extend arbitrary, at least for the ratio method. However, an intersection ratio of about five and a p-value around 0.05 for the Monte Carlo method as well as the stricter limits seem to deliver very similar results. Moreover, the clear distinction of the sources along the gamma-ray axis is reasonable regarding to the distribution of the FSRQs and BL Lacs themselves. In certain cases, both methods deviate in regions that are more intermittent between both blazar classes. This may well be caused by the different methods of calculating the compatibility

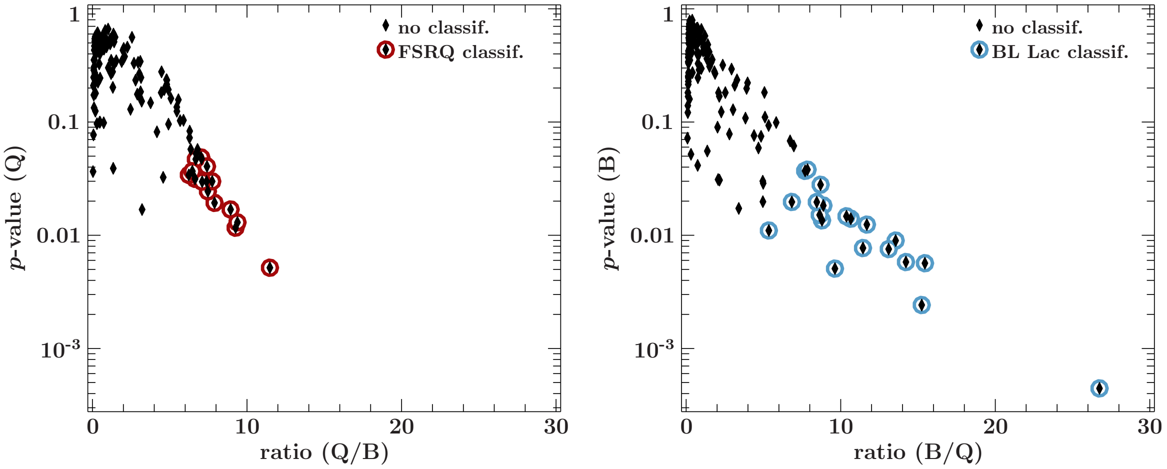

Figure 6.2.7.: p-value of Monte Carlo simulations against the ratio of volume intersections for the determination of BCU classification (see text). Left: for the classification of BCUs as FSRQs, right: for the classification as BL Lacs. The sources that are circled correspond to the classification criteria of a volume ratio of at least five and a p-value smaller than 0.05.

of a single BCU source with the probability density function of the FSRQs and BL Lacs: while the former method takes into account the entire Gaussian function of the BCU as well as its height and shape, the latter one counts simulated sources only within the $3\,\sigma$ error ellipse that is projected down on the Γ-Γ plane. This circumstance might result in a different weighting of the BCU uncertainties near significant features in the 2D probability density function of the blazar classes, like sharp peaks (bright sources or accumulation of sources) or wave-like structures (accumulation of gamma-bright but X-ray-faint sources).

In any case, both methods still produce comparable results, especially for sources that are estimated high-significance classifications. In order to further test how similar both methods function for the given data sets, the derived metrics are plotted in Fig. 6.2.7. The graphs show the derived ratio of volume intersection against the p-value of the Monte Carlo method. The most significant classifications are marked accordingly. Sources that are not classified with any method accumulate at low ratios and high p-values in the upper left corner as expected, while significant classifications form a trend of low p-values and large volume ratios. The distribution of sources in the graphs scatter significantly below a ratio of approximately five, featuring sources that are associated with p-values above 0.05 to 0.1. This scattering is notably less pronounced the higher the ratio is, for FSRQs even more so than for BL Lacs. The methods seem to converge for highly significant classifications with no notable outliers. Moreover, in the vast majority of cases, sources with ratios smaller than around five have p-values larger than 0.05, and can therefore not be considered a high-confidence classification.

As a convention, a classification is considered highly significant if the concerning sources pass the requirement of both methods. Sources that are already tentatively classified using, for example, the comparison with the overall luminosity or SED peak frequency distribution, provide an additional level of validation. There are 16 BCUs that can be classified as FSRQs using both methods with high confidence, including two sources that already have a tentative classification as this blazar type: J0728.0+6735 and J1310.7–5553. The FSRQ classification of J1329.0–5607 through the previous discussion of Γ_{BAT}, Γ_{LAT}, and $\nu_{\mathrm{s}}^{\mathrm{p}}$ is characterized by a volume ratio of 4.58, only slightly below 5, and with a significant p-value of 0.033. This source could therefore also be considered a likely FSRQ candidate. A similar case is given by J2318.2+1915, which could also be considered an FSRQ from the distribution of L_{LAT}. A volume ratio of 6.36 and a p-value of 0.057 also point towards this conclusion. Analogously, a total number of 19 BCUs can be classified as BL Lacs, with three sources that also have this suggested classification from previous discussions: J0820.1–2801, J1944.0+2117, and J2251.7–3208. The source J0317.8–4414, although tentatively a BL Lac following the distributions of the luminosity in both energy bands, features a p-value of only 0.183, which is not a significant result.

A small number of sources show results that are either inconclusive or incompatible with previous results regarding the distributions of the gamma-ray and X-ray parameters. The luminosity distribution of both energy bands suggests that the source J0331.1–5243 is likely a BL Lac. However, the classification methods here are not able to derive a conclusive answer. The volume ratio of 1.47 and p-value of 0.563 are reasonable because of the location of the source in the middle of the overlapping zone in the Γ-Γ plane, as is the case for many BCUs in the sample. The large uncertainties of the photon indices ($\Gamma_{\mathrm{BAT}} = 1.41 \pm 1.61$, $\Gamma_{\mathrm{LAT}} = 2.26 \pm 0.19$) on the other hand might well locate the source on the lower right area of the Γ-Γ plane, making a BL Lac classification much more likely. The classification of the BCU J1418.4+3543 in the discussions in Sect. 6.1 is not completely unambiguous. Here, the derived p-value of 0.017 but a volume ratio of 3.4 point at least partially towards a BL Lac. The source is also located in the intermittent region of the photon indices, although slightly on the BL Lac side ($\Gamma_{\mathrm{LAT}} = 2.11 \pm 0.02$). Interestingly, the BCU J1650.9+0429, which is associated above with a BL Lac because of its typical photon indices ($\Gamma_{\mathrm{BAT}} = 2.19 \pm 0.4$, $\Gamma_{\mathrm{LAT}} = 1.95 \pm 0.16$) and reasonable X-ray brightness, is not classified as a BL Lac using the methods introduced here (ratio = 2.8, $p = 0.078$). Because of its similar gamma-ray photon index as the FSRQ J0043.8+3425, a notable outlier source in Fig. 6.2.3 and 6.2.5a, the resulting contribution of the FSRQ's probability density function in this area could have the effect of reducing the probability of a clear BL Lac classification, skewing the result of the analysis.

In compiling the 4LAC catalog, Ajello et al. (2020) used an extensive procedure to classify the sources as different AGN types (FSRQs, BL Lacs, CSSs, SSRQs, and NLSy1s). The procedure included referencing the optical spectrum, the flatness / steepness of the radio spectrum, the presence of broadband emission, variability, polarization, and the potential earlier classification in the literature. Any object with a selected counterpart in the BZCAT catalog (listed as a BZU object) or with multiwavelength data that suggests a typical blazar-like double-humped SED structure was designated as a BCU. Furthermore, the authors state that the sub-set of BCUs likely has a similar composition as the rest of the known blazars in the 4LAC catalog, which, based on the limited data derived in this analysis, can be confirmed. Although the authors present the gamma-ray parameters of the sources in the 4LAC sample, including photon index, SED peak frequency, flux, and redshift, the classification of the listed source types is solely derived from the procedure stated above, and not the distribution of any of the calculated parameters. This work introduces a classification method that only relies on the spectral shapes in the hard X-ray and gamma-ray bands, and is independent of further multiwavelength databases and surveys. As such, it may prove as a well-suited method of BCU classification for larger high-energy data sets and / or hard X-ray measurements of higher sensitivity. Also, a classification procedure using different metrics like flux or luminosity might be a viable alternative to the photon index.

It needs to be stated, that the distinction of FSRQs and BL Lacs in terms of spectral shape in this analysis is primarily determined by the gamma-ray band data, with additional restrictions that be can made using hard X-ray measurements for the most X-ray-bright sources. Only a rather small number of sources can confidently be attributed to the FSRQ or BL Lac class regarding the total 4LAC sample size. The described methodology and used survey data sets, however, demonstrate a viable approach to the challenge of blazar candidate classification, which, in this study, is mostly limited by the hard X-ray survey sensitivity especially in the case of this set of gamma-ray-bright blazars. In order to classify a larger set of blazar candidate sources from the X-ray-bright sub-set further observations or deeper survey measurements in the hard X-ray range would be required. One solution is given by longer exposure time for *Swift*/BAT all-sky survey, which would deliver only diminishing results since the signal quality of the long-term survey only climbs further with the square root of time. The more sensible approach would be the analysis of further hard X-survey / monitoring data from more sensitive instruments and / or the stacking of archival map data from, for example, *AstroSat*, *INTEGRAL*, and *NuSTAR*. *NuSTAR* especially would be the prime choice for dedicated source observations in the desired energy band because of its relatively high sensitivity and therefore possibly low required exposure times. If the analysis would be extended to the soft X-ray band, archival spectra and new large and deep surveys from, for example, eROSITA could possibly increase the number of confident BCU classifications significantly.

Based on the above analysis it can be estimated which sources in this X-ray-bright sub-sample would be preferred targets for X-ray follow-up observations with the goal of increasing the number of confident BCU classifications from the used procedure. Below, the targets, that are estimated to provide the best results are listed. The BCU targets are chosen to be in the region of $\Gamma_{\mathrm{LAT}} > 2.5$ and $\Gamma_{\mathrm{LAT}} < 2.1$, away from the overlapping center, while having a photon index uncertainty (90%) in the X-ray band of $d\Gamma_{\mathrm{BAT}} > 1$, corresponding to a BAT S/N of $\approx 1\,\sigma - 2.5\,\sigma$. All BCUs that have already been classified with both methods above, are excluded. This leaves a number of 46 sources with no or just one classification criterion fulfilled. Sources with larger photon index uncertainties would benefit the most from additional data since their location in the Γ-Γ-plane determines the probability of a certain classification. This also means, that the probability density function of the given FSRQs and BL Lacs has to be known precisely. Further measurements of such sources with large uncertainties ($d\Gamma_{\mathrm{BAT}} > 1$) would therefore restrict the shape of the probability profile and mitigate the wave-like structure as seen in Fig. 6.2.5. The 26 listed FSRQs below represent all FSRQs with $\Gamma_{\mathrm{LAT}} = 1.8 - 2.4$, while the 42 BL Lacs are characterized by a range of $\Gamma_{\mathrm{LAT}} = 1.8 - 2.1$. The desired accuracy for new measurements of the hard X-ray spectrum would be at least as good as $d\Gamma \approx 0.5$ (90% uncertainty), which corresponds to a BAT measurement at a significance of $\approx 4\,\sigma - 5\,\sigma$:

- FSRQ
  J0042.2+2319, J0043.8+3425, J0102.8+5824, J0113.4+4948, J0116.0–1136, J0217.0–0821, J0217.8+0144, J0310.9+3815, J0317.7–2804, J0423.3–0120, J0457.0–2324, J0510.0+1800, J0742.6+5443, J0808.2–0751, J1239.5+0443, J1246.7–2548, J1308.5+3547, J1321.1+2216, J1700.0+6830, J1716.1+6836, J2000.9–1748, J2035.4+1056, J2212.0+2356, J2236.3+2828, J2328.3–4036, J2332.1–4118

- BL Lac

  J0040.3+4050, J0138.0+2247, J0140.6–0758, J0143.7–5846, J0255.8+0534, J0316.2–2608, J0333.7+7851, J0422.3+1951, J0430.3–2507, J0441.5+1505, J0546.9–2206, J0621.8+1746, J0700.2+1304, J0723.0–0732, J0730.4+3308, J0738.1+1742, J0812.0+0237, J0828.3+4152, J0854.3+4408, J0950.2+4553, J1015.0+4926, J1022.7–0112, J1058.6+5627, J1203.1+6031, J1230.2+2517, J1253.2+5301, J1253.8+6242, J1257.6+2413, J1301.6+4056, J1411.8+5249, J1442.7+1200, J1456.0+5051, J1508.8+2708, J1704.5–0527, J1736.0+2033, J1744.0+1935, J1749.0+4321, J1917.7–1921, J1921.3–1231, J2131.5–0916, J2152.0–1205, J2319.1–4207

- BCU

  J0021.0+0322, J0131.2+5547, J0248.6+5131, J0250.7+5630, J0317.8–4414, J0414.8–5338, J0420.3–6016, J0442.7+6142, J0526.7–1519, J0557.3–0615, J0647.0–5138, J0651.4+6525, J0751.4+2655, J0754.0+0451, J1014.7+3210, J1411.5–0723, J1427.4–1823, J1441.7+1836, J1447.0–2657, J1507.3+3341, J1549.8–3044, J1810.7+5335, J1826.0–5037, J2037.9–0504, J2137.4–3209, J2340.5+3854, J2343.9+0546, J2359.1+1719, J0214.2–7025, J0242.6+1735, J0507.9+4647, J0533.3–5549, J0741.2–5140, J0943.7+6137, J1047.9+0055, J1631.2+1046, J1632.8–1048, J1648.0+2221, J1706.8+3004, J2056.4–4904, J2123.8–3148, J2136.2–0642, J2239.4+5130, J2253.2–1232, J2318.2+1915, J2327.5–3259

Table 6.2.2.: Results of the X-ray-bright 4LAC BCU classification

4FGL Name	Class$^{(a)}$ (Volume)	Ratio$^{(a)}$ (Volume)	Class$^{(b)}$ (MC)	p-value$^{(b)}$ (MC)	Class$^{(c)}$	derived from
J0003.3–1928	Q	1.3	Q	0.278		
J0021.0+0322	B	4.39	B	0.076		
J0028.9+3553	Q	1.4	Q	0.511		
J0035.8+6131	**Q**	6.46	**Q**	0.037		
J0039.1–2219	**B**	8.69	**B**	0.028		
J0047.9+5448	**B**	14.22	**B**	0.006		
J0115.1+2622	Q	1.01	B	0.659		
J0131.2+5547	B	2.09	B	0.181		
J0143.5–3156	Q	2.56	Q	0.561		
J0151.4–3607	Q	1.32	Q	0.202		
J0214.2–7025	**Q**	6.76	Q	0.054		
J0242.6+1735	Q	4.82	Q	0.235		
J0248.6+5131	B	4.96	**B**	0.02		
J0250.7+5630	B	2.14	B	0.169		
J0303.2+3149	Q	3.14	Q	0.247		
J0304.5+6821	**Q**	7.1	**Q**	0.03		
J0317.8–4414	**B**	5.06	B	0.183	B	$L_{\rm X}, L_\gamma$
J0322.4+6606	**Q**	5.46	Q	0.125		
J0331.1–5243	Q	1.47	Q	0.563	B	$L_{\rm X}, L_\gamma$
J0333.1+8227	B	1.51	B	0.31		
J0350.8–2814	**B**	8.45	**B**	0.02		
J0352.0–2516	Q	2.08	Q	0.379		
J0401.0–5353	**B**	10.37	**B**	0.015		
J0420.3–6016	B	1.83	B	0.279		
J0442.7+6142	B	3.03	B	0.128		
J0447.4–2747	Q	2.26	Q	0.459		
J0456.2+2702	Q	3.18	Q	0.153		
J0500.2+5237	**B**	8.64	**B**	0.015		
J0505.6+6405	Q	3.07	Q	0.166		
J0507.9+4647	**Q**	6.7	Q	0.053		
J0508.2+5211	B	1.09	B	0.424		
J0509.9–6417	B	4.98	**B**	0.029		
J0526.1+6318	B	1.09	B	0.5		
J0526.7–1519	B	4.96	**B**	0.03		
J0533.3–5549	Q	4.47	Q	0.278		
J0552.8+0313	Q	2.79	Q	0.234		
J0557.3–0615	**B**	5.1	B	0.111		
J0608.9–5456	**Q**	7.75	**Q**	0.03		
J0623.0–3010	Q	4.17	Q	0.082		
J0644.4–6712	B	2.06	**B**	0.031		
J0647.0–5138	**B**	6.96	B	0.062		
J0651.4+6525	B	2.03	B	0.09		
J0658.1–5840	B	1.48	B	0.417		
J0703.3–0050	Q	1.2	Q	0.268		
J0709.2–1527	**B**	13.1	**B**	0.008		
J0715.3–6828	Q	1.36	Q	0.599		
J0725.8–0054	B	2.16	**B**	0.031		
J0728.0+6735	**Q**	6.24	**Q**	0.034	Q	$\Gamma_\gamma, \nu_{\rm s}^{\rm p}$
J0732.7–4638	**Q**	7.47	**Q**	0.024		
J0733.4+5152	**B**	10.65	**B**	0.014		
J0741.2–5140	**Q**	5.56	Q	0.157		
J0748.0–1638	**Q**	6.68	**Q**	0.047		
J0751.4+2655	B	1.69	B	0.356		

Table 6.2.2.: continued.

4FGL Name	Class$^{(a)}$ (Volume)	Ratio$^{(a)}$ (Volume)	Class$^{(b)}$ (MC)	p-value$^{(b)}$ (MC)	Class$^{(c)}$	derived from
J0754.0+0451	B	4.84	B	0.075		
J0804.9–0624	**B**	8.88	**B**	0.018		
J0805.0+6746	B	1.4	B	0.483		
J0820.1–2801	**B**	9.63	**B**	0.005	B	$\Gamma_{\mathrm{X}}, \Gamma_{\gamma}$
J0822.4–2630	B	1.22	B	0.576		
J0827.6–3735	**Q**	7.38	**Q**	0.03		
J0856.8+8559	Q	1.14	Q	0.537		
J0900.6–7408	**Q**	7.41	**Q**	0.041		
J0922.7–3959	**Q**	6.64	**Q**	0.032		
J0923.5+3852	**Q**	9.38	**Q**	0.013		
J0943.7+6137	**Q**	6.28	Q	0.073		
J1014.3+4112	Q	2.95	Q	0.337		
J1014.7+3210	B	3.91	B	0.198		
J1027.6+8251	Q	1.41	Q	0.326		
J1042.9+0054	**B**	7.85	**B**	0.038		
J1046.0+5448	Q	1.97	Q	0.431		
J1047.9+0055	Q	4.79	Q	0.237		
J1047.9–3738	**B**	7.69	**B**	0.037		
J1243.9–0218	Q	1.02	B	0.297		
J1254.2–2205	Q	1.15	Q	0.491		
J1310.7–5553	**Q**	8.94	**Q**	0.017	Q	L_{γ}
J1329.0–5607	Q	4.58	**Q**	0.033	Q	$\nu_{\mathrm{s}}^{\mathrm{p}}, \Gamma_{\mathrm{X}}, \Gamma_{\gamma}$
J1344.4–3656	Q	1.89	Q	0.343		
J1354.2+6934	Q	3.03	Q	0.267		
J1411.5–0723	B	1.63	B	0.339		
J1416.1+1320	Q	3.76	Q	0.148		
J1418.4+3543	B	3.4	**B**	0.017	Q/B	$L_{\mathrm{X}}, \nu_{\mathrm{s}}^{\mathrm{p}}, \Gamma_{\gamma}$
J1427.4–1823	B	4.68	B	0.059		
J1441.7+1836	B	3.84	B	0.108		
J1446.0–3039	Q	2.0	Q	0.362		
J1447.0–2657	**B**	5.34	B	0.093		
J1451.5+1415	Q	4.64	Q	0.194		
J1453.0–1318	B	1.15	B	0.457		
J1507.3+3341	B	3.29	B	0.236		
J1508.5–4951	**Q**	11.48	**Q**	0.005		
J1512.9–5639	Q	2.46	Q	0.13		
J1547.9–6403	**Q**	7.03	**Q**	0.049		
J1549.8–3044	**B**	6.73	B	0.068		
J1602.1+3324	Q	1.54	Q	0.348		
J1632.8–1048	**Q**	6.8	Q	0.057		
J1648.0+2221	**Q**	5.68	Q	0.103		
J1650.9+0429	B	2.8	B	0.078	B	$\Gamma_{\mathrm{X}}, \Gamma_{\gamma}$
J1706.8+3004	Q	4.91	Q	0.193		
J1738.0+8717	Q	1.21	Q	0.352		
J1752.6–1010	Q	3.12	Q	0.185		
J1810.7+5335	B	2.53	B	0.182		
J1814.0+3828	B	1.12	B	0.461		
J1815.2–2715	Q	2.69	Q	0.331		
J1823.6–3453	**B**	11.44	**B**	0.008		
J1826.0–5037	B	3.14	B	0.211		
J1830.2–4443	**Q**	7.9	**Q**	0.019		
J1907.7–1232	Q	3.1	Q	0.343		
J1929.4+6146	Q	4.45	Q	0.182		

Table 6.2.2.: continued.

4FGL Name	Class$^{(a)}$ (Volume)	Ratio$^{(a)}$ (Volume)	Class$^{(b)}$ (MC)	p-value$^{(b)}$ (MC)	Class$^{(c)}$	derived from
J1930.3+0911	**Q**	7.06	**Q**	0.047		
J1944.0+2117	**B**	26.74	**B**	0.0	B	$\Gamma_\mathrm{X}, \Gamma_\gamma$
J1949.4+1247	Q	2.02	Q	0.447		
J2001.9–5737	B	1.87	B	0.268		
J2002.4–7119	**B**	11.69	**B**	0.012		
J2025.3+3341	**Q**	9.26	**Q**	0.012		
J2026.6+3449	B	1.23	B	0.42		
J2037.9–0504	B	3.97	B	0.222		
J2056.4–4904	**Q**	5.46	Q	0.136		
J2056.7+4939	**B**	15.24	**B**	0.002		
J2110.3+0404	B	1.34	B	0.363		
J2123.8–3148	Q	4.81	Q	0.215		
J2132.0–5418	Q	2.9	Q	0.176		
J2136.2–0642	**Q**	5.08	Q	0.162		
J2137.4–3209	**B**	5.83	B	0.099		
J2239.4+5130	**Q**	5.89	Q	0.104		
J2246.7–5207	**B**	15.45	**B**	0.006		
J2251.7–3208	**B**	8.79	**B**	0.014	B	$\nu_\mathrm{s}^\mathrm{p}$
J2253.2–1232	Q	4.92	Q	0.096		
J2318.2+1915	**Q**	6.36	Q	0.057	Q	L_X
J2327.5–3259	**Q**	6.29	Q	0.083		
J2340.5+3854	B	2.94	B	0.294		
J2343.9+0546	B	2.27	B	0.123		
J2347.9+5436	**B**	13.55	**B**	0.009		
J2358.5–1808	**B**	6.84	**B**	0.02		
J2359.1+1719	B	2.37	B	0.318		

Notes. $^{(a)}$ Classification determined from the ratio of intersecting volumes of one single BCU source (2D Gaussian) and the cumulative probability density functions of FSRQs and BL Lacs. Instances where the ratio is larger than 5 are marked in boldface. $^{(b)}$ Classification from the Monte Carlo approach, whereas instances in boldface mark p-values smaller than 0.05 and with a p-value of the alternate classification larger than 0.05. The listed results correspond to the $3\,\sigma$ error regions of the modeled BCU sources in the Γ-Γ plane (see text). $^{(c)}$ Tentative classification from previous discussions in Sect. 6.2.1. The additional information refers to the distribution of luminosities L, photon indices Γ, or synchrotron peak frequencies $\nu_\mathrm{s}^\mathrm{p}$ the discussion is based on.

6.3 Summary

Continuing from the previous chapters, this analysis focuses on the gamma-ray-selected 4LAC sample, the newest and largest AGN catalog in the GeV regime, derived from eight years of continuous *Fermi*/LAT all-sky observations. From the 3207 mostly beamed sources, in the sample only 459 can be characterized as X-ray-bright, on the basis of the 105-month hard X-ray all-sky *Swift*/BAT survey. The 4LAC sample mainly consists of low-peaked FSRQs, low- to high-peaked BL Lacs, and a larger number of blazar candidate sources of unknown type (BCUs). The general trend as well as a number of individual sources are discussed regarding the X-ray characteristics and behavior regarding gamma-ray emission and SED properties. The main results of the hard X-ray analysis are listed as follows.

- The average BAT signal strength depends on the source type, whereas FSRQs are the brightest, followed by BL Lacs and BCUs. Only 97 sources (3% of the sample) have S/N values of $5\,\sigma$ or higher. Compared to the MOJAVE and TANAMI sample, the X-ray brightness is significantly lower, with only 35%–41% of the entire sample remaining after subtracting the background noise component.

- The distribution of X-ray luminosities is very similar to the radio-selected samples, with the FSRQs being the most luminous, followed by BL Lacs and non-blazar sources. BCUs cover a wide range with a number of them probably being FSRQs. The X-ray photon indices show relatively broad distributions because of the low signal strength, but center around 1.7 for FSRQs, and 2.5 for BL Lacs. KS tests show that distributions of the individual blazar types are significantly different from those of the MOJAVE-1.5 sample (p values $< 10^{-3}$).

- The $\log N$-$\log S$ distributions in the X-ray and gamma-ray band exhibit a variety of shapes due to a wide range of SED peak frequencies, data selection biases, and likely flux evolution. While the slope of the X-ray distribution of FSRQs ($\alpha = 1.33$) is comparable with the MOJAVE sample, the slope for BL Lacs ($\alpha = 1.63$) is significantly steeper than the radio-selected counterpart, which is largely due to the contribution of intermediate- and high-peaked sources.

- Especially BL Lacs exhibit a dependency of the photon index to the flux and luminosity due to a variety of SED peak frequencies. The group of X-ray-bright BL Lacs are not randomly drawn from the 4LAC sample. Furthermore, the 4LAC sample cannot be classified as a complete sample in the hard X-ray band. A more suitable way of classification in the context of X-ray surveys would not be the synchrotron peak, but the spectral gap frequency, leading to low-, mid-, and high-gap sources.

- Both the X-ray and gamma-ray fluxes are correlated. Non-blazar sources are generally more X-ray-bright, likely because of additional emission mechanisms besides beamed jet emission, like radio lobe hotspots and ICM X-ray emission. Blazars show notably higher gamma-ray luminosity at high z compared to the X-ray band, indicating different evolution of the emission. The Γ-Γ plane shows a clear separation of FSRQs and BL Lacs, mostly along the gamma-ray axis and a tentative trend along X-ray axis.

- On the basis of the distribution of the FSRQs and BL Lacs in the Γ-Γ plane, empiric pdfs can be determined, which facilitate the classification of the BCUs in the sample.

> Combining two complementary methods yields 16 FSRQ and 19 BL Lac classifications with high confidence. Up to nine BCU classifications derived from the X-ray and gamma-ray properties are confirmed in this analysis. A list of 4LAC sources is given, whose X-ray follow-up observations would notably increase the number of classified BCUs, requiring only a precision of a fitted power law of $d\Gamma \approx 0.5$.

The large 4LAC gamma-ray-selected AGN sample exhibits fundamentally different characteristics in the hard X-ray regime compared to its radio-selected counterparts, MOJAVE and TANAMI. Sources are overall fainter and show different photon index distributions, which can largely be explained by its composition, including intermediate- and high-peaked sources, as well as the gamma-ray selection bias. Besides a small number of suggested reclassifications and faulty listed redshift data, for several blazar candidate sources a tentative blazar classification can be derived with high confidence using the data sets from the GeV and keV range. Future X-ray surveys and dedicated observations of single sources will enable further restrictions of the nature of the blazar candidates using the methods introduced in this study. Although the 4LAC sample is not representative of X-ray-bright beamed AGN in the sky, both instruments and their rich all-sky survey data permit the characterization of high-energy regime of a large (sub) sample of gamma-ray-bright blazar and non-blazar sources.

7. Summary and conclusions

In this work, the main focus was the characterization of the hard X-ray properties of samples of known bright blazars, which are under-represented in surveys. Since AGN, and especially blazars, are emitting strongly throughout the electromagnetic spectrum by the means of non-thermal processes, they are studied with a large array of telescopes and detectors. The X-ray and gamma-ray parts of the spectrum are only accessible using satellite observatories, which survey the entire sky for familiar and new AGN populations and record their broadband high-energy characteristics. While extensive surveys for AGN in the optical and soft X-ray bands revealed millions of sources, the higher-energy domains, specifically the hard X-rays, registered a comparatively low number, with only hundreds of sources between 10 keV and a few MeV, but a few thousand above, around GeV energies, a regime that is dominated by blazars. The question that was addressed in this work was whether the scarcity of blazars in the hard X-ray band is due to systematics like the limited sensitivity of the available instruments or an intrinsically low brightness of this AGN type. For this, the 105-month count-rate maps of the *Swift*/BAT all-sky survey were used, which provide accumulated flux measurements from 20 keV to 100 keV. Although the extraction of data from the BAT survey maps is a standard task, the processing of very-low count rate spectra is not. In doing so, the specifically implemented PGSTAT fit statistic was used, as well as a dedicated Monte Carlo approach to derive the spectral properties from the extracted BAT data set. Modeling the noise component of the background-subtracted survey maps allowed assessments to be made about the signal strength of a source sample as a whole. An in-depth analysis of the *Swift*/BAT spectral data from the integrated survey maps showed that, although blazars are not featured strongly in this energy band, a significant part of blazars from other pre-defined samples is detected, just below the conservative catalog thresholds of about $5\,\sigma$. This thesis includes the X-ray studies of differently selected samples of beamed AGN, mostly blazars, which are also composed of different proportions of blazar sub-types. This approach allowed to address the issue why so few hard X-ray emitting blazars are cataloged, taking into consideration various potential factors, like selection biases, blazar evolution, and variability.

The first part of this thesis centers around the radio-bright and flux-limited AGN samples MOJAVE-1 (135 sources) and MOJAVE-1.5 (181 sources), from the same monitoring program at 15 GHz for relativistic extragalactic jets on the Northern hemisphere, both dominated by low-peaked blazars. Although most of the sources have low BAT S/N values, a great majority of both samples is not compatible with random background noise, that is, about 90% in the case of the MOJAVE-1 sample. The blazar sub-types of FSRQs and BL Lacs as well as radio galaxies occupy distinct X-ray parameter ranges, such as flux, luminosity, and photon index, which can be associated with the SED peak frequency / the spectral shape coinciding with the BAT band. The question why a small percentage of the MOJAVE blazars is gamma-ray-faint can be addressed using the distribution of spectral shapes in the hard X-rays, which are significantly “flatter” than gamma-ray-bright ones, indicating an HE peak well before the GeV domain, reducing the gamma-ray (*Fermi*/LAT) signal strength. While the sample's radio fluxes in a $\log N$-$\log S$ diagram shows for the most part a Euclidean distribution, the X-ray data reveals a very flat slope (index $\alpha = 1.13 \pm 0.04$), indicative of the relative scarcity of faint to even moderately bright blazars in the hard X-rays. This difference is interpreted as likely being due to different evolutionary paths in both emission bands, with a maximum of the X-ray evolution at $z \approx 1.5$, as shown by the fitting of the X-ray and radio luminosity functions. Compared to X-ray-selected blazar samples the contribution of this radio-selected population only contributes a very low amount to the CXB, 0.2% to 0.3%.

The study of the radio-bright MOJAVE blazars is supplemented by the sample sources from the TANAMI monitoring program (126 sources) for the Southern hemisphere, observing radio-loud beamed, gamma-ray-bright and VHE-detected AGN in the GHz range. The two different TANAMI sub-samples which are radio-loud and gamma-ray-bright, respectively, both tend to be relatively X-ray-bright, compatible with the MOJAVE samples. In fact, the very similar $\log N$-$\log S$ distributions of the MOJAVE and TANAMI samples indicate the same blazar population regarding the hard X-ray emission characteristics. Based on these X-ray properties some of the many unclassified TANAMI sources can be given a likely classification, that is, FSRQ, BL Lac, or radio galaxy. It is suggested that the larger MOJAVE-1.5 sample and the radio-loud TANAMI sub-sample (M18R) could serve as a statistically solid basis for studies of beamed AGN in the BAT energy band. Future studies of the multiwavelength properties of blazars, which would involve instruments in the hard X-ray range, such as *INTEGRAL*, *Astrosat*, *NuSTAR*, or other observatories can benefit from this robust radio-loud source sample. On its own, the main TANAMI sample, although including many interesting high-energy sources, lacks the statistical completeness from the MOJAVE samples, which needs to be taken into account for sample studies like in the analyzed hard X-ray band.

In the second part, the hard X-ray characteristics of the sizable gamma-ray-selected 4LAC sample from the *Fermi*/LAT all-sky survey are discussed. Compared to the radio samples in the previous part the 3207 *Fermi* sources, which are mostly blazars, have on average a significantly lower X-ray brightness. Of the sample, only 459 sources can be considered X-ray-bright, with most of them still being fainter that $5\,\sigma$. Only 35% to 41% are not compatible with random background noise. Although similar in their intrinsic luminosity to the radio sample sources, the 4LAC blazars are characterized by different spectral shapes, most notably the BL Lacs, which show rather flat photon indices, around $\Gamma = 2.5$, indicating high-peaked SEDs. These BL Lacs also contribute to a very steep $\log N$-$\log S$ distribution in the X-rays. Generally, the 4LAC sample features a wide array of synchrotron peak frequencies, which greatly influences the signal strength in the BAT band, being subject to the relative location of the SED's big emission bumps and the gap region in-between. In any case, the derived spectral shapes allow the sample, which includes a large number of unclassified blazar candidates, to be parametrized by their gamma-ray and hard X-ray photon indices. The distinct regions that form for FSRQs and BL Lacs in this two-dimensional parameter space allow the classification of 35 candidate sources with high confidence. Using the methodology introduced by the combination of hard X-ray and GeV spectral data, many more blazar candidates can be estimated in the future. A list of dozens of promising candidate sources together with poorly restricted FSRQs and BL Lacs are given, which might merit dedicated X-ray observations by more sensitive instruments, only requiring a low to moderate precision of a fitted power law of $d\Gamma \approx 0.5$.

Especially this last part of the study proves the potential and viable applications of the systematic combination of these high-energy surveys, which are particularly useful for highly beamed AGN populations. With *SRG* and eROSITA the next large all-sky survey in the (soft) X-rays is already underway, which will undoubtedly prove invaluable for large-scale AGN population studies at high energies. However, the hard X-ray band, although technically challenging, has shown to be an important observation window for characterizing the shape of the still enigmatic high-energy bump and for providing X-ray coverage for SED modeling. The latter will be an important ingredient in finding target sources for telescopes in the GeV and TeV domain, like, for example, the CTA. Future missions that would perform measurements of a large number of sources or run an all-sky survey in the MeV regime with better sensitivities than the BAT would be able to further close the gap of observational data in this energy range and contribute to the debated field of gamma-ray-faint MeV blazars.

A. 4LAC hard X-ray fitting results

In the following, the results of the spectral analysis of the 4LAC sample in the hard X-ray band (20 keV–100 keV) from the 105-month *Swift*/BAT survey maps are listed in Table A.0.1. Only the sources which are fitted with a power law and non-fitted sources that produce non-upper-limit flux values are included (546 sources). The complete list in the fits format of all 3207 4LAC sources and the results of the spectral extraction and calculation of photon index, flux, and luminosity as well as the individual spectra can be found in the zip file appended to this document.

Table A.0.1.: Results of the spectral hard X-ray analysis of the 4LAC sample in the 20 keV–100 keV band.

4FGL Name^a	Common Name	RA^b	Dec^b	S/N^c	Γ^d	$F_{20-100\,\mathrm{keV}}{}^e$	$L_{20-100\,\mathrm{keV}}{}^f$	z^g	Type^h	SED Type^i
J0001.2–0747	PMN J0001-0746	0.315	-7.797	2.03	1.39 ± 1.82	< 2.58			B	LSP
J0003.2+2207	2MASX J00032450+2204559	0.806	22.13	2.91	2.16 ± 0.98	4.0 ± 1.43	$(1.03 \pm 0.37) \cdot 10^{44}$	0.1	B	LSP
J0003.3–1928	PKS 0000-197	0.847	-19.468	2.12	1.64 ± 1.37	3.24 ± 1.46			BCU	LSP
J0006.3–0620	PKS 0003-066	1.599	-6.349	2.31	1.89 ± 1.18	3.73 ± 1.52	$(1.46 \pm 0.62) \cdot 10^{45}$	0.347	B	LSP
J0009.1+0628	TXS 0006+061	2.297	6.483	2.5	1.4 ± 1.4	3.33 ± 1.51	$(2.97 \pm 1.38) \cdot 10^{46}$	1.563	B	LSP
J0019.6+7327	S5 0016+73	4.903	73.456	3.65	1.5 ± 0.78	4.26 ± 1.27	$(5.53 \pm 1.66) \cdot 10^{46}$	1.781	Q	LSP
J0021.0+0322	2MASS J00205023+0323578	5.257	3.378	1.81	0.45 ± 1.46	3.6 ± 1.63			BCU	
J0022.0+0006	RX J0022.0+0006	5.515	0.113	3.44	1.32 ± 0.9	4.76 ± 1.58	$(1.2 \pm 0.42) \cdot 10^{45}$	0.306	B	HSP
J0023.7–6820	PKS 0021-686	5.935	-68.338	3.96		4.09 ± 1.01	$(1.61 \pm 0.4) \cdot 10^{45}$	0.354	BCU	LSP
J0028.9+3553	GB6 J0028+3550	7.225	35.89	0.93	2.14 ± 1.89	< 2.13			BCU	LSP
J0035.8+6131	LQAC 008+061	8.968	61.523	5.26	2.24 ± 0.59	5.49 ± 1.3			BCU	
J0035.9+5950	1ES 0033+595	8.982	59.833	21.2	2.84 ± 0.23	16.01 ± 1.31			B	HSP
J0037.9+2612	WISE J003719.15+261312.6	9.482	26.201	1.61	1.17 ± 1.73	2.51 ± 1.34	$(1.32 \pm 0.74) \cdot 10^{44}$	0.148	B	
J0039.1–2219	PMN J0039-2220	9.778	-22.328	0.88	1.45 ± 1.84	< 2.39	$< 2.1 \cdot 10^{43}$	0.062	BCU	
J0040.3+4050	B3 0037+405	10.099	40.836	2.72	1.78 ± 1.37	2.81 ± 1.25			B	LSP
J0042.2+2319	PKS 0039+230	10.558	23.327	2.04	0.78 ± 1.09	4.05 ± 1.48	$(1.73 \pm 0.76) \cdot 10^{46}$	1.426	Q	LSP
J0043.8+3425	GB6 J0043+3426	10.972	34.432	1.61	1.61 ± 1.25	3.13 ± 1.32	$(1.16 \pm 0.5) \cdot 10^{46}$	0.966	Q	LSP
J0047.9+5448	1RXS J004754.5+544758	11.987	54.802	4.71	2.6 ± 0.73	4.74 ± 1.27			BCU	HSP
J0049.6–4500	PMN J0049-4457	12.419	-45.009	3.51		3.22 ± 1.0	$(1.2 \pm 0.37) \cdot 10^{44}$	0.121	BCU	LSP
J0050.0–5736	PKS 0047-579	12.52	-57.616	3.93	1.89 ± 0.91	3.75 ± 1.28	$(7.42 \pm 2.54) \cdot 10^{46}$	1.797	Q	LSP
J0101.8–7543	PKS 0101-76	15.473	-75.732	3.25	1.27 ± 0.98	3.73 ± 1.32	$(1.21 \pm 0.45) \cdot 10^{46}$	1.017	Q	
J0102.8+5824	TXS 0059+581	15.701	58.409	2.88	0.92 ± 1.14	3.38 ± 1.29	$(3.49 \pm 1.56) \cdot 10^{45}$	0.644	Q	LSP
J0105.1+3929	GB6 J0105+3928	16.291	39.496	2.19	1.52 ± 1.68	2.35 ± 1.22	$(1.4 \pm 0.78) \cdot 10^{45}$	0.44	B	LSP
J0109.7+6133	TXS 0106+612	17.445	61.562	2.14		3.66 ± 1.05	$(8.02 \pm 2.3) \cdot 10^{45}$	0.783	Q	LSP
J0113.4+4948	S4 0110+49	18.368	49.805	0.89	0.88 ± 1.88	< 2.27	$< 8.33 \cdot 10^{44}$	0.389	Q	LSP
J0115.1+2622	1RXS J011451.8+262337	18.778	26.373	1.08	1.51 ± 1.93	< 2.23			BCU	ISP
J0115.8+2519	RX J0115.7+2519	18.954	25.332	4.67	1.37 ± 0.67	5.58 ± 1.54	$(2.0 \pm 0.58) \cdot 10^{45}$	0.358	B	HSP
J0116.0–1136	PKS 0113-118	19.001	-11.606	2.43	1.84 ± 1.47	3.06 ± 1.4	$(5.5 \pm 2.59) \cdot 10^{45}$	0.67	Q	LSP
J0123.1+3421	1ES 0120+340	20.791	34.354	9.32	2.6 ± 0.45	8.07 ± 1.42	$(2.15 \pm 0.38) \cdot 10^{45}$	0.272	B	HSP
J0126.0–2221	PKS 0123-226	21.52	-22.361	2.03	1.19 ± 1.28	3.38 ± 1.43	$(5.08 \pm 2.36) \cdot 10^{45}$	0.72	Q	LSP
J0131.2+5547	TXS 0128+554	22.821	55.785	1.5	2.15 ± 1.68	2.33 ± 1.18	$(7.24 \pm 3.68) \cdot 10^{42}$	0.036	BCU	
J0132.7–1654	PKS 0130-17	23.176	-16.91	2.74		3.81 ± 1.16	$(1.51 \pm 0.46) \cdot 10^{46}$	1.02	Q	LSP
J0136.5+3906	B3 0133+388	24.142	39.1	4.54	1.93 ± 0.71	5.03 ± 1.39			B	HSP
J0137.0+4751	OC 457	24.26	47.864	3.01	1.87 ± 0.9	3.92 ± 1.33	$(1.3 \pm 0.45) \cdot 10^{46}$	0.859	Q	LSP
J0137.6–2430	PKS 0135-247	24.407	-24.516	4.23	2.01 ± 0.76	4.88 ± 1.43	$(1.64 \pm 0.48) \cdot 10^{46}$	0.835	Q	LSP
J0137.9+5814	TXS 0134+579	24.496	58.249	4.17		4.43 ± 1.02			B	HSP
J0138.0+2247	GB6 J0138+2248	24.506	22.796	1.74	1.72 ± 1.4	3.06 ± 1.38			B	HSP
J0140.6–0758	RX J0140.7-0758	25.163	-7.975	1.03	1.61 ± 2.06	< 2.05	$< 1.6 \cdot 10^{45}$	0.49	B	HSP
J0143.5–3156	PKS 0140-322	25.898	-31.947	2.6	2.3 ± 1.65	2.46 ± 1.24	$(1.31 \pm 0.68) \cdot 10^{45}$	0.375	BCU	LSP
J0143.7–5846	SUMSS J014347-584550	25.948	-58.772	2.26	2.6 ± 1.77	2.14 ± 1.12			B	HSP
J0145.0–2732	PKS 0142-278	26.259	-27.536	4.46	2.01 ± 0.81	4.48 ± 1.38	$(3.32 \pm 1.03) \cdot 10^{46}$	1.148	Q	LSP
J0151.4–3607	PMN J0151-3605	27.87	-36.127	4.83	1.62 ± 0.59	5.78 ± 1.43	$(9.63 \pm 2.45) \cdot 10^{45}$	0.681	BCU	ISP

Table A.0.1.: continued.

4FGL Name[a]	Common Name	RA[b]	Dec[b]	S/N[c]	Γ[d]	$F_{20-100\,\mathrm{keV}}$[e]	$L_{20-100\,\mathrm{keV}}$[f]	z[g]	Type[h]	SED Type[i]
J0156.9–5301	1RXS J015658.6-530208	29.233	-53.031	5.11		4.5 ± 0.93			B	HSP
J0157.7–4614	PMN J0157-4614	29.435	-46.243	1.37	1.61 ± 1.5	2.56 ± 1.19	$(6.45 \pm 3.01) \cdot 10^{46}$	2.287	Q	LSP
J0158.5–3932	PMN J0158-3932	29.646	-39.536	2.4		3.07 ± 0.99			B	ISP
J0205.0–1700	PKS 0202-17	31.264	-17.002	3.74		5.27 ± 1.12	$(6.83 \pm 1.45) \cdot 10^{46}$	1.74	Q	LSP
J0208.5–0046	PKS 0205-010	32.135	-0.777	1.98		3.8 ± 1.15	$(9.9 \pm 3.0) \cdot 10^{46}$	2.025	B	LSP
J0214.2–7025	PMN J0214-7027	33.556	-70.424	1.91	2.01 ± 1.88	< 1.99			BCU	LSP
J0214.3+5145	TXS 0210+515	33.595	51.757	7.59		6.93 ± 1.07	$(3.91 \pm 0.6) \cdot 10^{43}$	0.049	B	HSP
J0217.0–0821	PKS 0214-085	34.252	-8.359	2.71	1.72 ± 1.51	2.92 ± 1.38	$(3.92 \pm 1.93) \cdot 10^{45}$	0.607	Q	LSP
J0217.2+0837	ZS 0214+083	34.316	8.623	1.41	1.18 ± 1.51	3.09 ± 1.49	$(5.18 \pm 2.56) \cdot 10^{43}$	0.085	B	LSP
J0217.4+7352	S5 0212+73	34.353	73.88	14.74	1.47 ± 0.18	18.91 ± 1.39	$(4.33 \pm 0.32) \cdot 10^{47}$	2.367	Q	LSP
J0217.8+0144	PKS 0215+015	34.462	1.735	1.53	2.21 ± 1.89	< 2.43	$< 5.92 \cdot 10^{46}$	1.715	Q	LSP
J0222.6+4302	3C 66A	35.67	43.036	4.16	2.25 ± 0.72	5.0 ± 1.39	$(3.96 \pm 1.12) \cdot 10^{45}$	0.444	B	ISP
J0224.9+1843	TXS 0222+185	36.229	18.719	11.55	1.86 ± 0.27	14.94 ± 1.66	$(7.36 \pm 0.82) \cdot 10^{47}$	2.69	Q	LSP
J0228.7+6718	4C +67.05	37.198	67.306	2.93	2.8 ± 1.17	3.25 ± 1.23	$(4.86 \pm 1.86) \cdot 10^{45}$	0.523	Q	LSP
J0232.8+2018	1ES 0229+200	38.214	20.316	12.38	2.1 ± 0.3	13.69 ± 1.66	$(7.14 \pm 0.88) \cdot 10^{44}$	0.139	B	HSP
J0235.6–2939	PHL 1389	38.901	-29.652	7.73	1.42 ± 0.41	8.59 ± 1.45	$(1.2 \pm 0.21) \cdot 10^{46}$	0.66	B	HSP
J0237.7+0206	PKS 0235+017	39.441	2.102	1.89	1.37 ± 1.82	< 2.52	$< 2.63 \cdot 10^{42}$	0.022	G	ISP
J0237.8+2848	4C +28.07	39.474	28.804	4.14		4.51 ± 1.24	$(2.61 \pm 0.72) \cdot 10^{46}$	1.206	Q	LSP
J0238.6+1637	PKS 0235+164	39.668	16.618	2.56	1.73 ± 1.02	4.15 ± 1.53	$(1.55 \pm 0.58) \cdot 10^{46}$	0.94	B	LSP
J0239.7+0415	PKS 0237+040	39.94	4.264	3.64	1.51 ± 0.69	5.79 ± 1.65	$(2.05 \pm 0.6) \cdot 10^{46}$	0.978	Q	LSP
J0242.3+1102	OD 166	40.595	11.048	1.75	2.27 ± 1.56	2.97 ± 1.42	$(2.47 \pm 1.19) \cdot 10^{47}$	2.68	Q	LSP
J0242.6+1735	NVSS J024248+173700	40.659	17.598	1.96	1.46 ± 1.75	2.59 ± 1.39	$(2.48 \pm 1.43) \cdot 10^{45}$	0.551	BCU	
J0243.2–0550	PKS 0240-060	40.818	-5.847	3.63	1.74 ± 0.79	4.97 ± 1.51	$(8.55 \pm 2.6) \cdot 10^{46}$	1.805	Q	LSP
J0244.6–5819	RBS 0351	41.158	-58.326	7.69	2.48 ± 0.55	5.84 ± 1.25	$(1.42 \pm 0.31) \cdot 10^{45}$	0.265	B	HSP
J0245.9–4650	PKS 0244-470	41.497	-46.846	1.31	1.32 ± 1.57	2.39 ± 1.19	$(1.55 \pm 0.8) \cdot 10^{46}$	1.385	Q	LSP
J0248.6+5131	WN B0245.0+5118	42.159	51.533	1.94	1.27 ± 1.14	3.49 ± 1.38			BCU	
J0250.7+5630	RX J0250.7+5629	42.698	56.514	2.6	2.88 ± 1.56	2.6 ± 1.24			BCU	HSP
J0253.2–5441	PKS 0252-549	43.306	-54.694	1.01	2.8 ± 1.96	1.92 ± 1.05	$(3.11 \pm 1.71) \cdot 10^{45}$	0.539	Q	LSP
J0255.8+0534	PMN J0255+0533	43.962	5.577	1.08	1.66 ± 1.8	< 2.48	$< 4.21 \cdot 10^{45}$	0.681	B	LSP
J0257.9–1215	PMN J0257-1211	44.492	-12.264	1.54	1.72 ± 1.62	2.65 ± 1.32	$(2.45 \pm 1.24) \cdot 10^{46}$	1.391	Q	LSP
J0303.2+3149	B2 0259+31	45.808	31.821	1.31	0.49 ± 1.66	2.97 ± 1.53			BCU	
J0303.6+4716	4C +47.08	45.91	47.276	3.56	1.54 ± 1.03	3.77 ± 1.41			B	LSP
J0304.5+6821	TXS 0259+681	46.141	68.354	2.66	2.11 ± 1.47	2.61 ± 1.19			BCU	LSP
J0310.9+3815	B3 0307+380	47.73	38.255	2.36	1.36 ± 1.2	3.58 ± 1.47	$(1.06 \pm 0.46) \cdot 10^{46}$	0.945	Q	LSP
J0312.9+4119	B3 0309+411B	48.244	41.329	5.61	1.76 ± 0.46	8.19 ± 1.58	$(3.91 \pm 0.77) \cdot 10^{44}$	0.136	G	LSP
J0316.2–2608	RBS 0405	49.069	-26.145	2.36	1.39 ± 1.42	2.82 ± 1.29	$(1.62 \pm 0.8) \cdot 10^{45}$	0.443	B	HSP
J0317.7–2804	PKS 0315-282	49.426	-28.079	1.79	1.93 ± 1.61	2.43 ± 1.2	$(1.76 \pm 0.88) \cdot 10^{46}$	1.166	Q	LSP
J0317.8–4414	PKS 0316-444	49.472	-44.238	4.25	2.13 ± 1.14	3.05 ± 1.19	$(4.37 \pm 1.73) \cdot 10^{43}$	0.076	BCU	HSP
J0319.8+4130	NGC 1275	49.958	41.512	58.5	3.17 ± 0.12	41.85 ± 1.53	$(3.12 \pm 0.11) \cdot 10^{43}$	0.018	G	LSP
J0322.4+6606	LQAC 050+066	50.615	66.11	1.64	1.18 ± 0.98	3.85 ± 1.36			BCU	
J0324.8+3412	1H 0323+342	51.206	34.212	10.41	1.97 ± 0.28	14.0 ± 1.64	$(1.25 \pm 0.15) \cdot 10^{44}$	0.061	NLSY1	HSP
J0325.5–5635	1RXS J032521.8-563543	51.379	-56.591	4.99	1.77 ± 0.65	4.73 ± 1.25	$(4.07 \pm 1.08) \cdot 10^{43}$	0.06	B	HSP
J0325.7+2225	TXS 0322+222	51.442	22.433	4.03		5.82 ± 1.33	$(1.09 \pm 0.25) \cdot 10^{47}$	2.066	Q	LSP

Table A.0.1.: continued.

4FGL Name[a]	Common Name	RA[b]	Dec[b]	S/N[c]	Γ^d	$F_{20-100\,\mathrm{keV}}{}^e$	$L_{20-100\,\mathrm{keV}}{}^f$	z^g	Type[h]	SED Type[i]
J0331.1–5243	PGC 013066	52.794	-52.733	1.19	1.41 ± 1.61	2.31 ± 1.16	$(2.39 \pm 1.21) \cdot 10^{43}$	0.067	BCU	LSP
J0333.1+8227	1RXS J033208.6+822654	53.297	82.45	1.77	1.87 ± 1.63	2.26 ± 1.14			BCU	
J0333.7+7851	WN B0326.7+7840	53.445	78.85	2.85	3.07 ± 1.14	3.35 ± 1.2	$(2.72 \pm 0.98) \cdot 10^{45}$	0.4	B	ISP
J0334.2–4008	PKS 0332-403	53.557	-40.145	3.77	1.69 ± 0.78	4.25 ± 1.22	$(4.18 \pm 1.21) \cdot 10^{46}$	1.445	B	LSP
J0336.4+3224	NRAO 140	54.102	32.411	15.42	1.7 ± 0.17	23.76 ± 1.66	$(1.71 \pm 0.12) \cdot 10^{47}$	1.259	Q	LSP
J0336.5–0348	1RXS J033623.3-034727	54.13	-3.812	3.44	1.7 ± 0.9	4.42 ± 1.49	$(3.03 \pm 1.05) \cdot 10^{44}$	0.162	B	HSP
J0337.8–1157	PKS 0335-122	54.474	-11.96	1.27	1.38 ± 1.82	< 2.37	$< 1.01 \cdot 10^{47}$	3.442	Q	LSP
J0338.1–2443	2E 0336.0-2453	54.531	-24.721	2.63	1.1 ± 1.26	3.2 ± 1.34	$(5.02 \pm 2.27) \cdot 10^{44}$	0.251	B	HSP
J0339.5–0146	PKS 0336-01	54.877	-1.777	2.93	1.35 ± 0.87	4.75 ± 1.52	$(1.11 \pm 0.37) \cdot 10^{46}$	0.85	Q	LSP
J0347.0+4844	IVS B0343+485	56.753	48.738	1.1	1.49 ± 1.5	2.91 ± 1.38	$(5.01 \pm 2.38) \cdot 10^{46}$	2.043	Q	LSP
J0349.4–1159	1ES 0347-121	57.354	-11.994	9.33	2.2 ± 0.41	9.02 ± 1.52	$(9.34 \pm 1.6) \cdot 10^{44}$	0.188	B	HSP
J0349.8–2103	PKS 0347-211	57.47	-21.058	2.4	1.49 ± 1.45	2.79 ± 1.29	$(1.02 \pm 0.47) \cdot 10^{47}$	2.944	Q	LSP
J0350.8–2814	GALEXASC J035051.31-281633.0	57.71	-28.249	2.15	1.1 ± 1.31	3.01 ± 1.31			BCU	HSP
J0352.0–2516	TXS 0350-253	58.003	-25.273	1.48	0.29 ± 1.43	3.16 ± 1.44			BCU	LSP
J0353.0–6831	PKS 0352-686	58.274	-68.528	10.36	2.72 ± 0.4	8.32 ± 1.27	$(1.67 \pm 0.26) \cdot 10^{44}$	0.087	B	HSP
J0358.1–5954	AT20G J035814-595233	59.539	-59.908	0.63	1.96 ± 2.06	< 1.8	$< 9.54 \cdot 10^{42}$	0.048	B	
J0358.9+6004	TXS 0354+599	59.733	60.077	2.71	2.48 ± 1.27	3.17 ± 1.3	$(2.91 \pm 1.22) \cdot 10^{45}$	0.455	Q	LSP
J0359.6+5057	NRAO 150	59.916	50.959	7.44	1.72 ± 0.33	11.67 ± 1.59	$(1.33 \pm 0.18) \cdot 10^{47}$	1.52	Q	LSP
J0401.0–5353	1RXS J040111.9-535456	60.265	-53.899	2.2	1.15 ± 1.82	< 2.07			BCU	
J0403.9–3605	PKS 0402-362	60.975	-36.087	7.75	1.75 ± 0.43	7.71 ± 1.37	$(7.68 \pm 1.37) \cdot 10^{46}$	1.417	Q	LSP
J0405.6–1308	PKS 0403-13	61.419	-13.144	5.87	1.77 ± 0.6	6.01 ± 1.52	$(7.17 \pm 1.86) \cdot 10^{45}$	0.571	Q	LSP
J0414.8–5338	RBS 0526	63.71	-53.648	1.24	-2.05 ± 1.53	< 1.92			BCU	ISP
J0416.2–4353	SUMSS J041613-435057	64.072	-43.888	1.88	1.18 ± 1.49	2.51 ± 1.2	$(1.06 \pm 0.56) \cdot 10^{45}$	0.398	Q	LSP
J0418.2+3807	3C 111	64.563	38.122	41.58	2.05 ± 0.07	58.15 ± 1.67	$(3.24 \pm 0.09) \cdot 10^{44}$	0.049	G	LSP
J0420.3–6016	1RXS J042012.8-601446	65.078	-60.27	3.03	1.6 ± 1.13	3.11 ± 1.22			BCU	
J0422.3+1951	MS 0419.3+1943	65.587	19.862	3.13	2.22 ± 1.24	3.77 ± 1.55	$(4.2 \pm 1.76) \cdot 10^{45}$	0.512	B	LSP
J0423.3–0120	PKS 0420-01	65.826	-1.334	1.33	1.51 ± 1.48	3.08 ± 1.44	$(9.43 \pm 4.61) \cdot 10^{45}$	0.916	Q	LSP
J0424.7+0036	PKS 0422+00	66.195	0.603	0.57	1.14 ± 1.6	2.94 ± 1.49	$(5.33 \pm 2.94) \cdot 10^{44}$	0.268	B	LSP
J0428.6–3756	PKS 0426-380	67.173	-37.94	4.52	1.98 ± 0.76	4.31 ± 1.27	$(2.88 \pm 0.85) \cdot 10^{46}$	1.11	B	LSP
J0430.3–2507	PMN J0430-2507	67.575	-25.128	1.37	1.85 ± 1.6	2.43 ± 1.21	$(2.36 \pm 1.23) \cdot 10^{45}$	0.516	B	ISP
J0433.0+0522	3C 120	68.262	5.37	41.55	1.98 ± 0.07	57.85 ± 1.71	$(1.45 \pm 0.04) \cdot 10^{44}$	0.033	G	LSP
J0433.1+3227	NVSS J043307+322840	68.29	32.461	1.43	5.0 ± 0.0	< 1.23			B	HSP
J0433.6–6030	PKS 0432-606	68.401	-60.511	1.24	1.79 ± 1.38	2.59 ± 1.16	$(9.84 \pm 4.49) \cdot 10^{45}$	0.93	Q	LSP
J0440.8+2749	B2 0437+27B	70.22	27.832	4.18	1.23 ± 0.6	7.29 ± 1.8			B	ISP
J0441.5+1505	1RXS J044127.8+150455	70.39	15.091	2.28	2.29 ± 1.88	2.62 ± 1.43	$(8.24 \pm 4.6) \cdot 10^{43}$	0.109	B	HSP
J0442.6–0017	PKS 0440-00	70.661	-0.296	1.76	1.51 ± 1.01	4.21 ± 1.56	$(2.6 \pm 1.02) \cdot 10^{45}$	0.449	Q	LSP
J0442.7+6142	GB6 J0442+6140	70.678	61.705	2.27	1.56 ± 1.35	3.0 ± 1.34			BCU	
J0447.2–2539	2MASS J04472149-2539302	71.812	-25.651	0.56	-2.33 ± 1.02	< 1.73			BCU	ISP
J0447.4–2747	MRC 0445-278	71.869	-27.8	1.32	1.79 ± 1.55	2.49 ± 1.21			BCU	
J0455.7–4617	PKS 0454-46	73.946	-46.287	4.46	2.0 ± 0.63	5.02 ± 1.26	$(1.79 \pm 0.45) \cdot 10^{46}$	0.858	Q	LSP
J0456.2+2702	MG2 J045613+2702	74.067	27.04	2.39	1.83 ± 1.23	3.84 ± 1.59			BCU	LSP
J0457.0+0646	4C +06.21	74.255	6.78	0.96	2.25 ± 1.93	< 2.54	$< 1.61 \cdot 10^{45}$	0.405	Q	LSP
J0457.0–2324	PKS 0454-234	74.261	-23.415	2.77	1.55 ± 1.13	3.42 ± 1.36	$(1.31 \pm 0.53) \cdot 10^{46}$	1.003	Q	LSP

Table A.0.1.: continued.

4FGL Name[a]	Common Name	RA[b]	Dec[b]	S/N[c]	Γ[d]	$F_{20-100\,\mathrm{keV}}$[e]	$L_{20-100\,\mathrm{keV}}$[f]	z[g]	Type[h]	SED Type[i]
J0500.2+5237	GB6 J0500+5238	75.074	52.633	3.61	2.11 ± 0.86	4.56 ± 1.47			BCU	
J0505.6+6405	TXS 0500+640	76.424	64.088	0.85	1.42 ± 2.2	< 1.74			BCU	LSP
J0507.7–6104	PMN J0507-6104	76.933	-61.081	3.64	1.87 ± 0.93	3.55 ± 1.23	$(2.08 \pm 0.73) \cdot 10^{46}$	1.089	Q	LSP
J0507.9+4647	TXS 0503+466	76.979	46.795	2.04	0.78 ± 1.24	3.89 ± 1.58			BCU	
J0507.9+6737	1ES 0502+675	76.996	67.622	5.67	2.21 ± 0.62	5.62 ± 1.4	$(3.75 \pm 0.95) \cdot 10^{45}$	0.416	B	HSP
J0508.2+5211	NVSS J050809+521256	77.059	52.189	2.31	1.8 ± 1.2	3.5 ± 1.43			BCU	
J0509.9–6417	RBS 0625	77.488	-64.289	3.52	1.36 ± 0.81	4.14 ± 1.26			BCU	HSP
J0510.0+1800	PKS 0507+17	77.518	18.014	1.34	1.97 ± 2.02	< 2.5	$< 1.54 \cdot 10^{45}$	0.416	Q	LSP
J0519.6–4544	Pictor A	79.906	-45.744	24.11	1.97 ± 0.14	23.23 ± 1.36	$(6.6 \pm 0.39) \cdot 10^{43}$	0.035	G	LSP
J0521.2+1637	3C 138	80.314	16.631	3.6		4.64 ± 1.44	$(1.08 \pm 0.33) \cdot 10^{46}$	0.759	CSS	LSP
J0522.9–3628	PKS 0521-36	80.737	-36.469	20.92	2.02 ± 0.16	20.91 ± 1.39	$(1.57 \pm 0.1) \cdot 10^{44}$	0.056	AGN	LSP
J0525.4–4600	PKS 0524-460	81.372	-46.007	8.46	1.51 ± 0.32	10.45 ± 1.37	$(9.19 \pm 1.21) \cdot 10^{46}$	1.479	Q	LSP
J0526.1+6318	GB6 J0526+6317	81.547	63.304	1.3	1.42 ± 1.94	< 2.24			BCU	LSP
J0526.7–1519	NVSS J052645-151900	81.692	-15.321	1.59	1.05 ± 1.1	3.9 ± 1.47			BCU	
J0530.9+1332	PKS 0528+134	82.736	13.54	4.89	1.06 ± 0.46	10.17 ± 1.85	$(1.12 \pm 0.21) \cdot 10^{47}$	2.07	Q	LSP
J0533.3+4823	TXS 0529+483	83.334	48.383	1.39	0.98 ± 1.27	3.71 ± 1.55	$(1.27 \pm 0.6) \cdot 10^{46}$	1.16	Q	LSP
J0533.3–5549	PMN J0533-5549	83.331	-55.825	1.68	2.03 ± 2.09	< 1.83			BCU	
J0536.4–3401	PKS 0534-340	84.104	-34.017	2.38	2.05 ± 2.02	< 1.95	$< 4.12 \cdot 10^{45}$	0.684	Q	LSP
J0538.8–4405	PKS 0537-441	84.709	-44.086	4.27	1.03 ± 0.7	4.98 ± 1.32	$(1.06 \pm 0.31) \cdot 10^{46}$	0.892	B	LSP
J0539.9–2839	PKS 0537-286	84.995	-28.659	11.23	1.34 ± 0.25	14.04 ± 1.46	$(4.64 \pm 0.48) \cdot 10^{47}$	3.104	Q	LSP
J0546.9–2206	1RXS J054656.9-220500	86.727	-22.112	1.32	2.02 ± 1.66	2.48 ± 1.26	$(6.14 \pm 3.26) \cdot 10^{44}$	0.28	B	
J0550.5–3216	PKS 0548-322	87.625	-32.277	24.59	2.23 ± 0.16	21.89 ± 1.42	$(2.57 \pm 0.17) \cdot 10^{44}$	0.069	B	HSP
J0552.8+0313	PKS 0550+032	88.218	3.232	2.12	1.81 ± 1.25	3.73 ± 1.57			BCU	LSP
J0555.6+3947	B2 0552+39A	88.902	39.788	5.83	1.84 ± 0.51	8.06 ± 1.72	$(2.9 \pm 0.62) \cdot 10^{47}$	2.365	Q	LSP
J0557.3–0615	1RXS J055717.0-061705	89.344	-6.265	1.29	1.25 ± 1.67	2.82 ± 1.47			BCU	
J0600.3+1244	NVSS J060015+124344	90.082	12.744	2.7		4.87 ± 1.44			BCU	HSP
J0600.6–3939	PKS 0558-396	90.151	-39.651	3.24		3.93 ± 1.04	$(4.61 \pm 1.22) \cdot 10^{46}$	1.661	Q	LSP
J0601.8–2003	PMN J0601-2004	90.473	-20.059	1.75	1.6 ± 1.7	2.52 ± 1.31	$(1.55 \pm 0.82) \cdot 10^{46}$	1.216	Q	LSP
J0608.1–1521	PMN J0608-1520	92.03	-15.364	1.53	1.39 ± 1.25	3.48 ± 1.47	$(1.45 \pm 0.63) \cdot 10^{46}$	1.094	Q	LSP
J0608.1–6028	PKS 0607-605	92.028	-60.476	1.73	2.16 ± 1.74	2.11 ± 1.11	$(1.57 \pm 0.83) \cdot 10^{46}$	1.1	Q	LSP
J0608.9–5456	PKS 0607-549	92.239	-54.943	3.8	1.6 ± 0.86	3.89 ± 1.26			BCU	LSP
J0621.8+1746	RX J0621.7+1747	95.452	17.779	0.95	1.21 ± 1.71	3.01 ± 1.6			B	
J0622.4–6433	RX J062308.0-643619	95.614	-64.558	4.8	1.35 ± 0.67	4.78 ± 1.29	$(1.93 \pm 0.53) \cdot 10^{44}$	0.129	Q	LSP
J0623.0–3010	PMN J0623-3010	95.765	-30.183	3.59	2.8 ± 0.96	4.03 ± 1.31			BCU	
J0625.8–5441	PMN J0625-5438	96.452	-54.692	2.85	1.89 ± 0.96	3.51 ± 1.25	$(9.54 \pm 3.39) \cdot 10^{46}$	2.051	Q	LSP
J0629.3–1959	PKS 0627-199	97.348	-20.0	2.28	1.86 ± 1.21	3.38 ± 1.39	$(5.86 \pm 2.42) \cdot 10^{46}$	1.724	B	LSP
J0635.6–7518	PKS 0637-75	98.902	-75.305	8.79	1.91 ± 0.33	10.16 ± 1.39	$(1.78 \pm 0.25) \cdot 10^{46}$	0.653	Q	LSP
J0638.6+7320	S5 0633+73	99.671	73.344	2.94	0.97 ± 1.04	3.74 ± 1.35	$(3.04 \pm 1.18) \cdot 10^{46}$	1.85	Q	LSP
J0640.0–1253	TXS 0637-128	100.021	-12.896	4.52	2.76 ± 1.09	4.07 ± 1.47	$(2.17 \pm 0.8) \cdot 10^{44}$	0.135	B	HSP
J0641.7–0320	PMN J0641-0320	100.437	-3.347	5.31	1.37 ± 0.55	7.8 ± 1.76	$(3.88 \pm 0.9) \cdot 10^{46}$	1.196	Q	LSP
J0644.4–6712	PKS 0644-671	101.105	-67.212	1.55	-0.04 ± 1.6	< 2.66			BCU	LSP
J0647.0–5138	1ES 0646-515	101.773	-51.638	1.82	2.49 ± 1.77	2.14 ± 1.13			BCU	HSP
J0648.7+1516	RX J0648.7+1516	102.191	15.281	4.4	3.66 ± 1.18	4.23 ± 1.52	$(4.99 \pm 1.82) \cdot 10^{44}$	0.179	B	HSP

Table A.0.1.: continued.

4FGL Name[a]	Common Name	RA[b]	Dec[b]	S/N[c]	Γ[d]	$F_{20-100\,\mathrm{keV}}$[e]	$L_{20-100\,\mathrm{keV}}$[f]	z[g]	Type[h]	SED Type[i]
J0650.7+2503	1ES 0647+250	102.699	25.055	3.31		4.76 ± 1.37	$(5.52 \pm 1.6) \cdot 10^{44}$	0.203	B	HSP
J0651.4+6525	NVSS J065125+652458	102.862	65.423	1.42	-0.29 ± 1.41	< 3.38			BCU	ISP
J0656.3–0322	TXS 0653-033	104.077	-3.369	3.95	1.44 ± 0.73	5.73 ± 1.72	$(7.41 \pm 2.32) \cdot 10^{45}$	0.634	Q	LSP
J0658.1–5840	PMN J0658-5840	104.539	-58.672	0.97	1.05 ± 1.86	< 2.14	$< 9.77 \cdot 10^{44}$	0.421	BCU	LSP
J0700.2+1304	GB6 J0700+1304	105.075	13.067	2.75	3.07 ± 1.46	3.43 ± 1.54			B	HSP
J0701.5–4634	PKS 0700-465	105.391	-46.573	2.33	2.08 ± 1.37	2.76 ± 1.2	$(9.36 \pm 4.13) \cdot 10^{45}$	0.822	Q	LSP
J0703.2–3914	1RXS J070312.7-391417	105.824	-39.248	2.19	5.0 ± 0.0	< 1.55			B	LSP
J0703.3–0050	TXS 0700-007	105.837	-0.844	1.91	1.49 ± 1.6	3.1 ± 1.53			BCU	ISP
J0709.2–1527	PKS 0706-15	107.31	-15.451	6.76	2.45 ± 0.69	5.77 ± 1.53			BCU	HSP
J0710.4+5908	1H 0658+595	107.623	59.135	14.35	2.39 ± 0.26	14.39 ± 1.49	$(6.16 \pm 0.65) \cdot 10^{44}$	0.125	B	HSP
J0710.8–3851	AT20G J071043-385037	107.725	-38.851	2.84		3.48 ± 1.08	$(1.44 \pm 0.45) \cdot 10^{44}$	0.129	Q	LSP
J0712.4+5724	RX J0712.3+5719	108.125	57.41	1.17	1.8 ± 1.87	< 2.21	$< 4.92 \cdot 10^{43}$	0.095	B	
J0715.3–6828	PMN J0715-6829	108.828	-68.483	1.25	1.85 ± 1.56	2.36 ± 1.15			BCU	
J0721.9+7120	S5 0716+71	110.488	71.341	5.37	0.84 ± 0.46	8.12 ± 1.43	$(2.99 \pm 0.54) \cdot 10^{44}$	0.127	B	ISP
J0723.0–0732	1RXS J072259.5-073131	110.752	-7.544	2.25	1.17 ± 1.47	3.19 ± 1.52			B	HSP
J0725.8–0054	PKS 0723-008	111.47	-0.913	5.89	1.51 ± 0.47	9.17 ± 1.77	$(3.72 \pm 0.73) \cdot 10^{44}$	0.128	BCU	LSP
J0728.0+6735	NVSS J072854+673225	112.021	67.599	1.2	2.16 ± 2.05	< 1.97	$< 7.52 \cdot 10^{45}$	0.846	BCU	LSP
J0730.3–1141	PKS 0727-11	112.578	-11.689	3.83	1.5 ± 0.64	6.24 ± 1.66	$(6.35 \pm 1.71) \cdot 10^{46}$	1.589	Q	LSP
J0730.4+3308	1RXS J073026.0+330727	112.624	33.134	1.82	1.41 ± 1.48	3.17 ± 1.5	$(9.62 \pm 4.67) \cdot 10^{43}$	0.112	B	HSP
J0732.7–4638	PKS 0731-465	113.177	-46.649	2.15	0.47 ± 1.29	3.39 ± 1.39			BCU	LSP
J0733.4+5152	NVSS J073326+515355	113.362	51.88	4.65	3.08 ± 1.24	3.41 ± 1.33	$(3.72 \pm 1.47) \cdot 10^{43}$	0.065	BCU	HSP
J0734.4–7711	PKS 0736-770	113.612	-77.185	2.55	1.31 ± 0.9	3.95 ± 1.3			Q	LSP
J0738.1+1742	PKS 0735+17	114.539	17.707	0.66	1.45 ± 2.18	< 2.02	$< 1.08 \cdot 10^{45}$	0.424	B	LSP
J0739.2+0137	PKS 0736+01	114.82	1.622	3.58	1.51 ± 0.66	6.36 ± 1.74	$(5.92 \pm 1.67) \cdot 10^{44}$	0.189	Q	LSP
J0740.9+3203	LEDA 1979979	115.234	32.058	1.92	2.55 ± 1.34	3.4 ± 1.44	$(3.35 \pm 1.45) \cdot 10^{44}$	0.179	B	HSP
J0741.2–5140	PMN J0740-5137	115.31	-51.674	2.31	1.54 ± 1.37	2.75 ± 1.24			BCU	
J0742.6+5443	GB6 J0742+5444	115.672	54.727	1.91	1.53 ± 1.71	2.35 ± 1.24	$(4.25 \pm 2.36) \cdot 10^{45}$	0.72	Q	LSP
J0743.0–5622	PMN J0743-5619	115.77	-56.377	1.81	1.39 ± 1.48	2.62 ± 1.23	$(5.22 \pm 2.48) \cdot 10^{46}$	2.319	Q	LSP
J0746.0–0039	PKS 0743-006	116.525	-0.654	1.18	1.33 ± 1.75	2.7 ± 1.45	$(8.78 \pm 5.01) \cdot 10^{45}$	0.994	Q	
J0746.4+2546	B2 0743+25	116.602	25.768	11.84	1.4 ± 0.24	17.24 ± 1.72	$(5.77 \pm 0.58) \cdot 10^{47}$	2.987	Q	LSP
J0748.0–1638	TXS 0745-165	117.006	-16.644	0.85	1.38 ± 2.05	< 2.31			BCU	LSP
J0750.8+1229	OI 280	117.701	12.494	2.65	1.04 ± 0.98	4.83 ± 1.65	$(1.02 \pm 0.39) \cdot 10^{46}$	0.889	Q	
J0751.0+7908	JVAS J0750+7909	117.768	79.139	0.99	-2.16 ± 0.96	< 1.99			BCU	LSP
J0751.4+2655	MG2 J075139+2657	117.866	26.928	1.63	0.05 ± 1.65	< 3.16	$< 6.67 \cdot 10^{44}$	0.334	BCU	LSP
J0752.2+3313	OI 380	118.055	33.232	1.46	1.15 ± 2.11	< 2.27	$< 2.42 \cdot 10^{46}$	1.936	Q	
J0754.0+0451	GB6 J0754+0452	118.521	4.857	1.11	1.8 ± 1.86	< 2.53			BCU	
J0754.7+4823	GB1 0751+485	118.693	48.393	2.27	0.38 ± 1.0	4.62 ± 1.5	$(1.35 \pm 0.55) \cdot 10^{45}$	0.377	B	LSP
J0757.1+0956	PKS 0754+100	119.286	9.949	3.88	3.03 ± 1.56	3.12 ± 1.47	$(8.7 \pm 4.18) \cdot 10^{44}$	0.266	B	LSP
J0804.9–0624	1RXS J080458.3-062432	121.233	-6.406	2.5	1.89 ± 1.2	3.65 ± 1.5	$(2.35 \pm 1.0) \cdot 10^{45}$	0.43	BCU	
J0805.0+6746	GB6 J0805+6745	121.252	67.768	0.86	1.57 ± 1.86	< 2.12			BCU	LSP
J0805.2–0110	PKS B0802-010	121.3	-1.181	4.77	1.35 ± 0.53	8.03 ± 1.74	$(5.36 \pm 1.18) \cdot 10^{46}$	1.388	Q	LSP
J0805.4+6147	TXS 0800+618	121.356	61.794	6.15	1.16 ± 0.45	8.07 ± 1.43	$(1.99 \pm 0.36) \cdot 10^{47}$	3.033	Q	LSP
J0808.2–0751	PKS 0805-07	122.065	-7.856	2.75	1.2 ± 1.36	3.5 ± 1.55	$(3.56 \pm 1.63) \cdot 10^{46}$	1.837	Q	LSP

Table A.0.1.: continued.

4FGL Name[a]	Common Name	RA[b]	Dec[b]	S/N[c]	Γ[d]	$F_{20-100\,\mathrm{keV}}$[e]	$L_{20-100\,\mathrm{keV}}$[f]	z[g]	Type[h]	SED Type[i]
J0808.5+4950	OJ 508	122.13	49.834	1.2	1.04 ± 1.56	2.65 ± 1.32	$(1.45 \pm 0.78) \cdot 10^{46}$	1.435	Q	LSP
J0812.0+0237	PMN J0811+0237	123.009	2.629	3.04	2.04 ± 1.02	4.23 ± 1.57			B	
J0812.3+1143	GB6 J0812+1141	123.099	11.727	2.0	0.95 ± 1.33	3.63 ± 1.58			B	
J0820.1–2801	1RXS J082021.9-280206	125.04	-28.026	5.3	1.49 ± 0.59	6.42 ± 1.56			BCU	
J0822.4–2630	NVSS J082236-263125	125.617	-26.502	1.66	1.66 ± 1.87	< 2.3			BCU	
J0824.7+5552	OJ 535	126.198	55.882	2.86	1.92 ± 0.99	3.64 ± 1.32	$(4.18 \pm 1.52) \cdot 10^{46}$	1.417	Q	LSP
J0825.9–2230	PKS 0823-223	126.499	-22.506	3.26	1.78 ± 0.81	4.9 ± 1.51	$(1.76 \pm 0.55) \cdot 10^{46}$	0.91	B	LSP
J0826.4–6404	SUMSS J082627-640414	126.623	-64.076	3.56	2.16 ± 0.9	3.86 ± 1.28			B	HSP
J0827.6–3735	PKS B0826-373	126.914	-37.592	2.17	1.9 ± 1.3	3.09 ± 1.32			BCU	
J0828.3+4152	B3 0824+420	127.088	41.879	2.34	1.41 ± 1.62	2.61 ± 1.3	$(1.01 \pm 0.5) \cdot 10^{40}$	0.001	B	
J0830.8+2410	S3 0827+24	127.702	24.173	3.34	1.03 ± 0.96	4.59 ± 1.54	$(1.08 \pm 0.4) \cdot 10^{46}$	0.939	Q	LSP
J0831.5+1747	GB6 J0831+1746	127.887	17.788	0.45	5.0 ± 0.0	< 0.94			B	ISP
J0834.6+4402	B3 0831+442	128.667	44.05	1.82	2.16 ± 1.63	2.54 ± 1.25			B	LSP
J0841.3+7053	4C +71.07	130.342	70.889	37.53	1.65 ± 0.08	40.73 ± 1.38	$(1.0 \pm 0.03) \cdot 10^{48}$	2.218	Q	LSP
J0847.2+1134	RX J0847.1+1133	131.812	11.569	2.0	1.66 ± 1.61	2.87 ± 1.43	$(3.04 \pm 1.59) \cdot 10^{44}$	0.198	B	ISP
J0854.3+4408	B3 0850+443	133.593	44.149	1.3	1.81 ± 1.91	< 2.09	$< 9.96 \cdot 10^{44}$	0.382	B	ISP
J0854.8+2006	OJ 287	133.707	20.116	3.84	1.3 ± 0.89	4.68 ± 1.52	$(1.17 \pm 0.41) \cdot 10^{45}$	0.306	B	LSP
J0856.8+8559	NVSS J085740+860344	134.224	85.995	1.94	1.84 ± 1.41	2.58 ± 1.17			BCU	
J0900.6–7408	AT20G J085959-741401	135.172	-74.144	2.19	1.21 ± 0.96	3.8 ± 1.32			BCU	LSP
J0902.5–4801	PMN J0903-4805	135.647	-48.023	4.37		4.86 ± 1.08			BCU	
J0906.3–0905	PMN J0906-0905	136.583	-9.093	2.16	2.74 ± 1.32	3.53 ± 1.47			B	
J0912.5+1556	RX J0912.5+1555	138.137	15.934	1.52	1.14 ± 1.99	< 2.43	$< 2.7 \cdot 10^{44}$	0.212	B	HSP
J0913.3+8133	1RXS J091324.6+813318	138.346	81.566	0.77	0.99 ± 2.02	< 2.05	$< 2.16 \cdot 10^{45}$	0.639	B	
J0917.3–0342	NVSS J091714-034315	139.334	-3.704	2.94	2.55 ± 1.49	3.08 ± 1.45	$(1.09 \pm 0.53) \cdot 10^{45}$	0.308	B	HSP
J0920.9+4441	S4 0917+44	140.229	44.699	3.15	1.98 ± 0.96	3.66 ± 1.29	$(1.28 \pm 0.45) \cdot 10^{47}$	2.186	Q	LSP
J0921.6+6216	OK 630	140.419	62.271	2.32	0.93 ± 1.22	3.13 ± 1.27	$(1.57 \pm 0.71) \cdot 10^{46}$	1.446	Q	LSP
J0922.7–3959	PKS 0920-39	140.692	-39.987	3.15	0.69 ± 0.86	5.05 ± 1.49	$(4.01 \pm 1.45) \cdot 10^{45}$	0.595	BCU	LSP
J0923.5+3852	B2 0920+39	140.885	38.874	3.82	1.07 ± 0.68	5.32 ± 1.43			BCU	LSP
J0930.3+8612	S5 0916+864	142.599	86.202	2.52	1.97 ± 1.17	2.94 ± 1.18			B	LSP
J0930.5+4951	1ES 0927+500	142.625	49.858	4.77		4.41 ± 0.98	$(4.26 \pm 0.95) \cdot 10^{44}$	0.187	B	HSP
J0934.5–1720	RXC J0934.4-1721	143.628	-17.339	4.93		4.46 ± 1.19	$(8.24 \pm 2.19) \cdot 10^{44}$	0.25	B	ISP
J0943.7+6137	FIRST J094420.3+613550	145.926	61.619	-0.07	1.25 ± 2.09	< 1.86	$< 3.51 \cdot 10^{45}$	0.792	BCU	
J0945.2+5200	WISE J094452.09+520233.4	146.316	52.005	0.94	1.18 ± 2.19	< 1.64	$< 1.45 \cdot 10^{45}$	0.563	Q	LSP
J0948.9+0022	PMN J0948+0022	147.244	0.372	4.66	0.8 ± 0.58	7.61 ± 1.67	$(6.14 \pm 1.56) \cdot 10^{45}$	0.585	NLSY1	LSP
J0949.0+4038	4C +40.24	147.262	40.637	5.38	2.04 ± 0.67	4.95 ± 1.29	$(4.65 \pm 1.22) \cdot 10^{46}$	1.25	Q	LSP
J0950.2+4553	RX J0950.2+4553	147.565	45.886	1.15	1.42 ± 2.26	< 1.5	$< 6.94 \cdot 10^{44}$	0.399	B	LSP
J0952.2+7503	RBS 0804	148.063	75.056	1.99	5.0 ± 0.0	< 1.06	$< 1.6 \cdot 10^{44}$	0.181	B	HSP
J0955.1+3551	1RXS J095508.2+355054	148.782	35.858	4.12	1.62 ± 0.86	4.03 ± 1.31	$(1.07 \pm 0.36) \cdot 10^{46}$	0.834	B	ISP
J0957.3–1348	PMN J0957-1350	149.331	-13.814	3.4	1.19 ± 0.97	4.62 ± 1.61	$(2.43 \pm 0.89) \cdot 10^{46}$	1.323	Q	LSP
J0958.0+3222	3C 232	149.522	32.369	2.76		3.43 ± 1.03	$(3.13 \pm 0.94) \cdot 10^{45}$	0.531	Q	LSP
J1010.2–3119	1RXS J101015.9-311909	152.572	-31.321	4.83		5.34 ± 1.21	$(2.86 \pm 0.65) \cdot 10^{44}$	0.143	B	HSP
J1010.8–0158	PKS 1008-01	152.704	-1.982	3.27	1.97 ± 1.18	3.68 ± 1.49	$(1.44 \pm 0.59) \cdot 10^{46}$	0.896	Q	LSP
J1014.3+4112	GB6 J1014+4112	153.591	41.208	1.11	1.67 ± 1.93	< 1.99			BCU	LSP

Table A.0.1.: continued.

4FGL Name[a]	Common Name	RA[b]	Dec[b]	S/N[c]	Γ[d]	$F_{20-100\,\mathrm{keV}}$[e]	$L_{20-100\,\mathrm{keV}}$[f]	z[g]	Type[h]	SED Type[i]
J1014.7+3210	NVSS J101445+320725	153.685	32.173	1.45	1.49 ± 1.6	2.47 ± 1.22	$(6.92 \pm 3.68) \cdot 10^{44}$	0.315	BCU	LSP
J1014.8+2257	OL 220	153.716	22.955	2.39	1.82 ± 1.52	2.61 ± 1.25	$(3.11 \pm 1.55) \cdot 10^{45}$	0.566	Q	LSP
J1015.0+4926	1H 1013+498	153.768	49.434	2.93	1.36 ± 1.1	3.16 ± 1.23	$(3.66 \pm 1.5) \cdot 10^{44}$	0.212	B	HSP
J1022.4–4231	PMN J1022-4232	155.622	-42.524	2.18	5.0 ± 0.0	< 1.17			B	LSP
J1022.7–0112	RX J1022.7-0112	155.684	-1.207	1.81	1.92 ± 2.04	< 2.33	$< 1.0 \cdot 10^{45}$	0.36	B	HSP
J1023.1+3949	4C +40.25	155.789	39.823	4.5	1.98 ± 0.9	3.68 ± 1.24	$(3.83 \pm 1.3) \cdot 10^{46}$	1.333	Q	LSP
J1027.6+8251	2MASS J10284195+8253398	156.923	82.861	1.52	1.51 ± 1.68	2.18 ± 1.12			BCU	
J1028.4–0234	PMN J1028-0237	157.121	-2.583	3.16	1.54 ± 0.97	4.29 ± 1.55	$(3.05 \pm 1.16) \cdot 10^{45}$	0.476	Q	LSP
J1031.1+7442	S5 1027+74	157.793	74.702	2.76	1.22 ± 1.38	2.66 ± 1.2	$(9.61 \pm 4.48) \cdot 10^{43}$	0.123	B	ISP
J1031.3+5053	1ES 1028+511	157.845	50.884	6.21	2.9 ± 0.92	3.75 ± 1.16	$(2.18 \pm 0.68) \cdot 10^{45}$	0.36	B	HSP
J1031.6+6019	TXS 1028+605	157.909	60.318	3.52	2.43 ± 1.13	2.99 ± 1.15	$(3.71 \pm 1.43) \cdot 10^{46}$	1.231	Q	LSP
J1036.2+2202	OL 256	159.053	22.04	2.16		3.22 ± 1.06	$(3.81 \pm 1.26) \cdot 10^{45}$	0.595	Q	LSP
J1037.7–2822	PKS B1035-281	159.427	-28.382	2.59		4.19 ± 1.28	$(1.84 \pm 0.56) \cdot 10^{46}$	1.066	Q	LSP
J1038.8–5312	MRC 1036-529	159.713	-53.207	4.24	1.64 ± 1.07	3.65 ± 1.39	$(3.48 \pm 1.34) \cdot 10^{46}$	1.45	Q	LSP
J1040.5+0617	GB6 J1040+0617	160.15	6.285	2.26	1.84 ± 1.8	2.4 ± 1.3			B	LSP
J1042.9+0054	RBS 0895	160.727	0.906	2.11	1.38 ± 1.57	2.92 ± 1.45	$(5.01 \pm 2.65) \cdot 10^{45}$	0.73	BCU	HSP
J1044.6+8053	S5 1039+81	161.164	80.894	6.52	1.24 ± 0.41	8.14 ± 1.33	$(4.02 \pm 0.68) \cdot 10^{46}$	1.254	Q	LSP
J1046.0+5448	7C 1043+5505	161.519	54.814	2.42	1.94 ± 1.34	2.62 ± 1.13	$(4.87 \pm 2.19) \cdot 10^{44}$	0.249	BCU	
J1047.9+0055	TXS 1045+011	161.985	0.923	2.29	1.55 ± 1.47	3.08 ± 1.43	$(4.32 \pm 2.12) \cdot 10^{45}$	0.641	BCU	LSP
J1047.9–3738	GALEXASC J104756.99-373730.1	161.988	-37.646	1.38	1.97 ± 1.42	3.24 ± 1.45			BCU	
J1058.4+0133	4C +01.28	164.624	1.564	3.67		3.84 ± 1.17	$(1.39 \pm 0.43) \cdot 10^{46}$	0.89	B	LSP
J1058.6+5627	TXS 1055+567	164.665	56.463	2.1	1.94 ± 1.73	1.98 ± 1.05	$(1.08 \pm 0.59) \cdot 10^{44}$	0.143	B	ISP
J1102.9+3014	B2 1100+30B	165.74	30.244	3.37	1.88 ± 0.97	3.56 ± 1.27	$(1.76 \pm 0.65) \cdot 10^{45}$	0.384	Q	LSP
J1103.6–2329	1ES 1101-232	165.909	-23.496	7.15		7.89 ± 1.27	$(7.56 \pm 1.22) \cdot 10^{44}$	0.186	B	HSP
J1104.4+3812	Mkn 421	166.119	38.207	120.3	2.78 ± 0.05	80.24 ± 1.28	$(1.7 \pm 0.03) \cdot 10^{44}$	0.03	B	HSP
J1107.0–4449	PKS 1104-445	166.775	-44.832	2.3	1.42 ± 0.98	4.17 ± 1.51	$(4.0 \pm 1.47) \cdot 10^{46}$	1.598	Q	LSP
J1112.5+3448	TXS 1109+350	168.147	34.802	1.43	1.47 ± 1.36	2.73 ± 1.22	$(4.16 \pm 1.87) \cdot 10^{46}$	1.949	Q	LSP
J1118.2–0415	PMN J1118-0413	169.575	-4.254	2.67	1.37 ± 1.53	3.08 ± 1.5			AGN	LSP
J1118.6–1235	PKS 1115-12	169.653	-12.596	2.59	1.36 ± 1.08	4.31 ± 1.65	$(4.61 \pm 1.8) \cdot 10^{46}$	1.739	Q	
J1119.0+1235	OM 127	169.766	12.587	2.34		3.99 ± 1.12	$(7.96 \pm 2.23) \cdot 10^{46}$	2.126	Q	LSP
J1129.1+3703	CRATES J112916+370317	172.296	37.064	1.52	1.79 ± 1.58	2.27 ± 1.12	$(1.53 \pm 0.79) \cdot 10^{45}$	0.445	B	LSP
J1129.8–1447	PKS 1127-14	172.465	-14.796	12.62	1.77 ± 0.25	16.93 ± 1.8	$(1.12 \pm 0.12) \cdot 10^{47}$	1.184	Q	LSP
J1131.0+3815	B2 1128+38	172.755	38.257	3.43	2.37 ± 0.8	4.07 ± 1.21	$(1.2 \pm 0.36) \cdot 10^{47}$	1.733	Q	LSP
J1134.8–1729	1RXS J113443.6-172853	173.714	-17.498	1.62	2.38 ± 1.62	3.0 ± 1.5	$(4.71 \pm 2.38) \cdot 10^{45}$	0.571	B	
J1136.4+6736	RX J1136.5+6737	174.118	67.613	9.83	2.52 ± 0.36	8.45 ± 1.22	$(4.44 \pm 0.65) \cdot 10^{44}$	0.136	B	HSP
J1144.9+1937	3C 264	176.239	19.628	1.04	1.28 ± 2.14	< 1.8	$< 1.9 \cdot 10^{42}$	0.022	G	HSP
J1145.7–6949	PKS 1143-696	176.438	-69.831	4.82	1.9 ± 0.6	5.7 ± 1.43	$(1.0 \pm 0.26) \cdot 10^{45}$	0.244	Q	LSP
J1146.9+3958	S4 1144+40	176.741	39.978	3.5		3.68 ± 0.93	$(1.7 \pm 0.43) \cdot 10^{46}$	1.089	Q	LSP
J1148.5+2629	TXS 1145+268	177.141	26.499	1.45	1.93 ± 1.74	2.14 ± 1.14	$(7.53 \pm 4.08) \cdot 10^{45}$	0.867	Q	LSP
J1152.8+3308	B2 1150+33A	178.212	33.142	5.88	1.89 ± 0.54	5.89 ± 1.33	$(6.38 \pm 1.44) \cdot 10^{46}$	1.398	Q	LSP
J1153.4+4931	4C +49.22	178.351	49.517	7.75	1.9 ± 0.41	7.28 ± 1.26	$(2.62 \pm 0.46) \cdot 10^{45}$	0.334	Q	LSP
J1154.0+6018	RX J1154.0+6022	178.519	60.311	2.93		3.5 ± 0.91	$(1.72 \pm 0.45) \cdot 10^{46}$	1.12	Q	LSP
J1159.5+2914	Ton 599	179.884	29.245	4.42	1.56 ± 0.7	4.66 ± 1.3	$(8.75 \pm 2.52) \cdot 10^{45}$	0.729	Q	LSP

Table A.0.1.: continued.

4FGL Name[a]	Common Name	RA[b]	Dec[b]	S/N[c]	Γ[d]	$F_{20-100\,\mathrm{keV}}$[e]	$L_{20-100\,\mathrm{keV}}$[f]	z[g]	Type[h]	SED Type[i]
J1202.4+4442	B3 1159+450	180.61	44.715	9.0	2.45 ± 0.4	7.7 ± 1.23	$(2.44 \pm 0.4) \cdot 10^{45}$	0.297	B	ISP
J1203.1+6031	SBS 1200+608	180.788	60.518	2.0	1.38 ± 1.38	2.48 ± 1.11	$(2.44 \pm 1.11) \cdot 10^{43}$	0.065	B	LSP
J1208.9+5441	TXS 1206+549	182.226	54.7	2.26	1.34 ± 1.17	2.84 ± 1.14	$(1.77 \pm 0.73) \cdot 10^{46}$	1.345	Q	LSP
J1213.0+5129	1RXS J121301.8+512942	183.26	51.484	2.21	1.69 ± 1.82	< 1.85	$< 4.59 \cdot 10^{45}$	0.796	B	ISP
J1213.3–2618	RBS 1080	183.336	-26.314	3.07		3.99 ± 1.32	$(9.37 \pm 3.1) \cdot 10^{44}$	0.278	B	ISP
J1215.0+1656	TXS 1212+171	183.774	16.937	1.18	0.52 ± 1.87	< 2.46	$< 5.72 \cdot 10^{45}$	1.132	Q	LSP
J1217.9+3007	B2 1215+30	184.476	30.118	3.53	2.11 ± 0.98	3.46 ± 1.24	$(1.56 \pm 0.57) \cdot 10^{44}$	0.13	B	HSP
J1221.3+3010	PG 1218+304	185.345	30.168	10.32	2.51 ± 0.44	7.39 ± 1.29	$(7.69 \pm 1.37) \cdot 10^{44}$	0.184	B	HSP
J1221.5+2814	W Comae	185.378	28.238	2.6		2.96 ± 0.94	$(7.73 \pm 2.46) \cdot 10^{43}$	0.102	B	ISP
J1222.5+0414	4C +04.42	185.627	4.239	12.85	1.37 ± 0.23	17.42 ± 1.64	$(5.42 \pm 0.53) \cdot 10^{46}$	0.964	Q	LSP
J1223.8+8039	S5 1221+80	185.971	80.66	2.63	1.9 ± 1.25	2.74 ± 1.14			B	LSP
J1224.4+2436	MS 1221.8+2452	186.116	24.614	2.3		3.0 ± 0.97	$(4.13 \pm 1.33) \cdot 10^{44}$	0.219	B	HSP
J1224.9+2122	4C +21.35	186.228	21.381	11.53	1.87 ± 0.28	12.27 ± 1.44	$(8.02 \pm 0.97) \cdot 10^{45}$	0.434	Q	LSP
J1225.6–7313	PMN J1225-7313	186.408	-73.232	1.36	5.0 ± 0.0	< 1.06			BCU	
J1228.7+4858	TXS 1226+492	187.179	48.983	1.69	1.18 ± 1.52	2.27 ± 1.11	$(1.99 \pm 1.01) \cdot 10^{46}$	1.716	Q	LSP
J1229.0+0202	3C 273	187.268	2.045	192.14	1.75 ± 0.02	240.34 ± 1.67	$(1.58 \pm 0.01) \cdot 10^{46}$	0.158	Q	LSP
J1230.2+2517	ON 246	187.56	25.298	2.21	1.28 ± 1.85	< 2.08	$< 9.19 \cdot 10^{43}$	0.135	B	ISP
J1239.5+0443	MG1 J123931+0443	189.885	4.728	2.01	1.3 ± 1.47	3.07 ± 1.45	$(3.19 \pm 1.54) \cdot 10^{46}$	1.761	Q	LSP
J1243.9–0218	PMN J1243-0218	190.985	-2.308	1.43	0.98 ± 1.44	3.3 ± 1.54			BCU	LSP
J1244.5+1616	SDSS J124444.35+161621.7	191.136	16.28	1.68	1.99 ± 1.48	2.76 ± 1.26	$(2.12 \pm 1.0) \cdot 10^{45}$	0.456	B	
J1245.1+5709	1RXS J124510.5+571020	191.288	57.158	1.07	2.23 ± 1.9	< 1.75	$< 3.33 \cdot 10^{46}$	1.545	B	ISP
J1246.7–2548	PKS 1244-255	191.689	-25.802	2.48	1.17 ± 1.03	4.68 ± 1.7	$(5.33 \pm 2.12) \cdot 10^{45}$	0.635	Q	LSP
J1253.2+5301	S4 1250+53	193.307	53.017	2.5	1.87 ± 1.28	2.53 ± 1.07			B	LSP
J1253.5–3934	1RXS J125341.2-393200	193.398	-39.567	2.84	1.44 ± 0.94	4.53 ± 1.59	$(3.71 \pm 1.35) \cdot 10^{44}$	0.179	B	HSP
J1253.8+6242	1RXS J125400.1+624303	193.467	62.705	1.52	0.91 ± 2.08	< 1.85	$< 3.45 \cdot 10^{45}$	0.867	B	LSP
J1254.2–2205	NVSS J125422-220413	193.552	-22.087	-0.12	1.71 ± 1.8	2.75 ± 1.49			BCU	
J1254.9+1138	ON 187	193.733	11.65	5.69	1.74 ± 0.57	6.41 ± 1.52	$(2.03 \pm 0.49) \cdot 10^{46}$	0.872	Q	LSP
J1256.1–0547	3C 279	194.042	-5.789	12.78	1.53 ± 0.21	19.89 ± 1.75	$(1.85 \pm 0.17) \cdot 10^{46}$	0.536	Q	LSP
J1257.6+2413	1ES 1255+244	194.419	24.22	2.22	1.43 ± 1.49	2.63 ± 1.24	$(1.3 \pm 0.64) \cdot 10^{44}$	0.141	B	HSP
J1258.7–0452	RBS 1194	194.685	-4.868	2.58	1.72 ± 1.1	4.09 ± 1.58	$(5.06 \pm 2.02) \cdot 10^{45}$	0.586	B	
J1300.4+1416	OW 197	195.12	14.27	1.51	1.79 ± 1.72	2.36 ± 1.24	$(1.36 \pm 0.72) \cdot 10^{46}$	1.109	Q	LSP
J1301.6+4056	RX J1301.7+4056	195.401	40.948	2.33	2.23 ± 1.22	2.71 ± 1.1	$(5.55 \pm 2.29) \cdot 10^{45}$	0.652	B	LSP
J1308.5+3547	5C 12.291	197.129	35.792	1.32	1.77 ± 1.53	2.3 ± 1.1	$(1.16 \pm 0.57) \cdot 10^{46}$	1.055	Q	LSP
J1309.7+1153	4C +12.46	197.438	11.897	3.06		$< 3.76\dagger$			B	LSP
J1310.7–5553	PMN J1310-5552	197.684	-55.887	9.41	1.46 ± 0.28	13.81 ± 1.59	$(3.61 \pm 0.42) \cdot 10^{44}$	0.104	BCU	HSP
J1321.1+2216	TXS 1318+225	200.296	22.281	0.08	1.04 ± 2.16	< 2.03	$< 4.85 \cdot 10^{45}$	0.943	Q	LSP
J1322.6–0936	PKS B1319-093	200.664	-9.608	2.24	1.32 ± 0.81	5.43 ± 1.73	$(6.42 \pm 2.08) \cdot 10^{46}$	1.864	Q	LSP
J1325.5–4300	Cen A	201.381	-43.017	606.89	1.87 ± 0.0	813.08 ± 1.7	$(5.8 \pm 0.01) \cdot 10^{42}$	0.002	G	LSP
J1329.0–5607	PMN J1329-5608	202.267	-56.119	1.78	2.78 ± 1.64	2.65 ± 1.31			BCU	LSP
J1332.0–0509	PKS 1329-049	203.02	-5.161	6.05	1.47 ± 0.5	8.57 ± 1.76	$(1.62 \pm 0.33) \cdot 10^{47}$	2.15	Q	LSP
J1337.4+5502	S4 1335+55	204.367	55.042	1.64	-2.58 ± 1.05	< 0.9	$< 1.99 \cdot 10^{44}$	1.1	Q	LSP
J1337.6–1257	PKS 1335-127	204.424	-12.952	5.74	1.93 ± 0.53	7.97 ± 1.78	$(8.92 \pm 2.03) \cdot 10^{45}$	0.539	Q	LSP
J1341.2+3958	SDSS J134105.10+395945.4	205.321	39.974	4.09	2.48 ± 0.86	3.67 ± 1.16	$(3.25 \pm 1.05) \cdot 10^{44}$	0.172	B	HSP

Table A.0.1.: continued.

4FGL Name^a	Common Name	RA^b	Dec^b	S/N^c	Γ^d	$F_{20-100\,\mathrm{keV}}{}^e$	$L_{20-100\,\mathrm{keV}}{}^f$	z^g	Type^h	SED Type^i
J1341.8–2053	PKS B1339-206	205.461	-20.89	4.29	1.72 ± 0.76	5.69 ± 1.77	$(7.05 \pm 2.2) \cdot 10^{46}$	1.582	Q	LSP
J1344.4–3656	PKS 1341-366	206.125	-36.934	0.87	1.61 ± 1.66	2.88 ± 1.45			BCU	ISP
J1346.3–6026	Cen B	206.591	-60.446	21.11		$< 27.61\dagger$	$< 1.03 \cdot 10^{43}$	0.013	G	LSP
J1353.3+1434	OP 186	208.336	14.576	2.71	2.67 ± 1.52	2.69 ± 1.28	$(1.97 \pm 0.95) \cdot 10^{45}$	0.405	B	LSP
J1354.2+6934	87GB 135252.8+694626	208.573	69.568	2.81		$< 3.2\dagger$			BCU	LSP
J1354.8–1041	PKS 1352-104	208.718	-10.693	3.74	1.76 ± 0.89	4.91 ± 1.66	$(1.65 \pm 0.58) \cdot 10^{45}$	0.33	Q	LSP
J1357.1+1921	4C +19.44	209.29	19.361	4.1	2.22 ± 0.96	3.78 ± 1.32	$(9.91 \pm 3.5) \cdot 10^{45}$	0.72	Q	
J1402.6–3330	PMN J1402-3334	210.665	-33.505	2.02	1.73 ± 1.24	3.64 ± 1.52	$(9.11 \pm 3.81) \cdot 10^{46}$	2.14	Q	
J1403.4+4319	NVSS J140319+432018	210.868	43.323	2.23	2.4 ± 1.57	2.19 ± 1.05	$(2.39 \pm 1.17) \cdot 10^{45}$	0.493	B	ISP
J1406.6–3934	1RXS J140630.3-393508	211.666	-39.573	1.49	-2.52 ± 1.01	< 1.42	$< 1.61 \cdot 10^{44}$	0.37	B	ISP
J1411.5–0723	NVSS J141133-072252	212.886	-7.398	1.81	0.27 ± 1.3	4.33 ± 1.8			BCU	ISP
J1411.8+5249	SBS 1410+530	212.969	52.828	2.59	0.54 ± 1.7	2.17 ± 1.13	$(2.8 \pm 1.5) \cdot 10^{43}$	0.076	B	HSP
J1413.1–6519	Circinus galaxy	213.294	-65.332	145.91	2.37 ± 0.02	176.17 ± 1.52	$(8.13 \pm 0.07) \cdot 10^{41}$	0.001	Sey	
J1416.1+1320	PKS B1413+135	214.029	13.347	1.7	1.0 ± 1.64	2.67 ± 1.38	$(3.95 \pm 2.24) \cdot 10^{44}$	0.247	BCU	LSP
J1418.4+3543	87GB 141615.9+355650	214.623	35.719	1.37	1.41 ± 1.38	2.6 ± 1.16	$(4.29 \pm 1.94) \cdot 10^{46}$	2.085	BCU	HSP
J1419.5+3821	B3 1417+385	214.894	38.366	1.37	1.76 ± 1.54	2.23 ± 1.08	$(4.03 \pm 1.95) \cdot 10^{46}$	1.831	Q	LSP
J1427.4–1823	NVSS J142726-182303	216.867	-18.396	0.9	1.42 ± 1.41	3.59 ± 1.63			BCU	ISP
J1427.9–4206	PKS 1424-41	216.987	-42.106	4.19	1.63 ± 0.57	6.8 ± 1.62	$(7.11 \pm 1.71) \cdot 10^{46}$	1.522	Q	LSP
J1428.1+1629	MG1 J142813+1629	217.047	16.491	1.32	5.0 ± 0.0	< 1.15			BCU	
J1428.5+4240	H 1426+428	217.129	42.678	15.89	2.65 ± 0.26	12.04 ± 1.21	$(5.71 \pm 0.58) \cdot 10^{44}$	0.129	B	HSP
J1428.9+5406	S4 1427+543	217.229	54.111	1.7	1.45 ± 1.08	2.9 ± 1.12	$(1.06 \pm 0.41) \cdot 10^{47}$	3.013	Q	LSP
J1433.0–1801	PKS 1430-178	218.254	-18.02	2.25	0.54 ± 1.1	4.92 ± 1.78	$(3.55 \pm 1.82) \cdot 10^{46}$	2.331	Q	LSP
J1440.6–3846	1RXS J144037.4-384658	220.155	-38.78	2.19	1.87 ± 1.19	3.54 ± 1.45	$(1.41 \pm 0.6) \cdot 10^{45}$	0.35	B	HSP
J1441.7+1836	NVSS J144143+183706	220.44	18.607	1.28	1.84 ± 1.76	2.24 ± 1.2			BCU	ISP
J1442.7+1200	1ES 1440+122	220.698	12.013	3.44	2.59 ± 1.41	3.04 ± 1.35	$(2.42 \pm 1.11) \cdot 10^{44}$	0.163	B	HSP
J1443.1+5201	3C 303	220.779	52.029	4.38	2.19 ± 0.72	4.07 ± 1.12	$(2.22 \pm 0.63) \cdot 10^{44}$	0.141	G	LSP
J1446.0–3039	PMN J1445-3036	221.523	-30.662	1.45	1.38 ± 1.37	3.45 ± 1.53			BCU	LSP
J1447.0–2657	NVSS J144657-265713	221.765	-26.962	2.62	2.05 ± 1.25	3.67 ± 1.53			BCU	
J1451.5+1415	NVSS J145126+141626	222.888	14.261	1.55	1.71 ± 1.82	< 2.23	$< 2.18 \cdot 10^{45}$	0.529	BCU	
J1453.0–1318	TXS 1450-131	223.26	-13.312	1.34	2.2 ± 1.31	3.7 ± 1.59			BCU	
J1454.4–3744	PKS 1451-375	223.616	-37.75	3.19	1.79 ± 0.66	5.78 ± 1.58	$(1.75 \pm 0.49) \cdot 10^{45}$	0.314	Q	LSP
J1456.0+5051	RGB J1456+508	224.018	50.85	2.12	1.53 ± 1.8	< 1.84	$< 1.4 \cdot 10^{45}$	0.49	B	LSP
J1459.0+7140	3C 309.1	224.753	71.673	3.98	1.85 ± 0.73	4.17 ± 1.18	$(1.56 \pm 0.45) \cdot 10^{46}$	0.91	CSS	ISP
J1503.5+4759	TXS 1501+481	225.896	47.996	1.16	1.76 ± 1.62	2.05 ± 1.04	$(7.6 \pm 4.07) \cdot 10^{44}$	0.345	B	LSP
J1504.4+1029	PKS 1502+106	226.103	10.498	14.79	2.22 ± 0.23	17.66 ± 1.6	$(5.2 \pm 0.47) \cdot 10^{47}$	1.839	Q	LSP
J1506.1+3731	B2 1504+37	226.535	37.518	2.78	1.97 ± 1.17	2.87 ± 1.16	$(5.57 \pm 2.29) \cdot 10^{45}$	0.673	Q	LSP
J1507.3+3341	87GB 150531.0+334938	226.835	33.687	1.43	2.0 ± 1.5	2.42 ± 1.12			BCU	LSP
J1508.5–4951	PMN J1508-4953	227.144	-49.862	8.39	1.27 ± 0.28	13.51 ± 1.54			BCU	LSP
J1508.8+2708	RBS 1467	227.205	27.141	2.82	1.61 ± 1.0	3.52 ± 1.29	$(7.26 \pm 2.78) \cdot 10^{44}$	0.27	B	HSP
J1509.6–4334	PMN J1509-4340	227.416	-43.578	2.73	1.39 ± 1.4	3.08 ± 1.4	$(6.08 \pm 2.93) \cdot 10^{45}$	0.776	Q	LSP
J1512.8–0906	PKS 1510-089	228.215	-9.106	18.75	1.24 ± 0.12	35.9 ± 1.8	$(1.25 \pm 0.07) \cdot 10^{46}$	0.36	Q	LSP
J1512.9–5639	PMN J1512-5640	228.25	-56.655	3.74	1.79 ± 0.74	4.88 ± 1.4			BCU	LSP
J1517.7–2422	AP Librae	229.425	-24.373	5.51	1.75 ± 0.44	9.36 ± 1.7	$(5.02 \pm 0.91) \cdot 10^{43}$	0.048	B	LSP

Table A.0.1.: continued.

4FGL Name[a]	Common Name	RA[b]	Dec[b]	S/N[c]	Γ[d]	$\mathrm{F}_{20-100\,\mathrm{keV}}$[e]	$\mathrm{L}_{20-100\,\mathrm{keV}}$[f]	z[g]	Type[h]	SED Type[i]
J1518.6+0614	TXS 1516+064	229.65	6.242	2.7	1.69 ± 0.71	5.56 ± 1.63	$(1.44 \pm 0.43) \cdot 10^{44}$	0.102	G	HSP
J1521.8+4338	B3 1520+437	230.465	43.634	3.84	1.79 ± 0.71	4.28 ± 1.2	$(1.19 \pm 0.33) \cdot 10^{47}$	2.168	Q	LSP
J1527.3+3117	B2 1525+31	231.849	31.299	2.24	1.79 ± 1.57	2.36 ± 1.15	$(2.33 \pm 1.15) \cdot 10^{46}$	1.392	Q	
J1532.7–1319	TXS 1530-131	233.197	-13.326	1.67		5.48 ± 1.42			Q	LSP
J1536.8–3155	PKS 1533-317	234.213	-31.922	2.13	2.34 ± 1.68	2.57 ± 1.31			B	LSP
J1539.9+4220	87GB 153741.6+422719	234.977	42.338	1.54	1.13 ± 1.29	2.79 ± 1.19			B	LSP
J1543.6+0452	CGCG 050-083	235.906	4.869	2.62	0.82 ± 1.52	3.2 ± 1.54	$(1.14 \pm 0.55) \cdot 10^{43}$	0.04	AGN	ISP
J1546.5+1816	MG1 J154628+1817	236.634	18.283	2.26	1.59 ± 1.3	3.14 ± 1.37	$(1.25 \pm 0.56) \cdot 10^{46}$	1.005	B	LSP
J1547.9–6403	PMN J1548-6401	236.992	-64.051	3.16		< 3.77†			BCU	LSP
J1549.5+0236	PKS 1546+027	237.385	2.608	2.69		4.28 ± 1.36	$(2.24 \pm 0.71) \cdot 10^{45}$	0.414	Q	LSP
J1549.8–3044	NVSS J154946-304501	237.451	-30.749	1.9	2.22 ± 2.02	< 2.12			BCU	HSP
J1555.7+1111	PG 1553+113	238.931	11.188	3.46	2.15 ± 0.78	4.94 ± 1.47	$(2.28 \pm 0.69) \cdot 10^{45}$	0.36	B	HSP
J1602.1+3324	OS 300	240.531	33.414	0.99	1.83 ± 1.57	2.36 ± 1.16	$(1.37 \pm 0.68) \cdot 10^{46}$	1.1	BCU	LSP
J1603.8+1104	MG1 J160340+1106	240.96	11.07	1.93	0.97 ± 1.24	3.62 ± 1.49	$(1.73 \pm 0.74) \cdot 10^{44}$	0.143	B	LSP
J1604.5–4441	PMN J1604-4441	241.128	-44.69	1.59	0.8 ± 1.2	3.54 ± 1.4			B	LSP
J1608.7+1029	4C +10.45	242.176	10.494	2.33	0.82 ± 0.94	4.69 ± 1.53	$(1.57 \pm 0.61) \cdot 10^{46}$	1.226	Q	LSP
J1617.3–5849	MRC 1613-586	244.349	-58.826	2.84		3.77 ± 1.22	$(3.1 \pm 1.0) \cdot 10^{46}$	1.414	Q	LSP
J1617.9–7718	PKS 1610-77	244.481	-77.304	4.31	1.25 ± 0.64	5.39 ± 1.42	$(5.02 \pm 1.35) \cdot 10^{46}$	1.71	Q	LSP
J1625.7+4134	4C +41.32	246.447	41.571	0.72	1.32 ± 1.7	2.17 ± 1.13	$(4.81 \pm 2.54) \cdot 10^{46}$	2.55	Q	LSP
J1626.0–2950	PKS B1622-297	246.515	-29.849	5.75	1.61 ± 0.44	8.38 ± 1.5	$(2.09 \pm 0.38) \cdot 10^{46}$	0.815	Q	LSP
J1626.8+4337	MG4 J162551+4346	246.714	43.625	2.24	0.74 ± 1.23	3.18 ± 1.27	$(7.54 \pm 3.79) \cdot 10^{45}$	1.048	Q	
J1630.6+8234	NGC 6251	247.669	82.574	2.78	1.69 ± 1.12	3.03 ± 1.19	$(3.95 \pm 1.55) \cdot 10^{42}$	0.024	G	LSP
J1631.2+1046	MG1 J163119+1051	247.804	10.775	0.84	-2.44 ± 1.07	< 1.59			BCU	LSP
J1632.8–1048	TXS 1630-107	248.204	-10.813	0.99	1.27 ± 1.05	3.91 ± 1.46			BCU	LSP
J1635.2+3808	4C +38.41	248.817	38.14	4.3	1.43 ± 0.53	6.31 ± 1.37	$(7.94 \pm 1.74) \cdot 10^{46}$	1.814	Q	LSP
J1637.7+4717	4C +47.44	249.434	47.291	1.99	2.34 ± 1.67	2.13 ± 1.08	$(6.28 \pm 3.22) \cdot 10^{45}$	0.735	Q	LSP
J1638.1+5721	OS 562	249.525	57.358	3.17	1.75 ± 0.86	3.68 ± 1.2	$(8.26 \pm 2.75) \cdot 10^{45}$	0.751	Q	LSP
J1642.9+3948	3C 345	250.734	39.816	7.7	1.42 ± 0.34	9.85 ± 1.36	$(1.09 \pm 0.16) \cdot 10^{46}$	0.593	Q	LSP
J1647.5+2911	B2 1645+29	251.884	29.184	0.71	1.39 ± 1.5	2.61 ± 1.24	$(1.11 \pm 0.55) \cdot 10^{44}$	0.132	B	ISP
J1647.5+4950	SBS 1646+499	251.892	49.834	3.72	1.8 ± 0.87	3.66 ± 1.21	$(2.05 \pm 0.68) \cdot 10^{43}$	0.049	B	LSP
J1648.0+2221	MG2 J164800+2224	252.023	22.352	0.54	1.13 ± 2.14	< 2.03	$< 3.88 \cdot 10^{45}$	0.823	BCU	LSP
J1650.7+0831	MG1 J165034+0824	252.7	8.518	1.76	1.95 ± 1.09	3.49 ± 1.35	$(9.11 \pm 3.53) \cdot 10^{46}$	1.965	Q	LSP
J1650.9+0429	1RXS J165053.5+043009	252.739	4.498	5.14	2.19 ± 0.4	9.04 ± 1.5			BCU	
J1653.8+3945	Mkn 501	253.474	39.76	48.98	2.43 ± 0.08	44.38 ± 1.33	$(1.13 \pm 0.03) \cdot 10^{44}$	0.033	B	HSP
J1656.3–3301	2MASS J16561677-3302127	254.095	-33.019	18.43	1.45 ± 0.1	33.35 ± 1.45	$(7.68 \pm 0.34) \cdot 10^{47}$	2.4	Q	LSP
J1657.7+4808	4C +48.41	254.438	48.137	2.23	2.14 ± 1.31	2.66 ± 1.14	$(5.65 \pm 2.43) \cdot 10^{46}$	1.669	Q	LSP
J1659.0+2627	4C +26.51	254.77	26.464	1.66	2.0 ± 1.51	2.57 ± 1.2	$(7.6 \pm 3.61) \cdot 10^{45}$	0.793	Q	LSP
J1700.0+6830	TXS 1700+685	255.022	68.504	2.42	1.71 ± 1.08	3.07 ± 1.17	$(8.27 \pm 3.29) \cdot 10^{44}$	0.301	Q	LSP
J1704.5–0527	NVSS J170433-052839	256.138	-5.462	2.18	1.43 ± 1.3	3.17 ± 1.36			B	ISP
J1706.8+3004	87GB 170454.3+300758	256.722	30.067	1.26	1.36 ± 1.0	3.59 ± 1.3	$(1.87 \pm 0.72) \cdot 10^{45}$	0.425	BCU	ISP
J1714.0–2029	1RXS J171405.2-202747	258.522	-20.486	2.13		4.29 ± 1.24			BCU	HSP
J1716.1+6836	S4 1716+68	259.032	68.606	2.68	-0.02 ± 1.44	< 2.81	$< 2.47 \cdot 10^{45}$	0.777	Q	
J1722.6+6104	GB6 J1722+6105	260.662	61.073	1.94	0.28 ± 1.5	2.69 ± 1.29	$(1.22 \pm 1.24) \cdot 10^{46}$	2.058	Q	LSP

Table A.0.1.: continued.

4FGL Name^a	Common Name	RA^b	Dec^b	S/N^c	Γ^d	$F_{20-100\,\mathrm{keV}}{}^e$	$L_{20-100\,\mathrm{keV}}{}^f$	z^g	Type^h	SED Type^i
J1724.9+7654	S5 1726+76	261.233	76.915	2.35	1.13 ± 0.78	4.13 ± 1.21	$(5.31 \pm 1.69) \cdot 10^{45}$	0.68	Q	LSP
J1727.4+4530	S4 1726+45	261.852	45.511	1.47	0.51 ± 1.1	3.65 ± 1.31	$(3.75 \pm 1.86) \cdot 10^{45}$	0.717	Q	LSP
J1730.6+0024	PKS 1728+004	262.663	0.41	3.53	1.54 ± 0.59	5.97 ± 1.47	$(4.31 \pm 1.07) \cdot 10^{46}$	1.335	Q	LSP
J1733.0–1305	PKS 1730-13	263.263	-13.086	3.55	1.24 ± 0.53	6.9 ± 1.48	$(1.72 \pm 0.39) \cdot 10^{46}$	0.902	Q	LSP
J1734.3+3858	B2 1732+38A	263.598	38.976	2.57	2.07 ± 1.24	2.88 ± 1.19	$(1.49 \pm 0.62) \cdot 10^{46}$	0.976	Q	LSP
J1736.0+2033	NVSS J173605+203301	264.019	20.556	0.38	1.64 ± 1.74	2.23 ± 1.18			B	HSP
J1738.0+8717	6C B175708+871924	264.501	87.285	0.77	0.91 ± 1.69	2.24 ± 1.17			BCU	
J1740.5+5211	4C +51.37	265.136	52.193	4.36	1.34 ± 0.6	5.29 ± 1.31	$(3.48 \pm 0.88) \cdot 10^{46}$	1.381	Q	LSP
J1744.0+1935	S3 1741+19	266.008	19.596	1.07	2.66 ± 2.04	< 2.0	$< 3.69 \cdot 10^{43}$	0.084	B	HSP
J1749.0+4321	B3 1747+433	267.255	43.362	2.34	1.62 ± 1.52	2.43 ± 1.15			B	LSP
J1751.5+0938	OT 081	267.878	9.646	3.42	1.54 ± 0.84	4.26 ± 1.35	$(1.27 \pm 0.42) \cdot 10^{45}$	0.322	B	LSP
J1752.6–1010	MRC 1749-101	268.16	-10.176	2.05	1.51 ± 0.87	4.17 ± 1.36			BCU	LSP
J1800.6+7828	S5 1803+784	270.173	78.467	4.98	1.68 ± 0.6	5.14 ± 1.29	$(8.81 \pm 2.26) \cdot 10^{45}$	0.68	B	LSP
J1806.8+6949	3C 371	271.711	69.827	2.51		2.94 ± 0.96	$(1.73 \pm 0.57) \cdot 10^{43}$	0.05	B	LSP
J1810.7+5335	2MASS J18103800+5335016	272.678	53.593	0.39	1.06 ± 2.14	< 1.88			BCU	HSP
J1814.0+3828	2MASS J18140339+3828107	273.502	38.477	1.82	1.23 ± 1.35	2.82 ± 1.25	$(5.55 \pm 2.65) \cdot 10^{44}$	0.275	BCU	HSP
J1814.4+2953	B2 1811+29	273.615	29.894	1.8	5.0 ± 0.0	< 1.37	$< 1.96 \cdot 10^{47}$	1.351	Q	
J1815.2–2715	NVSS J181510-271304	273.813	-27.257	0.38	1.61 ± 2.17	< 1.64			BCU	
J1823.6–3453	NVSS J182338-345412	275.911	-34.895	2.37	2.05 ± 1.75	2.24 ± 1.19			BCU	HSP
J1824.7–3243	PKS 1821-327	276.177	-32.718	3.93	1.37 ± 0.57	6.18 ± 1.46	$(2.18 \pm 0.54) \cdot 10^{45}$	0.355	AGN	
J1826.0–5037	SUMSS J182551-503914	276.518	-50.625	1.51	2.78 ± 2.39	< 1.9			BCU	
J1829.2–5813	PKS 1824-582	277.311	-58.232	2.84	1.61 ± 0.89	3.95 ± 1.33	$(4.11 \pm 1.4) \cdot 10^{46}$	1.531	Q	
J1829.5+4845	3C 380	277.4	48.765	7.46	1.75 ± 0.36	9.09 ± 1.35	$(1.7 \pm 0.26) \cdot 10^{46}$	0.695	CSS	LSP
J1830.2–4443	PMN J1830-4441	277.55	-44.72	2.03	1.21 ± 0.72	5.01 ± 1.44			BCU	LSP
J1833.6–2103	PKS 1830-211	278.41	-21.057	26.05	1.41 ± 0.08	44.22 ± 1.47	$(1.06 \pm 0.04) \cdot 10^{48}$	2.507	Q	LSP
J1842.3+6810	S4 1842+68	280.585	68.169	1.05	1.44 ± 1.65	2.16 ± 1.11	$(1.45 \pm 0.81) \cdot 10^{45}$	0.472	Q	LSP
J1849.2+6705	S4 1849+67	282.319	67.091	5.08	2.15 ± 0.86	3.73 ± 1.19	$(7.45 \pm 2.42) \cdot 10^{45}$	0.657	Q	LSP
J1907.7–1232	NVSS J190748-123221	286.94	-12.538	1.62	1.51 ± 1.63	2.72 ± 1.35			BCU	
J1911.2–2006	PKS B1908-201	287.808	-20.114	1.19	1.12 ± 1.43	3.0 ± 1.39	$(1.07 \pm 0.54) \cdot 10^{46}$	1.119	Q	LSP
J1917.7–1921	1H 1914-194	289.438	-19.363	2.61	1.14 ± 1.0	4.13 ± 1.47	$(1.84 \pm 0.68) \cdot 10^{44}$	0.137	B	HSP
J1921.3–1231	TXS 1918-126	290.344	-12.526	0.9	1.83 ± 1.66	2.59 ± 1.33			B	
J1924.8–2914	PKS B1921-293	291.214	-29.247	6.89	2.12 ± 0.4	9.3 ± 1.54	$(4.06 \pm 0.69) \cdot 10^{45}$	0.353	Q	LSP
J1926.8+6154	87GB 192614.4+614823	291.71	61.915	2.66	1.18 ± 0.89	3.84 ± 1.24			B	HSP
J1929.4+6146	TXS 1928+616	292.369	61.775	1.79	2.1 ± 1.46	2.44 ± 1.1	$(3.25 \pm 1.52) \cdot 10^{44}$	0.212	BCU	ISP
J1930.3+0911	NVSS J193016+091037	292.585	9.198	1.42	1.07 ± 1.44	2.99 ± 1.39			BCU	
J1931.1+0937	RX J1931.1+0937	292.784	9.631	2.79	1.84 ± 0.71	5.18 ± 1.5			B	HSP
J1934.3+6541	TXS 1933+655	293.595	65.689	2.74	0.95 ± 0.86	4.0 ± 1.24	$(2.69 \pm 0.91) \cdot 10^{46}$	1.687	Q	LSP
J1937.2–3958	PKS 1933-400	294.309	-39.983	2.91	1.67 ± 0.8	4.77 ± 1.47	$(1.83 \pm 0.57) \cdot 10^{46}$	0.965	Q	LSP
J1941.3–6210	PKS 1936-623	295.347	-62.175	5.47	1.56 ± 0.48	7.69 ± 1.51			Q	LSP
J1944.0+2117	MG2 J194359+2118	296.005	21.29	14.52	2.23 ± 0.22	16.72 ± 1.49			BCU	
J1949.4+1247	TXS 1947+126	297.371	12.793	1.27	0.97 ± 1.75	2.6 ± 1.38			BCU	
J1955.4+5132	OV 591	298.858	51.543	3.61	1.78 ± 0.67	4.69 ± 1.26	$(3.32 \pm 0.9) \cdot 10^{46}$	1.214	Q	LSP
J1958.3–3010	1RXS J195815.6-301119	299.581	-30.181	3.12		3.77 ± 1.25	$(1.37 \pm 0.45) \cdot 10^{44}$	0.119	B	

Table A.0.1.: continued.

4FGL Name^a	Common Name	RA^b	Dec^b	S/N^c	Γ^d	$F_{20-100\,\mathrm{keV}}{}^e$	$L_{20-100\,\mathrm{keV}}{}^f$	z^g	Type^h	SED Type^i
J2000.0+6508	1ES 1959+650	300.011	65.148	23.21	2.75 ± 0.2	18.21 ± 1.28	$(9.81 \pm 0.69) \cdot 10^{43}$	0.047	B	HSP
J2000.9–1748	PKS 1958-179	300.235	-17.816	2.93	2.38 ± 1.3	3.52 ± 1.48	$(7.78 \pm 3.3) \cdot 10^{45}$	0.652	Q	LSP
J2001.9–5737	1RXS J200205.7-573644	300.491	-57.631	0.88	1.93 ± 1.7	2.4 ± 1.26			BCU	
J2002.4–7119	SUMSS J200227-711940	300.6	-71.324	2.93	2.14 ± 1.02	3.65 ± 1.34			BCU	
J2009.4–4849	PKS 2005-489	302.36	-48.825	4.52		5.75 ± 1.2	$(7.01 \pm 1.47) \cdot 10^{43}$	0.071	B	HSP
J2010.0+7229	4C +72.28	302.516	72.487	0.87	1.88 ± 1.77	1.98 ± 1.06			B	LSP
J2011.6–1546	PKS 2008-159	302.916	-15.774	6.15	1.88 ± 0.55	7.42 ± 1.72	$(5.29 \pm 1.23) \cdot 10^{46}$	1.178	Q	LSP
J2015.5+3710	MG2 J201534+3710	303.892	37.176	9.89	2.17 ± 0.31	11.31 ± 1.41	$(4.5 \pm 0.56) \cdot 10^{46}$	0.859	Q	LSP
J2022.5+7612	S5 2023+760	305.646	76.201	2.66	1.94 ± 0.94	3.44 ± 1.2	$(4.86 \pm 1.74) \cdot 10^{45}$	0.594	B	LSP
J2025.3+3341	B2 2023+33	306.341	33.689	4.87	1.55 ± 0.51	6.94 ± 1.44	$(8.94 \pm 1.92) \cdot 10^{44}$	0.219	BCU	LSP
J2025.6–0735	PKS 2023-07	306.422	-7.595	1.85	5.0 ± 0.0	< 1.65	$< 2.64 \cdot 10^{47}$	1.388	Q	LSP
J2026.6+3449	NVSS J202638+345022	306.653	34.829	1.21	0.46 ± 1.77	2.49 ± 1.34			BCU	
J2035.4+1056	PKS 2032+107	308.852	10.938	2.57	1.87 ± 1.13	3.71 ± 1.45	$(5.23 \pm 2.1) \cdot 10^{45}$	0.601	Q	LSP
J2037.9–0504	PMN J2037-0508	309.477	-5.068	2.02	1.91 ± 1.5	3.12 ± 1.47			BCU	
J2040.2–7115	PKS 2035-714	310.066	-71.264	3.56	2.34 ± 1.09	3.53 ± 1.33	$(2.66 \pm 1.03) \cdot 10^{44}$	0.162	B	
J2056.2–4714	PKS 2052-47	314.072	-47.237	6.38	1.77 ± 0.59	6.79 ± 1.69	$(7.72 \pm 1.93) \cdot 10^{46}$	1.489	Q	LSP
J2056.4–4904	SUMSS J205613-490415	314.122	-49.072	0.52	2.21 ± 1.9	< 2.43			BCU	
J2056.7+4939	RGB J2056+496	314.191	49.666	8.71	2.57 ± 0.39	8.38 ± 1.29			BCU	HSP
J2056.7–3209	PKS 2053-323	314.178	-32.161	2.42	1.07 ± 0.97	5.1 ± 1.73			B	LSP
J2110.3+0404	NVSS J211019+040418	317.594	4.083	1.95	1.24 ± 1.34	3.6 ± 1.58			BCU	ISP
J2123.8–3148	PMN J2123-3155	320.967	-31.805	0.64	1.1 ± 1.92	< 2.82			BCU	
J2131.5–0916	RBS 1752	322.891	-9.268	0.35	1.31 ± 1.86	< 2.73	$< 1.57 \cdot 10^{45}$	0.449	B	HSP
J2132.0–5418	PMN J2132-5420	323.023	-54.313	1.51	2.17 ± 1.5	2.94 ± 1.37			BCU	LSP
J2134.2–0154	PKS 2131-021	323.57	-1.904	2.24	1.63 ± 1.79	< 2.67	$< 1.91 \cdot 10^{46}$	1.283	B	LSP
J2136.2–0642	TXS 2133-069	324.071	-6.716	2.9	2.46 ± 1.46	3.41 ± 1.57	$(2.08 \pm 0.96) \cdot 10^{46}$	0.94	BCU	LSP
J2137.4–3209	NVSS J213726-320755	324.364	-32.155	0.72	1.62 ± 1.75	2.89 ± 1.53			BCU	
J2143.5+1743	OX 169	325.894	17.731	4.04	1.14 ± 0.54	7.4 ± 1.61	$(8.13 \pm 1.85) \cdot 10^{44}$	0.211	Q	LSP
J2144.3–7802	PKS 2141-781	326.085	-78.034	1.23	1.68 ± 1.55	2.53 ± 1.22	$(5.14 \pm 2.58) \cdot 10^{45}$	0.732	Q	LSP
J2147.1+0931	PKS 2144+092	326.783	9.518	2.82	1.57 ± 0.77	5.19 ± 1.63	$(2.57 \pm 0.82) \cdot 10^{46}$	1.113	Q	LSP
J2147.3–7536	PKS 2142-75	326.827	-75.602	5.34	1.01 ± 0.5	7.36 ± 1.47	$(2.49 \pm 0.54) \cdot 10^{46}$	1.138	Q	LSP
J2148.6+0652	PKS 2145+06	327.163	6.879	4.39	2.35 ± 0.94	4.56 ± 1.56	$(2.95 \pm 1.01) \cdot 10^{46}$	0.99	Q	LSP
J2151.8–3027	PKS 2149-306	327.966	-30.46	32.8	1.53 ± 0.08	52.03 ± 1.83	$(1.26 \pm 0.04) \cdot 10^{48}$	2.345	Q	LSP
J2152.0–1205	RBS 1791	328.024	-12.092	1.32	-2.44 ± 1.02	< 1.88	$< 4.32 \cdot 10^{43}$	0.121	B	ISP
J2156.0–6942	PKS 2153-69	329.025	-69.707	5.12	1.48 ± 0.56	6.38 ± 1.49	$(1.15 \pm 0.27) \cdot 10^{43}$	0.028	G	LSP
J2158.8–3013	PKS 2155-304	329.714	-30.225	4.08	1.91 ± 0.96	4.73 ± 1.68	$(1.63 \pm 0.59) \cdot 10^{44}$	0.116	B	HSP
J2200.3+1029	TXS 2157+102	330.089	10.496	13.6		$< 16.34\dagger$	$< 1.33 \cdot 10^{45}$	0.172	B	LSP
J2201.8+5048	NRAO 676	330.453	50.805	8.73	1.68 ± 0.32	10.25 ± 1.36	$(1.86 \pm 0.25) \cdot 10^{47}$	1.899	Q	LSP
J2202.7+4216	BL Lac	330.695	42.282	16.9	1.69 ± 0.16	20.64 ± 1.4	$(2.34 \pm 0.16) \cdot 10^{44}$	0.069	B	LSP
J2207.6+0053	PMN J2207+0052	331.914	0.891	2.98		4.22 ± 1.27			BCU	
J2212.0+2356	PKS 2209+236	333.019	23.933	2.5	1.91 ± 1.71	2.43 ± 1.27	$(1.58 \pm 0.84) \cdot 10^{46}$	1.125	Q	LSP
J2212.8+0647	TXS 2210+065	333.214	6.786	1.99	0.98 ± 1.53	3.18 ± 1.54	$(1.02 \pm 0.56) \cdot 10^{46}$	1.12	Q	LSP
J2219.2–0342	PKS 2216-03	334.824	-3.71	1.74	1.93 ± 1.83	2.63 ± 1.44	$(1.01 \pm 0.56) \cdot 10^{46}$	0.901	Q	LSP
J2225.6+2120	PKS 2223+21	336.414	21.342	3.06	1.65 ± 0.62	5.97 ± 1.55	$(1.12 \pm 0.29) \cdot 10^{47}$	1.959	Q	LSP

Table A.0.1.: continued.

4FGL Name[a]	Common Name	RA[b]	Dec[b]	S/N[c]	Γ[d]	$F_{20-100\,\mathrm{keV}}$[e]	$L_{20-100\,\mathrm{keV}}$[f]	z[g]	Type[h]	SED Type[i]
J2225.7–0457	3C 446	336.432	-4.954	2.45	1.4 ± 1.2	4.09 ± 1.66	$(2.92 \pm 1.21) \cdot 10^{46}$	1.404	Q	LSP
J2226.5+6901c	NVSS J222625+690207	336.629	69.021	1.48		2.99 ± 0.99			BCU	
J2229.7–0832	PKS 2227-08	337.426	-8.545	6.05	1.13 ± 0.47	9.73 ± 1.81	$(6.75 \pm 1.3) \cdot 10^{46}$	1.56	Q	LSP
J2232.6+1143	CTA 102	338.153	11.731	10.11	1.42 ± 0.26	15.89 ± 1.68	$(6.02 \pm 0.65) \cdot 10^{46}$	1.037	Q	LSP
J2236.3+2828	B2 2234+28A	339.096	28.483	1.07	1.83 ± 1.56	2.58 ± 1.26	$(6.83 \pm 3.42) \cdot 10^{45}$	0.79	Q	LSP
J2239.4+5130	LQAC 340+051	339.872	51.506	0.96	1.51 ± 2.01	< 1.94			BCU	
J2246.7–5207	RBS 1895	341.683	-52.126	5.9	2.54 ± 0.77	5.0 ± 1.42	$(1.27 \pm 0.37) \cdot 10^{44}$	0.098	BCU	HSP
J2250.0+3825	B3 2247+381	342.514	38.425	2.77		3.63 ± 1.04	$(1.32 \pm 0.38) \cdot 10^{44}$	0.119	B	HSP
J2251.7–3208	1RXS J225146.9-320614	342.944	-32.14	6.93		$< 8.15\dagger$	$< 1.57 \cdot 10^{45}$	0.246	BCU	HSP
J2253.2–1232	TXS 2250-127	343.308	-12.542	3.25		$< 4.3\dagger$			BCU	LSP
J2253.9+1609	3C 454.3	343.496	16.151	55.05	1.52 ± 0.05	74.41 ± 1.6	$(1.99 \pm 0.04) \cdot 10^{47}$	0.859	Q	LSP
J2258.1–2759	PKS 2255-282	344.529	-27.984	3.1	1.32 ± 0.71	5.83 ± 1.69	$(1.62 \pm 0.49) \cdot 10^{46}$	0.926	Q	LSP
J2300.1+4053	NVSS J230012+405224	345.034	40.898	3.4		$< 4.63\dagger$			B	HSP
J2302.8–1841	PKS 2300-18	345.715	-18.699	7.48		$< 8.8\dagger$	$< 3.8 \cdot 10^{44}$	0.129	G	LSP
J2311.0+3425	B2 2308+34	347.768	34.422	3.01	1.47 ± 0.98	3.75 ± 1.35	$(4.94 \pm 1.8) \cdot 10^{46}$	1.817	Q	LSP
J2318.2+1915	TXS 2315+189	349.557	19.256	2.02	0.83 ± 1.29	3.52 ± 1.48	$(3.21 \pm 1.52) \cdot 10^{46}$	2.163	BCU	LSP
J2319.1–4207	PKS 2316-423	349.776	-42.117	3.28		$< 3.86\dagger$	$< 2.57 \cdot 10^{43}$	0.055	B	HSP
J2325.4–4800	PKS 2322-482	351.35	-48.002	1.37	0.58 ± 1.49	3.01 ± 1.43	$(3.26 \pm 1.73) \cdot 10^{44}$	0.221	B	ISP
J2327.5+0939	PKS 2325+093	351.896	9.654	9.5	1.38 ± 0.29	14.36 ± 1.68	$(1.78 \pm 0.21) \cdot 10^{47}$	1.843	Q	LSP
J2327.5–3259	NVSS J232747-330130	351.883	-32.987	2.2	1.71 ± 1.5	2.94 ± 1.38			BCU	
J2328.3–4036	PKS 2325-408	352.082	-40.604	3.1	2.13 ± 1.03	3.82 ± 1.41	$(1.23 \pm 0.45) \cdot 10^{47}$	1.972	Q	LSP
J2330.6–3726	PKS 2327-376	352.66	-37.435	1.93	2.59 ± 1.94	2.3 ± 1.25	$(6.49 \pm 3.64) \cdot 10^{44}$	0.279	B	LSP
J2332.1–4118	PKS 2329-415	353.025	-41.302	1.97	1.66 ± 1.62	2.65 ± 1.32	$(4.34 \pm 2.26) \cdot 10^{45}$	0.671	Q	LSP
J2340.5+3854	GALEXASC J234042.83+385510.7	355.128	38.905	0.73	1.43 ± 1.66	2.38 ± 1.22			BCU	HSP
J2343.9+0546	1RXS J234354.4+054713	355.991	5.779	2.83		$< 3.84\dagger$			BCU	HSP
J2347.0+5141	1ES 2344+514	356.766	51.697	7.06	2.46 ± 0.54	6.1 ± 1.29	$(2.82 \pm 0.6) \cdot 10^{43}$	0.044	B	HSP
J2347.9+5436	NVSS J234753+543627	356.981	54.607	3.89	2.1 ± 1.21	2.92 ± 1.2			BCU	
J2354.9+8151	S5 2353+81	358.741	81.867	1.94	0.99 ± 1.55	2.46 ± 1.19	$(1.13 \pm 0.61) \cdot 10^{46}$	1.344	Q	LSP
J2358.5–1808	1RXS J235836.3-180701	359.639	-18.141	1.47	1.59 ± 1.27	3.51 ± 1.5	$(2.72 \pm 1.17) \cdot 10^{43}$	0.058	BCU	HSP
J2359.0–3038	H 2356-309	359.772	-30.637	9.36	2.24 ± 0.44	8.57 ± 1.56	$(6.67 \pm 1.23) \cdot 10^{44}$	0.165	B	HSP
J2359.1+1719	NVSS J235901+171926	359.776	17.323	1.61	1.59 ± 1.47	3.01 ± 1.4			BCU	ISP

Notes. (a) Name listed in 4FGL catalog, (b) Equatorial coordinates (J2000) in degrees, (c) *Swift*/BAT S/N (14 keV – 150 keV), (d) Photon Index for 20 keV – 100 keV, (e) X-ray flux in $10^{-12}\mathrm{erg\,s^{-1}\,cm^{-2}}$ († indicates upper limits caused by contamination of a nearby source) (f) X-ray luminosity in $\mathrm{erg\,s^{-1}}$, (g) Redshift, form 4LAC catalog DR2 (Lott et al., 2020), (h) Classification from 4FGL catalog (Abdollahi et al., 2020) Q: Flat Spectrum Radio Quasar, B: BL Lac, BCU: Blazar candidate of uncertain type, G: radio galaxy, Sey: Seyfert, NLSY1: Narrow-Line Seyfert-1, CSS: Compact Steep Spectrum radio source, AGN: non-blazar active galaxy, (i) SED classification from the 4LAC catalog (Ajello et al., 2020): LSP, ISP, and HSP for low-, intermediate-, and high-synchrotron-peaked SEDs, respectively.

B. BAT source spectra

In the following, a number of *Swift*/BAT source spectra, which have been analyzed in this work, are presented. Since the number of extracted and analyzed source spectra is around 3500 the figure only shows a small excerpt from the MOJAVE-1, MOJAVE-1.5, TANAMI, and 4LAC AGN samples. All displayed spectra are truncated to show only the fitted range of 20 keV to 100 keV, that is, five out of a total of eight energy channels. The complete BAT spectra themselves in fits/pha format are saved in the zip file appended to this thesis.

Figure B.0.1 presents (a) 1253–055 (3C 279) that is included in the MOJAVE-1 sample, and (b) 0241+622 (TXS 0241+622), which is only in the MOJAVE-1.5 sample. The second row includes the TANAMI sources of (c) 1322–428 (Centaurus A) and (d) 0426–380 (PKS 0426–380). The third row shows the two sources (e) 3FGL J1653.9+3945 (4FGL J1653.8+3945, Mrk 501) and (f) 3FGL J2202.7+4214 (4FGL J2202.7+4216, BL Lac).

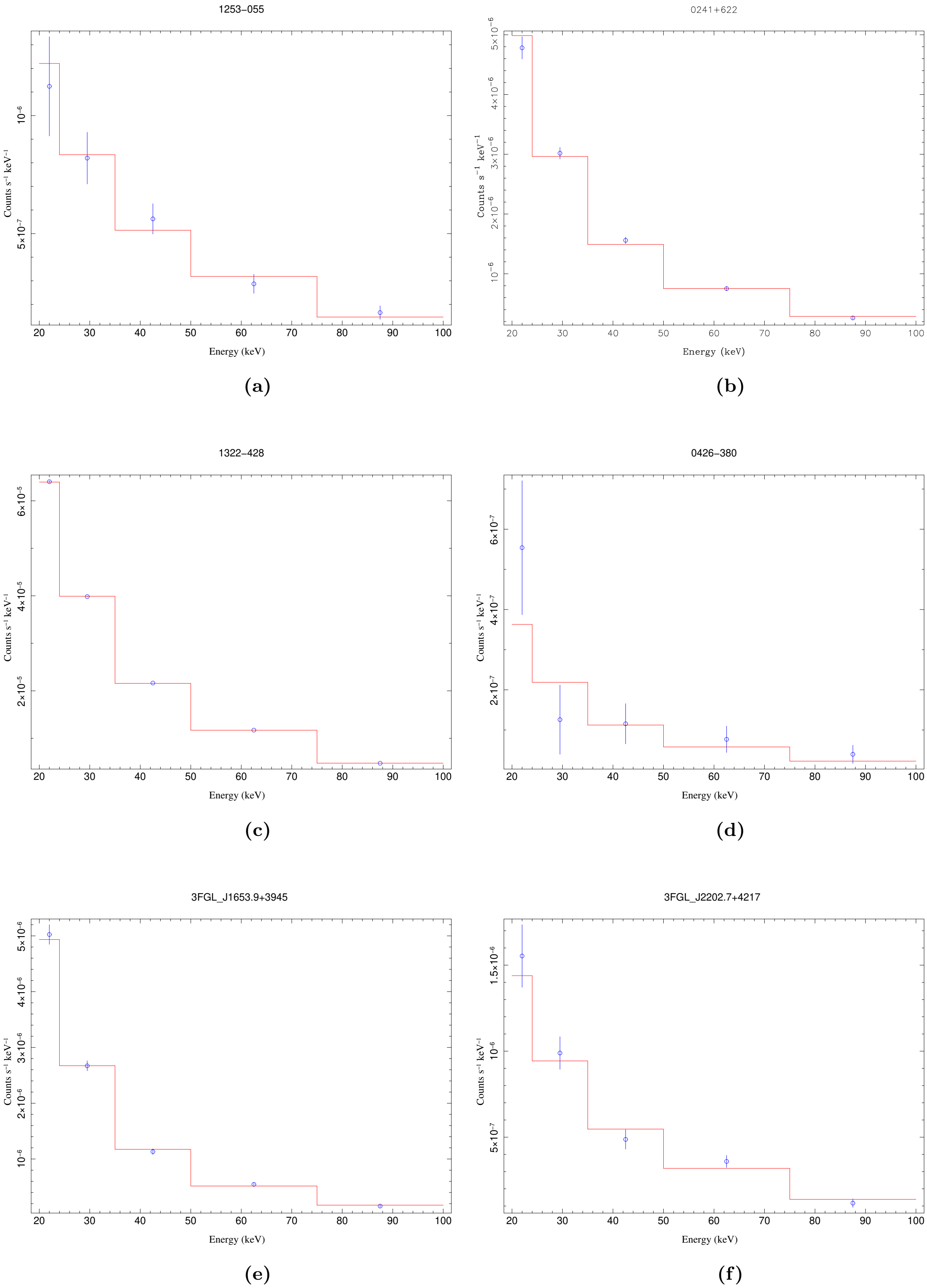

(a) (b) (c) (d) (e) (f)

Figure B.0.1.: *Swift*/BAT 5-channel spectra of the analyzed source samples in this work. (a) and (b): MOJAVE and MOJAVE-1.5 sources, (c) and (d): TANAMI sources, and (e) and (f): 4LAC sources. The red line indicates the fitted power law.

C. Supplementary studies

This section presents analyses in scientific studies led by other scientists that I have contributed to during the course of my doctoral study. My contributions to these works comprise the extraction and analysis of BAT spectra from the 105-month survey maps or the earlier 70-month maps for individual sources or smaller samples. The steps were performed analogously to the analysis chain outlined in the previous chapters. Additionally, I re-processed and illustrated light curve data from the BAT transient monitor for a small set of sources.

C.1 Light curve analysis of BAT transient sources

From 2019 I was involved in the observation program of our working group of the bright and TeV-detected BL Lacs Mrk 421, Mrk 501, and 1ES 1959+650, which are high-peaked sources that exhibited flaring behavior in the past. The program was initiated in 2012, aiming to gain quasi-simultaneous multiwavelength coverage of the pre-, during, and post-flare states, using the Effelsberg 100 m radio telescope, *XMM-Newton*, *Swift*, and *INTEGRAL*/IBIS for the observation of the synchrotron component of the SEDs, and *Fermi*/LAT as well as FACT for the HE and VHE components, respectively. The analysis of the multiwavelength data of Mrk 421, for example, has been reported in Kreikenbohm (2019) and Gokus et al. (2022). See these studies for a list of the contributing authors in this program. The multiwavelength observations are scheduled to provide good temporal coverage by multiple instruments. The X-ray range is supported by weekly observations by *XMM-Newton* and *Swift*, while FACT provides nightly measurements in the TeV band. In the hard X-rays, the continuous light curve data from the *Swift*/BAT transient monitor (15 keV – 50 keV) delivers daily and orbital-binned (90 min) data, which are accessible on-line. For this project I regularly monitored the BAT light curves in order to alert the working group if the count rate of any of the three sources should increase in a matter of one to a few days. In case a source exhibits a flaring state, additional observations by *INTEGRAL*, *Swift*, and *XMM-Newton* are triggered. Similarly, an outburst of a source can be determined by the quick-look analysis that is provided by FACT. In the post-flare phase, short daily observations by *Swift*/XRT are planned for a time of 25 days.

A recent flare of the source Mrk 421 on June 9 2019 was first observed by FACT, and prompted dedicated observations by the X-ray instruments, which also recorded a significant increase in brightness over the following few days. Figure C.1.1 shows the most recent state of the BAT light curve of Mrk 421 and a zoomed-in version around the time of the flare. The highest S/N value in the light curve around the flare has been measured as $(8.11/1.36) \cdot 10^{-3}\,\mathrm{ph\,s^{-1}\,cm^{-2}} = 5.96\,\sigma$ on MJD 58645, one day after the FACT trigger. Data obtained from *XMM-Newton* revealed unprecedentedly high count rates of the source and intra-day variability.

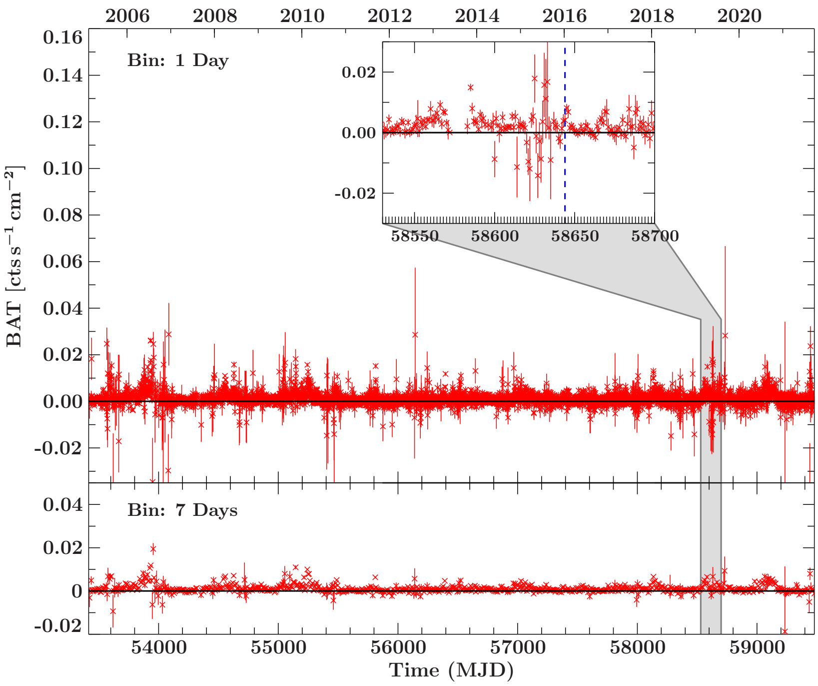

Figure C.1.1.: Light curve data from the BL Lac Mrk 421 as recorded from the *Swift*/BAT transient monitor in the band of 15 keV to 50 keV. The top and bottom panels show daily and weekly binning of the light curve, respectively. The inlay presents a zoomed-in version around the flare (FACT) on June 9, 2019, indicated by the blue dashed line.

C.2 Water-Maser Galaxies

I performed the extraction of BAT spectra from the 105-month survey and the processing of weaker spectra using template spectral shapes (see Sect. 3.2.4) for two specific studies that include the hard X-ray characteristics of maser-emitting AGN.

The Ph.D. project of Eugenia Fink involves a sample of 133 maser sources which are compiled as part of the megamaser cosmology project, that aims to derive the Hubble constant to a high precision using extragalactic masers. Also, a control group of 98 non-maser active galaxies is implemented. With the aim to describe the physical processes in water maser galaxies and their broadband properties, a data set of the hard X-ray characteristics is prepared, a waveband that is little affected by intrinsic absorption, contrary to the soft X-rays. I determined the flux and corresponding upper limits where applicable, photon indices, and luminosity values of the sample sources in the 20 keV – 100 keV band, as well as the Crab-weighted S/N values from the 14 keV – 150 keV range. Furthermore, I performed the subtraction of the S/N distribution of the random background component from the sample S/N distribution to obtain the fraction of each sample that is not compatible with the random background noise. In addition to the hard X-ray characteristics of both samples, a correlation analysis of the X-ray luminosity and the emission from the radio continuum at 20 cm and the water maser line emission was conducted.

In her Ph.D. project, Katharina Leiter defines sub-sets of 53 maser and 54 non-maser sources, which have all been observed by *XMM-Newton*, based on the above source samples. The characterization of these controlled and uniform samples in the X-rays will help to refine the selection criteria for more efficient maser surveys in the future. The study includes detailed analyses of the spectra obtained by *XMM-Newton* and the calculation of correlation measures between quantities like X-ray flux, maser flux, N_H, line equivalent width, and luminosities in the soft and hard bands, with the latter given by the BAT data. For this part, I derived the Kendall's τ correlations coefficients for the censored and uncensored data sets, as well as for partial correlation for the case of luminosity versus luminosity. Furthermore, I used Monte Carlo methods to estimate the validity of the results of the correlations that are derived from data with substantial uncertainties.

C.3 AGN studies - multiwavelength data

For a number of studies of individual AGN and small samples I also extracted and analyzed the BAT data from the survey maps. In most cases, I computed a single data point or upper-limit value for the SED of a source, whose flux was too faint for the survey threshold in the BAT catalogs (Baumgartner et al., 2013; Oh et al., 2018) and / or participated in scientific discussions. In the following, I list all works to which I contributed. The usual energy range of 20 keV to 100 keV for the extracted and fitted BAT spectra is named “BAT band” hereafter.

In Krauß et al. (2014), we compiled a study of the multiwavelength data of the six radio-loudest TANAMI sources that are coincidental with the position of the two IceCube PeV neutrino events 20 and 14 (named “Ernie” and “Bert”). Under the assumption that the neutrino production is facilitated by the photo-production of pions that stem from accelerated protons, the estimated flux of the neutrino emission of all sources is compatible with the observed events. Therein, the value of the neutrino flux is derived from the flux of the gamma-ray band, approximated by the integrated emission of the fitted SEDs in the range of 1 keV to 5 GeV. For the multiwavelength data set I computed the upper-limit flux values for five TANAMI sources in the complete 14 keV – 195 keV band using the 70-month BAT survey maps. Figure C.3.1 shows the SED of the source 1714–336 including the log-parabola fits of the data. In ANTARES Collaboration et al. (2015), we put constraints on the blazar origin of said neutrino events. The analysis showed that the TANAMI sources 1653–329 and 1714-336 were the most likely points of origin of the neutrino signals. Following these studies, in (Kadler et al., 2016) we then reported on the high-confidence association of the IceCube 2 PeV neutrino event 35, dubbed “Big Bird”, with the blazar 1424–418, a gamma-ray-bright TANAMI source. The blazar exhibited an outburst in the 100 GeV to 300 GeV band for several months before and after the neutrino event. Furthermore, we compiled fitted broadband SEDs for the time of the 2LAC integration period, as well as for the main outburst phase of Jul 2012 to Apr 2013, which featured an increased fluence and consequently a high probability of the neutrino originating from 1424–418 instead of other gamma-ray sources in the field. Quasi-simultaneous data from the radio up to the GeV domain was included for the SED. Since the source was not listed in the at that point most recent BAT 70-month catalog, I derived the flux in the BAT band from the 105-month survey maps, which happened to fit well with the SED for the 2LAC data, whose observation times overlap (2008 – 2010 for *Fermi*/LAT, 2004 – 2013 for *Swift*/BAT). The corresponding plot is shown in Fig. C.3.1.

Using multi-epoch, quasi-simultaneous SED data, in Krauß et al. (2016) we studied the spectral evolution of a sample of 22 radio-loud AGN from the TANAMI program between quiescent and flaring states. In total, 81 SEDs were fitted with log-parabolas, including the *Swift*/BAT data points that I extracted and derived from the 105-month survey in the BAT band for each source. Low and intermediate states of source activity have shown to exhibit SEDs that generally follow the behavior described by the blazar sequence, indicated by the correlation of the gamma-ray photon index and the synchrotron peak frequency. High

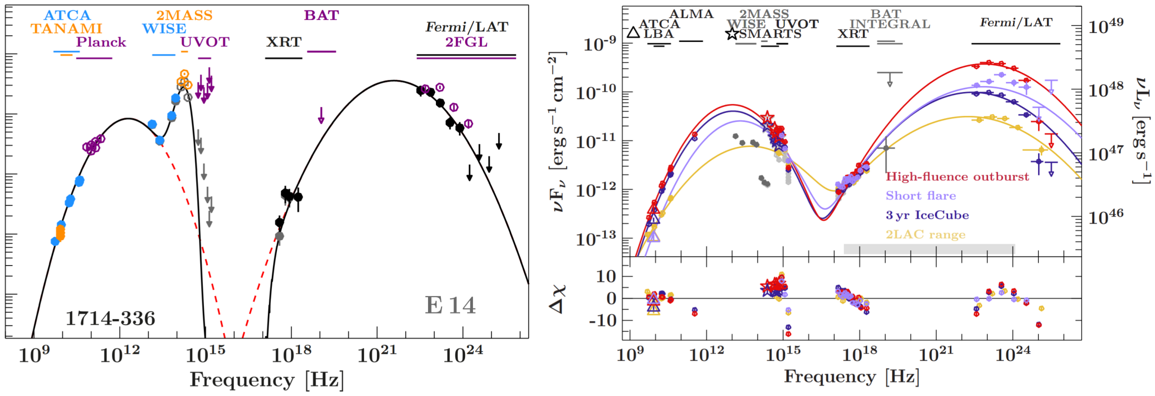

Figure C.3.1.: Left: broadband SED of the source 1714–336, with fitted log-parabolas. The filled symbols indicate data taken in the IceCube observation period of May 2010 to May 2012, while the open symbols show data from outside this time, image credit: Krauß et al. (2014). Right: multi-epoch SEDs of 1424–418, with log-parabola fits. The gray area indicates the energy range for the calculation of the neutrino fluence, image credit: Kadler et al. (2016)

states on the other hand do not follow this trend. The same observation has been made for the harder-when-brighter trend in the X-ray band, that is also expected from the blazar sequence.

In the first multiwavelength study of the gamma-ray-bright and TeV-detected AGN IC310 (Ahnen et al., 2017), I also contributed a spectral data point in the BAT band from the 105-month survey maps and derived the S/N value for the source. The observation campaign was conducted from Nov 2012 to Jan 2013 using VLBI arrays, measurements by *Swift* and *INTEGRAL*, and also *Fermi* and MAGIC. The final SED of IC310 was fitted using a single-zone SSC model with parameters that are found for the model of mis-aligned blazars. Here, the extracted BAT data point is in good agreement with the SED. Both the X-ray and VHE emission showed the harder-when-brighter trend that is typical for the assumed SSC model.

The Ph.D. thesis of Kreikenbohm (2019) includes the study of the peculiar active galaxy PKS 2004–447, that has been classified as a gamma-ray emitting narrow-line Seyfert 1 galaxy. As the source is part of the TANAMI sample I contributed the already extracted and processed spectral data point in the BAT band for the SEDs of the source which have been compiled for different flux states. However, because of the low count rate in the integrated BAT maps, only an upper-limit value could be used, which on the other hand is compatible with all fitted SED profiles. The X-ray spectroscopy below 10 keV showed a non-thermal hard spectrum with a medium amount of variability in terms of flux and spectral shape. Time-resolvd broudband data revealed that the radio jet can be associated with the high-energy emission, while the jet's low-energy / synchrotron emission can explain the observed optical part of the spectrum.

Furthermore, I participated in scientific discussions of other papers, that is, Beuchert et al. (2018) and Krauß et al. (2018a). In the former, we presented a detailed study of the extended X-ray emission of PKS 1718–649, a young AGN in an optical host galaxy. The latter study presents the high-energy SEDs of about 200 *Fermi*/LAT counterpart sources of 100 TeV – 1 PeV IceCube neutrino events.

List of Figures

List of Tables

Acronyms

2LAC	Second LAT AGN Catalog
3FGL	Third *Fermi* Large Area Telescope source catalog
3LAC	Third LAT AGN Catalog
4FGL	Fourth *Fermi* Large Area Telescope source catalog
4LAC	Fourth LAT AGN Catalog
ACZ	Acceleration and Collimation Zone
ADU	Analog-to-Digital Unit
AGN	Active Galactic Nucleus / Nuclei
ALMA	Atacama Large Millimeter/Submillimeter Array
ARF	Ancillary Response File
BAT	Burst Alert Telescope
BCU	Blazar Candidate of Unknown Type
BL Lac	BL Lacertae Object
BLRG	Broad-Line Radio Galaxy
CCD	Charge-Coupled Device
CD	Compton Dominance
CMB	Cosmic Microwave Background
CSS	Compact Steep Spectrum radio source
CXB	Cosmic X-ray Background
CZT	Cadmium-Zinc-Teluride
EBL	Extragalactic Background Light
EC	External-Compton
FR	Fanaroff-Riley (classification)
FOV	Field Of View
FSRQ	Flat Spectrum Radio Quasar
FWHM	Full Width Half Maximum
GRB	Gamma-ray Burst
GBM	Gamma-ray Burst Monitor
GSFC	Goddard Space Flight Center
HE	High-Energy
HPD	Half-Power Diameter
HRC	High-Resolution Camera
HSP	High-Synchrotron-Peaked (source)
IACT	Imaging Atmospheric Cherenkov Telescope
ICM	Intracluster Medium
IGM	Intergalactic Medium
IR	Infrared
ISM	Interstellar Medium
ISP	Intermediate-Synchrotron-Peaked (source)

LAT	Large Area Telescope
LBA	Long Baseline Array
LOFAR	LOw Frequency Array
ISP	Intermediate-Synchrotron-Peaked source
LSP	Low-Synchrotron-Peaked (source)
MOJAVE	Monitoring Of Jets in Active galactic nuclei with VLBA Experiments
NED	NASA Extragalactic Database
NIR	Near Infrared
NLRG	Narrow-Line Radio Galaxy
NLSY1	Narrow-Line Seyfert-1
NRAO	National Radio Astronomy Observatory
PSF	Point Spread function
QE	Quantum Efficiency
QSO	Quasi-Stellar Object
RLF	Radio Luminosity Function
RMF	Redistribution Matrix File
RQQ	Radio-Quiet Quasars
RSP	Response file
S/N	Signal-to-Noise ratio
SED	Spectral Energy Distribution
SFG	Star-Forming Galaxy
SNR	Supernova Remnant
SRG	Spectrum-Roentgen-Gamma
SSC	Synchrotron Self-Compton
SSRQ	Steep Spectrum Radio Quasar
TANAMI	Tracking Active Galactic Nuclei with Austral Milliarcsecond Interferometry
TES	Transition-Edge Sensor
URA	Uniformly Redundant Array
UV	Ultraviolet
VHE	Very High Energy
VLA	Very Large Array
VBLA	Very Long Baseline Array
VLBI	Very Long Baseline Interferometry
X-IFU	X-ray Integral Field Unit
XLF	X-ray Luminosity Function
ZEA	Zenithal Equal Area

Bibliography

Abbott B.P., Abbott R., Abbott T.D., et al., 2016, Phys. Rev. Lett. 116, 061102

Abdo A.A., Ackermann M., Agudo I., et al., 2010a, ApJ 716, 30

Abdo A.A., Ackermann M., Ajello M., et al., 2010b, ApJS 188, 405

Abdo A.A., Ackermann M., Ajello M., et al., 2010c, ApJ 723, 1082

Abdo A.A., Ackermann M., Ajello M., et al., 2010d, ApJ 722, 520

Abdollahi S., Acero F., Ackermann M., et al., 2020, ApJS 247, 33

Abdollahi S., Ackermann M., Ajello M., et al., 2017, ApJ 846, 34

Accadia T., Acernese F., Alshourbagy M., et al., 2012, J. Instrum. 7, 3012

Acero F., Ackermann M., Ajello M., et al., 2015, ApJS 218, 23

Ackermann M., Ajello M., Allafort A., et al., 2011, ApJ 741, 30

Ackermann M., Ajello M., Atwood W.B., et al., 2015, ApJ 810, 14

Adrián-Martínez S., Al Samarai I., Albert A., et al., 2012, Astropart. Phys. 36, 204

Agudo I., Thum C., Gómez J.L., Wiesemeyer H., 2014, A&A 566, A59

Ahnen M.L., Ansoldi S., Antonelli L.A., et al., 2017, A&A 603, A25

Aird J., Coil A.L., Georgakakis A., et al., 2015, MNRAS 451, 1892

Ajello M., Alexander D.M., Greiner J., et al., 2012a, ApJ 749, 21

Ajello M., Angioni R., Axelsson M., et al., 2020, ApJ 892, 105

Ajello M., Atwood W.B., Baldini L., et al., 2017, ApJS 232, 18

Ajello M., Costamante L., Sambruna R.M., et al., 2009, ApJ 699, 603

Ajello M., Greiner J., Sato G., et al., 2008a, ApJ 689, 666

Ajello M., Rau A., Greiner J., et al., 2008b, ApJ 673, 96

Ajello M., Shaw M.S., Romani R.W., et al., 2012b, ApJ 751, 108

Akaike H., 1973, Second International Symposium on Information Theory (Tsahkadsor, 1971) Akadémiai Kiadó, Budapest, 267–281

Akritas M.G., Siebert J., 1996, MNRAS 278, 919

Akylas A., Georgantopoulos I., 2019, A&A 625, A131

Aleksić J., Alvarez E.A., Antonelli L.A., et al., 2012, Astropart. Phys. 35, 435

Allison J.R., Sadler E.M., Meekin A.M., 2014, MNRAS 440, 696

Ananna T.T., Treister E., Urry C.M., et al., 2020, ApJ 889, 17

Angioni R., Ros E., Kadler M., et al., 2019, A&A 627, A148

Angioni R., Ros E., Kadler M., et al., 2020, A&A 641, A152

ANTARES CollaborationAdrián-Martínez S., Albert A., et al., 2015, A&A 576, L8

Antonucci R., 1993, ARA&A 31, 473

Arnaud K.A., Dorman B., Gordon C., 2018, version 12.10.1, HEASARC, NASA/GSFC

Arnaud K.A., Smith R.K., Siemiginoska A., 2011, Handbook of X-ray astronomy (First Edition), Vol. 7, Cambridge Univ. Press, Cambridge

Arshakian T.G., Torrealba J., Chavushyan V.H., et al., 2010, A&A 520, A62

Arsioli B., Fraga B., Giommi P., et al., 2015, A&A 579, A34

Atwood D., Sakdinawat A., 2017, X-Rays and Extreme Ultraviolet Radiation: Principles and Applications (Second Edition), Cambridge Univ. Press, Cambridge

Atwood W., Albert A., Baldini L., et al., 2013, arXiv:1303.3514

Atwood W.B., Abdo A.A., Ackermann M., et al., 2009, ApJ 697, 1071

Barbosa F.K.B., Storchi-Bergmann T., Cid Fernandes R., et al., 2009, MNRAS 396, 2

Barret D., Lam Trong T., den Herder J.W., et al., 2018, In: den Herder J.W.A., Nikzad S., Nakazawa K. (eds.) Space Telescopes and Instrumentation 2018: Ultraviolet to Gamma Ray, Vol. 10699. Society of Photo-Optical Instrumentation Engineers (SPIE) Conference Series, p. 106991G

Barthelmy S.D., Barbier L.M., Cummings J.R., et al., 2005, Space Sci. Rev. 120, 143

Bastia P., 2019, J. Instrum. 14, C10009

Baumgartner W.H., Tueller J., Markwardt C.B., et al., 2013, ApJS 207, 19

Becker R.H., White R.L., Edwards A.L., 1991, ApJS 75, 1

Beckmann V., Jean P., Lubiński P., et al., 2011, A&A 531, A70

Beckmann V., Soldi S., Ricci C., et al., 2009, A&A 505, 417

Beckmann V., Soldi S., Shrader C.R., et al., 2006, ApJ 652, 126

Berriman G., Schmidt G.D., West S.C., Stockman H.S., 1990, ApJS 74, 869

Beuchert T., 2017, Ph.D. Thesis, Multiwavelength observations of Active Galactic Nuclei from the radio to the hard X-rays, Dr. Karl Remeis-Sternwarte Bamberg, ECAP/FAU, Erlangen

Beuchert T., Rodríguez-Ardila A., Moss V.A., et al., 2018, A&A 612, L4

Biland A., Bretz T., Buß J., et al., 2014, J. Instrum. 9, P10012

Bird A.J., Bazzano A., Malizia A., et al., 2016, ApJS 223, 15

Bird A.J., Malizia A., Bazzano A., et al., 2007, ApJS 170, 175

Biteau J., Prandini E., Costamante L., et al., 2020, Nat. Astron. 4, 124

Blandford R., Meier D., Readhead A., 2019, ARA&A 57, 467

Blandford R.D., Königl A., 1979, ApJ 232, 34

Blandford R.D., Levinson A., 1995, ApJ 441, 79

Blandford R.D., Payne D.G., 1982, MNRAS 199, 883

Blandford R.D., Znajek R.L., 1977, MNRAS 179, 433

Błażejowski M., Sikora M., Moderski R., Madejski G.M., 2000, ApJ 545, 107

Blobel V., Lohrmann E., 2012, Statistische und numerische Methoden der Datenanalyse, `http://www-library.desy.de/elbook.html` Accessed: 2019-10-11

Bloom S.D., Marscher A.P., 1996, ApJ 461, 657

Böck M., Kadler M., Müller C., et al., 2016, A&A 590, A40

Böhringer H., Werner N., 2010, A&A Rev. 18, 127

Boller T., Freyberg M.J., Trümper J., et al., 2016, A&A 588, A103

Bosch K., 1998, Statistik-Taschenbuch (Dritte Auflage), Oldenbourg, München

Bottacini E., Ajello M., Greiner J., 2012, ApJS 201, 34

Böttcher M., Dermer C.D., Finke J.D., 2008, ApJ 679, L9

Böttcher M., Reimer A., Sweeney K., Prakash A., 2013, ApJ 768, 54

Boula S., Mastichiadis A., Kazanas D., 2022, In: 37th International Cosmic Ray Conference. 12-23 July 2021. Berlin., p. 678

Bradascio F., 2019, In: 36th International Cosmic Ray Conference (ICRC2019), Vol. 36. International Cosmic Ray Conference, p. 845

Brandt W.N., Alexander D.M., 2015, A&A Rev. 23, 1

Brandt W.N., Hasinger G., 2005, ARA&A 43, 827

Brenneman L.W., Reynolds C.S., 2009, ApJ 702, 1367

Bromberg O., Nakar E., Piran T., Sari R., 2011, ApJ 740, 100

Brown A.M., Adams J., 2012, MNRAS 421, 2303

Browne I.W.A., Savage A., Bolton J.G., 1975, MNRAS 173, 87P

Bruni G., Savolainen T., Lobanov A., et al., 2021, In: 43rd COSPAR Scientific Assembly. Held 28 January - 4 February, Vol. 43., p. 1436

Burbidge G.R., 1956, ApJ 124, 416

Burke B.F., Graham-Smith F., 2010, An Introduction to Radio Astronomy (Third Edition), Cambridge University Press, Cambridge

Burnham K.P., Anderson D.R., 2004, Sociological Methods & Research 33, 261–304

Burrows D.N., Hill J.E., Nousek J.A., et al., 2005, Space Sci. Rev. 120, 165

Caccianiga A., Moretti A., Belladitta S., et al., 2019, MNRAS 484, 204

Cadež A., Calvani M., 2005, MNRAS 363, 177

Calabretta M.R., Greisen E.W., 2002, A&A 395, 1077

Callingham J.R., Ekers R.D., Gaensler B.M., et al., 2017, ApJ 836, 174

Caplar N., Lilly S.J., Trakhtenbrot B., 2015, AJ 811, 148

Cara M., Lister M.L., 2008, ApJ 674, 111

Caroli E., Butler R.C., Di Cocco G., et al., 1984, Nuovo Cimento C Geophysics Space Physics C 7, 786

Caroli E., Stephen J.B., Di Cocco G., et al., 1987, Space Sci. Rev. 45, 349

Carroll B.W., Ostlie D.A., 2007, An Introduction to Modern Astrophysics, Pearson Addison-Wesley, San Francisco, Calif. ; Munich

Casandjian J.M., Grenier I.A., 2008, A&A 489, 849

Cash W., 1979, ApJ 228, 939

Cavaliere A., Lapi A., 2013, Physics Reports 533, 69

Cerruti M., 2020, Galaxies 8, 72
Chang C.S., 2010, Ph.D. Thesis, Active Galactic Nuclei throughout the Spectrum: M 87, PKS 2052-47, and the MOJAVE sample, Universität Köln, Köln
Chang Y.L., Arsioli B., Giommi P., Padovani P., 2017, A&A 598, A17
Chen B., Dai X., Baron E., 2012, ApJ 762, 122
Churazov E., Forman W., Jones C., Böhringer H., 2003, ApJ 590, 225
Cohen A.S., Lane W.M., Cotton W.D., et al., 2007, AJ 134, 1245
Condon J.J., Cotton W.D., Greisen E.W., et al., 1998, AJ 115, 1693
Conselice C.J., Wilkinson A., Duncan K., Mortlock A., 2016, ApJ 830, 83
Corwin, H. G. J., Emerson D., 1982, MNRAS 200, 621
Costamante L., 2020, MNRAS 491, 2771
Costamante L., Ghisellini G., Giommi P., et al., 2001, A&A 371, 512
Craig N., Fruscione A., 1997, AJ 114, 1356
Croton D.J., Springel V., White S.D.M., et al., 2006, MNRAS 365, 11
Cutri R.M., Wright E.L., Conrow T., et al., 2013, Explanatory Supplement to the AllWISE Data Release Products, Explanatory Supplement to the AllWISE Data Release Products
da Costa L.N., Pellegrini P.S., Davis M., et al., 1991, ApJS 75, 935
D'Abrusco R., Massaro F., Paggi A., et al., 2014, ApJS 215, 14
Danziger I.J., Goss W.M., 1979, MNRAS 186, 93
Davis J.E., 2001, ApJ 548, 1010
De Angelis A., Mallamaci M., 2018, EPJ Plus 133, 324
Degenaar N., Wijnands R., Miller J.M., et al., 2015, J. High Energy Astrophys. 7, 137
Dermer C.D., Schlickeiser R., Mastichiadis A., 1992, A&A 256, L27
Dicken D., Tadhunter C., Morganti R., et al., 2008, ApJ 678, 712
Dihingia I.K., Vaidya B., Fendt C., 2021, MNRAS 505, 3596
Donato D., Ghisellini G., Tagliaferri G., Fossati G., 2001, A&A 375, 739
Drinkwater M.J., Webster R.L., Francis P.J., et al., 1997, MNRAS 284, 85
Dutka M.S., Ojha R., Pottschmidt K., et al., 2013, ApJ 779, 174
Ebrero J., Carrera F.J., Page M.J., et al., 2009, A&A 493, 55
Edge D.O., Shakeshaft J.R., McAdam W.B., et al., 1959, MEMRAS 68, 37
Esparza-Arredondo D., Gonzalez-Martín O., Dultzin D., et al., 2021, A&A 651, A91
Event Horizon Telescope CollaborationAkiyama K., Alberdi A., et al., 2019, ApJ 875, L1
Fabian A.C., Iwasawa K., Reynolds C.S., Young A.J., 2000, PASP 112, 1145
Falomo R., Maraschi L., Tanzi E.G., Treves A., 1987, ApJ 318, L39
Falomo R., Pesce J.E., Treves A., 1993, ApJ 411, L63
Fanaroff B.L., Riley J.M., 1974, MNRAS 167, 31P
Feng J., Wu Q., 2017, MNRAS 470, 612
Fenimore E.E., Cannon T.M., 1978, Appl. Opt. 17, 337
Finke J.D., 2016, ApJ 830, 94
Fossati G., Maraschi L., Celotti A., et al., 1998, MNRAS 299, 433
Gaskell C.M., Goosmann R.W., Merkulova N.I., et al., 2012, ApJ 749, 148
Gehrels N., Chincarini G., Giommi P., et al., 2004, ApJ 611, 1005
Ghisellini G., 2015, J. High Energy Astrophys. 7, 163
Ghisellini G., 2016, Galaxies 4, 36
Ghisellini G., Celotti A., Fossati G., et al., 1998, MNRAS 301, 451
Ghisellini G., Righi C., Costamante L., Tavecchio F., 2017, MNRAS 469, 255
Ghisellini G., Tavecchio F., 2008, MNRAS 387, 1669
Giblin J.T., Shertzer J., 2012, ISRN A&A 2012, 848476
Giommi P., Colafrancesco S., Cavazzuti E., et al., 2006, A&A 445, 843
Giommi P., Padovani P., 2015, MNRAS 450, 2404
Giommi P., Polenta G., Lähteenmäki A., et al., 2012, A&A 541, A160
Globus N., Levinson A., 2016, MNRAS 461, 2605
Gokus A., Kreikenbohm A., Leiter K., et al., 2022, In: 37th International Cosmic Ray Conference. 12-23 July 2021. Berlin., p. 869
Gold B., Odegard N., Weiland J.L., et al., 2011, ApJS 192, 15
Graham J.A., 1978, PASP 90, 237
Grimm H.J., Gilfanov M., Sunyaev R., 2002, A&A 391, 923

Gunson J., Polychronopulos B., 1976, MNRAS 177, 485
Hammersley A., Ponman T., Skinner G., 1992, Nucl. Instrum. Methods Phys. Res. A 311, 585
Hanish D.J., Capak P., Teplitz H.I., et al., 2015, ApJS 217, 17
Harrison F.A., Aird J., Civano F., et al., 2016, ApJ 831, 185
Harrison F.A., Craig W.W., Christensen F.E., et al., 2013, ApJ 770, 103
Hartman R.C., Bottcher M., Aldering G., et al., 2001, ApJ 553, 683
Hasinger G., Miyaji T., Schmidt M., 2005, A&A 441, 417
Hawkins M.R.S., 2007, A&A 462, 581
Heald G.H., Pizzo R.F., Orrú E., et al., 2015, A&A 582, A123
Healey S.E., Romani R.W., Cotter G., et al., 2008, ApJS 175, 97
Heidt J., Tröller M., Nilsson K., et al., 2004, A&A 418, 813
Hewitt A., Burbidge G., 1989, ApJS 69, 1
Hickox R.C., Markevitch M., 2006, ApJ 645, 95
Högbom J.A., 1974, A&AS 15, 417
Hogg D.W., 1999, astro–ph/9905116
Holt J., Tadhunter C.N., Morganti R., 2008, MNRAS 387, 639
Homan D.C., Lister M.L., Kovalev Y.Y., et al., 2015, ApJ 798, 134
Hong J., Mori K., Hailey C.J., et al., 2016, ApJ 825, 132
Houck J.C., Denicola L.A., 2000, In: Manset N., Veillet C., Crabtree D. (eds.) Astronomical Data Analysis Software and Systems IX, Vol. 216. Astronomical Society of the Pacific Conference Series, p. 591
Howell S.B., 2006, Handbook of CCD Astronomy (Second Edition), Cambridge University Press, Cambridge
Hunstead R.W., Murdoch H.S., 1980, MNRAS 192, 31
Hunstead R.W., Murdoch H.S., Shobbrook R.R., 1978, MNRAS 185, 149
IceCube Collaboration 2013, Science 342, 1242856
IceCube CollaborationAartsen M.G., Ackermann M., et al., 2018, Science 361, eaat1378
Ighina L., Caccianiga A., Moretti A., et al., 2019, MNRAS 489, 2732
Inskip K.J., Tadhunter C.N., Morganti R., et al., 2010, MNRAS 407, 1739
in't Zand J.J.M., 1992, Ph.D. Thesis, A coded-mask imager as monitor of Galactic X-ray sources, University of Utrecht, Utrecht
in't Zand J.J.M., 1996, Coded aperture camera imaging concept, `https://universe.gsfc.nasa.gov/archive/cai/coded_intr.html#section1` Accessed: 2019-10-29
Intema H.T., Jagannathan P., Mooley K.P., Frail D.A., 2017, A&A 598, A78
Jackson C.A., Wall J.V., Shaver P.A., et al., 2002, VizieR Online Data Catalog J/A+A/386/97
Jackson N., Badole S., Morgan J., et al., 2022, A&AHogg 658, A2
Jacobs D.C., Aguirre J.E., Parsons A.R., et al., 2011, ApJ 734, L34
James F., 1994, CERN Program Library Long Writeup D506 (Geneva: CERN)
Jansen F., Lumb D., Altieri B., et al., 2001, A&A 365, L1
Jauncey D.L., Batty M.J., Gulkis S., Savage A., 1982, AJ 87, 763
Jauncey D.L., Batty M.J., Wright A.E., et al., 1984, ApJ 286, 498
Jauncey D.L., Wright A.E., Peterson B.A., Condon J.J., 1978, ApJ 219, L1
Jenness T., Robson E.I., Stevens J.A., 2010a, MNRAS 401, 1240
Jenness T., Robson E.I., Stevens J.A., 2010b, MNRAS 401, 1240
Jennison R.C., Das Gupta M.K., 1953, Nature 172, 996
Johnston K.J., Fey A.L., Zacharias N., et al., 1995, AJ 110, 880
Jones D.H., Read M.A., Saunders W., et al., 2009, MNRAS 399, 683
Jones D.H., Saunders W., Colless M., et al., 2004, MNRAS 355, 747
Jorstad S., Marscher A., 2016, Galaxies 4, 47
Jorstad S.G., Marscher A.P., Mattox J.R., et al., 2001, ApJS 134, 181
Jorstad S.G., Marscher A.P., Stevens J.A., et al., 2007, AJ 134, 799
Kadler M., Krauß F., Mannheim K., et al., 2016, Nat. Phys. 12, 807
Kadler M., Ojha R., TANAMI Collaboration 2015, Astron. Nachr. 336, 499
Kaiser C.R., Best P.N., 2007, MNRAS 381, 1548
Kamraj N., Harrison F.A., Baloković M., et al., 2018, ApJ 866, 124
Kapanadze B.Z., 2013, AJ 145, 31
Karamanavis V., Fuhrmann L., Krichbaum T.P., et al., 2016, A&A 586, A60
Kataoka J., Reeves J.N., Iwasawa K., et al., 2007, PASJ 59, 279
Katsuta J., Tanaka Y.T., Stawarz Ł., et al., 2013, A&A 550, A66

Keenan M., Meyer E.T., Georganopoulos M., et al., 2021, MNRAS 505, 4726

Kellermann K.I., Lister M.L., Homan D.C., et al., 2004, ApJ 609, 539

Kellermann K.I., Vermeulen R.C., Zensus J.A., Cohen M.H., 1998, AJ 115, 1295

Kendall M.G., 1938, Biometrika 30, 81

Kitayama T., Sasaki S., Suto Y., 1998, Publ. Astron. Soc. Jpn. 50, 1

Kollgaard R.I., Wardle J.F.C., Roberts D.H., 1990, AJ 100, 1057

Kollmeier J., Onken C., Kochanek C., et al., 2008, ApJ 648, 128

Komissarov S.S., Barkov M.V., Vlahakis N., Königl A., 2007, MNRAS 380, 51

Komossa S., Voges W., Xu D., et al., 2006, AJ 132, 531

Koss M., Mushotzky R., Veilleux S., et al., 2011, ApJ 739, 57

Kovalev Y.Y., 2009, ApJ 707, L56

Krauß F., Deoskar K., Baxter C., et al., 2018a, A&A 620, A174

Krauß F., Kadler M., Mannheim K., et al., 2014, A&A 566, L7

Krauß F., Kreter M., Müller C., et al., 2018b, A&A 610, L8

Krauß F., Wilms J., Kadler M., et al., 2016, A&A 591, A130

Kreikenbohm A., 2019, Ph.D. Thesis, Classifying the high-energy sky with spectral and timing methods, Universität Würzburg, Würzburg

Krimm H.A., Holland S.T., Corbet R.H.D., et al., 2013, ApJS 209, 14

Krivonos R., Tsygankov S., Lutovinov A., et al., 2012, A&A 545, A27

Krivonos R., Tsygankov S., Lutovinov A., et al., 2015, MNRAS 448, 3766

Krolik J.H., 1999, Active galactic nuclei: from the central black hole to the galactic environment, Princeton University Press, Princeton

Kuehr H., Witzel A., Pauliny-Toth I.I.K., Nauber U., 1981, A&AS 45, 367

La Franca F., Fiore F., Comastri A., et al., 2005, ApJ 635, 864

Langejahn M., Kadler M., Wilms J., et al., 2020, A&A 637, A55

Lanyi G.E., Boboltz D.A., Charlot P., et al., 2010a, AJ 139, 1695

Lanyi G.E., Boboltz D.A., Charlot P., et al., 2010b, AJ 139, 1695

Larionov V.M., Villata M., Raiteri C.M., 2010, A&A 510, A93

Lauberts A., Valentijn E.A., 1989, The surface photometry catalogue of the ESO-Uppsala galaxies, (Garching: European Southern Observatory)

Lauer T.R., Postman M., Strauss M.A., et al., 2014, ApJ 797, 82

Lea S.M., Silk J., Kellogg E., Murray S., 1973, ApJ 184, L105

Lee J.A., Sohn B.W., Jung T., et al., 2017, ApJS 228, 22

Lewis K.T., Eracleous M., Sambruna R.M., 2003, ApJ 593, 115

Liang E.W., Yi S.X., Zhang J., et al., 2010, ApJ 725, 2209

Lin C., Fan J.H., Xiao H.B., 2017, Res. Astron. Astrophys. 17, 066

Lister M.L., Aller H.D., Aller M.F., et al., 2009a, AJ 137, 3718

Lister M.L., Aller M., Aller H., et al., 2011, ApJ 742, 27

Lister M.L., Aller M.F., Aller H.D., et al., 2018, ApJS 234, 12

Lister M.L., Aller M.F., Aller H.D., et al., 2013, AJ 146, 120

Lister M.L., Aller M.F., Aller H.D., et al., 2016, AJ 152, 12

Lister M.L., Aller M.F., Aller H.D., et al., 2015, ApJ 810, L9

Lister M.L., Cohen M.H., Homan D.C., et al., 2009b, AJ 138, 1874

Lister M.L., Homan D.C., 2005, AJ 130, 1389

Lister M.L., Homan D.C., Hovatta T., et al., 2019, ApJ 874, 43

Liu T., Tozzi P., Tundo E., et al., 2015, ApJS 216, 28

Longair M.S., 2011, High Energy Astrophysics (Third Edition), Cambridge Univ. Press, Cambridge

Lott B., Gasparrini D., Ciprini S., 2020, arXiv:2010.08406

Lucchini M., Markoff S., Crumley P., et al., 2019, MNRAS 482, 4798

Luo B., Brandt W.N., Xue Y.Q., et al., 2017, ApJS 228, 2

Lusso E., Comastri A., Simmons B.D., et al., 2012, MNRAS 425, 623

MacLeod C.L., Ivezić Ž., Sesar B., et al., 2012, ApJ 753, 106

MAGIC CollaborationAcciari V.A., Ansoldi S., et al., 2020, A&A 637, A86

Mahony E.K., Sadler E.M., Croom S.M., et al., 2011, MNRAS 417, 2651

Malizia A., Bassani L., Bazzano A., et al., 2012, MNRAS 426, 1750

Malizia A., Landi R., Molina M., et al., 2016, MNRAS 460, 19

Malkan M.A., Sargent W.L.W., 1982, ApJ 254, 22

Mannheim K., 1993, A&A 269, 67
Mannheim K., 1995, Astropart. Phys. 3, 295
Mao L.S., 2011, New Astron. 16, 503
Maraschi L., Ghisellini G., Celotti A., 1992, ApJ 397, L5
Marcotulli L., Di Mauro M., Ajello M., 2020, ApJ 896, 6
Markowitz A.G., Krumpe M., Nikutta R., 2014, MNRAS 439, 1403
Markwardt C.B., Barthelmy S.D., Cummings J.C., et al., 2007, The SWIFT BAT Software Guide, `https://swift.gsfc.nasa.gov/analysis/bat_swguide_v6_3.pdf` version 6.3, Accessed: 2019-10-17
Maselli A., Cusumano G., Massaro E., et al., 2010a, A&A 520, A47
Maselli A., Cusumano G., Massaro E., et al., 2010b, A&A 520, A47
Masetti N., Mason E., Landi R., et al., 2008, A&A 480, 715
Masini A., Comastri A., Civano F., et al., 2018, ApJ 867, 162
Massaro E., Giommi P., Leto C., et al., 2009, A&A 495, 691
Massaro F., Giroletti M., D'Abrusco R., et al., 2014, Astrophys. J. Suppl. Ser. 213, 3
Massaro F., Thompson D.J., Ferrara E.C., 2015, A&A Rev. 24, 2
Mateos S., Barcons X., Carrera F.J., et al., 2005, A&A 444, 79
Mateos S., Warwick R.S., Carrera F.J., et al., 2008, A&A 492, 51
Maughan B.J., Reiprich T.H., 2019, OJ Ap. 2, 9
McLean I.S., 2008, Electronic Imaging in Astronomy: Detectors and Instrumentation (Second Edition), Springer-Verlag Berlin Heidelberg, Berlin
Meegan C., Lichti G., Bhat P.N., et al., 2009, ApJ 702, 791
Meléndez M., Mushotzky R.F., Shimizu T.T., et al., 2014, ApJ 794, 152
Merloni A., Heinz S., 2013, Evolution of Active Galactic Nuclei, Springer, Dordrecht
Merloni A., Predehl P., Becker W., et al., 2012, arXiv:1209.3114
Meyer E.T., Fossati G., Georganopoulos M., Lister M.L., 2011, ApJ 740, 98
Miller J.S., Goodrich R.W., 1990, ApJ 355, 456
Mink J., 2014, In: Manset N., Forshay P. (eds.) Astronomical Data Analysis Software and Systems XXIII, Vol. 485. Astronomical Society of the Pacific Conference Series, p. 231
Mirabel I.F., Rodríguez L.F., 1999, ARA&A 37, 409
Mitsuda K., Bautz M., Inoue H., et al., 2007, PASJ 59, S1
Miyaji T., Hasinger G., Salvato M., et al., 2015, ApJ 804, 104
Moretti A., Campana S., Lazzati D., Tagliaferri G., 2003, ApJ 588, 696
Morganti R., Holt J., Tadhunter C., et al., 2011a, A&A 535, A97
Morganti R., Holt J., Tadhunter C., et al., 2011b, A&A 535, A97
Mufakharov T., Mingaliev M., Sotnikova Y., et al., 2015, MNRAS 450, 2658
Müller C., Kadler M., Ojha R., et al., 2014, A&A 569, A115
Müller C., Kadler M., Ojha R., et al., 2018, A&A 610, A1
Müller C., Krauß F., Dauser T., et al., 2015, A&A 574, A117
Murphy K., Yaqoob T., 2009, In: Wolk S., Fruscione A., Swartz D. (eds.) Chandra's First Decade of Discovery., p. 166
Murphy T., Sadler E.M., Ekers R.D., et al., 2010, MNRAS 402, 2403
Myers J.D., 2006, Swift's Burst Alert Telescope (BAT), `https://swift.gsfc.nasa.gov/about_swift/bat_desc.html` Accessed: 2019-10-16
Nesci R., Edwards P., Stevens J., et al., 2011a, ATEL 3819, 1
Nesci R., Ojha R., Kadler M., et al., 2011b, ATEL 3660, 1
Netzer H., 2015, ARA&A 53, 365–408
Nolan P.L., Abdo A.A., Ackermann M., et al., 2012, ApJS 199, 31
O'Dea C.P., 1998, PASP 110, 493
Ogle P.M., Davis S.W., Antonucci R.R.J., et al., 2005, ApJ 618, 139
Oh K., Koss M., Markwardt C.B., et al., 2018, ApJS 235, 4
Ojha R., Kadler M., Böck M., et al., 2010, A&A 519, A45
Orienti M., Dallacasa D., Stanghellini C., 2007, A&A 475, 813
Otrupcek R.E., Wright A.E., 1991, Proc. Astron. Soc. Australia 9, 170
Padovani P., 2016, A&A Rev. 24, 13
Padovani P., Alexander D.M., Assef R.J., et al., 2017, A&A Rev. 25, 2
Padovani P., Bonzini M., Miller N., et al., 2014, In: Mickaelian A.M., Sanders D.B. (eds.) Multiwavelength AGN Surveys and Studies, Vol. 304., p.79

Paliya V.S., Koss M., Trakhtenbrot B., et al., 2019, ApJ 881, 154
Paliya V.S., Stalin C.S., 2016, ApJ 820, 52
Pandey A., Gupta A.C., Wiita P.J., 2018, ApJ 859, 49
Panessa F., Tarchi A., Castangia P., et al., 2015, MNRAS 447, 1289
Pavlidou V., Angelakis E., Myserlis I., et al., 2014, MNRAS 442, 1693
Pearson T.J., Unwin S.C., Cohen M.H., et al., 1981, Nature 290, 365
Perley R.A., Chandler C.J., Butler B.J., Wrobel J.M., 2011, ApJ 739, L1
Perlman E.S., Padovani P., Giommi P., et al., 1998, AJ 115, 1253
Perlman E.S., Padovani P., Landt H., et al., 2001, In: Padovani P., Urry C.M. (eds.) Blazar Demographics and Physics, Vol. 227. Astronomical Society of the Pacific Conference Series, p. 200
Perri M., Maselli A., Giommi P., et al., 2007, A&A 462, 889
Peterson B.A., Savage A., Jauncey D.L., Wright A.E., 1982, ApJ 260, L27
Peterson B.A., Wright A.E., Jauncey D.L., Condon J.J., 1979, ApJ 232, 400
Petrov L., Natusch T., Weston S., et al., 2015, PASP 127, 516
Phillips M.M., 1979, ApJ 227, L121
Pian E., Foschini L., Beckmann V., et al., 2005, A&A 429, 427
Piran T., 2005, Rev. Mod. Phys. 76, 1143
Ponti G., Cappi M., Dadina M., Malaguti G., 2004, A&A 417, 451
Prantzos N., Boehm C., Bykov A.M., et al., 2011, Rev. Mod. Phys. 83, 1001
Predehl P., Andritschke R., Arefiev V., et al., 2021, A&A 647, A1
Predehl P., Andritschke R., Böhringer H., et al., 2010, In: Arnaud M., Murray S.S., Takahashi T. (eds.) Space Telescopes and Instrumentation 2010: Ultraviolet to Gamma Ray, Vol. 7732. Society of Photo-Optical Instrumentation Engineers (SPIE) Conference Series, p. 77320U
Pushkarev A.B., Butuzova M.S., Kovalev Y.Y., Hovatta T., 2019, MNRAS 482, 2336
Raiteri C.M., Villata M., Capetti A., et al., 2009, A&A 507, 769
Rajput B., Stalin C.S., Rakshit S., 2020, A&A 634, A80
Ramos Almeida C., Levenson N.A., Rodríguez Espinosa J.M., et al., 2009, ApJ 702, 1127
Ramos Almeida C., Tadhunter C.N., Inskip K.J., et al., 2011, MNRAS 410, 1550
Ranalli P., Koulouridis E., Georgantopoulos I., et al., 2016, A&A 590, A80
Rau A., Schady P., Greiner J., et al., 2012, A&A 538, A26
Reynolds C.S., Fabian A.C., 2008, ApJ 675, 1048
Ricci C., Trakhtenbrot B., Koss M.J., et al., 2017, ApJS 233, 17
Roming P.W.A., Kennedy T.E., Mason K.O., et al., 2005, Space Sci. Rev. 120, 95
Ross N.P., McGreer I.D., White M., et al., 2013, ApJ 773, 14
Ruschel-Dutra D., Storchi-Bergmann T., Schnorr-Müller A., et al., 2021, MNRAS 507, 74
Sadler E.M., Ekers R.D., Mahony E.K., et al., 2014, MNRAS 438, 796
Sahakyan N., Baghmanyan V., Zargaryan D., 2018, A&A 614, A6
Saikia P., Körding E., Falcke H., 2016, MNRAS 461, 297
Sandage A., 1965, ApJ 141, 1560
Sandrinelli A., Covino S., Treves A., 2014, A&A 562, A79
Sargsyan L., Weedman D., Lebouteiller V., et al., 2011, ApJ 730, 19
Sartori L.F., Trakhtenbrot B., Schawinski K., et al., 2019, ApJ 883, 139
Sazonov S., Revnivtsev M., Krivonos R., et al., 2007, A&A 462, 57
Sbarufatti B., Ciprini S., Kotilainen J., et al., 2009, AJ 137, 337
Schmidt M., 1963, Nature 197, 1040
Schmidt M., 1968, ApJ 151, 393
Schwarz G., 1978, Ann. Statist. 6, 461–464
Seibert M., Wyder T., Neill J., et al., 2012, In: American Astronomical Society Meeting Abstracts #219, Vol. 219. American Astronomical Society Meeting Abstracts, p. 340.01
Seward F.S., Charles P.A., 2010, Exploring the X-ray Universe (Second Edition), Cambridge Univ. Press, Cambridge
Shaver P.A., Wall J.V., Kellermann K.I., 1996, MNRAS 278, L11
Shaw M.S., Romani R.W., Cotter G., et al., 2012, ApJ 748, 49
Shaw M.S., Romani R.W., Cotter G., et al., 2013, ApJ 764, 135
Shklovsky I.S., 1953, DAN SSSR 90, 983
Sikora M., Begelman M.C., Rees M.J., 1994, ApJ 421, 153
Sikora M., Moderski R., Madejski G.M., 2008, ApJ 675, 71

Skrutskie M.F., Cutri R.M., Stiening R., et al., 2006a, AJ 131, 1163

Skrutskie M.F., Cutri R.M., Stiening R., et al., 2006b, AJ 131, 1163

Smith J.E., Young S., Robinson A., et al., 2002, MNRAS 335, 773

Smith R.J., Lucey J.R., Hudson M.J., et al., 2000, MNRAS 313, 469

Snyder J.P.P., 1993, Flattening the Earth: Two Thousand Years of Map Projections, Univ. of Chicago Press, Chicago

Soldi S., Beckmann V., Baumgartner W.H., et al., 2014, A&A 563, A57

Spruit H.C., Foglizzo T., Stehle R., 1997, MNRAS 288, 333

Starling R.L.C., Page M.J., Branduardi-Raymont G., et al., 2005, Ap&SS 300, 81

Steinle H., 2006, ChJ Astron. Astrophys. Suppl. 6, 106

Stickel M., Fried J.W., Kuehr H., 1989, A&AS 80, 103

Stickel M., Meisenheimer K., Kuehr H., 1994, A&AS 105, 211

Suh H., Hasinger G., Steinhardt C., et al., 2015, ApJ 815, 129

Sulentic J.W., Stirpe G.M., Marziani P., et al., 2004, A&A 423, 121

Tadhunter C.N., Morganti R., di Serego Alighieri S., et al., 1993, MNRAS 263, 999

Tavecchio F., Ghisellini G., 2015, MNRAS 451, 1502

Tavecchio F., Ghisellini G., Bonnoli G., Foschini L., 2011, MNRAS 414, 3566

Tempel E., Kipper R., Tamm A., et al., 2016, A&A 588, A14

Thompson D.J., Djorgovski S., de Carvalho R., 1990, PASP 102, 1235

Titov O., Pursimo T., Johnston H.M., et al., 2017, AJ 153, 157

Truebenbach A.E., Darling J., 2017, ApJS 233, 3

Tsunemi H., Hiraga J., Yoshita K., Hayashida K., 1999, Nucl. Instrum. Methods Phys. Res. A 421, 90

Tueller J., Mushotzky R.F., Barthelmy S., et al., 2008, ApJ 681, 113

Ueda Y., Akiyama M., Ohta K., Miyaji T., 2003, ApJ 598, 886

Ulrich M.H., Boksenberg A., Bromage G.E., et al., 1984, MNRAS 206, 221

Urry C.M., Padovani P., 1995, PASP 107, 803

van Haarlem M.P., Wise M.W., Gunst A.W., et al., 2013, A&A 556, A2

Vaughan S., Fabian A.C., 2004, MNRAS 348, 1415

Véron-Cetty M.P., Véron P., 2003, A&A 412, 399

Véron-Cetty M.P., Véron P., 2006, A&A 455, 773

Véron-Cetty M.P., Véron P., 2010, A&A 518, A10

Villata M., Raiteri C.M., Larionov V.M., et al., 2008, A&A 481, L79

Voges W., Aschenbach B., Boller T., et al., 1999, A&A 349, 389

Voges W., Aschenbach B., Boller T., et al., 2000, IAU Circ. 7432, 3

von Kienlin A., Meegan C.A., Paciesas W.S., et al., 2020, ApJ 893, 46

Vrieze S.I., 2012, Psychol. Methods 17, 228–243

Wagner S.J., Witzel A., Heidt J., et al., 1996, AJ 111, 2187

Wakely S.P., Horan D., 2008, In: International Cosmic Ray Conference, Vol. 3., p.1341

Wang S., Liu J., Qiu Y., et al., 2016, ApJS 224, 40

Warwick R.S., Saxton R.D., Read A.M., 2012, A&A 548, A99

Weisskopf M.C., Brinkman B., Canizares C., et al., 2002, PASP 114, 1

West R.M., Tarenghi M., 1989, A&A 223, 61

White G.L., Jauncey D.L., Savage A., et al., 1988, ApJ 327, 561

Wierzcholska A., Siejkowski H., 2016, MNRAS 458, 2350

Williams R.E., Blacker B., Dickinson M., et al., 1996, AJ 112, 1335

Willingale R., 1979, Ph.D. Thesis, Analysis of x-ray images and spectra, University of Leicester, Leicester

Wilms J., Allen A., McCray R., 2000, ApJ 542, 914

Wilson A., Tsvetanov Z., 1994, AJ 107

Winkler C., Courvoisier T.J.L., Di Cocco G., et al., 2003, A&A 411, L1

Winter L.M., Mushotzky R.F., Reynolds C.S., Tueller J., 2009, ApJ 690, 1322

Winter L.M., Veilleux S., McKernan B., Kallman T.R., 2012, ApJ 745, 107

Wisotzki L., Christlieb N., Bade N., et al., 2000, A&A 358, 77

Wootten A., Thompson A.R., 2009, IEEE Proceedings 97, 1463

Wright A., Otrupcek R., 1990, PKS Catalog (1990) 0

Wright E.L., Chen X., Odegard N., et al., 2009, ApJS 180, 283

Wu X.B., Hao G., Jia Z., et al., 2012, AJ 144, 49

Xie W., Lei W.H., Zou Y.C., et al., 2012, Res. Astron. Astrophys. 12, 817

Yao S., Yuan W., Zhou H., et al., 2015, MNRAS 454, L16
Yoo S., An H., 2020, ApJ 902, 2
York D.G., Adelman J., Anderson, John E. J., et al., 2000, AJ 120, 1579
Zacharias M., Wagner S.J., 2016, A&A 588, A110
Zakamska N.L., Schmidt G.D., Smith P.S., et al., 2005, AJ 129, 1212
Zaw I., Rosenthal M.J., Katkov I.Y., et al., 2020, ApJ 897, 111

Acknowledgments

I want to thank my doctoral supervisors Prof. Dr. Matthias Kadler and Prof. Dr. Jörn Wilms for their continuous and patient support during my thesis, both scientific and in terms of navigating the academic landscape as well as for letting me participate in a number of tasks as a tutor and in different outreach projects. I think, we made a good team. Furthermore, I want to thank Prof. Dr. Karl Mannheim for the opportunity to work for the past couple of years and to produce my doctoral thesis at the Lehrstuhl für Astronomie at the Julius-Maximilians-Universität in Würzburg.

During this time I was also given the opportunity and financial support to visit several national and international conferences, which were valuable and interesting experiences, and for which I am grateful. On two separate occasions I was given the chance to visit at the NASA Goddard Space Flight Center in Greenbelt, Maryland for collaboration work, an experience that I also greatly appreciate. In this context I want to thank Dr. Neil Gehrels, Dr. Wayne Baumgartner, Dr. Craig Markwardt, and Dr. Jeremy Perkins for their time and the fruitful discussions. Also great thanks go to Dr. Roopesh Ojha for his help in organizing my stay and of course Dr. Katja Pottschmidt for her help and letting me stay at her place while at the GSFC.

In the last couple of years the Lehrstuhl für Astronomy and the Dr. Karl Remeis Observatory in Bamberg grew together more and more. I am proud to have gained a lot of friends and good colleagues at both institutes. For the many scientific discussions, less scientific conversations, and the proof-reading of my thesis I want to thank Paul R. Burd, Andrea Gokus, Eugenia Fink, Florian Rösch, Dr. Tobias Beuchert, Dr. Matthias Bissinger, Dr. Felicia Krauss, Dr. Thomas Dauser, and Dr. Michael Kreter.

The greatest thank you for your close support during our work, our astronomy-related side projects, and way, way beyond goes to Katha Leiter and Dr. Annika Kreikenbohm. My time in our office and after that would not have been the same without you both.

Finally, I want to express my gratitude to my family and all my other friends for their long-lasting support, their endorsements, and help in more than one way. I doubt that I could have done it without you.

This work was partially funded by the DFG-Graduiertenkolleg 1147/1, and by the Bundesministerium für Wirtschaft und Technologie under Deutsches Zentrum für Luft- und Raumfahrt (DLR grant numbers 50OR1607 and 50OR1709).

This research has made use of data from the MOJAVE database that is maintained by the MOJAVE team (Lister et al., 2009a). The Very Long Baseline Array (VLBA) is an instrument of the National Radio Astronomy Observatory (NRAO). NRAO is a facility of the National Science Foundation, operated by Associated Universities Inc. This work has made use of data provided by the multiwavelength monitoring program TANAMI and its participating facilities. The Australian Long Baseline Array and the Australia Telescope Compact Array are part of the Australia Telescope National Facility which is funded by the Commonwealth of Australia for operation as a National Facility managed by CSIRO.

This research has made use of a collection of ISIS scripts provided by the Dr. Karl Remeis Observatory, Bamberg, Germany at http://www.sternwarte.uni-erlangen.de/isis/. This research has made use of the Interactive Spectral Interpretation System (ISIS, Houck & Denicola, 2000). Figures are rendered using the slxfig interface of S-Lang, developed by J. E. Davis.

This work has made use of the data obtained by *Swift*, a NASA mission with international participation. This research has made use of the NASA/IPAC Extragalactic Database (NED) which is operated by the Jet Propulsion Laboratory, California Institute of Technology, under contract with the National Aeronautics and Space Administration. This research has made use of the VizieR catalogue access tool and the SIMBAD database, CDS, Strasbourg, France. Part of this work is based on archival data, software or online services provided by the Space Science Data Center - ASI.